Investigation of polymer systems with mechano- and photoresponsive fluorophore systems

Von der Fakultät für Mathematik und Naturwissenschaften der RWTH Aachen University zur Erlangung des akademischen Grades eines Doktors der Naturwissenschaften genehmigte Dissertation

vorgelegt von

Damian Schöngen, M.Sc.

aus

Heinsberg, Germany

Berichter: Universitätsprofessor Dr. rer. nat. Dominik Wöll

Universitätsprofessor Dr. rer. nat. Walter Richtering

Tag der mündlichen Prüfung: 09.10.2026

Diese Dissertation ist auf den Internetseiten der Universitätsbibliothek verfügbar.

Eidestattliche Erklärung

Damian Schöngen erkärt hiermit, dass diese Dissertation und die darin dargelegten Inhalte die eigenen sind und selbstständig, als Ergebnis der eigenen originären Forschung, generiert wurden.
Hiermit erkläre ich an Eides statt

1. Diese Arbeit wurde vollständig oder größtenteils in der Phase als Promovierender dieser Fakultät und Universität angefertigt;
2. Sofern irgendein Bestandteil dieser Dissertation zuvor für einen akademischen Abschluss oder eine andere Qualifikation an dieser oder einer anderen Institution verwendet wurde, wurde dies klar angezeigt;
3. Wenn immer andere eigene- oder Veröffentlichungen Dritter herangezogen wurden, wurden diese klar benannt;
4. Wenn aus anderen eigenen- oder Veröffentlichungen Dritter zitiert wurde, wurde stets die Quelle hierfür angegeben. Diese Dissertation ist vollständig meine eigene Arbeit, mit der Ausnahme solcher Zitate;
5. Alle wesentlichen Quellen von Unterstützung wurden benannt;
6. Wenn immer ein Teil dieser Dissertation auf der Zusammenarbeit mit anderen basiert, wurde von mir klar gekennzeichnet, was von anderen und was von mir selbst erarbeitet wurde;
7. Ein Teil dieser Arbeit wurden zuvor veröffentlicht und zwar in:
    - D. Schöngen, D. Wöll, “Synthesis and Characterization of a Novel Photocleavable Fluorescent Dye Dyad for Diffusion Imaging”, *Chemical & Biomedical Imaging* **2025**, *3*,199–207, DOI 10.1021/cbmi.4c00084

Aachen,

_____

Damian Schöngen

Die vorliegende Arbeit wurde im Zeitraum November 2021 bis April 2026 am Institut für Physikalische Chemie der Rheinisch-Westfälischen Technischen Hochschule Aachen (RWTH Aachen University) angefertigt.

Parts of this thesis were published previously or presented at conferences:

Publications

- D. Schöngen, D. Wöll, "Synthesis and Characterization of a Novel Photocleavable Fluorescent Dye Dyad for Diffusion Imaging", *Chemical & Biomedical Imaging* **2025**, *3*,199–207, DOI 10.1021/cbmi.4c00084

Conferences

- D. Schöngen, D. Wöll, oral presentation at the CECP24 in Bad Hofgastein, Austria, February 2024: *Synthesis, characterisation and application of a novel efficient photocleavable fluorescent dye dyad*
- D. Schöngen, D. Wöll, oral presentation at the PhotoIUPAC24 in Valencia, Spain, July 2024: *High accuracy diffusion measurements with a novel photocleavable fluorescent dye dyad*
- D. Schöngen, D. Wöll, poster presentation at the ICP25 in Aachen, Germany, July 2025: *FEDUP: extending the range of feasible diffusion imaging*

Danksagung

Hiermit möchte ich mich bei allen bedanken, die mich während meiner Promotion unterstützt haben.
Besonderer Dank gilt Prof. Dominik Wöll. Er gab mir die Möglichkeit, nach meiner Masterarbeit meine wissenschaftliche Karriere in Form einer Promotion in seinem Arbeitskreis fortzusetzen, die nun in dieser Doktorarbeit mündet. Ohne seine ständige Beratung und Unterstützung wäre diese anspruchsvolle Arbeit schlichtweg unmöglich gewesen. Selbst wenn die Ergebnisse mal wieder nicht ganz meinen eigenen Erwartungen entsprachen, hat er mich immer wieder ganz natürlich dazu motiviert, nicht aufzugeben. Gleichzeitig gewährte er mir den benötigten Freiraum, um frei zu forschen. Die Jahre meiner Arbeit in seiner Forschungsgruppe werden sich mit Sicherheit als einige der prägendsten Jahre meiner fachlichen und persönlichen Entwicklung erweisen.
Weiterhin danke ich Prof. Walter Richtering dafür, dass er die Rolle des Zweitgutachters übernommen hat. Er und sein gesamter Arbeitskreis waren stets in jeglicher Hinsicht hilfsbereit, ein Angebot, das ich viel zu selten wahrgenommen habe.
Auch Prof. Robert Göstl und seiner Arbeitsgruppe danke ich für die angenehme Kooperation. Nur weil ich an seiner innovativen Forschung teilhaben durfte, konnte ich Einblicke in gänzlich neue Forschungsgebiete gewinnen. In diesem Zusammenhang gilt mein besonderer Dank Siyang He, mit dem ich mich jederzeit intensiv über unsere kooperative Arbeit austauschen konnte und der mir bereitwillig unzählige Proben zur Verfügung gestellt oder sogar extra angefertigt hat.
Ebenso möchte ich mich ganz herzlich bei allen aktuellen und ehemaligen Mitgliedern des Arbeitskreises Wöll bedanken, die mich während meiner Promotion begleitet haben. Ich habe mich zu jeder Zeit als Teil eines eingeschworenen Teams empfunden. Wissenschaftliche Diskussionen waren stets zielführend, und bisher konnte noch praktisch jedes fachliche Problem gemeinsam gelöst werden. Niemand hat mir mehr verdeutlicht, wie wichtig der lebhafte Austausch in der Wissenschaft ist, und so manche “meiner” Erkenntnisse, auch in dieser Arbeit, können letztendlich auf den Input von einem von euch zurückgeführt werden. Ohne die Hilfe gleich mehrerer technischer Angestellter wäre ich vermutlich auch niemals mit meiner Synthese fertig geworden. Insbesondere möchte ich denjenigen unter euch danken, die sich die Mühe gemacht haben, diese nicht ganz kurze Arbeit (teilweise) gegenzulesen. Ihr wart wirklich eine große Hilfe. Ich danke auch allen Student:innen, die mich mit ihrer Arbeit unterstützt haben. Es war mir eine Ehre, euch anzuleiten, und eine es war eine besondere Freude, einige von euch in der Welt der Wissenschaft aufsteigen zu sehen, manche sogar zu engen Mitarbeitern.
Zu guter Letzt möchte ich meiner Familie und meinen Freunden danken. Ohne ihre beständige Unterstützung wäre ich niemals so weit gekommen.

It is very easy to answer many of these fundamental biological questions; you just look at the thing!

- Richard Feynman

Abstract

Fluorescence microscopy is a highly versatile tool for the investigation of structural properties of polymer systems. Its primary strength lies in the ability to selectively visualize specific nanoscopic structural aspects whose observation is otherwise difficult. Visualization, however, requires the right method paired with a suitable fluorophore system. In this context, this work focuses on the improvement of two different newly established fluorescence microscopy methods and corresponding fluorophore systems.

The first part is dedicated to the visualization of bond scission with mechanoresponsive fluorophores (mechanofluorophores). A recently developed mechanofluorophore system is incorporated into different polymer systems as crosslinker. Mechanical activation is either achieved *ex-situ*, e.g., via ultrasonication of polymer solutions, or attempted *in-situ* via atomic force microscopy (AFM). The mechano-optical response is imaged with fluorescence lifetime imaging (FLIM). Combined FLIM and AFM measurements are not yet well established in literature for the investigation of polymer systems labeled with mechanofluorophores. The results indicate a general insufficiency of the mechanofluorophore system, in particular low photostability, unspecific activation and low contrast between the unactivated and the activated form. Overall, little improvements are achieved in respect to the resolution and information content available to fluorescence microscopy. The diverse problems and approaches to solve them are identified. Moreover, an as of yet unrecognized correlation is revealed between topological changes of mechanoresponsive polymer films and the apparent optical response of the here employed mechanofluorophores.

The second part is dedicated to the visualization of diffusion on a sub-pixel level with the recently established FRET efficiency diffusion measurement upon photocleavage (FEDUP) method. To this purpose, a photocleavable energy transfer dyad is synthesized, characterized and finally employed for diffusion measurements in a variety of polymer films. Measurements at elevated temperatures allow the investigation of the glass transition in selected examples. Both the dyad itself and the novel measurement approach represent improvements to the FEDUP method in specific aspects. Diffusion coefficients between $D \approx 10^{-22} - 10^{-19}$ $\mathrm{m^2\,s^{-1}}$ are measured with reasonable accuracy. The suitability of the fluorophore system for the investigation of the glass transition of specific polymer systems is discussed in detail.

This work extends the toolbox of fluorescence microscopy, while highlighting potential pitfalls of specific methods and the importance of suitable complementary techniques.

Zusammenfassung

Fluoreszenzmikroskopie ist eine der vielfältigsten Methoden, die für die Untersuchung von strukturellen Eigenschaften von Polymersystemen zur Verfügung steht. Die Hauptstärke liegt in ihrer Fähigkeit, spezifische nanoskopische strukturelle Aspekte selektiv zu visualisieren, deren Beobachtung sich ansonsten schwierig gestaltet. Allerdings erfordert Visualisierung sowohl die richtige Methode, als auch ein geeignetes Fluorphorsystem. In diesem Zusammenhang konzentriert sich diese Arbeit auf die Verbesserung von zwei neu etablierten Fluoreszenzmikroskopiemethoden und zugehörigen Fluorophorsystemen.

Der erste Teil ist der Visualisierung von Bindungsbrüchen mit mechanoresponsiven Fluorophoren (Mechanofluorophore) gewidmet. Ein kürzlich entwickeltes Mechanofluorophorsystem ist in verschiedene Polymersysteme als Vernetzer eingebaut. Mechanische Aktivierung wird entweder *ex-situ* erreicht, z.B. mit Ultraschallbestrahlung von Polymerlösungen, oder *in-situ* mit Rasterkraftmikroskopie (AFM). Die mechano-optische Reaktion wird mit Fluoreszenzlebensdauer-Mikroskopie (FLIM) abgebildet. Kombinierte FLIM und AFM Messungen sind in der Literatur noch nicht weitläufig etabliert für die Untersuchung von Polymersystemen, die mit Mechanofluorophoren markiert sind. Die Ergebnisse deuten auf allgemeine Mängel des Mechanofluorophorsystems hin, insbesondere auf geringe Photostabilität, unspezifische Aktivierung und geringen Kontrast zwischen der unaktivierten und der aktivierten Form. Insgesamt werden nur geringe Verbesserungen erreicht hinsichtlich der Auflösung und des Informationsgehaltes, die mit Fluoreszenzmikroskopie erreicht werden können. Die diversen Probleme und zugehörigen Lösungsansätze werden identifiziert. Zudem wird eine noch unerkannte Korrelation zwischen den topologischen Veränderungen des mechanoresponsiven Polymerfilms und der anscheinenden optischen Reaktion des hier verwendeten Mechanofluorophors offenbart.

Der zweite Teil ist der Visualisierung von Diffusion auf einem Subpixel-Niveau mit der kürzlich etablierten FRET-Effizienz-Diffusionsmessung-nach-Photospaltung (FEDUP) Methode gewidmet. Zu diesem Zweck wird eine photospaltbare Energietransfer Dyade synthetisiert, charakterisiert und letztendlich für Diffusionsmessungen in einer Vielzahl von Polymerfilmen verwendet. Messungen bei erhöhten Temperaturen erlauben die Untersuchung des Glasübergangs in ausgewählten Beispielen. Sowohl die Dyade selbst, als auch die neue Messstrategie repräsentieren Verbesserungen der FEDUP Methode in spezifischen Aspekten. Diffusionskoeffizienten zwischen $D \approx 10^{-22} - 10^{-19}$ $\mathrm{m^2\,s^{-1}}$ werden mit hinreichender Genauigkeit gemessen. Die Anwendbarkeit des Fluorophorsystems für die Untersuchung des Glasübergangs von bestimmten Polymersystemen wird eindringlich diskutiert.

Diese Arbeit erweitert die Anwendungsmöglichkeiten der Fluoreszenzmikroskopie, während sie mögliche versteckte Probleme von spezifischen Methoden, sowie die Unerlässlichkeit von geeigneten komplementären Techniken aufzeigt.

Contents

1 Introduction **1**
1.1 Aim of this work . . . 2

2 Scientific background **6**
2.1 Fluorescence . . . 6
2.1.1 Fluorescence and absorption spectroscopy . . . 9
2.1.2 Fluorescence quenching . . . 10
2.2 Förster resonance energy transfer . . . 11
2.3 Fluorescence microscopy . . . 13
2.3.1 Widefield microscopy . . . 16
2.3.2 Total internal reflection fluorescence microscopy . . . 17
2.3.3 Confocal microscopy . . . 18
2.3.4 Fluorescence lifetime imaging . . . 20
2.3.5 Super-resolution fluorescence microscopy . . . 21
2.3.6 Single molecule tracking . . . 25
2.3.7 FRET efficiency diffusion measurements upon photocleavage . . . 27
2.4 Atomic force microscopy . . . 31
2.5 Photolabile protecting groups . . . 33
2.5.1 Photocleavage mechanism . . . 33
2.6 Polymer systems . . . 35
2.6.1 Glass transition . . . 35
2.6.2 Viscosity . . . 36
2.6.3 Thermoresponsive polymers . . . 37
2.6.4 Microgels . . . 37
2.6.5 Mechanophores . . . 38

3 Visualization of bond scission in polymer systems with mechanofluorophores **40**
3.1 Introduction . . . 40
3.2 Characterization of the system . . . 41
3.2.1 Characterization of the mechanofluorophores . . . 42
3.2.2 Characterization of the microgels . . . 49
3.3 (Combined) AFM and FLIM measurements . . . 54
3.3.1 The polymer systems - PVCL, VIM and PHMA . . . 54
3.3.2 FLIM measurements of microgels . . . 55
3.3.3 Combined AFM and FLIM measurements of PHMA networks . . . 58

3.4 Summary and conclusion . . . 65

4 Synthesis, characterization and application of a novel fluorescent dye dyad 68
4.1 Introduction . . . 68
4.2 Synthesis of the dyad . . . 70
4.3 Spectroscopic characterization of the dyad . . . 74
4.3.1 Dyad in methanol . . . 74
4.3.2 Dyad in water . . . 79
4.4 Irradiation experiments . . . 84
4.4.1 UV irradiation in bulk . . . 85
4.4.2 Visible light irradiation in bulk . . . 96
4.4.3 Performance on the single molecule level . . . 102
4.5 Summary and conclusion (Part 1) . . . 118
4.6 Diffusion measurements in various (polymer) systems . . . 120
4.6.1 Example measurement and analysis . . . 121
4.6.2 Poly(vinyl acetate) . . . 141
4.6.3 Poly(butyl methacrylate) . . . 149
4.6.4 Polyethylene glycol . . . 153
4.6.5 Diffusion measurements in further (polymer) systems . . . 157
4.7 Summary and conclusion (Part 2) . . . 166

5 Summary and outlook 169

6 Methods and materials 173
6.1 Additional scientific background . . . 173
6.1.1 Dynamic light scattering . . . 173
6.1.2 Nuclear magnetic resonance . . . 174
6.1.3 Mass spectrometry . . . 175
6.1.4 High perfomance liquid chromatography . . . 176
6.1.5 Differential scanning calorimetry . . . 176
6.1.6 Defocused microscopy . . . 177
6.2 Syntheses . . . 177
6.2.1 Synthesis of methyl(2-nitrophenyl)acetate (**1**) . . . 178
6.2.2 Synthesis of methyl 2-(2-nitrophenyl)pent-4-ynoate (**2**) . . . 178
6.2.3 Synthesis of 2-(2-nitrophenyl)pent-4-yn-1-ol (**3**) . . . 179
6.2.4 Synthesis of tert-butyl (2-(2-nitrophenyl)pent-4-yn-1-yl) ethane-1,2-diyldicarbamate (**4**, protected photocleavable linker) . . . 179
6.2.5 Synthesis of the photocleavable linker 2-(2-nitrophenyl)pent-4-yn-1-yl (2-aminoethyl)carbamate (**5**) . . . 180
6.2.6 Synthesis of the reference donor (**6**) . . . 181
6.2.7 Synthesis of the reference acceptor (**7**) . . . 181
6.2.8 Synthesis of the dyad (**8**) . . . 182

6.3 Spectroscopy . . . 182
6.3.1 UV-Vis Spectroscopy . . . 182
6.3.2 Fluorescence Spectroscopy . . . 182
6.3.3 Quantum Yields . . . 183
6.4 Sample preparation . . . 183
6.4.1 Cleaning of glass substrates . . . 183
6.4.2 TCSPC . . . 184
6.4.3 PAINT . . . 184
6.4.4 FLIM . . . 184
6.4.5 FEDUP . . . 184
6.5 Confocal microscopy . . . 185
6.5.1 Lifetime measurements and FCS . . . 185
6.5.2 FLIM . . . 185
6.6 Irradiation experiments . . . 185
6.7 Widefield microscopy . . . 186
6.7.1 PAINT measurements . . . 186
6.7.2 FEDUP measurements . . . 186
6.7.3 Defocused microscopy . . . 187
6.8 AFM . . . 188
6.9 DLS . . . 188
6.10 NMR . . . 188
6.11 MS . . . 189
6.12 HPLC . . . 189
6.13 DSC . . . 189

7 Supplementary information 190
7.1 Spectra . . . 190
7.1.1 Absorption coefficients of BTD reference compounds . . . 190
7.1.2 Irradiation experiments . . . 191
7.1.3 Emission map of ATTO647N . . . 193
7.1.4 Comparison of dyad **8** in water and methanol . . . 194
7.1.5 Stern-Volmer Analysis . . . 195
7.2 TCSPC curves . . . 199
7.2.1 Lifetimes of the mechanofluorophore reference compounds . . . 199
7.2.2 Lifetimes of the FLIM images . . . 201
7.2.3 Lifetimes of the FEDUP system before and after UV irradiation . . . 203
7.2.4 Lifetimes of the FEDUP system after irradiation with red light . . . 213
7.3 FCS curves . . . 216
7.4 Microscopy measurements . . . 217
7.4.1 Defocused images . . . 217
7.4.2 FEDUP images . . . 218
7.4.3 FEDUP data . . . 219

7.5 AFM images of thin polymer films . . . 229
7.6 DSC curves . . . 232
7.7 NMR spectra . . . 235
7.7.1 2-Nitrosotoluene . . . 235
7.7.2 Synthesis . . . 238
7.8 ESI-MS spectra . . . 241
7.9 HPLC . . . 244
7.10 ATTO-TEC product information . . . 246

8 Lists **250**
8.1 List of Tables . . . 250
8.2 List of Figures . . . 253
8.3 List of Abbreviations . . . 281
8.4 List of Symbols . . . 284
8.5 Glossary . . . 285
8.5.1 Glossary of Chapter 3 . . . 285
8.5.2 Glossary of Chapter 4 . . . 286

9 Bibliography **289**

1 Introduction

Polymers have long become an integral part of the modern world. From advanced composite materials for large, yet lightweight and robust components in the aerospace, railway and automobile industries,[1,2] to the widespread use of relatively simple plastic packaging materials,[3,4] to biomaterials for implants or medical devices such as pacemakers,[5,6] polymers of all shapes and sizes are used in nearly every aspect of modern life. A world without these specialized materials is frankly no longer imaginable. Hence, it is not surprising that polymers in general are still a hot topic of various ongoing studies. The development of new, cheaper, more sustainable,[7] recyclable[8,9] or more durable[10–12] materials might be the most obvious necessary research. But it is also obligatory to improve our understanding of the properties of these materials. In this context, countless studies investigate bulk properties such as the elasticity,[13–16] durability[17–21] or chemical or thermal degradation.[22–26]

True understanding, however, can arguably only be achieved through detailed investigations of the nanoscopic structure of functional polymeric materials and the interplay between properties and structure. Consequently, accurate visualization of structural features on the molecular level is invaluable. Methods such as scanning electron microscopy (SEM) or transmission electron microscopy (TEM) achieve the required resolution. SEM has been used to visualize and study the self-assembly of supramolecular nanoparticles[27] or the behavior of colloidal polymeric particles at interfaces,[28] whereas TEM has revealed the structure and assembly of block copolymers.[29,30] Despite being powerful techniques, these methods have inherent limitations. The need for an intrinsic contrast often makes their application infeasible.[31] The required high-energy light sources can easily lead to irreversible damage of the samples. Furthermore, sample preparation is generally complicated and time-consuming.[32]

Excellent alternatives for the visualization of nanoscopic structures are fluorescence microscopy (FM) techniques. Advantageously, FM methods are non-invasive, benefit from a good inherent contrast, their sample preparation is well-established and depending on the dyes used they can be applied to nearly all systems, including live cells and various polymer systems. Disadvantageously, classical FM suffers from a severely restricted spatial resolution of hundreds of nanometers.[33] This resolution limit, however, can be surpassed with modern super-resolution techniques. Methods like stimulated emission depletion (STED),[34] photoactivation localization microscopy (PALM),[35,36] (direct) stochastic optical reconstruction microscopy ((d)STORM)[37–39] and point accumulation for imaging in nanoscale topography (PAINT)[40] all achieve a resolution more than an order of magnitude better than conventional microscopy. These methods essentially differ only in the nature of the required fluorescent labels, the methodology for precise localization of the fluorescence signals and the (re)construction of the resulting microscopy image. These subtle differences also allow for the combination of different techniques to access complementary information, sometimes even within a single experiment or measurement.[41–43]

Fundamentally, the investigated problem dictates the suitable FM technique. In this context, new techniques are constantly developed, too. For example, FLIM has long been a common tool for studying

the environment of a system, as fluorescence lifetimes are highly sensitive to different solvents or the rigidity of the surroundings.[44] Achieving super-resolved FLIM with a (d)STORM-like approach then led to the simultaneous visualization of structure and environmental factors.[45,46] Aside from new methods, the development of special dyes can also help to investigate specific problems. For instance, fluorophores with strong solvatochromic properties can be used as polarity sensors based solely on the shift in fluorescence emission.[47] The fluorescence lifetimes of molecular rotors, in contrast, reveal more about the microviscosity of a system.[48] A relatively new type of dyes are mechanofluorophores. These are fluorophores whose fluorescence emission is responsive to mechanical forces. Thus, the resulting fluorescence can be used to sense or even map mechanical stress in polymer systems.[49] Depending on the mechanofluorophore used, this is extended to sensing bond scission, and thereby the study of material failure.[50] Chapter 3 of this work is dedicated to the visualization of bond scission via mechanofluorophores using a not yet established combination of FLIM and AFM.

For other problems, visualization is not a matter of structural resolution, but rather, accessible information. For instance, significant ongoing research is dedicated to the study of diffusion in polymeric materials. From polyelectrolytes as membranes for batteries and fuel cells[51] to the kinetic investigation of radical polymerization,[52] the study of movement within polymer systems is a field in itself with various applications. Here, visualization does not necessarily include imaging of the structure itself, but rather mapping of compartments with varying mobility. Analyzing and visualizing diffusion is overall more suitable for describing the heterogeneity of a polymer film. Again, FM offers the tools to solve this exact problem. In particular, single particle tracking (SPT)[53] and single molecule tracking (SMT)[54] have become methods for the measurement of mobility in polymer systems. Nevertheless, both techniques have a logical lower limit. Their accuracy depends on several factors, including the mechanical stability of the setup,[55] the number of collected photons,[56] signal-to-noise ratio (SNR)[57] and dye orientation.[58] In consequence, diffusion coefficients below $D \approx 10^{-17}$ $\mathrm{m^2\,s^{-1}}$ are unavailable to either SPT or SMT.[59] Unfortunately, certain aspects of polymer dynamics, such as the still not fully understood glass transition, occur on significantly longer time scales. Investigation or even visualization of the dynamic processes during glass transitions of polymers require more sophisticated single molecule approaches, such as minimal fluorescence photon fluxes microscopy (MINFLUX), which can circumvent the accuracy-determined limit of classical tracking methods.[60] In MINFLUX, clever, but costly, instrumentation allows for even more accurate measurements. A more cost-efficient method to surpass the boundaries of SMT is the newly established FEDUP technique, which is based on the distance dependence of the energy transfer between two dyes.[55,59] Chapter 4 of this work is dedicated to the further development of the FEDUP method.

1.1 Aim of this work

This work is divided into two parts. The first part (Chapter 3) builds on the *Göstl group's* existing work on mechanofluorophores.[49,50,61,62] In particular, one of the developed multicolor mechanofluorophores (see Figure 1.1) is investigated in closer detail.[50]

The mechanofluorophore in question consists of two anthracene units bound via triple bonds to a central benzo thiadiazole (BTD) unit. Throughout this work, the entire system will be abbreviated as BTD,

according to the distinguishing central unit. The anthracene units are further modified. The central aromatic ring of the anthracene forms a Diels–Alder adduct with a maleimide moiety. An α-halogenated ester is attached to the nitrogen atom of the maleimide. This qualifies the system for use as an initiator and inhibitor in an atom transfer radical polymerization (ATRP). Since there are two such moieties per mechanofluorophore, the system also acts as crosslinker.

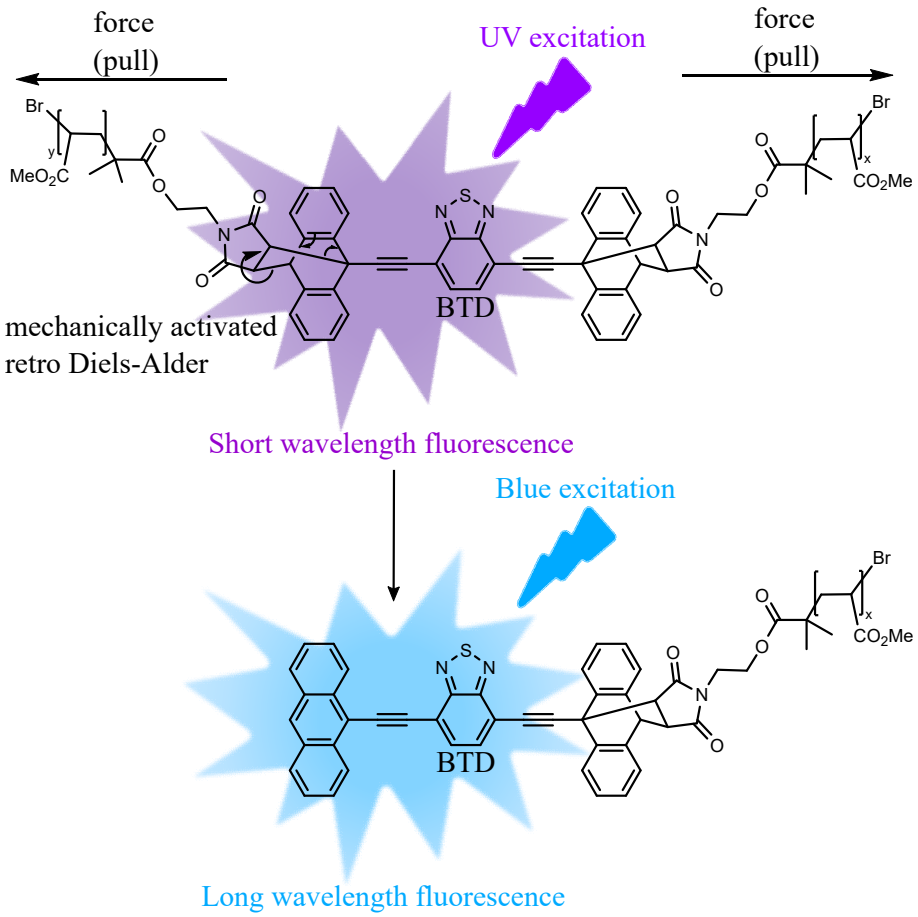

Figure 1.1: Schematic depiction of the activation of the BTD mechanofluorophore investigated in Chapter 3. Before activation, the chromophore can only be excited with ultraviolet (UV) light (violet lightning) and emits fluorescence from roughly 400–600 nm (violet star).[50] It is assumed that when (opposing) pulling forces act upon the linked polymer strands x and y (depicted in the brackets, here polyacrylate), one of the two Diels–Alder anthracene-maleimide adducts undergoes a retro Diels–Alder reaction restoring the aromaticity of the central anthracene moiety (see also Section 2.6.5). This results in a spectral shift, such that excitation with blue light (blue lightning) becomes possible and the fluorescence emission shifts to the range of 450–800 nm (blue star).[50] The color scheme shown here is used consistently throughout this work, i.e., the unactivated mechanofluorophore is coded in violet, whereas the activated mechanofluorophore is coded in blue.

After polymerization, polymer strands are affixed to the ester on either side of the BTD. It is assumed that mechanical forces act on the mechanofluorophore by pulling on both polymer strands through directed or random forces. It is also assumed that the Diels–Alder adducts represent the weakest bonds in the system. If sufficiently strong forces act on the polymer strands and consequently on the Diels–Alder anthracene-maleimide adduct, a retro Diels–Alder reaction is initiated, restoring the aromaticity of the anthracene unit. This is accompanied by a significant shift in the absorption and emission spectra of

the chromophore. It is hypothesized that only one of the two modified anthracene units undergoes the mechanically activated retro Diels–Alder reaction. After bond scission, the BTD is in a mechanically inactive terminal position of the polymer chain. The singly activated BTD can move more freely and can adapt to forces acting on the remaining polymer strand. Thus, no sufficient force can be applied to activate the second anthracene-maleimide Diels–Alder adduct.[50] The described concept, including the shifts in absorption and emission, is shown in Figure 1.1.
A proof of concept has already been published for the shown system.[50] However, only diffraction limited confocal imaging has been achieved so far. In this work, it is striven for an improvement of the imaging resolution and available information content. To this end, the BTD mechanofluorophore is used as crosslinker in polymer films and microgels (see Section 2.6.4 for theory of microgels). Imaging of the activated and, if applicable, unactivated BTD is attempted with FM techniques, such as FLIM (see also Section 2.3.4). Since the established super-resolution methods are likely to be unfeasible (see also Section 2.3.5), a new specialized method is being developed. Essentially, it is reasoned that the BTD can be activated selectively with AFM (see also Section 2.4). This allows for the activation of a sparse subset of fluorophores, which is one fundamental requirement of essentially all super-resolution methods (see Section 2.3.5). Conveniently, the structure is simultaneously imaged with AFM, while bond scission is imaged with FLIM. This way, it is aimed for an improved visualization of material failure.

The second part (Chapter 4) continues the work of the *Wöll group* on accurate diffusion measurements in highly rigid thin polymer films.[55,59] Specifically, the FEDUP method is further developed.
FEDUP measurements require a photocleavable Förster resonance energy transfer (FRET) dyad. The original work presented a dyad based on perylene diimide (PDI) and terrylene diimide (TDI) as chromophores and a methyl phenacyl derivative as photolabile linker.[55] The dyes are extraordinarily photostable and the system delivers excellent results. However, photocleavage requires UV light with a wavelength around 300 nm which is challenging to guide through the same optical elements as the excitation lasers. In consequence, an external light-emitting diode (LED) is used for photocleavage. Furthermore, the dyad is highly apolar, making application in more hydrophilic environments impossible. Recently, a new dyad (see Figure 1.2) addressing both disadvantages was synthesized and characterized.[59] The new dyad, henceforth called dyad **8** or just the dyad (see Section 4.2 for names of all relevant compounds), consists of the two commercially available fluorophores ATTO565 and ATTO647N as FRET-donor and -acceptor, respectively. The chromophores are linked via a modified version of the photolabile protecting group 2-(2-nitrophenyl)propyloxycarbonyl (NPPOC) which is known for its high photocleavage efficiency and regular use in photolithographic oligonucleotide synthesis.[63–65] Since both chromophores are molecular cations (see Section 4.3 for structures), the solubility in polar media is vastly increased compared to the dyad in the original work. The NPPOC-based linker can be efficiently cleaved with wavelengths of up to 400 nm allowing the use of standard UV lasers for photocleavage and the coupling of excitation and photocleavage lasers into a single optical pathway (see Section 2.3.7 for a depiction of the setup).
The FEDUP method is based on the distance dependence of FRET (see Section 2.2). Before photocleavage, the two chromophores are in close proximity to each other. Therefore, energy transfer is highly efficient. After photocleavage, the two chromophores can move independently of each other. Over time, they will statistically move further apart, resulting in a gradual decrease in FRET efficiency. Since

the effective FRET-range is typically in the range of 10 nm, it becomes feasible to measure accurate diffusion at the sub-pixel level based on fluorescence intensities or lifetimes alone. The above described concept of FEDUP is shown schematically in Figure 1.2.

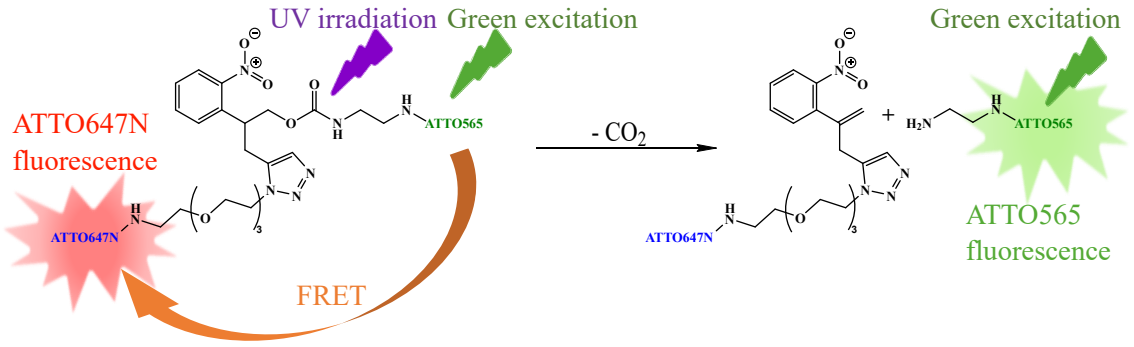

Figure 1.2: Schematic depiction of the photocleavage of the dyad **8** investigated in Chapter 4. Before irradiation with UV light (purple lightning), the dyad exhibits efficient energy transfer from the ATTO565 moiety to the ATTO647N moiety. Upon irradiation with UV light, the central NPPOC moiety undergoes photocleavage (for mechanism, see Section 2.5.1). After photocleavage, the two chromophores can move independently from each other. Thereby, they will statistically move further apart than the distance required for energy transfer (about 10 nm, see Section 2.2). The color scheme shown here is used consistently throughout this work, i.e., donor fluorescence is coded in bright green, acceptor fluorescence in red, FRET in orange and the chromophores ATTO565 and ATTO647N are coded in olive and blue, respectively.

In this work, an extended characterization of the new dyad is presented. Subsequently, dyad **8** is applied in FEDUP measurements of various (hydrophilic) polymer films at different temperatures. Thereby, it is attempted to increase the range of feasible diffusion measurements to lower diffusion coefficients than possible with classical fluorescence microscopy methods, while also increasing the range of materials that can be investigated. Moreover, it is hoped that the glass transition can be studied with unprecedented resolution.

2 Scientific background

All introduced abbreviations, quantity symbols and (novel) technical terms are appropriately defined during their first incidence. A (linked) alphabetical list of abbreviations and symbols, as well as a (chapter-specific) glossary, can be found in Sections 8.3, 8.4 and 8.5, respectively.

2.1 Fluorescence

Spectroscopy is the study of the interaction of matter with electromagnetic radiation. If the energy of an incoming photon matches the energy difference ΔE between two states, and the lower state is occupied, the photon can be absorbed and, as a consequence, the molecule in question is excited to the corresponding higher state, provided that the transition is quantum-mechanically allowed. This is generally formulated in Bohr's frequency condition:

$$\Delta E = h\nu = h\frac{c}{\lambda} \tag{2.1}$$

where ν and λ are the frequency and wavelength of the photon, respectively, and c is the speed of light in vacuum. During the transition, an electron is promoted to an orbital of higher energy without a change of spin, such that its spin remains anti-parallel to that of the electron it was paired with before. The transition to a new orbital, or, expressed differently, to a new volume of probability density, is accompanied by a physical shift of electrons. Hence, although fast, it cannot be instantaneous. Typically, absorption occurs on a timescale of femtoseconds.

Depending on the wavelength of the photon, either rotational, vibrational or electronic states may be excited. Each of these transitions has its own set of selection rules derived from the universal law that the transition dipole moment $\hat{\mu}$ must not be zero. If the wavelength is decreased even further, the molecule or atom will eventually be ionized, as the photon carries enough energy to promote an electron into the continuum, i.e., outside the boundary of the attractive Coulomb interaction between atomic nucleus and electrons. Absorption almost exclusively occurs from the vibrational ground state of the electronic ground state, since no other states are significantly populated at room temperature.

After excitation, different relaxation pathways are possible. Most common is radiationless relaxation via vibrational relaxation (VR) and internal conversion (IC). VR describes the energy dissipation due to collisions with surrounding molecules resulting in a fast relaxation to the vibrational ground state ($v = 0$) of a given electronic state S_N. IC denotes the isoenergetic transition from, typically, the vibrational ground state ($v = 0$) of a given electronic state S_N to an overlapping higher vibrational state ($v > 0$) of the next lowest electronic state S_{N-1} of the same multiplicity. Both processes take place on a timescale of picoseconds. An isoenergetic transition to a state of different multiplicity is also possible, particularly when promoted by heavy atoms. This type of transition is called intersystem crossing (ISC).

Some molecules also have additional radiative relaxation pathways. Radiative relaxation is generally termed luminescence. This is, in turn, differentiated into fluorescence and phosphorescence, depending on whether an allowed transition occurs between two electronic states of the same multiplicity, or if a forbidden transition takes place between two states of different multiplicity. Since phosphorescence is a spin-forbidden transition following ISC, it is several orders of magnitude slower than the other relaxation pathways (taking up to hundreds of seconds to occur).[66] All of these processes are typically summarized in a Jablonski diagram (see Figure 2.1). The following theory will focus particularly on fluorescence.

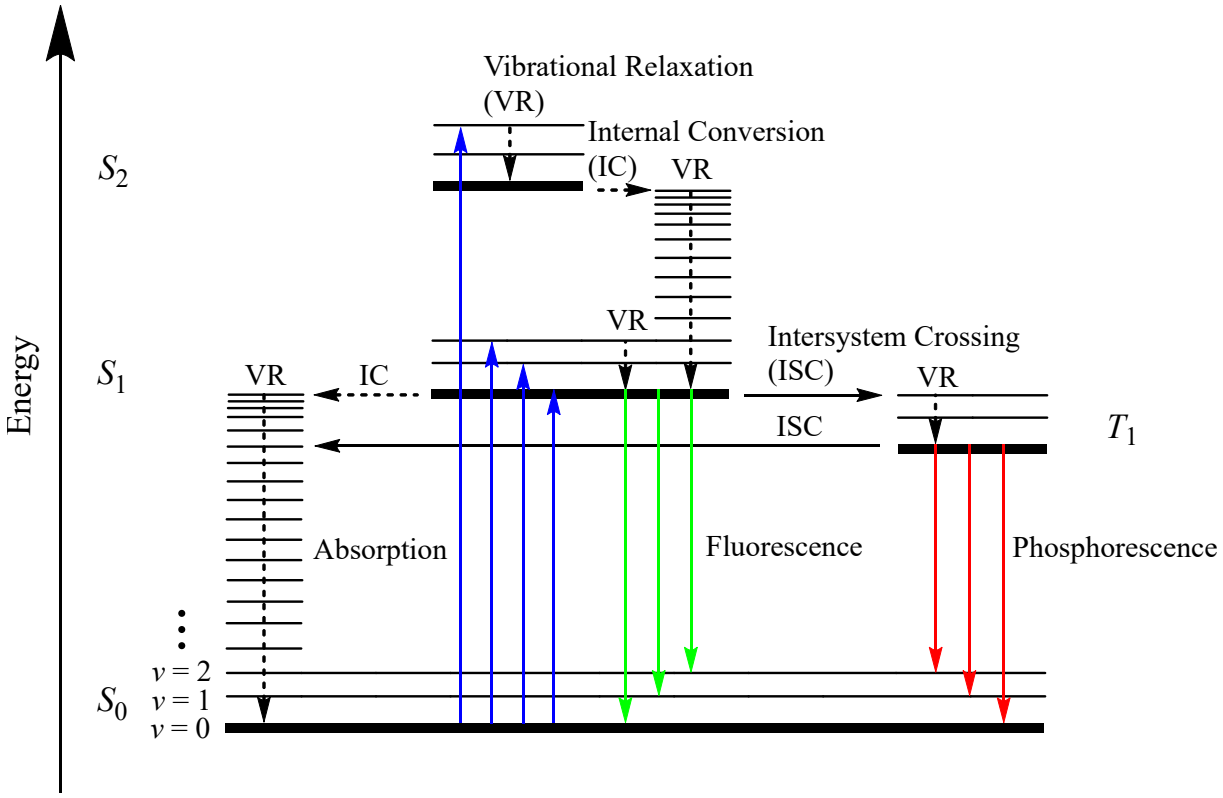

Figure 2.1: Schematic Jablonski diagram depicting excitation and various radiative and non-radiative relaxation pathways of an arbitrary fluorophore. The bold horizontal lines constitute the vibrational ground state of any particular electronic state. The thin horizontal correspond to the various excited vibrational states of any particular electronic state. Vibrational states are also indicated with the vibrational quantum number v. Electronic singlet states are denoted S_N with $N = 0, 1, 2, ...$ for the electronic ground state and higher excited states, respectively. Electronic triplet states are likewise denoted T_N. The vertical blue arrows represent the absorption process resulting in excitation into higher electronic states. The vertical green arrows illustrate fluorescence and the vertical red arrows illustrate phosphorescence, respectively. The dashed vertical black arrows mark VR within any particular electronic state. The dashed horizontal black arrows represent IC from any particular electronic state to another electronic state of the same multiplicity. The solid horizontal black arrows depict ISC from any particular electronic state to another electronic state of different multiplicity.

A molecule that can emit light within the visible spectrum due to a spin-allowed radiative transition is known as a fluorophore. After excitation into an arbitrary electronic state, the molecule returns to the vibrational ground state of the lowest excited singlet state S_1 via rapid radiationless relaxation via VR and IC. Since the energy gap between the electronic ground state S_0 and the first excited state S_1 is significantly larger than the gap between higher excited states, there is less overlap of the energy

hypersurfaces. Consequently, IC becomes considerably less likely and radiative relaxation becomes feasible. Therefore, in most cases, fluorescence occurs from the $S_{1,v=0}$ state, independent of the excitation wavelength. This is called the Kasha rule. The lifetime of the first excited electronic state is typically in the order of nanoseconds.

Due to the radiationless relaxation preceding fluorescence, the emitted light is shifted to longer wavelength compared to the absorbed light. Only the $S_{0,v=0} \leftrightarrow S_{1,v=0}$ transition can theoretically occur at the same wavelength in both directions. However, additional effects can cause further shifts. For example, the solvent shell of a fluorophore often rearranges to stabilize the excited state more effectively. Since the rearrangement can only occur after excitation (or de-excitation), the initial transition requires more energy than the transition from the stabilized state. These effects are collectively termed the Stokes shift.

All electronic transitions, both absorption and emission, are vertical transitions. This means that the involved electron movement is much faster than the atomic rearrangement of the nuclei adapting to the new electron configuration. This is called the Franck–Condon principle. However, the nuclear geometry alters little after electronic excitation and the spacing of the vibrational energy levels of different electronic states is similar.[66] Due to the vertical nature of transitions and the geometric similarity of electronic states, transition probabilities are similar for absorption and emission. In other words, the transitions $S_{0,v=0} \rightarrow S_{1,v=n}$ and $S_{1,v=0} \rightarrow S_{0,v=n}$ are equally likely. In consequence, absorption and emission spectra of a fluorophore are mirror images of each other.

Aside from absorption, emission and excitation spectra (see also Section 2.1.1), fluorescence is often characterized by the fluorescence quantum yield Φ and the fluorescence lifetime τ_{fl}. The former describes the ratio of emitted photons to absorbed photons as shown in equation (2.2):

$$\Phi = \frac{\text{Number of emitted photons}}{\text{Number of absorbed photons}} \tag{2.2}$$

$$= \frac{k_{\mathrm{fl}}}{k_{\mathrm{fl}} + k_{\mathrm{nr}}} = k_{\mathrm{fl}} \tau_{\mathrm{fl}} \tag{2.3}$$

Quantum yields can be determined either relative to a standard or absolutely, using an Ulbricht sphere and equation (2.2). An Ulbricht sphere is a closed chamber with a highly reflective coating, such as barium sulfate. There are only two small openings: one for the excitation light and one for the optical path to the detector. Almost no light is lost within the Ulbricht sphere, hence the detection of photons is quantitative. The number of emitted and absorbed photons can be calculated from the integrated emission spectrum of the sample and the difference of the integrated areas of the excitation signal in the sample and the pure solvent, respectively. When quantum yields are determined relative to a standard, emission and absorption spectra are quantitatively compared. Assuming a constant photon flux, the unknown quantum yield Φ_i of compound i is calculated according to equation (2.4) from the integrated emission spectra F_i and F_s of sample and standard, respectively, the fraction of absorbed light $f_x = 1 - 10^{-A_x}$ (with $x = i, s$), the refractive indices of sample and reference solution n_i and n_s, and the known quantum yield of the standard Φ_s.[67]

$$\Phi_i = \frac{F_i f_s n_i^2}{F_s f_i n_s^2} \Phi_s \tag{2.4}$$

The fluorescence quantum yield can also be expressed according to equation (2.3) as the ratio of the fluorescence rate constant k_{fl} to the sum of the fluorescence rate constant and all non-radiative rate constants k_{nr}, i.e., the rate constants of IC, ISC and any quenching rate constants (see Section 2.1.2). In this context, the fluorescence lifetime is defined as the inverse of all relaxation rate constants. Thus, there is a direct relationship between fluorescence quantum yield and lifetime. In lifetime measurements, the lifetime is calculated from the temporal decay function of the fluorescence[66]:

$$I(t) = \sum_i A_i \exp\left(-\frac{t}{\tau_{\mathrm{fl},i}}\right) \tag{2.5}$$

In the simplest case, this is a mono-exponential decay function, as the decay of the excited state can often be reasonably approximated as a first-order kinetic reaction. However, more complicated decay functions with more than one fluorescence lifetime component are also possible. The relative occurrence of a lifetime component i is calculated from the ratio of all amplitudes A_i. Generally, the fluorescence lifetime is strongly dependent on the environment, e.g., the solvent, and can be used as an environmental sensor. Lifetimes can be determined either with time correlated single photon counting (TCSPC) or the phase modulation method (see also Sections 2.3.3 and 2.3.4).
Throughout this work, most fluorophores are characterized according to their absorption and emission spectra, fluorescence quantum yield and lifetime. The latter two are measured using an Ulbricht sphere and TCSPC, respectively, unless stated otherwise.

2.1.1 Fluorescence and absorption spectroscopy

The above described phenomena of absorption and emission can be recorded as absorption-, emission- and excitation spectra. In absorption spectroscopy, also known as UV-vis spectroscopy, the sample is scanned with light in the ultraviolet (UV) and visible (vis) region. The intensity I of the transmitted light is measured in an 180° arrangement behind the sample holder. The measured values are then compared to the intensity I_0 of the light transmitted by a reference, i.e., a solution containing only solvent but no sample. The intensity I decreases compared to the reference intensity I_0. The exact loss of intensity is dependent on the concentration c_i of the sample i and the path length d the light has to traverse. In non-turbid solutions, the differential decrease of intensity $\mathrm{d}I$ in dependence of the thickness $\mathrm{d}x$ can be described as follows:

$$\mathrm{d}I = -I\sigma(\lambda)N_i\mathrm{d}x \tag{2.6}$$

Here, N_i is the number of light-absorbing molecules i per volume and $\sigma(\lambda)$ is the wavelength-dependent effective cross-section of absorption which is a characteristic quantity for each fluorophore. Solving differential equation (2.6) with the boundary condition $I = I_0$ at $x = 0$ and a sample thickness of d yields the Lambert–Beer law:

$$\ln\frac{I_0}{I} = \sigma(\lambda)N_i d \tag{2.7}$$

Equation (2.7) is usually modified further. The absorption cross-section is replaced by the absorption coefficient $\varepsilon(\lambda)$ which is defined as follows:

$$\varepsilon(\lambda) = \frac{\sigma(\lambda) N_A}{\ln 10} \tag{2.8}$$

where N_A is the Avogadro constant. Concomitantly, the particle density N_i is replaced by the concentration $c_i = N_i \times N_A^{-1}$. Rearrangement then leads to the Lambert–Beer law as it is commonly used:

$$A = \log \frac{I_0}{I} = \varepsilon(\lambda) c_i d \tag{2.9}$$

The logarithmic ratio of intensities A is called absorbance. In typical absorption spectra the absorbance is plotted against the wavelength. Absorption spectra are an essential part of the characterization of all dyes in this work, especially in Chapter 4. In particular, absorption coefficients are used to discuss and compare different fluorophores or to calculate concentrations according to equation (2.9).

Fluorescence spectroscopy differs from UV-vis spectroscopy in the crucial aspect that emission instead of transmission is investigated. To this end, the methods differ most fundamentally in their measurement geometry; in fluorescence spectroscopy the detector is positioned in a 90° angle to the excitation light. Fluorescence tends to be isotropic since molecules in solution can usually move freely and adopt on average all possible conformations in respect to the incident light with equal likelihood. Hence, a 90° angle allows for the measurement of emission while omitting the excitation light. Excitation is achieved with high energy light sources like xenon arc lamps or mercury-vapor lamps. A monochromator narrows the excitation light to a narrow band of excitation wavelengths. The nearly monochrome light beam is channeled through the sample to excite the fluorophores. The generated fluorescence is separated by another monochromator and finally detected on the detector.

Fluorescence spectroscopy is divided into emission and excitation spectroscopy. In emission spectroscopy, the excitation wavelength is selected and the fluorescence emission is scanned to yield an emission spectrum. Consequently, the measured intensity at any wavelength is only dependent on the transition probability of the respective transition. In excitation spectroscopy, a specific emission wavelength is selected while the excitation wavelength is varied. The measured intensity is only dependent on the absorption coefficient at the respective excitation wavelength. Therefore, an excitation spectrum offers basically the same information as an absorption spectrum. In this work, emission spectra are measured for all fluorescent compounds as means of characterization.

2.1.2 Fluorescence quenching

All effects which decrease the intensity of fluorescence are collectively termed quenching. The exact mechanism of quenching can vary. Among others, energy transfer (see also Section 2.2), electron transfer and induced ISC due to the spin-orbit coupling of heavy atoms are common.[66] Usually, a second species aside from the fluorophore is involved in the quenching process, although self-quenching is also possible. The second species is called the quencher.

Quenching can be differentiated into static and dynamic quenching. The former applies when a fluorophore in ground state forms a non-fluorescent complex with the quencher.[66] The latter is based on

collisions of the excited fluorophore with the quencher and is therefore also called collisional quenching. In the following, dynamic quenching is explained in greater detail.
The influence of a collisional quencher can be described most easily by an addition of a new relaxation pathway and therefore a new rate constant to equation (2.3). The rate constant in question is the bimolecular quenching constant k_q which is added together with the quencher concentration c_Q to the denominator:

$$\Phi_{\mathrm{fl,q}} = \frac{k_\mathrm{fl}}{k_\mathrm{fl} + k_\mathrm{nr} + k_\mathrm{q} c_\mathrm{Q}} \tag{2.10}$$

Dividing equation (2.3) by equation (2.10) yields the Stern–Volmer equation (2.11).

$$\frac{F_0}{F} = 1 + K_\mathrm{SV} c_\mathrm{Q} = 1 + k_q \tau_{\mathrm{fl},0} c_\mathrm{Q} \tag{2.11}$$

The Stern–Volmer quenching constant K_SV is an indicator for the sensitivity of the fluorphore to the quencher.[66] As can be seen from equation (2.11), K_SV can be obtained from a linear regression by plotting the ratio of the unquenched fluorescence intensity F_0 to the quenched fluorescence intensity F against the quencher concentration c_Q. If the fluorescence lifetime in absence of a quencher $\tau_{\mathrm{fl},0}$ is known, the bimolecular quenching constant k_q, and thereby the true indicator of the quenching efficiency, becomes accessible, too. It can be shown that in the case of diffusion-controlled quenching the bimolecular quenching constants adopt values around $10^{10}\ \mathrm{L\,mol^{-1}\,s^{-1}}$. Smaller values indicate either steric shielding of the fluorophore or a low quenching efficiency of the quencher. Larger values on the other hand suggest a binding interaction between quencher and fluorophore, thus a deviation from purely collisional quenching.[66]
In this work, a variety of Stern–Volmer experiments are performed. They are essential in the characterization of the dyad, which contains an intramolecular quenching nitrophenyl moiety, all reference compounds and their different photocleavage products (see Section 4.3).

2.2 Förster resonance energy transfer

Two fluorophores whose emission and absorption spectra overlap can undergo Förster resonance energy transfer (FRET) from one dye to the other, provided they are in close proximity to each other. Typical FRET distances are about 10 nm. The energy is transferred radiationless from the excited (FRET-)donor to the (FRET-)acceptor via a dipole–dipole interaction. The donor fluorophore can be thought of as an oscillating dipole which can exchange energy with a nearby acceptor with a similar resonance frequency.[66] Thus, no intermediate photon is produced. It has to be noted that the simple dipole–dipole mechanism is a simplification which is no longer valid for two dyes in very close proximity.[68] However, for most applications, including the ones throughout this work, the Förster theory[69] is a suitable approximation. Since the donor fluorescence is decreased with the energy transfer, FRET can be viewed as a specific form of quenching (see Section 2.1.2). The acceptor does not even necessarily need to be fluorescent itself, although in most applications of FRET it has proven convenient to use FRET-pairs consisting of two dyes. FRET is commonly illustrated with a modified Jablonski diagram, as depicted in Figure 2.1. The donor is excited normally. Instead of the radiative relaxation to the ground state

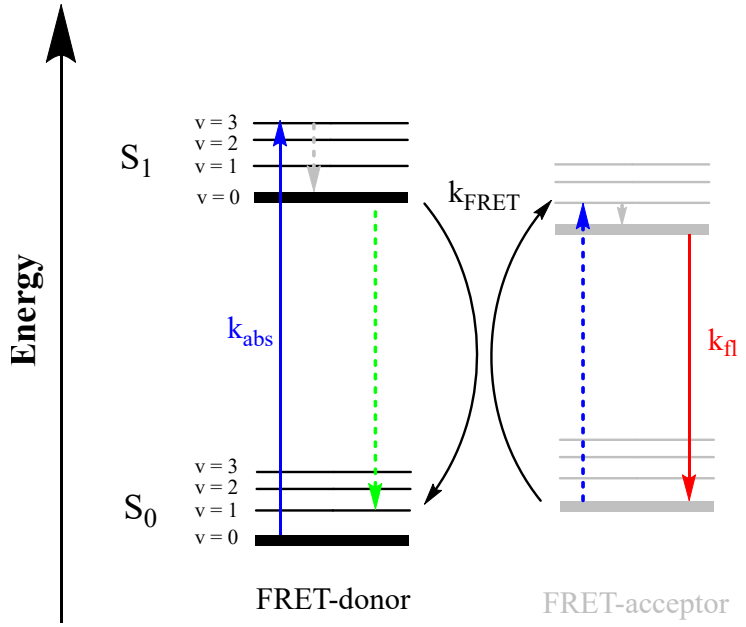

Figure 2.2: Schematic Jablonski diagram depicting the FRET mechanism. The bold horizontal lines constitute the vibrational ground state of any particular electronic state. The thin horizontal lines correspond to the various excited vibrational states of any particular electronic state. Vibrational states are also indicated with the vibrational quantum number v. Electronic singlet states are denoted S_N with $N = 0, 1, 2, ...$ for the electronic ground state and higher excited states, respectively. The solid vertical blue arrow represents the absorption process resulting in excitation into higher electronic states. The dashed vertical green arrow illustrates the non-radiative relaxation of the FRET-donor that replaces relaxation via fluorescence emission. The dashed vertical blue arrow represents the excitation of the FRET-acceptor via energy transfer. The curved black arrows indicate the energy transfer from donor to acceptor. The vertical red arrow marks the fluorescence of the acceptor following the energy transfer. The dashed vertical grey arrows depict VR within any particular electronic state.

via fluorescence, the energy is transferred to the nearby acceptor with the transfer rate k_{FRET}, if the involved states overlap. The acceptor then undergoes regular relaxation, including radiative relaxation via fluorescence. The transfer rate k_{FRET} is calculated according to the following equation:

$$k_{\mathrm{FRET}} = \frac{1}{\tau_D}\left(\frac{R_0}{r}\right)^6 \tag{2.12}$$

where r is the distance between donor and acceptor, R_0 is the Förster distance[69] at which the FRET efficiency is exactly 50% and τ_D is the lifetime of the donor in absence of any energy transfer. In this context, the FRET efficiency η_{FRET} is defined as follows:

$$\eta_{\mathrm{FRET}} = \frac{k_{\mathrm{FRET}}}{\tau_D^{-1} + k_{\mathrm{FRET}}} = \frac{1}{1 + \left(\frac{r}{R_0}\right)^6} \tag{2.13}$$

As shown in equation (2.14), the FRET efficiency can also be defined via the quenching efficiency of the donor fluorescence, i.e., via the decrease of the donor fluorescence in presence of the acceptor, F_{DA}, compared to the donor fluorescence in absence of the acceptor, F_D, if both values are normalized to the concentration of the donor.[70]

$$\eta_{\mathrm{FRET}} = 1 - \frac{F_{DA}}{F_D} = 1 - \frac{\tau_{DA}}{\tau_D} \tag{2.14}$$

Equivalently, the FRET efficiency can be calculated using the average donor decay times, τ_{DA} and τ_D, in presence and absence of the acceptor, respectively, instead of the intensities. However, this necessitates that the donor lifetime is only altered by the energy transfer and not by the potential binding to the acceptor.[66] Due to the dependency on the inverse sixth power of the distance as shown in equation (2.13), FRET is highly sensitive to distance changes, especially around the Förster distance. The Förster distance R_0, in turn, can also be calculated theoretically with equation (2.15).

$$R_0^6 = \frac{9\ln(10)\kappa^2\Phi_D}{128\pi^5 n^4 N_A} \int_0^\infty F_D(\lambda)\varepsilon_A(\lambda)\lambda^4 \mathrm{d}\lambda \tag{2.15}$$

As can be seen from equation (2.15), the Förster distance is dependent on various factors. Most important is the overlap integral of the normalized donor emission spectrum $F_D(\lambda)$ and the absorption coefficient of the acceptor $\varepsilon_A(\lambda)$ over all wavelengths λ. The smaller the spectral overlap, the more the Förster distance approaches a value of zero, i.e., energy transfer becomes less likely or ultimately impossible. Further, the Förster distance is highly dependent on the fluorescence quantum yield of the donor, Φ_D, although the donor does not emit an intermediate photon during the energy transfer process. However, the donor quantum yield indirectly expresses the stability of the excited state. A low quantum yield indicates a high efficiency of IC and thus a short lifetime of the excited state. Consequently, the donor has less time to undergo energy transfer. The Förster distance also changes with the refractive index n of the medium the FRET-pair is dissolved in. Lastly, the parameter κ denotes the orientation factor. The energy transfer can only occur if the transition dipoles of donor and acceptor are not orientated perfectly perpendicular to one another, in which case $\kappa^2 = 0$. There has to be at least some degree of parallelism present. In the case of head-to-tail parallel transition dipoles the orientation factor reaches its maximum value, $\kappa^2 = 4$. For freely rotating molecules, as is usually given in solution, it can be shown that the orientation factor assumes the average value $\kappa^2 = 2/3$.[66]

Since the Förster distance can be calculated from known values and constants, measurements of the donor intensity or lifetime alone reveal accurate distances between donor and acceptor when combining equations (2.13) and (2.14). For this reason, FRET is often called a "spectroscopic ruler".[71] There are numerous examples of research using FRET to study, for example, the folding of proteins[72,73] or the structure of DNA[74] and its interaction with other biomolecules.[75]

In this work, the distance dependence of FRET is utilized to investigate molecular dynamics, in particular the diffusion of single molecules in rigid environments (see Section 2.3.7 for more theory on the method and Chapter 4 for results).

2.3 Fluorescence microscopy

Compared to conventional microscopy, fluorescence microscopy (FM) offers several advantages, namely specificity, selectivity, sensitivity and a natural high contrast.[76] All these factors arise from the need for fluorescent labels. At first glance, the necessity of labeling seems like a major disadvantage, as a

non-trivial chemical reaction and subsequent purification step is introduced in the sample preparation process. However, labeling procedures are optimized, the labeling reaction is usually an easy click-type reaction, and purification can often be achieved reasonably simply by dialysis or centrifugation. The labels do have the potential to alter the chemical nature of the sample, but most times it can be assumed that the, compared to the sample, small amounts of small (organic) molecules do not significantly influence the investigated structures. Thus, the above mentioned advantages of fluorescent labels far outweigh the apparent disadvantages.

Specificity is related to the choice of the labeling sites and corresponding dye; since the investigated structure has to be labeled anyway, it is possible to select dyes which bind to specific sites only. Thereby, it is possible to image only the structure of interest in a possibly larger frame of context. This is especially advantageous in the investigation of biological samples, e.g., live cells, where there are several structures of interest within one microscopic system. If only one part can be labeled with one specific dye, whereas another part is labeled with a different dye, the structures can be differentiated on the basis of the labels already. The advantage of selectivity becomes immediately obvious here, too. Due to the possibility of labeling specific (sub)structures with different dyes, it is also possible to selectively image these specific (sub)structures. Either different monochromatic excitation light sources, i.e., lasers, are utilized to selectively excite a subset of the employed labels, or emission filters are used to observe only the fluorescence of a few selected fluorophores while omitting all unwanted fluorescence. The sensitivity and high contrast are both based on the nature of fluorescence. Due to the Stokes shift, it becomes comparatively simple to spectrally separate excitation and emission light. Contrary to conventional microscopy, the typically monochrome excitation light can be filtered out almost completely. Furthermore, the fluorescent labels are excited selectively, thus only those contribute to the fluorescence emission, that is, the final image. Hence, the background in FM is dark, whereas all signals stemming from the fluorescent labels are bright, resulting in a much better contrast than can be achieved in conventional microscopy. Thanks to the low background and the high detection efficiency of modern cameras, the sensitivity of FM is enhanced, too.

Despite its many inherent advantages, FM is still subject to the classical resolution limit as it was defined by Abbe.[33] The closest distance d that two objects can be resolved individually is dependent on the wavelength of light λ and the numerical aperture (NA) of the objective $\mathrm{NA} = n \sin\theta$ where θ is the aperture angle and n the refractive index of the immersion medium.

$$d = \frac{\lambda}{2\mathrm{NA}} \tag{2.16}$$

For typical microscopes, this results in a resolution limit of about half the wavelength used, thus about 200 – 300 nm. More sophisticated techniques are necessary to circumvent this physical limit (see Section 2.3.5). The resolution limit restricts the imaging of certain features. A notional zero-dimensional point object can only be projected as a broad spot. The point object diffracts the incident light into a spherical wave. Only a part of that spherical wave can traverse the imaging lens, since it has a finite aperture angle. Thereby, the diffraction pattern is modified. The generated parallel wave front in the back focal plane of the lens is fully coherent and imaged into infinity. To project the diffraction pattern, a tube lens is placed behind the objective lens. At the focus in the image plane, constructive interference is achieved. However, in a circular zone around that spot destructive interference occurs which is followed

by another ring of constructive interference, and so on. This interference pattern is called the Airy pattern; the brightest central spot is termed the Airy disk. In consequence, the image of a zero-dimensional point is not a likewise zero-dimensional point but a broad spot with a characteristic intensity profile. This profile is called the point spread function (PSF) of the imaging lens.[76] The resolution limit can also be understood on the basis of the Airy pattern; for two point objects to be resolved individually, the centers of their Airy disks have to be positioned inside the interference minimum of the other object or further apart.

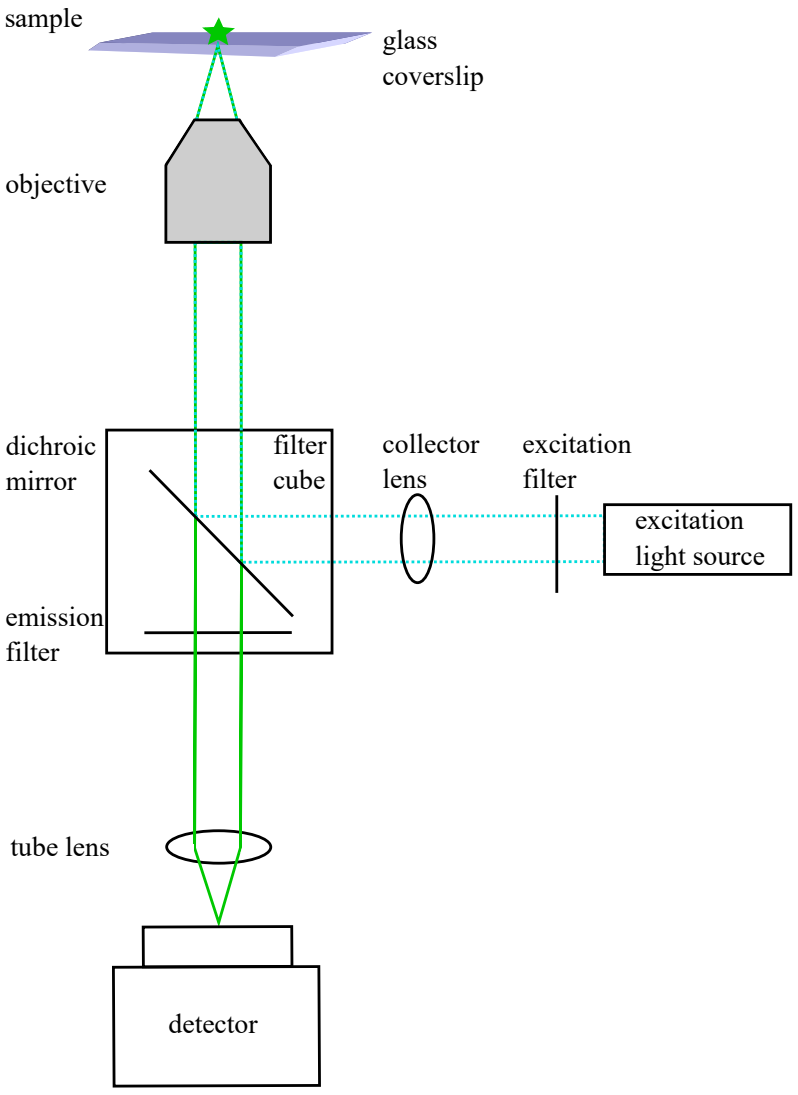

Figure 2.3: Schematic setup of an inverted fluorescence microscope. The excitation beam is colored in light blue, the emission light is colored in green.

Fluorescence microscopes are typically inverted microscopes. A schematic setup of an inverted fluorescence microscope is shown in Figure 2.3. The excitation light, generally a laser, is reflected by a dichroic mirror and guided through the objective to illuminate the sample on top (see Section 2.3.1 and 2.3.2 for a more detailed description of the possible illumination setups). The generated longer wavelength fluorescence light is collected by the same objective, which projects the image towards infinity. The light is then transmitted through the same dichroic mirror reflecting the excitation light

before. Suitable emission filters block leaking excitation light and unwanted background luminescence. The tube lens projects the image again in a finite focal plane. The fluorescence is ultimately detected with a digital camera positioned in the focal plane of the tube lens, if no further magnifying lenses are positioned here instead. In this case, the camera is placed in the focal plane of the last additional lens. The described optical elements are present in even the simplest fluorescence microscope. Depending on the application, further optical elements are installed in the excitation and emission path (see Subsections 2.3.1 – 2.3.7).

2.3.1 Widefield microscopy

Widefield microscopy is the most conventional technique in fluorescence microscopy. The entire field-of-view is illuminated as homogeneously as possible and all fluorophores within are excited at the same time. Thus, all signals are recorded simultaneously,[77] which is invaluable for all dynamic microscopy measurements like single molecule tracking (SMT) (see Section 2.3.6 and 2.3.7). Disadvantageously, a widefield image is superimposed with out-of-focus fluorescence from below or above the focal plane.[78] This out-of-focus fluorescence blurs the resulting image, independent of the actual resolution.

Two optical setups are most common for the illumination system: critical illumination and Köhler illumination. In the following, both illumination techniques are described schematically for classical transmission microscopy. In critical illumination, the light source is imaged by a lens, the so-called condenser lens, into the front focal plane of the objective. An aperture in the front focal plane of the condenser lens controls the amount of illumination light. The light source should be large and featureless, as any inhomogeneities of the light source are translated to the object plane and thus lead to uneven illumination of the sample.[76] Köhler illumination, named after its developer August Köhler, is the more widespread setup nowadays. Here, the light source is imaged by a collector lens, sometimes also called widefield lens, on the front focal plane of a second lens, the condenser lens. The condenser aperture is placed in this focal plane and closed or opened until it is completely filled by the image of the light source. Behind the condenser lens, all light rays are parallel, only to be focused by the objective onto its back focal plane to form again the image of the light source. The front focal plane of the condenser lens and the back focal plane of the objective lens are thereby conjugate to each other.[76]

Apart from these two setups, two illumination configurations can be distinguished: dia-illumination and epi-illumination. In dia-illumination, also called bright-field illumination, the sample is placed between light source and objective lens. Both transmitted light and light diffracted by the sample is gathered by the objective lens. For fluorescence microscopy, however, epi-illumination in combination with inverted microscopes is more convenient. As described in Section 2.3, the sample is illuminated by light transmitted through the objective lens, and likewise, the sample image is collected by the objective (compare Figure 2.3). There is no designated condenser, instead the objective lens serves as condenser lens, too. Thus, the front focal plane of the condenser lens corresponds to the back focal plane of the objective lens. Köhler illumination can be achieved in epi-illumination as long as the light source is imaged correctly onto the back focal plane of the objective lens.[76]

In this work, widefield microscopy is employed in all diffusion measurements in Chapter 4 and some minor microscopy experiments in Chapter 3 as well. Since the FEDUP method is not an imaging

technique *per se*, but a single molecule technique to measure diffusion, blurring due to out-of-focus fluorescence is not the biggest issue. It is more important to measure all signals simultaneously to achieve reasonable statistics (see Section 2.3.7). For most widefield measurements in this work, Köhler illumination is utilized. Only in some FEDUP measurements, total internal reflection fluorescence (TIRF) (see Section 2.3.2) is used instead. Bright-field images are only taken sporadically to show some general structures, whereas all fluorescence microscopy is carried out in epi-illumination.

2.3.2 Total internal reflection fluorescence microscopy

There exist different approaches to reduce the out-of-focus background signal in FM. One option is the manipulation of the emission path, as is the case in confocal microscopy (see Section 2.3.3). However, this approach comes at the cost of all widefield benefits (see also Section 2.3.1), in particular the simultaneous recording of all signals in the field of view. An approach compatible with a widefield setup is total internal reflection fluorescence (TIRF) microscopy. Here, the illumination itself is manipulated so that only fluorophores are excited which are positioned within axial distances approximately 100 nm above the glass substrate–sample interface.[79] TIRF is based on the properties of refraction when light propagates from one medium with refractive index n_1 to another medium with refractive index n_2. In microscopy, this occurs at the glass substrate–sample interface. Refraction is classically described by Snell's law:

$$n_1 \sin\theta_{\text{in}} = n_2 \sin\theta_{\text{out}} \tag{2.17}$$

Here, θ_{in} denotes the angle of incidence and θ_{out} the angle of the refracted beam. Depending on the refractive indices and the angle of incidence, light rays are either (partly) transmitted or (partly) reflected from the interface. Total reflection is achieved if the refracted light rays propagate tangentially along the direction of the interface or even away from the interface back into the first medium.[79] This condition is expressed by equation (2.17) when the angle of the refracted light beam is at least $\theta_{\text{out}} = 90^\circ$ and consequently $\sin 90^\circ = 1$. The critical angle, θ_c, which is the minimum incident angle for total internal reflection to occur, is thus defined as follows:

$$\theta_c = \sin^{-1}\frac{n_2}{n_1} \tag{2.18}$$

Equation (2.18) is only solvable if $n_2 < n_1$. Hence, TIRF can only be employed if the refractive index of the second medium is lower than that of the first medium and the angle of incidence is equal to or greater than the critical angle.

The equations above describe how light is refracted at an interface. However, they do not include the proportions of reflected and transmitted light. It can be shown that even in the case of total internal reflection an electric component of light traverses the boundary and an electric field is established in the second medium. This field is called the evanescent field.[79] The intensity of the field, I_z, decays exponentially in dependence on the axial distance z from the interface, according to equation (2.19):

$$I_z = I_0 \exp\left(-\frac{z}{d}\right) \tag{2.19}$$

where I_0 is the intensity of the field at the interface ($z = 0$) and d is the penetration depth of the evanescent field. The penetration depth is in turn defined as follows:

$$d = \frac{\lambda}{4\pi\sqrt{n_1^2 \sin\theta_{\text{in}} - n_2^2}} \tag{2.20}$$

From equation (2.20), it becomes clear that the penetration depth is linearly dependent on the excitation wavelength λ and inversely linearly dependent on the NA of the objective, since $\text{NA} = n_1 \sin\theta_{\text{in}}$ (see also Section 2.3). Therefore, the longer the wavelength of the excitation light, the deeper the evanescent field penetrates the sample, while a higher NA objective reduces the penetration depth.

TIRF has three general advantages. First, as mentioned above already, out-of-focus background is reduced and SNR is increased. This is particularly helpful if measurements take place under unfavorable conditions such as high dye concentrations. Second, the intensity I_0 at the surface is significantly higher than the incident intensity. Hence, fluorophores at the interface are actually brighter in TIRF than in other illumination setups. Third, if parallel polarized incidence is used, an elliptically polarized evanescent field is created. This excites even fluorophores with dipoles in a perpendicular arrangement to the surface. Otherwise, it would be almost impossible to excite these, since the transition dipole moment approaches zero (see also Section 2.1).[76]

There are two ways to implement TIRF in a microscope. For one, a prism can be optically coupled to a glass coverslip. The other option is to use high NA objectives (NA$> n_2$). The excitation beam is diverged from the central axis in the back focal plane of the objective and directed along the periphery of the objective lens. Consequently, the beam exits the front aperture at high angles.[76] Of both methods, prism-based TIRF is typically more cost-effective and achieves a purer evanescent field. In this context, purity means how well the decay of the evanescent field can be described by a single exponential profile as defined in equation (2.19). However, the coupling of the prism to the glass coverslip requires more effort and the angle of incidence is more restricted. In contrast, objective-based TIRF is easier to handle and a larger range of incident angles is available, if sufficiently high NA objectives are used. In return, designated TIRF objectives tend to be very expensive and still generate a less pure evanescent field.[79]

In this work, objective-based TIRF is employed for a series of FEDUP measurements in Chapter 4. Out-of-focus light is less of an issue in those measurements. However, they benefit from the higher intensity at the surface. Furthermore, most diffusion measurements take place in rigid polymer films which even restrict rotational movement to some degree. Therefore, it is possible that several fluorophores are stuck with their dipole perpendicular to the surface. Using TIRF ensures the excitation of all fluorophores in the field of view.

2.3.3 Confocal microscopy

Confocal microscopy directly addresses the shortcomings of widefield microscopy, i.e., the blurring of the images due to out-of-focus fluorescence. To this end, a pinhole is placed in the focal plane of the tube lens. Only in-focus light can pass this pinhole (green lines in Figure 2.4). Thus, the pinhole is confocal with the focus point. After the pinhole, the light is focused by another arrangement of lenses onto the detector. The detector in confocal microscopy is typically a photomultiplier tube or a single photon avalanche diode (SPAD) instead of a digital camera, as it is used in widefield. Notable exceptions include

spinning disk confocal microscopy (SDCM) (see below), where often charge-coupled device (CCD) cameras are in use.[76] The effectively observed three-dimensional section of light passing the pinhole is called the confocal volume. Light originating from below or above the focal plane, as well as light originating from the focal plane around the focus, is blocked (blue and red lines, respectively, in Figure 2.4). Generally, the smaller the pinhole, the less out-of-focus light is transmitted and therefore the better the resolution. At the same time, smaller pinholes mean a significant loss of signal intensity.[76]

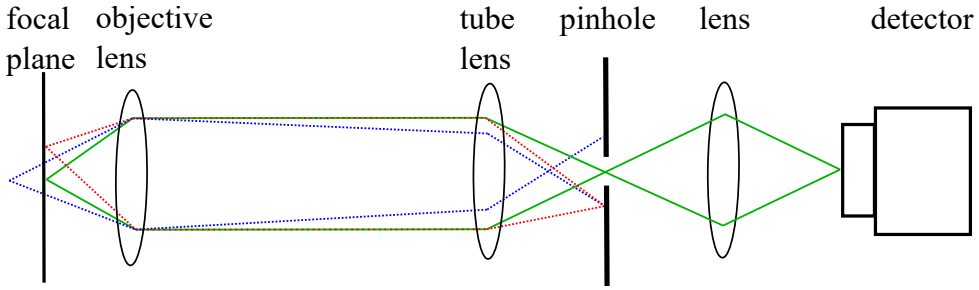

Figure 2.4: Schematic representation of the imaging path in a confocal microscope. The solid green lines represent the in-focus fluorescence, whereas the dotted blue lines represent fluorescence from a position outside of the focal plane and the dotted red lines depict fluorescence from a position in the focal plane but outside of the focus.

As a trade-off for the improved resolution, only the fluorescence from the confocal volume is detected. Hence, the field-of-view at any given point in time is drastically reduced compared to widefield microscopy. To image larger structures, the sample has to be scanned systematically. This approach is called confocal laser scanning microscopy (CLSM). In the earlier days of confocal microscopy, the sample stage was moved in a precise raster pattern. Most common today is a variable laser beam. The laser beam is moved across the lateral directions of the sample by using two mirrors driven by galvanometers and controlled by a computer.[80] A slightly different approach is spinning disk confocal microscopy (SDCM). Here, a rotatable disk with a series of pinholes arranged in an Archimedean spiral is placed in the position of the pinhole. Due to the geometry of the pattern, each section of an image is scanned equally long during a single revolution of the disk.[76] With SDCM, it is possible to image multiple in-focus spots at once, thereby increasing the acquisition rate compared to CLSM.
Apart from an improved resolution in imaging, confocal microscopy can also be used for time-dependent fluorescence measurements, in particular fluorescence correlation spectroscopy (FCS) and time correlated single photon counting (TCSPC). In FCS, intensity fluctuations are measured and analyzed. These fluctuations hold information about the number of fluorophores inside the confocal volume and their average traversing time. If the size of the confocal volume is known, this information can be converted to average concentration and translational diffusion coefficients.[76] The fluorescence signal fluctuates in dependence on fluorophores entering or leaving the confocal volume within a diffusion time τ_D. Within a time period shorter than τ_D, the fluorophore moves about only a little, hence the signal remains similar. The longer the observed time period, the more likely it is for the fluorophore to leave the confocal volume completely and the fluorescence signal of this specific fluorophore to cease before a new fluorophore is detected. The resulting fluctuations are analyzed with an autocorrelation function.[76]
TCSPC is a common method for the determination of fluorescence lifetimes (see also Section 2.1). Excitation is achieved with a pulse of light as short as possible. Then, the arrival time of a fluorescence

photon at the detector is measured before another excitation pulse occurs. In practice, the time between the arrival and the next pulse is recorded instead.[76] This cycle is repeated several thousands of times and the arrival times of each photon are plotted in a histogram. When a sufficient amount of photons is detected, the histogram represents an accurate statistic of arrival times which can be described with the temporal decay function (2.5).[66] After the arrival of a photon at the detector, there is a short dead time when the detector can no longer register incoming signals. These dead times are due to the fact that the counting electronics is slower than the pulse rate of the laser. Hence, it would not be possible to correctly measure all arrival times if every cycle generated a photon.[76] Consequently, the intensity of the excitation pulse and the concentration of the fluorophore have to be adjusted so that at most one fluorophore in the confocal volume is excited per cycle. Otherwise, the histogram is shifted towards shorter lifetimes. There may also be several cycles in which no signal is detected whatsoever, as long as there are enough photons overall for a reasonable statistical analysis. The empty cycles do not contribute to the overall histogram. Since the time between photon arrival and the next pulse is measured instead of the time between pulse and photon arrival, it is simple to exclude these empty cycles. Cycles are only included in the analysis if a signal is detected and the correct arrival time is calculated retrospectively.[76]
In principle, it is also possible to implement TCSPC in a widefield setup.[81] However, more convenient, and more common, is the implementation in a confocal microscope. The combination of TCSPC with CLSM gives rise to fluorescence lifetime imaging (FLIM) (see Section 2.3.4).
In this work, confocal microscopy is mostly used in the context of TCSPC and FLIM. All fluorophores, both in Chapter 3 and 4, are characterized by lifetime measurements with TCSPC. Furthermore, most fluorescence images in Chapter 3 are FLIM images. Lastly, some FCS measurements are performed in Chapter 4.

2.3.4 Fluorescence lifetime imaging

As mentioned before, there are two methods to determine fluorescence lifetimes; the phase modulation method and time correlated single photon counting (TCSPC). Both methods can be used to perform fluorescence lifetime imaging (FLIM). In the following, time-domain FLIM, or TCSPC-FLIM, is discussed in greater detail, whereas frequency-domain FLIM is mostly neglected. However, most principles apply to both methods.
FLIM offers several advantages over regular intensity measurements. Contrary to intensity, fluorescence lifetimes are mostly independent of fluorophore concentration. In consequence, changes of intensity can be analyzed with FLIM to determine whether these fluctuations are caused by alteration of the quantum yield, a (local) variation of the fluorophore concentration, or both.[81] If the dependency of the lifetime on the concentration of a certain substance is known, the (local) concentration of this substance can be determined with FLIM, independently of the fluorophore concentration.[66] Generally, FLIM reveals more information about the environment of a fluorophore, as lifetimes are highly sensitive to environmental influences. In some cases, this can introduce an additional contrast, as the dye used might have comparable intensities in different environments but more distinguishable lifetimes.[81] In other cases, this can be used to investigate specific environmental questions. For example, many dyes, especially red-emitting dyes, are weakly quenched by water and other solvents bearing O – H groups. The quenching efficiency can be drastically reduced by using deuterated solvents instead.[44,82] This allows

the determination of the water content in the solvent sphere of a fluorophore label in microgels[45] (see Section 2.6.4 for theory on microgels) or better visualization of the drying process of hydrogels.[46]
The main principle of FLIM is straightforward. CLSM is used to create an image by sequentially measuring all pixels in the image. At each pixel the decay curve is measured. Reasonable photon statistics are obtained thanks to the high repetition rate of the laser (several dozen MHz). At dwell times of several microseconds or more per pixel, thousands of pulses image each pixel per scan. The overall measurement time is dependent on the desired accuracy and the complexity of the fluorescence decay. A single-exponential decay can be determined reasonably well with some hundreds of photons, whereas a double-exponential decay needs at least one hundred times as many photons to be determined with the same accuracy.[66] In these cases, either the dwell time has to be increased drastically or the region of interest has to be scanned several times until a trustworthy photon statistic is recorded. The instrumentation of TCSPC-FLIM, in contrast, is rather complicated. Both specialized hardware and software is required to both correctly count the photon arrival times and identify the position of the laser beam on the sample. Complete systems are commercially available.
It is also possible to measure FLIM with a widefield setup, especially when employing frequency-domain FLIM.[66] On one hand, this increases the acquisition speed and decreases possible photo-induced damage. On the other hand, SNR and camera sensitivity, and consequently resolution, are worse than in a confocal approach.[81] Instead of CLSM, multiphoton-laser scanning microscopy (MP-LSM) can be employed. In MP-LSM, a high density of low energy, high wavelength photons is required. Two (or more) photons of half (or third, etc.) the energy required for excitation come together spontaneously to excite the fluorophores. The dependency of multiphoton excitation on the photon density effectively restricts excitation to a small focal volume, comparable to the confocal volume, without the need for a pinhole. The main advantage of MP-LSM lies in the use of photons in the near-infrared region, which exhibit a deeper penetration depth than photons from the visible spectrum. Thus, MP-LSM FLIM is particularly useful for tissue imaging.[81]
In Chapter 3 of this work, CLSM-TCSPC-FLIM is employed to image microgels and polymer films crosslinked with mechanofluorophores. FLIM is used to increase the contrast between the unactivated and the activated mechanofluorophores, since the shifts of fluorescence lifetimes upon (mechanical) activation are even more pronounced than the intensity changes and shifts in the emission spectrum. Or, to be more precise, the enhanced contrast in FLIM is more convenient to observe the controlled activation additional to the inevitable non-specific activation. Moreover, confocal microscopy in general is better suited for the attempted increase in resolution, since no conventional widefield super-resolution fluorescence microscopy (SRFM) technique is used (compare Section 2.3.5).

2.3.5 Super-resolution fluorescence microscopy

In recent years, a multitude of microscopy techniques emerged that surpass the resolution limit as defined in equation (2.16) (see also Section 2.3). Altogether, these techniques are termed super-resolution fluorescence microscopy (SRFM). SRFM enhances the resolution compared to conventional microscopy by at least one order of magnitude.[31,83] The importance of the improved resolution was internationally recognized in 2014 when the Nobel prize in chemistry was awarded for the development of SRFM.[84]
Since the resolution limit is based on the physical properties of real optical setups, even most

sophisticated instrumentation is restricted to this technical limit. Thus, even in SRFM, diffraction limited images, or image parts, are generated first. However, there are three main approaches to extract sub-diffraction information from diffraction limited images.

The first approach is to encode the sub-diffractional information directly in the measured images by using spatially structured excitation light. Correspondingly, the most common relevant technique is termed structured illumination microscopy (SIM).[85] A diffraction grating is placed in the excitation path to modulate the illumination in a precise manner. Upon interaction of the structured beam with the unknown sample structure, both patterns are superposed multiplicatively to form moiré fringes. Since the illumination pattern is known, it is possible to deconvolute the moiré fringes and obtain the otherwise unobtainable pattern of the structure, which reveals high resolution information.[85] The resolution is improved about twofold compared to conventional microscopy and therefore significantly less than the methods discussed below. In return, it might be the most universally applicable method.

The second approach is also based on a precise manipulation of the excitation beam. This time, the illumination is constructed in a way which allows the imaging of a smaller subset of fluorophores.[86] To generate the whole image, the field of view has to be scanned systematically in a CLSM-like manner. Two lasers are required; one regular excitation laser and a second highly structured laser beam that features spatially confined minima.[87] The most typical laser geometry is a broad, intense, doughnut-shaped laser. The first laser excites all fluorophores within the targeted confocal volume, whereas the second laser depletes all excited states again, except at the sub-diffraction-sized minima of its illumination. The most prominent techniques based on this principle are stimulated emission depletion (STED)[34] and reversible saturable optical fluorescence transitions (RESOLFT)[87]. The necessary high laser powers for the depletion process in STED can sometimes prove damaging to samples, and the method is restricted to CLSM-type measurements.

The last approach relies on the statistical switching of all fluorophores in the field of view between a fluorescent bright state and a long-lived non-fluorescent dark state. As long as all fluorophores in their bright state are separated by distances exceeding the diffraction limit, it is possible to localize single emitters with sub-diffraction accuracy. These types of SRFM methods are denominated single molecule localization microscopy (SMLM). In the following, the basic principle of SMLM and three of the most prominent methods are presented in greater detail. The general methodology is also shown in Figure 2.5.

The basic idea of SMLM is, as the name implies, to localize single emitters. The point spread function (PSF) of a single emitter, which can be considered a point-like light-source, is not a single point but a broad spot called the Airy disk (see Section 2.3). The intensity profile of the true PSF can be reasonably well described with an idealized PSF, such as a two dimensional Gaussian. Fitting the PSF of a single emitter with such idealized PSFs allows to determine the centroid with high accuracy.[31] This centroid is assumed to be the true position of the emitter which can be represented by a single point. Requirement for this localization procedure is to ensure that at any given time only a single emitter contributes to any imaged PSF. This is achieved by temporarily switching most fluorophores within the field of view to a non-fluorescent dark state, such that only a sparse subset of emitters separated by distances larger than the diffraction limit contribute to a single frame of a measurement video. These single emitters can then be localized as described above, before they are turned off again, and a new, spatially separated subset is recovered from its non-fluorescent dark state to its regular fluorescent bright state instead. The process

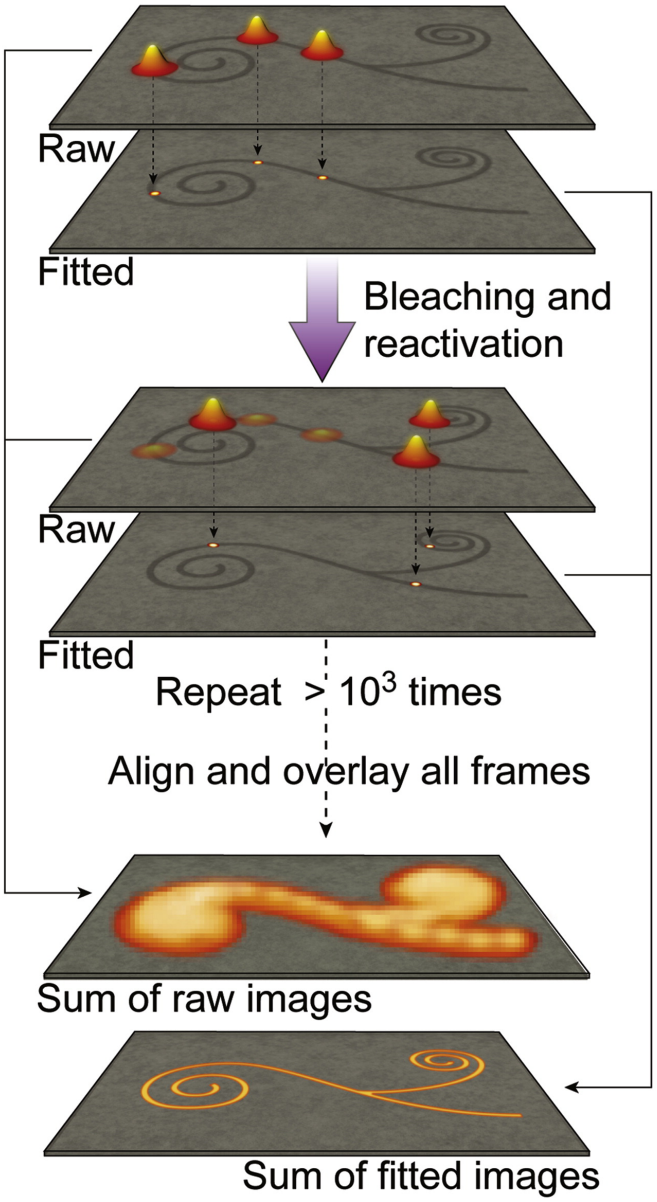

Figure 2.5: General principle of single molecule localization microscopy (SMLM). The structure of interest is symbolized by the spiral pattern. Single molecule fluorescence is depicted as broad orange two-dimensional signals appearing along the structure. The centroids are determined by fitting two-dimensional Gaussians to the measured signals. The sum of all these localizations results in a super-resolved image. Reprinted from Developmental Cell, *23*, P. Sengupta, S. Van Engelenburg, J. Lippincott-Schwartz, Visualizing Cell Structure and Function with Point-Localization Superresolution Imaging, 1092–1102, **2012**, with permission from Elsevier.[31]

of switching fluorophores between a fluorescent bright state and a non-fluorescent dark state is referred to as blinking.[88] This measurement sequence is repeated until statistically every single emitter has been localized at least once. All sub-images of accurately localized single molecules are consequently summed up to yield one final super-resolved image of the entire imaged structure (compare Figure 2.5). The achievable resolution is dependent on the average localization accuracy of the emitters and the labeling density.[89] The former, in turn, is dependent on the number N of detected photons, the pixel size

a of the detector, the average background signal b^2 and the standard deviation of the PSF σ. With these experimental values, the localization accuracy σ_{loc} can be calculated according to equation (2.21).[56]

$$\sigma_{\text{loc}} = \sqrt{\left(\frac{\sigma^2 + \frac{a^2}{12}}{N}\right)\left(\frac{16}{9} + \frac{8\pi\left(\sigma^2 + \frac{a^2}{12}\right)b^2}{Na^2}\right)} \tag{2.21}$$

Since σ, a and b are given parameters that can be influenced only little, the most important factor of the localization accuracy is the number of detected photons per emitter. The labeling density also directly influences the achievable resolution. Logically, the more labels are present, the better the structure can be resolved, provided that each label can be localized individually. The theoretical resolution is given by the Nyquist–Shannon sampling theorem.[90] In essence, the mean distance between two neighboring localizations should be less than half of the desired resolution.[39] Mathematically, the correlation between the Nyquist resolution σ_{Nyquist} and the labeling density ρ_{label} can be expressed by equation (2.22).[89]

$$\sigma_{\text{Nyquist}} = 2\rho_{\text{label}}^{-\frac{1}{d}} \tag{2.22}$$

where d denotes the number of dimensions. The overall image resolution σ_{final} is a convolution of the localization accuracy σ_{loc} and the Nyquist resolution σ_{Nyquist}.[89]

$$\sigma_{\text{final}}^2 = \sigma_{\text{loc}}^2 + \sigma_{\text{Nyquist}}^2 \tag{2.23}$$

SMLM methods essentially differ in their approach to induce the necessary blinking behavior. Three of the most common are shortly presented in the following. In photoactivation localization microscopy (PALM), photoswitches are utilized.[35] Photoswitches are molecules which can undergo a reversible intramolecular reaction in their excited state. Hence, every excitation either results in fluorescence or the deactivation of the photoswitch by intramolecular rearrangement to its non-fluorescent form. Reactivation, i.e., the reverse reaction, is also achieved by light, often of a different (shorter) wavelength. Fine tuning of the light intensities for deactivation and reactivation is required to ensure blinking in a random statistical way that allows for the localization of single emitters. An irreversible deactivation by photodamage, usually called photobleaching, is also possible. Photobleaching is the ultimate limitation of all SRFM techniques, since it restricts the number of blinking cycles a molecule can perform overall. The original (direct) stochastic optical reconstruction microscopy ((d)STORM) method is similarly based on the switching of fluorophores with two lasers, one for deactivation and one for activation.[37] Typically, pairs of two different dyes are required. One dye can be excited with longer wavelengths and is used for imaging. The second dye, which has to be in close proximity to the first, is excited with shorter wavelengths and serves to recover the first dye to its bright state. The pair thereby forms a kind of photoswitch.[37] This method is simply termed STORM. More common today is direct STORM or dSTORM.[38,39] Here, only one laser is required. In addition, a so-called blinking buffer has to be added. This buffer contains reducing agents like primary thiols. Statistically, all excited fluorophores undergo ISC to the excited triplet state at some point. The reducing agents selectively quench the triplet state without returning the molecules to their singlet ground state, thereby considerably prolonging the

dark state of the fluorophores. It is assumed that a stable radical anion is formed. Return to the singlet ground state occurs via oxidization with oxygen dissolved in the solution.[39] The recovery rate can be further influenced by the addition of oxygen scavengers. The exact blinking mechanism is still up to debate and is likely dependent on the dye and the blinking buffer. There exists evidence that cyanine dyes, for example, form a stable non-fluorescent adduct with the reducing agent of the blinking buffer that dissociates under high laser powers.[91,92]

The point accumulation for imaging in nanoscale topography (PAINT)[40] method operates on a slightly different principle. Contrary to the other methods, the structure-of-interest is not covalently labeled with fluorophores. Instead, a solution of freely diffusing fluorescent probes is added to the sample. The fluorophores exhibit an increased binding affinity to the structure-of-interest.[40] While still in solution, the fluorophores move too fast to be localized. Only upon (temporary) binding to the structure, localization becomes possible. Blinking is achieved either by photobleaching of the bound probes or by dissociation. In this context, photobleaching is less of a problem for the overall photon budget, since bleached fluorophores can be constantly replaced by fresh probes diffusing in the solution. Solvatochromic dyes such as Nile Red are particularly convenient as probes in PAINT, since the fluorescence in aqueous solution can be easily distinguished from the fluorescence in more apolar surroundings. In the case of Nile Red, fluorescence is almost completely quenched in aqueous solution.[93] A special variant of the method is DNA-PAINT. Here, the freely diffusing probes are attached to small DNA-strands, while the structure-of-interest is labeled with complementary DNA-strands.[94]

In this work, the established SRFM methods only play a minor role. In Chapter 3, a new kind of SMLM is attempted. The employed mechanofluorophores are not photoswitches and are unlikely to be photochemically controlled in a (d)STORM-like approach. Therefore, a new method has to be developed. However, the fundamental principles remain comparable; single emitters are supposed to be activated in an individual fashion with AFM, such that they can be accurately localized. In the end, they are turned off again by photobleaching. Methods like STED are deemed unsuitable due to the low photostability of the dyes used. PAINT is used on a few suitable occasions for comparative images.

2.3.6 Single molecule tracking

FM is not only a powerful tool for imaging of structures, it can also be used to reveal dynamic information about the system. Several techniques have been developed to measure diffusion. Methods like fluorescence correlation spectroscopy (FCS)[95] (see Section 2.3.3) or fluorescence recovery after photobleaching (FRAP)[96] are particularly useful in investigating dynamic biological problems like cellular binding.[97] Powerful as they are, these methods measure ensemble averages and cannot reveal diffusional or structural inhomogeneities.[52,98] To address this shortcoming, single molecule tracking (SMT)[54] has been developed. Similar to the SMLM techniques described in Section 2.3.5, SMT is based on the accurate localizations of single emitters separated by distances exceeding the diffraction limit. To achieve the obligatory spatial separation, very low labeling densities are employed. However, the localizations are not added up to form a super-resolved image. In fact, the low labeling density in classical SMT does not allow for super-resolution according to the Nyquist–Shannon theorem (compare equations (2.22 and (2.23)). Instead, the single molecule positions in subsequent images are compared.

Whenever a localization in frame $i+1$ is found within a predetermined radius R around a localization in frame i, it is considered the same molecule and the distance between both localizations is taken as the trajectory.[76] If more than one localization is found within the critical radius, the trajectory has to be rejected. The size of the radius is dependent on the diffusion rate and blinking behavior of the used fluorophores. If molecules are transferred to a dark state by some inherent mechanism, it is possible that localizations of specific molecules are missing for several frames. Therefore, it is part of the analysis to determine if a reappearing signal belongs to a specific observed trajectory or if it is more sensible to cut the old trajectory and start a new one. Both the connection of localizations to trajectories as well as the rejection of some tracks is achieved by different available algorithms.[99–101] The above described principle of SMT is also shown in Figure 2.6.

The interpretation of the reconstructed trajectories is commonly performed via an analysis of the mean square displacement (MSD).[76] The MSD analysis does not only allow the determination of accurate diffusion coefficients, but is also able to distinguish different modes of motion, such as normal, anomalous, directed or confined diffusion.[98] To this end, the displacement r is calculated from the linear distances between two localizations belonging to the same fluorophore measured at different lag times t_{lag}. The n-dimensional diffusion coefficient D can then be obtained from the increase of the MSD $\langle r^2 \rangle$ with t_{lag}.

$$\langle r^2 \rangle = 2nDt_{\text{lag}}^{\alpha} \tag{2.24}$$

The parameter α in equation (2.24) differentiates normal from anomalous diffusion. In the case of normal diffusion applies $\alpha = 1$, whereas for directed (super-)diffusion applies $\alpha > 1$ and for anomalous (sub-)diffusion applies $0 < \alpha < 1$.[102] There exists a certain dependence of the single molecule diffusion coefficient on the track length. In particular, the diffusion coefficient becomes more reliable the longer the track.[103]

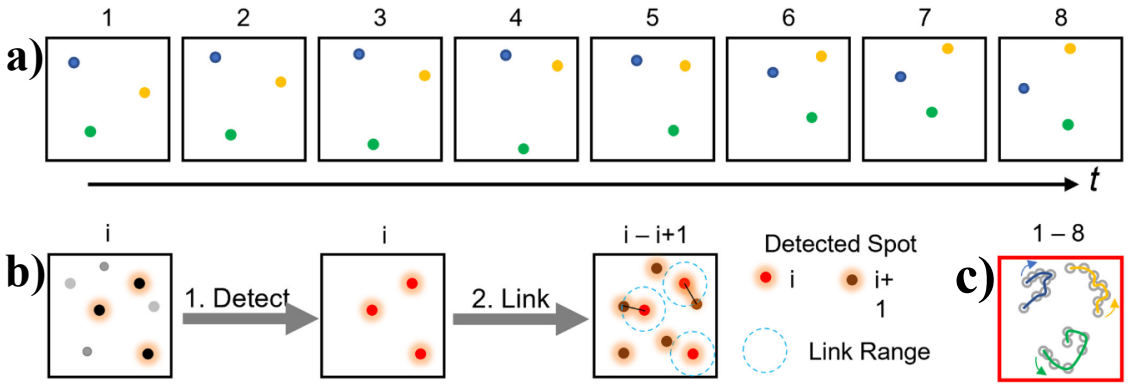

Figure 2.6: Schematic procedure of a single molecule tracking (SMT) measurement. (**a**) Schematic representation of the fluorescence signals of three single molecules at eight different points in time. (**b**) Detection and linking of single molecule positions. The distance threshold (here "link range") is symbolized by the dashed blue circles. (**c**) The resulting single-molecule trajectories of the three single molecules captured in the eight frames shown in (**a**). Reprinted from K.-H. Tran-Ba, K. Foreman, "Single-Molecule Tracking of Dye Diffusion in Synthetic Polymers: A Tutorial Review", *J. Appl. Phys.* **2023**, *133*, 101101, with the permission of AIP Publishing.[104]

There are a number of limitations to the SMT method. First, the labeling density, and in the same context the purity of the sample, determines the amount of false positives during the analysis. In this context, a false positive is an accepted connection between two localizations that do not actually belong to the same molecule.[103] The number of false positives increases drastically in too densely labeled samples or samples with radiant impurities, which cannot be precisely differentiated from fluorescent labels. Second, in the case of fast diffusion ($D > 10^{-13}$ $\mathrm{m^2\,s^{-1}}$), the number of false negatives becomes too great for a reliable analysis. False negatives occur when the connection between two localizations is not recognized.[103] To counter false negatives, larger radii R of acceptance would be required. This in turn is only possible if the labeling density is low enough, thereby reducing the overall number of available trajectories. Lastly, the localization accuracy determines the lower limit of measurable diffusion coefficients. If the fluorophores move so slowly that two subsequent localizations of the same emitter are closer together than their localization accuracy, then no accurate displacement r can be determined. It would need increasingly long measurement times to observe motion that results in two distinctly separate localizations. The overall measurement time, however, is ultimately restricted by photobleaching.[60] Further complications limiting the localization accuracy may occur due to the instability of the measurement setup,[55] dye orientation,[58] and low SNR due to low signal or non-negligible background.[57] With finite measurement times on a real microscope these limitations result in a lower limit of approximately $D \approx 10^{-17}$ $\mathrm{m^2\,s^{-1}}$.[59] To circumvent this lower limit, more sophisticated single molecule approaches are required (see Section 2.3.7).

2.3.7 FRET efficiency diffusion measurements upon photocleavage

There exist currently two FM methods to measure diffusion coefficients below the lower limit presented by SMT (see Section 2.3.6). One method is termed minimal fluorescence photon fluxes microscopy (MINFLUX).[60] In MINFLUX, precise laser geometries similar to STED are employed. The difference, however, is the functions of the lasers. A doughnut-shaped, or otherwise minima-structured, laser is used in both cases. In MINFLUX, there is no second excitation laser filling out the sub-diffraction sized excitation minimum in the first laser. Instead, the excitation minimum is positioned in a way that the fluorophore only minimally excited. Whenever the fluorophore moves to the edge of the excitation minimum and reaches the illumination area of the doughnut-shaped laser, the position is corrected until no fluorescence is detected anymore. This way, it is possible to localize single molecules with sub-diffractional accuracy without the need for high photon counts, as stated in equation (2.21) (see Section 2.3.5). Thus, photobleaching is significantly reduced and longer measurement times become feasible, which in turn makes it possible to measure diffusion coefficients far below the limit of SMT. Nevertheless, the MINFLUX method is not part of this thesis and is only mentioned for the sake of completeness. In the following, the second method for high accuracy single molecule diffusion measurements is presented.

First developed in 2013 by *Dill et al.*[55] and officially named in 2025 by *Schöngen et al.*[59], FRET efficiency diffusion measurement upon photocleavage (FEDUP) makes use of the strong distance dependency of FRET to measure movement on a sub-pixel level. The basic idea is to use a photocleavable FRET dyad which can be selectively cleaved in a controlled manner at a defined point in time. Before cleavage, FRET-donor and -acceptor can perform translational motion only as a single unit. Due to their

close proximity, FRET efficiency is high. In this context it has to be noted that the Förster theory of FRET is too simple a model at distances as short as in the dyad before cleavage.[68] For the analysis of a FEDUP measurement, this distinction is not relevant, since the Förster theory is sufficiently accurate at distances r close to the Förster distance R_0. It is of primary importance that the changes of donor and acceptor fluorescence can be accurately described with the well-known dependence on the sixth power of the distance, as defined in equation (2.13) (see Section 2.2).[59] After photocleavage, however, donor and acceptor can move independently of each other. For two freely and randomly moving dyes in close proximity, it is statistically most likely to move apart eventually in all three dimensions. Hence, the FRET efficiency, as defined in equation (2.14), decreases on average as the fluorescence emission of the donor increases. The fluorescence intensities then hold information about the distance between donor and acceptor. Assuming perfect spectral separation of donor and acceptor fluorescence, equations (2.13) and (2.14) are rewritten as equations (2.25) and (2.26) to incorporate the spatiotemporal dependency into the FRET efficiency, η.

$$\eta(r,t) = \frac{1}{1+\left(\frac{r(t)}{R_0}\right)^6} \tag{2.25}$$

$$\eta(t,D) = 1 - \frac{F_{\text{donor}}(t,D)}{F_{\text{donor}}(\infty,D)} \tag{2.26}$$

$$= \frac{F_{\text{acceptor}}(t,D)}{F_{\text{acceptor}}(0,D)} \tag{2.27}$$

Most notably, the vaguely defined donor intensities in presence and absence of the acceptor of equation (2.14) have been replaced with the donor intensity $F_{\text{donor}}(t,D)$, measured at time t, due to the relative diffusion of donor and acceptor with diffusion coefficient D, and the final donor intensity $F_{\text{donor}}(\infty,D)$ that is reached after a period of time long enough for donor and acceptor to move beyond the boundaries of any energy transfer. Equivalently, the FRET efficiency can be expressed by the ratio of acceptor fluorescence $F_{\text{acceptor}}(t,D)$ at time t to the acceptor fluorescence at the moment of photocleavage $F_{\text{acceptor}}(0,D)$. In theory, the same FRET efficiency should be obtained in both cases. In practice, effects like crosstalk (see the Glossary 8.5), direct excitation of the acceptor and photobleaching can introduce a disparity between equation (2.26) and equation (2.27). In that case, correction terms have to be introduced.[55] It is shown later on that neither crosstalk nor direct excitation are detected for the investigated dyad under the chosen measurement condition (see Chapter 4).

If the Förster distance R_0 is known (equation (2.15)), the distance between acceptor and donor can be determined at each point in time from the measured fluorescence intensities. In other words, a distribution of magnitudes of three-dimensional random vectors with independent coordinates is obtained. Such a three-dimensional probability distribution $P_{3\text{D}}(x)$ is described by the Maxwell distribution (2.28).

$$P_{3\text{D}}(x) = \sqrt{\frac{2}{\pi}}\frac{x^2}{\sigma^3}\exp\left(-\frac{x^2}{2\sigma^2}\right) \tag{2.28}$$

where x denotes the magnitude of the three-dimensional vector and σ is the standard deviation. The Maxwell distribution is reformulated to match the problem at hand. Assuming free diffusion after photocleavage with an average relative diffusion coefficient D, the probability P to find two fluorophores

at a distance r can be expressed by equation (2.29).

$$P_{3D}(r,t,D) = \frac{1}{2\sqrt{\pi(Dt)^3}} r^2 \exp\left(-\frac{r^2}{4Dt}\right) \tag{2.29}$$

Equation (2.29) is derived from equation (2.28) by setting $x = r$ and $\sigma = \sqrt{2Dt}$. This enables the calculation of the FRET efficiency with equation (2.30).

$$\eta(t,D) = \int_0^\infty P_{3D}(r,t,D)\eta(r,t)\mathrm{d}r \tag{2.30}$$

An average relative diffusion coefficient D of a FRET pair (see also the Glossary 8.5) is therefore determined by measuring the FRET efficiency at different points in time according to equations (2.26) or (2.27) and fitting the obtained values with equation (2.30). In this context, the diffusion coefficient D is the most important parameter in fit function (2.30). The maximum donor intensity $F_{\text{donor}}(\infty,D)$ or the maximum acceptor intensity $F_{\text{acceptor}}(0,D)$ are the only other variable but fixed parameters in the model. Both time, t, and relative distances, r, are treated as variables. The Förster distance R_0 is a fixed parameter that can be calculated separately with equation (2.15). Beneficially, two equivalent fitting approaches can be performed simultaneously, depending on the calculation of the FRET efficiency with donor intensities or acceptor intensities.

The model predicts a continuous decrease of the FRET efficiency over time. While this prediction is valid on a large statistical scale, the model fails to accurately describe the random nature of the relative movement of individual FRET pairs, in particular temporary decreases of the relative distance between donor and acceptor due to random movement toward each other. Although it is theoretically possible to determine a diffusion coefficient for every single FRET pair, and thereby image the entire field of view in respect of the distribution of diffusion coefficients, fitting of such single molecule time-dependent FRET intensities with equation (2.30) is subject to high inaccuracy. Apart from the arbitrary direction of the relative motion, effects like blinking, restricted rotational movement and photobleaching introduce additional uncertainties. In a sufficiently large ensemble, however, the deviations of individual FRET pairs from the model become statistically irrelevant. If enough FRET pairs contribute to the Maxwell distribution, it does not matter if some emitters are temporarily in a dark state unrelated to the energy transfer. Every emitter is going to be in a dark state at some point, but the effect is statistically counterbalanced by the on average constant amount of fluorophores in their bright state at the same time. Likewise, the angle between the direction of motion of one specific FRET pair becomes irrelevant in the overall statistic, as every angle contributes equally likely to the Maxwell distribution at any given point in time. Hence, while the time-dependent FRET efficiency of individual FRET pairs exhibits inevitable strong deviations from the model, the time-dependent FRET efficiency of a sufficiently large ensemble is described correctly.

Similarly, there exists no theoretical lower limit to the method, whereas in practice photobleaching and finite measurement times do introduce technical limitations. Upper limits, in contrast, are unequivocally reached when the movement of the cleaved FRET pair exceeds the temporal resolution, thus when the FRET efficiency changes on a time scale similar to the camera exposure time. More technical details of the analysis are presented in Section 4.6.

The diffusion coefficient D describes the relative movement of donor and acceptor. Hence, it is

technically not a single molecule diffusion coefficient. However, the FEDUP method is meant to measure diffusion on a level so low that translational motion is almost frozen, i.e., both dye fragments can be regarded as practically immobilized. In this state, translational motion is considered to be a kind of wriggling, which in turn is assumed to behave according to random walk statistics in a very narrow, restricted volume. Hence, it is estimated that the effectively observed relative movement of donor and acceptor is approximately equivalent to the motion of single molecules.

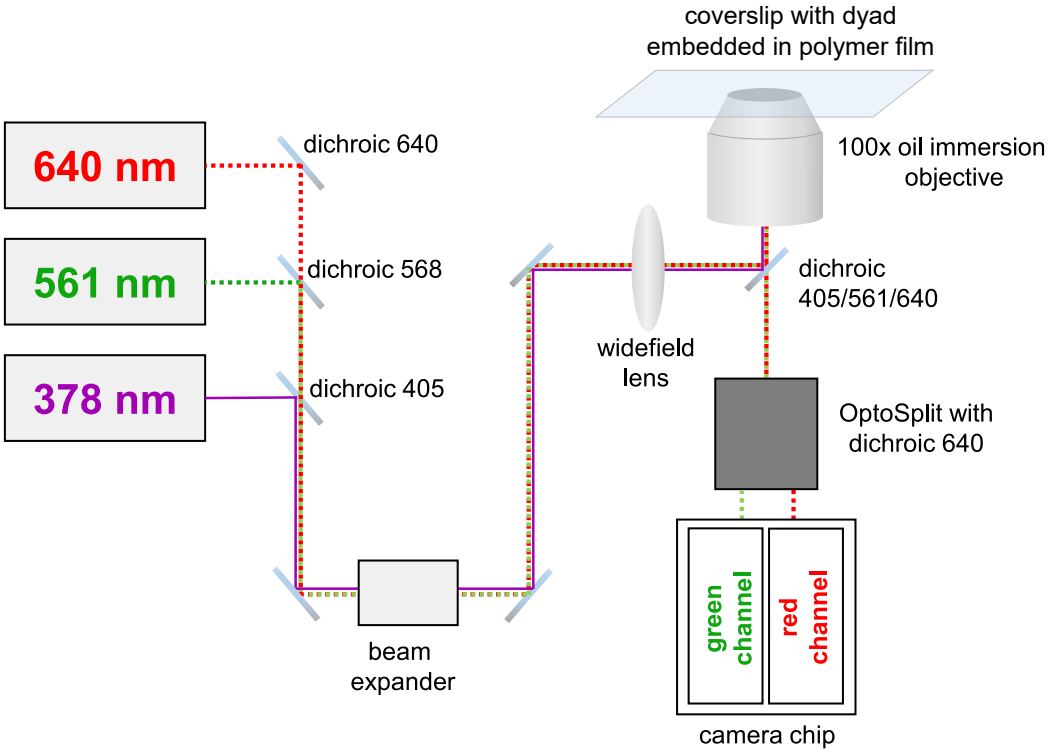

Figure 2.7: Schematic microscopy setup for all FEDUP measurements in Chapter 4. All laser beams (640 nm, red, acceptor excitation, 561 nm, green, donor excitation, 378 nm, violet, photocleavage) are guided along the same optical path. Fluorescence emission is split into two spectral channels. The green channel records all emission between 570 – 633 nm, the red channel records all emission above 655 nm.

The technical implementation of the FEDUP method has to achieve several things. The FRET donor has to be excited as selectively as possible, donor and acceptor fluorescence have to be detected both spectrally separately and time-correlated to the photocleavage, photocleavage has to be achieved in a spatiotemporal controlled manner, and, last but not least, photobleaching has to be identified. Photobleaching results in false positive signals. Due to the relaxation of the donor excited state via energy transfer, basically only the acceptor is in danger of premature photodamage. If photobleaching occurs before the energy transfer fades, this also results in a sudden increase of donor fluorescence, which might be mistaken for the spatial separation of donor and acceptor. Thus, the diffusion coefficient would be shifted to larger values. To detect photobleaching, a third laser parallel to the FRET excitation laser and the photocleavage laser is required, which selectively excites only the acceptor. As long as a signal is detected related to the selective excitation of the acceptor, no photobleaching has yet occurred.
A schematic FEDUP microscopy setup is shown in Figure 2.7. As described above, three lasers are employed for (selective) excitation of donor and acceptor and for controlled photocleavage, respectively.

All three laser beams are guided along the same optical path. The beams are broadened via a beam expander. Widefield illumination is ensured with an appropriate lens in front of the objective (compare Section 2.3.1). A multiband dichroic mirror is required to reflect the UV-, green and red laser into the objective and transmit both the red fluorescence of the FRET-acceptor and the yellow-orange fluorescence of the FRET-donor. The fluorescence emission is subsequently separated spectrally via a second dichroic and imaged on a single camera. Two spatially equivalent but spectrally distinct channels are generated. Further suitable filters restrict the detection range of the two channels to the fluorescence emission of the FRET-donor and -acceptor, respectively (for more details on the used setup, see Section 6.7.2). Measurements are performed using alternating laser excitation (ALEX).[105] Photocleavage is achieved with a single UV-laser pulse. FEDUP measurements are the main focus of Chapter 4.

2.4 Atomic force microscopy

While fluorescence microscopy is a versatile tool that allows the visualization of many different structural aspects, it is an inconvenient method to investigate the topography of samples like polymer films or microgels (see also Section 2.6). An alternative presents itself with atomic force microscopy (AFM). In AFM, distance-dependent interactions are measured between a sample and small tip attached to a spring-like cantilever. The cantilever, in turn, is attached to a more rigid chip. The forces exerted on the tip, and in consequence the cantilever, correspond to a certain distance between sample and tip which can be translated to the height of the sample at the position of the tip. Typically, the forces between sample and tip are in the range of 10 pN – 1 µN.[106] Since interatomic forces are in the order of nN,[106] both non-destructive imaging and controlled irreversible damage are possible, although the latter is unsuited for topography measurements and only important for special applications (see also Chapter 3). The sample is scanned in two dimensions and at each tip position, corresponding to a pixel of a real image, the height is reconstructed from the deformation of the cantilever. Overall, a topological image with nanometer resolution is obtained.[107] Visualization is usually achieved by representing the height with a color scale. Apart from simple height measurements, the sensing of van der Waals, electrostatic, magnetic, or capillary forces yields information about charge distributions, magnetic domain wall structure and liquid film distribution. The detection of frictional forces and elastic or plastic deformations is also possible.[106] AFM can be used for both conductive and insulating materials, contrary to most other scanning probe techniques which require the material to be conductive.[106]
A schematic AFM setup is shown in Figure 2.8. Fundamentally, two modes of operation can be distinguished: the static mode, also called dc-mode or contact mode, and the dynamic mode, also called ac-mode or tapping mode.[106] Throughout this work, the terms contact and tapping mode are used. As the name suggests, in contact mode the tip of the cantilever is brought into contact with the sample. The critical force resulting from tip–sample interaction upon contact is predefined. Whenever the threshold force is reached, this is interpreted as contact between sample and tip. To measure the acting force, a laser is deflected from the backside of the cantilever onto a quad photodiode. Given the spring-like nature of the cantilever, the interactions between tip and sample result in deformations of the cantilever, i.e., the cantilever is bent towards, or away from, the sample surface. In consequence, the laser deflected from the backside of the cantilever moves axially and laterally on the photodiode. The change

from the equilibrium position is measured and translated into a force and corresponding height. As the sample is scanned, the distance between tip and sample is constantly adjusted so that the predefined force interpreted as contact is kept constant. To this end, a feedback loop is established between the photodiode and a piezoelectric drive of either the chip or the sample holder.[107] Since the tip is in permanent contact, the sample can be damaged by the drag of the tip during lateral movement.[108]

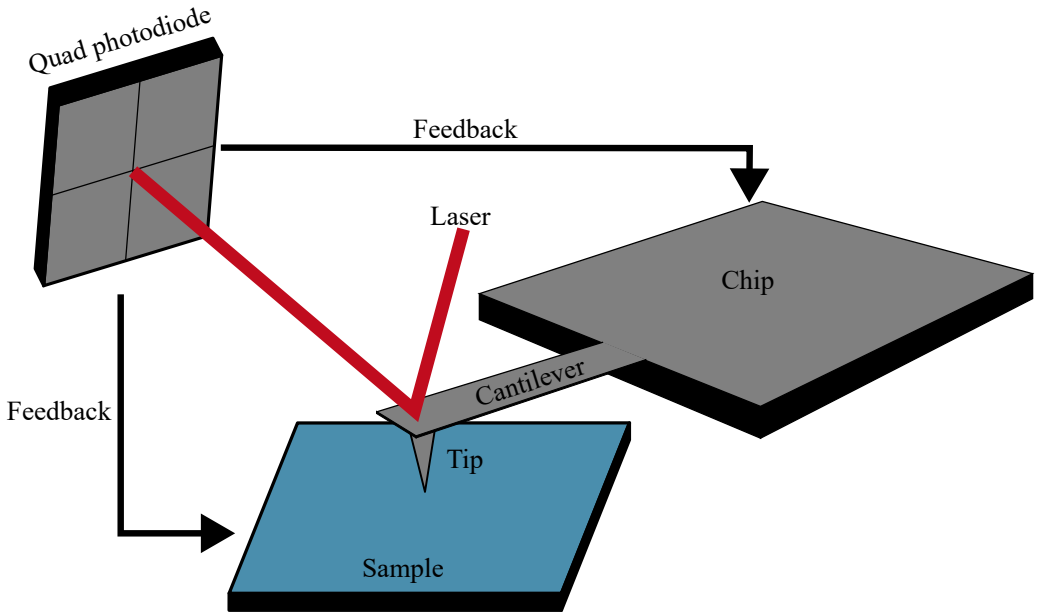

Figure 2.8: Schematic AFM setup. A laser beam is reflected from the backside of the cantilever and detected on the quad photodiode. Upon interaction of the tip with the sample, the cantilever deforms, thereby changing the reflection of the laser beam on the quad photodiode. A feedback loop between the photodiode and the chip or the sample holder constantly adjusts the height between cantilever and the surface of the sample to keep the interaction between tip and sample constant.

Tapping mode, in contrast, is a less harmful approach. The cantilever is oscillating close to its resonance frequency.[106] This way, several cycles of the cantilever approaching and retracting from the sample are performed at every measured position. In principle, the cantilever experiences the same change of forces during approach and retraction. The exact force-distance curve might differ slightly due to additional effects, but the obtained information is the same. As the cantilever approaches the sample surface, attractive dipole-dipole interactions bend the cantilever towards the sample even if the tip is not in contact.[108] Upon a further approach short range repulsive forces eventually take over. These weaken the amplitude of the cantilever oscillation. Instead of keeping the force constant like in contact mode, the feedback loop now ensures constant amplitude of the cantilever oscillation as the sample is scanned. Equivalently, an amplitude threshold is predefined that is interpreted as contact between tip and sample.[108] Since tip and sample are effectively out of contact for most of the time, tapping mode is less damaging to the sample.

In this work, AFM is utilized for several tasks. In Chapter 3, AFM is used as a precision tool to damage the sample in a controlled manner. Thereby, it is attempted to selectively activate the mechanofluorophores incorporated in different polymer systems as crosslinkers. Simultaneously, the topography is imaged. In Chapter 4, AFM serves to determine the thickness of the investigated polymer films. All measurements are performed in tapping mode, if not explicitly stated otherwise.

2.5 Photolabile protecting groups

Not every chemical reaction is a straightforward process in which two or more reactants combine to give a single desired product. More often than not, the reactants bear several moieties that may react, too, and lead to undesired side-products. To circumvent these secondary reactions, the bothersome functionalities can be shielded during the synthesis with so-called protecting groups, which inhibit the protected moieties' reactivity during the critical steps. Subsequently, the protecting groups are removed under specific conditions, e.g., at lower or higher pH, with elevated temperatures, or, in the case of a photolabile protecting group (PPG), with light of specific wavelengths.
A pure PPG, which is effectively solely removable by a light-induced reaction, is naturally orthogonal to classical protecting groups. In this context, orthogonality is defined as the possibility to remove two different protecting groups shielding two different moieties, possibly in a single reactant, independently.[109] This is often achieved using protecting groups which are sensitive to different pH-values. Obviously, PPGs offer an easily exploitable orthogonality to non-photolabile protecting groups, if they are insensitive to other factors. It has to be noted that many PPGs do react under other specific conditions, like certain pH-values, too. PPGs can also be chromatically orthogonal. Chromatic orthogonality is achieved when two PPGs are cleaved by light of different wavelengths.[110]
Apart from their inherent orthogonality, PPGs offer other advantages over classical protecting groups. For one, irradiation and consequently deprotection of the sample can be controlled spatially.[111] Furthermore, irradiating the sample, or a defined area of the sample, leads to simultaneous excitation and, depending on the cleavage quantum yield, likewise simultaneous cleavage of the PPGs. Unlike chemically cleavable protecting groups, the reactant (i.e. light) is independent of diffusion or steric hindrance. These properties make PPGs attractive for the synthesis of DNA chips and DNA micro-arrays. Both terms refer to systems with densely DNA-functionalized surfaces.[112] The surfaces are typically first coated with PPGs. Then, they are selectively deprotected and functionalized with DNA strands.
A common PPG is the *o*-nitrobenzyl group. Different functionalities have been realized based on this template, such as ethers, esters, carbonates, carbamates and acetals.[109] In Chapter 4 of this work, an *o*-nitrobenzyl based carbamate, derived from the 2-(2-nitrophenyl)propyloxycarbonyl (NPPOC) protecting group,[63,64] is employed as a photolabile linker between two different dyes. The NPPOC protecting group is well-known for its use in DNA and DNA-chip syntheses.[113,114] Other applications include photo-induced thiol Michael-additions. Here, the base catalyst amine is protected by NPPOC. The start of the reaction can then be controlled by a precise deprotection of the amines by irradiation with UV light.[115] Similarly, in this work, the controlled photocleavage of the NPPOC is used to mark the start of a FEDUP measurement (see also Section 2.3.7).

2.5.1 Photocleavage mechanism

In the following, the photocleavage mechanism of the NPPOC protecting group is discussed in greater detail. The mechanism is displayed in Figure 2.9. For convenience, the mechanism is shown for dyad **8**, so that all possible cleavage products are identified. The different cleavage pathways and their various products are subject of the characterization of the dyad in Section 4.3. The depicted mechanism is adapted from previous works.[111,116–119]

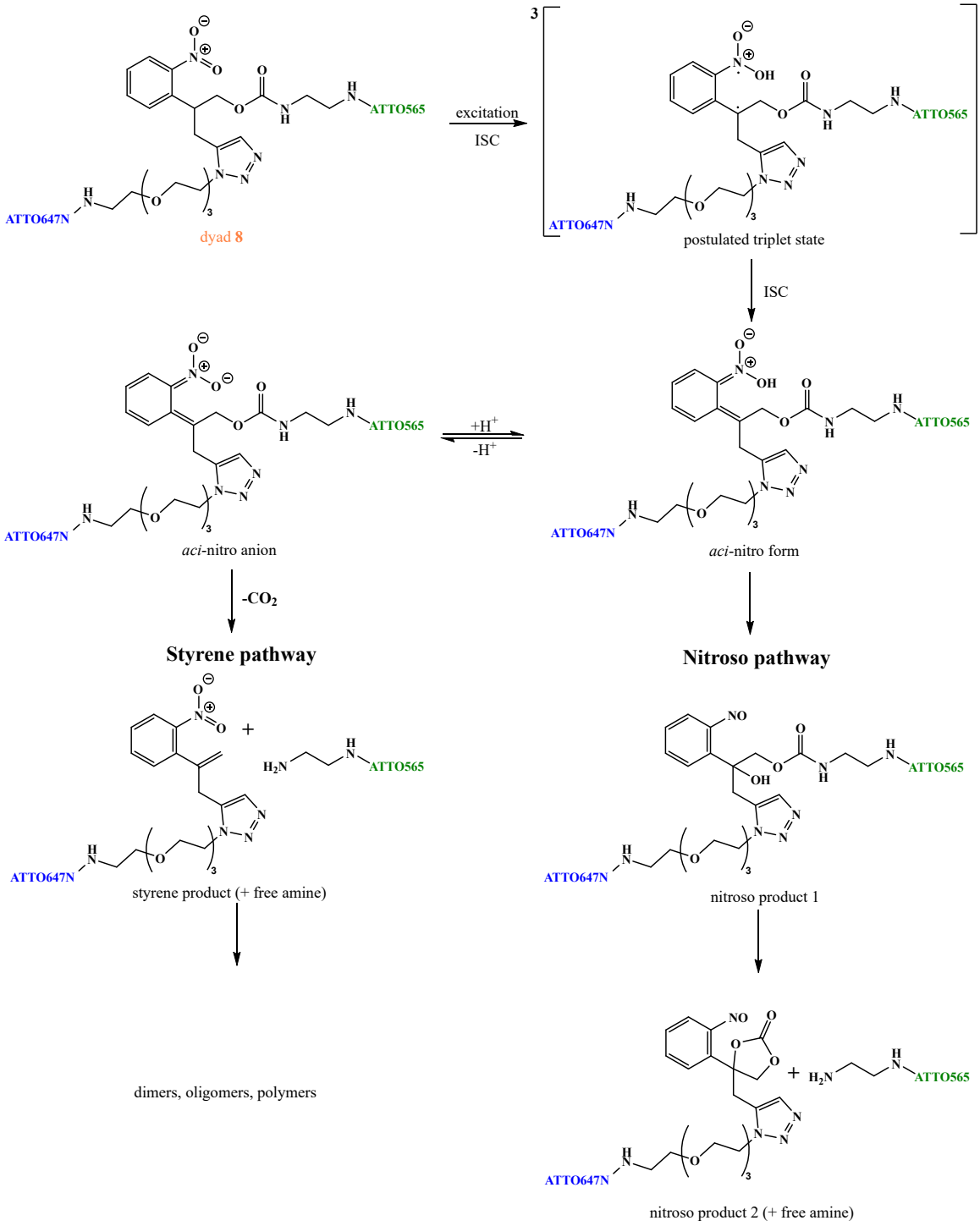

Figure 2.9: Proposed photocleavage mechanism adapted from literature.[111] Dependent on the reaction conditions, either the styrene or the nitroso pathway is the main reaction pathway. The formation of the nitroso product 2 is mainly dependent on the solvent.[111]

After excitation of the NPPOC to its first excited singlet state of $^1n\pi^*$-character, an intersystem crossing (ISC) to the triplet state can occur. The energetically lowest triplet state is also of $^1n\pi^*$-character.[119] The triplet state is short-lived. However, the lifetime is sufficient for the benzylic hydrogen to be transferred to the nitro-moiety, resulting in a biradical. So far, this intermediate is only hypothesized since the

subsequent relaxation to the *aci*-nitro form via ISC is too fast to allow the observation of the intermediate. It is up for debate if the triplet species are involved in the mechanism at all. However, sophisticated experiments involving a sensitizer covalently linked to the NPPOC could verify the presence of triplet species.[117]

The reaction conditions dictate the final deprotection steps. In the presence of suitable proton acceptors, the acid-base equilibrium of the *aci*-nitro form is shifted towards the corresponding anion. The *aci*-nitro anion then fragments into an *o*-nitrostyrene compound, carbon dioxide and the deprotected amine.[111] Throughout this work, this reaction pathway is called the styrene pathway and the cleavage products are denominated the styrene product and the free donor. In contrast, if no proton acceptor is present in the reaction mixture, it is most likely that a nitroso compound is formed instead (nitroso product 1 in Figure 2.9). It is assumed that the nitroso compound is generated via an intramolecular cyclization. Dependent on the solvent, the nitroso compound can undergo another intramolecular cyclization, which ultimately leads to photocleavage, too (nitroso product 2 in Figure 2.9).[111] Throughout this work, the second reaction pathway is called the nitroso pathway. To avoid misunderstandings, nitroso product 1 is called the uncleaved nitroso product, whereas nitroso product 2 is denominated the cleaved nitroso product. The other cleavage product is identical to the product in the styrene pathway and thus is termed free donor.

2.6 Polymer systems

Polymers are a vast class of materials with various beneficial properties that make them invaluable for modern industry and everyday life. A full review is far outside the scope of this work and the reader is referred to existing reviews on the history of polymers[120] or reviews of specific properties, like strength and toughness[121] or thermoresponsivity[122]. The following text is restricted to polymer characteristics relevant to the discussion throughout this work, i.e., glass transitions (Section 2.6.1), viscosity (Section 2.6.2) and thermoresponsive behavior (Section 2.6.3). Special polymer systems used in this work are discussed in Sections 2.6.4 and 2.6.5.

2.6.1 Glass transition

Glass transition is a phenomenon that, although well described, is not fully understood yet.[123] It is convenient to start the discussion from the better defined melting process and then extend the theoretical description to lower temperatures. The melting temperature, T_m, of a liquid can be defined as the first order transition between the liquid and the crystalline phase. The crystallization often results in a decrease of the specific volume. The most prominent exception in that regard is probably water. Any liquid, including polymer melts, that is cooled below its melting temperature T_m without crystallizing is called a supercooled liquid. As the temperature of the supercooled liquid is decreased further, its viscosity increases and molecular motion decreases. Eventually, a temperature is reached when molecular rearrangement becomes too slow to be observed on regular experimental time scales. However, the equilibrium value of the specific volume might not have been reached yet, i.e., crystallization is not yet complete and the structure is stuck in its thermodynamically metastable amorphous state. The frozen material is then called a glass. Thus, the glass transition is not a phase transition, but a kinetic

phenomenon that occurs whenever the time scale of molecular rearrangement surpasses the time scale of feasible observation. Although described as frozen melts, certain material properties of glasses more resemble that of crystalline solids than that of liquids. Most notably, the thermal expansion coefficient of the glass is significantly smaller than of the supercooled liquid and similar to the crystalline state. In consequence, the glass transition temperature T_g can be defined according to the change of the thermal expansion coefficient, although other definitions are in use, too. If consistently defined, the glass transition temperature is among the most important parameters to estimate mechanical properties of polymers.[123]

2.6.2 Viscosity

Viscosity is a quantity describing the resistance of a liquid to flow.[123] Typically, viscosity decreases with increasing temperature, as molecular motion increases and thus liquids flow more easily. The temperature dependence of the viscosity, η, of regular liquids is described with Arrhenius-type behavior. For supercooled liquids and glasses, however, a better description is offered by the Vogel-Fulcher-Tammann (VFT) equation (2.31):

$$\eta = \eta_0 \exp\left(\frac{B}{T - T_\infty}\right) \tag{2.31}$$

where η_0 is the viscosity at $T = 0$ K, T is the temperature, T_∞ is the Vogel-temperature and B is a material constant. In the case of $T_\infty = 0$ K, equation (2.31) becomes the regular Arrhenius equation and $B = E_a/k_B$, with E_a the activation energy and k_B the Boltzmann constant. If $T_\infty = 0$ K, the viscosity is predicted to become infinite at T_∞.[123] This is not observed experimentally due to finite measurement times and unfeasibly long equilibration times.[124] Viscosity of glasses is commonly described in terms of different relaxation processes. The most important process is termed α-relaxation.[124] It is the main relaxation process of polymers at temperatures close to their glass transition temperature and the process responsible for the non-Arrhenius behavior defined in equation (2.31). The α-relaxation is associated to the (micro-)Brownian motion of entire polymer chains.[125] In contrast, β-relaxation is associated to the motion, internal vibrations or rotation of smaller polymer chain segments.[126] This process shows more regular Arrhenius-type temperature dependence.[124] Further minor relaxation processes have been identified,[124] which are not discussed here. Most polymers investigated throughout this work are studied below or close to their glass transition temperature, T_g. It is assumed that α-relaxation is the most relevant relaxation process.

The viscosity of a polymer can be investigated with fluorescent probes. Molecular rotors, for example, allow to quantify the viscosity of (polymeric) systems on a microscopic scale.[48] In Chapter 4 of this work, viscosity is investigated in the context of diffusion. Diffusion and viscosity stand in a direct relation. Assuming spherical geometry with a hydrodynamic radius R_H of the diffusing probe, the diffusion coefficient D can be expressed by the Stokes–Einstein equation (2.32).

$$D = \frac{k_B T}{6\pi\eta R_H} \tag{2.32}$$

Hence, measurements of (single-molecule) diffusion coefficients allow to draw conclusions about the (micro-)viscosity of the investigated system.

2.6.3 Thermoresponsive polymers

Polymers can be made responsive to various external stimuli by precise engineering of the incorporated functional groups.[122] Among stimuli-responsive materials, thermoresponsivity of polymers is probably the one which has been investigated the most. Thermoresponsivity refers to a reversible phase transition upon temperature changes. The phase transition is initiated at a certain temperature termed the lower critical solution temperature (LCST). The phenomenon of the LCST is best understood for aqueous solutions of hydrophilic polymers, such as poly(*N*-isopropylacrylamide) (PNIPAM). Below the LCST, the PNIPAM amide groups form stable hydrogen bonds with the surrounding water molecules. Thus, the polymer chains are dissolved completely. Above the LCST, however, the hydrogen bonds to the solvent are weakened and intra- and intermolecular interactions of the polymer chains become more dominant. The formerly dissolved polymer coils form more hydrophobic and ultimately insoluble globules.[122] The process is supported by an increase in entropy upon the release of the solvent molecules from the hydration sphere of the polymer chains. Eventually, the aqueous solution turns from fully transparent to opaque as the polymer forms aggregates of sizes larger than the wavelengths of visible light.[122]
The LCST can be purposefully adjusted by incorporating more hydrophilic or hydrophobic functional groups into the polymer, usually by copolymerization or end group functionalization. The polymer architecture, molecular mass and even other external stimuli such as the ionic strength can have a profound influence on the LCST, too.[122] The possibility to engineer polymers with thermoresponsive behavior at physiological temperatures gives rise to promising biomedical applications such as drug delivery[127,128] or tissue engineering.[129,130] In this work, thermoresponsive polymers play a role in the context of microgels (see Section 2.6.4).

2.6.4 Microgels

The International Union of Pure and Applied Chemistry (IUPAC) defines microgels as colloidal crosslinked polymer networks with diameters between 0.1 – 100 µm which are swollen in a solvent.[131] Although their shape is in principle arbitrary, microgels are commonly roughly spherical and their morphology is often described as a fuzzy sphere.[132] They are usually prepared by emulsion or precipitation polymerization, which leads to the typical core-shell structure.[133] Under regular reaction conditions, the comparatively rigid core exhibits a higher polymer density and higher degree of crosslinking, whereas the fuzzy shell consists of more or less individual dangling polymer chains.
The most interesting property of microgels is their reversible swelling behavior. Depending on the monomer used, the captured solvent can be expelled under specific external stimuli leading to the collapse of the microgel. In this context, thermoresponsivity (see also Section 2.6.3) is among the best studied features. Microgels based, for example, on the commonly employed polymers PNIPAM or poly(vinyl caprolactam) (PVCL) show thermoresponsive behavior. The effect is particularly noteworthy close to the LCST of the respective polymers, thus at approximately 32 °C[134,135] for both PNIPAM and PVCL. Above the LCST, the polymer-solvent interactions weaken considerably resulting in the precipitation of the polymer. Consequently, solvent trapped inside a microgel is expelled. Since this

temperature-dependent transition is accompanied by a collapse of the microgel, the critical temperature is called volume phase transition temperature (VPTT). The VPTT tends to be similar to the LCST of the corresponding linear polymer.[133] The collapse is usually reversible, thus the microgel swells up to its former size when lowering the temperature below the VPTT. Apart from temperature, microgels can be made responsive to other external stimuli like pH, ionic strength, light or pressure.[136]
The inducible collapse makes microgels promising candidates for applications such as drug delivery[137] or biocatalysis.[138,139] Especially PNIPAM and PVCL microgels are under closer investigation, since their VPTTs are similar to physiological temperatures. But pH-responsivity can also be highly advantageous for biological applications. For example, the different pH-values of tumor cells can be exploited for targeted drug release when employing pH-responsive microgels as drug carriers.[140]
In biocatalysis, the aqueous micro-environment of a microgel can help to protect enzymatic activity from potentially detrimental exposure to other solvents.[139] Moreover, the triggered collapse can lead to a macroscopic phase separation and thus a convenient purification of products without the necessity of damaging excess energies.[138] Other investigated applications of microgels include tissue regeneration[133,141] or targeted enzyme inhibition.[142]
In this work, PVCL microgels are investigated. In particular, it is attempted to achieve visualization of bond scission in Chapter 3. The microgels contain mechanofluorophores (see also Section 2.6.5) as crosslinkers, which are activated *ex-situ* via ultrasonication. They are characterized spectrally and with dynamic light scattering (DLS), and ultimately imaged with FLIM.

2.6.5 Mechanophores

Mechanophores are compounds that convert mechanical forces into chemical reactions, usually by reversible or irreversible cleavage of a mechanically labile bond.[143] They have attracted a great deal of recent scientific attention, especially in regard to the study of mechanical stress and bond scission in polymers.[49,50,61,62,143–152] To that purpose, mechanophores are incorporated in polymers, for example as crosslinkers[50,62,144,152] or in the form of microcapsules that rupture to release reporter dyes or healing agents.[143,153] Potential applications range from simple warning signs of material failure to autonomous materials with self-healing capabilities[143] or even targeted drug release using mild stimuli such as ultrasound.[154]
Although every compound which is chemically responsive to mechanical forces is per definition a mechanophore, the greatest research focus lies on mechanochromic materials. These are mechanophores which alter their spectroscopic characteristics, i.e., their absorption and/or emission, upon mechanical activation.[143] The most important class of mechanochromic compounds are mechanofluorophores which, as the name implies, exhibit shifts of their fluorescence upon the application of mechanical force. Mechanofluorophores are particularly interesting in their role as optical force probes (OFPs).[149] They unite the optical advantages of FM (see Section 2.3) with the unique sensing of mechanical stress of mechanophores. That is, they offer the possibility of highly sensitive and selective detection and even visualization of mechanical failure.[61] However, the specificity of most OFPs is somewhat reduced by the fact that their activation can also be achieved by heat or light.[143]
Among the most relevant motifs for mechano(fluoro)phores are spiropyrans,[150,151] Diels–Alder adducts of anthracene,[50,61] dioxetane,[155] latent persistent radicals[147], excimer formation or dissociation[145]

and disulfides with carbonate moieties in β-position.[148,154] These motifs all differ in the nature of their chemical and optical response to mechanical forces. However, they are similar in that the shift of absorption and emission is in all cases related to the scission of mechanolabile bonds, inter- and intramolecular. In the following, the chemical transformation of Diels-Alder adducts of anthracene is explained in greater detail, since this type of mechanofluorophore is most relevant to this work (see Chapter 3). Anthracene consists of three conjugated aromatic rings. It is possible to form a Diels–Alder adduct with one of the aromatic rings using an electrophilic dienophile such as maleimide. The π-electron conjugation of the resulting Diels–Alder adduct is disrupted, shifting the absorption and emission spectrum further into the UV region. Incorporation of the motif into a polymer becomes possible by suitable substitutents on the anthracene and the dienophile. Mechanical force is exerted onto the mechanofluorophore via any (opposing) forces acting on the crosslinked polymer strands. The application of mechanical force, heat, or exposure to excessive light can initiate a retro-Diels–Alder reaction restoring the conjugated π-system of the anthracene unit.[49] Theoretically, the reaction is reversible and, under heat, the Diels–Alder adduct might form again. In practice, when incorporating the motif as a crosslinker in a polymer, it is highly unlikely for the two reactants to come in close enough proximity for a reaction again. Hence, the activation of the mechanofluorophore can be considered irreversible for all purposes.

There exist different methods to exert the force necessary for the activation of mechanophores. For solid-state polymeric systems, compression and tension,[156] shear loading,[157] laser-induced stress waves,[158] or solvent ingress[159] are in common use. In contrast, polymer solutions are usually ultrasonicated to induce cavitation.[160] For polymers at interfaces, more subtle methods like AFM are more favorable.[161]

In Chapter 3 of this work, a special multicolor mechanofluorophore[50] is investigated in closer detail in the context of the visualization of bond scission. The mechanofluorophore in question is a Diels–Alder adduct of anthracene and maleimide and is employed as crosslinker in microgels and polymer films. It is attempted to increase the achievable resolution and information content, in particular by selective activation of the mechanofluorophores by means of AFM. The visualization is achieved with FLIM. For comparison, in some measurements activation is performed *ex-situ*. To this end, microgel solutions are sonicated and polymer films are physically cut or compressed by different means.

3 Visualization of bond scission in polymer systems with mechanofluorophores

A reasearch assignment on combined AFM *and* FLIM *measurements of mechanofluorophore-crosslinked microgels and polymer films, conducted by Christian Metzen, was supervised by the author and contributes to this chapter (Section 3.3).*
All samples (microgels, polymer films, reference compounds) were synthesized and provided by the Göstl group.

3.1 Introduction

Nothing lasts forever. No matter how much the chemical, thermal and mechanical resistance and durability of polymer systems is going to be improved, eventual material failure is inevitable. Typically, material failure is only detected when it is already too late. Visible breaks, tears, cracks or splits in any material are only the macroscopic symptoms of a long propagation of microscopic events that can ultimately be attributed to the scission of individual molecular bonds.[49,50,146] Early detection of these crucial molecular processes are invaluable for damage prevention.[146] One approach, for example, is to incorporate self-healing agents that are activated by the same mechanical force that induces the build-up to material failure.[143] While self-reporting or even self-healing materials might represent an obvious commercial interest, they can also be used to study the still badly understood processes that lead to material failure.
The most promising candidates in this regard are mechanofluorophores. These are molecules or molecular motifs whose optical properties, in particular the emission, are altered by the application of mechanical force (see also Section 2.6.5). The shift of (fluorescence) emission allows their use as highly sensitive optical force probes (OFPs), i.e., mechanofluorophores allow for a microscopic visualization of mechanical forces and the material response to these forces. A lot of recent research is focused on this kind of visualization of early signs of material failure. The mechano-optical response of spiropyrans covalently embedded in both elastomeric and glassy polymer strands could be observed both visually and with UV-vis spectroscopy.[150,151] Fracture of fiber-reinforced polymer composites was visualized with FLIM of a rhodamine-spirolactam employed as epoxy resin crosslinker.[144] Material degradation, i.e., the shortening of polymer strands due to bond scission, was investigated in linear and crosslinked polymers[61], hydrogels[152] and microgels[62] with π-extended anthracene mechanophores. Despite the spectroscopic and even microscopic visualization in all given examples, the resolution is of yet restricted to diffraction limited confocal imaging. A strategy for super-resolution measurements proves to be challenging.[149]
In this work, it is striven to improve the resolution that can be achieved with OFPs in polymer systems. In

particular, this work is directly based on the results presented by *Baumann et al.*[50] One of the developed multicolor mechanofluorophores based on π-extended anthracene is used throughout all measurements presented in this chapter. The mechanophore, henceforth called benzo thiadiazole (BTD) according to its central moiety determining its optical properties, is used as a crosslinker in poly(hexyl methacrylate) (PHMA) films and also as crosslinker in poly(vinyl caprolactam) (PVCL) microgels. Mechanical activation is performed with a variety of methods. In first experiments, the microgels are activated *ex-situ* with ultrasonication. The polymer films are activated by manual cutting or unspecific application of local pressure. The spectral changes are observed with FLIM (see Section 3.2 for the reasoning of using FLIM instead of conventional confocal microscopy). Ultimately, it is hoped that activation can be achieved quasi-selectively with AFM. Ideally, this leads to individual activated mechanofluorophores which can be located with greater precision due to the spatial separation of individual emitters. This way, it is aimed for an improved resolution exceeding confocal diffraction limited imaging (see also Section 2.3.5 for the general requirements of super-resolution techniques). It has been shown before that spatially selective activation of π-extended anthracene mechanophores with AFM is possible.[161] However, the mechanophore was located at the interface between polymer brushes and silica wafer surfaces and fluorescence was recorded comparatively crudely.[161] A similar concept in polymer systems has not yet been investigated as extensively. The effect of the mechanical force induced by the AFM tip has been generally neglected when employing AFM for structure investigations.[62] A potential SRFM approach based on the selective activation of mechanophores with AFM has not yet been reported.
In the following, the employed mechanoresponsive dye system and the investigated microgels are characterized in greater detail (Section 3.2). A brief general introduction of the investigated polymer systems is given in Section 3.3.1. (Combined) FLIM and AFM measurements are presented in Section 3.3. A summary and conclusion of Chapter 3 is given in Section 3.4.

3.2 Characterization of the system

Before microscopy measurements can be attempted, it is obligatory to understand the investigated dye and polymer system in greater detail. To this end, reference compounds for the unactivated and the activated BTD mechanophore were synthesized. The unactivated reference is the actual crosslinker and ATRP initiator used in the polymerization of the PHMA films and PVCL microgels, whereas the activated reference shows some minor structural differences which are not expected to significantly alter the optical properties. The structures of the reference compounds are shown in Figure 3.1. To remain consistent with the nomenclature introduced in the literature,[50] the unactivated reference compound is henceforth called “BTD initiator”, or depending on the context, “BTD crosslinker” or “unactivated BTD”. The activated reference compound is simply termed “BTD reference” or “activated BTD”. The terms “activated and unactivated BTD” are primarily used for the mechanofluorophore covalently embedded in a polymer system. The polymer systems are termed “unactivated / activated (BTD) microgels” and “BTD-PHMA networks” (all introduced technical terms are summarized in the Glossary 8.5). Absorption and emission spectra, as well as fluorescence quantum yields and lifetimes of both reference compounds are compared in Section 3.2.1. Moreover, the photobleaching behavior is briefly investigated. An additional, preliminary characterization of the investigated microgels is presented in

Section 3.2.2. This includes DLS measurements and comparative Nile-Red PAINT SRFM images (see Section 6.1.1 for additional scientific background on DLS and Section 2.3.5 for scientific background on PAINT). To grant a sense of coherence, all data related to the unactivated BTD is coded in purple, whereas all data related to the activated BTD is coded in bright blue, if feasible.

3.2.1 Characterization of the mechanofluorophores

The absorption and emission spectra in toluene, as well as the structures of the two reference compounds, unactivated BTD initiator and activated BTD reference, are shown in Figure 3.1. Excitation wavelengths of 380 nm and 488 nm were chosen, respectively, since these were close to the respective local absorption maxima and also represent common available laser wavelengths (see Section 3.3). Fluorescence lifetimes are summarized in Table 3.1. TCSPC curves can be found in the appendix (Section 7.2.1). Fluorescence quantum yields and photobleaching quantum yields are summarized in Table 3.2. Experimental details of spectroscopic and lifetime measurements can be found in Sections 6.3 and 6.5.1.

The absorption of the BTD initiator dominates in the UV region between 300 – 400 nm. Two local maxima are observed at 325 nm and 382 nm. Above 400 nm, absorption decreases rapidly. However, weak absorption is still observed until approximately 525 nm. The most red-shifted local absorption maximum of the BTD reference is at 465 nm. Above 500 nm absorption also decreases rapidly. The absorption of the BTD reference extends into the UV region, too. The absorption coefficient between 325 – 400 nm is very similar for both reference compounds. In particular, small local maxima are observed at 330 nm and 372 nm for the BTD reference. Both wavelength and absorptivity are comparable to the local maxima of the BTD initiator. This indicates that these absorption bands are related to the central BTD moiety, whereas the absorption band around the maximum at 465 nm is related to the extended π-system of the anthracene moiety. Likewise, the increased absorptivity below 325 nm is likely related to the restored electronic conjugation. It is estimated that in the unactivated BTD the anthracene-maleimide Diels–Alder adduct prevents efficient absorption around 300 nm.

The emission spectra of both compounds differ even more strongly than the absorption spectra. The unactivated BTD exhibits fluorescence emission between approximately 400 – 600 nm at 380 nm excitation with a maximum at 447 nm. The activated BTD, in contrast, is notably red-shifted with fluorescence emission between approximately 500 – 750 nm at 488 nm excitation and a maximum at 555 nm. No noteworthy fluorescence is observed for the BTD initiator at 488 nm excitation with the used spectrometer (see also Section 6.3.2). Thus, fluorescence emission of unactivated and activated BTD appears to be reasonably separable in the planned microscopy measurements with a combination of suitable filters and excitation wavelengths. However, the fluorescence quantum yield decreases by about an order of magnitude upon activation. Using the reference method (see Section 2.1), quantum yields of 73% and 7% were determined for the BTD initiator and the BTD reference in acetonitrile (MeCN), respectively. The determined quantum yields are reasonably similar to the literature values in MeCN (84% and 9%).[50] In this context, it has to be noted that the emission of the BTD reference appears to be highly sensitive to the environment, i.e., the solvent. The emission maximum of the BTD reference in MeCN is red-shifted by about 60 nm compared to the emission in toluene (see Figure 3.2). A strong dependency of the fluorescence quantum yield on the solvent has been reported, too.[50] In comparison, solvent-dependent spectral shifts and changes of the quantum yield of the BTD initiator are insignificant.

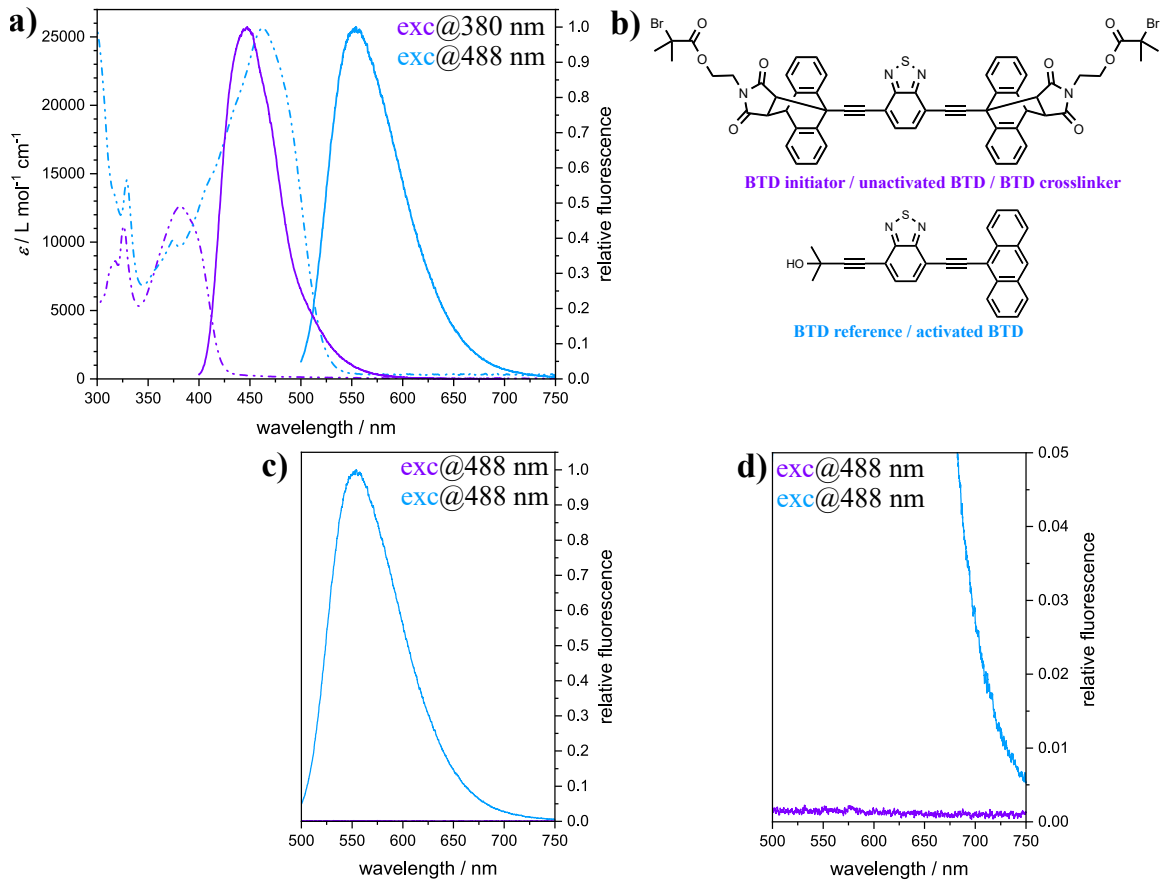

Figure 3.1: (**a**) Absorption (dotted-dashed lines) and normalized emission spectra (solid lines) of the BTD initiator (violet, 380 nm excitation) and the BTD reference (blue, 488 nm excitation) in toluene. Both emission spectra are normalized to their maximum intensity at 447 nm and 555 nm, respectively. The absorption spectra are scaled to the absorption coefficients determined at the local absorption maxima at 382 nm and 465 nm, respectively. (**b**) Structure of the unactivated (purple, BTD initiator / crosslinker) and activated (blue, BTD reference) reference compounds. (**c**) Comparative emission spectra of both reference compounds at 488 nm excitation. The emission intensity of both spectra is given relative to the maximum of the BTD reference at 555 nm. (**d**) Close-up of (**c**).

Fluorescence lifetimes were determined for both reference compounds at 488 nm excitation. FLIM measurements are all performed at 488 nm excitation, too (see Section 3.3). The absorption coefficient of the BTD initiator at 488 nm is very low, but not necessarily zero. Likewise, emission is too weak to be measured with the used spectrometer, but likely existent. The lifetimes are measured at this excitation wavelength to emphasize the expected background signal in the FLIM measurements. Technical limitations of the used setup (see also Section 6.5.1) prevented the determination of comparative lifetimes of the unactivated BTD with more suitable UV excitation. Consequently, the determined lifetimes, especially of the BTD initiator in Table 3.1, should be treated with caution. Lifetimes were determined once in toluene and once in a rigid polymer matrix (poly styrene (PS)) to grant a better comparability to the FLIM measurements both in microgels and PHMA networks. The TCSPC curves can be found in the appendix (Figure 7.13 – 7.16).

The BTD reference in toluene has two distinct lifetime components, $\tau_1 = 5.19$ ns and $\tau_2 = 1.6$ ns, in a ratio of approximately 15:2. Likewise, in PS one long and short lifetime component, $\tau_1 = 6.9$ ns

Table 3.1: Fluorescence lifetimes τ of the BTD initiator and the BTD reference in toluene and in thin PS films. Lifetimes were determined at 488 nm excitation in a spectral window from 532 – 715 nm. The relative amplitudes of the fluorescence lifetime components τ_1, τ_2 and τ_3 are mentioned in square brackets after the lifetimes. The errors of the lifetime components are always in the order of magnitude of the last decimal place specified.

Compound	system	τ_1 / ns	τ_2 / ns	τ_3 / ns
BTD initiator	toluene	6.1 [14%]	2.0 [40%]	0.52 [46%]
BTD initiator	PS	5.6 [20%]	2.5 [59%]	0.38 [21%]
BTD reference	toluene	5.19 [87%]	1.6 [13%]	-
BTD reference	PS	6.9 [62%]	1.1 [38%]	-

and $\tau_2 = 1.1$ ns, are found, albeit in a ratio of approximately 3:2. The elongation of the main lifetime component, τ_1, is assumed to be related to the more restricted rotational movement and conformational freedom of the dye in the more rigid polymer matrix. The long lifetime component matches well to the reported lifetime of anthracene in comparable solvents, up to the dependency on the viscosity.[162] The shorter lifetime component, τ_2, can be considered unchanged in magnitude within the accuracy of the measurement. The origin of the shorter lifetime component is not entirely clear, but is likely related to the central BTD moiety of the dye.

For the BTD initiator in toluene, three lifetime components, $\tau_1 = 6.1$ ns [14%], $\tau_2 = 2.0$ ns [40%] and $\tau_3 = 0.52$ ns [46%], are measured. Similar lifetime components in a similar ratio are observed in PS ($\tau_1 = 5.6$ ns [20%], $\tau_2 = 2.5$ ns [59%] and $\tau_3 = 0.38$ ns [21%]). It is estimated that the shortest lifetime component τ_3 is in both cases a measurement artifact most likely related to a reflection of the excitation laser (compare Figure 7.14). The other two lifetime components are similar to the lifetime components of the BTD reference within the accuracy of the measurement. It is assumed that a tiny fraction of the BTD initiator has been activated by excessive exposure to light or local heat due to the laser (see also Section 2.6.5). It has been shown that both stimuli can initiate the required retro-Diels–Alder reaction.[49] The unspecific activation can still be considered insignificant compared to targeted mechanical activation. In light of the results presented in Section 3.3, it has to be noted that it is also possible that the observed lifetime components of the BTD initiator are valid characteristics of the unactivated BTD. Due to the inefficient excitation of the BTD initiator at 488 nm, however, neither the determined magnitudes nor the relative amplitudes can be considered reliable.

Photostability of the mechanofluorophores

One of the most essential demands on a dye for SRFM is good photostability (see also Section 2.3.5). Only with sufficient photostability can a reasonable amount of photons be collected from a single emitter, and thus a good localization accuracy is reached (compare equation (2.21)). Not much is known about the comparatively new dyes investigated here in this regard. Studies on structurally related compounds like 9,10-bis(phenylethynyl)anthracene determined an extraordinarily good photostability.[163] Still, it is obligatory to test the novel mechanofluorophore dye system, too. To this end, the BTD initiator and the BTD reference were dissolved in MeCN and irradiated with light of wavelengths close to their respective absorption maxima. The BTD initiator was irradiated with a 365 nm LED at 400 $\mathrm{W\,m^{-2}}$. The BTD

reference was irradiated with a 455 nm LED at 300 $\mathrm{W\,m^{-2}}$. The irradiation was interrupted in arbitrary time intervals to measure absorption and emission spectra. The detailed experimental setup is presented in Section 6.6. The absorption and emission spectra of the two reference compounds (see also figure 3.1) at different irradiation times, as well as the temporal evolution of the absorption and emission maxima are shown in Figure 3.2. A second measurement series was performed for both reference compounds with a 400 nm LED at 210 $\mathrm{W\,m^{-2}}$. At this wavelength, the absorption coefficients of the BTD initiator and reference are approximately equal, granting optimal comparability. The comparative measurement at 400 nm irradiation is shown in the appendix in Figure 7.2. The photobleaching quantum yields determined from the different irradiation experiments are compared in Table 3.2.

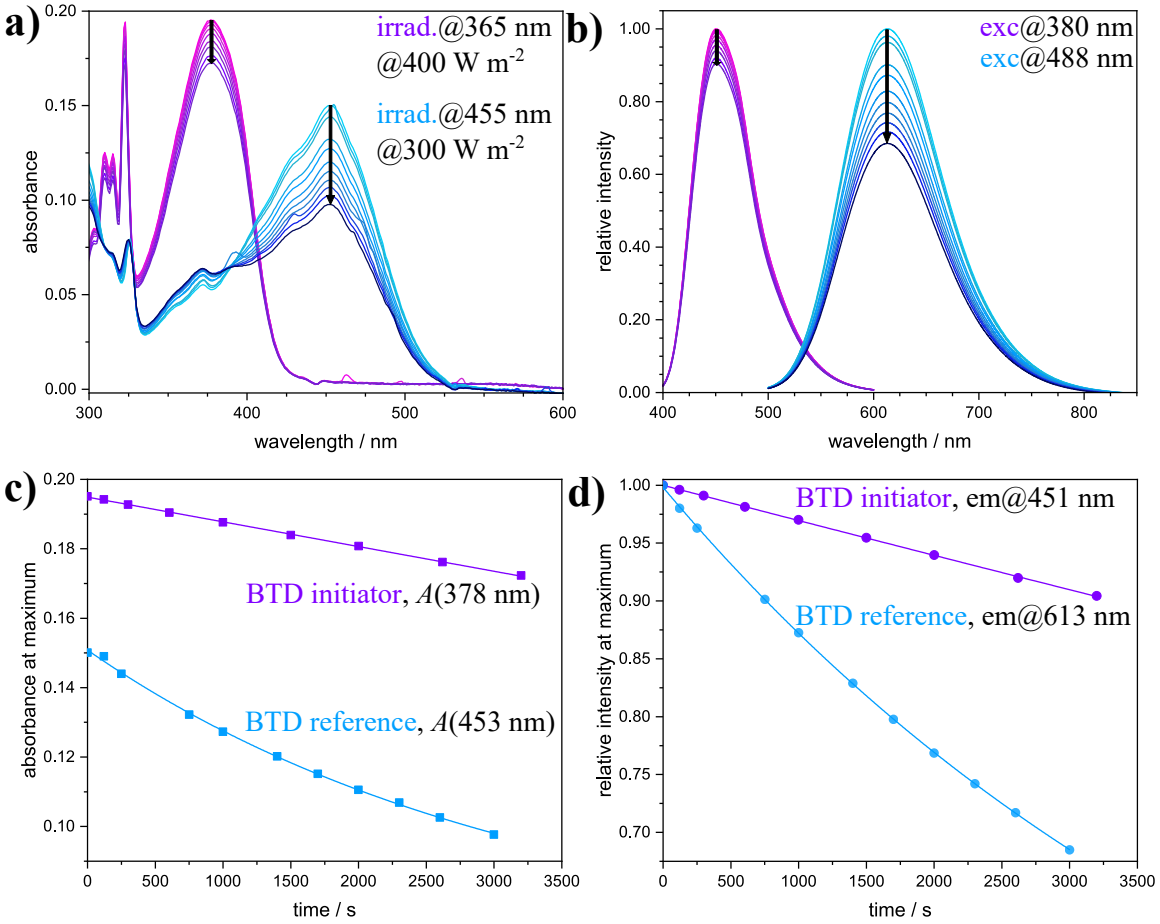

Figure 3.2: Spectral changes of BTD initiator and BTD reference in MeCN during selected irradiation times with a 365 nm LED @ 400 $\mathrm{W\,m^{-2}}$ and a 455 nm LED @ 300 $\mathrm{W\,m^{-2}}$, respectively. Changes of (**a**) absorption spectra and (**b**) relative emission spectra at 380 nm and 488 nm excitation for the BTD initiator (light to dark violet) and the BTD reference (light to dark blue) respectively. The black arrows indicate the changes with increasing irradiation time. Emission intensity is given relative to the maximum intensity of the respective compound at 0 s irradiation. (**c**) Temporal evolution of the absorbance at the different wavelengths of the (local) maxima shown in (**a**). (**d**) Temporal evolution of the relative fluorescence intensities at the different wavelengths of the (local) maxima depicted in (**b**). All solid lines in (**c**) and (**d**) represent fits with single exponential decay functions. The colors correspond to the primary colors of the color gradients used for the spectra of the different compounds in (**a**) and (**b**).

The absorbance A at the absorption maximum at 453 nm decreases by about 33% for the BTD reference in 3000 s of irradiation with 455 nm at 300 $\mathrm{W\,m^{-2}}$. Likewise, the relative emission intensity F at

the emission maximum also decreases by about 33%. Both decreases are well described with single exponential decay functions with comparable time constants τ ($X(t) = X_0 + \Delta X[1 - \exp(-t/\tau)]$, with $X = A, F$ and $\tau_A = 3200 \pm 300$ s and $\tau_F = 5000 \pm 200$ s, respectively). This indicates (quasi-) first order kinetics of the photodegradation reaction. It is estimated that both the triplet state of the dye and the concentration of oxygen play vital roles in the reaction. In particular, the triplet state produces reactive singlet oxygen, which reacts efficiently with the anthracene moiety to form an endoperoxide.[163] Despite the reaction conditions (closed cuvette), it is assumed that oxygen is present in excess. Furthermore, it is assumed that the rate limiting step is the generation of singlet oxygen and not the subsequent photodegradation reaction. Therefore, the limiting factor is the presence of the excited triplet states, resulting in quasi-first order kinetics. The absorption and emission maxima of the BTD initiator at 378 nm and 451 nm, respectively, decrease by about 10% in a similar time interval (3200 s) of irradiation with 365 nm at 400 $\mathrm{W\,m^{-2}}$. The decreases are reasonably well described by single exponential decays. The notable drop of absorption and emission indicates a low photostability. In comparable experiments with the commercial SRFM dyes ATTO565 and ATTO647N, decreases are significantly less pronounced (compare Section 4.4). To quantify the assessment, photobleaching quantum yields Φ_b are calculated. The theoretical derivation is presented in the following. An example calculation is given for the 455 nm irradiation experiment of the BTD reference. Analogous to the fluorescence quantum yield, the photobleaching quantum yield is formally defined according to equation (3.1).

$$\Phi_\mathrm{b} = \frac{\text{number of reacted molecules}}{\text{number of absorbed photons}} = \frac{N_\mathrm{r}}{N_\mathrm{ph}} \tag{3.1}$$

Thus, reasonable estimates for the number of reacted molecules N_r and the number of absorbed photons N_ph have to be found. N_ph can be estimated from the absorbed power density P_a of the LED and the irradiation time. The power density is measured once behind the cuvette filled with solvent ($P_{a,0} = 294.5\ \mathrm{W\,m^{-2}}$) and at every time t behind the sample ($P_{a,s}(t)$, $P_{a,s}(750\ \mathrm{s}) = 232.2\ \mathrm{W\,m^{-2}}$). The difference in measured power density $\Delta P_a = P_{a,0} - P_{a,s}(t) = 62.3\ \mathrm{W\,m^{-2}}$ corresponds to the overall absorption. However, both the BTD initiator and the BTD reference also emit fluorescence when excited with the investigated irradiation wavelengths, therefore the equivalence is not valid. Instead, the amount of absorbed light at time t is approximated by the transmission T as determined by the measured absorbance at the irradiation wavelength $\lambda_\mathrm{irrad.} = 455$ nm, i.e., $T = 10^{-A(t,\lambda_\mathrm{irrad.})}$, $T = 10^{-A(750\ \mathrm{s},455\ \mathrm{nm})} = 10^{-0.131} = 0.261$. Since the absorbance decreases as the reaction proceeds, the transmission increases over time. To account for the decrease of absorbance during the irradiation, the average of the absorbance $\bar{A}(t_1, t_2, \lambda_\mathrm{irrad.}) = 0.137$ at times $t_1 = 250$ s and $t_2 = 750$ s is used for the calculation. The absorbed power density P_a is thus calculated according to equation (3.2).

$$P_a = P_{a,0}(1 - T) \tag{3.2}$$

$$\begin{aligned} P_a &= P_{a,0}(1 - 10^{-\bar{A}(t_1,t_2,\lambda_\mathrm{irrad.})}) \\ &= 294.5\ \mathrm{W\,m^{-2}}(1 - 10^{-0.137}) \\ &= 79.8\ \mathrm{W\,m^{-2}} \end{aligned} \tag{3.3}$$

The exemplary value is reasonably similar to the measured difference, ΔP_a, which is slightly underestimated due to the contribution of the fluorescence emission to the value $P_{a,s}(t)$. Multiplication of P_a with the irradiation time $\Delta t = t_2 - t_1 = 750\text{ s} - 250\text{ s} = 500\text{ s}$ between two spectral measurements and the irradiation area $a = 1\text{ cm}^2$ yields the overall absorbed energy E_{abs} in the observed time interval. Dividing the overall absorbed energy by the energy of a single photon, $E = h\nu = hc/\lambda_{\text{irrad.}} = 4.37 \times 10^{-19}\text{ J}$, then yields the number of absorbed photons in the time interval Δt.

$$\begin{aligned} N_{\text{ph}} &= \frac{P_a \cdot \Delta t \cdot a}{E_{\text{abs}}} = \frac{P_{a,0}(1 - 10^{-A(t,\lambda)}) \cdot \Delta t \cdot a}{h \cdot \frac{c}{\lambda_{\text{irrad.}}}} \\ &= \frac{79.8\text{ W m}^{-2} \cdot 500\text{ s} \cdot 0.0001\text{ m}^2}{4.37 \times 10^{-19}\text{ J}} \\ &= 9.1 \times 10^{18} \end{aligned} \tag{3.4}$$

The number of reacted molecules, N_{r}, can be approximated from the absorption spectrum under two conditions. One, the absorption coefficient of the sample is known and does not change upon irradiation. Second, the product of the photobleaching reaction does not absorb at the evaluated wavelength, i.e., it does not contribute to the measured absorbance. The concentration at each measured time t can then be determined with the Lambert–Beer law (2.9). To this end, the absorption coefficients of the BTD initiator and the BTD reference were determined in MeCN at 378 nm ($\varepsilon(378\text{ nm}) = 12600\text{ L mol}^{-1}\text{ cm}^{-1}$) and 453 nm ($\varepsilon(453\text{ nm}) = 21600\text{ L mol}^{-1}\text{ cm}^{-1}$), respectively. The determination of the absorption coefficients with the Lambert-Beer law (2.9) is shown in Figure 7.1 in the appendix, the calculated absorption coefficients ε are listed in Table 3.2. It is assumed that the photobleaching products do not contribute significantly to the absorbance values at the absorption maxima. The difference $\Delta A = A(t_1) - A(t_2) = A(250\text{ s}) - A(750\text{ s}) = 0.143 - 0.131 = 0.012$ of the absorbance measured at two subsequent times then corresponds to the concentration c_r of reacted molecules according to the Lambert-Beer law (2.9) with a pathway of $d = 1.0\text{ cm}$. Since the reaction volume $V = 3\text{ mL}$ is known and constant, the concentration can be transformed into the amount of substance n. Multiplication with the Avogadro number N_A yields the number of reacting molecules N_{r} in the time interval Δt.

$$N_{\text{r}} = n \cdot N_A = c_r \cdot V \cdot N_A \tag{3.5}$$

$$\begin{aligned} N_{\text{r}} &= \frac{\Delta A}{\varepsilon \cdot d} \cdot V \cdot N_A \\ &= \frac{0.012}{21600\text{ L mol}^{-1}\text{ cm}^{-1} \cdot 1.0\text{ cm}} \cdot 0.003\text{ L} \cdot 6.022 \times 10^{23}\text{mol}^{-1} \\ &= 1.0 \times 10^{15} \end{aligned} \tag{3.6}$$

Consequently, the photobleaching quantum yield in the specific time interval Δt equates to:

$$\Phi_b = \frac{N_{\text{r}}}{N_{\text{ph}}} = \frac{1.0 \times 10^{15}}{9.1 \times 10^{18}} = 1.1 \times 10^{-4}$$

The calculation can be repeated for every time interval individually. Since the actual amount of reacted molecules is compared to the actual amount of photons absorbed, the photobleaching quantum yield is theoretically independent of the dye concentration, provided that oxygen is present in excess. Likewise,

the irradiation time and the power density of the LED do not influence the calculation conceptually. In the presented example, photobleaching quantum yields from $\Phi_{b,\text{min}} = 3.73 \times 10^{-5}$ to $\Phi_{b,\text{max}} = 1.67 \times 10^{-4}$ are calculated. An average value of $\Phi_b = 0.009 \pm 0.003\%$ is obtained. All photobleaching quantum yields listed in Table 3.2 are average values calculated accordingly.

Table 3.2: Absorption coefficients ε, fluorescence quantum yields Φ and photobleaching quantum yields Φ_b at different irradiation wavelengths $\lambda_\text{irrad.}$ of the BTD initiator and the BTD reference in MeCN. Absorption coefficients were determined according to the Lambert–Beer law at 378 nm and 453 nm for the BTD initiator and the BTD reference, respectively. Fluorescence quantum yields were determined at 366 nm and 488 nm excitation in MeCN relative to the standard Rhodamine 6G in ethanol ($\Phi_s = 94\%$)[67] according to equation (2.4).

Compound	ε / L mol^{-1} cm^{-1}	Φ / %	$\lambda_\text{irrad.}$ / nm	Φ_b / %	$\sigma(\Phi_\text{b})$ / %
BTD initiator	12600	73	365	0.0045	±0.0003
BTD initiator	12600	73	400	0.008	±0.003
BTD reference	21600	7	400	0.014	±0.002
BTD reference	21600	7	455	0.009	±0.003

The method is subject to significant uncertainties. The reliability of nearly every measured value, apart from the irradiation time, is questionable, including the exact irradiation wavelength. The used LEDs have a typical spectral width of about 15 nm. Absorption measurements are prone to errors and the measured power density is subject to fluctuations. Furthermore, several assumptions and inaccurate average values are included in the calculation. Nevertheless, a reasonable accuracy is reached overall. The relative standard deviation of about 33% indicates the validity of the method. Given the mentioned uncertainties, the error is justifiable. Within the accuracy of the measurement, the same photobleaching quantum yield is obtained for the BTD reference at 400 nm excitation ($\Phi_b = 0.014\% \pm 0.002\%$). Likewise, reasonably similar photobleaching quantum yields are obtained for the BTD initiator at 365 nm and 400 nm excitation ($\Phi_b = 0.0045\% \pm 0.0003\%$ and $\Phi_b = 0.008\% \pm 0.003\%$). This, too, indicates the validity of the method. The determined photobleaching quantum yields are several orders of magnitude higher than those reported in the literature for similar compounds.[163] It should be noted that the method, minor, yet significant, structural aspects and even the definition of the photobleaching quantum yield differ from what has been presented here. Therefore, the comparability is limited.

The precision of the determined photobleaching quantum yields should be treated with caution. Semi-quantitative conclusions, however, are possible. For one, it seems that the BTD initiator is slightly more photostable than the BTD reference. The irradiation experiments shown in Figure 3.2 at first make it appear as if the initiator is substantially less prone to photobleaching. The slower apparent photobleaching rate, however, is most likely related to the less efficient absorption of the initiator, i.e., the absorption coefficient at the investigated irradiation wavelengths is significantly smaller than the respective absorption coefficient of the BTD reference. Second, both dyes are several orders of magnitude less photostable than typical high performance dyes. At 365 nm irradiation, no photobleaching whatsoever is observed for either ATTO565 or ATTO647N under comparable conditions (see Section 4.4). At prolonged 645 nm irradiation under otherwise reasonably comparable conditions, the photobleaching quantum yield of ATTO647N calculated with equations (3.1) – (3.5) equates to $\Phi_b(\text{ATTO647N}) = 1.0 \pm 0.6 \times 10^{-6}\%$, thus more than three orders of magnitude lower than of either

BTD reference compound.

The low fluorescence quantum yield and comparatively high photobleaching quantum yield of the activated BTD are severe hindrances for the intended SRFM measurements with the dye system, even if activation of individual mechanofluorophores with AFM turns out possible as a means of quasi-blinking. The low fluorescence quantum yield indicates that only few photons are emitted per excitation cycle, leading to a low achievable localization accuracy even if single emitters can be localized (see equation (2.21)). The high photobleaching quantum yield limits the total number of excitation cycles. Whereas dyes like ATTO647N can be excited up to several million times to yield potentially millions of photons overall, the activated BTD can be statistically excited less than one hundred thousand times to yield less than ten thousand photons overall. Typically, several hundreds of photons are required to localize a single emitter with reasonable accuracy in a single frame of a measurement video. Given the low performance of the dye system, a substantial increase in resolution seems unfeasible.
However, it might still be possible to increase the information content generated in FM measurements. The lifetime measurements imply a reasonably sensitive detection of the mechanical activation via the fluorescence lifetimes. In particular, the long lifetime component of the π-extended anthracene moiety appears to be a clear indicator of bond scission. While the low emission and high photobleaching rate prevent good localization accuracy, they still grant reasonably accurate determination of lifetimes. Even if no true SRFM is possible, sophisticated combined FLIM and AFM measurements might still yield valuable insights that surpass simple (spectrally resolved) confocal imaging. Disadvantageously, the used setup can only be employed for FLIM of the activated BTD. No efficient UV excitation for the unactivated BTD is available and no comparative FLIM images can be generated. The multicolor properties of the mechanofluorophore are thus not fully realized in the microscopy measurements in Section 3.3.

3.2.2 Characterization of the microgels

Apart from characterization of the dye system, it is also important to characterize the investigated polymer system, in particular the BTD microgels. Two different, albeit similar, microgel samples are investigated in Section 3.3. In the following, these microgel samples are further characterized with DLS (Figure 3.3), absorption and fluorescence spectroscopy (Figure 3.4). DLS is a standard technique for the size determination of colloidal particles like microgels. Most conveniently, the volume phase transition temperature (VPTT) can be observed directly (see also Section 2.6.4). Additional scientific background on DLS is given in Section 6.1.1, the experimental setup is described in Section 6.9. Furthermore, comparative PAINT measurements of BTD microgels are shown (Figure 3.5).
The two microgel samples differ essentially only in their exact composition. Microgel sample **A** consists only of PVCL. BTD crosslinker was added in a concentration of about 1 wt% of the total monomer mass. Microgel sample **B** has the same amount and type of crosslinker, but 20 wt% of the monomer mass has been replaced by N-vinyl-imidazole (VIM) as co-monomer. The compositions of microgels **A** and **B** are also noted in the Glossary 8.5. A fraction of both samples was activated *ex-situ* by 30 s of ultrasonication. Comparative PAINT measurements were performed for a different microgel sample that was synthesized equivalently to microgels **A**.
The LCST of PVCL, and thus the VPTT of the microgels investigated here, is typically around 32 °C.[135]

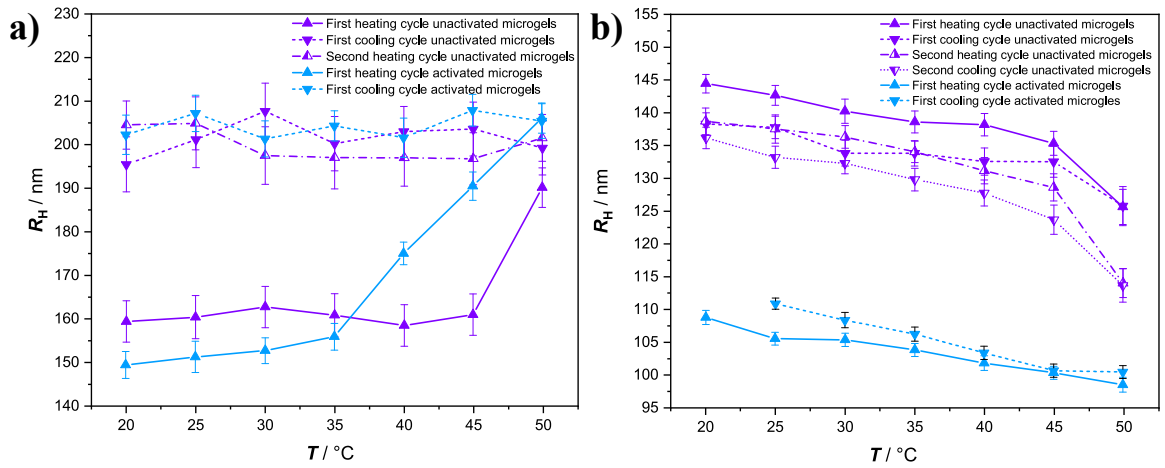

Figure 3.3: Hydrodynamic radii R_H determined via DLS at various temperatures for unactivated BTD microgels (violet) and activated BTD microgels (blue). Upright triangles denote heating cycles (increasing temperature), downright triangles signify cooling cycles (decreasing temperature). The microgels in (**a**) are synthesized with the following ratios by mass: 100% PVCL (monomer), 1.0% of the total monomer mass BTD crosslinker (microgels **A**). The microgels in (**b**) are synthesized with the following ratios by mass: 80% PVCL (monomer), 20% VIM (co-monomer), 1.0% of the total monomer mass BTD crosslinker (microgels **B**). Activation was in both cases achieved with 30 s of ultrasonication.

However, neither microgels **A** nor **B** show the expected thermoresponsive behavior, neither before nor after activation. No definitive collapse of the microgels is observed between 20 – 50 °C. There are some indications that microgels **B** might undergo a phase transition between 45 – 50 °C, but the data is inconclusive and DLS data at higher temperatures is required to confirm the assessment.

Nevertheless, both microgels **A** and **B** show an unexpected form of thermoresponsiveness. At temperatures between 20 – 35 °C, the unactivated and the activated microgels **A** are almost identical in size ($R_H = 160$ nm and $R_H = 150$ nm, respectively). No size decrease is observed around the expected VPTT. Instead, the hydrodynamic radius increases abruptly. The increase is observed above 35 °C and 45 °C for the activated and the unactivated microgels **A**, respectively. At 50 °C, the hydrodynamic radii of both activated and unactivated microgels **A** reach their apparent maxima of 200 nm. It cannot be stated if the hydrodynamic radius of the microgels **A** increases further at higher temperatures. However, the changes appear to be irreversible. The sizes of microgels **A** remain unchanged within the accuracy of the measurement, even upon cooling down to 20 °C again or upon a second heating cycle to 50 °C. A similar increase in size above the expected VPTT has been reported before for comparable mechanophore microgels after activation.[62] The behavior was assigned to the precipitation of fragmented polymer chains above the LCST. After dialysis, regular thermoresponsive behavior was regained. However, neither a comparable behavior was reported for unactivated microgels, nor the size increase was irreversible, and, upon cooling below the VPTT, the approximate original sizes were restored.[62] It is not known if microgels **A** were purified again after activation.

The origin of the size increase of microgels **A** is not clear. It might indicate irreversible aggregation of the microgels or of microgels and cleaved polymer strands, or a temperature-dependent activation of the BTD crosslinker. A (partial) collapse induced activation is also fathomable. Aggregation seems to be the less likely explanation, as the increase of the hydrodynamic radius is only about 33%. Although microgels can interpenetrate each other quite severely depending on particle softness, internal crosslinker

density distribution and temperature,[164] an even bigger increase in average particle size is expected upon aggregation. The size increase before dialysis reported in literature corresponds to 60 – 100% at comparable hydrodynamic radii and composition of the microgels.[62] Partial thermal or collapse induced mechanical activation of unactivated BTD crosslinker can explain the size increase, provided the activated microgels **A** still contain comparable amounts of unactivated BTD crosslinker to the unactivated microgels. The similar sizes of the unactivated and activated microgels do indeed indicate that this is the case. As the crosslinker density decreases, the polymer network becomes less rigid and can potentially swell up to larger sizes. A decrease in size due to fragmentation of the network, in particular of the more loosely crosslinked corona, is also possible (see below), but not inevitable.
The thermoresponsive behavior of the microgels **B** does not fully support the hypothesis. The activated microgels **B** do not show any noteworthy thermoresponsiveness. Hydrodynamic radii between 110 – 100 nm are obtained between 20 – 50 °C. The same sizes are determined in a second measurement cycle with decreasing temperatures. A slight dependence of the hydrodynamic radius on the temperature seems to be present, but not to the amount that is expected around the VPTT of PVCL microgels.[62] Contrary to microgels **A**, the *ex-situ* activation of the microgels **B** seems to have a significant influence on the size. This is consistent with older studies. It is estimated that the microgels are partially fragmented during activation.[62] Therefore, the unactivated microgels **B** are significantly larger. Between 20 – 45 °C, hydrodynamic radii between 145 – 130 nm are determined. Again, a slight decrease of the sizes with increasing temperature is observed. At 50 °C, the hydrodynamic radius decreases down to 115 nm, at least during the second measurement cycle. It is not clear if the VIM co-monomer increases the VPTT dramatically, or if the significant size decrease of the unactivated microgels **B** between 45 – 50 °C is related to the hypothesized thermal activation of the BTD crosslinker. Studies of comparable microgels indicate an increase of the VPTT by up to 15 °C when incorporating up to 5 mol% VIM in PVCL microgels.[165,166] However, the influence at neutral pH seems to be less significant and the VPTT is only notably increased under acidic conditions.[166] The pH of the microgel solution **B** was not measured. Thermal or collapse induced mechanical activation of the BTD crosslinker, in contrast, should result in an irreversible alteration of the hydrodynamic radius. The unactivated microgels **B** appear to become smaller in subsequent measurement cycles. However, no clear irreversibility like for microgels **A** is observed. It is estimated that the results imply both an increased VPTT due to the high VIM content and partial unspecific activation of the BTD crosslinker at temperatures above $T > 45$ °C.

The (mechanical) activation of the BTD crosslinker cannot only be observed by changes of the particle size, but also by spectral changes. To this end, absorption and emission spectra are recorded of aqueous solutions of unactivated and activated microgels **B** (Figure 3.4). The DLS measurements indicate a more quantitative activation of microgels **B** compared to **A**, hence a clearer spectral response is expected. The absorption spectra of the unactivated and the activated microgels **B** solutions are similar. The local maxima around 380 nm in both spectra are estimated to be related to the absorption of unactivated BTD crosslinker. No local maximum around 450 nm corresponding to the activated BTD is observed. However, the significant increase of the absorbance below 350 nm of the activated microgels compared to the unactivated microgels indicates at least partial activation. The BTD reference also exhibited higher absorptivity in the UV region (see Figure 3.1 **a**). The absorption spectra are superimposed by scattering, hence true quantitative comparisons based on the absorption spectra are infeasible.

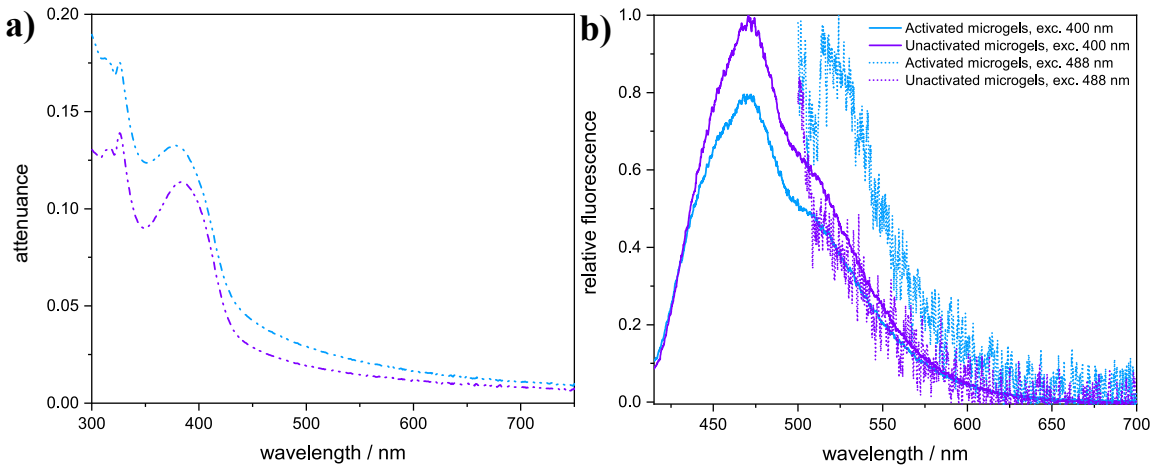

Figure 3.4: Absorption (**a**) and emission spectra (**b**) of an aqueous solution of microgels **B** before (violet) and after activation (blue). Emission spectra were once recorded at 400 nm excitation (solid lines) and once at 488 nm excitation (dotted lines). The intensity at 400 nm and at 488 nm excitation is given relative to the maximum intensity of the emission spectrum of the unactivated and the activated microgels, respectively.

At 400 nm excitation, the (normalized) emission spectra of the unactivated and the activated microgels **B** are essentially identical. The emission spectra with (local) maxima at about 470 nm are assumed to be associated to the unactivated BTD crosslinker. At 488 nm excitation, however, the two emission spectra differ significantly. Whereas the emission spectrum of the unactivated microgels matches the tailing fluorescence of the BTD crosslinker at 400 nm excitation, the emission spectrum of activated microgels exhibits a new (local) weak maximum at about 520 nm. It is assumed that the new local maximum is an indicator of the presence of activated BTD. The shift of the emission maximum compared to the BTD reference in toluene or MeCN is reasonable in light of the solvatochromic effect of the dye (see Section 3.2.1). Hence, the (partial) activation of the microgels **B** by ultrasonication is confirmed spectrally. Nevertheless, the activation is not quantitative, and a substantial amount of BTD crosslinker remains. Moreover, the spectral response is less significant than expected. In particular, the fluorescence emission of the activated BTD in aqueous environment seems to be even weaker than in organic solvents, while the fluorescence emission of the unactivated BTD at longer excitation wavelengths increases significantly.

Last, comparative Nile Red PAINT measurements are performed for unactivated and activated microgels with comparable composition to microgels **A**. The results are presented in Figure 3.5. The experimental setup is described in Section 6.7.1. The measurements are meant to emphasize how SRFM images of the activated and unactivated BTD microgels should approximately look like. It is refrained from analyzing the data more quantitatively. Likewise, the exemplary images of single microgels in Figure 3.5 **b,c** and **f,g** should be treated with caution. For a valid comparison, several microgels would have to be compared. Any differences observed here are not necessarily systematic and might be random. Widefield measurements of the microgels without Nile Red additive did not yield any interpretable results at either 378 nm or 488 nm excitation.

The structure of the microgels as imaged by PAINT is essentially as expected, especially for the unactivated microgels. Both before and after activation, the swollen microgels are spherical. The typical core-shell structure of microgels can be recognized, with a comparatively dense core and decreasing

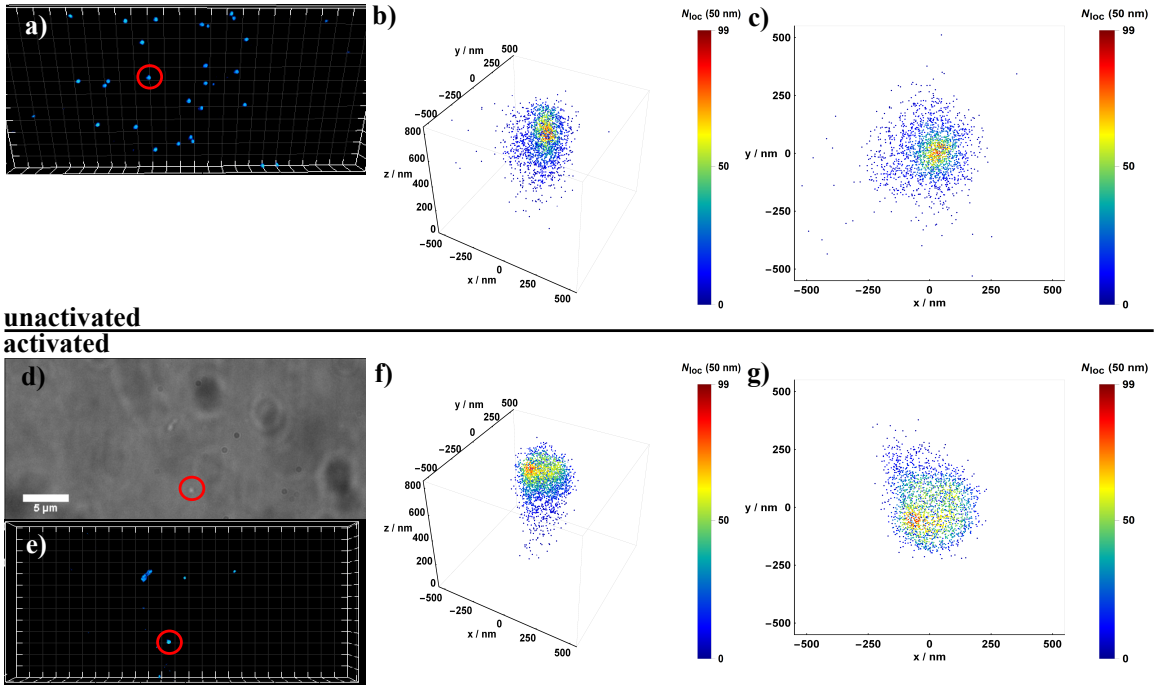

Figure 3.5: Widefield microscopy measurements of BTD microgels before (**a** – **c**) and after 30 s of sonication (**d** – **g**). A different sample with comparable composition to the ones investigated in the DLS and FLIM measurements is shown. (**a**, **e**) Fluorescence image of the field of view. The red circle marks the single microgels shown in (**b,c**) and (**f,g**), respectively. (**b,f**) 3D Nile Red PAINT images of the microgels marked in (**a,e**), respectively. 3D data was measured with astigmatism. (**c,g**) XY-projection of the microgels shown in (**b,f**), respectively. The color scale denotes the amount of localizations in a 50 nm radius around any given localization. (**d**) Brightfield image of the field of view shown in (**e**).

polymer density towards the corona. It appears as if the radial distribution of polymer density does change upon activation. The PAINT measurements indicate that the core is opening up, whereas a substantial amount of the dangling chains in the corona is cleaved. This results randomly in particles of equal size, but drastically different polymer distribution. This could explain the marginal size difference of activated and unactivated microgels **A** as observed by DLS. More measurements are required to validate the observations. Nonetheless, even this simple analysis might help to explain observations in later FLIM measurements.

Although the material failure of microgels is of great scientific interest, microgels might be too complicated a polymer system to test the performance of the mechanofluorophores in combined AFM and FLIM measurements. The absorption and emission spectra imply a worse spectral separation of unactivated and activated BTD in the aqueous environment of the polymer network than of the reference compounds in organic solvents. The fluorescence emission of especially the activated BTD seems to be weaker, too. The DLS measurements indicate irregular thermoresponsive behavior and even (partial) unspecific activation of the mechanophores by heat or by the mechanical stress during the phase transition. This could potentially result in an unfaithful visualization of bond scission. The PAINT measurements appear more promising for the investigation of structural changes in first tests. In return, the effect of bond scission on the structure and not bond scission itself is visualized.

3.3 (Combined) AFM and FLIM measurements

Despite the discouraging results obtained throughout Section 3.2, FLIM measurements of microgels **A** and **B** before and after *ex-situ* activation are performed (Section 3.3.2). In light of the results, it is refrained from combining the FLIM measurements with AFM. A combination of both techniques is used for the investigation of PHMA networks instead (Section 3.3.3). For one, the polymer system is less complex and it is assumed that fewer detrimental secondary effects occur, e.g., the collapse of the microgels. Second, PHMA networks crosslinked with BTD crosslinker have been studied before.[50] Thus, it is attempted to reproduce and improve on these results. The experimental setups for FLIM and AFM measurements can be found in Sections 6.5.2 and 6.8, respectively. The sample preparation is described in Section 6.4.4. All FLIM images were recorded at 488 nm excitation in a spectral window of 500 – 715 nm. The global TCSPC curves of all presented FLIM images can be found in the appendix in Section 7.2.2. A brief introduction on the two investigated polymer systems is given in Section 3.3.1.

3.3.1 The polymer systems - PVCL, VIM and PHMA

PVCL is a common polymer used in the synthesis of microgels. The LCST in water is close to body temperature and the polymer exhibits a good biocompatibility. Both make PVCL, and in particular PVCL microgels, a promising candidate for biomedical applications (see also Section 2.6.4 for more theory on microgels).[167] VIM is often incorporated into microgel networks to introduce an additional pH-responsiveness.[165] Quaternized VIM can introduce beneficial electrostatic interactions, e.g. for the electrostatic immobilization of negatively charged enzymes.[168] Depending on the pH and the VIM content, the VPTT of the microgels can change drastically.[166] The thermoresponsiveness of the PVCL/VIM microgels employed in this work has been investigated in Section 3.2.2. The structure of PVCL and VIM is shown in Figure 3.6 **a**. Given the potential biomedical applications, the mechanisms of material degradation of PVCL microgels are of considerable scientific interest. To this purpose, one suitable approach is the implementation of mechanophores or mechanofluorophores into the polymer network. PVCL microgels crosslinked with mechanofluorophores comparable to the BTD crosslinker employed here have been studied before.[62] However, an investigation of these polymer systems with microscopy methods is not yet well established. Studies on PVCL/VIM microgels with incorporated mechanophores are rare in general.

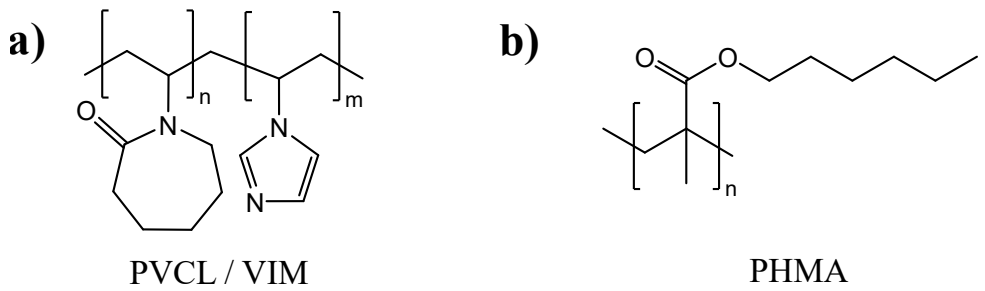

Figure 3.6: Structure of (**a**) PVCL (co-polymerized with VIM) and (**b**) PHMA. Microgels **A** have a ratio of $n : m = 1 : 0$, microgels **B** have a ratio of $n : m = 4 : 1$. Both microgels and PHMA networks in this work are crosslinked with BTD crosslinker.

PHMA is a typical polymer of the poly(alkyl methacrylate) class, comparable to the more common

poly(methyl methacrylate) (PMMA) or poly(butyl methacrylate) (PBMA) (see also Section 4.6.3). Typical applications of PHMA or its monomer include hydrophobic coatings[169] or the use as a reactive diluent to improve the viscosity of polymer adhesives.[170] The structure of PHMA is depicted in Figure 3.6 **b**. PHMA networks crosslinked with BTD crosslinker or comparable mechanoresponsive Diels–Alder adducts have been investigated before.[50,61,171] However, an investigation with FLIM and AFM is not yet well established.

3.3.2 FLIM measurements of microgels

In Figure 3.7, FLIM images of unactivated and activated microgels **A** are shown (top and bottom, respectively). The global TCSPC curves of both samples were fitted with an n-exponential tail fit with $n = 4$ (see also Figure 7.17). For the unactivated microgels **A**, the following four lifetime components were determined: $\tau_1 = 11.0$ ns [7%], $\tau_2 = 4.63$ ns [36%], $\tau_3 = 1.70$ ns [36%] and $\tau_4 = 0.63$ ns [22%]. For the activated microgels **A**, the following four lifetime components were determined: $\tau_1 = 13.0$ ns [3%], $\tau_2 = 5.15$ ns [31%], $\tau_3 = 1.87$ ns [36%] and $\tau_4 = 0.59$ ns [29%]. The determined errors of the lifetime components are always in the order of magnitude of the last decimal place specified. The lifetimes of microgels **A** and **B** before and after activation are also summarized in Table 3.3. In all cases, it is assumed that the shortest lifetime component, τ_4, is a measurement artifact as it was observed already for the BTD initiator in toluene (see Section 3.2.1 and Table 3.1). Similarly, it is estimated that the longest lifetime component, τ_1, is not directly related to the mechanofluorophore. First, the lifetime component τ_1 is significantly longer than any lifetime component observed for either BTD reference compound (see Table 3.1). Second, the relative amplitude is comparatively small. Third, its occurrence does not seem to coincide with the regions of interest containing microgels except randomly. Instead, the lifetime component τ_1 is essentially uniformly distributed throughout the entire FLIM image with approximately equal intensity. The other lifetime components are also detected outside the boundaries of the microgels to some degree, but with significantly lower intensity and density than inside the microgels. Hence, the discussion of the FLIM images is focused on the two dominant lifetime components, τ_2 and τ_3, which match well to the lifetime components of the BTD reference in solution (compare Table 3.1 and 3.3).

Table 3.3: Fluorescence lifetimes τ determined in the FLIM images of microgels **A** and **B**. The excitation wavelength was 488 nm, the analyzed emission wavelengths 500 – 715 nm. The relative amplitudes of the fluorescence lifetime components τ_1, τ_2, τ_3 and τ_4 are mentioned in the square brackets. The errors of the lifetime components are in the order of magnitude of the last decimal place specified.

Figure	microgel sample	τ_1 / ns	τ_2 / ns	τ_3 / ns	τ_4 / ns
3.7 **a,b,c**	**A**, unactivated	11.0 [7%]	4.63 [36%]	1.70 [36%]	0.63 [22%]
3.7 **d,e,f**	**A**, activated	13.0 [3%]	5.15 [31%]	1.87 [36%]	0.59 [29%]
3.8 **a,b,c**	**B**, unactivated	14.0 [12%]	5.2 [42%]	2.0 [34%]	0.68 [12%]
3.8 **d,e,f**	**B**, activated	11.0 [9%]	4.4 [34%]	1.85 [37%]	0.66 [20%]

The four lifetime components of the unactivated and activated microgels **A** are very similar both in magnitude and amplitude. Given the low accuracy due to the overall low photon count, the lifetime components can be considered identical. The slightly shorter lifetime components τ_2 and τ_3 for the unactivated microgels **A** are not significant and should not be considered to be an indicator of unactivated

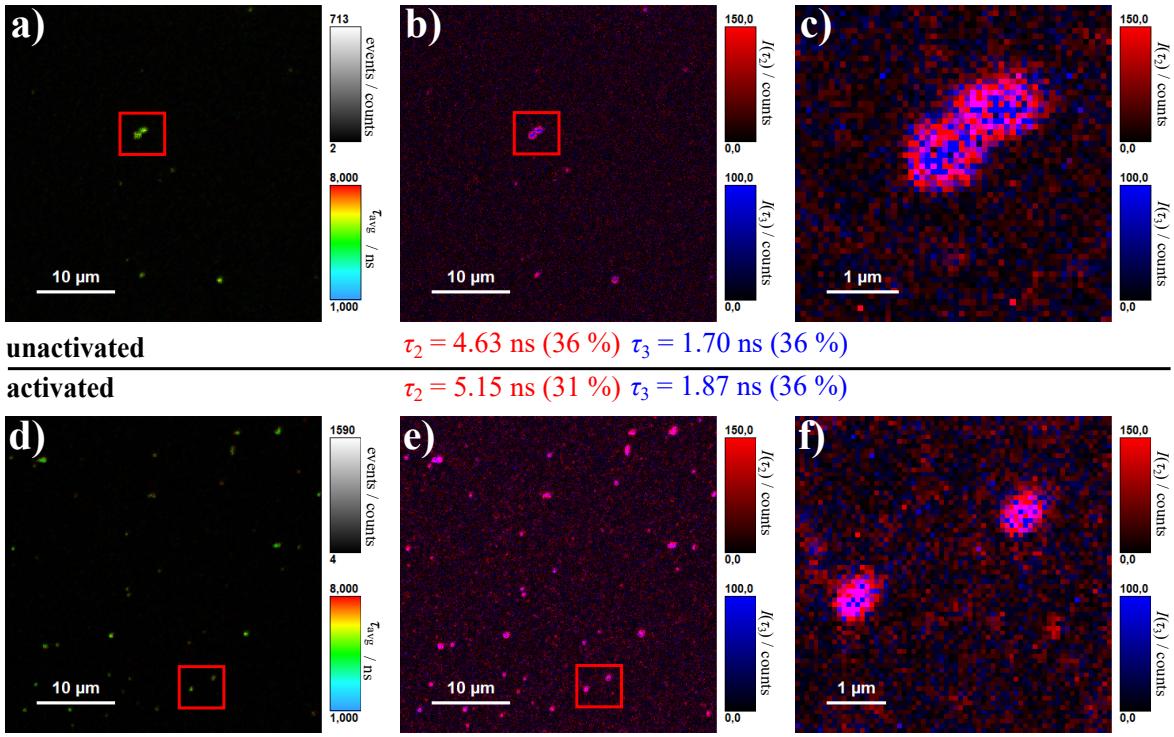

Figure 3.7: FLIM images of unactivated (top) and activated (bottom) microgels **A**. A 40×40 µm region of interest was imaged with 512×512 pixels and a pixel dwell time of 1.3 µs. 100 and 250 frames were recorded, respectively. Each FLIM fit was performed with four lifetime components. Unactivated: $\tau_1 = 11.0$ ns [7%], $\tau_2 = 4.63$ ns [36%], $\tau_3 = 1.70$ ns [36%] and $\tau_4 = 0.63$ ns [22%]. Activated: $\tau_1 = 13.0$ ns [3%], $\tau_2 = 5.15$ ns [31%], $\tau_3 = 1.87$ ns [36%] and $\tau_4 = 0.59$ ns [29%]. (**a,d**) The color scale represents the average lifetime, the grey scale depicts the measured intensity. (**b,e**) The intensity of the fluorescence ascribed to the two dominant lifetime components (τ_2, τ_3) is depicted in scales of red and blue for the long and the short lifetime component, respectively. (**c,f**) Close-up of the region of interest marked by the red square in (**a,b**) and (**d,e**), respectively.

vs. activated BTD. In this context, it should be noted here already that the situation is exactly the other way around for microgels **B**. Therefore, it is assumed that the difference of about 0.5 ns for τ_2 of unactivated and activated microgels **A** is irrelevant. Likewise, the relative amplitudes are considered equal within the accuracy of the measurement. In light of the similar lifetime components, it is not surprising that the FLIM images depicting the average lifetimes τ_{avg} look essentially identical for unactivated and activated microgels **A**. The difference in maximum intensity is well correlated to the overall amount of frames recorded during the measurement. However, even when the image is broken down into the two dominant lifetime components τ_2 and τ_3 (depicted as red and blue, respectively), no meaningful difference between the unactivated and the activated microgels **A** can be recognized. In both cases, single microgels are marked uniformly by both lifetime components in approximately equal ratio.

In Figure 3.8, FLIM images of unactivated and activated microgels **B** are shown. The global TCSPC curves of both samples were fitted with an n-exponential tail fit with $n = 4$ (see also Figure 7.18). For the unactivated microgels **B**, the following four lifetime components were determined: $\tau_1 = 14.0$ ns [12%], $\tau_2 = 5.2$ ns [42%], $\tau_3 = 2.0$ ns [34%] and $\tau_4 = 0.68$ ns [12%]. For the activated microgels **B**, the following four lifetime components were determined: $\tau_1 = 11.0$ ns [9%], $\tau_2 = 4.4$ ns [34%], $\tau_3 = 1.85$ ns [37%]

and $\tau_4 = 0.66$ ns [20%]. The lifetimes are also summarized in Table 3.3. The same assumptions as for microgels **A** are made, i.e., the longest and least common lifetime component, τ_1, is ignored, the shortest lifetime component, τ_4, is estimated to be a measurement artifact and only the lifetime components τ_2 and τ_3 are considered relevant. The 0.8 ns and 8% variance of magnitude and relative amplitude of lifetime component τ_2 for unactivated and activated microgels **B** is not considered significant given the high measurement uncertainty.

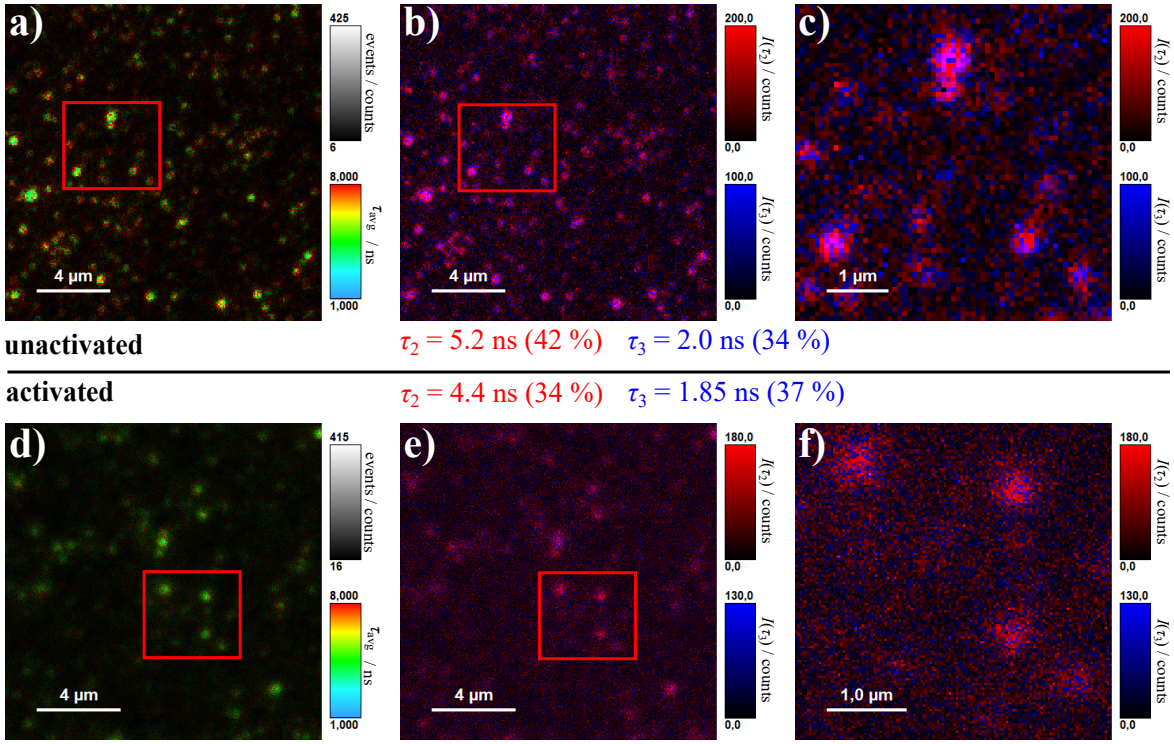

Figure 3.8: FLIM images of unactivated (top) and activated (bottom) microgels **B**. A cut-out is shown of the 40×40 µm region of interest which was imaged with 512×512 pixels and a pixel dwell time of 1.3 µs. 250 frames were recorded. Four lifetime components were determined in both cases. Unactivated: $\tau_1 = 14.0$ ns [12%], $\tau_2 = 5.2$ ns [42%], $\tau_3 = 2.0$ ns [34%] and $\tau_4 = 0.68$ ns [12%]. Activated: $\tau_1 = 11.0$ ns [9%], $\tau_2 = 4.4$ ns [34%], $\tau_3 = 1.85$ ns [37%] and $\tau_4 = 0.66$ ns [20%]. (**a,d**) The color scale represents the average lifetime, the grey scale depicts the measured intensity. (**b,e**) The intensity of the fluorescence ascribed to the two dominant lifetime components (τ_2, τ_3) is depicted in scales of red and blue for the long and the short lifetime component, respectively. (**c,f**) Close-up of the region of interest marked by the red square in (**a,b**) and (**d,e**), respectively.

Like for microgels **A**, the differences of the unactivated and the activated microgels **B** as observed via FLIM are marginal. Essentially, the same four lifetime components in the same ratio are determined. The average lifetimes of the microgels in the FLIM images can be considered equal within the accuracy of the measurement. The composition of the microgels, as encoded by the lifetime components τ_2 and τ_3, does not differ significantly before and after activation.

It is not entirely clear why the FLIM images of unactivated and activated BTD crosslinked microgels appear to be so similar. Unspecific activation of the unactivated microgels, e.g. due to inappropriate sample preparation, is one possibility. It is fathomable that the BTD crosslinker is activated due to the (shear) forces experienced during spincoating or even during volume transfer with a pipette. Dropcasting

of the microgel solutions as an alternative preparation method, however, did not influence the results. Unspecific activation might also occur during the drying process and the inevitable collapse of the microgels in their dry state. The DLS measurements already indicated that unspecific activation upon phase transition might occur (see Section 3.2.2). In principle, the unspecific activation could also be related to aging effects and uncontrolled progressing material failure over time.
Just as well, it is possible that the similarity of the FLIM images is related to the spectral properties of the unactivated and activated BTD in the environment of (dry) microgels. Although differences are observed in the emission spectra of the activated and the unactivated microgels at 488 nm excitation, the emission intensity, even as measured with a spectrometer, is similar (see Figure 3.4). In comparison, the fluorescence emission of the BTD reference vastly exceeded the emission of the BTD crosslinker at 488 nm excitation in all tested organic solvents (see Figure 3.1). Moreover, for both activated and unactivated microgels, a considerable amount of intact BTD crosslinker remains, as evidenced by the essentially identical fluorescence emission at 400 nm excitation. Therefore, it is possible that the FLIM images both before and after activation show mostly the BTD crosslinker instead of activated BTD. In light of the TCSPC measurements of the reference compounds (see Section 3.2.1), it is possible that lifetimes before and after activation do not differ substantially. The observed lifetime components of the BTD crosslinker at 488 nm were ascribed to unspecific activation before. However, it cannot be excluded that the lifetime components correspond to the unactivated BTD, after all. With that assumption in mind, the main difference of the lifetimes is not the magnitude of the values, but the ratio of the long and the short lifetime component, which switches from a ratio favoring the shorter component to a ratio favoring the longer component. The approximately equal ratio of the two considered lifetimes observed in all FLIM images then indicates the presence of roughly equal amounts of activated and unactivated BTD in all microgels. Given the low reliability of the measurements, this assessment should be treated with considerable caution. Overall, it is estimated that the FLIM images indicate a mixture of both unspecific activation and insufficient spectral resolution of the unactivated and activated BTD.
A third and most trivial explanation is the existence of a fluorescent impurity in the polymer system. At 488 nm excitation, random luminescence events are common. Essentially, there will always be some emission events detectable on a microscope with lasers of sufficiently short wavelengths (see also the impurity signals in the polymer films of Chapter 4 at 561 nm vs. 640 nm excitation, e.g., Figure 7.45). The fluorescence quantum yield of the activated BTD is very low, therefore it is also possible that the fluorescence is mostly hidden by unspecific emission events. However, the dominant lifetime components, τ_2 and τ_3, are in all cases reasonably comparable to the lifetime components of the BTD reference, therefore it is improbable that unspecific excitation of any possible impurities are solely responsible for the similarity of the FLIM images before and after activation.
Since no noteworthy difference is observed even for *ex-situ* activated and unactivated microgels, it is refrained from attempting a controlled activation via AFM. It is reasoned that even if controlled activation is possible, the activation cannot be visualized with FLIM.

3.3.3 Combined AFM and FLIM measurements of PHMA networks

As microgels turned out to be too complex polymer systems for the investigation of bond scission with the employed mechanofluorophore, it is attempted to reduce the complexity by taking one step backwards

and use BTD-PHMA networks instead. It has already been shown that (quantitative) visualization of bond scission on the basis of activated BTD in PHMA networks is possible.[50] Here, it is attempted to increase the information value by using FLIM instead of regular CLSM in combination with AFM for controlled activation. The samples were prepared equivalently to the procedure described in literature (see also 6.4.4).[50] For a reasonable alignment of AFM and FLIM images, the films are cut with a scalpel. The cut and the surrounding polymer film are imaged with both methods successively. Characteristic features of the cut, in particular of the edges, are visible and well comparable with both methods and help with the visual orientation. Advantageously, the cuts also manually activate the mechanofluorophores and thus serve as an intrinsic control. Three different BTD-PHMA networks are investigated which differ only in the thickness of the film and the date of production.

Unfortunately, the measurements were met by serious problems. In most measurements, in particular the visually most impressive ones, the global TCSPC curves exhibit a second maximum at about 10 ns which impedes any real analysis with exponential tail fits (compare Figures 7.19 – 7.21 in the appendix). The origin of that second maximum is not entirely clear but it is estimated that it is related to interaction of the AFM cantilever and the imaging laser. Simple reflection of the laser by the cantilever is improbable given the time scale; 10 ns correspond to about 3 m of traveling distance for light moving at regular speeds. When retracted, the AFM head is at most 10 cm above the substrate surface. It cannot be reproduced retroactively which factors differed in the few measurements in which the second maximum does not occur or is present to a negligible degree only. However, no comparable phenomenon was observed for any FLIM measurement of microgels in Section 3.3.2, therefore an influence of the AFM cantilever seems likely. It is estimated that the distance of the retracted AFM head to the substrate represents the most crucial factor, i.e., in all faulty measurements, the cantilever is still comparatively close to the substrate surface, whereas in the more regular measurements, the cantilever is retracted further away.

In the following, all FLIM images fitted with only two lifetime components correspond to such faulty measurements (Figures 3.9 and 3.10). Fitting with more lifetime components leads to physically unreasonable lifetimes with negative relative amplitude or likewise illogical negative background in the fitting model. More regular measurements (Figure 3.11) are marked by four lifetime components, as was already the case for the microgel samples in Section 3.3.2. The FLIM images with only two lifetime components are highly inaccurate with respect to the lifetime data and the lifetime information ultimately has to be considered meaningless. The images should be essentially viewed as regular CLSM images. Nonetheless, specific faulty measurements are included, as they highlight other potential issues that are independent of the lifetime analysis.

In Figure 3.9, FLIM and AFM images of a cut in an approximately 5 µm thick BTD-PHMA network are shown. The cut was once imaged in a comparatively large field of view (Figure 3.9 **a,b**) and once in closer detail with higher resolution (Figure 3.9 **d,e**). Only two lifetime components can be determined in both cases. Although the measurement is faulty (see above), lifetimes are determined to offer at least qualitative insight. The lifetime components ($\tau_1 = 7.2$ ns [31%] and $\tau_2 = 1.66$ ns [69%] for the large field of view, $\tau_1 = 7.9$ ns [34%] and $\tau_2 = 1.81$ ns [66%] for the detailed view, respectively) are similar in magnitude and relative amplitude and match well to the lifetime of BTD reference in PS (see Section 3.2.1). However, the lifetimes should be treated with utmost caution (see above). The contours of the cut in the detailed FLIM images are reproduced in the AFM image, proving the good alignment of AFM

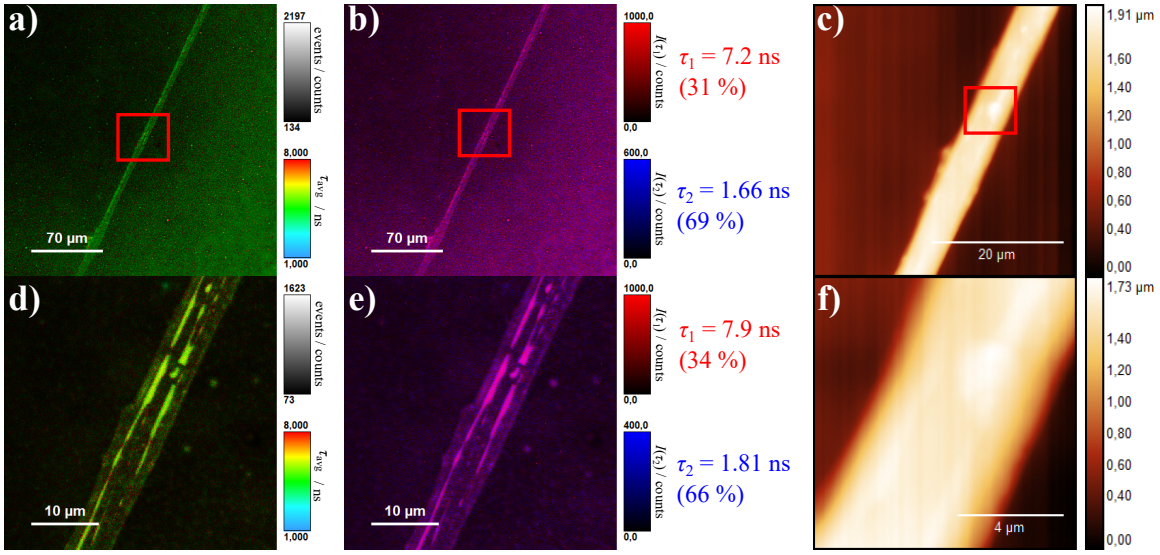

Figure 3.9: FLIM (**a,b,d,e**) and AFM height images (**c,f**) of a manually activated PHMA network crosslinked with BTD crosslinker. Images (**d,e,f,**) are separate measurements with higher resolution of the regions of interest marked by the red square in images (**a,b,c**). Images (**c,d,e**) all show approximately the same region of interest. (**a,b**) A 264 µm × 264 µm, (**c,d,e**) a 40 µm × 40 µm and (**f**) a 10 µm × 10 µm region of interest was imaged. All FLIM images were recorded with 512 × 512 pixels, 1.3 µs dwell time and 250 frames. Due to technical measurement problems, only two lifetime components yielded any reasonable fit of the global TCSPC curves. Lifetime components of (**a,b**) $\tau_1 = 7.2$ ns [31%] and $\tau_2 = 1.66$ ns [69%], as well as (**d,e**) $\tau_1 = 7.9$ ns [34%] and $\tau_2 = 1.81$ ns [66%], were determined. (**a,d**) The color scale represents the average lifetime, the grey scale depicts the measured intensity. (**b,e**) The intensity of the fluorescence ascribed to the two lifetime components τ_1 and τ_2 is depicted in scales of red and blue, respectively. (**c,f**) The color scale depicts the relative height.

tip and imaging laser. In contrast to most other cuts, the polymer film is not scraped away at the area of the cut and the material is not pushed to the edges (see below). Instead, the exact opposite occurred and AFM shows that the area of the cut is elevated by about 1.5 µm relative to the rest of the polymer film. The cut was performed with the blunt back side of the scalpel. It is estimated that the polymer stuck to the blade and was lifted upwards thereby.

The FLIM images are subject to considerable background. Essentially, the entire field of view is fluorescent with approximately equal fluorescence lifetimes. However, the area of the cut is distinctly brighter, in particular in the detailed views. This indicates that unspecific activation of the BTD crosslinker occurs frequently, but controlled activation still results in a visual spectral response. The images match well to the CLSM images of cuts reported in the literature.[50] It has to be noted, however, that the intensity of the fluorescence in the entire film correlates exceptionally well with the height as determined by AFM. In the detailed views in Figure 3.9 **d,e**, small strips of high intensity within the area of the cut can be recognized. The AFM height image reveals corresponding peaks on the hill that is the area of the cut. Thus, it is possible that the increase in intensity is not entirely related to the mechanical activation of the BTD crosslinker, but at least to some degree a result of a locally thicker film and consequently a higher density of (activated) BTD. The correlation between film thickness and fluorescence intensity is observed in all combined AFM and FLIM measurements, but is recognized most unequivocally in this particular measurement.

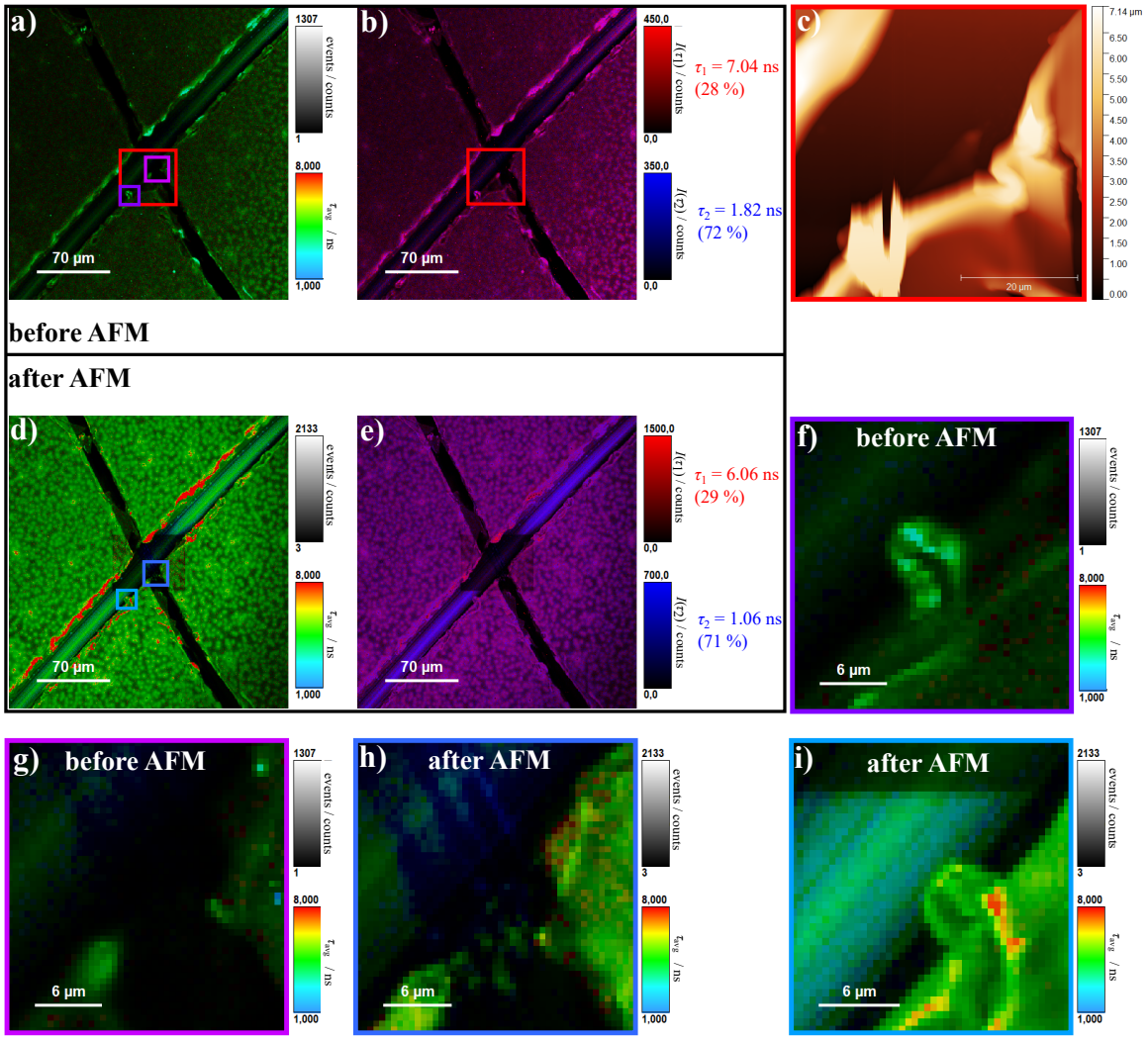

Figure 3.10: FLIM images before (**a,b,f,g**) and after (**d,e,h,i**) an AFM measurement, as well as the corresponding AFM height image (**c**) of a cut PHMA network crosslinked with BTD crosslinker. The red square in (**a,b**) marks the approximate area of the AFM scan shown in (**c**). In the FLIM images (**d,e**), an apparent change of intensity occurred in a precise rectangular area corresponding approximately to the area of the AFM scan. The violet / magenta and dark / light blue squares in (**a**) and (**d**) mark the regions of interest shown in greater magnification in (**f,g**) and (**h,i**), respectively. (**a,b,d,e**) A 264 µm × 264 µm and (**c**) a 40 µm × 40 µm region of interest was imaged with FLIM and AFM respectively. All FLIM images were recorded with 512 × 512 pixels, 1.3 µs dwell time and 250 frames. Due to technical measurement problems, only two lifetime components yielded any reasonable fit of the global TCSPC curves. Lifetime components of (**a,b,f,g**) $\tau_1 = 7.4$ ns [28%] and $\tau_2 = 1.82$ ns [72%], as well as (**d,e,h,i**) $\tau_1 = 6.06$ ns [29%] and $\tau_2 = 1.06$ ns [71%] were determined. (**a,d,f,g,h,i**) The color scale represents the average lifetime, the grey scale depicts the measured intensity. (**b,e**) The intensity of the fluorescence ascribed to the two lifetime components τ_1 and τ_2 is depicted in scales of red and blue, respectively. (**c**) The color scale depicts the relative height.

In Figure 3.10, FLIM images of a cross-shaped cut in an approximately 9 µm thick BTD-PHMA network are shown before (**a,b,f,g**) and after (**d,e,h,i**) an AFM measurement (**c**). In the measurement after AFM, only two lifetime components, $\tau_1 = 6.06$ ns [29%] and $\tau_2 = 1.06$ ns [71%], similar to those in the first measurement could be determined. Although the FLIM images before the AFM measurement can be

fitted more regularly with four lifetime components, a fit with two lifetime components, $\tau_1 = 7.4$ ns [28%] and $\tau_2 = 1.82$ ns [72%], was performed to grant at least some comparability.

As before, fluorescence is observed in the entire field of view, both before and after the AFM measurement. However, the fluorescence intensity is not homogeneous. Instead, countless densely but randomly distributed spots of higher intensity are visible throughout the polymer film. These are particularly well visible after the AFM measurement, but also occur distances of several dozen micrometers away from the scan region of the AFM and are thus unlikely to be related to the same. These spots of increased fluorescence intensity probably correspond to unspecifically activated BTD crosslinker throughout the PHMA network. In this context, it seems as if the distribution of the crosslinker is not homogeneous. This is likely related to a different polymerization rate of monomer and crosslinker, leading to microscopic phase separation. The intensity is even more noticeably increased at the edges of the cut where the film thickness is increased according to the AFM measurement. Any apparent increase of fluorescence lifetimes at these edges after AFM should not be treated as significant and is most likely a sign of the faulty analysis of the TCSPC curve (see above). The overall higher intensity in the FLIM images 3.10 **d** and **e** compared to **a** and **b** should not be considered significant, either.

However, one noteworthy difference is observed between the FLIM images before and after the AFM measurement. In the approximate area of the AFM scan, a spectral response is visible in the FLIM images in the form of a highly regular rectangular shape. The lifetimes within the rectangular shape do not differ significantly from the surroundings. Only the intensity of all fluorescence in this region seems to be drastically reduced. Due to the reduced intensity, the area is henceforth called “shadow” or “shaded rectangle”. The origin of this locally restricted phenomenon is not clear and could not be reproduced in any successive measurement. The presence of a literal shadow could be excluded, since the considered area could be moved by changing the field of view. It is estimated that the AFM tip picked up some loose polymer material at an early point in the scan. The accidentally modified tip might be responsible for the shaded rectangle, although neither the mechanism nor the actual effect is understood at this point. There exists some evidence that the AFM tip picked up an unknown amount of polymer at one point. Before the AFM measurement, the lower right channel of the cut as marked by the bright purple square in Figure 3.10 **a** appears open. For a better recognition, the considered area is depicted in greater magnification in Figure 3.10 **g**. The AFM measurement itself, however, shows a continuous edge of the crossing channel. In the FLIM images after the AFM measurement (dark blue square in Figure **d** corresponding to image **h**), this edge can be seen as a series of weakly fluorescing spots. Furthermore, one peninsular spot marked by the violet / light blue square in 3.10 **a** and **d**, respectively, seemed to have changed shape after the AFM measurement. A close-up of the considered area before and after AFM is compared in images **f** and **i**. The peninsular spot coincides with the irregular spot in the lower left corner of the AFM image 3.10 **c**. The change of the peninsular spot in **f** and **i** might indicate polymer being picked up by the AFM tip, whereas the change in images **g** and **h** might show polymer being deposited by the tip.

Nonetheless, it remains highly questionable if the rectangular shadow was produced by the AFM tip at all. Since the effect could not be reproduced, it cannot be stated that it is any sign of controlled activation of mechanofluorophores with AFM. It has to be assumed that the recognition of the effect in the first place is merely a bias introduced by the regularity of the shape and the approximate coincidence with

the area of the AFM scan. The FLIM images are shown here for the sole reason that they represent the only noteworthy spectral response to the AFM in all combined measurements of BTD-PHMA networks. Moreover, they serve as a reminder not to over-interpret single measurements.

The combined AFM and FLIM measurements around the cross-shaped cut in an approximately 3 µm thick BTD-PHMA network shown in Figure 3.11 represent all valid measurements. Again, FLIM images were recorded before (3.11 **a,b**) and after AFM measurements (3.11 **c,d,f,g**). Figures 3.11 **f,g** are separate close-ups of the approximate area of the AFM scans presented in 3.11 **e**. All FLIM images were fitted with four lifetime components highly comparable in magnitude and ratio to the four lifetime components observed for all microgel samples in Section 3.3.2 (compare Tables 3.3 and 3.4). The lifetimes are summarized in Table 3.4. Within the accuracy of the measurement, the lifetimes can be considered equal in magnitude and relative amplitude for all three separate FLIM images. The interpretation of the lifetimes is the same as for the microgel samples, i.e., the shortest lifetime component τ_4 is considered to be a measurement artifact, whereas the longest lifetime component τ_1 is assumed to be unrelated to the mechanofluorophore system. Only the two dominant lifetime components τ_2 and τ_3, which are comparable to the lifetimes of the BTD reference (see Section 3.2.1), are considered relevant.

Table 3.4: Fluorescence lifetimes τ determined in the various FLIM images shown in Figure 3.11. The excitation wavelength was 488 nm. The relative amplitudes of the fluorescence lifetime components τ_1, τ_2, τ_3 and τ_4 are mentioned in the square brackets. The errors of the lifetime components are in the order of magnitude of the last decimal place specified.

Figure	before / after AFM	τ_1 / ns	τ_2 / ns	τ_3 / ns	τ_4 / ns
3.11 **a,b**	before	10.80 [9%]	4.60 [36%]	1.82 [34%]	0.72 [21%]
3.11 **c,d**	after	11.00 [10%]	4.88 [34%]	2.10 [32%]	0.80 [24%]
3.11 **f,g**	after	12 [8%]	5.5 [33%]	2.38 [35%]	0.80 [24%]

In an attempt to reproduce the results of the measurement in Figure 3.10, sixteen different successive AFM measurements were performed with varying settings. In particular, the overall scan time was varied while keeping the size of the region of interest and the amount of pixels constant. Furthermore, the setpoint, which determines the maximum exerted force, was varied (see Section 2.4 for more theory on AFM). Essentially, the longer the measurement time and the smaller the setpoint, the higher the overall exerted force acting on the BTD-PHMA network. The region of interest was systematically moved so that a grid of sixteen AFM images with varying overall exerted force was measured. The sixteen AFM images form one comprehensive larger image of the same region of interest as shown in the FLIM images, in particular images 3.10 **f,g**. At high set points and long measurement times, however, the AFM measurements fail, probably due to a loss of contact of the tip and the sample surface. The FLIM images 3.10 **c,d,f,g** were all recorded after the AFM grid, i.e., the next day.

Despite the more trustworthy FLIM fits, the measurement does not yield any new insights. As before, the entire background is speckled with fluorescent spots. At the edges of the cut, the fluorescence intensity is increased with a good correlation to the local film thickness. Neither the average lifetimes, nor the dominant lifetime components differ significantly between the background and the more intense edges of the cut. Neither any of the sixteen separate AFM measurements caused any notable spectral changes.

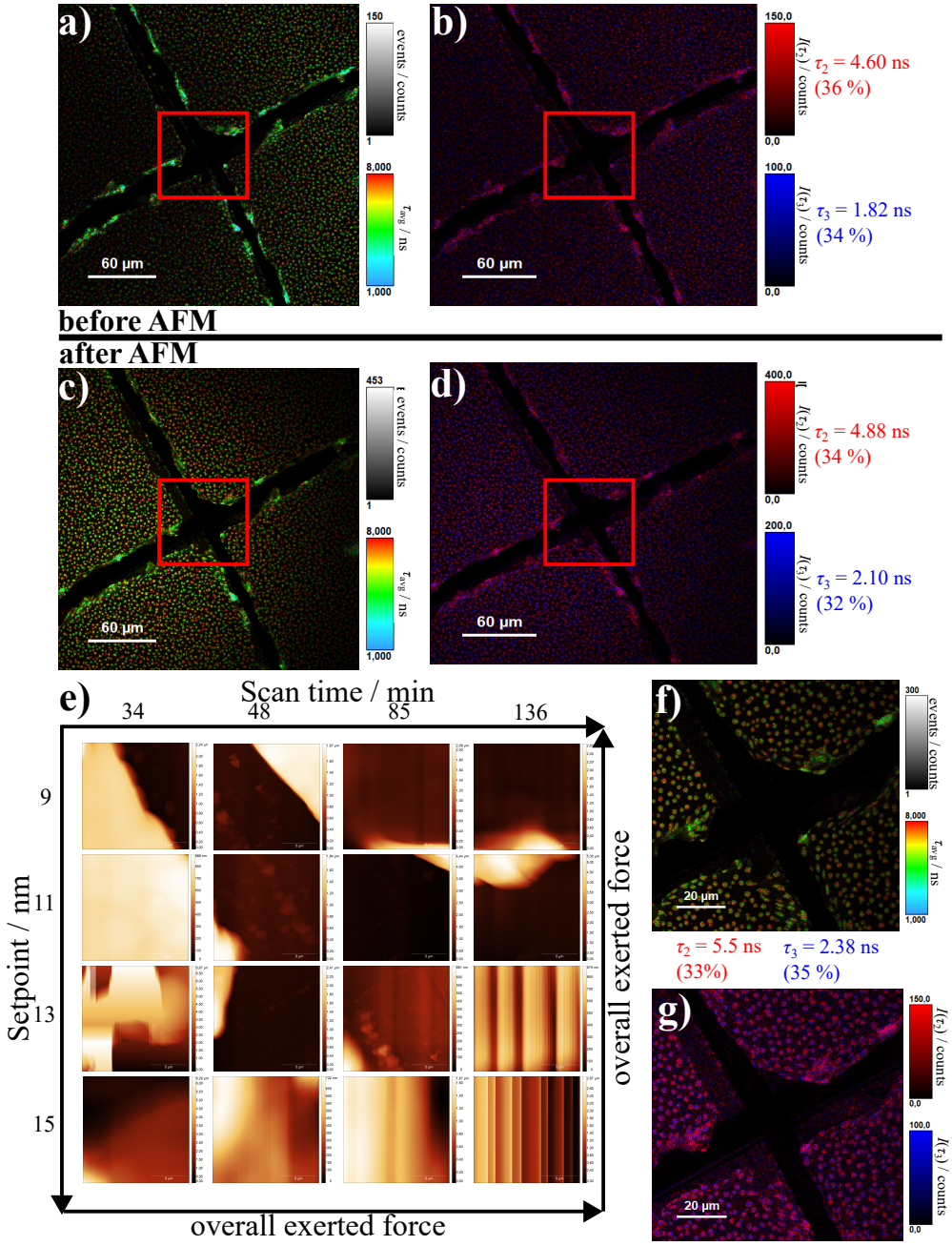

Figure 3.11: FLIM images before (**a,b**) and after (**d,e,f,g**) sixteen AFM measurements with varying settings, as well as the corresponding AFM height images (**e**) of a cut PHMA network crosslinked with BTD crosslinker. The red square in (**a,b,c,d**) marks the approximate area of the AFM scan shown in (**e**) and the separate FLIM measurement shown in (**f,g**). (**a,b,c,d,f,g**) All FLIM images were recorded with 512×512 pixels, 3 µs dwell time and 250 frames. Four lifetime components were determined in each case (see Table 3.4). (**a,c,f**) The color scale represents the average lifetime, the grey scale depicts the measured intensity. (**b,d,g**) The intensity of the fluorescence ascribed to the two dominant lifetime components τ_2 and τ_3 is depicted in scales of red and blue, respectively. (**e**) The color scale depicts the relative height.

The results are representative for all performed measurements, including measurements further away from any manual cuts or at the natural border of the films. Hence, it can be stated with high certainty that

the background is not fluorescent due to propagation of the manual activation into the bulk, but either due to unspecific activation or fluorescence of the unactivated BTD crosslinker.

3.4 Summary and conclusion

Material failure, although one of the most critical aspects of material science, is a still badly understood process. Logically, however, it has to start ultimately with the scission of individual molecular bonds.[49] Therefore, it is of utmost importance to develop methods to investigate bond scission on the molecular level. One of the most promising tools in this regard is FM in combination with mechanoresponsive fluorophores, or mechanofluorophores, which report quantitatively and representatively on critical forces. In this chapter, a mechanofluorophore system was employed as a crosslinker in PVCL/VIM microgels and PHMA networks in an attempt to visualize material damage with a combination of FLIM and AFM. The work was a direct continuation of preceding studies of *Baumann et al.*[50] In particular, it was attempted to improve the resolution and information content available to FM.

In Section 3.2, the BTD mechanofluorophore system used throughout this chapter and the BTD-PVCL/VIM microgels were investigated in closer detail. Absorption and emission spectra of mechanically activated and unactivated BTD reference compounds were recorded and compared, their fluorescence lifetimes and quantum yields were measured and the photostability was tested. The (altered) thermoresponsiveness of the microgels was investigated with DLS, activation of the incorporated BTD crosslinker was confirmed spectrally, and comparative PAINT measurements were performed. The preliminary tests already indicated that the mechanofluorophore used here has severe inherent limitations. For one, the activated BTD exhibited both a low fluorescence quantum yield and a low photostability. Unactivated BTD had a comparatively high fluorescence quantum yield, but an equally low photostability and even worse excitation efficiency. Consequently, the fluorophore system was considered unsuited for conventional SRFM methods, whose resolution is dependent on the total number of emitted fluorescence photons. Instead of attempting an improvement of the resolution, it was decided to focus on increasing the information content by imaging the lifetimes with FLIM. The lifetime measurements of the unactivated and activated BTD reference compounds indicated a reasonable contrast of lifetimes at 488 nm excitation. In particular, the restoration of the conjugated π-system of the anthracene unit seemed to be identifiable by a lifetime comparable to that of anthracene[162].

The investigation of the BTD microgels, however, revealed further complications. The DLS measurements hinted at a thermal or collapse-induced random activation of the BTD crosslinker and overall irregular thermoresponsive behavior of the microgels. Spectral measurements implied little differences in the emission spectra of *ex-situ* activated and unactivated microgels. The emission at 400 nm excitation, which is associated to the unactivated BTD, was comparable for microgels before and after activation. Only the activated microgels exhibited an emission maximum at about 520 nm at 488 nm excitation. The emission was associated to the activated BTD. Disadvantageously, the emission intensity at 488 nm excitation appeared to be very weak and the relative fluorescence intensity of the unactivated microgels at this excitation wavelength was overall comparable aside from the absence of the maximum at 520 nm. The PAINT measurements, however, seemed to be capable of resolving internal structural differences between activated and unactivated microgels that should also be reflected to some

degree in FLIM measurements.

Despite the manifold problems indicated by the simple preliminary experiments, (combined) FLIM and AFM measurements of BTD crosslinked polymer systems were attempted in Section 3.3. First, unactivated and *ex-situ* activated microgels were investigated with FLIM. Finally, BTD-PHMA networks were studied with a combination of FLIM and AFM. No significant differences were observed between the unactivated and the activated microgels. The global TCSPC curves of all FLIM images were fitted with four comparable lifetime components in a similar ratio. In all cases, the two dominant lifetime components matched well to the two lifetime components of the BTD reference compound in toluene. The shortest lifetime component was considered to be a measurement artifact. The longest lifetime component had the distinctly smallest relative amplitude and was assumed to be unrelated to the mechanofluorophore. Most surprising was the fact that the activated and the unactivated microgels yielded essentially the same FLIM images in regard to lifetimes, the distribution of lifetimes and the fluorescence intensity. It could not be determined if this was a sign of unspecific activation of the BTD crosslinker during sample preparation, or if this effect was ultimately attributed to the worse spectral properties of the mechanofluorophore in the aqueous environment of the microgels. Thus, the FLIM images either showed approximately equal amounts of activated BTD crosslinker in all cases, or approximately equal amounts of unactivated BTD crosslinker instead, if the spectral contrast attested in Section 3.2 was insufficient, after all.

The combined FLIM and AFM measurements of the PHMA networks were met by similar problems. For one, even without obvious mechanical activation the entire polymer film was already laced with fluorescent spots. These probably indicate unspecific activation and microscopic phase separation during the polymerization. Mechanical activation by cutting the polymer films resulted in an apparent increase of fluorescence intensity at the site of the cut. However, the fluorescence lifetimes of the unactivated background and the activated areas did not differ significantly. Similar lifetime components in a comparable ratio to the lifetimes of BTD in microgels were determined in all valid measurements. Moreover, AFM measurements revealed that the increase in intensity at areas of mechanical activation coincided exceptionally well with the local film thickness. Hence, the increase in intensity might be simply related to the higher apparent two-dimensional labeling density in thicker films instead of mechanical activation of the mechanofluorophores. Again, it is not entirely clear how these results have to be interpreted. Either, the polymer films underwent major unspecific activation beforehand, e.g., due to heating during the polymer synthesis or rapid degradation of the samples in general. Alternatively, the spectral separation and contrast in lifetimes of the unactivated and the activated BTD attested on the basis of the preliminary tests was insufficient under the actual measurement conditions.

No controlled activation with AFM was achieved. In light of the aforementioned results, it has to be noted that this is likely a matter of the insufficiency of the fluorophore system and not indicative of a general impossibility of a controlled activation of mechanophores with AFM. Only in one single measurement an apparent change was observed in form of a highly regularly shaped area with reduced intensity in the approximate area of the AFM scan. Unfortunately, the result could not be reproduced. It was neither possible to unequivocally determine the origin, nor to accurately explain the observed intensity decrease. There existed experimental evidence that the AFM tip picked up some loose polymer material, but it was not clear if and how this related to the observed spectral change.

All in all, the aim of this chapter was not met. Neither the resolution could be improved, nor the information content of any FM images could be substantially increased. On the contrary, the results presented here even raise questions about the reliability of older studies. The combination of FLIM and AFM measurements revealed a reasonable correlation between film thickness and fluorescence intensity, but not fluorescence lifetime. This can be seen as an indicator that the assumption that the polymer network is activated by cutting it manually is already wrong. Instead, the majority of the mechanofluorophores might be already activated beforehand and the observed increase in fluorescence is caused by the piling up of polymer material at the edges of the cut and the resulting higher apparent two-dimensional labeling density. The influence of topological changes introduced by any mechanical activation has been neglected by most studies so far and has to be investigated in closer detail.
However, it is equally likely that the samples investigated here do not represent valid representative systems. Handling, transport and storage of all samples might have been faulty to begin with. Therefore, they should not be seen as any kind of counterevidence against previous results, but as a reminder that fluorescence microscopy is just one technique of many that might not reveal the whole picture. From the FLIM images alone, it is impossible to recognize the correlation of intensity and film thickness. This is only be revealed by complementary methods like AFM. Consequently, the microscopy images are easily misinterpreted, as the results match the initial expectations.
Likewise, the results should not be seen as an indicator that the general approach of visualizing bond scission with mechanofluorophores is misguided. Instead, they should be regarded as an indicator of current insufficiencies. First and foremost, the system is not yet understood well enough. It is not clear how faithfully the employed mechanofluorophores report on damage. Expressed differently, it is not clear if the hypothesized unspecific activation of the mechanofluorophores is a reasonable explanation for the observations. Supporting theoretical calculations have to be performed to accurately evaluate the bond strength of the mechanolabile bonds in comparison to the average bond strength in the polymer network. Furthermore, simulations could reveal the random or directed forces that can be expected to occur in polymer strands under different conditions. Only then it can be stated if random activation of the mechanofluorophores is a statistically representative event, or just an over-reporting inevitability.
Second, for an improvement of the resolution a different fluorophore system is required altogether. The photostability has to be vastly improved, the fluorescence quantum yield should be considerably higher after activation and the spectral separation of unactivated and activated state should be improved, too. In the best case, a mechanoresponsive photoswitch is designed, i.e., a photoswitch that can only be operated after mechanical activation. This could potentially lead to a PALM-like SRFM approach. Controlled activation with AFM is also fathomable, provided the mechanofluorophore is a faithful reporter of material damage. Given the results presented here, a modified AFM tip, e.g., a colloidal probe, might be more suitable for this purpose.

4 Synthesis, characterization and application of a novel fluorescent dye dyad

Part of this chapter have been published in D. Schöngen, D. Wöll, "Synthesis and Characterization of a Novel Photocleavable Fluorescent Dye Dyad for Diffusion Imaging", Chemical & Biomedical Imaging ***2025****, 3, 199-207, DOI https://doi.org/10.1021/cbmi.4c00084.*[59] *A research assignment on the synthesis (Section 4.2), conducted by Alexandra Markus, and a research assignment on* FEDUP *measurements in* PVAc *(Section 4.6.2), conducted by Hridya M. Biju, were supervised by the author and contribute to this chapter.*

4.1 Introduction

Although polymers are among the most common materials in everyday life, several aspects of their properties are not yet fully understood. One of the most important characteristics, that is still topic of ongoing scientific debates, is the glass transition (see also Section 2.6.1). When cooling polymer melts to their glass transition temperature, T_g, molecular motion of the polymer chains decreases to the point that molecular rearrangement to the thermal equilibrium becomes unfeasible to observe on experimental time scales.[123] An improved understanding of this phenomenon arguably requires methods to observe or better yet visualize molecular movement on the nanoscale, as accurate information on the dynamics of the glass transition are invaluable for the ongoing discussion. However, most established methods for the measurement of diffusion processes are either limited to temperatures far above T_g, since their accuracy is insufficient to resolve motion on the time scales occurring at typical glass transitions,[59,172] or they lack the power to reveal diffusional and structural inhomogeneities,[52,98,173] which are expected to be of utmost importance for any discussion of glass transitions. Methods like pulsed field gradient nuclear magnetic resonance (PFG-NMR),[174,175] fluorescence recovery after photobleaching (FRAP),[97,176,177] or fluorescence correlation spectroscopy (FCS)[103,178,179] fall into the second category. They have been used to study dynamic processes, like, for example, the diffusion paths in zeolite materials,[175] the binding interactions of proteins,[97] or the hybridization of deoxyribonucleic acid (DNA),[179] respectively. Powerful as these techniques are, they provide only ensemble averaged molecular parameters and thus are unsuitable for the investigation of inhomogeneous processes like the glass transition of polymers. Methods like single particle tracking (SPT)[98,180] and single molecule tracking (SMT)[54,181] offer the possibility to visualize movement on the molecular level. They are, however, limited by the realistically achievable accuracy. Limitations are mainly dictated by the number of collected photons[56] and photostability,[60] the mechanical stability of the measurement setup,[55] signal-to-noise ratio (SNR)[57] and dye orientation.[58] It can be shown that diffusion coefficients below $D \approx 10^{-17}$ $\mathrm{m^2\,s^{-1}}$ are no longer accessible by either SPT or SMT,[59] at least not within reasonable

measurement times using a real setup and without using notional dyes impervious to photodamage.
A recently developed method with the potential to surpass the limitations of SPT and SMT is minimal fluorescence photon fluxes microscopy (MINFLUX). The technique can be employed for both imaging and tracking. MINFLUX achieves higher localization accuracy with significantly fewer photons than regular localization methods (see also Section 2.3.7).[60] Thereby, photodamage of the fluorophores is reduced to a minimum, while the measurement accuracy is improved. Hence, the determination of very low diffusion rates, as they can be expected near the glass transition temperature of any polymer, becomes feasible, since the most critical limitations of classical tracking are circumvented. However, research on MINFLUX-based tracking seems to focus on exploring the *upper* limit of classical tracking, in particular in the context of biological systems.[182] Most publications on MINFLUX-based tracking investigate the diffusion behavior in living cell membranes,[183] in lipid (bi)layers,[184–186] or in solutions emulating the viscosity of cellular environments,[187] or they study fast protein dynamics, like the stepping motion of motor proteins,[188] movement along DNA-strands,[189] or the diffusion of specific proteins in bacteria.[60,190] All mentioned examples explore fast diffusion rates at or above the upper limit accessible with classical tracking methods (compare 2.3.6). At the date of writing this thesis, no publication was found on the application of MINFLUX-based tracking to polymer systems, in particular polymer systems below or close to their glass transition temperature.
Undeniably, the investigation of polymer glass transitions with MINFLUX-based tracking bears of yet unrecognized potential. Still, it is of arguably equal importance to develop competing techniques for the posed problem. Like different SRFM methods may grant access to complementary information or alternatively verify results, different techniques for diffusion imaging in highly viscous media are necessary to reveal the complexity of glass transitions in their entirety. Moreover, they act as verification for the reliability of any competing method. In this context, the method FRET efficiency diffusion measurement upon photocleavage (FEDUP) is going to be developed further throughout this chapter. Introduced in 2013 by *Dill et al.*[55] and officially termed FEDUP in 2025 by *Schöngen et al.*[59], the method fundamentally differs from all other tracking techniques, including MINFLUX. No absolute coordinates of single molecules are required whatsoever, instead only relative positions based on FRET efficiencies are determined (compare equation (2.25)). Therefore, the accuracy of the method is not intrinsically correlated to the achievable localization accuracy. This results in the maybe biggest advantage of FEDUP over MINFLUX, apart from its more cost-efficient and comparatively simple instrumentation; the theoretical independence from setup stability, i.e., sample drift. As long as the field of view is illuminated homogeneously, sample drift is basically irrelevant since three-dimensional spatial information is entirely encoded in the intensity or lifetimes of FRET-donor and -acceptor. Sample drift can be easily corrected without disturbing any dynamic analysis since the absolute positions of any single molecule pair are not included in the analysis. In contrast, sample drift might be one of the last inevitable imperfections of MINFLUX.[60] In return, FEDUP has its own set of inaccuracies that can be avoided entirely with MINFLUX, namely experimentally imperfect spectral separation and a need for high photostability. The almost diametrically opposed advantages and disadvantages make both methods rather complementary to each other than competing. Further inaccuracies in the FEDUP method are introduced due to several model assumptions. First and foremost, the dipole–dipole interaction originally proposed by Förster[69] is shown to be an inaccurate description of the energy transfer mechanism at

very short distances.[68] Nevertheless, at distances close to the Förster distance the well-known distance dependence to the power of six holds reasonably well.[59] Hence, analysis of FEDUP data using equations (2.25) – (2.30) is still valid within certain model-imposed limitations, which are going to be discussed in greater detail later.

In this chapter, the latest development of the FEDUP method is presented. Whereas the original work employed an apolar FRET-dyad,[55] the dyad used in this work is soluble in more polar media.[59] Furthermore, the photocleavable linker of FRET-donor and -acceptor was modified to be responsive to longer wavelength UV-irradiation. Thereby, the range of materials that can be investigated is enlarged while the optical instrumentation is vastly improved. Photocleavage is no longer achieved with an external LED, but is achieved in a more spatiotemporally controlled manner via a UV-laser coupled into the same excitation path as the imaging lasers (see also Figure 2.7 for a schematic representation of the setup). Further instrumental improvements include a better spectrally correlated spatiotemporal resolution. Spectral separation is now achieved via a second dichroic mirror coupled with suitable filters in the emission path, so that simultaneous recording of donor and acceptor emission becomes possible. Before, spectral separation was achieved in a timed fashion by a sequential changing of filters.[55] Furthermore, the analysis procedure was slightly reworked to include three-dimensional diffusion. In the original work, the analysis was based on a two-dimensional probability model.[55] However, FRET intensities and lifetimes encode three-dimensional relative positions. Therefore, an analysis based on the Maxwell–probability distribution (see Section 2.3.7) is more appropriate.

In the following, the synthesis of the novel dyad **8** (see Figure 4.1 for naming scheme) is presented (Section 4.2). Next, the dye system is characterized spectroscopically (Section 4.3) and its bulk and single molecule behavior upon irradiation with visible and UV-light is investigated in closer detail (Section 4.4). The results of Sections 4.2 – 4.4 are summarized in an intermediary conclusion in Section 4.5. Finally, FEDUP measurements are performed in various (hydrophilic) polymer systems (Section 4.6). In most cases, the measurements take place (far) below the respective glass transition temperature T_g. For three selected polymers (poly(vinyl acetate) (PVAc), poly(butyl methacrylate) (PBMA) and poly(ethylene glycol) (PEG)) measurements are performed at different temperatures, including temperatures close to or slightly above T_g. It is aimed to demonstrate the potential of the method for the investigation of difficult to access polymer dynamics, in particular the glass transition. There exist very few, if any, comparable single molecule diffusion studies for any of the investigated polymer systems.

4.2 Synthesis of the dyad

In the following, a brief overview of the complete synthesis (see also Figure 4.1) of the new dyad **8** and the reference compounds donor **6** and acceptor **7** is given. The detailed synthesis protocols, as well as the full IUPAC names and structures of the compounds and their characterization with nuclear magnetic resonance (NMR) and/or electrospray ionization (ESI)-mass spectrometry (MS), can be found in Section 6.2.

The biggest synthetic effort is presented by the synthesis of the photolabile linker **5** with two orthogonal functional groups to which different dyes can be attached selectively. The main requirement

is for the two reactive sites to be separated by the photocleavable moiety. The linker is based on the common PPG 2-(2-nitrophenyl)propyloxycarbonyl (NPPOC)[63,64] which gained considerable popularity in DNA-related syntheses.[113,114] NPPOC was chosen as linker primarily for its efficient photocleavage with long wavelength UV-A light (up to approximately 400 nm). Furthermore, the photocleavage mechanism has been studied extensively already[111,117–119] and cleavage products and potential side-products are known (compare Section 2.5.1). However, commercially available variants of NPPOC do not include two reactive sites and are usually simple chloroformates (compare the intermediate product shown in Figure 4.1) that can be used for the protection of alcohols and amines. Hence, a synthesis scheme had to be devised.

The synthesis started with the esterification of *o*-nitrophenyl acetic acid (starting material in 4.1) with methanol to methyl(2-nitrophenyl)acetate **1**, according to comparable literature procedures.[191] Concentrated sulfuric acid was used as catalyst. The ester **1** is also commercially available, but at prices several hundred times higher than the corresponding acid. The esterification is necessary for a better reactivity of the benzylic position and a more facile reduction to the corresponding alcohol **3** in synthesis step 3.

The ester **1** was consequently functionalized at its benzylic position with propargyl bromide resulting in ester **2**. The dehydrogenation of a single benzylic proton was achieved with the strong but bulky base tertiary potassium butanolate (KO^{t}Bu). The procedure for this and the next step was taken directly from literature.[192] The terminal triple bond represents the first reactive site to attach a dye label to later on. This triple bond also represents the main difference between the original NPPOC structure[63,64] and all following related structures.

Subsequently, the ester **2** was reduced with sodium borohydride to the corresponding alcohol **3**. The alcohol **3** in turn was phosgenated to the chloroformate intermediate. For safety reasons, trichloromethyl chloroformate (diphosgene) was used instead of phosgene. The intermediate product is highly sensitive to water. Therefore, isolation of the chloroformate intermediate was eschewed and the reaction mixture was used without purification. It followed the condensation of the intermediate with *N*-Boc-ethylene diamine to the amine-protected photolabile carbamate **4**. Mono protected diamine has to be used to avoid a double condensation with the same diamine. It is likely for the second amine to be even more reactive after the condensation of the first amine to the carbamate moiety. The reaction procedure for both sub-steps was adapted from similar literature reactions.[193]

The deprotection of the primary amine of compound **4** to the final photolabile linker **5** was performed under mild conditions to avoid hydrolysis of the carbamate moiety. One thousand molar equivalents of 1 M hydrochloric acid in a 1:1 mixture of ethyl acetate and water were employed for this purpose.[194] The deprotection of the primary amine reveals the second reactive site for labeling with dyes. Any azide- and NHS ester-functionalized dye can now be attached to the photolabile linker **5**. Irradiation with UV-light leads to a cleavage at the carbamate moiety. The azide-functionalized dye will thus remain attached to nitrophenyl residue after photocleavage whereas the NHS ester-functionalized dye is released as a primary amine (for the exact mechanism and photocleavage products, see Section 2.5.1). Contrary to the apolar precursors **1**–**4**, linker **5** exhibits moderate solubility in aqueous solutions.

Compounds **2**–**5** were all purified with normal phase chromatography. Compound **1** was purified by recrystallization. After purification, compounds **1**–**4** can be sufficiently characterized with ^{1}H-NMR.

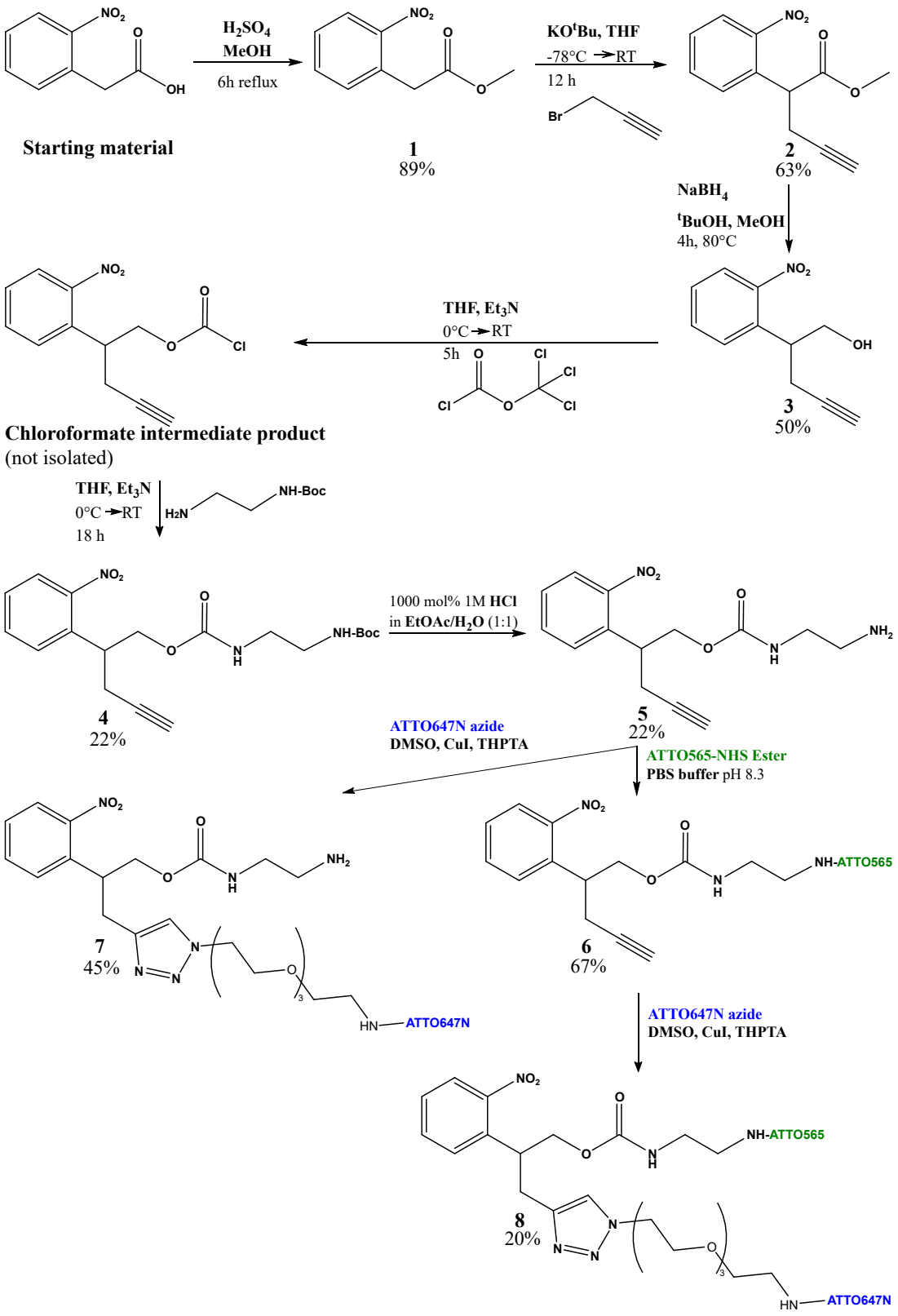

Figure 4.1: Overview of the synthesis route of the dyad **8**. Reactants and solvents are written in bold next to the reaction arrows. Reaction yields are given below the compound numbers. For the most essential reactants, the structure is given next to the reaction arrows, too. The structures of the commercially available dyes ATTO565 NHS ester (olive) and ATTO647N azide (blue) can be found in Figure 4.2.

Upon deprotection of the primary amine, however, the ^{1}H-NMR spectrum of linker **5** loses most discernible characteristic features (compare spectra 7.74–7.77 with spectrum 7.78 in the appendix). Characterization is instead achieved with ^{13}C-NMR and ESI-MS. For a better control of the purity of linker **5**, an ESI-MS of compound **4** is measured, too. No remains of compound **4** are observed in the MS of linker **5**. A short scientific summary of NMR and (ESI-)MS is given in Section 6.1, the measurement conditions are listed in Section 6.10 and 6.11, respectively. The relevant spectra can be found in the appendix in Sections 7.7.2 and 7.8.

Starting from the photolabile linker **5**, the two reference compounds, donor **6** and acceptor **7**, were synthesized. The reaction conditions were directly taken from the labeling procedures as specified by the dye manufacturer (ATTO-TEC™, see Figure 7.89 in the appendix). Donor **6** consists of the commercially available NHS ester-functionalized dye ATTO565 attached to the primary amine of linker **5**, acceptor **7** consists of the commercially available azide-functionalized dye ATTO647N attached to the terminal triple bond of linker **5**. The NHS ester reacts with the primary amine under mild buffer conditions without further additives or heat. The alkyne-azide click reaction is promoted by Cu(I) and suitable stabilizing ligands. The full structures of both dyes are shown in Figure 4.2 **c**. The dyes have been chosen for their good spectral overlap and thus efficient energy transfer, high photostability, excellent brightness and their solubility in aqueous solutions. Since both dyes are molecular cations, they are expected to increase the solubility of the entire organic framework in polar media. Compounds **6** – **8** are all well soluble in methanol and moderately well soluble in aqueous solutions. Donor **6** and acceptor **7** are not only two possible precursors of dyad **8**, they are also required as reference compounds in the spectroscopic characterization and irradiation experiments (Sections 4.3 and 4.4).

Of the two possible precursors, donor **6** was chosen for the final reaction to dyad **8** due to a more convenient purification procedure. Acceptor **7** and dyad **8** exhibit similar elution behavior in reverse-phase chromatography, whereas donor **6** can be quantitatively separated using a different eluent mixture. The final reaction conditions were thus identical to the synthesis of acceptor **7**. Compounds **6** – **8** are identified with ESI-MS (see Section 7.8) and fully characterized spectroscopically (Section 4.3). To verify the purity of dyad **8**, small amounts were subjected to high performance liquid chromatography (HPLC). Some residues of free ATTO647N azide could be separated. In return, finely dispersed column material contaminated the eluted product fraction. The following characterization and irradiation experiments (Sections 4.3 and 4.4, respectively) are done with the manually purified dyad **8**. It was reasoned that the contamination, which is most difficult to be removed again due to the small amount of substance, is a more significant influence on the spectra than the insubstantial amount of free ATTO647N azide. No relevant spectral changes are observed in the fluorescence spectrum after HPLC, whereas in the absorption spectrum all structure is lost in the UV-region (compare the HPLC-purified spectra in Figure 7.86 with the spectra in Figure 4.2). A brief scientific summary of HPLC is given in Section 6.1.4, the measurement conditions are listed in Section 6.12. The chromatogram and comparative spectra after HPLC can be found in the appendix (Section 7.9).

4.3 Spectroscopic characterization of the dyad

It is obligatory to study the behavior of the fluorophore system in solution, before the new dyad can be employed in FEDUP measurements (Section 4.6). The first measurements were performed on the system before photocleavage. Absorption and emission spectra were recorded for the unreacted dyes **ATTO565 NHS ester** and **ATTO647N azide**, the reference compounds donor **6** and acceptor **7**, and the dyad **8**. Furthermore, quantum yields and lifetimes of all substances were determined. The spectroscopic characterization is conducted once for all compounds dissolved in methanol (Section 4.3.1) and one more time for all compounds dissolved in water (Section 4.3.2). The photoresponsiveness of the system is investigated in Section 4.4. For a both qualitative and quantitative comparison of the different dye systems, it was attempted to adjust all compounds to the same concentration. In the case of obvious significant diversion from equal concentration, relevant data, i.e., emission spectra, are normed to the concentration of the respective compound. Concentrations are calculated with the Lambert–Beer law (equation (2.9)), using the maximum absorption coefficients of ATTO565 and ATTO647N as specified by the manufacturer for aqueous phosphate-buffered saline (PBS) solutions: $\varepsilon_{\mathrm{ATTO565}}(564\ \mathrm{nm}) = 120000\ \mathrm{L\,mol^{-1}\,cm^{-1}}$ and $\varepsilon_{\mathrm{ATTO647N}}(646\ \mathrm{nm}) = 150000\ \mathrm{L\,mol^{-1}\,cm^{-1}}$, respectively (see also Figures 7.87 and 7.88 in the appendix). It is assumed that neither the presence of the photolabile linker, nor different polar solvents, i.e., methanol, significantly change the absorption coefficient, even if spectra are shifted to different wavelengths. As mentioned in the introduction of this thesis already (Section 1.1), a consistent color scheme is used to better identify the different fluorescent compounds. The unreacted dyes **ATTO565 NHS ester** and **ATTO647N azide** are coded in olive and blue, respectively. The reference compounds donor **6** and acceptor **7** are represented by the colors bright green and red, respectively. The dyad **8** is shown in orange (compare Figure 4.2). An intermediate summary and conclusion of both the spectroscopic characterization and all irradiation experiments will be given in Section 4.5 before turning to the FEDUP measurements in Section 4.6.

4.3.1 Dyad in methanol

In the following, the characterization of the dyad and all reference compounds dissolved in methanol is discussed. Absorption spectra of all substances are shown in Figure 4.2 **a**, corresponding emission spectra are depicted in Figures 4.2 **b** and **d** for 530 nm and 600 nm excitation, respectively. The concentration of all compounds was adjusted to approximately 0.6 $\mu\mathrm{mol\,L^{-1}}$. Hence, a quantitative comparison of the emission spectra is feasible. The color-coded structures of **ATTO565 NHS ester**, **ATTO647N azide**, donor **6**, acceptor **7** and dyad **8** are given in Figure 4.2 **c**. Lifetimes and fluorescence quantum yields are listed in Table 4.1. All TCSPC curves can be found in the appendix (Section 7.2.3). Between 450 – 700 nm, the absorption spectra consist of predominantly the absorption of the ATTO565 or ATTO647N chromophore. The absorption of the ATTO647N chromophore in the red region is essentially identical for the unreacted dye, acceptor **7** and dyad **8**. The absorption maximum for all three compounds is at 642 nm. The absorption maximum of the ATTO565 chromophore, in contrast, is shifted from 552 nm for the unreacted dye to 556.5 nm for donor **6** and 557 nm for dyad **8**. It is likely that the insignificant difference between donor **6** and dyad **8** is caused by the overlapping absorption of the ATTO647N chromophore in that spectral region. The absorption spectrum of dyad

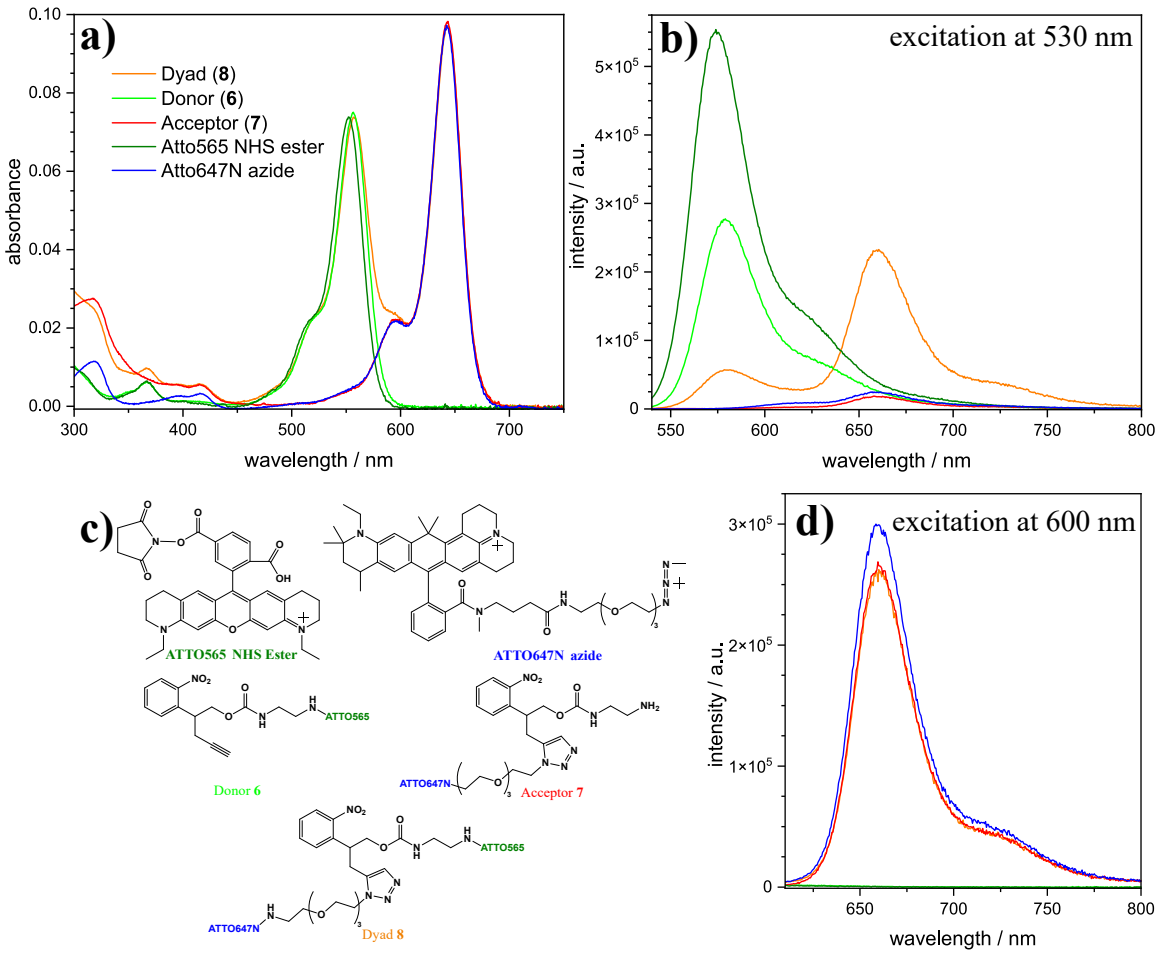

Figure 4.2: (**a**) Absorption and (**b**) emission (excitation at 530 nm) spectra of **ATTO565 NHS ester** (olive), **ATTO647N azide** (blue), reference donor **6** (bright green), reference acceptor **7** (red), and dyad **8** (orange) in methanol (MeOH). The structures of all compounds are shown in (**c**). The corresponding emission spectra with 600 nm excitation are presented in (**d**). No significant excitation was observed for the compounds without ATTO647N moiety. The concentration of all compounds was adjusted to approximately 0.6 µmol L^{-1}.[59]

8 is overall an overlap of the corresponding absorption spectra of reference donor **6** and acceptor **7**, thereby indicating no relevant interaction of the dyes in the ground state.[59] The ratio of the absorbances $A(557\text{ nm})/A(642\text{ nm}) = 0.77$ at the two absorption maxima at 557 nm and 642 nm matches the ratio of the maximum absorption coefficients $\varepsilon_{\text{ATTO565}}(557\text{ nm})/\varepsilon_{\text{ATTO647N}}(642\text{ nm}) = 0.8$ of ATTO565 and ATTO647N. Thus, the purity of dyad **8** is assured (see also Section 4.2). In the UV-region of the spectra the absorbances of donor **6** and **ATTO565 NHS ester** are identical. The absorbance of acceptor **7** is increased compared to **ATTO647N azide**, however, the structure of the spectrum remains distinctly the same. The absorption spectrum of dyad **8** shows the increased absorbance of acceptor **7** overlain with the fine structure of donor **6**, most notable in the form of the small local maximum at 368 nm.

Excitation with 530 nm predominantly excites the ATTO565 chromophore. Direct excitation of the ATTO647N chromophore is observable for both **ATTO647N azide** and acceptor **7**, but fluorescence emission is weak compared to all other dyes. Interestingly, the emission of both compounds exhibits a side band between 575 – 625 nm which is not visible at 600 nm excitation (compare Figure 4.2

c and **d**) A systematic investigation reveals that the side band becomes more pronounced for shorter excitation wavelengths but disappears above approximately 550 nm excitation (see appendix Figure 7.4). It it estimated that the emission side band is an indicator of some degree of anti-Kasha behavior, i.e., fluorescence emission from a higher vibronic or excited state.

Table 4.1: Fluorescence lifetimes τ and fluorescence quantum yields Φ of compounds **ATTO565 NHS ester**, **ATTO647N azide**, energy donor reference compound **6**, energy acceptor reference compound **7**, and dyad **8** in methanol. Quantum yields were determined with either 510 nm or 600 nm excitation. Lifetimes were determined either with 527 nm or 635 nm excitation. For the lifetimes of **ATTO565 NHS ester** and donor **6** the emission between 545 – 620 nm was analyzed. For the lifetimes of **ATTO647N azide** and acceptor **7** the emission between 655 – 715 nm was analyzed. For dyad **8**, both spectral windows were analyzed separately. The amplitudes of the fluorescence lifetime components τ_1 and τ_2 are mentioned in square brackets after the lifetimes. The errors of the lifetime components are always in the order of magnitude of the last decimal place specified.

Compound	Φ / %	λ_{exc} / nm	λ_{em} / nm	τ_1 / ns	τ_2 / ns
ATTO565 NHS ester	97[a]	527	545 – 620	4.13 [100%]	-
Donor **6**	61[a]	527	545 – 620	2.95 [73%]	2.19 [27%]
Dyad **8**	58[a]	527	545 – 620	3.43 [69%]	1.94 [31%]
ATTO647N azide	75[b]	635	655 – 715	4.30 [100%]	-
Acceptor **7**	66[b]	635	655 – 715	4.20 [100%]	-
Dyad **8**	61[b]	635	655 – 715	3.76 [100%]	-
Dyad **8**	58[a]	527	655 – 715	3.67 [100%]	-

[a] Fluorescence quantum yield Φ determined at 510 nm excitation.
[b] Fluorescence quantum yield Φ determined at 600 nm excitation.

The emission spectra of **ATTO565 NHS ester** and donor **6** at 530 nm excitation resemble each other in shape, apart from a 5 nm shift of the maximum from 575 nm to 580 nm. Most noteworthy, however, is the reduction of the intensity by almost half for the donor **6** compared to the unreacted dye. The qualitative observation is also quantified by a similar drop of the fluorescence quantum yield, from an almost quantitative quantum yield of 97% for **ATTO565 NHS ester** to 61% of the reference donor **6**. The reduction of the quantum yield is attributed to an intramolecular quenching process caused by the nitrophenyl group of the photocleavable linker. For one, nitrophenyl is a known fluorescence quencher.[195,196] Second, Stern-Volmer experiments with various nitro-arenes also verify the existence of a quenching effect (see appendix Figures 7.6–7.8 for spectra, Figure 7.12 for the Stern-Volmer plot and Table 7.1 for an overview of the results). The values of the bimolecular quenching constants indicate moderately efficient, but not yet diffusion-controlled quenching (see also Section 2.1.2). It is assumed that the quenching efficiency is drastically increased in the intramolecular case. The hypothesis of intramolecular quenching by the nitrophenyl moiety is further confirmed by a matching alteration of fluorescence lifetimes. Whereas ATTO565 exhibits a single long lifetime, $\tau = 4.13$ ns, donor **6** has two shorter lifetime components, $\tau_1 = 2.95$ ns and $\tau_2 = 2.19$ ns, in a ratio of approximately 3:1 (see Table 4.1). It is estimated that the donor **6** in solution can freely adopt a wide variety of conformations with differing quenching efficiencies due to variable distances and orientations between the quenching moiety and

the chromophore. The two lifetime components then represent average values corresponding to several rapidly interchanging conformations. Since it is not expected that the crucial distances between quencher and chromophore differ all that much for the various adopted conformations, and hence quenching efficiencies are also comparable, the two observed lifetime components are similar, too. At 600 nm excitation, no significant fluorescence emission is observed for either the unreacted dye or donor **6**.
Intramolecular quenching is also observed for acceptor **7**, but significantly less pronounced. Comparing the emission spectra of **ATTO647N azide** and the reference acceptor **7**, especially at 600 nm excitation, reveals a slight decrease of fluorescence intensities for the acceptor. The drop is most notable around the emission maximum at 660 nm. Otherwise, the emission spectra are identical. The phenomenon is again quantified by a minor drop of quantum yields and lifetimes. The fluorescence quantum yield is reduced from 75% for the unreacted dye to 66% for acceptor **7**. Likewise, the lifetime drops from 4.3 ns to 4.2 ns. Contrary to donor **6**, only a single lifetime component is observed for acceptor **7** (see also the TCSPC curves in the appendix, Section 7.2.3). A lower (intramolecular) quenching efficiency of ATTO647N than of ATTO565 is consistent with the results of the Stern–Volmer experiments (appendix, Table 7.1). Bimolecular quenching of ATTO647N with nitro-arenes is in all tested cases less efficient than quenching of ATTO565. Hence, quenching of ATTO647N with nitro-arenes is considered to be not diffusion controlled. The weak quenching indicates either steric shielding of the ATTO647N chromophore or a low quenching efficiency of the quencher (see also Section 2.1.2). This effect seems to be translated to the intramolecular case.
Excitation of the dyad **8** at 530 nm leads to a global emission maximum at 660 nm which is associated with the ATTO647N chromophore. The intensity vastly exceeds the observed emission of acceptor **7** due to direct excitation at 530 nm. Thus, the presence of efficient energy transfer is confirmed. Assuming a FRET mechanism, the Förster distance can be calculated with equation (2.15). The overlap integral is calculated with the normalized emission spectrum of donor **6** and the absorption spectrum of acceptor **7** normed to the known maximum absorption coefficient $\varepsilon(642\ \text{nm}) = 150000\ \text{L}\,\text{mol}^{-1}\,\text{cm}^{-1}$. The determined quantum yield of donor **6** is used and free rotation of both dyes is assumed ($\kappa^2 = 2/3$). A Förster distance of $R_0 = 6.23$ nm is thus calculated for the reference donor-acceptor pair. Using the spectra and quantum yield of the precursor dyes, a Förster distance of $R_0 = 6.61$ nm is obtained. Both values are reasonably close to the Förster distance as specified by the manufacturer for the dye pair used in aqueous solution ($R_0 = 6.9$ nm, see also Figure 7.90), especially given the smaller spectral overlap in methanol than in water (see also Section 4.3.2) and the lower quantum yield of donor **6** compared to the unreacted dye.
Interestingly, a weaker local emission maximum is observed at 580 nm which is associated with the ATTO565 chromophore. Compared to the emission of donor **6**, the intensity at 580 nm is reduced by about 80%. Hence, the FRET efficiency according to equation (2.14) is approximately $\eta_{\text{FRET}} = 80\%$. In light of the large calculated Förster distance, a more quantitative FRET efficiency was expected. Using the determined FRET efficiency to calculate the distance of the two chromophores in the dyad with equation (2.13) yields a distance of almost 5 nm. Given the structure of the dyad, and in particular the photolabile linker (see also Figure 4.2 **c**), the distance seems unreasonably large. It is not entirely clear what causes the non-quantitative FRET efficiency of the dyad. In the following, several possible reasons are discussed and evaluated. The most trivial explanations for the apparent incomplete energy

transfer are unspecific partial cleavage due to, for example, insufficient protection from UV-light or a contamination of the dyad **8** with donor **6** due to insufficient purification (see also Section 6.2.8 for the detailed synthesis protocol of the dyad). The latter hypothesis is highly unlikely, however, given the almost perfect ratio of the experimental absorption maxima in the absorption spectrum of dyad **8** compared to the theoretical ratio based on the absorption coefficients of ATTO565 and ATTO647N (0.77 vs. 0.8, see above). Moreover, HPLC analysis confirms that none of the precursor **6** remains after synthesis and purification of dyad **8** (see also Section 7.9 in the appendix). Unspecific cleavage can be excluded based on the lifetime measurements before and after controlled photocleavage (see below). None of the easily distinguishable cleavage products (see Section 4.4.1) are found in the non-irradiated samples. Instead, the lifetime measurements, like the spectral measurements, imply that a minor fraction of donors fluoresces regularly instead of transferring their excitation energy.

In this context, three unconfirmed hypotheses seem more likely. Either, the assumption of free rotation of both dyes in the dyad is invalid and hence a wrong value of $\kappa^2 = 2/3$ is used, leading to an overestimation of the Förster distance and consequently the distance between the chromophores in the dyad. Defocused measurements of the dyad in polymer films (see Section 4.6) do not fully support this hypothesis, however, as rotational restrictions of the emitting dipoles are only observed in very specific cases of some rigid polymers. It is also possible that the dyad adopts a conformation highly unfavorable for energy transfer, i.e., a conformation maximizing the distance between the chromophores, due to electrostatic repulsion of the dyes. Both dyes are slightly positively charged under acidic and neutral conditions, hence repulsive electrostatic interactions are possible. However, given the distribution of single positive charges over extended conjugated π-systems and further possible attractive electrostatic effects like $\pi-\pi$-stacking, the hypothesis does not seem intuitive to the mind of a chemist. Furthermore, on the single molecule level the apparent FRET efficiency seems to be more quantitative (see Section 4.4.3). Lastly, a strong diversion from the Förster energy transfer model cannot be excluded. Additional effects like the quenching by the nitrophenyl moiety and the shortened lifetime of the donor excited state might influence the FRET behavior in unrecognized ways. Reverse FRET from the ATTO647N chromophore to the ATTO565 chromophore is also a possibility, especially given the hypothesized anti-Kasha behavior of ATTO647N upon excitation with short wavelengths (see above). The spectral overlap of the emission spectrum of acceptor **7** (excited at 530 nm) with the absorption spectrum of donor **6**, although small, is not zero. At 600 nm or longer wavelength excitation, however, the overlap integral approaches zero. Depending on the quantum yield of acceptor **7** at 530 nm excitation, a theoretical Förster distance of up to $R_0 = 3.01$ nm is calculated for the energy transfer from the ATTO647N chromophore to the ATTO565 chromophore. The value above was calculated with the quantum yield determined at 600 nm (66%). In the case of regular Kasha behavior, fluorescence quantum yields are independent of the excitation wavelength. In light of the potential anti-Kasha behavior of ATTO647N, the quantum yield at 530 nm might change significantly, and the calculated reverse-Förster distance is likely considerably overestimated. Moreover, only the anti-Kasha part of the emission shows any overlap with the absorption of ATTO565, thus valid calculation of the reverse-Förster distance might require knowledge of the quantum yield of this specific process. Nevertheless, even at fluorescence quantum yields as low as 0.1%, which is definitely an underestimation in any way, the Förster distance still equates to $R_0 = 1.0$ nm. Given the overall size of dyad **8**, this implies that reverse FRET is possible,

albeit with a significantly worse efficiency than in the intended direction. Simulations and theoretical calculations are required to ultimately answer this question.
The fluorescence lifetime of dyad **8** matches well with the lifetimes discussed so far. Analyzing the spectral window between 545 – 620 nm, where the ATTO565 chromophore is dominant, reveals two lifetime components, $\tau_1 = 3.43$ ns and $\tau_2 = 1.94$ ns. Both magnitude and amplitude, i.e., ratio of the two components, are reasonably comparable to the lifetime components of the donor **6**. The divergence is within the uncertainty of the measurement, especially given the inevitably imperfect spectral separation of donor and acceptor fluorescence in the dyad. Some of the photons contributing to the TCSPC curve stem from the ATTO647N chromophore which is excited either directly or by energy transfer and exhibits fluorescence emission from approximately 575 – 800 nm (compare Figure 4.2 b). Analyzing the spectral window between 655 – 715 nm yields a single lifetime component, regardless of whether the ATTO565 chromophore is excited at 527 nm or the ATTO647N chromophore is excited more directly at 635 nm (3.67 ns and 3.76 ns, respectively). Both lifetimes are considered equal within the margin of error. Imperfect spectral separation can even rationalize the slightly smaller value of the lifetime at 527 nm excitation, as the TCSPC statistic is insignificantly contaminated with the shorter lifetime components of the ATTO565 chromophore. Overall, the presence of energy transfer in the dyad **8** is once more confirmed. However, the deviation of the lifetimes of acceptor **7** and the dyad **8** (compare Table 4.1) indicate some further unspecified changes of the photophysical properties of the dyad compared to the reference compounds. Imperfect spectral separation cannot explain the variance, since the absorption of the ATTO565 chromophore at 635 nm approaches zero. Later bulk measurements (see Section 4.4.2) confirm that the photochemical properties of dyad **8** are not completely identical to the reference compounds, hence a likewise alteration of the photophysical properties seems possible. Nonetheless, quantum yield (61%) and emission spectrum of the dyad **8** at 600 nm excitation are the same as for acceptor **7** within the accuracy of the measurements.

4.3.2 Dyad in water

In the following, the characterization of the dyad and all reference compounds dissolved in water is discussed. Absorption spectra of all substances are shown in Figure 4.3 **a**, corresponding emission spectra are depicted in Figures 4.3 **b** and **c** for 530 nm and 600 nm excitation, respectively. For better clarity, the emission spectrum shown in Figure 4.3 **b** is presented once more in Figure 4.3 **d** with approximately tenfold zoom of the *y*-axis to better highlight the weakly fluorescent species. Adjustment of the concentrations was not feasible due to additional effects in the absorption spectrum of the dyad (see below). Instead, all emission spectra are normed to the concentration of the respective fluorescent compound. Concentrations of dyad **8**, acceptor **7** and **ATTO647N azide** were determined with the Lambert-Beer law (2.9) using the absorbance values at the absorption maxima at 650 nm and 645 nm, respectively. Concentration of donor **6** and **ATTO565 NHS ester** were determined with the Lambert-Beer law (2.9) using the absorbance values at the absorption maxima at 568 nm and 565 nm, respectively. Quantum yields and lifetimes of all dyes are listed in Table 4.2. All TCSPC curves can be found in the appendix (Section 7.2.3). The same color scheme is used as before.
Like for the methanol solutions (Section 4.3.1), the absorption spectrum between 450 – 700 nm is dominated by the absorption of the ATTO565 and ATTO647N chromophore. In this spectral region, the

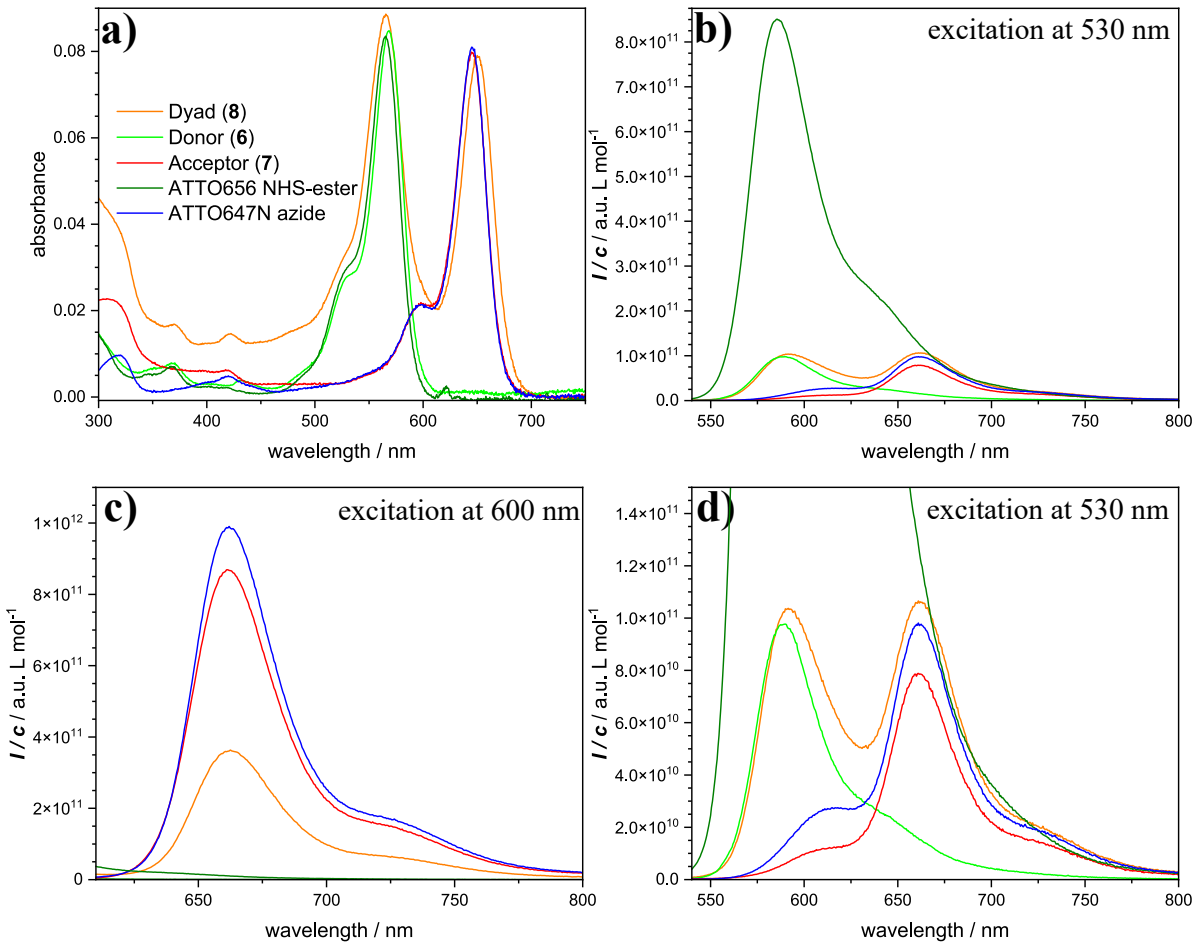

Figure 4.3: (**a**) Absorption and (**b**) emission (excitation at 530 nm) spectra of **ATTO565 NHS ester** (olive), **ATTO647N azide** (blue), reference donor **6** (green), reference acceptor **7** (red), and dyad **8** (orange) in water. The corresponding emission spectra with 600 nm excitation are presented in (**c**). No significant excitation was observed for the compounds without ATTO647N moiety. (**d**) Emission spectra (**b**) in about ten-fold enhancement for a better visualization of the weakly fluorescent species. The intensity I of all emission spectra is normed to the concentration c of the respective compound.

absorption of **ATTO647N azide** and acceptor **7** is essentially the same, reaching the global maximum at 645 nm. In the UV region, the acceptor **7** exhibits slightly increased absorption compared to the unreacted dye. The absorption spectra of **ATTO565 NHS ester** and donor **6** are also similar, apart from a small shift of the absorption maximum from 565 nm to 568 nm. Otherwise, no differences are observed for these two compounds. Most peculiar, however, is the behavior of the dyad **8**. First, the absorption maximum associated to the ATTO647N chromophore is shifted by 5 nm to 650 nm. Second, the absorption maximum associated to the ATTO565 chromophore does not coincide with the absorption maximum of the donor and is seemingly shifted back to 565 nm. Most striking is the fact that the absorbance of the absorption maximum at 565 nm is now higher than of the second maximum at 650 nm despite the higher absorption coefficient of the ATTO647N chromophore. Additionally, all absorbance values at shorter wavelengths than the absorption maximum at 565 nm are significantly higher than for the reference compounds. Thus, the absorption spectrum is not simply the sum of the absorption spectra of donor **6** and acceptor **7**. It appears as if some sort of scattering increases the absorption over basically

the entire spectrum. Scattering could also explain the shift of the absorption maximum of the ATTO565 chromophore compared to donor **6**, but not the shift of the ATTO647N chromophore. Impurities in form of scattering particles from the column during purification cannot be excluded definitively. Nevertheless, they are still unlikely, given that the exact same sample does not show any scattering effects in methanol. In this context, it is possible that all the described effects are caused by clustering of dyad molecules or by an interaction of the dyes in their ground states. The first hypothesis is supported by the fact that the exact same amount of dyad **8** dissolved in equal volumes of methanol and water does not yield the same absorbance values at either absorption maximum. Instead, it appears as if the concentration in water is only a third of that in methanol, when it should be exactly equal (compare Figure 7.5 in the appendix). It appears that the solubility of the dyad in water is considerably worse than the solubility of the reference compounds, leading to clustering and also a preference of the dyad to stick to the glass walls of the cuvette and thereby an apparent reduction of concentration.

Table 4.2: Fluorescence lifetimes τ and fluorescence quantum yields Φ of compounds **ATTO565 NHS ester**, **ATTO647N azide**, energy donor reference compound **6**, energy acceptor reference compound **7**, and dyad **8** in water. Quantum yields were determined with either 510 nm or 600 nm excitation. Lifetimes were determined either with 527 nm or 635 nm excitation. For the lifetimes of **ATTO565 NHS ester** and donor **6** the emission between 545 – 620 nm was analyzed. For the lifetimes of **ATTO647N azide** and acceptor **7** the emission between 655 – 715 nm was analyzed. For dyad **8**, both spectral windows were analyzed separately. The amplitudes of the fluorescence lifetime components τ_1, τ_2 and τ_3 are mentioned in square brackets after the lifetimes. The errors of the lifetime components are always in the order of magnitude of the last decimal place specified.

Compound	Φ / %	λ_{exc} / nm	λ_{em} / nm	τ_1 / ns	τ_2 / ns	τ_3 / ns
ATTO565 NHS ester	92[a]	527	545 – 620	4.01 [100%]	-	-
Donor **6**	8[a]	527	545 – 620	4.04 [49%][c]	2.4 [28%]	0.95 [23%]
Dyad **8**	12[a]	527	545 – 620	3.98 [35%][c]	2.42 [40%]	0.91 [25%]
ATTO647N azide	59[b]	635	655 – 715	3.88 [94%]	1.7 [6%]	-
Acceptor **7**	35[b]	635	655 – 715	3.34 [65%]	1.24 [35%]	-
Dyad **8**	19[b]	635	655 – 715	3.71 [75%]	1.80 [25%]	-
Dyad **8**	12[a]	527	655 – 715	3.60 [75%]	1.6 [25%]	-

[a] Fluorescence quantum yield Φ determined at 510 nm excitation.
[b] Fluorescence quantum yield Φ determined at 600 nm excitation.
[c] The long lifetime component is contributed to free ATTO565. The amplitude is vastly overestimated, since the quantum yield of free ATTO565 in water is about 8 – 12 times higher than that of nitrophenyl-containing compounds, leading to a strong bias in the photon statistics. Spectral analysis indicates that the compound underwent minor degradation during storage, but not to the extent implied by the (uncorrected) amplitudes of the lifetime components.

The emission spectrum at 600 nm excitation also differs from its counterpart in Section 4.3.1. **ATTO647N azide**, acceptor **7** and dyad **8** all exhibit an emission maximum at 662 nm, thus about 2 nm red-shifted compared to the methanol solutions. However, the intensity of all three compounds varies more significantly. **ATTO647N azide** still shows the strongest emission of all compounds containing the ATTO647N chromophore. Compared to the methanol solutions, the quantum yield (59%) is considerably reduced and instead of a single long lifetime two shorter lifetime components, $\tau_1 = 3.88$ ns [94%]

and $\tau_2 = 1.7$ ns [6%], are detected. This is consistent with the phenomenon of universal quenching of many (red-emitting) dyes by O–H-vibrations.[44] The additional O–H-bond per water molecule compared to methanol decreases the quantum yield and lifetime of most regular (red-emitting) dyes, that among ATTO647N.[44] Quantum yield and lifetime are reasonably similar to the values specified by the manufacturer for ATTO647N in aqueous PBS solution (65% and 3.5 ns, respectively, see also Figure 7.88). More interesting is the difference of the emission of acceptor **7** and dyad **8**. In methanol, emission spectrum and quantum yields at 600 nm excitation are essentially the same for both compounds and only the lifetimes are different. Both acceptor **7** and dyad **8** show only minor intensity decreases in methanol compared to **ATTO647N azide** due to inefficient intramolecular quenching. In water, the emission intensity of the dyad **8** is further reduced compared to acceptor **7**. The emission intensity of acceptor **7** seems similarly reduced compared to **ATTO647N azide** as in methanol. However, the quantum yield (35%) and lifetime components of acceptor **7**, $\tau_1 = 3.34$ ns [65%] and $\tau_2 = 1.24$ ns [35%], indicate a more drastic change than can be observed in the emission spectrum. The drop of the quantum yield is much more significant than in methanol. Likewise, both lifetime components are considerably shorter than the two lifetime components of **ATTO647N azide**, thereby indicating a more efficient intramolecular quenching by the nitrophenyl-moiety in water than in methanol. It is not clear why two lifetime components are observed in water when only one lifetime component is detected for all compounds containing the ATTO647N chromophore in methanol. The manufacturer reports only a single lifetime component for ATTO647N in aqueous PBS solution (see also Figure 7.88). The quantum yield of the dyad (19%) is even further reduced, reflecting the observed decrease in intensity. Curiously, the lifetime components of the dyad in the spectral window between 655 – 715 nm at 635 nm excitation, $\tau_1 = 3.71$ ns [75%] and $\tau_2 = 1.80$ ns [25%], are more comparable to the lifetime components of **ATTO647N azide**. Within the accuracy of the measurements, the same magnitude and amplitude of the lifetime components of the dyad are obtained when exciting with 527 nm ($\tau_1 = 3.60$ ns [75%] and $\tau_2 = 1.6$ ns [25%]). The differences, especially in lifetimes, once more indicate that the photophysical properties of the dyad are altered in unexpected ways compared to acceptor **7**.

The emission spectrum at 530 nm excitation is even more curious. While **ATTO647N azide** and acceptor **7** behave similarly as in methanol, with only minor direct excitation observable and the same insignificant red-shift as mentioned above, the fluorescence emissions of donor **6** and dyad **8** are vastly different. Of all compounds containing the ATTO565 chromophore, only the unreacted **ATTO565 NHS ester** exhibits a strong emission with a maximum at 586 nm. The strength of the emission is also reflected in the high quantum yield of 92% and a single long lifetime component of 4.01 ns. Both values are comparable to the respective figures obtained in methanol and match the values as specified by the manufacturer for ATTO565 in aqueous PBS solution (90% and 4.0 ns, respectively, see Figure 7.87). The slight decrease compared to methanol is consistent with the quenching effect of water as described above. The effect has been proven to exist to a lesser extent for ATTO565 than for dyes with a more red-shifted emission.[44] In contrast, the intensity of the donor **6** is only about a tenth of the intensity of the unreacted dye at the slightly shifted maximum at 589 nm. This is also reflected in the small quantum yield of only 8% and the short observed lifetime components. There are three lifetime components detected. The longest and largest component, $\tau_1 = 4.04$ ns [49%], is attributed to free ATTO565. It is estimated that donor **6** was partly cleaved during storage in water prior to the lifetime measurement. Spectral analysis of the

solution used for the lifetime measurement indicates minor degradation, but not to the amount implied by the amplitude of the long lifetime component. It is likely that the photon statistic is falsified due to the fact that after photocleavage the quantum yield of the free dye increases about tenfold (see also Section 4.4.1). Hence, a single molecule of the cleaved donor contributes about ten times more photons than an uncleaved donor molecule. Consequently, the ratio of the long lifetime component is vastly overestimated. No degradation is observed in methanol solutions in comparable time periods under similar storage conditions. It is estimated that unspecific cleavage occurs due to slow hydrolysis of the carbamate moiety, leading to a chemical cleavage similar to the styrene pathway of the photocleavage. Therefore, no nitroso products are present and only one additional long lifetime due to the free ATTO565 chromophore is observed. Since the lifetimes after cleavage according to the styrene pathway are more comparable to the lifetimes before cleavage when measuring the ATTO647N chromophore, no similar effect is observed for either acceptor **7** or dyad **8** in the spectral window between 655 nm – 715 nm (compare lifetimes after photocleavage in Section 4.4.1). However, it is assumed that the donor **6** actually exhibits two lifetimes, $\tau_2 = 2.4$ ns and $\tau_3 = 0.95$ ns, in about equal ratio. As before, both lifetimes are believed to be average values of different conformations with varying quenching efficiencies due to a variable distance to the quenching nitrophenyl-moiety. The longer of the two lifetime components is comparable to the two lifetime components obtained for methanol solutions. The other lifetime component is significantly shorter and indicates that the reference donor adopts a highly unfavorable conformation in water with a very high quenching efficiency.

Corresponding to the drastic decrease of fluorescence emission of donor **6**, similar effects are observed for dyad **8** at 530 nm excitation. The emission maximum at 592 nm, which is associated to the ATTO565 chromophore, shows essentially the same intensity as the emission maximum of donor **6**. The slight shift and even insubstantial increase of intensity is caused by the overlap with the emission of the directly excited ATTO647N chromophore. Contrary to methanol solutions, the emission intensity due to direct excitation of the acceptor **7** at 530 nm is comparable to the emission intensity of donor **6**, hence the spectral overlap has a greater influence on the convoluted spectrum. In that context, no significant energy transfer is observed and the emission maximum of the dyad at 663 nm is essentially the sum of the fluorescence emission of donor **6** and acceptor **7**. The quantum yield (12%) and the three lifetime components in the spectral window between 545 – 620 nm, $\tau_1 = 3.98$ ns [35%], $\tau_2 = 2.42$ ns [40%] and $\tau_3 = 0.91$ ns [25%], are almost identical to the values obtained for donor **6**, too, albeit with a slightly different ratio of the lifetime components. Again, it is assumed that the longest lifetime component is associated to free ATTO565 due to partial unspecific cleavage. The ratio of the two actual lifetime components is less meaningful than in methanol solutions, as it is falsified by the disproportionately high emission of the cleaved fragment bearing the ATTO565 chromophore. Given the observed partial cleavage, it should be noted that the influence on the lifetimes of the dyad **8** and acceptor **7** at 635 nm is less significant. The alteration of quantum yields and lifetimes after photocleavage is considerably less pronounced for the fragment bearing the ATTO647N chromophore, at least in aqueous solutions (see Section 4.4.1). Hence, the lifetime data presented above does not show the same extent of falsification as the lifetimes associated to the ATTO565 chromophore.

Despite the basically nonexistent energy transfer of the dyad in water, the Förster distance can still be calculated with equation (2.15). The overlap integral is calculated using the normalized emission

spectrum of donor **6** and the absorption spectrum of acceptor **7** normed to the maximum absorption coefficient. The fluorescence quantum yield of the donor is used as determined. A Förster distance of $R_0 = 4.55$ nm is calculated. The marginally larger spectral overlap than in methanol is more than compensated by the drastically reduced quantum yield. In contrast, for the unreacted dyes a Förster distance of $R_0 = 6.95$ nm is calculated which coincides with the value specified by the manufacturer (6.9 nm, see also Figure 7.90). Here, the larger spectral overlap than in methanol more than compensates for the slightly lower quantum yield of ATTO565. A theoretical calculation of the distance of the two chromophores in the dyad with equation (2.13) is not feasible, since the apparent FRET efficiency is too close to zero. Depending on the fluorescence quantum yield of acceptor **7** (see Section 4.3.1), a theoretical Förster distance of up to $R_0 = 4.24$ nm is calculated for the energy transfer from the ATTO647N chromophore to the ATTO565 chromophore when using the normalized emission spectrum of acceptor **7** at 530 nm excitation and the absorption spectrum of donor **6** normed to the maximum absorption coefficient. This implies that FRET is almost equally likely in both directions in water. The existence of comparatively efficient reverse FRET could also explain the apparent low FRET efficiency. Overall, the spectral properties in water seem to be highly unfavorable for any microscopy application. However, it is also possible that they offer unique opportunities. For example, both donor **6** and dyad **8** might be used as water sensors. The determination of local water content can be achieved by measuring super-resolved FLIM of red-emitting dyes due to their partial quenching by water.[45,46] It is fathomable that an equivalent approach based on donor **6** and dyad **8** is applicable, with potentially even more significant changes of fluorescence lifetimes and intensities reporting on the local environment. A Nile-Red PAINT approach seems also possible, as the low fluorescence emission of donor **6** and dyad **8** in water might grant a low background comparable to Nile-Red in water. First simple tests were performed in that regard, and an aqueous solution with nanomolar amounts of donor **6** or dyad **8** was added to a sample of spincoated PNIPAM microgels. Unfortunately, the binding affinity of both compounds for the glass substrate appears to be higher than for the tested polymer structures and the produced images are incomparable to real Nile-Red PAINT images of the same microgels. Nonetheless, the drastically different properties of donor **6** and dyad **8** in two so similar media like water and methanol might prove useful for specific applications.

4.4 Irradiation experiments

Several different experiments are discussed in the following section. In Subsection 4.4.1, the photocleavage of the dyad and all reference compounds is investigated in closer detail. To this end, the dye systems are irradiated with a 365 nm LED at 450 $\mathrm{W\,m^{-2}}$ in a spatiotemporal controlled manner. This is done once in methanol and once in water. In Subsection 4.4.2, the photobleaching behavior in bulk is studied by irradiating the dyes with visible light. The experiment is essentially equivalent to the UV-irradiation study, but employing a 645 nm LED at 1.675 $\mathrm{kW\,m^{-2}}$ instead. The photobleaching investigation is restricted to methanol solutions. For a detailed description of the experimental setup of all irradiation experiments, see Section 6.6. Finally, the performance of the dyad on the single molecule level is evaluated qualitatively in Subsection 4.4.3. The investigation is conceptually similar to the bulk irradiation experiments. The dye system is embedded in polymer films and subjected to UV- and

vis-irradiation while the response is observed with binary spectral resolution. A visual proof of concept is delivered, the FEDUP measurement conditions (see also Section 6.7.2) are tested and photobleaching on the single molecule level is briefly investigated. No quantitative analysis is performed yet. However, the data shown in Section 4.4.3 will be used in an exemplary evaluation in Section 4.6.1. A summary and first conclusion of all results gathered in Sections 4.3 and 4.4 is given in Section 4.5.

4.4.1 UV irradiation in bulk

One of the most essential properties of dyad **8** is its ability to be cleaved by UV light. The photolabile NPPOC-type linker is sensitive to UV irradiation and upon excitation it can undergo an intramolecular fragmentation leading to cleavage at the carbamate moiety. Thereby, two fragments are obtained. One fragment consists of a short primary amine attached to ATTO565 and the other fragment consists of the ATTO647N chromophore attached to the residue of the photolabile linker. For all purposes, the first fragment can be considered equal to the pure ATTO565 chromophore. With about 40% quantum efficiency, the photoreaction works extraordinarily well and reliably.[116] Two possible cleavage pathways have been identified for NPPOC in previous works.[111,116–118] Either the residue of the photolabile linker is transformed into an *o*-nitrostyrene, or one of two nitroso products. The formation of the second nitroso product through a rearrangement of the first nitroso product is dependent on the solvent. It has been shown that the rearrangement does occur in methanol.[111] Still, it is assumed that the styrene pathway is the dominant photocleavage reaction. However, both pathways are going to play an important role in the following discussion. The full photocleavage mechanism of the dyad is depicted in Figure 2.9. An overview of the two possible pathways and the resulting photocleavage products is also given in Figure 4.4. Hereafter, the influence of UV irradiation on all compounds characterized in Section 4.3 is investigated.

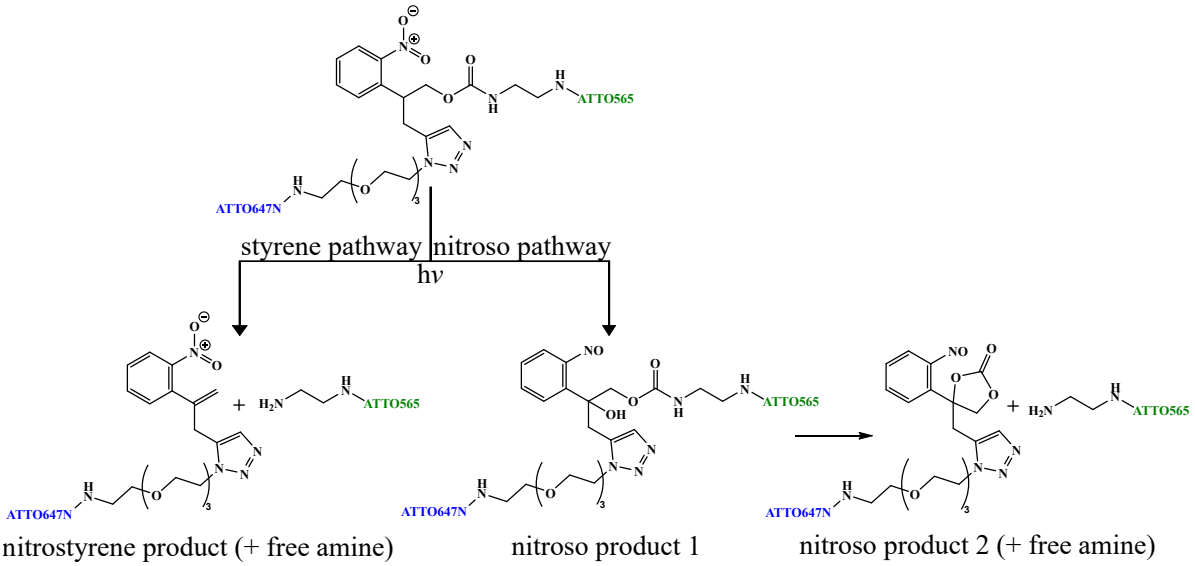

Figure 4.4: Overview of the possible photocleavage products of dyad **8**.

Methanol solutions

To investigate the photocleavage in methanol, **ATTO565 NHS ester**, **ATTO647N azide**, donor **6**, acceptor **7** and dyad **8** were irradiated with 365 nm UV light at 450 $\mathrm{W\,m^{-2}}$. At regular, but increasing, time intervals, the illumination was stopped and absorption and emission spectra were recorded. Overall illumination time was 1500 s. In the case of acceptor **7**, the solution was irradiated for additional 2200 s at approximately tripled power density afterwards (see below). The concentration of all compounds was adjusted to approximately 0.6 $\mu\mathrm{mol\,L^{-1}}$ to enable direct comparability of the emission spectra. Quantum yields and lifetimes were determined only for the fully irradiated samples, i.e., after no significant spectral changes were observed anymore. Only for acceptor **7**, both were determined once after 1500 s of irradiation and once more after the additional illumination time. The spectra and their temporal evolution are shown in Figure 4.5. The quantum yields and lifetimes before and after irradiation are compared in Table 4.3. All TCSPC curves can be found in the appendix (Section 7.2.3).

The unreacted dyes **ATTO565 NHS ester** and **ATTO647N azide** do not possess any known UV-sensitive moieties. Hence, no significant photoreaction, aside from photobleaching, is expected for either dye. Indeed, no obvious photoreaction and only minor photodegradation is observed. Absorption and emission spectra of both dyes remain essentially constant. Likewise, quantum yields and lifetimes remain constant within the error of measurement.

In contrast, donor **6** undergoes several (spectral) changes under the same conditions. The absorbance at the maximum at 557 nm decreases marginally by overall approximately 4%. The decrease can be reasonably well described by a single exponential decay function ($A(t) = A_0 + \Delta A[1 - \exp(-t/\tau)]$ with $\tau = 278$ s). It is estimated that the decrease is not related to the photocleavage, but to an enhanced photobleaching process compared to the unreacted dye, induced by the photolabile linker. At the same time, the fluorescence intensity at the emission maximum at 580 nm increases by about 40%. This is most likely caused by the physical separation of the ATTO565 chromophore from the quenching nitrophenyl moiety (see the possible cleavage products in Figure 4.4). Thereby, the efficient intramolecular quenching is interrupted and only significantly less efficient intermolecular quenching is possible. Like the decrease of absorbance, the increase in intensity can be accurately described by a single exponential function ($F(t) = F_0 + \Delta F[1 - \exp(-t/\tau)]$ with $\tau = 312$ s). This indicates first order kinetics of the photocleavage. A quantum yield of the photoreaction can be estimated from the amount of photons absorbed during any time interval of the irradiation experiment and the conversion of donor **6** to the corresponding free ATTO565 chromophore, as estimated from the change of emission intensity in that time interval relative to the overall alteration. An average value of about 20% is calculated, which matches the literature value reasonably well, given the high uncertainty of the calculation.[116]

The observed enhancement of fluorescence intensity is quantified by a matching increase of the fluorescence quantum yield from 61% to 83%. A similar alteration is observed for the fluorescence lifetimes. Before photocleavage, two similar, and compared to free ATTO565, short lifetime components are detected ($\tau_1 = 2.95$ ns [73%] and $\tau_2 = 2.19$ ns [27%]). After photocleavage, two lifetime components, $\tau_1 = 4.03$ ns [75%] and $\tau_2 = 1.56$ ns [25%], in a similar ratio are observed, but the values differ drastically. The longer lifetime component is equivalent to the lifetime of irradiated **ATTO565 NHS ester** and represents the fraction of fully cleaved donor fluorophores. Most likely, this coincides well with the fraction of donor molecules reacting according to the styrene photoreaction pathway (see Figure

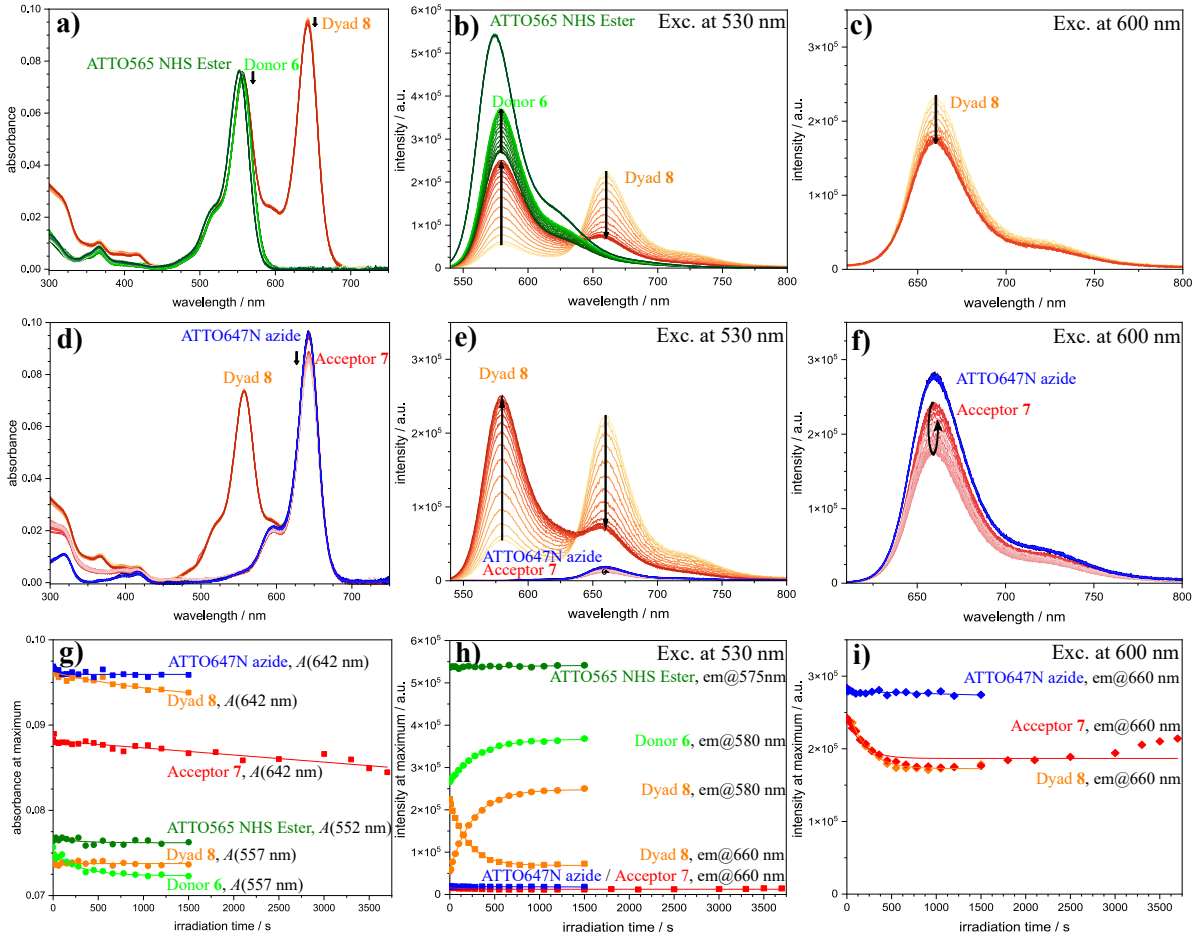

Figure 4.5: Spectral changes of **ATTO565 NHS ester**, **ATTO647N azide**, the reference donor **6**, the reference acceptor **7** and the dyad **8** in methanol during selected irradiation times with a 365 nm LED @ 450 $W\,m^{-2}$. The first column from the left shows the changes of absorption spectra, the second column depicts changes of emission spectra at 530 nm excitation and the third column represents changes of the emission spectra at 600 nm excitation. Changes of (**a**) absorption and (**b**) / (**c**) emission spectra of **ATTO565 NHS ester** (light to dark olive), the reference donor **6** (dark to light green) and the dyad **8** (light to dark orange), respectively. Changes of (**d**) absorption and (**e**) / (**f**) emission spectra of **ATTO647N azide** (dark to light blue), the reference acceptor **7** (dark to light red) and the dyad **8** (light to dark orange), respectively. The black arrows in subfigures (**a**) – (**f**) indicate the changes with increasing irradiation time. (**g**) Temporal evolution of the absorbance at the different wavelengths of the (local) maxima shown in (**a**) and (**d**). (**h**) Temporal evolution of the fluorescence intensities (excitation at 530 nm) at the different wavelengths of the (local) maxima depicted in (**b**) and (**e**). (**i**) Temporal evolution of the fluorescence intensities (excitation at 600 nm) at the different wavelengths of the (local) maxima presented in (**c**) and (**f**). In subfigures (**g**) – (**i**), circles refer to absorbance and emission maxima values related to the ATTO565 chromophore, while squares denote absorbance and emission maxima values related to the ATTO647N chromophore. All solid lines represent fits with single exponential decay functions. The colors correspond to the primary colors of the color gradients used for the spectra of the different compounds in subfigures (**a**) – (**f**).[59]

4.4). In this context, it is assumed that the shorter lifetime represents the fraction of donor molecules that reacts according to the nitroso photoreaction pathway, but does not undergo the rearrangement to the cleaved nitroso product 2. Even if the rearrangement can occur in methanol, it is not entirely clear to which extent or how fast this reaction takes place.[111] Stern–Volmer experiments proof that quenching

of both employed dyes by nitroso-arenes is significantly more efficient than quenching by comparable nitro-arenes (see Figures 7.9 – 7.11 in the appendix for the spectra, Figure 7.12 for the Stern–Volmer plots, and Table 7.1 for a comparison of the results). Contrary to quenching by nitro-arenes, quenching by nitroso-arenes appears to be diffusion-controlled (see also Section 2.1.2). Thus, the existence of an (uncleaved) nitroso photocleavage product rationalizes the observed short lifetime component, as well as the incomplete restoration of the quantum yield of ATTO565. If the ATTO565 chromophore was cleaved completely, the quantum yield should be even closer to the value of the unreacted dye (97 – 99%), since the concentration of the quencher (about 0.6 $\mu mol L^{-1}$) is too small to cause efficient intermolecular quenching, even if donor **6** reacted entirely according to the nitroso pathway (compare the quenching effect of several orders of magnitude higher concentrated nitroso arenes in Figure 7.11 in the appendix). It should be noted, however, that the ratio of the two lifetime components is likely falsified due to the difference in quantum yields of the free ATTO565 chromophore and the intramolecularly quenched uncleaved nitroso product. Like discussed in Subsection 4.3.2 already, the contribution of the component with the higher quantum yield to the decay curve is overestimated due to a disproportionately high contribution of photons. A more trivial explanation for the observed lifetimes and quantum yield, like an incomplete photoreaction, can be excluded based on the consistency of absorption and emission spectra between approximately 800 – 1500 s irradiation time. Neither absorption nor emission spectra change significantly anymore after 800 s of irradiation, indicating a quantitative photoreaction.

Like donor **6**, acceptor **7** also shows minor photodegradation which is indicated by the decrease of the absorbance at the absorption maximum at 642 nm by about 2% after 1500 s. Simultaneously, the fluorescence intensity at the emission maximum at 660 nm decreases by about 27%, which clearly exceeds the expected decrease due to photobleaching. The decrease until this point in time is well described by a single exponential decay function with a time constant ($\tau = 263$ s) similar to the one obtained for donor **6**. Thus, the underlying photoreaction appears to exhibit similar first order kinetics. The decrease is quantified by a drop of fluorescence quantum yield from 66% to 58%. The fluorescence decay kinetics show matching alterations. Before photocleavage, a single long lifetime of 4.20 ns is observed. After 1500 s of UV irradiation, two lifetime components, $\tau_1 = 4.17$ ns [89%] and $\tau_2 = 1.3$ ns [11%], are detected instead. It is assumed that the longer lifetime component corresponds to the fraction of acceptor molecules reacting according to the styrene photocleavage pathway. Stern-Volmer experiments show that quenching by nitrostyrene is comparable to quenching by other nitro-arenes, but with slightly higher quenching efficiency. The stronger quenching does not seem to be reflected in the intramolecular case. It is possible that the conformational freedom of the nitrostyrene cleavage product is restricted compared to the uncleaved nitrophenyl compound **7**. Hence, the cleavage product could be restricted to conformations slightly less favorable for intramolecular quenching. This effect might counterbalance the increased quenching efficiency of nitrostyrene compared to similar compounds without the double bond. The shorter lifetime component is ascribed to the possible nitroso products of the photocleavage. The ATTO647N chromophore remains attached to the quenching moiety irrespective of the photocleavage pathway, hence shorter lifetimes than for the free chromophore are to be expected. The existence of nitroso compounds even rationalizes the fact that the second lifetime component of acceptor **7** is shorter still than the short lifetime component of donor **6** after photocleavage. Contrary to nitro-arenes, nitroso-arenes are shown to quench ATTO647N more efficiently than ATTO565 (see

Table 4.3: Fluorescence lifetimes τ and fluorescence quantum yield Φ of compounds **ATTO565 NHS ester**, **ATTO647N azide**, energy donor reference compound **6**, energy acceptor reference compound **7**, and dyad **8** in methanol before and after 1500 s of irradiation with a 365 nm LED @ 450 $\mathrm{W\,m^{-2}}$. Quantum yields were determined with either 510 nm or 600 nm excitation. Lifetimes were determined either with 527 nm or 635 nm excitation. For **ATTO565 NHS ester** and donor **6** the emission between 545 – 620 nm was analyzed. For **ATTO647N azide** and acceptor **7** the emission between 655 – 715 nm was analyzed. For dyad **8**, both spectral windows were analyzed separately. The amplitudes of the fluorescence lifetime components τ_1 and τ_2 are mentioned in square brackets underneath the lifetimes. The errors of the lifetime components are always in the order of magnitude of the last decimal place specified.

Compound	Φ (no $h\nu$) / %	Φ ($h\nu$) / %	λ_{exc} / nm	λ_{em} / nm	τ_1 (no $h\nu$) / ns	τ_2 (no $h\nu$) / ns	τ_1 ($h\nu$) / ns	τ_2 ($h\nu$) / ns
ATTO565 NHS ester	97[a]	99[a]	527	545 – 620	4.13 [100%]	-	4.07 [100%]	-
Donor **6**	61[a]	83[a]	527	545 – 620	2.95 [73%]	2.19 [27%]	4.03 [75%]	1.56 [25%]
Dyad **8**	58[a]	57[a]	527	545 – 620	3.43 [69%]	1.94 [31%]	4.12 [91%]	1.68 [9%]
ATTO647N azide	75[b]	73[b]	635	655 – 715	4.30 [100%]	-	4.27 [100%]	-
Acceptor **7**[c]	66[b]	58[b]	635	655 – 715	4.20 [100%]	-	4.17 [89%]	1.3 [11%]
Dyad **8**	61[b]	55[b]	635	655 – 715	3.76 [100%]	-	4.17 [82%]	1.04 [18%]
Dyad **8**	58[a]	57[a]	527	655 – 715	3.67 [100%]	-	3.93 [71%]	1.01 [29%]

[a] Fluorescence quantum yield Φ determined at 510 nm excitation.
[b] Fluorescence quantum yield Φ determined at 600 nm excitation.
[c] After additional 2200 s of UV irradiation at approximately tripled power density, the lifetimes and quantum yield increase to $\tau_1(3700\ \mathrm{s}) = 4.21$ ns [95%], $\tau_2(3700\ \mathrm{s}) = 1.7$ ns [5%] and $\Phi(3700\ \mathrm{s}) = 66\%$.

also appendix, Table 7.1), resulting in even shorter lifetimes of the possible nitroso cleavage products of acceptor **7**. The lifetimes are somewhat comparable despite belonging to entirely different dyes, since the lifetimes of ATTO565 and ATTO647N are quite similar in methanol.

Upon closer inspection, it was noticed that the fluorescence emission intensity of acceptor **7** actually increases again after approximately 1000 s. To investigate this phenomenon in closer detail, the acceptor was irradiated for an additional 2200 s at approximately tripled power density. Despite further decreases of the absorption due to, probably, photobleaching by some additional 2%, the emission intensity continues to rise until the end of the experiment. About 88% of the original fluorescence intensity is restored at the emission maximum at 660 nm. The effect is also quantified by an increase of the quantum yield from 58% back to 66% and further alteration of the lifetime components. Two lifetime components are observed after overall 3700 s irradiation. The longer lifetime component can be considered unchanged within the accuracy of the measurement ($\tau_1(1500\ \mathrm{s}) = 4.17$ ns [89%] vs. $\tau_1(3700\ \mathrm{s}) = 4.21$ ns [95%]). The shorter lifetime component, however, increases significantly, from $\tau_2(1500\ \mathrm{s}) = 1.3$ ns [11%] to $\tau_2(3700\ \mathrm{s}) = 1.7$ ns [5%]. Dimerization of nitroso compounds in solution is known to occur.[197] Likewise, a reversible photoreaction under UV irradiation is possible.[198] Both

processes could play a role in the further alteration of the photophysical properties.
Lastly, fluorescence correlation spectroscopy (FCS) measurements were performed for **ATTO647N azide**, acceptor **7** and the dyad **8** before and after irradiation (see Section 7.3 in the appendix for the FCS curves and Section 6.5.1 for the measurement details). All FCS curves are analyzed employing a pure diffusion model. In all cases a single time component is found, with the only exception of acceptor **7** at prolonged irradiation times. Before photocleavage, the determined diffusion rates of all three dyes vary according to their different molecular weights. Diffusion coefficients of $D_{\mathrm{A647N}}(0\ \mathrm{s}) = 681\ \mu\mathrm{m}^2\,\mathrm{s}^{-1}$, $D_{\mathrm{A7}}(0\ \mathrm{s}) = 521\ \mu\mathrm{m}^2\,\mathrm{s}^{-1}$ and $D_{\mathrm{D8}}(0\ \mathrm{s}) = 478\ \mu\mathrm{m}^2\,\mathrm{s}^{-1}$ are obtained for **ATTO647N azide**, acceptor **7** and dyad **8**, respectively. After 1500 s of UV irradiation, the same diffusion coefficient is determined within the margin of error for both acceptor **7** ($D_{\mathrm{A7}}(1500\ \mathrm{s}) = 567\ \mu\mathrm{m}^2\,\mathrm{s}^{-1}$) and dyad **8** ($D_{\mathrm{D8}}(1500\ \mathrm{s}) = 576\ \mu\mathrm{m}^2\,\mathrm{s}^{-1}$). The value of the diffusion coefficient approaches, if not quite reaches, the value of the diffusion coefficient of **ATTO647N azide**, which remains unaffected by the UV irradiation ($D_{\mathrm{A647N}}(1500\ \mathrm{s}) = 672\ \mu\mathrm{m}^2\,\mathrm{s}^{-1}$). Thereby, it is confirmed that the photocleavage of acceptor **7** and dyad **8** is essentially equivalent. After 3700 s of irradiation, the FCS curve of acceptor **7** exhibits a second time component. The first component corresponds to a similar diffusion coefficient as before ($D_{\mathrm{A7,1}}(3700\ \mathrm{s}) = 624\ \mu\mathrm{m}^2\,\mathrm{s}^{-1}$ [85%]), whereas the second minor component corresponds to an about threefold lower diffusion coefficient ($D_{\mathrm{A7,2}}(3700\ \mathrm{s}) = 196\ \mu\mathrm{m}^2\,\mathrm{s}^{-1}$ [15%]). This indicates some degree of oligo- or polymerization of the nitrostyrene photocleavage product under UV irradiation. The behavior of the system under prolonged UV irradiation has not been tested for the other dyes, but similar results are expected for dyad **8** and to some degree even donor **6**.
The photocleavage of dyad **8** displays characteristics very similar to the ones discussed for donor **6** and acceptor **7** above. The drop of the absorbance at the maximum at 642 nm is highly comparable to the photodegradation of acceptor **7**. The absorption maximum at 557 nm remains essentially constant. The less significant photodamage of the ATTO565 chromophore compared to donor **6** indicates protection of the donor moiety by transfer of the excitation energy to the ATTO647N chromophore, at least before photocleavage. In the emission spectra, the irradiation time-dependent decrease of FRET due to the physical separation of the two chromophores can be observed. At 530 nm excitation, cleavage of the linker leads to a reduction of the fluorescence emission associated to the ATTO647N chromophore around the local maximum at 660 nm by overall about 70%. Simultaneously, the fluorescence emission associated to the ATTO565 chromophore around the local maximum at 580 nm increases by overall about 350%. The increase significantly surpasses the increase of emission intensity of donor **6** due to the physical separation from the quenching nitrophenyl moiety (about 40%). Both increase and decrease of the local emission maxima are well described by first order kinetics with time constants of 258 s and 195 s, respectively. The values are reasonably similar within the accuracy of their determination. No significant energy transfer remains after approximately 800 s of irradiation. The resulting emission spectrum is the sum of the emission spectra of the (cleaved) reference donor and acceptor. At 600 nm excitation, the fluorescence emission of dyad **8** behaves essentially identical to the fluorescence emission of acceptor **7**. The emission intensity around the maximum at 660 nm decreases by overall about 22%, which is reminiscent of the decrease observed for acceptor **7** within the same irradiation time (27%). Even a similar marginal increase of the intensity is detected at the end of irradiation experiment. It was refrained from irradiating the dyad **8** for longer times. However, it is assumed that the emission behavior

at 600 nm excitation remains identical to acceptor **7**. The decrease in emission intensity at 660 nm can be well described with a single exponential decay function with a time constant of 200 s. The value perfectly matches the time constants of the increase and decrease of fluorescence emission at 530 nm excitation. The similarity of the first order kinetics of dyad **8** and both reference compounds suggests that all three dye systems react comparably under UV irradiation.
Not only the semi-quantitative spectral changes of dyad **8** are analogous to donor **6** and acceptor **7**, likewise the lifetimes are altered in a comparable fashion. Analyzing the emission window between 545 – 620 nm, two lifetime components, $\tau_1 = 4.12$ ns [91%] and $\tau_2 = 1.68$ ns [9%], are found. Both values coincide with the lifetime components detected for donor **6** after photocleavage. Hence, the interpretation of the two lifetime components is also the same. It is assumed that the longer lifetime component belongs to the free ATTO565 chromophore, whereas the shorter lifetime component indicates the presence of the uncleaved nitroso product. The ratio of the two lifetime components, however, is different. Given the estimated inaccuracies due to disproportionate contributions to the photon statistics by the different photocleavage fragments, the difference is not deemed significant. Moreover, a slight variation of the photochemical reactivity is to be expected for two systems this chemically different. The fluorescence quantum yield remains unaltered within the accuracy of the measurement. Since both chromophores absorb at 510 nm, the determined quantum yield is highly inaccurate and not as meaningful as for the reference compounds. Analyzing the emission window between 655 – 715 nm, two lifetime components are observed which are reasonably similar in magnitude and amplitude to the lifetime components of acceptor **7** after 1500 s of UV irradiation, irrespective of the excitation wavelengths ($\tau_1 = 4.17$ ns [82%] and $\tau_2 = 1.04$ ns [18%] at 635 nm excitation vs. $\tau_1 = 3.93$ ns [71%] and $\tau_2 = 1.01$ ns [29%] at 527 nm excitation). The slight difference of the determined lifetimes of dyad **8** can be explained by imperfect spectral separation of the ATTO647N emission from the ATTO565 emission at 527 nm excitation. The different lifetime components are also estimated to reflect the two different photocleavage pathways. The fluorescence quantum yield decreases from 61% before irradiation to 55% after irradiation, which mirrors the behavior of the reference acceptor. Thus, all results confirm that the photocleavage products of dyad **8** are a mixture of the cleavage products of donor **6** and acceptor **7**.

Aqueous solutions

Given the vastly different behavior of the system in methanol and in water even before any photoreaction (compare Sections 4.3.1 and 4.3.2), a more systematic investigation of the photocleavage in water is obligatory. The investigation is restricted to the UV-responsive compounds donor **6**, acceptor **7** and dyad **8**, since no significant photoreactions are observed for the unreacted dyes **ATTO565 NHS ester** and **ATTO647N azide** in methanol. It is assumed that the precursor dyes are likewise unreactive under the same illumination conditions in water. The measurements are performed the same way as before, i.e., the samples were irradiated for at least 1500 s. Absorption and emission spectra were recorded at the same increasing time intervals. Donor **6** was irradiated for additional 1200 s since the emission spectrum was still undergoing significant changes after 1500 s of irradiation. This already indicates a less efficient photocleavage in water than in methanol, where the reaction appears to be completed after about 800 s of irradiation at the same power density. Acceptor **7** was irradiated for additional 1500 s to see if a similar behavior under prolonged irradiation times is observed. Lifetimes and quantum yields

were determined after full irradiation of each compound, i.e., when no significant spectral changes were observed anymore. The absorption and emission spectra at different irradiation times, as well as the temporal evolution of absorption and emission maxima, are shown in Figure 4.6. The lifetimes and quantum yields before and after UV irradiation are compared in Table 4.4. All TCSPC curves can be found in the appendix (Section 7.2.3). Since adjustment of the different compounds to comparable concentrations was not feasible (see also Section 4.3.2), the intensities in all emission spectra in Figure 4.6 are normed to the concentrations of the respective dyes. The concentration of donor **6** was calculated with the Lambert–Beer law (2.9) using the maximum absorbance value at 568 nm and the specified maximum absorption coefficient of ATTO565. The concentrations of acceptor **7** and dyad **8** were determined with the Lambert–Beer law (2.9) using the maximum absorbance value at 646 nm and 650 nm, respectively, and the specified maximum absorption coefficient of ATTO647N.

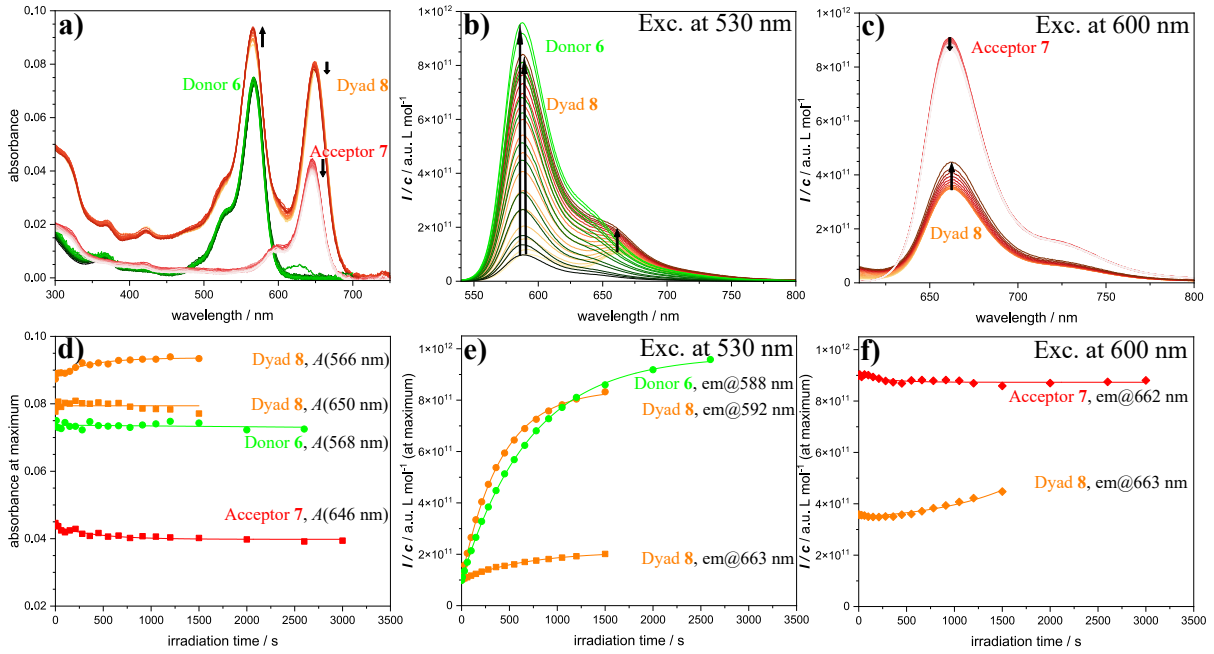

Figure 4.6: Spectral changes of the reference donor **6**, the reference acceptor **7** and the dyad **8** in water during selected irradiation times with a 365 nm LED @ 450 W m^{-2}. The first column from the left shows the changes of absorption spectra, the second column depicts changes of emission spectra at 530 nm excitation and the third column represents changes of the emission spectra at 600 nm excitation. Changes of (**a**) absorption and (**b**) / (**c**) emission spectra of the reference donor **6** (dark to light green), the reference acceptor **7** (dark to light red) and the dyad **8** (light to dark orange), respectively. The black arrows in subfigures (**a**) – (**c**) indicate the changes with increasing irradiation time. (**d**) Temporal evolution of the absorbance at the different wavelengths of the (local) maxima shown in (**a**). (**e**) Temporal evolution of the fluorescence intensities (excitation at 530 nm) at the different wavelengths of the (local) maxima depicted in (**b**). (**f**) Temporal evolution of the fluorescence intensities (excitation 600 nm) at the different wavelengths of the (local) maxima presented in (**c**). In subfigures (**d**) – (**f**), circles refer to absorbance and emission maxima values related to the ATTO565 chromophore, while squares denote absorbance and emission maxima values related to the ATTO647N chromophore. All solid lines represent fits with single exponential decay functions. The colors correspond to the primary colors of the color gradients used for the spectra of the different compounds in subfigures (**a**) – (**c**). The intensity I of all emission data is normed to the concentration c of the respective compound.

All investigated UV-sensitive compounds behave generally differently in water than in methanol under UV irradiation. The changes of the absorption spectra of all dyes are even less pronounced than in methanol. No significant reduction of the absorbance at the absorption maximum at 568 nm is observed for donor **6**. The absorption maximum shifts to marginally shorter wavelengths, though, approaching the position of unreacted **ATTO565 NHS ester** in water (see Figure 4.3). The fact that the spectrum shifts slightly but remains otherwise constant confirms the assumption that the photolabile linker does not significantly alter the absorption of the ATTO565 chromophore, in particular the absorption coefficient. The absorbance at the absorption maximum of acceptor **7** at 646 nm decreases by about 10% overall. The drop occurs almost entirely in the first 800 s of irradiation, while no significant change is observed between 800 s – 3000 s of irradiation. Similarly, the absorbance at the absorption maximum of the dyad **8** at 650 nm is lowered by approximately 4% after 1500 s of irradiation. Surprisingly, the absorbance at the absorption maximum of the dyad **8** at 566 nm even increases by overall about 7%. It is not clear which effect causes the increase of the absorption spectrum of the dyad between approximately 500 nm – 600 nm. No equivalent effect is observed for either donor **6** or acceptor **7**. No noteworthy shifts are observed, but it is likely that any possible shifts, especially of the absorption maximum at 650 nm, are covered by the unexplained increase.

Table 4.4: Fluorescence lifetimes τ and fluorescence quantum yield Φ of the energy donor reference compound **6**, the energy acceptor reference compound **7**, and the dyad **8** in water before and after up to 3000 s of irradiation with a 365 nm LED @ 450 $\mathrm{W\,m^{-2}}$. Quantum yields were determined with either 510 nm or 600 nm excitation. Lifetimes were determined either with 527 nm or 635 nm excitation. For donor **6** the emission between 545 – 620 nm was analyzed. For acceptor **7** the emission between 655 – 715 nm was analyzed. For dyad **8**, both spectral windows were analyzed separately. The amplitudes of the fluorescence lifetime components τ_1, τ_2 and τ_3 are mentioned in square brackets underneath the lifetimes. The errors of the lifetime components are always in the order of magnitude of the last decimal place specified.

Compound	Φ (no $h\nu$) / %	Φ ($h\nu$) / %	λ_{exc} / nm	λ_{em} / nm	τ_1 (no $h\nu$) / ns	τ_2 (no $h\nu$) / ns	τ_3 (no $h\nu$) / ns	τ_1 ($h\nu$) / ns	τ_2 ($h\nu$) / ns
Donor **6**	8[a]	55[a]	527	545 – 620	4.04 [49%][c]	2.4 [28%]	0.95 [23%]	4.10 [89%]	2.1 [11%]
Dyad **8**	12[a]	25[a]	527	545 – 620	3.98 [35%][c]	2.42 [40%]	0.91 [25%]	4.04 [86%]	2.0 [14%]
Acceptor **7**	35[b]	53[b]	635	655 – 715	3.34 [64%]	1.21 [36%]	-	3.43 [69%]	1.45 [31%]
Dyad **8**	19[b]	20[b]	635	655 – 715	3.71 [75%]	1.80 [25%]	-	3.47 [69%]	1.24 [31%]
Dyad **8**	12[a]	25[a]	527	655 – 715	3.60 [75%]	1.6 [25%]	-	4.00 [86%]	1.7 [14%]

[a] Fluorescence quantum yield Φ determined at 510 nm excitation.

[b] Fluorescence quantum yield Φ determined at 600 nm excitation.

[c] The long lifetime component is contributed to free ATTO565. The amplitude is vastly overestimated, since the quantum yield of free ATTO565 in water is about 8 – 15 times higher than that of nitrophenyl-containing compounds, leading to a strong bias in the photon statistics. Spectral analysis indicates that the compound underwent minor degradation during storage, but not to the extent implied by the (uncorrected) amplitudes of the lifetime components.

At 530 nm excitation, the intensity of donor **6** at the emission maximum at 588 nm increases even more drastically than in methanol, by overall about 880%. The increase is perfectly described by first order kinetics with a time constant of about 715 s, thus the reaction rate is about halved compared to the photocleavage in methanol. The intensity appears to approach a constant value. However, the plateau is not yet fully reached after 2700 s of irradiation. A non-quantitative photoreaction is also a reasonable explanation for the determined quantum yield and lifetimes after irradiation. The quantum yield increases from 8% to 55%. Although this represents a massive increase, the quantum yield does not yet quite reach the level of free ATTO565 (about 90%). Likewise, a matching change of lifetimes is observed. To evaluate these alterations correctly, the discussion of the lifetimes before photocleavage in Section 4.3.2 is briefly summarized here. Before photocleavage, three lifetime components are observed. It is assumed that the longest and largest component is due to unspecific cleavage by hydrolysis during storage. It is further estimated that hydrolysis results entirely in a chemical cleavage similar to the styrene pathway of the photocleavage. Thus, only the longest lifetime component, which is associated to free ATTO565, is related to the hydrolysis. In the following, the longest lifetime component before controlled cleavage is ignored in the discussion of the lifetimes of donor **6** and dyad **8** in the spectral window between 545 nm – 620 nm. However, the relevant lifetime components are still called according to their designation in Table 4.4. In this context, the fluorescence decay kinetics change from two short lifetime components, $\tau_2(0\text{ s}) = 2.4$ ns [28%] and $\tau_3(0\text{ s}) = 0.95$ ns [23%], in about equal ratio to one long lifetime component, $\tau_1(2700\text{ s}) = 4.10$ ns [89%], and one short lifetime component, $\tau_2(2700\text{ s}) = 2.1$ ns [11%], in about a nine to one ratio. As before, it is likely that the ratio is distorted by the disproportionate contributions of the different fluorescent compounds to the photon statistic. Nevertheless, the long lifetime component matches the lifetime of free ATTO565 in water (about 4.0 ns). The short lifetime component is estimated to be an average value of the two short lifetime components observed before photocleavage. It is unlikely that the short lifetime component is related to any possible uncleaved nitroso products. First, a much shorter lifetime is expected in that case due to the higher quenching efficiency of nitroso-arenes compared to nitro-arenes (see also Table 7.1 in the appendix). Second, it is estimated that the styrene pathway is even more dominant in water than in methanol due to the higher basicity of water and the dependency of the styrene pathway on the presence of a (weak) base (see the mechanism in Figure 2.9). Hence, both quantum yield and lifetimes also indicate that the photoreaction is not finished after the experimental irradiation time.

The emission spectrum of acceptor **7** at 600 nm excitation changes significantly less in water than in methanol upon UV irradiation. The emission maximum at 662 nm decreases marginally by overall about 2%. The drop can be explained by photobleaching. Even the time dependency of the emission and absorption decrease is essentially the same (compare the temporal evolution of absorption and emission maximum in Figure 4.6 **d** and **f**, respectively). However, given the photobleaching rate as determined from the decreased absorption, an even stronger drop of emission is expected. The photobleaching seems to be mostly offset by an increase of the fluorescence quantum yield from 35% to 53%. It is not clear why the quantum yield increases this significantly, although the ATTO647N chromophore remains attached to the quenching nitrophenyl moiety in any case. It appears that the quenching efficiency of nitrostyrene, the assumed main cleavage product, is reduced in water compared to the original nitrophenyl moiety. The increase of the fluorescence quantum yield is to some degree also reflected in the lifetimes of

acceptor **7**. Two lifetime components, $\tau_1(3000\text{ s}) = 3.43$ ns [69%] and $\tau_2(3000\text{ s}) = 1.45$ ns [31%], are observed. Magnitude and amplitude are very similar to the lifetime components before photocleavage ($\tau_1(0\text{ s}) = 3.34$ ns [64%] and $\tau_2(0\text{ s}) = 1.21$ ns [36%]) and can be considered equal within the accuracy of the measurement. Still, the increase, especially of the second lifetime component, can be seen as an indicator that the quenching efficiency of the cleavage product in water is indeed lower than of the uncleaved acceptor **7**. Moreover, it is likely that the lifetimes before photocleavage are somewhat falsified by the above discussed unspecific hydrolysis of the carbamate moiety. Since the lifetimes before and after photocleavage are still very similar, the falsification is not detected as clearly as for donor **6** and dyad **8** in the spectral window between 545 nm – 620 nm. However, it should be noted that quantum yield measurements are prone to bigger errors than lifetime measurements and that the increase of the quantum yield could simply be overestimated. In this context, the subtle alteration of the lifetime components of acceptor **7** fits better to the observed combined change of the absorption and emission spectra than the more significant increase of the quantum yield.

The emission spectrum of dyad **8** at 530 nm excitation undergoes almost identical changes as the emission spectrum of donor **6**. After 1500 s of irradiation, the intensity at the emission maximum at 592 nm increases by about 740%, almost perfectly matching the increase of donor **6** in the same irradiation time (see Figure 4.6 **e**). Although both resulting intensity-time curves have clearly the same shape, however, the reaction rate of the photocleavage seems to be higher for dyad **8** and a time constant of 411 s is obtained. Again, the photoreaction appears not be completed yet, but the curve indicates that a plateau is about to be reached. Despite cleavage and subsequent interruption of any possible energy transfer, the intensity of the second local maximum of the dyad at 663 nm also increases over time. At the same time the structure of the spectrum changes from a clearly visible second maximum to a strongly pronounced shoulder. The increase is entirely explainable by the increase of the tailing fluorescence of the ATTO565 chromophore in that spectral region. The fluorescence of the ATTO647N chromophore does not change significantly, as proven by the insignificant alteration discussed for acceptor **7** above. Even before photocleavage, no energy transfer can be observed for the dyad in water. At every time, the emission spectrum at 530 nm excitation can be seen as the sum of the emission spectra of ATTO565 and ATTO647N. The same explanation applies for the observed increase of the intensity of the emission spectra at 600 nm excitation. While donor **6** shows basically no fluorescence at this excitation wavelength, free ATTO565 does show weak fluorescence (see Figure 4.3). As the dyad is cleaved, free ATTO565 is formed and contributes to the emission spectrum at 600 nm excitation. The contribution of free ATTO565 exceeds the expected decrease of the ATTO647N emission due to photobleaching.

All described phenomena are also quantified by quantum yield and lifetime measurements. The quantum yield at 510 nm excitation increases from 12% to 25%. As described in the discussion of the photocleavage in methanol, the quantum yield at 510 nm is subject to heavy uncertainties due to the fact that both chromophores absorb light of this wavelength. Therefore, the quantum yield at 510 nm excitation is less meaningful for dyad **8** than for donor **6**. Otherwise, an increase more similar to the increase of donor **6** can be expected. In contrast, the lifetimes of dyad **8** in the spectral window between 545 nm – 620 nm match the lifetimes of donor **6** perfectly. The same two lifetime components, $\tau_1(1500\text{ s}) = 4.04$ ns [86%] and $\tau_2(1500\text{ s}) = 2.0$ ns [14%], in the same ratio are measured within the margin of error. The interpretation of both lifetime components also corresponds to the

explanation given above. The fact that the magnitude and especially the amplitude of both lifetime components are so similar to the lifetime components of donor **6** despite different irradiation times also suggests that the reaction rate of dyad **8** is higher. The quantum yield at 600 nm excitation remains unchanged for dyad **8**. The result is less meaningful than for the reference compounds due to the minor contribution of absorption and emission of the ATTO565 chromophore at this wavelength in water. The lifetimes at 635 nm excitation, on the other hand, change analogously to the lifetimes of acceptor **7**. Whereas the lifetimes of the dyad and the reference acceptor differed more strongly before cleavage, after UV irradiation essentially the same two lifetime components, $\tau_1(1500\ \mathrm{s}) = 3.47$ ns [69%] and $\tau_2(1500\ \mathrm{s}) = 1.24$ ns [31%], in the same ratio are found. When observing the same spectral window (655 nm – 715 nm) at 527 nm excitation, the two detected lifetime components, $\tau_1(1500\ \mathrm{s}) = 4.00$ ns [86%] and $\tau_2(1500\ \mathrm{s}) = 1.7$ ns [14%], are more comparable to the lifetimes in the lower spectral window, both in magnitude and amplitude. The two lifetime components most likely belong to the ATTO565-bearing fragment, which is excited more efficiently at 527 nm and whose fluorescence in the observed spectral region in water far exceeds the fluorescence due to direct excitation of the ATTO647N chromophore (see also Figure 4.3 **b**). This effect is more pronounced in water than in methanol, since the emission spectrum of ATTO565 is bathochromically shifted by almost 10 nm in water. No similar shift is observed for the emission of ATTO647N. Hence, the spectral overlap of the emissions of ATTO565 and ATTO647N is greater in water than in methanol.

4.4.2 Visible light irradiation in bulk

FEDUP measurements do not only rely on photocleavage by UV-light, the main signal detection is achieved with visible light illumination, in particular with green (561 nm) and red (640 nm) lasers. Therefore, it is important to investigate the response of the dye systems to exposure to light of these wavelengths. Analogous experiments to the UV-irradiation experiments in Section 4.4.1 were performed with 567 nm and 645 nm LEDs. However, the maximum power density of the available green LED (112 $\mathrm{W\,m^{-2}}$) was too low to induce any significant spectral changes even after several consecutive hours of irradiation (see Figure 7.3 in the appendix). The experiment was not continued. Instead, the focus of this section lies on the influence of the about one order of magnitude stronger available red LED (1.675 $\mathrm{kW\,m^{-2}}$) on the dye system. To this end, **ATTO647N azide**, donor **6**, acceptor **7** and dyad **8** (all in methanol) were irradiated for up to 73 h at 645 nm at 1.675 $\mathrm{kW\,m^{-2}}$. The concentration of all compounds was adjusted to approximately 0.6 $\mu\mathrm{mol\,L^{-1}}$. Slight deviations from the target concentration are ignored here, as all compounds react entirely differently to the irradiation anyway. In particular, the photobleaching rates, and consequently concentrations over time, vary drastically. The absorption of ATTO565 at 645 nm is negligible and donor **6** is only included in the irradiation experiment as a negative control. Given the insignificant spectral changes of donor **6** (see below), it was abstained from also including **ATTO565 NHS ester**. Since the dyad **8** shows by far the most noteworthy response to red light irradiation, and is also the compound that was studied first, much of the following discussion is based on the most interesting features of the spectral changes of the dyad. The behavior of the other compounds is compared directly, even if they do not exhibit the same features. For a more logical structure of the discussion, the dyad is still discussed last. Absorption and emission spectra, as well as the temporal evolution of absorption and emission maxima are shown in Figure 4.7. The lifetimes and

quantum yields before and after irradiation are compared in Table 4.7. All TCSPC curves can be found in the appendix (Section 7.2.4).

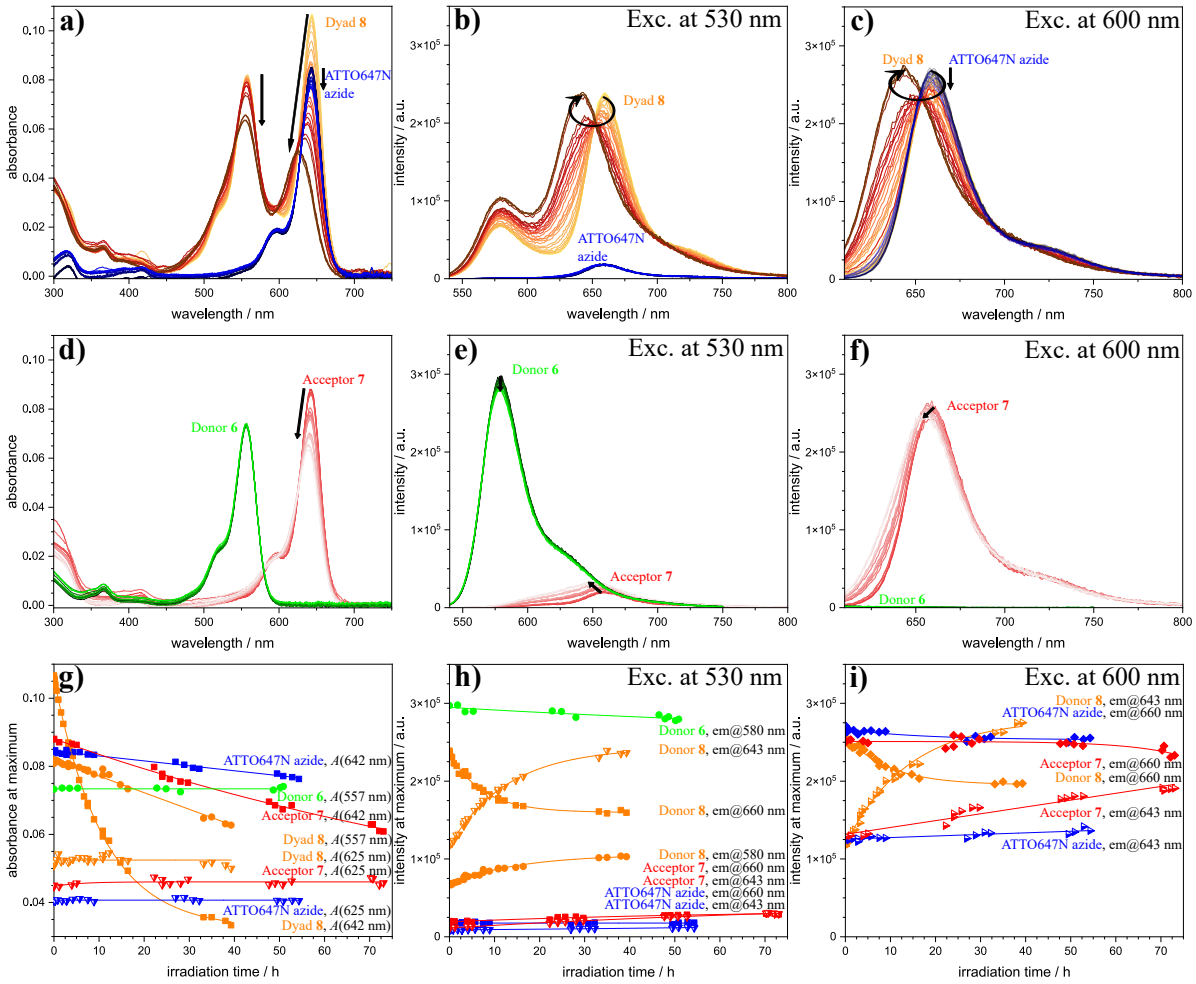

Figure 4.7: Spectral changes of ATTO647N azide, the reference donor **6**, the reference acceptor **7** and the dyad **8** in methanol during selected irradiation times with a 645 nm LED @ 1.675 kW m^{-2}. The first column from the left shows the changes of absorption spectra, the second column depicts changes of emission spectra at 530 nm excitation and the third column represents changes of the emission spectra at 600 nm excitation. Changes of (**a**) absorption and (**b**) / (**c**) emission spectra of ATTO647N azide (dark to light blue) and the dyad **8** (light to dark orange), respectively. Changes of (**d**) absorption and (**e**) / (**f**) emission spectra of the reference donor **6** (dark to light green) and the reference acceptor **7**, respectively. The black arrows in subfigures (**a**) – (**f**) indicate the changes with increasing irradiation time. (**g**) Temporal evolution of the absorbance at the different wavelengths of the (local) maxima shown in (**a**) and (**d**). (**h**) Temporal evolution of the fluorescence intensities (excitation at 530 nm) at the different wavelengths of the (local) maxima depicted in (**b**) and (**e**). (**i**) Temporal evolution of the fluorescence intensities (excitation 600 nm) at the different wavelengths of the (local) maxima presented in (**c**) and (**f**). In subfigures (**g**) – (**i**), circles refer to absorbance and emission maxima values related to the ATTO565 chromophore, while squares denote absorbance and emission maxima values related to the ATTO647N chromophore. Triangles denote the absorbance and emission values at the wavelengths of the shifted maxima of the dyad **8**. All solid lines represent fits with single exponential decay functions. The colors correspond to the primary colors of the color gradients used for the spectra of the different compounds in subfigures (**a**) – (**f**).

As expected, irradiation with red light has little to no influence on donor **6**. Even after about 51 h of irradiation, the absorption spectrum does not show any measurable alterations. The intensity at the emission maximum at 580 nm decreases slightly by overall approximately 6% which indicates at least some minor photobleaching. Both fluorescence quantum yield (55%) and lifetimes ($\tau_1(51\text{ h}) = 3.05$ ns [70%] and $\tau_2(51\text{ h}) = 2.15$ ns [30%]) remain constant within the accuracy of the measurements. Both the values and the ratio of the lifetime components are the same as before irradiation. Thus, it is confirmed that donor **6** does not undergo any photoreactions aside from negligible photodegradation upon irradiation with red light.

The spectra of **ATTO647N azide** also exhibit only minor changes. The absorbance at the absorption maximum at 642 nm decreases by about 10% after 54 h of irradiation. Fittingly, the intensity at the emission maximum at 660 nm decreases by about 5% in the same time. Concomitantly, the intensity of the emission spectra at 600 nm excitation increases slightly between 610 nm – 650 nm. In light of the below discussed results of the dyad **8**, it makes sense to observe the gain at 643 nm. Here, the intensity rises by almost 10%. A very similar behavior is observed at 530 nm excitation, albeit the increase at 643 nm is even more significant (about 27%). Neither increase nor decrease are reasonably described by single exponential functions. However, it seems probable that there exist too few data points over too short a time period to recognize the kinetics correctly. Two possible explanations for the observed spectral changes come to mind; either there exist very slow photoreactions aside from photobleaching, or (one of) the products of photobleaching are also fluorescent, but undergo minor hypsochromic shifts compared to the non-irradiated dye. However, these changes are too small to be reflected in the quantum yield (72%) and lifetime ($\tau(54\text{ h}) = 4.29$ ns) which both remain constant. Overall, the experiment primarily shows the extraordinary photostability of ATTO647N (see also Section 3.2.1).

Acceptor **7** behaves similarly to **ATTO647N azide**, but with vastly more pronounced spectral changes. The absorbance at the absorption maximum at 642 nm decreases by about 31% after 73 h of irradiation with the red LED. Even at irradiation times more comparable to the overall irradiation time of **ATTO647N azide**, the drop of the absorbance is about twice as strong as for the unreacted dye. This indicates that the photostability of the ATTO647N chromophore is lowered by the presence of the photolabile linker, in particular the nitrophenyl moiety. A similar observation was made in the UV-irradiation experiments (Section 4.4.1). Simultaneously, the absorption maximum shifts by about 3 nm to 639 nm. It is not clear if a similar shift is also present for **ATTO647N azide**, whose photoreaction rate is much slower. Interestingly, the lowered absorption is not reflected in the emission spectra. At 600 nm excitation, the emission maximum at 660 nm decreases by only 8% overall. The drop is highly comparable to the unreacted dye. Matching to the shift of the absorption spectrum, the maximum shifts by about 4 nm to 656 nm over the course of the irradiation. The shift is accompanied by a noticeable increase of the intensity between 610 nm – 650 nm, which is also observed for **ATTO647N azide**. Quantifying the rise at 643 nm yields an increase by almost 50%. The changes of the emission spectra at 530 nm excitation are even more curious. Here, the intensity at the original maximum at 660 nm even increases by overall 43%. Additionally, the maximum is shifted by almost 10 nm to 650 nm. The increase of the intensity at shorter wavelengths is also more significant at 530 nm excitation and the intensity at 643 nm increases by overall 170%. It seems that the overall increase of the fluorescence at shorter wavelengths even surpasses the expected decrease of fluorescence at the original maximum at 660 nm,

Table 4.5: Fluorescence lifetimes τ and fluorescence quantum yield Φ of compounds **ATTO647N azide**, energy donor reference compound **6**, energy acceptor reference compound **7**, and dyad **8** in methanol before and after up to 73 h of irradiation with a 645 nm LED @ 1.675 kW m^{-2}. Quantum yields were determined with either 510 nm or 600 nm excitation. Lifetimes were determined either with 527 nm or 635 nm excitation. For donor **6** the emission between 545 – 620 nm was analyzed. For **ATTO647N azide** and acceptor **7** the emission between 655 – 715 nm was analyzed. For dyad **8**, both spectral windows were analyzed separately. The amplitudes of the fluorescence lifetime components τ_1 and τ_2 are mentioned in square brackets underneath the lifetimes. The errors of the lifetime components are always in the order of magnitude of the last decimal place specified.

Compound	Φ (no $h\nu$) / %	Φ ($h\nu$) / %	λ_{exc} / nm	λ_{em} / nm	τ_1 (no $h\nu$) / ns	τ_2 (no $h\nu$) / ns	τ_1 ($h\nu$) / ns	τ_2 ($h\nu$) / ns
Donor **6**	61[a]	55[a]	527	545 – 620	2.95 [73%]	2.19 [27%]	3.05 [70%]	2.15 [30%]
Dyad **8**	58[a]	50[a]	527	545 – 620	3.43 [69%]	1.94 [31%]	3.67 [38%]	1.86 [62%]
ATTO647N azide	75[b]	72[b]	635	655 – 715	4.30 [100%]	-	4.29 [100%]	-
Acceptor **7**	66[b]	70[b]	635	655 – 715	4.20 [100%]	-	4.25 [100%]	-
Dyad **8**	61[b]	59[b]	635	655 – 715	3.76 [100%]	-	4.04 [92%]	1.5 [8%]
Dyad **8**	58[a]	50[a]	527	655 – 715	3.67 [100%]	-	3.90 [76%]	1.78 [24%]

[a] Fluorescence quantum yield Φ determined at 510 nm excitation.
[b] Fluorescence quantum yield Φ determined at 600 nm excitation.

thereby causing the apparent rise at this wavelength, too. All in all, the shape of the emission spectra changes even more drastically than for the emission spectra at 600 nm excitation, although the alteration is distinctly similar. Like in the discussion of **ATTO647N azide**, it is not clear if these changes are related to photoreactions aside from photodegradation, or if (one of) the products of the photodegradation is also fluorescent, but with hypsochromically shifted emission. Given the alteration of the emission spectrum at 530 nm, a third explanation comes to mind. ATTO647N seems to exhibit some anti-Kasha behavior that leads to an increased fluorescence emission between approximately 575 nm – 625 nm when lowering the excitation wavelength (see also Figure 7.4). It is possible the ATTO647N chromophore undergoes a photoreaction resulting in a similar, yet more rigid chromophore for which emission from higher vibronic states is even more favored. This could explain the different, if similar, changes of the emission spectra at 530 nm and 600 nm excitation while also offering a reasonable explanation why the lowered absorption is not reflected in an equally lowered emission. However, neither quantum yield nor lifetime measurements fully support either of the hypotheses. Both quantum yield (70%) as well as lifetime ($\tau(73\text{ h}) = 4.25$ ns) are essentially the same as before irradiation. The small increase of both can not be considered significant, or at least not significant enough to explain the changes observed in the spectra.

Of all investigated compounds, dyad **8** exhibits by far the most noteworthy spectral changes upon irradiation with red light. The absorbance at the absorption maximum at 642 nm is reduced by about

69% after only 39 h of irradiation. The absorption maximum is shifted simultaneously by 17 nm to 625 nm. Interestingly, 625 nm represents an isosbestic point for all compounds bearing the ATTO647N chromophore, i.e., the absorbance at this wavelength remains constant over the course of the irradiation for dyad **8**, acceptor **7** and **ATTO647N azide** (compare the data represented by triangles in Figure 4.7 **g**). Overall, the decrease of the absorption associated to the ATTO647N chromophore can be considered similar for all relevant compounds, albeit with vastly different decay rates. These observations, in particular the identical isosbestic point, indicate that all three compounds undergo the same, or at least highly comparable, photoreactions, only with different reaction rates. In this context, only for dyad **8** the drop of the absorbance is well described with first order kinetics, yielding a time constant of about 11 h. Given the much slower reaction rates of acceptor **7** and the unreacted dye, time constants of several dozen or even hundreds of hours can be expected for these two compounds. As already hypothesized above, it seems likely that the amount of data points and the reaction time do not suffice to recognize the correct kinetics.

Curiously, the absorbance at the absorption maximum at 557 nm, which is associated to the ATTO565 chromophore, also drops by about 23%. This exceeds the expected decrease due to the lowered absorption of the ATTO647N chromophore in that spectral region by far. No shifts or further significant alterations can be observed. Thus, the presence of the ATTO647N chromophore seems to enhance the photodegradation of the covalently linked ATTO565 chromophore. No comparable decrease of absorption is observed in the control experiment with donor **6**. Reverse FRET, as postulated in Section 4.3, is an unlikely explanation. At the irradiation wavelength (645 nm) the emission of ATTO647N does not exhibit the hypothesized anti-Kasha behavior which is required for a reasonable spectral overlap with the absorption spectrum of ATTO565. The overlap integral approaches zero at sufficiently long excitation wavelengths (see Section 4.3.1). In the course of the experiment, however, the emission spectrum of the ATTO647N chromophore in the dyad is hypsochromically shifted, which increases the spectral overlap and therefore the potential reverse energy transfer. An entirely different energy transfer mechanism is also fathomable, for example, excited electron transfer from the ATTO647N chromophore to the photocleavable NPPOC moiety. The enhanced photoreactivity of the ATTO565 chromophore in the dyad might then be related to excited NPPOC linker. The higher photoreactivity of acceptor **7** compared to **ATTO647N azide** confirms the involvement of NPPOC in the photoreactions.

Of all investigated compounds, the emission spectra of dyad **8** also undergo the most significant changes upon irradiation with red light. Due to the drastically lowered absorption of the ATTO647N chromophore, a strong increase of the ATTO565 fluorescence at the emission maximum at 580 nm and a simultaneous drop of the ATTO647N fluorescence at the emission maximum at 660 nm was expected. At 530 nm excitation, the fluorescence at 660 nm does drop by about 33%, however the maximum clearly shifts by 17 nm to 643 nm, reaching about the same intensity at this wavelength as is observed at the original maximum before irradiation. The intensity of the fluorescence emission at the new maximum increases by almost 97% over the course of the experiment. Likewise, the intensity at the local emission maximum at 580 nm does indeed increase by about 52%. Nonetheless, this increase is orders of magnitude below the increase due to the interruption of energy transfer as described in Section 4.4.1. Most likely, the rise is simply caused by the shift of the emission associated to the ATTO647N chromophore to shorter wavelength. An increased reverse FRET is also possible (see above). Hence,

despite the photodegradation as observed in the absorption spectra, in particular of the ATTO647N chromophore, the energy transfer still persists in about equal or even higher efficiency. The emission spectra of dyad **8** at 600 nm excitation show essentially the same behavior. The maximum shifts from 660 nm to 643 nm. The intensity at 660 nm decreases by about 25% while the intensity at 643 nm increases by about 140%, thereby reaching about the level of intensity of the original maximum before irradiation. Comparing the emission spectra of **ATTO647N azide**, acceptor **7** and dyad **8**, a distinctly similar variation is observed, especially at 600 nm excitation. The main difference seems to be the timescale of the underlying photoreaction. Again, the intensity changes of dyad **8** are all reasonably well described by first order kinetics yielding time constants between 7 – 15 h, which is comparable to the time constant of the absorbance decay.

Dyad **8** is also the only compound that exhibits significant alterations of lifetimes. The quantum yields, in contrast, remain essentially constant within the error of the measurement ($\Phi(510\text{ nm}) = 50\%$ and $\Phi(600\text{ nm}) = 59\%$). The two lifetime components in the spectral window between 545 nm – 620 nm do not change significantly in magnitude, however, their ratio is turned around from approximately 2:1 to 1:2 ($\tau_1(39\text{ h}) = 3.67$ ns [38%] and $\tau_2(39\text{ h} = 1.86$ ns [62%]). It is not clear if the alterations are related to the possible induced photoreaction of the ATTO565 chromophore or if they are related to the shift of the emission of the ATTO647N chromophore and the consequently worse spectral separation. However, the similarity of the lifetime components before and after irradiation show that the ATTO565 chromophore undergoes only minor photoreactions. More noteworthy are the changes of the lifetimes in the spectral window between 655 nm – 715 nm. Before irradiation, a single lifetime was found irrespective of the excitation wavelength. After irradiation, two lifetime components are observed in both cases. At 635 nm excitation, one long lifetime component, $\tau_1(39\text{ h} = 4.04$ ns [92%], and one short lifetime component, $\tau_1(39\text{ h} = 1.5$ ns [8%], in a ratio of about 10:1, are detected. Neither lifetime component matches the lifetime of ATTO647N in methanol or the lifetimes of any other component bearing the ATTO647N chromophore so far (see Table 4.5). The lifetimes are more reminiscent of the lifetime components of donor **6** after photocleavage (compare Table 4.3). This could be seen as evidence for a reverse energy transfer process, but is more likely a coincidence. It is estimated that both lifetime components stem from the products of the photoreaction of the ATTO647N chromophore. Similar lifetime components are found in the same spectral window at 527 nm excitation, albeit in a different ratio ($\tau_1(39\text{ h}) = 3.90$ ns [76%] and $\tau_2(39\text{ h} = 1.78$ ns [24%]). The divergence is most probably related to the imperfect spectral separation of the ATTO647N emission from the ATTO565 emission.

Altogether the results show that the (photo-)reactivity of the ATTO647N chromophore is not only increased by the presence of the photolabile linker, but also by the covalently linked second chromophore. Moreover, the results indicate that the plain picture of photobleaching as a process that simply destroys a chromophore to yield a non-fluorescent species is too simplified, at least under the experimental irradiation conditions. When embedding the dye system in thin polymer films and irradiating with significantly higher irradiation power densities, a different photodegradation behavior is observed (see Section 4.4.3). Lastly, the results show that the dye system exhibits more complex interactions and reactivities than at first expected.

4.4.3 Performance on the single molecule level

Before the dyad is employed in diffusion measurements (Section 4.6), it is crucial to have a more detailed look at the behavior of the dye system on the single molecule level. To this end, the irradiation experiments in Section 4.4 are conceptually repeated on a microscope with spatially separated single dye molecules. The donor **6**, acceptor **7** and dyad **8** are separately embedded in thin tempered poly(vinyl acetate) (PVAc) films (Sigma-Aldrich, $M_W = 184000\ \mathrm{g\,mol^{-1}}$, see also Section 6.4.5 for more details on the sample preparation). The conditions are equivalent to the FEDUP measurements presented later. PVAc has been chosen as polymer test system for two reasons. For one, PVAc is a comparatively polar polymer which is well soluble in methanol. Second, the glass transition temperature of PVAc is just above ambient temperature.[199,200] Therefore, low mobility is expected at room temperature, resulting in small translational diffusion coefficients unavailable to classical SMT. Still, it is also possible to perform measurements directly at or above the glass transition with relatively little experimental effort (see also Section 4.6.2).
In all FEDUP measurements, the emission is separated in two spatially equivalent, but spectrally separate channels on the same (scientific) complementary metal-oxide-semiconductor ((s)CMOS) camera (see also Section 2.3.7 and 6.7.2). It is expected that the fluorescence of the ATTO565 chromophore dominates in the short wavelength channel (570 – 633 nm) at 561 nm excitation. Accordingly, the channel is henceforth called donor channel. At 640 nm excitation, the short wavelength channel only records intrinsic noise and background and hence is discarded entirely. In contrast, it is expected that the fluorescence of the ATTO647N chromophore dominates in the long wavelength channel (> 655 nm). Depending on the excitation wavelength, the long wavelength channel is henceforth called the FRET channel (561 nm excitation) or acceptor channel (640 nm excitation).
First, the measurement conditions are tested. In particular, it is controlled for crosstalk, i.e., how much fluorescence of the ATTO565 chromophore leaks into the FRET channel and how much fluorescence of the ATTO647N chromophore is observed in the FRET channel due to direct excitation. Then, a visual proof of concept of FEDUP measurements with the new dyad is delivered. Last, photobleaching on the single molecule level is investigated. All experiments offer invaluable insights that are required for an appropriate evaluation of the actual FEDUP measurements.

Crosstalk

To test for crosstalk, picomolar amounts of donor **6** and acceptor **7** are separately added to an approximately 8 wt% PVAc solution in methanol. A drop of the solution is subsequently spincoated onto a clean coverslip and tempered under vacuum at 80 °C (see also Section 6.4.5 for more details about the sample preparation). The measurement procedure is analogous to a FEDUP measurement (see also Section 6.7.2 for details about the measurement settings). Ten frames are rapidly recorded with 561 nm and 640 nm excitation in alternating fashion, then a 0.5 s UV-laser pulse (378 nm at 0.1 $\mathrm{kW\,cm^{-2}}$) is applied. The amount of UV photons per irradiated area is in the same order of magnitude as the amount of photons emitted by the UV-LED in the bulk irradiation experiments within 800 s (compare Section 4.4.1). This was shown to be a sufficient amount of photons for a near quantitative photocleavage reaction in methanol and it is assumed that photocleavage in a PVAc matrix is comparably quantitative employing the UV laser. After the UV pulse, alternating laser excitation (ALEX)[105] is employed again.

Each frame corresponds to 220 ms of irradiation. The laser power density (on average 0.028 kW cm^{-2} and 0.022 kW cm^{-2} for the 561 nm and 640 nm laser, respectively) is comparable to a typical FEDUP measurement. Between each cycle of green and red excitation a variable delay time without any excitation is inserted. The length of the delay time in FEDUP measurements has to be adjusted depending on the glass transition temperature, the measurement temperature and the photobleaching rate (see also Section 4.6). These considerations are irrelevant for the crosstalk tests and an otherwise unreasonably short delay time of 0.5 s is employed. However, to assure maximum comparability the procedure is otherwise unchanged. In particular, a UV-laser pulse is applied to investigate if similar spectral changes of donor **6** and acceptor **7** upon UV irradiation (Section 4.4.1) are observed in bulk and the single molecule level. Similar crosstalk control experiments are performed for every polymer investigated in Section 4.6. However, the results do not differ significantly from those discussed below. Hence, all of the following results regarding crosstalk can be seen as universally valid throughout the remainder of this work. All measurements in this chapter are performed employing Köhler illumination (see also Section 2.3.1), if not explicitly stated otherwise.

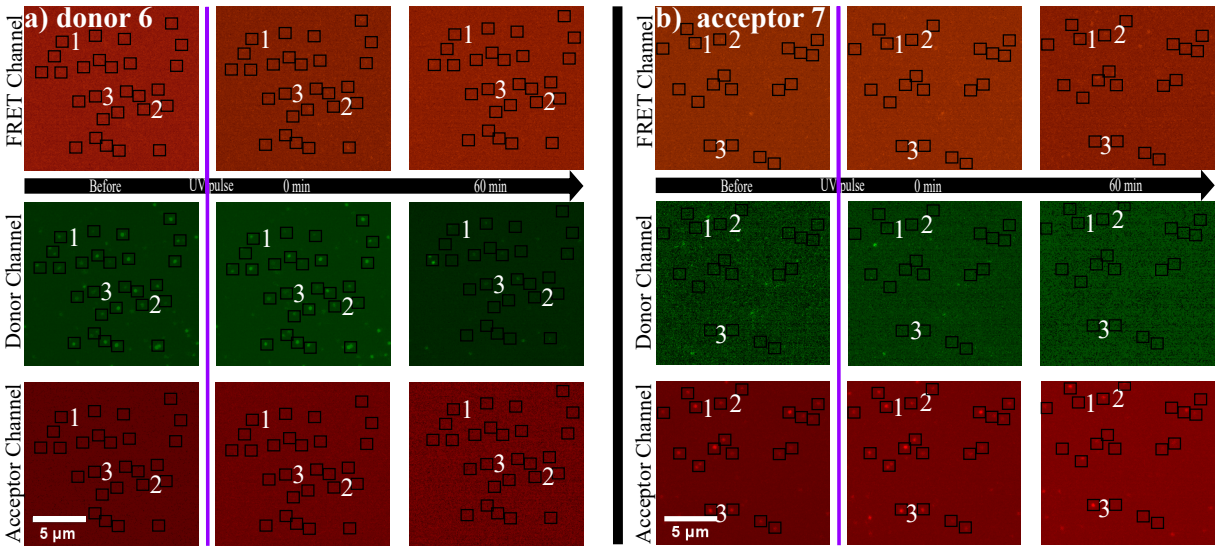

Figure 4.8: Series of false-color images taken from a widefield microscopy movie of (**a**) donor **6** and (**b**) acceptor **7** in a tempered PVAc film before and after 0.5 s of UV irradiation (378 nm at 100 W cm^{-2}). A selection of images recorded with 200 ms integration time is shown which were taken at the times indicated in the central time arrow. In the top row, the long wavelength channel ($>$ 655 nm) at 561 nm excitation is shown (orange, FRET channel). In the middle row, the short wavelength channel (570 – 633 nm) at 561 nm excitation is displayed (green, donor channel). In the bottom row, the long wavelength channel at 640 nm excitation is shown (red, acceptor channel). All images were colored according to the established color scheme. The vertical purple line symbolizes the UV irradiation. The imaging pixel size was 65 nm. A few selected signals are marked with black squares to help guide the eye. The squares were positioned over the clearly visible signals in the donor and the acceptor channel, respectively, and then translated to the corresponding coordinates in the other channels. Three arbitrarily chosen signals of each sample are additionally labeled with numbers. The corresponding intensity-time traces are shown in Figure 4.9.

In Figure 4.8, a series of false-color images of donor **6** (**a**) and acceptor **7** (**b**) in a thin PVAc film at different times relative to the UV pulse is shown. The original recorded grayscale pictures were colored in according to the established color scheme to grant a better sense of coherence. Correspondingly, the

FRET channel is depicted in shades of orange, the donor channel in shades of green and the acceptor channel in shades of red. Furthermore, the contrast was improved in post production to grant the best visibility of all signals. Consequently, a quantitative comparison of the images based on the brightness is not feasible and the images have to be taken as purely qualitative. For a more quantitative comparison, the reader is referred to Figure 4.9 and the corresponding discussion. The images in Figure 4.8 are precise cut-outs from the entire recorded field of view, as to enhance the details. In the case of the FRET channel and the acceptor channel, the exact same coordinates were used to crop the original images. In the case of the donor channel, the corresponding coordinates were determined using a spatial correlation with TetraSpeck™ beads, which fluoresce brightly over the whole range of the visible spectrum. Hence, it is certified that the images of the different channels all show the same region of interest, at most insignificantly shifted by a few pixels. The correlation, as well as all further computational steps involved in the data analysis, are presented step by step in Section 4.6.1.

At first glance most surprising might be the fact that in the acceptor sample there are some sparse signals visible in the donor channel (compare Figure 4.8 **b**). However, these signals are not spatially correlated with the signals detected in the acceptor channel. In this context, spatial correlation denotes the fact that signals are measured in corresponding areas in two or three measurement channels. A control experiment imaging a PVAc film without any dye additives proves that these signals stem from unspecified impurities in the polymer, for example remaining catalyst from the polymerization (see Figure 7.45 in the appendix). In comparison, the amount and intensity of probably impurity-related signals in the FRET and acceptor channel, although present to a minor degree, are negligible in the control experiment. Likewise, some weak signals can be observed in the FRET channel of the acceptor sample. Only few of these fluorescence signals seem to be spatially correlated to the signals in the acceptor channel. Hence, it is likely that most signals in the FRET channel are also related to impurities in the polymer. Some signals might also represent random noise that is interpreted as fluorescence. In most cases, no noteworthy fluorescence is detected in the FRET channel at the pixels corresponding to any signal detected in the acceptor channel. This is quantified by the intensities measured in these pixels over time, as shown for a few selected examples in Figure 4.9 (right). Henceforth, the depiction of the intensity measured over time in corresponding areas in donor, FRET and acceptor channel is termed intensity-time trace. The generation of intensity-time traces is explained in greater detail in Section 4.6.1. The acceptor intensity-time traces 2 and 3 highlight that neither direct excitation in the FRET channel, nor any signal in the donor channel is detected. The associated (background corrected) intensity-time traces fluctuate around the zero value. These fluctuations correspond to the base noise level (see Section 4.6.1). The majority of all evaluated signals, whose fluorescence is detected in the acceptor channel, exhibit similar intensity-time traces. Only in a few specific cases a signal in the FRET channel is observed, e.g., trace 1. There are two possible reasons. First, the power density of the 561 nm laser is not entirely homogeneous over the entire field of view. The power might be higher at the corresponding spot leading to more direct excitation and consequently a higher intensity in the FRET channel. This phenomenon is independent of the 640 nm excitation and any signal in the acceptor channel, therefore there is no correlation between the intensities in these two channels. Second, one of the long wavelength fluorescent impurities could randomly be at the associated spot in the FRET channel. Overall, however, direct excitation appears to be negligible under the tested measurement conditions.

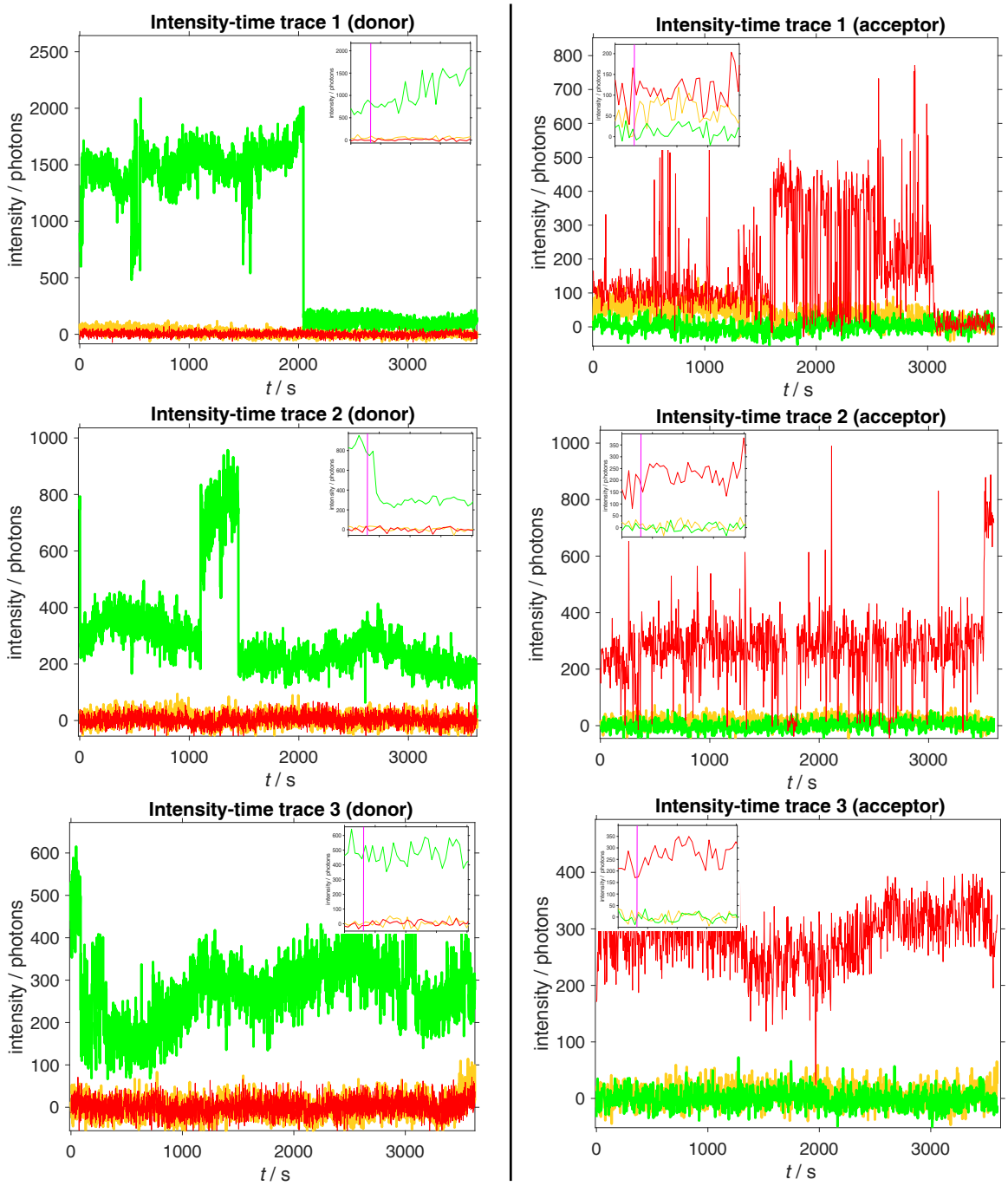

Figure 4.9: Typical intensity-time traces of donor **6** (left) and acceptor **7** (right) in PVAc. The numbers above each graph coincide with the labels given in Figure 4.8 **a** and **b**. The intensities detected in the different spectral channels are shown as orange, green and red lines for the FRET, donor and acceptor channel, respectively. The time is given relative to the UV pulse. The insets depict the measured intensity in the first five frames before and the first few dozen frames after the UV pulse which is symbolized by the vertical purple line. All signals are corrected for background (see Section 4.6.1 for a more detailed description of the analysis algorithm).

The signal intensity in the acceptor channel seems to remain approximately constant until the end of the measurement, or alternatively, until photobleaching occurs. However, all intensity-time traces, both of acceptor and donor, are subject to fluctuations from frame to frame, including brief off-times when

the intensity turns to zero for a few frames. This intrinsic blinking is assumed to be related to the photophysics of the dye and not an artifact introduced by the photolabile linker. Conceptually, it is also possible that the quenching nitrophenyl moiety might extend the dark state under certain circumstances. The on temporal average constant intensity in the acceptor channel before and after the UV pulse indicates that the stryrene pathway is the more favored photocleavage reaction under the measurement conditions. It was shown already that the nitrostyrene photocleavage product of acceptor **7** exhibits very similar photophysical properties to the uncleaved molecule, whereas the nitroso product shows a higher quenching efficiency and hence lower intensities and lifetimes (see Section 4.4.1). Nevertheless, no drop of the average intensity similar to the behavior in bulk is observed for the acceptor after application of the UV pulse. In fact, no general immediate spectral changes seem to be induced by the UV irradiation (see insets in Figure 4.9). The spontaneous decrease of the intensity of acceptor trace 1 at approximately 3000 s is assumed to be caused by photobleaching (see below). Hence, the UV laser does not seem to facilitate any secondary photoreactions of either acceptor **7** or the polymer matrix, apart from sporadic photodegradation of the dye.

In the donor sample, clear signals are detected only in the donor channel. Additionally, some very weak signals are detected in the FRET channel. No signals are detected in the acceptor channel in the field of view whatsoever. Again, there seems to be no noteworthy spatial correlation between the signals in the donor and the FRET channel. This implies that no significant leakage of the donor fluorescence into the FRET channel is observed under the measurement conditions. The intensity-time traces of donor **6** in Figure 4.9 (left) confirm that no leakage is observed. Only donor fluorescence is detected whereas no corresponding signals are measured in either FRET or acceptor channel. In this context, it has to be noted that the impurity signals (see above) in the donor channel cannot be differentiated from the ATTO565 signals. Only by comparing the signal density in Figure 4.8 **a** and **b**, as well as the SNR, it becomes clear that some signals in the donor channel have to stem from the ATTO565 chromophore.

The donor fluorescence intensity also remains roughly constant over the course of the measurement. No universal increase of fluorescence, as in the bulk irradiation experiment, is observed. This is not unexpected, since the mobility in the polymer film is so low that the quenching nitrophenyl moiety is forced to remain in close proximity to the ATTO565 chromophore even after photocleavage. A slow diffusion of the quencher into closer proximity of the ATTO565 chromophore is also fathomable. It is possible that the spontaneous temporary increases and decreases of the intensity in all donor traces are partially related to the diffusion of the nitrostyrene photocleavage product. The sudden drop of intensity of donor trace 1 about 2000 s after the UV pulse is assumed to be a sign of photodegradation to a non-fluorescent species (see below). Like for the acceptor, no immediate universal spectral response is observed upon application of the UV pulse. Thus, it appears as if photocleavage occurs according to the styrene pathway, whereas other photoreactions occur only to a minor degree. On temporal average, the intensity fluctuations of both donor and acceptor do not significantly exceed the typical variance of single molecule intensities. Hence, both donor and acceptor intensity can be regarded as constant before and after photocleavage in their respective channels.

All dye molecules remain stationary during the entire measurement. Both donor and acceptor seem to be fully immobilized inside the polymer film. The extraordinarily low mobility is most effectively seen when observing the acceptor channel of the acceptor sample. Even after 1 h of measurement time, all

signals remain in the same relative position. The only positional change is a collective shift of all signals due to sample drift. The donor molecules remain likewise stationary. However, their photostability seems to be drastically lower than that of the acceptor molecules under the experimental conditions, leading to significantly more photobleaching. Hence, it is unfeasible to recognize the signal pattern after 1 h. Photobleaching both of donor and acceptor is observed as a sharp disruption of the fluorescence signal (compare donor and acceptor trace 1 in Figure 4.9). No spectral shifts, as observed in similar bulk experiments with prolonged visible light irradiation, are detected (compare Section 4.4.2). The phenomenon of photobleaching is discussed in more detail below.

Proof of concept

In the following, a visual proof of concept is delivered. Analogous to the crosstalk experiments, dyad **8** is embedded in picomolar amounts in a thin PVAc film. The measurement procedure is identical albeit a significantly lower power density was reached with the UV-laser. This was counterbalanced by increasing the irradiation time to 4 s. Since the critical diffusion times are on a scale of dozens of minutes, the larger measurement error introduced by the slightly longer UV pulse is not significant. Furthermore, a longer delay time of 30 s was employed between each cycle of alternating excitation (see also Section 4.6.1). The recorded images were cropped to an even smaller region of interest than before to enhance the pattern recognition. A region with overall only six separate signals, and consequently six dyad molecules, was chosen. It was taken care that in the chosen area no impurity signals are visible in the donor channel. A series of selected images of the six chosen signals in all three measurement channels at different times relative to the UV pulse is shown in Figure 4.10. The corresponding intensity-time traces are depicted in Figure 4.11. A negative control experiment, in which the measurement is repeated without application of the UV pulse, is presented further below in the context of photobleaching on the single molecule level.

Before the application of the UV pulse, no signals are detected in the donor channel. This is already surprising given the apparent 80% FRET efficiency and remaining donor fluorescence observed in methanol (see Section 4.3.1). It is possible that a more quantitative FRET efficiency is reached in the polymer matrix, for example, due to a more favorable conformation of the dyad, which is likely to be more restricted in its conformational freedom. The higher apparent FRET efficiency is expressed by the weaker fluorescence emission of the donor compared to bulk measurements. However, it is not necessarily reflected in the brightness of the signal in the FRET channel. Despite higher excitation power of the 561 nm laser, the intensity of all signals in the FRET channel is comparable to, or even weaker than, the intensity of the corresponding signals in the acceptor channel. Most importantly, the intensity of any signals in the FRET channel clearly exceeds the intensity of any unspecific signals detected in the FRET channel of either the donor **6** or the acceptor **7** sample under similar conditions, provided that any fluorescence is detected in the FRET channel at all. To each signal detected in the FRET channel, a matching, spatially correlated signal is measured in the acceptor channel. This is a unique feature of the dyad **8**, which is not observed for the reference compounds (see above). As before, the fluorescence in all channels is also subject to intrinsic blinking. Hence, some dye molecules are turned off during some frames and the spatial correlation can only be recognized on temporal average and not necessarily in each single frame.

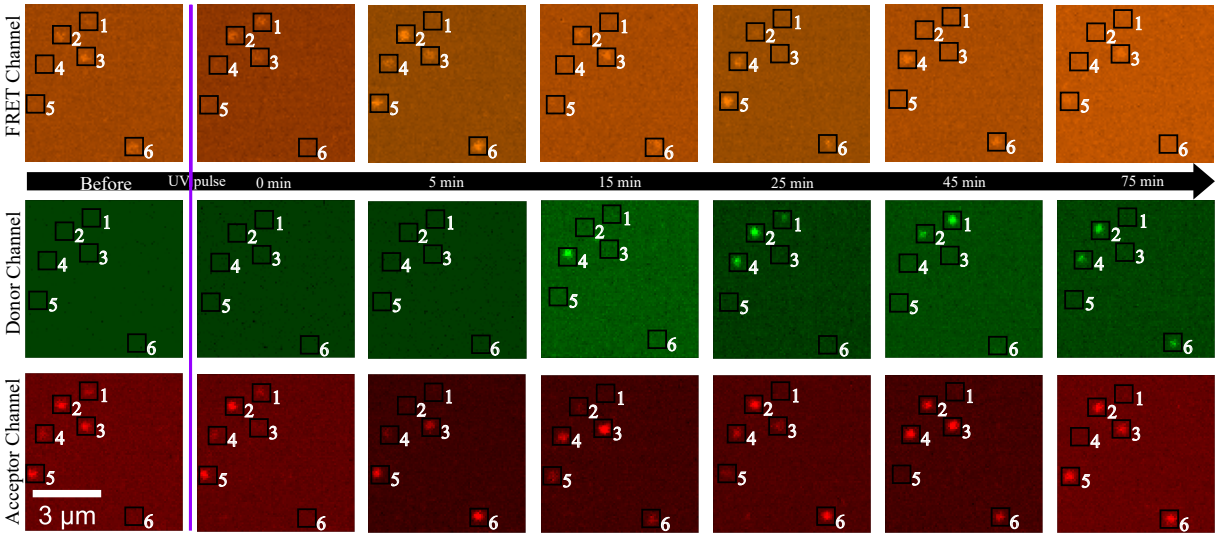

Figure 4.10: Series of false-color images taken from a widefield microscopy movie of dyad **8** in a tempered PVAc film before and at different times after 4 s of UV irradiation (378 nm at 50 $W\,cm^{-2}$). A selection of images recorded with 200 ms integration time is shown which were taken at the times indicated in the central time arrow. In the top row, the long wavelength channel (> 655 nm) at 561 nm excitation is shown (orange, FRET channel). In the middle row, the short wavelength channel (570 – 633 nm) at 561 nm excitation is displayed (green, donor channel). In the bottom row, the long wavelength channel at 640 nm excitation is shown (red, acceptor channel). All images were colored according to the established color scheme. The vertical purple line symbolizes the UV irradiation. The imaging pixel size was 65 nm. All signals are marked with black squares and labeled with white numbers to help with the recognition of the signal pattern. The corresponding intensity-time traces are shown in Figure 4.11.[59]

Application of the UV pulse does not cause any immediate general spectral changes (see insets in Figure 4.11). Thus, the influence of the UV irradiation on the system, apart from the targeted photocleavage and sporadic photodegradation of the dyes, seems to be negligible. After application of the UV pulse, the average intensity of all signals in the FRET channel decreases over the course of dozens of minutes and eventually drops to zero. In five of the six example cases, signals start appearing in the associated spots in the donor channel shortly after the intensity in the FRET channel is reduced to almost zero. Henceforth, any pair of signals that exhibits measurable intensities in the FRET, donor and acceptor channel at matching coordinates is called a “donor-acceptor pair”, as to notionally distinguish the molecule pair from its parent dyad molecule. Donor-acceptor pairs are then further subdivided into “initially identified donor-acceptor pairs” and “valid donor-acceptor pairs”, or equivalently, “FRET pairs”. The former category represents all signal pairs recognized by the analysis algorithm, including random signals that happen to match the spatial correlation, whereas the latter category only includes donor-acceptor pairs that fulfill a specified set of conditions that unequivocally identifies them as a cleaved dyad molecule based on their intensity-time traces (see Section 4.6.1, in particular steps 4 and 7 of the example analysis). The remaining donor-acceptor pairs are ascribed to three different categories of invalid donor-acceptor pairs. The various categories of donor-acceptor pairs are discussed in-depth in Section 4.6.1 (step 7) and are only mentioned in the following to grant a sense of coherence retrospectively.

On average, the signal intensity of the donor-acceptor pairs in the donor channel increases over time, even if temporary reversions are observed, too. Any temporary decrease of donor channel intensity is

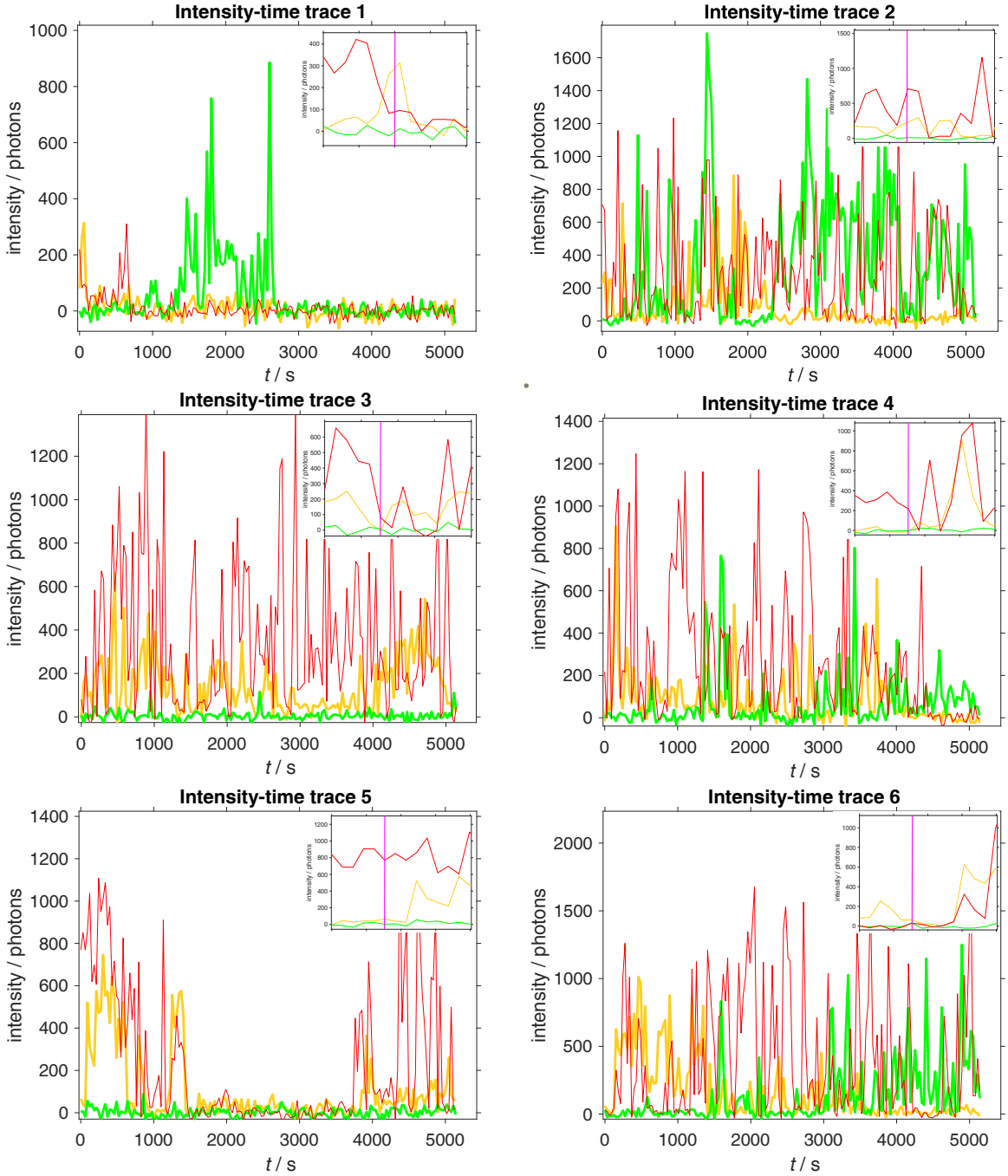

Figure 4.11: The intensity-time traces of the six signals identified in Figure 4.10. The time is counted relative to the UV pulse. The numbers above each graph coincide with the labels given in Figure 4.10. The intensities detected in the different spectral channels are shown as orange, green and red lines for the FRET, donor and acceptor channel, respectively. The insets in the upper right corner of each graph show the intensity in the first five frames before and the first few frames after the UV pulse which is symbolized by the vertical purple line.[59]

well correlated with a temporary increase of intensity in the FRET channel, and vice versa. This implies that the two cleaved dye fragments move independently from each other in two random directions. On both temporal and ensemble average, the relative distance between the donor-acceptor pair increases, as evidenced by the general reduction of the efficiency of the energy transfer between donor and

acceptor dye. However, movement in the other relative direction also occurs in appropriate likeliness, indicating neither significant repulsive nor attractive interaction between the two cleaved fragments of any donor-acceptor pair.

A continued signal in the acceptor channel is the most important control condition for the previous evaluation. Even if no spatial information is encoded in its intensity, a ceasing signal in the acceptor channel is the only indicator of photobleaching. The signal is produced by direct excitation of the acceptor in any donor-acceptor pair with red light, thus fluorescence is still emitted independently of the FRET efficiency during the excitation with green light. An irreversible termination of the signal is associated with photodegradation of the acceptor (see below). The intensity in the acceptor channel remains constant on a greater temporal average for the donor-acceptor pairs 2, 3, 4 and 6 (see Figure 4.11). Consequently, it is likely that these four donor-acceptor pairs in fact exhibit changes of their FRET efficiency due to diffusion (valid donor-acceptor pairs or FRET pairs, category I, see Section 4.6.1 step 7, or the Glossary 8.5 for the terminology). Donor-acceptor pair 3 is potentially excluded from this assessment due to uncertainty, i.e., due to the briefness and low intensity of any signal in the donor channel. In the case of donor-acceptor pair 1, however, the signal in the acceptor channel is interrupted sharply. No signal is detected afterwards. Concomitantly, a signal is detected in the donor channel. It has to be assumed that this is a typical recording of the photobleaching process of the acceptor in a donor-acceptor pair (see below). The appearance of the donor fluorescence is not related to diffusion of the two independent dye fragments and the donor-acceptor pair 1 is identified as invalid for the analysis (category II, see Section 4.6.1 or the Glossary 8.5). A similar effect is observed for the donor-acceptor pairs 2, 3 and 4 at a later measurement time (about 5000 s). However, signals are already detected in the donor channel before the possible occurrence of photobleaching, indicating that both dye fragments have diffused farther apart than the Förster distance, at least temporarily. The significance of this behavior for the (analysis of the) FEDUP method is discussed in greater detail in Section 4.6.1 (step 7 of the analysis). In comparison, intensity trace 5 exhibits anomalous behavior. At first, regular intensity-time traces are observed in the acceptor and FRET channel. About 1500 s after the UV pulse, however, no signal whatsoever is detected in any channel for about 2000 s before fluorescence is observed again in the FRET channel and to a greater extent in the acceptor channel. No noteworthy signal is detected in the donor channel in the measurement time. It is not entirely clear what causes the extraordinarily long off-time in all channels. Likewise, it is not clear if fluorescence in the donor channel would turn up at longer measurement times or after photobleaching of the acceptor, or if this is not a valid donor-acceptor pair at all. The intensity in the FRET channel indicates that energy transfer does occur, since no signals with comparable intensity in the FRET channel are observed in the control measurements. Given that no noteworthy intensity is detected in the donor channel, however, it cannot be stated unequivocally that the initially identified donor-acceptor pair 5 is indeed a cleaved dyad molecule (invalid donor-acceptor pair, category IV, see Section 4.6.1 or the Glossary 8.5).

The most curious behavior of donor-acceptor pair 5 is the long intermediary period without any fluorescence emission. A few similar cases of donor-acceptor pairs exhibiting extended dark times on all channels, including recovery on all channels, are observed throughout essentially all further measurements in various polymers, even in a control experiment without the application of an UV pulse for photocleavage (see Figure 4.12 **e**). However, the occurrence is uncommon compared to the more

regular behavior of the other five investigated donor-acceptor pairs and does not significantly influence the overall statistics, even if included in the same.
Overall, the experiment suffices as a proof of concept, especially if seen together with the last control experiment featured below that confirms that no unspecific photocleavage occurs. Despite typical single molecule intensity fluctuations, photobleaching and further photophysical and -chemical effects influencing the intensity-time traces, the gradual decrease of the FRET efficiency due to physical separation of donor and acceptor dye can be well recognized and differentiated from all other effects. The intensity in all channels behaves essentially as expected. The performance even surpasses expectations in some aspects, given the unexpectedly low crosstalk and higher apparent FRET efficiency compared to the one in solution.

Photobleaching on the single molecule level

The last control experiments before the diffusion measurements in Section 4.6 are about a more detailed investigation of photobleaching on the single molecule level. In particular, evidence is produced that detection of fluorescence in the donor channel due to photobleaching of the acceptor can be distinguished from distance-dependent FRET efficiency decrease. To this end, dyad **8** is again embedded in a thin PVAc film, and the measurement is repeated under identical conditions, but without the irradiation of the sample with any UV light. Typical intensity-time traces of the measurement with and without the UV pulse are compared in Figure 4.12. In further separate experiments, the photobleaching rates of donor **6**, acceptor **7** and dyad **8** are compared under different measurement conditions.
In the top half of Figure 4.12, three arbitrary intensity-time traces of the same measurement of the dyad in PVAc as before are shown (**a** – **c**). All traces have been identified as examples of premature photobleaching of the acceptor in a donor-acceptor pair, similar to trace 1 in Figure 4.11. In this context, premature denotes the fact that photobleaching of the acceptor occurs before any kind of signal is detected in the donor channel. The term is used later on to distinguish these cases from instances when photobleaching of the acceptor occurs after the FRET signal vanished and in the donor channel a signal turned up, at least temporarily (see Section 4.6.1, compare also the intensity-time traces of, e.g., donor-acceptor pairs 1 and 4). In all cases shown in Figure 4.12, the appearance of a fluorescence signal in the donor channel coincides with the disappearance of any signal in both the FRET and the acceptor channel. Whereas the former is to be expected, the latter has been established as a sign of fatal photodamage. Even if the intensity in the FRET channel was already decreasing, thereby indicating a growing distance between both chromophores, there is no longer any relative spatial information encoded in the intensities.
Conceptually similar behavior is observed in the control experiment without application of the UV pulse. Three typical intensity-time traces of three different identified donor-acceptor pairs are shown in the lower half of Figure 4.12. Compared to the regular measurement discussed before, the measurement time is increased by one order of magnitude as to allow for the possible occurrence of any slow secondary photoreactions. The intensity in both FRET and acceptor channel remains constant on temporal average in all shown cases, as long as there is any signal at all. The long, but still temporary off-time in all channels observed in the intensity-time traces of donor-acceptor pair **e** is assumed to be unrelated to either photobleaching or unspecific photocleavage (see above). In the case of the intensity-time traces shown in

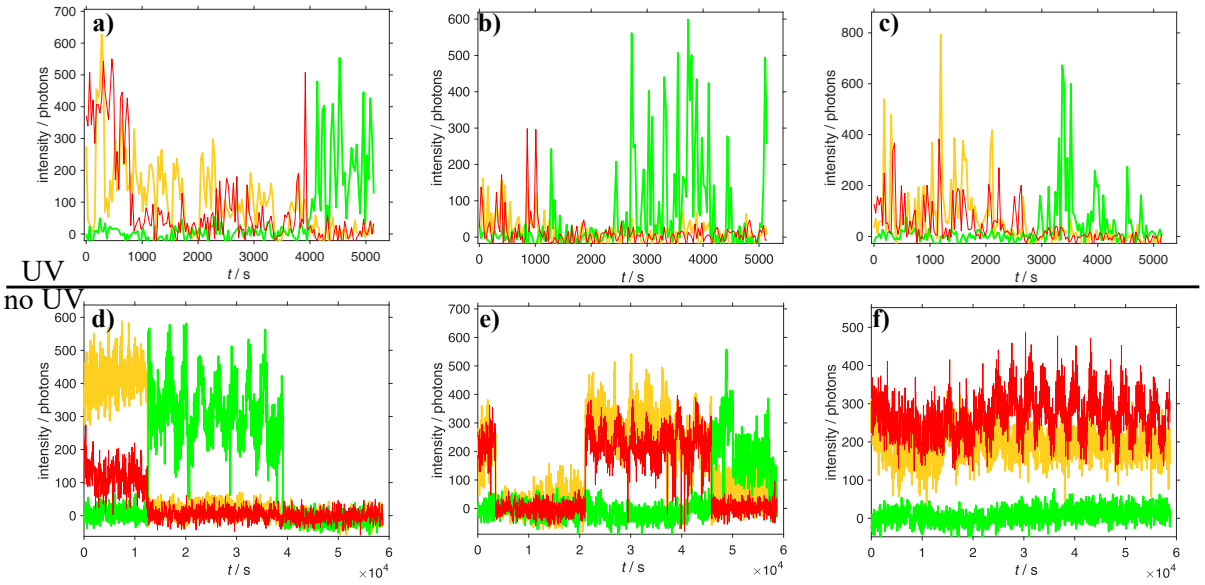

Figure 4.12: (**a** – **c**) Three exemplary intensity-time traces from the same measurement as the one shown in Figure 4.10. It is assumed that in all three cases photobleaching occurs, since the intensities in acceptor and donor channel are well correlated. (**d** – **f**) Three exemplary intensity-time traces from a control experiment without a UV pulse. Otherwise, the measurement was performed under identical conditions. The intensity-time traces of the donor-acceptor pairs depicted in **d** and **e** show conceptually similar behavior to their counterparts in **a** and **b**. The intensity-time traces of the FRET, donor and acceptor channel are shown in orange, green and red, respectively.

Figure 4.12 **d** and **e**, which represent about 33% of the 161 donor-acceptor pairs initially identified by the algorithm in the control measurement, the intensity in both the FRET and the acceptor channel sharply drops to zero simultaneously (category II, see Section 4.6.1 step 7 of the example analysis or the Glossary 8.5 for the terminology, see Figure 4.13 for an overview of the categorization). Likewise, the intensity in the donor channel rises sharply. The intensity remains constant on temporal average afterwards before eventually dropping abruptly to zero again. Since no controlled photocleavage was initiated, it has to be assumed that these intensity-time traces are examples of (premature) photobleaching of the acceptor, as well as eventual photobleaching of the donor.

In the case of intensity-time trace **f**, which represents another 27% of donor-acceptor pairs in the control experiment, the intensity in both FRET and acceptor channel remains constant on temporal average over the duration of the experiment (category IV, see Section 4.6.1 or the Glossary 8.5). This indicates that no unspecific photocleavage and no significant other photoreactions apart from photodegradation are observed on the single molecule level under the measurement conditions, in contrast to the bulk experiments. The different behavior is likely due to the low reaction rates of any competing photoreaction (see Section 4.4.2), the vast difference in power density and the different chemical environment.

All intensity-time traces exhibit an apparent periodicity in the intensity fluctuations. It is not clear what causes this regularity which is only recognizable on sufficiently long time scales. Closer inspection of the measurement videos reveals that the background remains approximately constant, whereas only the intensity of the fluorescence signals fluctuates roughly periodically. Thus, the effect is unlikely to be related to instabilities of the excitation lasers or the camera. It is possible that the fluctuations reflect

the working intervals of the dehumidifier. Periods of low intensity might correspond to higher humidity. The higher water content of the hydrophilic PVAc could potentially lead to an increased fluorescence quenching and thus lower intensities. It is not possible to verify the hypothesis retroactively and it was refrained from conducting corresponding experiments.

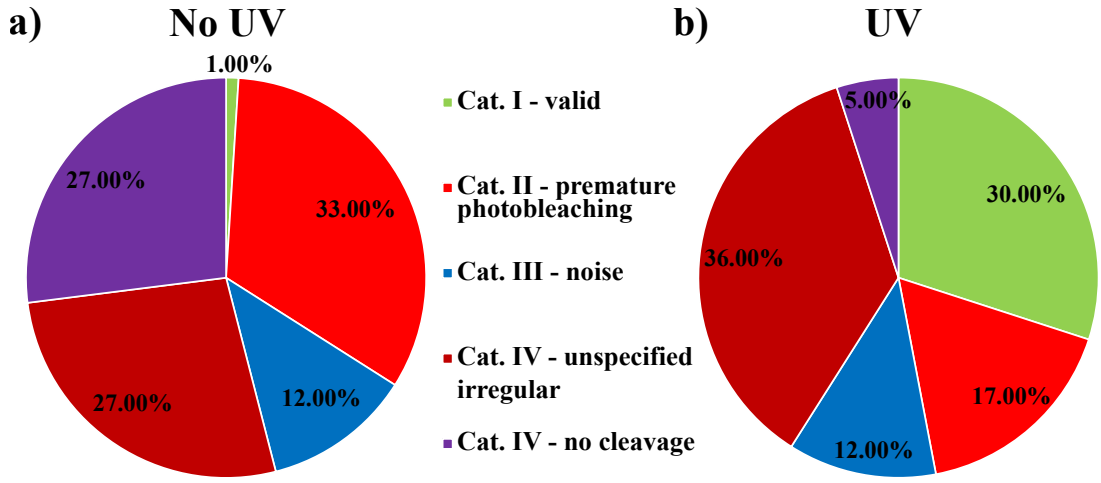

Figure 4.13: Categorization of the intensity-time traces of all initially identified donor-acceptor pairs in the experiments (**a**) without and (**b**) with application of a UV pulse. Category I, II and III donor-acceptor pairs are symbolized by green, red and blue. Category IV pairs are divided into the sub-categories "unspecified irregular" (dark red) and "no cleavage" (purple).

All three intensity-time traces (**d** – **f**) are typical results of the control experiment accounting for the majority of all identified donor-acceptor pairs. The intensity-time traces of about 12% of the initially identified donor-acceptor pairs can only be interpreted as noise, whereas 27% show various irregular and generally not interpretable behavior (categories III and IV, respectively, see Section 4.6.1 or the Glossary 8.5). Only about 1% percent of all identified pairs show behavior that could be falsely interpreted as FRET efficiency decrease due to diffusion, i.e., they show both a gradual decrease of the intensity in the FRET channel and a gradual increase of the intensity in the donor channel, while intensity in the acceptor channel remains approximately constant (category I, see Section 4.6.1 step 7 of the example analysis for a comprehensive explanation of the selection process). In contrast, about 30% of all initially identified donor-acceptor pairs in the proof of concept measurement exhibit the specified behavior (category I). Even most of the donor-acceptor pairs which undergo premature photobleaching of the acceptor (about 17%, category II) essentially show an on average decreasing FRET efficiency until photobleaching occurs. The remaining donor-acceptor pairs in the proof of concept measurement are again either interpreted as noise or they exhibit irregular, generally not interpretable behavior (category III and IV, respectively, see also Section 4.6.1). Only about 5% of the initially identified donor-acceptor pairs in a regular measurement exhibit behavior similar to the donor-acceptor pair shown in Figure 4.12 **f**, indicating that photocleavage with the UV laser is approximately quantitative. The categorization of the initially identified donor-acceptor pairs in the experiments with and without application of the UV pulse is summarized in Figure 4.13. Overall, it is proven that unspecific cleavage of the dyad is insignificant and that photobleaching can be recognized based solely on the intensity-time traces of all identified donor-acceptor pairs.

Even if the concept has been shown to work unequivocally, the problem of photobleaching has also

revealed itself as the biggest impediment of the FEDUP method. A significant ratio of all identified donor-acceptor pairs of a typical measurement, such as the one presented above, exhibit premature photobleaching of the acceptor. This could introduce a bias in the analysis, as donor-acceptor pairs with slower diffusion rates, and therefore longer irradiation times until the critical distance between both dyes is reached, also have more time to undergo premature photodegradation. Consequently, these pairs are more likely to be excluded from the analysis and the determined (average) diffusion coefficient is shifted to higher values (see Section 4.6.1 for more considerations on the FEDUP method). Hence, it is imperative to minimize photobleaching. There are essentially two ways of achieving this: minimizing the irradiation time and power, or suppressing the detrimental photoreactions.

When the laser power densities are turned to lowest reasonable levels, i.e., so that fluorescence signals can be reasonably seen and focused with the used set-up (see Section 6.7.2), there is little that can be done about the irradiation power. However, the delay time between two consecutive excitation cycles can be varied almost arbitrarily. Increasing the delay time at the cost of temporal resolution decreases the irradiation time and thereby also decreases the chances of photobleaching. Choosing a suitable delay time thus requires an understanding of the photobleaching kinetics under the experimental conditions, as photobleaching is one integral obstacle of the FEDUP method. To this end, donor **6**, acceptor **7** and dyad **8** are separately embedded in PVAc and poly(ethylene glycol) (PEG) films and irradiated according to the standard FEDUP measurement protocol. All fluorescence signals in the respective main channels are localized with the ImageJ plugin ThunderSTORM[201] and the normalized amount of localizations per frame is compared for PVAc and PEG. This is shown in Figure 4.14 **a** – **c** for the donor, the acceptor and the dyad, respectively.

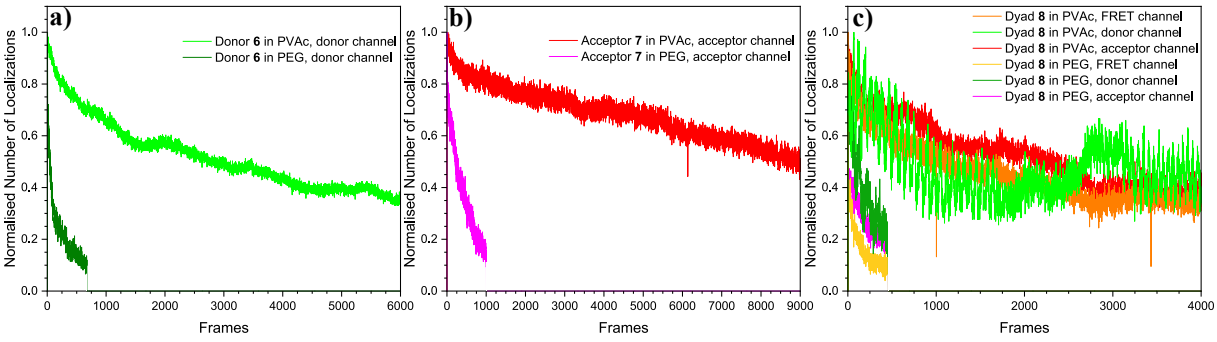

Figure 4.14: Comparison of photobleaching in PVAc and PEG. All fluorescence signals were localized with the ImageJ plugin ThunderSTORM[201]. Subsequently, the number of localizations were normalized to ensure comparability. Data shown in one particular graph was recorded on the same day under identical measurement conditions and analyzed with the same localization threshold value. All measurements were performed according to the regular FEDUP measurement protocol. Each frame corresponds to 220 ms of irradiation with a 561 nm laser (0.028 $kW\,cm^{-2}$) and additional 220 ms of irradiation with a 640 nm laser (0.022 $kW\,cm^{-2}$). Additionally, a 500 ms pulse with 378 nm laser (0.1 $kW\,cm^{-2}$) was applied between frame 5 and 6. All dye components were added in sub-nanomolar concentration to ensure single molecule behavior. (**a**) Localizations in the donor channel when embedding donor **6** in PVAc (light green) and PEG (olive), respectively. (**b**) Localizations in the acceptor channel when embedding acceptor **7** in PVAc (red) and PEG (magenta), respectively. (**c**) Localizations in the FRET channel (orange and dark yellow), the donor channel (light green and olive) and the acceptor channel (red and magenta) when embedding dyad **8** in PVAc and PEG, respectively.

There appears to be a strong dependence of the photostability of the dye system on the chemical environment, i.e., the polymer matrix. The photobleaching rate of both the dyad **8** and its reference compounds donor **6** and acceptor **7** is orders of magnitude higher in PEG than in PVAc. This is likely related to the different gas permeability of the two polymers, and consequently the different available oxygen concentration. The permeability coefficient of oxygen in PEG is about one order of magnitude bigger than in PVAc.[202,203] Photodegradation is believed to be an excited state reaction involving oxygen or other oxidative species from the surroundings. In particular, it is estimated that the triplet state of some dyes produces singlet oxygen, which consequently reacts with the molecule in its ground state.[163]
In PVAc, the amount of localizations detected for donor **6** in the donor channel is reduced by half after about 3000 frames which corresponds to 11 min of constant irradiation with each a 561 nm laser (0.028 $\mathrm{kW\,cm^{-2}}$) and a 640 nm laser (0.022 $\mathrm{kW\,cm^{-2}}$) at comparable power density. Moreover, about 5% of all signals are instantly bleached by the 0.5 s UV pulse (378 nm at 0.1 $\mathrm{kW\,cm^{-2}}$). Whereas the latter observation is consistent with the image series in Figure 4.8, the same suggests an even higher photobleaching rate. The third frame shown, taken 60 min after the UV pulse, is equivalent to about 3200 frames of recording. Only about 10% of the original signals can be seen here. However, the image does not show the entire measurement, but only a cut-out of the central area where the laser power density is likely to be higher than at the edges of the field of view. In the statistic shown in Figure 4.14, in contrast, the entire field of view is included. Additionally, the localization statistic is falsified by the indistinguishable impurity signals present in both PVAc and PEG to different degrees, in particular in the donor channel. The photostability of these impurities varies drastically for each individual case, ranging from very high to very low. Therefore, impurity signals are detected throughout most of the measurement. Furthermore, sporadic false localizations are detected by the algorithm in each frame.
Despite the uncertainty of the analysis, the lower photostability of donor **6** in PEG compared to PVAc is unambiguous. The UV pulse instantly destroys the fluorescence of about half of all emitters in PEG. After about eight hundred frames, equivalent to about 3 min of constant irradiation as specified above, only about 10% of the original localizations remain. It is assumed that a majority of the detected localizations at this point are wrongly recognized localizations and impurities. Likewise, it is reasonable to claim that the donor is less photostable than the acceptor. After the same irradiation time under the same conditions, the amount of localizations detected in the acceptor channel of the acceptor sample is reduced by about 25% in PVAc and 80% in PEG. The bleaching rate of the UV laser is approximately half of the donor. The laser power density of the red laser is slightly lower compared to the green laser. However, the influence on the photobleaching rate is arguably offset by the fact that the ATTO647N chromophore can also absorb light of 561 nm, whereas the ATTO565 chromophore cannot be excited by light of 640 nm. Hence, the lower photobleaching rate of the acceptor compared to the donor is evidenced.
Photobleaching of the dyad differs from the reference compounds. In PVAc, the photobleaching rate of the ATTO647N chromophore in the dyad **8** is vastly increased compared to the photobleaching rate of the same chromophore in the reference acceptor **7**. This is evidenced by the faster decrease of detected localizations in both the FRET and the acceptor channel. Both channels exhibit essentially the same behavior. The initial decay kinetics in the FRET channel are only slightly faster than in the acceptor channel due to additional interruption of FRET by photocleavage instead of photobleaching. Otherwise,

the UV pulse seems to have a similar influence on the amount of localizations detected as discussed before, at most with slightly higher destructive potential than for acceptor **7**. The higher photobleaching rate of the ATTO647N chromophore in the dyad is expected. Due to the efficient energy transfer, the excitation energy of the ATTO565 chromophore during excitation with the green laser (and also the UV laser) is transferred to the ATTO647N chromophore which is otherwise directly excited by green light only to a minor extent. Thereby, the acceptor in the dyad, or in a donor-acceptor pair, protects the donor from photobleaching by returning it to the electronic ground state. At the same time, the probability of photobleaching increases for the acceptor, as it spends more time in excited singlet and triplet states.
The temporary protection of the ATTO565 chromophore by energy transfer is also evidenced by the drastically different photobleaching behavior of the dyad in PVAc compared to reference donor **6**. Instead of a simple exponential decay of the amount of detected localizations in the donor channel, the amount of localizations first increases to its maximum shortly after the application of the UV pulse. Afterwards, the average amount of detected localizations decreases for almost 2000 frames before it increases again in a reasonable correlation with the decrease of localizations in the other two channels. Furthermore, the amount of localizations detected per frame fluctuates much more strongly than for the reference donor in subfigure **a**. The fluctuation appears to be highly periodic. Conceptually similar variations were observed in the intensity-time traces in Figure 4.12 on comparable time scales. It is possible that the regularity of the fluctuation is also caused by the working intervals of the dehumidifier (see above). The different decay kinetics of donor **6** and the dyad are an indicator that the ATTO565 chromophore in the dyad can only undergo destructive photoreactions after energy transfer is impossible due to either photodegradation of the acceptor or a sufficiently increased distance between donor and acceptor.
A similar behavior is also recognizable in PEG, although it is obscured by the significantly faster decay kinetics. Still, the relative amount of localizations in the donor channel decreases slower than in the acceptor and FRET channel, despite the higher photobleaching rate of donor **6** compared to acceptor **7** under the measurement conditions. Again, this is interpreted as protection of the ATTO565 chromophore by transfer of the excitation energy. Furthermore, the destructive potential of the UV on the ATTO647N chromophore in the dyad appears to be vastly higher than in the acceptor. About 55% of all dye molecules are irreversibly destroyed by the UV pulse.
The experiment shows the problem of photobleaching most clearly. In an ideal FEDUP measurement, the amount of localizations in the acceptor channel would remain constant, whereas the amount of localizations in the FRET and donor channel decrease and increase in perfect correlation. However, measurements are still possible as long as a reasonable amount of donor-acceptor pairs diffuses sufficiently far apart before photobleaching occurs. Even in PEG, where photostability seems to be extraordinarily low, it appears as if the amount of localizations in the FRET channel decreases faster than in the acceptor channel. Given the short time frame of this particular measurement (about ten minutes between the UV pulse and the last frame), this indicates a higher mobility of donor-acceptor pairs in PEG than in PVAc. Hence, a diffusion measurement can still be feasible, as the measurement time, and consequently the irradiation time, is reduced compared to PVAc, thereby counterbalancing the increased photodegradation. It is likely that the higher mobility is in part even responsible for the faster photobleaching rate, as both reactive sites and oxygen are more accessible. Still, the lower photostability of the dye system in PEG, or generally less rigid polymer systems, has to be taken into account in the

respective diffusion measurement, and in particular any potential bias introduced to the analysis thereby (see also Section 4.6.4).

Lastly, it is attempted to suppress the critical photodegradation reactions. It is assumed that only excited dyes and in particular dyes transferred to their triplet state can undergo any kind of reaction which leads to irreversible photodamage. Furthermore, it is assumed that most photodegradation reactions involve oxygen.[163]

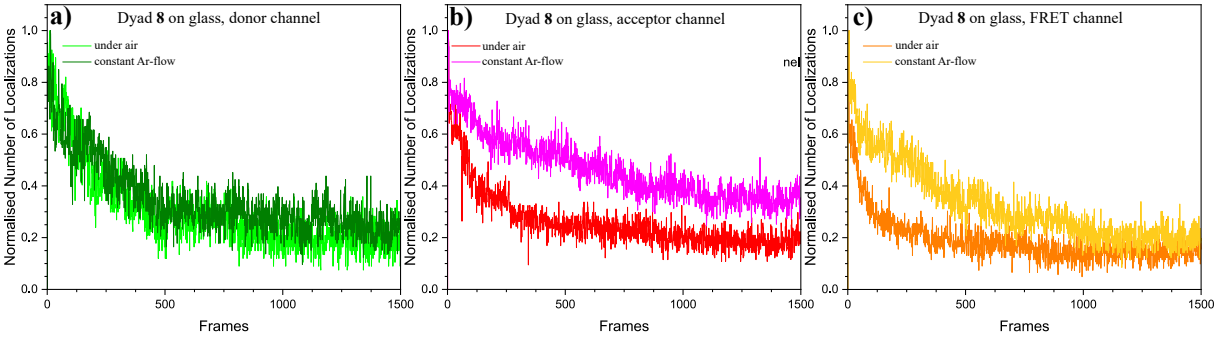

Figure 4.15: Comparison of photobleaching of dyad **8** on glass with and without a constant flow of Argon across the coverslip. All fluorescence signals were localized with the ImageJ plugin ThunderSTORM[201]. The number of localizations were normalized to ensure comparability. All data was recorded on the same day under identical measurement conditions and analyzed with the same localization threshold value. The same sample was used for both measurement series. All measurements were performed according to the regular FEDUP measurement protocol. Each frame corresponds to 220 ms of irradiation with a 561 nm laser (0.006 $kW\,cm^{-2}$) and additional 220 ms of irradiation with a 640 nm laser (0.003 $kW\,cm^{-2}$). Additionally, a 300 ms pulse with a 378 nm laser (0.1 $kW\,cm^{-2}$) was applied between frames 5 and 6. TIRF illumination was employed for all lasers. The dyad was added in sub-nanomolar concentration to ensure single molecule behavior. Normalized amounts of localizations are separately compared in the (**a**) donor channel, (**b**) acceptor channel and (**c**) FRET channel with (olive, magenta and dark yellow) and without (light green, red and orange) a constant Ar flow, respectively.

If any fluorescence is to be detected, excitation is unavoidable. Likewise, it is not trivial to chemically alter the system so that a return of any dye molecules in their triplet states to the ground state is facilitated without fundamentally disturbing the properties of the system to be investigated. Therefore, it can only be attempted to reduce the partial pressure of oxygen in the air surrounding the illuminated field of view. The best way of achieving this would be to put the entire microscope into a chamber filled with an inert gas like argon (Ar). This, however, is not feasible. Instead, a constant argon flow was directed onto the coverslip with the sample. It was taken care that the flow was gentle enough not to induce any additional mechanical instabilities or drifts, but strong enough that a decent local Ar atmosphere can be expected (see also Section 6.7.2). To show the influence of the Ar flow without any possible secondary influences caused by the polymer matrix, dyad **8** was deposited directly on a clean glass substrate. Two identical FEDUP-type measurements were performed according to the same procedure as described before, one with and one without an additional Ar flow across the sample. In Figure 4.15 **a** – **c**, the amount of normalized localizations detected in donor, acceptor and FRET channel is compared, respectively.
Despite the simple experimental design, the argon flow seems to reduce the photobleaching rate of the ATTO647N chromophore significantly. Both in the FRET and the acceptor channel, the amount of localizations detected per frame decreases considerably slower in the measurements with argon flow.

The photodegradation caused by the UV pulse also seems slightly lessened. In contrast, no recognizable difference is observed in the donor channel for the ATTO565 chromophore. It is not clear if the influence of an argon atmosphere on the photobleaching of the ATTO565 chromophore is simply less pronounced, if ATTO565 undergoes an entirely different photodegradation reaction in which oxygen is not the most critical factor, or if photobleaching is reduced but the effect is not correctly recognized in the simple experiment and analysis. Still, it is evidenced that photobleaching is at least partially related to the presence of oxygen and that a reduction of the partial pressure of oxygen can increase the photostability, at least of the ATTO647N chromophore. As the acceptor is the more critical factor anyway, given the protection of the donor by the acceptor (see above), it is advisable to incorporate strategies for the reduction of oxygen (and other oxidative species) in any measurement.

4.5 Summary and conclusion (Part 1)

Given the complexity and extent of Chapter 4, the results so far are briefly summarized and evaluated with regard to the suitability of the dye system for the main topic of this chapter, in form of the diffusion measurements in Section 4.6.

The work presented in this chapter seeks to extend the range of systems that can be investigated with the FEDUP method. The original work on the FEDUP method presented an apolar dyad for diffusion imaging that requires short wavelength UV irradiation for photocleavage.[55] In this work, in contrast, a dyad soluble in more polar solvents and cleavable with long wavelength UV was developed and successfully synthesized (Section 4.2). The solubility was increased by employing the cationic dyes ATTO565 and ATTO647N, the photocleavage wavelength could be tuned by basing the photolabile linker of these two dyes on the well-known NPPOC[63,64] PPG. Additional reference compounds were synthesized to grant a better understanding of the photochemical and -physical properties of the dye system. The dyad and its reference compounds, including the precursor dyes, were characterized by measuring absorption and emission spectra, as well as fluorescence lifetimes and quantum yields, and comparing them with each other (Section 4.3). The dye system was subjugated to UV and vis light irradiation and any spectral changes were monitored by again comparing spectra, lifetimes and quantum yields of the dyad and all reference compounds (Section 4.4). Both characterization and irradiation experiments were performed in solution. Almost all experiments were performed once in methanol and repeated once more in water. Lastly, the performance of the dyad on the single molecule level was tested qualitatively to confirm the suitability of the dye system for the upcoming diffusion measurements.

Most surprising, and potentially detrimental to the desired diffusion measurements, is the vastly different behavior of the dyad, and to lesser degree its reference compounds, in different chemical environments. It is estimated that primarily the nitrophenyl group of the photocleavable linker introduces this variance to the spectral properties due to its quenching ability. It could be demonstrated that the quantum yields and lifetimes of all dye compounds covalently bound to the nitrophenyl quencher are influenced more significantly by the solvent than their respective precursor dyes. This effect is particularly strongly pronounced for the reference donor and the dyad. Whereas the quantum yield (and lifetime) of ATTO565 only changes by a few percent when exchanging methanol for water, the quantum yield (and lifetimes) of the donor and the dyad decrease by an order of magnitude. Furthermore, a strong dependency of the

FRET efficiency on the solvent was recognized. Given the structure of the dyad and the consequentially short distances between donor and acceptor chromophore, a quantitative FRET efficiency was expected irrespective of the solvent. Both in methanol and water the calculated Förster distance exceeds the expected possible maximum distance of donor and acceptor when covalently bound to the same linker. However, in methanol, the apparent FRET efficiency is only about 80%, whereas in water the FRET efficiency is too low to be determined accurately. When embedded in a polymer matrix, in contrast, the FRET efficiency appears to be significantly higher than in either water or methanol. It is estimated that apart from the influence of the (intramolecular) quencher, the conformational freedom of the dyad, or rather of the donor relative to the acceptor in the dyad, plays a major role in the observed FRET efficiencies. The existence of reverse FRET from the ATTO647N chromophore to the ATTO565 chromophore cannot be excluded either.

All crucial photoreactions, in particular photocleavage and photobleaching, also show a strong dependency on the environment. Two possible reaction pathways have been postulated for the photocleavage of NPPOC-type PPGs.[111] The styrene pathway leads to a nitrostyrene cleavage product which exhibits similar quenching potential as the uncleaved linker and is therefore the more convenient reaction pathway for the intended diffusion measurements. The nitroso pathway leads to a nitroso cleavage product which exhibits significantly stronger quenching and thereby introduces undesirable spectral changes in the dye system unrelated to physical separation of the linked chromophores. Evidence could be produced that both reaction pathways take place in unequal ratio in methanol. In water and on the single molecule level in different polymer matrices, however, the styrene pathway seems to be favored. Similarly, a drastically different photodegradation behavior was observed in bulk and on the microscope. In bulk, strong spectral shifts of especially the dyad were observed. On the single molecule level, however, no shifts were detected, and instead, a more regular photobleaching behavior to a non-fluorescent species seems to occur. Both the varying irradiation conditions, in particular the diverging irradiation power densities, and the different chemical environments could be responsible for the observed differences.

The behavior of the dye system in bulk, especially in water, seems at first highly unfavorable for the intended diffusion measurements. Both the low apparent FRET efficiency and the overall low fluorescence emission of the dyad in water could prove as insurmountable obstacles for the FEDUP method. Nonetheless, the reasonably good performance on the single molecule level suggests otherwise. The proof of concept experiment confirms that, despite the often strange behavior in bulk, the dye system behaves essentially as expected on the single molecule level in polymer matrices. Additional unavoidable uncertainties are introduced to the method by the nonlinear photophysical and -chemical alterations of the dyes by the NPPOC linker. These uncertainties, however, do not impede the possibility of diffusion measurements completely and only have to be considered when evaluating the accuracy of the method later on.

The accuracy aside, the proof of concept experiment certainly achieves one essential aim; it provides a visualization of motion on the single molecule level. Translational motion in PVAc is virtually not visible by the “naked eye”. Even after several hours, fluorophores remain in exactly the same relative position, moving less than a pixel worth of distance. However, the FEDUP method manages to visualize sub-pixel movement by encoding the movement with color. The image series in Figure 4.10 shows unmistakably

that translational motion does occur, as each new detected signal in the donor channel that does not coincide with photobleaching of the acceptor corresponds to single molecule movement on a nanometer length scale. Irrespective of the reasonability of the quantification of that movement in the following Section 4.6, the simple fact that otherwise invisible translational movement becomes visible should not be undervalued.
Similarly, the at first glance detrimental properties of the dye system in water do not necessarily represent a disadvantage. It is fathomable that the low fluorescence emission in water is even favorable for specific applications. In biological systems, for example, it can be expected that the dyad only shows noteworthy FRET efficiency when attached to supermolecular structures, such as phospholipid membranes, but little to no fluorescence emission in the aqueous surroundings. This could prove advantageous for the visualization of targeted, comparatively apolar substructures, or for the visualization of the mobility in these substructures, in more polar environments. The use of the dyad or the reference donor as water sensing probes is also conceivable. Similar to the determination of local water content in polymer gels by the lifetime changes of red-emitting dyes due to partial quenching by water,[45] it seems likely that an equivalent principle is applicable for the dyad or the reference donor. A Nile Red PAINT-like SRFM approach is also conceivable, using nanomolar amounts of the reference donor or the dyad in water instead of aqueous Nile Red solutions. In simple tests with PNIPAM microgels, unfortunately, the binding affinity of the dye system for the deposited polymer gels was too low compared to the affinity of temporary binding to the glass substrate. An optimization of the measurement procedure is required for the proposed application. Last, the possibility of photocleavage and the connected changes of the photophysical properties, in particular the increased fluorescence emission in water, could also serve further specific applications not yet fully conceived.
All in all, it can be stated that the dyad seems almost surprisingly promising for the intended application of diffusion measurements in (hydrophilic) polymers. Properties of the dye system which are potentially detrimental for the intended application could in turn prove beneficial for entirely different applications.

4.6 Diffusion measurements in various (polymer) systems

The photocleavable dyad **8** was developed for high accuracy diffusion measurements, i.e., the FRET efficiency diffusion measurement upon photocleavage (FEDUP) method. The suitability of the dyad for this purpose was confirmed in Section 4.4. The actual application of the dyad in diffusion measurements is presented throughout the remainder of this chapter.
First, the measurement and analysis procedure is explained step by step in Section 4.6.1 on the basis of the same measurement presented before (see Section 4.4.3). A first evaluation of the measurement and analysis procedure is given, too. Then, the FEDUP method is used for extended diffusion measurements in three selected polymers (PVAc (Section 4.6.2), PBMA (Section 4.6.3) and PEG (Section 4.6.4)). Each of these three polymers is investigated once at room temperature and once at 40 °C, which corresponds to a temperature close to the glass transition temperature for PVAc and PBMA. In the case of semi-crystalline PEG, 40 °C corresponds to a temperature just below the determined melting temperature (see Section 4.6.4). Last, the limits of the FEDUP method are studied in Section 4.6.5 by applying the dyad both to polymers with significantly higher and lower glass transition temperatures

(poly(acrylic acid) (PAA) and poly(ethyl acrylate) (PEA), respectively) and to a water soluble biological polymer (dextran). Furthermore, it is shown that even diffusion on the glass surface of the substrate can be visualized to some extent. In all cases, it is refrained from repeating the analysis procedure and only the final results of the analysis are presented (i.e., step 8 and step 9, see below). The measurement and analysis are always performed equivalently to the example measurement and analysis presented in Section 4.6.1.

4.6.1 Example measurement and analysis

In the following, the measurement and analysis procedure of the FEDUP method is presented in greater detail. To this end, the measurement discussed qualitatively in Section 4.4.3 is now used as a quantitative example. The detailed measurement setup is described in Section 6.7.2. However, further crucial aspects of the measurement, which have direct influences on the analysis, are discussed here. The analysis consists of nine distinct steps, which are explained separately. Essentially, the donor and FRET channel have to be spatially correlated (step 1), the signals in all three relevant channels have to be localized (step 2), a drift correction has to be applied (step 3), donor-acceptor pairs have to be identified (step 4), a background correction has to be implemented (step 5), the intensity-time traces of all identified donor-acceptor pairs have to be extracted (step 6), the valid intensity-time traces have to be selected (step 7), the summed-up intensity-time traces have to be evaluated (step 8), and finally, the data has to be fitted with the established Maxwell distribution model (step 9). Apart from the localization of fluorescence events (part of step 1 and step 2), the analysis is entirely performed with a series of custom Matlab scripts. Localization is achieved with the ThunderSTORM[201] plugin of the microscopy video processing software ImageJ. The computational, time and general effort of the nine steps varies drastically. For example, whereas step 6 represents by far the largest computational effort, step 7 is the most crucial part of the analysis, which requires the most thorough considerations. Furthermore, not all steps are technically independent of each other (for example, step 5 and step 6), but are explained separately for a better overview of the analysis procedure. The measurement and the nine steps of the analysis are presented in their entirety first, then a first evaluation of possible pitfalls, introduced biases and other uncertainties, as well as advantages of the method is given, before turning to the extended diffusion measurements for the remainder of this chapter.

The measurement

The sequence of a FEDUP measurement has been presented in Section 4.4.3 already and is only briefly repeated here. Instead, the logic behind the procedure is explained in more detail.
The measurement is performed with alternating laser excitation (ALEX)[105] employing a 561 nm and 640 nm laser. The lasers are turned on and off by automated opening and closing of shutters. Five frames are recorded in quick succession with each laser, then a short powerful UV pulse (378 nm) is applied. The length of the UV pulse is also controlled by an individual shutter. Afterwards, ALEX is used again. Between each cycle of excitation, a variable delay time is inserted during which the sample is not irradiated in any way. The excitation cycles, delay time and length of the UV pulse are controlled with a single custom LabView script. Delay times between $t_{\text{delay}} = 0 - 32$ s can be set, the irradiation time of the excitation and photocleavage lasers can be chosen freely. For the typical employed laser

power densities (approximately 0.03 kW cm^{-2}, 0.02 kW cm^{-2} and 0.1 kW cm^{-2} for the 561 nm, 640 nm and 378 nm laser, respectively), about 200 ms of irradiation with visible light and about 1 s of irradiation with UV light seem to yield the best results. The irradiation times of the excitation lasers usually surpass the camera exposure time by at least 10 ms to account for the temporal resolution of the shutters. For the same reason, a delay of 200 ms is inserted between the closing of the shutter of the 561 nm laser and the opening of the shutter of the 640 nm laser.

The recorded frames before the UV pulse are not relevant for the actual analysis, since no photocleavage has occurred yet. However, it is obligatory to observe the system before application of the UV pulse at least briefly, so that possible undesired influences of the UV laser may be recognized. Moreover, the recorded frames can help with the identification of donor-acceptor pairs in step 4. Given the insignificant crosstalk (see Section 4.4.3), before application of the UV pulse, intensity should be measurable in the FRET and acceptor channel only, but not in the donor channel. This is an optional condition for the identification of donor-acceptor pairs. The condition has to be regarded as optional, since intrinsic blinking, especially of the ATTO647N chromophore, may in some cases lead to no detectable fluorescence in the few frames before photocleavage (see step 4). This could be countered by increasing the number of frames taken before the UV pulse. However, every additional frame recorded, which is not essential for the actual analysis, unnecessarily increases the chance of premature photobleaching (see the Glossary 8.5 for a brief explanation of all introduced technical terms). Recording each five frames with each excitation laser has been identified as a reasonable compromise between the demand to observe the system before photocleavage and the need to keep irradiation times and power as short and low as possible.

The delay time has been introduced for similar reasons. The shorter the delay time, the more frames are recorded per arbitrary time interval, leading to a better temporal resolution. However, the more often the dye system is excited, the more probable (premature) photobleaching becomes. Additionally, the more frames are recorded, the bigger the computational effort of the analysis (see step 6). The delay time represents a compromise between the required temporal resolution, the photobleaching rate and the available computational power. The example measurement is performed in PVAc films. In light of the glass transition temperature of PVAc, which is just above ambient temperature[199,200], translational diffusion is expected to be tardy. Hence, no high temporal resolution is required. It takes dozens of minutes, if not hours, for the relative movement of distances in the order of magnitude of the Förster distance. Even if the photobleaching rate in PVAc is comparably low, it is not necessary to record more than one or two frames per minute to achieve a suitable temporal resolution. Consequently, the delay time was set to its near maximum value of $t_{\mathrm{delay}} = 30$ s. The time interval between two subsequent frames in the same spectral channel is thus composed of the delay time ($t_{\mathrm{delay}} = 30$ s), the irradiation times of each excitation laser (200 ms) and the internal delay between the alternating laser excitation (200 ms). In the example measurement, this corresponds to $t_{\mathrm{cycle}} = 30.6$ s overall. Henceforth, the time interval between two subsequent frames is termed the cycle time t_{cycle}. The irradiation time of the UV laser is regarded as insignificant in comparison and the time point $t = 0$ s refers to the first frame taken with 561 nm excitation after UV irradiation, irrespective of the length of the UV pulse and the inevitable delay between the pulse and the first recorded frame. A FEDUP measurement in PVAc at room temperature typically takes several hours in which several thousands of frames are recorded.

Step 1: Spatial correlation of donor and FRET channel

Before any reasonable measurement can be performed, the donor and the FRET channel have to be calibrated once the measurement setup is fully aligned otherwise. Although both channels are spatially equivalent, the two channels do not match each other perfectly. For one, the sizes, that is, the overall amount of pixels, differ slightly. Second, both channels correspond to two separate imaging paths, which are recombined on the camera (see also Figure 2.7). Hence, the two channels have to be aligned manually so that the same field of view is obtained. This is inevitably prone to imperfections. Third, chromatic aberration causes wavelength-dependent shifts. The negative influence of these effects can be reduced by optimizing the technical instrumentation. Chromatic aberration is suppressed to the greatest possible extent by the use of an achromatic objective lens, which is employed in all measurements throughout this chapter. The quality of the alignment of both channels is dependent on the experimental expertise and patience of the experimenter. The size difference of the channels can be adjusted using corrective lenses in the respective optical paths and by cropping the separate images to yield a better match.

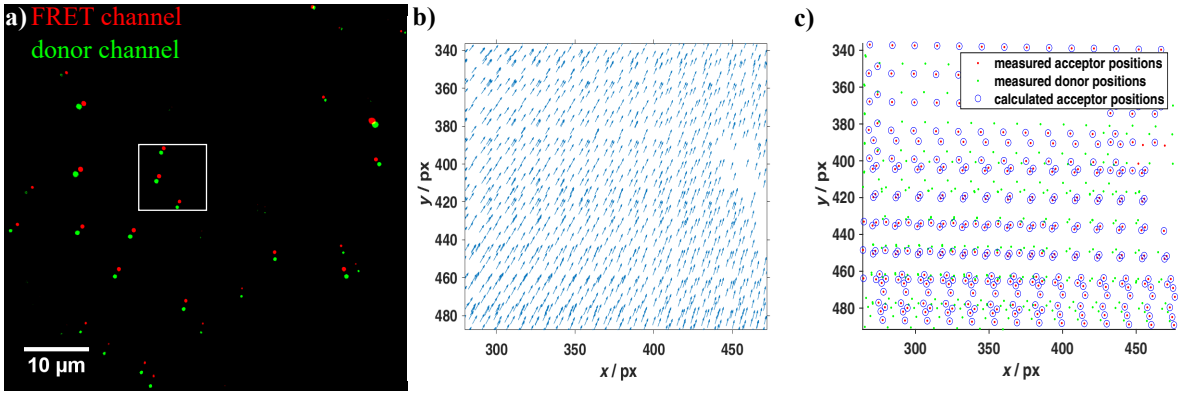

Figure 4.16: (**a**) Overlay of the FRET channel (red) and donor channel (green) of a single exemplary frame of the spatial correlation with TetraSpeck™ beads. The white square shows the approximate area that is referenced in subfigures **b** and **c**. (**b**) Calculated shift vectors connecting the pixels in the donor channel with the corresponding pixels in the FRET channel. A cut-out corresponding to the white square in subfigure **a** is shown. The magnitude of the vectors corresponds to the distance between correlated pixels in amount of pixels, the orientation of the vectors signifies the direction of the shift. (**c**) Application of the shift vectors to the donor signals (green, measured donor positions) from 250 summed up frames of the donor channel. Again, the approximate area of the white square in **a** is shown. The signals detected in the FRET channel are depicted in red (measured acceptor positions), the expected positions calculated by applying the shift vectors to the signals in the donor channel are marked by blue circles (calculated acceptor positions). The area signed by the white square in subfigure **a** approximately corresponds to the region of interest shown both in Figure 4.10 and 4.18.

Despite these measures, imperfections are unavoidable and there is a considerable mismatch in the absolute coordinates of both channels. This can be seen, for example, in Figure 4.16 **a**. Therefore, every pixel in the donor channel has to be ascribed to a corresponding pixel in the FRET channel. To this end, a sample of TetraSpeck™ beads is placed on the microscope and excited with the same 561 nm laser used in the actual FEDUP measurements. The used TetraSpeck™ beads are of subdiffractional size (approximately 100 nm). They can be excited with visible and UV light of nearly arbitrary wavelength and emit fluorescence over the whole range of the visible spectrum. Consequently, a bright signal is detected in both channels simultaneously when exciting the beads with green light. To obtain positional

information for as many pixels as possible, the sample is scanned systematically until about 1000 frames with different signal patterns are collected. The scanning is achieved with a piezo sample-stage that moves the sample in a defined pattern. The sample is moved in 1 µm steps to the left for 50 frames. Then, it is moved 1 µm to the top and subsequently moved to the right with the same step length for again 50 frames. This process is repeated until a sufficient amount of pixels have been screened.
With each frame, a single image containing both spectral channels is recorded. The single image is separated into two spatially approximately equivalent images containing the donor channel and the FRET channel, respectively. The signals in each frame of the separate channels are then localized with standard SRFM localization software, e.g., the ThunderSTORM[201] plugin of the ImageJ video processing software. The coordinates of the localizations in both channels are compared. Shift vectors are calculated based on the repeating pattern in each pair of frames with a customized Matlab script (see Figure 4.16 **c**). These shift vectors connect every detected localization in the donor channel with a matching localization in the FRET channel. Overall, a vector field is obtained that ascribes every pixel in the donor channel to a specific pixel in the FRET channel. Even if not every single pixel has been scanned during the spatial correlation, the corresponding shift vector can be reasonably approximated by the surrounding shift vectors forming a comprehensive local vector field. This vector field is the crucial result of the spatial correlation that can now be used to find the correct associated positions of any donor-acceptor pair, provided that a signal is detected in any of the two relevant channels. The spatial correlation is verified by applying the vector field to the localizations detected in the donor channel of the TetraSpeck™ beads sample (henceforth called the measured donor positions) and comparing the calculated positions in the FRET channel (the calculated acceptor positions) with the localizations actually detected in the FRET channel (the measured acceptor positions). The calculated acceptor positions have to coincide reasonably well with the measured acceptor positions for the spatial correlation to be accepted. The verification of the vector field shown in Figure 4.16 **b** is depicted in Figure 4.16 **c**.

Step 2: Localization of fluorescence signals

The actual data analysis can logically only begin once the FEDUP measurement is completed. First, the single images containing both donor and FRET channels are separated in the exact same fashion, i.e., using the same coordinates, as in the spatial correlation. The acceptor channel is cropped using the same coordinates as for the FRET channel. Afterwards, the fluorescence signals in all three channels are localized with the ThunderSTORM[201] plugin of the ImageJ video processing software. Contrary to SMT, the localizations are not required to determine a diffusion coefficient, as all spatial information is encoded in the intensity and/or lifetimes of a donor-acceptor pair. However, it is convenient to localize all fluorescence events for the initial identification of donor-acceptor pairs (step 4). Essentially, step 2 serves to mark all regions of interest that have to be investigated further in the later analysis. Additionally, the drift correction (step 3) requires absolute spatial information.

Step 3: Drift correction

The localizations detected in the three relevant channels are fed separately to a SMT routine. The sample drift is treated as regular movement of single molecules and analyzed with a standard SMT algorithm (see also Section 2.3.6). A circle with a radius of three pixels (equivalent to approximately 200 nm) is

drawn around every localization. If a localization in subsequent frames is located within the circle, it is recognized as the same emitter. To avoid unnecessary false positives, tracks are only accepted if emitters are in a dark state for at most two successive frames, and if the track length is at least three frames long. The tracks are compared to recognize any collective movement. Since diffusion in any of the investigated polymer films is expected to be both slow and random, measurable collective uniform movement can only stem from drift of the entire sample. A drift curve is obtained that defines the concerted shift of all signals per frame. This drift curve is applied to every detected signal, so that in the following analysis steps donor-acceptor pairs and the corresponding intensity-time traces are identified and extracted correctly for the entire measurement video (see below). A visual impression of the sample drift of the example measurement is shown in Figure 4.17. In subfigure **a**, the summed-up localizations in all frames of the acceptor channel are shown. Instead of local point clouds, parallel diagonal streaks of localizations can be seen. This indicates sample drift along that axis. In subfigure **b**, the calculated collective uniform movement over the whole measurement video is presented. The drift is equivalent in all three channels. The acceptor channel has been chosen as an example, since on temporal average it contains the most localizations and grants the best visibility of the sample drift.

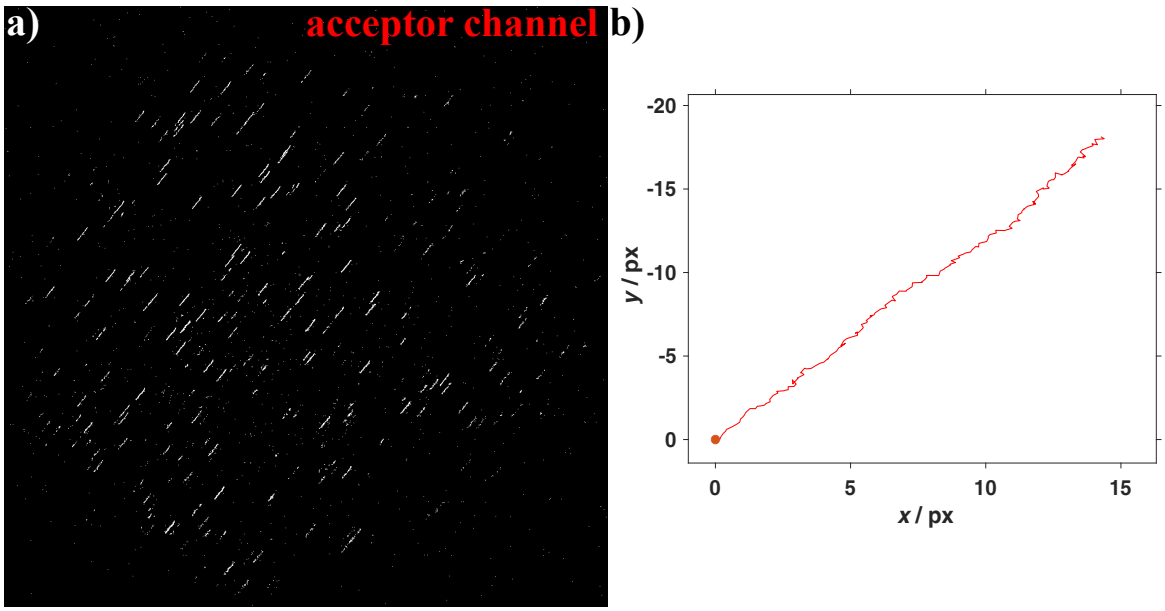

Figure 4.17: (**a**) Summed-up localizations of all frames of the acceptor channel. (**b**) The identified average collective movement of all localizations in the acceptor channel over the whole measurement time. The x- and y-axis show the relative drift in x- and y-direction, respectively. The distance from the first localization is expressed in numbers of pixels. The drift is equivalent in all three channels.

Step 4: Identification of donor-acceptor pairs

Not every localization detected in step 2 belongs to a donor-acceptor pair. A significant amount of signals, especially in the donor channel, is related to fluorescent impurities in the polymer film, as evidenced by the control experiment shown in Figure 7.45 in the appendix (see also Section 4.4.3). Moreover, wrongfully detected localizations occur in every channel due to, for example, random intensity fluctuations of the background which the localization algorithm recognizes as a fluorescent event. To investigate every single event by extracting the intensity-time trace is a waste of computational effort.

Instead, logical conditions are implemented to identify any possible donor-acceptor pair.

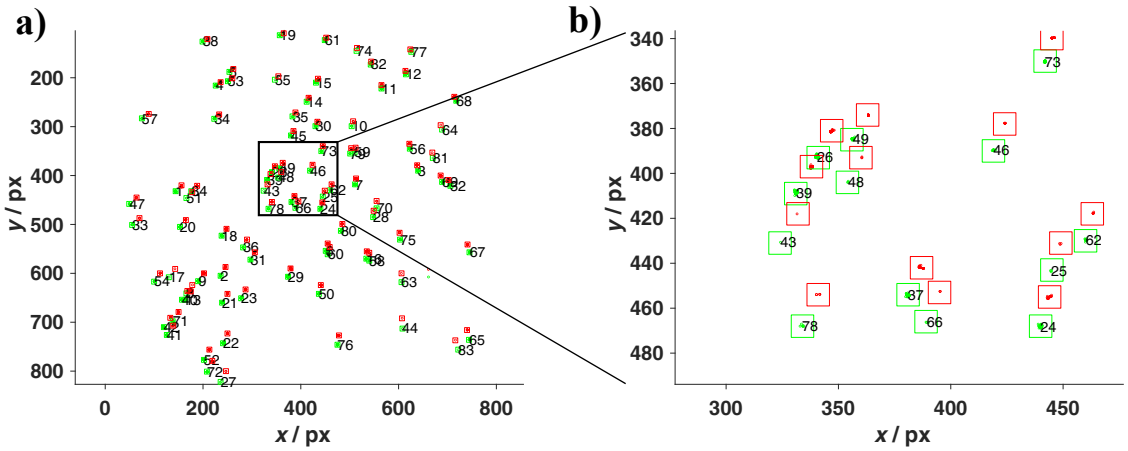

Figure 4.18: (**a**) All detected pairs of signals in the donor and the FRET channel that match the initial condition to be identified as donor-acceptor pairs. 84 donor-acceptor pairs were identified by the algorithm overall. (**b**) Close up of the region of interest marked by the black square. The calibrated local vector field of this specific region is shown in Figure 4.16 **c**. The donor-acceptor pairs marked with the numbers 49, 26, 48, 39, 43 and 37 by the identification algorithm correspond to the re-branded donor-acceptor pairs 1, 2, 3, 4, 5 and 6 in Figure 4.10. The green and red dots correspond to all localizations detected in the donor and FRET channel, respectively, after application of the drift correction. The green and red squares around the dots represent the accepted search radius when moving along the local shift vector to the correlated signal in the other channel. An overlap of green and red squares is not critical, as the areas are not spatially correlated. Only an overlap of two green or two red squares can lead to errors.

The strictest, inexorable condition is at least one detected localization in both the donor and the FRET channel at corresponding areas. It is not necessary that a localization is detected in both channels simultaneously at any point during the measurement. In fact, an arbitrary amount of frames may be recorded between the last localization in the FRET channel and the first localization in the donor channel. Any signal in either donor or FRET channel is identified as part of a given donor-acceptor pair if the signal in either channel is located in a five pixel radius around the precise associated spot as defined by applying the local shift vector to any localization in the other channel. The extended radius of acceptance is introduced to account for general measurement uncertainties, possible additional uncertainties implemented by both the spatial correlation and the drift correction and the finite localization accuracy. Consequently, different donor-acceptor pairs can only be resolved independently if the signals in one channel are at least five pixels apart. The mentioned uncertainties can be easily recognized in Figure 4.18, **b** which presents a small subset of the identified donor-acceptor pairs of the example measurement. Part of the same subset of donor-acceptor pairs is also basis of the discussion in Section 4.4.3. The entirety of the identified donor-acceptor pairs is shown in Figure 4.18 **a**. If the drift correction and localization procedure worked perfectly with maximum accuracy, in all cases only a single spot corresponding to hundreds of localizations would be visible. However, in some cases, slightly extended point clouds are observed. It is assumed that this is primarily related to imperfect drift correction and the localization accuracy, and not any noteworthy translational diffusion of the donor-acceptor pairs.

A second optional condition states that signal pairs are only identified as donor-acceptor pairs if any signal is detected in the FRET channel in the five frames before UV irradiation, while no signal is detected in the associated area in the donor channel. This condition, however, can be too strict in certain cases. For example, the donor-acceptor pairs 4 and 5 of the example measurement in Section 4.4.3 (39 and 43 in Figure 4.18) exhibit no fluorescence in the FRET channel before photocleavage. Still, the overall intensity-time traces of all three relevant channels confirm that at least donor-acceptor pair 4 is very likely a valid donor-acceptor pair (see step 7 for the terminology). It is assumed that this is a random, if common, phenomenon. It has been shown already that almost arbitrarily long dark states of all fluorophores are possible at any point in the measurement. Moreover, randomly detected signals in the donor channel before photocleavage could potentially prevent the identification of donor-acceptor pairs. Hence, it has to be decided for every measurement anew, if the second condition is implemented or not. For the example measurement discussed here, both possibilities are tested and compared, with a general focus on a suspension of the stricter identification rule.
Overall 84 signal pairs are detected in the example measurement with only the first condition active. For comparison, only 31 of these pairs are detected if the second condition is set as valid. At this step in the analysis, it cannot be stated if any of these pairs are valid donor-acceptor pairs, if they are donor-acceptor pairs that have undergone premature photobleaching or if they are just random signals that happen to match the identification condition. Consequently, the remaining analysis steps have to be performed for these 84 signal pairs. To distinguish these signal pairs from the selected pairs in step 7, all donor-acceptor pairs identified in step 4 are termed “initially identified donor-acceptor pairs”, whereas all donor-acceptor pairs selected in step 7 are termed “valid donor-acceptor pairs” and all excluded pairs are collectively called “invalid donor-acceptor pairs”. The latter category is further subdivided into different categories according to the nature of invalidity (see below).

Step 5: Background correction

Even when no fluorescence event is recorded, the intensity measured by the used (s)CMOS camera (see also Section 6.7.2) is not zero due to the camera offset, leakage of the laser through the emission filters and (intrinsic) noise. The intensity due to all these effects is collectively termed the background signal. In a first approximation, the background can be regarded as uniform over the entire field of view and, in most applications, can be treated as such. However, the background also shows local and temporal fluctuations due to, e.g., thermal noise. Additionally, the uniformity of the background noise is dependent on the homogeneity of the illumination. Background noise interferes with the analysis, since the fit model assumes no intensity in the donor channel at the beginning of the measurement and essentially no remaining intensity in the FRET channel at infinite measurement time, provided that any diffusion occurs at all and crosstalk is negligible (see also Section 4.4.3). Hence, the background has to be corrected to obtain more accurate results.
To account for the local and temporal variance of the background, a correction is calculated individually for all initially identified donor-acceptor pairs for each single frame in every channel. Any fluorescence signal localized in step 2 is approximated by a circle of radius r and the intensity of all pixels and sub-pixels within the area of the circle is summed up to yield the fluorescence intensity of that signal. Each quadratic pixel is subdivided into four artificial sub-pixel to allow for a better approximation of the

roughly circular fluorescence signals. Furthermore, the intensity is corrected for the average detection efficiency of the camera (82%), the photoelectrons per A/D count (0.46) and the camera offset (100 A/D counts). A second circle with radius $\sqrt{2}r$ is drawn around the first circle. Again, the sum is calculated of the intensity of all pixels and sub-pixels in the area of the second circle without the central inner area of the first circle. Thus, both areas are exactly equal in size. As long as no fluorescence emitter is located within the circumference of the second circle, the measured intensity in the area of the second circle corresponds to the local background. The summed-up intensity of the area of the second circle is then subtracted from the summed-up intensity of the area of the inner circle. This has to be done for every signal in every single frame of all three channels individually. The background correction has already been confirmed to be reasonably accurate. This can be seen, for example, in Figures 4.11, 4.12 and 4.19 in step 7. In all cases, the intensity fluctuates in a narrow range of values around the zero value when no fluorescence signal is detected in any one of the three channels. This fluctuation corresponds to the last inevitable (intrinsic) noise.

Step 6: Extraction of intensity-time traces

Although representing by far the biggest computational effort, step 6 can be summarized quickly. The intensity is calculated as described in step 5. This is done individually for all initially identified donor-acceptor pairs for all frames of the recording video. The intensity is calculated in the spatially correlated areas of all three channels. This yields intensity-time traces, as shown in Section 4.4.3 already. Technically, at this point, only intensity-frame traces are obtained and the frame number has to be converted to the measurement time in step 7 according to the employed cycle time (see above).

Step 7: Selection of valid intensity-time traces

The selection of all valid donor-acceptor pairs according to their intensity-time traces is the most crucial part of the analysis. It is also the step that introduces the biggest (personal) bias. The latter is discussed in more detail after step 9 of the example analysis. Here, the logic behind the selection process is explained. The initially identified donor-acceptor pairs can be broadly classified into four different categories on the basis of their intensity-time traces obtained in step 6:

(I) Valid donor-acceptor pairs / FRET pairs.

(II) Premature bleaching of the acceptor.

(III) Random noise or low intensity features hidden by noise.

(IV) Various irregular behavior.

Only donor-acceptor pairs of category I are included in the further analysis. In the following, it is reasoned for each category individually why it is justified to include or exclude the concerned donor-acceptor pairs based on their intensity-time traces.
Category I consists of all donor-acceptor pairs whose traces show a change of FRET efficiency due to diffusion of the donor relative to the acceptor. Only these valid donor-acceptor pairs are henceforth also called “FRET pairs”. In the example measurement, overall, 24 of 84 intensity-time traces are identified

as belonging to donor-acceptor pairs of category I. All 24 traces are shown in Figure 4.19. The traces are marked to a reasonable degree by the following distinct features:

1. The intensity in the FRET channel clearly exceeds the background noise at some point in the measurement.
    - The intensity shows an approximate decrease over time.
    - The intensity shows reasonable correlation with the intensity in the donor channel.
2. The intensity in the donor channel clearly exceeds the background noise at some point in the measurement.
    - The intensity shows an approximate increase over time.
    - The intensity is approximately zero at $t = 0$ s.
    - The intensity shows reasonable correlation with the intensity in the FRET channel.
3. The intensity in the acceptor channel clearly exceeds the background noise.
    - The intensity is approximately constant until photobleaching occurs.
    - The last signal is detected after the first signal in the donor channel is observed.

Essentially, there has to be a measurable intensity in all three channels at the correlated areas, which can be differentiated from random signals and which behaves approximately as expected for a randomly diffusing donor-acceptor pair. As seen in the control experiment without the UV pulse (see Section 4.4.3), constant intensity in all channels indicates that no photocleavage occurred. In contrast, the proof of concept experiment showed that the FRET efficiency decreases after photocleavage on temporal and ensemble average. This should be reflected to some degree in the intensity-time traces of donor and FRET channel. Good examples for the specified behavior are the intensity-time traces of the FRET pairs 2, 4 and 6 in Figure 4.11, which correspond to the FRET pairs 26, 39 and 37 in Figure 4.19, respectively. However, significant diversions from the specified behavior are common. For example, the maximum FRET efficiency is often observed several minutes after photocleavage and not at time point $t = 0$ s (compare, e.g., intensity-time traces 24, 32 and 47 in Figure 4.19). This could be related to diffusion of donor and acceptor towards each other, the higher rotational freedom of the donor-acceptor pair compared to the uncleaved dyad and therefore possibly larger κ^2 values resulting in an increased Förster distance, or simply blinking of the acceptor at earlier measurement times. Likewise, the intensity in the donor channel can temporarily decrease or even drop to zero due to photobleaching after an arbitrary amount of time (compare, e.g., intensity-time traces of the FRET pairs 14, 21, 23, 32, 34, 41, 47, 51 and 52). The uncertainty introduced by photobleaching of the donor is discussed in more detail below, in step 8 and the evaluation of the analysis procedure.
Photobleaching of the acceptor is signified by a spontaneous drop of the intensity in the acceptor channel (see Section 4.4.3). In the ideal case, the intensity in the acceptor channel remains constant over the course of the experiment. This, however, is not feasible in real single molecule measurements. Hence, the condition is weakened and it suffices when an interpretable signal in the acceptor channel is detected until a signal of reasonable intensity is detected in the donor channel. The corresponding donor-acceptor pair is counted as valid, even if the acceptor seems to have been photobleached shortly after both dyes



Figure 4.19: All intensity-time traces of the example measurement belonging to valid donor-acceptor pairs (category I). The numbers above each trace correspond to the numbers given to the initially identified donor-acceptor pairs in Figure 4.18.

have moved out of the effective FRET range. Although FRET is no longer possible even if donor and acceptor diffuse towards each other again, the behavior of the intensity in donor and FRET channel can still be regarded as valid. Diffusion by distances exceeding the Förster distance confirmably has occurred already and the situation is effectively the same as if donor and acceptor continued to move apart, which they appeared to have been doing anyway. Among the category I donor-acceptor pairs of the example measurement, the FRET pairs 6, 21, 24, 29, 39, 52 and 69 are examples of the specified behavior. This

equates to almost 30% of all FRET pairs. Given the overall low number of valid donor-acceptor pairs, it is estimated that the statistic is improved by including all of the examples above, despite the obvious bias.

The intensity-time traces of category II donor-acceptor pairs have already been discussed in Section 4.4.3 in the context of photobleaching on the single molecule level. In the example measurement, 14 of 84 donor-acceptor pairs are excluded on the basis of premature photobleaching. The intensity-time traces of all 14 concerned donor-acceptor pairs are shown in Figure 7.46 in the appendix. Contrary to the accepted fraction of donor-acceptor pairs of category I that show photobleaching of the acceptor, the intensity in the acceptor channel drops discontinuously to zero before any intensity is measured in the donor channel for all category II donor-acceptor pairs. In most cases, the disappearance of any signal in the acceptor channel is correlated perfectly with the appearance of a signal in the donor channel (see subfigure 7.46 **a**). In some cases, a short delay is present between the last observed frame with measurable intensity in the acceptor channel and the first frame with measurable intensity in the donor channel (see subfigure 7.46 **b**). Alternatively, no intensity is detected in the acceptor channel at any point during the measurement (see subfigure 7.46 **c**). In all these cases it has to be assumed that the acceptor was photobleached before the FRET efficiency decreased sufficiently by diffusion. The donor-acceptor pairs have to be discarded, as the encoded spatial information are falsified, even if otherwise expected behavior is observed in both other channels.

The intensity-time traces of category III donor-acceptor pairs are excluded on the basis of their uncertainty. In the example measurement, 10 of 84 initially identified donor-acceptor pairs are identified as noise or as exhibiting features hidden by noise. The corresponding intensity-time traces are depicted in Figure 7.47. All donor-acceptor pairs in this category exhibit comparatively low intensity in all three channels (about a fifth or less of the average intensity in the respective channels of all donor-acceptor pairs of category I). The signals are mostly indistinguishable from the noise of the detector, i.e., the unavoidable intensity fluctuations around the zero value (see step 5). At most, spare single peaks of intensity are observed. In some cases, this seems to be nothing but random noise (see subfigure 7.47 **a**). The intensity spikes lead to wrongfully detected localizations in step 2 which happen to fulfill the conditions set in step 4. In most cases, it is estimated that the low fluorescence intensity is caused by the locally low excitation power. When comparing Figures 4.18 and 7.47 **b**, it can be recognized that all considered donor-acceptor pairs are positioned at opposite edges of the field of view and thereby at the border of the illumination area. The intensity of the excitation laser is in a good approximation a Gaussian profile, hence the excitation power drops rapidly but not discontinuously at the edges of the field of view. Given the uncertainty, the intensity-time traces of these donor-acceptor pairs cannot be reasonably interpreted. Due to the sporadic nature of the intensity spikes that can be localized by the localization algorithm in step 2, most donor-acceptor pairs of category III are omitted by the algorithm, if the second condition in step 4 is set as valid (see below).

The remaining 36 of the 84 initially identified donor-acceptor pairs are summarized under the broad category IV. The corresponding intensity-time traces exhibit various irregular behavior. In 11% of all irregular cases (subfigure 7.48 **a**), an intensive signal is detected in the donor channel from the very beginning of the measurement. Similarly, in another 22% of all category IV donor-acceptor pairs, an intensive signal is detected in the donor channel unreasonably shortly after the UV pulse (subfigure 7.48

b). No correlated signal is detected after or at $t = 0$ s in the FRET channel. Hence, it can not be stated unequivocally if these represent valid donor-acceptor pairs. It is estimated that in most cases, these are intensity-time traces of impurities or of donor-acceptor pairs in too close proximity of impurities. Since several of these donor-acceptor pairs show fluorescence in the donor channel even before photocleavage, a considerable part of these pairs is also omitted if the second condition in step 4 is set as valid.
About 17% of the intensity-time traces exhibit negative intensity values significantly exceeding the background corrected base noise level in any of the three channels (subfigure 7.48 **e** and **d**). Most likely, another emitter was located in the second circle of the background correction (see step 5), leading to a wrongly calculated background value. These donor-acceptor pairs are excluded from the further analysis to prevent a falsification of the overall intensities by the negative intensity values.
In another 11% of the irregular cases, the intensity in the FRET channel remains approximately constant, indicating that no photocleavage occurred (subfigure 7.49 **a**). These cases include donor-acceptor pairs that show only brief and weak spikes of donor fluorescence, e.g., donor-acceptor pair 3 in Section 4.4.3 (intensity-time trace 48 in Figure 7.49 **a**). In about 25%, no correlated signal is detected in the donor channel, even after photobleaching of the acceptor, although a clear signal is measured in the FRET channel (subfigure 7.49 **b**). The situation is comparable to donor-acceptor pair 5 in Section 4.4.3. It is possible that the donor is bleached rapidly once energy transfer becomes impossible in most of these donor-acceptor pairs. However, without detection of a reasonable fluorescence signal in the donor channel it has to be assumed these are invalid donor-acceptor pairs which have been randomly detected by the identification algorithm.
For the remaining 14% of initially identified donor-acceptor pairs, noteworthy intensity is detected only in the acceptor channel (subfigure 7.49 **c**). It is estimated that these intensity-time traces correspond to remaining free ATTO647N from the synthesis (see Section 4.2 and 4.3). Random localizations in the FRET and donor channel, potentially due to temporal fluctuations of the crosstalk, lead to the recognition of these as donor-acceptor pairs in the first place.

For comparison, if the second criterion in step 4 is implemented, only 31 instead of 84 donor-acceptor pairs are initially identified. Of these 31 donor-acceptor pairs, 11 (35%) are classified as valid (category I, corresponding to the donor-acceptor pairs 7, 18, 21, 26, 29, 32, 37, 41, 67 and 69 in Figure 4.19). Thus, only about half of the category I donor-acceptor pairs are recognized. In return, only half as many category II donor-acceptor pairs are identified, too (7 pairs, 23%). Category III donor-acceptor pairs are reduced to 3 pairs overall (10%). Category IV shrinks from the largest fraction to more reasonable 10 donor-acceptor pairs (32%), which to some part might have been excluded due to personal bias. Specifically, most of the category IV donor-acceptor pairs exhibit behavior as shown in subfigures 7.48 **b** and subfigures 7.49 **a** and **b** (see above). On one hand, the identification criterion omits most of the unwanted donor-acceptor pairs right away. On the other hand, it also severely restricts the detection of valid donor-acceptor pairs.

Step 8: Evaluation of the summed-up intensity-time traces

The data are analyzed according to the model based on the Maxwell distribution presented in Section 2.3.7. To this end, the intensity-time traces of all valid donor-acceptor pairs shown in Figure 4.19 are summed-up to yield the summed-up intensity-time trace presented in Figure 4.20 **a**. The more

donor-acceptor pairs contribute to the overall statistic, the more accurately the established model can possibly describe the distribution of distances as encoded by the intensities in the donor and FRET channel. Apart from the total number of donor-acceptor pairs, however, further effects influence the accuracy of the method. Most important is the separate photobleaching of both the donor and the acceptor. Critical aspects of photobleaching are recognized on the basis of the shape of the summed-up intensity-time trace in Figure 4.20.

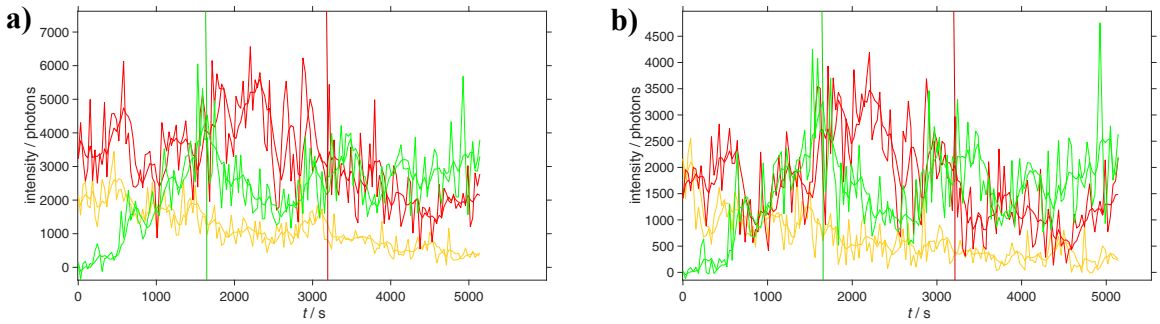

Figure 4.20: (**a**) Sum of the intensity-time traces of all valid donor-acceptor pairs depicted in Figure 4.19. (**b**) Sum of the intensity-time traces of all valid donor-acceptor pairs, if the second identification criterion in step 2 is implemented. The summed-up intensity values are shown as thin lines. The thick lines represent the moving average of the intensity values (binning size = 5). The intensity in the donor, FRET and acceptor channel is colored in green, orange and red, respectively. The vertical green line represents the point at which (partial) photobleaching of the donor appears to become significant, the vertical red line represents the point at which (partial) photobleaching of the acceptor appears to become significant.

The expected general decrease and increase of acceptor and donor fluorescence, respectively, is distinctly better recognizable in the sum of all intensity-time traces than in the individual cases. The intensity-time traces of individual FRET pairs show strong fluctuations on short time scales due to blinking and lesser fluctuations on longer time scales due to random diffusion of donor and acceptor both apart and towards each other. These fluctuations are almost entirely hidden in the overall statistic, as the missing intensity of individual donor-acceptor pairs in some frames is on average compensated by the whole ensemble. The summed-up intensity in the FRET channel decreases essentially continuously. Temporary increases, although still present, are less noteworthy. The summed-up intensity in the donor channel increases essentially continuously until approximately 1700 s after the UV pulse. However, it then decreases until approximately 2600 s, before increasing again until about 3000 s. An approximately constant value is adopted afterwards. Whereas the increase in summed-up donor intensity is reasonably well correlated with the decrease in summed-up FRET intensity between 0 – 1700 s, and also from 3000 s onwards, only little correlation is recognized between 1700 – 3000 s. When comparing the summed-up intensity-time trace in Figure 4.20 with the constituting individual intensity-time traces in Figure 4.19, it becomes evident that the uncorrelated decrease in the donor channel is partly related to photobleaching of the donor. About a quarter of the individual donor-acceptor pairs exhibit photobleaching of the donor in the specified time interval, i.e., no signal is detected in either donor or FRET channel any more, resulting in the (temporary) drop of summed-up donor intensity. It is estimated that similar features are less pronounced the more valid donor-acceptor pairs contribute to the overall statistic. The decrease of the

summed-up donor intensity represents a significant deviation from the Maxwell distribution fit model. The summed-up intensity in the acceptor channel remains approximately constant until 3200 s, before the average intensity noticeably decreases. This is well correlated with a simultaneous drop of the intensity in the FRET channel. Again, about a quarter of all individual intensity-time traces in Figure 4.19 exhibit photobleaching after the specified time interval, this time of the acceptor, i.e., no signal is detected in the acceptor channel any more, resulting in the drop of summed-up acceptor intensity.
In consequence, it is not sensible to include all data in the fit in step 9. The donor and FRET intensity-time traces are fitted independently anyway, since the FRET efficiency is determined independently as well according to equations (2.26) and (2.27), respectively. To obtain the best results for the donor-fit, it is thus most reasonable to fit the data until photobleaching of the donor becomes too dominant. Likewise, the best result for the acceptor-fit is obtained if only the data is used which is recorded before photobleaching of the acceptor becomes too dominant. This time restriction is henceforth called "analyzed time".

Interestingly, the shape of the summed-up intensity-time trace is almost unchanged when only the 11 donor-acceptor pairs are summed-up that are obtained if the second identification criterion in step 4 is implemented (see Figure 4.20 **b**). The most noteworthy difference is the overall lower summed-up intensity in all three channels and more significant relative intensity fluctuations. Otherwise, all crucial aspects are identical to the ones discussed above. This can be interpreted as a sign for the statistical robustness of the method, even with comparatively few FRET pairs.

Step 9: Fitting of the data

In the final step of the analysis, the summed-up intensity-time traces of step 8 are analyzed according to the established model based on the Maxwell distribution (equation (2.30), see Section 2.3.7). The measurement time t and the intensity-derived relative distances r are treated as variables. The Förster distance is set as a fixed parameter (equation (2.25)). The R_0 value calculated for donor **6** and acceptor **7** in methanol is used (6.23 nm, see Section 4.3.1). It is estimated that the Förster distance in any polymer matrix differs from the calculated values in solution (see also Section 4.4.3). However, it was impossible to determine an accurate Förster distance in any polymer matrix. It is assumed that the Förster distance is in all cases comparable to the determined Förster distance in methanol. Likewise, it is assumed that both donor and acceptor in the dyad or in a donor-acceptor pair have essentially no rotational restrictions, resulting in an orientation factor of $\kappa^2 = 2/3$. The assumption is largely verified by defocused measurements in all investigated systems (see also Sections 4.6.2 – 4.6.5).
A minor variable but fixed parameter is the maximum intensity in either the donor or the FRET channel ($F_{\text{donor}}(\infty, D)$ and $F_{\text{acceptor}}(0, D)$ in equations (2.26) and (2.27), respectively). The parameter is calculated anew for every data set. The intensities are treated as independent to allow for different detection efficiencies and quantum yields of donor and acceptor fluorescence. Under the experimental conditions, no significant crosstalk is observed (see Section 4.4.3), hence no further correction terms are introduced to either equation (2.26) or (2.27).
The only true fitting parameter is introduced in the form of the relative (ensemble-averaged) diffusion coefficient, D, of the relative movement of donor and acceptor. Fitting the donor and the FRET intensity-time trace each yields the relative diffusion coefficient D, which describes the relative movement of donor and acceptor. It is assumed that the relative movement is reasonably comparable to

the diffusion of single molecules (see Section 2.3.7). To distinguish the relative diffusion coefficients obtained by fitting donor and FRET intensities, the corresponding diffusion coefficients are termed $D = D_D$ and $D = D_F$, respectively.

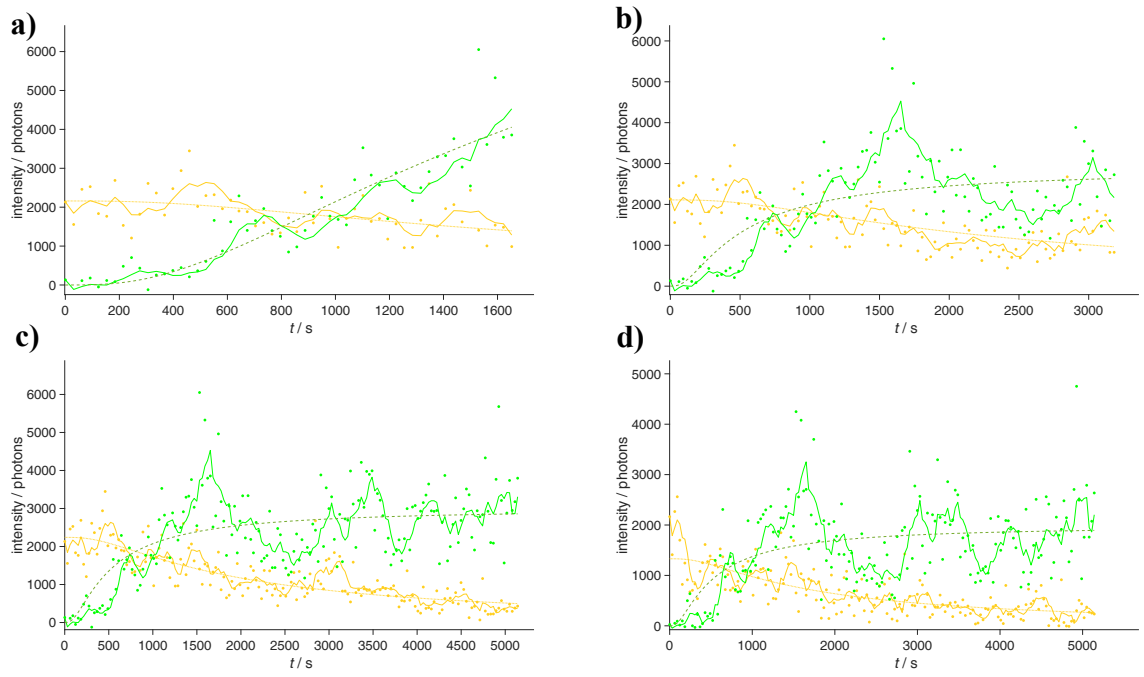

Figure 4.21: Separate fits of the summed-up FRET (orange) and donor (green) intensity-time traces shown in Figure 4.20 **a** until (**a**) photobleaching of the (free) donor becomes dominant, (**b**) photobleaching of the (free) acceptor becomes dominant, or (**c**) when including all data. (**d**) Separate fits of the summed-up FRET (orange) and donor (green) intensity-time traces shown in Figure 4.20 **b** when including all data. The dots represent the summed-up intensity values, the solid lines indicate the moving average of these values (binning size = 5). The cycle time is $t_{\text{cycle}} = 30.6$ s. The dotted orange line corresponds to the fit of the FRET intensity-time trace with a diffusion coefficient of (**a**) $D_F = 3.5 \times 10^{-21}$ m^2 s^{-1}, (**b**) $D_F = 3.0 \times 10^{-21}$ m^2 s^{-1}, (**c**) $D_F = 4.0 \times 10^{-21}$ m^2 s^{-1}, and (**d**) $D_F = 4.5 \times 10^{-21}$ m^2 s^{-1}, respectively. The dashed green line corresponds to the fit of the donor intensity-time trace with a diffusion coefficient of (**a**) $D_D = 3.5 \times 10^{-21}$ m^2 s^{-1} and (**b**, **c**, **d**) $D_D = 1.5 \times 10^{-20}$ m^2 s^{-1}, respectively. All fits are performed with equation (2.30).

In Figure 4.21, least squares fits of the summed-up intensity-time trace with equation (2.30) are shown. The various fits correspond to a restriction of the data until photobleaching of the donor becomes dominant (subfigure **a**, 1700 s, vertical green line in Figure 4.20), until photobleaching of the acceptor becomes dominant (subfigure **b**, 3200 s, vertical red line in Figure 4.20), or when including all data (**c**). For comparison, in subfigure 4.21 **d**, a fit is shown using all data of the 11 valid donor-acceptor pairs identified if the second condition in step 4 is included. The determined diffusion coefficients D_D and D_F are summarized in Table 4.6.

When comparing the different fits, it becomes evident that the analysis of the FRET intensity-time trace is significantly more robust than the analysis of the donor intensity-time trace. Essentially the same diffusion coefficient $D_F = 3.0 - 4.5 \times 10^{-21}$ m^2 s^{-1} is obtained within the accuracy of the method, regardless how many frames (equivalent to measurement time) are included in the fitting procedure. Even with a reduced set of donor-acceptor pairs, the result does not vary significantly. This indicates a

high precision of the method, largely independent of the accuracy. In all cases, the fit model describes the decrease of the summed-up FRET intensity reasonably well. In contrast, the diffusion coefficient derived from the donor intensity-time trace $D_D = 3.5 - 15 \times 10^{-21}$ m^2 s^{-1} differs more significantly depending on the number of included frames. While the increase of the summed-up donor intensity until 1700 s is well described by the model fit, the data at subsequent times deviates more strongly from the model, as was predicted in step 8 already. When including the data until 1700 s only, the same diffusion coefficient $D_F = D_D = 3.5 \times 10^{-21}$ m^2 s^{-1} is obtained for both fits. In all other cases, an about four times higher diffusion coefficient D_D is obtained. It can be estimated that the diffusion coefficient D_D is generally overestimated. Effects like photobleaching of the donor make it appear as if an approximately constant intensity value is reached earlier, as the initial increase of intensity suggests. As a constant (summed-up) intensity value corresponds to the logical end of a measurement, i.e., diffusion beyond the reach of energy transfer, an earlier reached apparent plateau of the intensity corresponds to a higher diffusion rate. Similar effects are less pronounced for the FRET intensity curve, as it conceptually does not matter if the intensity decreases due to interruption of the energy transfer or photobleaching of the acceptor, as long as photobleaching occurs after sufficient initial diffusion in diverging directions. Hence, it is assumed that the diffusion coefficient D_F is generally more accurate than the diffusion coefficient D_D.

Table 4.6: The relative diffusion coefficients D_D and D_F obtained from fitting the summed-up intensity-time trace of the example measurement until different analyzed times, corresponding to, in that order, photobleaching of the donor, acceptor or the overall measurement time, respectively. Donor and FRET intensity-time traces are fitted independently in each case to yield D_D and D_F, respectively.

analyzed time / s	2nd condition in step 4 is valid	D_D / 10^{-21} m^2 s^{-1}	D_F / 10^{-21} m^2 s^{-1}
1700	no	3.5	3.5
3200	no	15	3.0
5100	no	15	4.0
1700	yes	3.5	4.0
3200	yes	15	4.0
5100	yes	15	4.5

Overall, the method allows for a reasonable estimation of the ensemble-averaged single molecule diffusion coefficient in PVAc. The value $D \approx 4 \times 10^{-21}$ m^2 s^{-1} matches comparable diffusion coefficients, for example, the average single molecule diffusion coefficient in PBMA, which has a similar glass transition temperature like PVAc.[204] The diffusion coefficient is about eleven orders of magnitude lower than the diffusion coefficient of either the dyad or the acceptor in solution as determined by FCS (see Section 4.4.1) and four orders of magnitude lower than typically accessible by SMT or comparable methods. A more comprehensive discussion on the diffusion in PVAc is presented in Section 4.6.2.

The model can also be applied to each intensity-time trace of all individual FRET pairs shown in Figure 4.19 to obtain 24 single molecule diffusion coefficients. The corresponding fits are shown in Figure 7.50. The 24 determined relative single molecule diffusion coefficients, D_D and D_F, are plotted in a histogram in Figure 4.22. Three calculated D_D and two calculated D_F values significantly exceed a value of $D > 20 \times 10^{-21}$ m^2 s^{-1} and are not included in the histogram to grant a better overview. It is estimated that the respective values are highly inaccurate (see below).

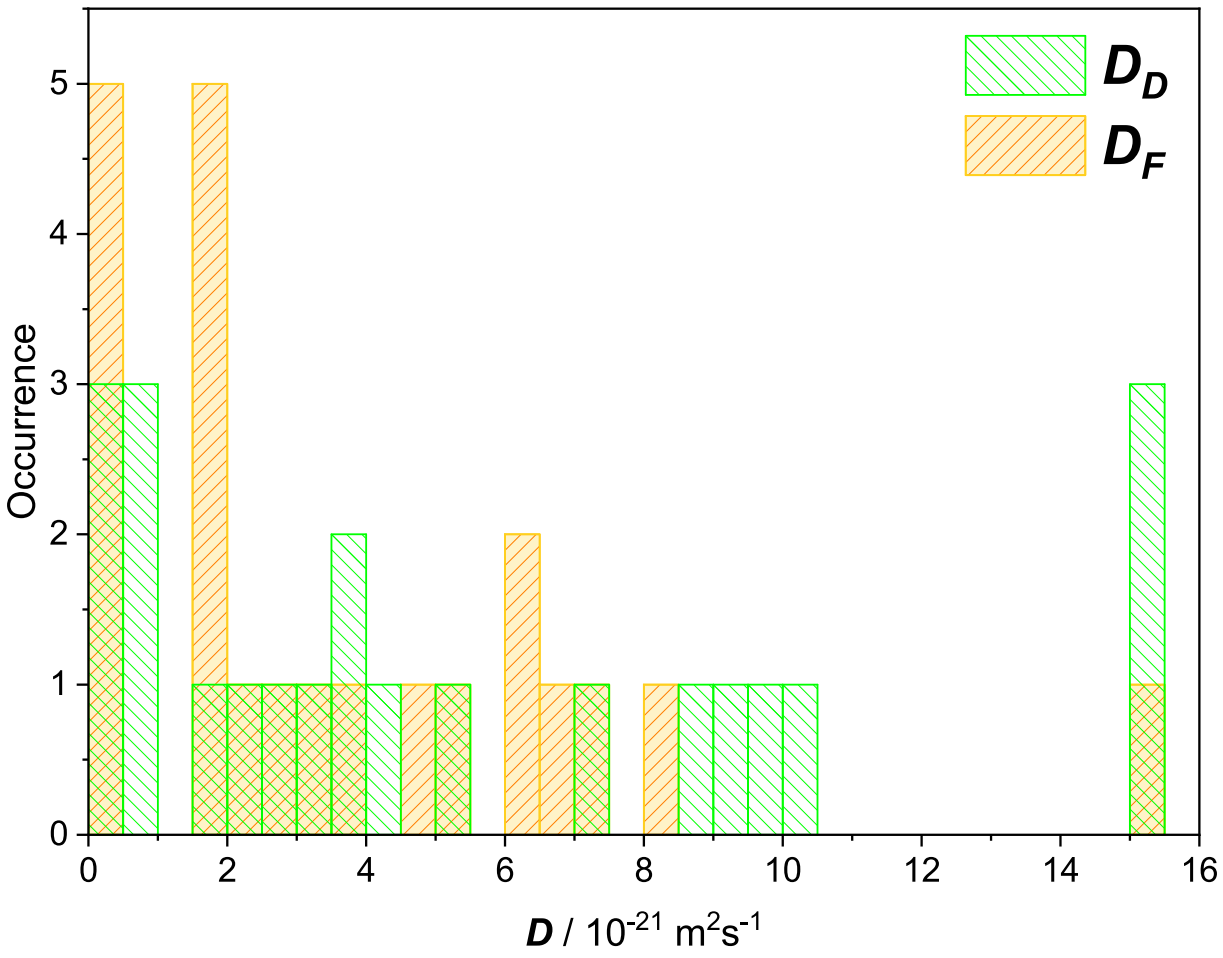

Figure 4.22: Histogram of the relative single molecule diffusion coefficients D_D (green) and D_F (orange). D_D and D_F were determined with separate fits of the individual FRET and donor intensity-time traces shown in Figure 4.19 (see Figure 7.50 for the fits). All fits are performed with equation (2.30).

As estimated in Section 2.3.7 already, it is difficult to extract reliable, accurate single molecule diffusion coefficients. The deviations of the intensity-time traces of individual FRET pairs from the model are significant in all cases (see Figure 7.50). The model cannot describe the intensity fluctuations due to photophysical switching of both donor and acceptor. Likewise, the model fails to capture the intensity fluctuations due to the random positive and negative changes of the relative distance between individual donor-acceptor pairs. The model describes a probability of finding donor and acceptor at a certain distance at certain times, and statistically, it is most probable for both dyes to move apart over time. Although all valid donor-acceptor pairs eventually move apart, as signified by the general decrease of FRET efficiency, they do not necessarily move apart continuously. This, however, is not well described by the Maxwell distribution. Hence, both accuracy and precision are low. The low accuracy and precision are signified by the broad and essentially uniform distribution of single molecule diffusion coefficients, respectively. The single molecule diffusion coefficients summarized in histogram 4.22 range from $D = 0.01 - 90 \times 10^{-21}$ $m^2\,s^{-1}$ for both D_D and D_F. It is estimated that diffusion coefficients below $D < 1 \times 10^{-22}$ $m^2\,s^{-1}$ and above $D > 2 \times 10^{-20}$ $m^2\,s^{-1}$ correspond to harsh errors of the analysis, as the accuracy of the least square fits with equation (2.30) is too low in the respective cases.

Despite the low accuracy of the fits, the FEDUP method is currently the only way to extract any

reasonable information of single molecule diffusion on this level of translational immobility. However, given the amount of unreasonable single molecule diffusion coefficients obtained, it is refrained from repeating the procedure in the following measurements. Instead, only ensemble-averaged relative single-molecule diffusion coefficients are discussed.

Evaluation of the measurement and analysis procedure

The method offers one noteworthy advantage over other methods, even if those were capable measuring diffusion rates this low; the possibility of drift correction (step 3). This represents a huge benefit compared even to MINFLUX. Any translational motion as slow as that registered in PVAc at room temperature is entirely hidden by the inevitable sample drift over hours of measurement on a real setup, irrespective of the achievable localization accuracy. Only the independence from any absolute coordinates allows the quantification of the movement as it is observed via the FRET efficiency.
The accuracy of the method, in contrast, is yet to be optimized on several accounts. For one, there are technical inaccuracies, most importantly the inhomogeneity of the excitation laser profile. A correction accounting for the local laser power increases the accuracy of the detected intensity values, especially if the sample is subject to significant drift during the measurement. Donor-acceptor pairs could be shifted from areas of locally high excitation power to areas of locally low excitation power, and vice versa. The resulting decrease or increase in intensity could be easily misinterpreted. Second, the accuracy of the determined diffusion coefficients is dependent on the quality of the fit model. It has been shown that the model delivers a reasonable description of the summed-up single molecule FRET behavior. However, for a better accuracy, the fit model has to be adjusted to include other effects influencing the (summed-up) intensity, most prominently photobleaching of both donor and acceptor, but also the blinking kinetics. The implementation of both an excitation power correction and of fit model adjustments is conceptually easy but difficult to achieve in reality. For example, the laser profile has to be accurately measured first before any correction can be attempted. The reliability of the correction is likewise questionable. The badly understood mechanisms of both photodegradation and the photophysical reactions make it difficult to implement sensible corrective terms to the statistical analysis model. A possible approach is a variable normalization of the summed-up intensity-time traces to the amount of donor-acceptor pairs contributing at each specific measurement time. This, however, is not trivial to implement computationally. In the framework of this thesis, neither excitation power correction nor further adjustment to the model are undertaken. It is estimated that the error introduced by the inhomogeneity of the laser is negligible in comparison to the overall achievable accuracy. Furthermore, it is assumed that the model is reasonably accurate if a sufficiently large number of FRET pairs contributes to the overall statistic and the fit is restricted according to observed photobleaching of donor and acceptor (see 4.6.1 step 9).
Apart from the potential incompleteness of the model, it is also worth considering the applicability of the model. It is theoretically possible to extract diffusion coefficients for each valid donor-acceptor pair. Given the irregularities of the intensity-time traces of even confirmed individual FRET pairs (Figure 4.19), however, a quantification of single molecule diffusion coefficients with the Maxwell distribution model is both inaccurate and imprecise. Although each intensity-time trace represents a visualization of the diffusion in polymer films, the statistical validity of individual intensity-time traces is low. Apart from effects like blinking and photobleaching, the single molecule intensity-time traces

are strongly influenced by the random nature of the diffusion, i.e., the angle between the directions of motion of donor and acceptor is both random and variable. Donor and acceptor can move parallel to or even towards each other (see Section 2.3.7). The random nature of the diffusion is theoretically implemented in the Maxwell distribution. In fact, it is one of the prerequisites for the applicability of the model. On the single molecule level, however, the statistical nature of the distance-dependent FRET and donor fluorescence cannot be accurately described by the established model, which describes the overall statistic on long time scales and not the statistical fluctuations on shorter time scales. This leads to significant deviations when analyzing individual donor-acceptor pairs. Nevertheless, the FEDUP method is the only currently established method to extract even approximate single molecule diffusion coefficients at this level of immobility. Moreover, these deviations become irrelevant when analyzing the ensemble statistic, as the various donor-acceptor pairs compensate for each other. Both dark frames and any kind of intensity fluctuations are essentially hidden by the ensemble average. Thus, the Maxwell distribution model is more suitable for the determination of ensemble-averaged (relative) single molecule diffusion coefficients. An entirely new model for a reasonable extraction of single molecule diffusion data has yet to be conceived. However, even if the model represents an accurate description of the observed FRET efficiency, it is not clear how accurate the determined ensemble-averaged diffusion coefficients really are. It can only be stated with some confidence that they are precise.

Another important reason for possible inaccuracies of the method are the detection and selection biases. These are almost unavoidable and have to be discussed in detail to be recognized correctly. The detection and selection biases are not entirely independent of each other. Detection bias denominates the fact that certain donor-acceptor pairs cannot be detected under the measurement conditions, whereas the selection bias refers to both the personal influence as well as the influence of the measurement conditions on the selection process in step 7. The bias due the interplay of detection and selection is signified by two notional extreme cases; very fast and very slow diffusion. The detection of these extreme cases is directly dependent on the employed cycle time, i.e., fast diffusion can only be observed with short cycle times, whereas slow diffusion requires long cycle times. During the selection process, in turn, fast diffusing molecules might not be recognized as valid donor-acceptor pairs, if the time scale of their movement is comparable to the cycle time, whereas slow diffusing molecules are subject to more significant premature photobleaching the shorter the cycle time, and consequently, the longer the overall illumination time. Alternatively, slow diffusing donor-acceptor pairs might be interpreted as uncleaved dyad molecules. Highly heterogeneous polymer films can potentially exhibit a large distribution of diffusion coefficients, which is then not recognized correctly. It is assumed in all measurements that the investigated polymer films are homogeneous and consequently diffusion is approximately uniform for all donor-acceptor pairs. This, however, is not necessarily true, even if AFM measurements indicate an approximately homogeneous surface and film thickness (see Sections 4.6.2 – 4.6.5). In the example measurement, a significant amount of intensity-time traces of the category IV donor-acceptor pairs could have been misinterpreted in the above specified way. It is assumed that the donor-acceptor pairs which exhibit intensity in the donor channel at early times are falsified by impurity signals in the polymer, but it is also fathomable that these donor-acceptor pairs represent the fraction of faster diffusing molecules instead. Likewise, some of the prematurely photobleached or apparently uncleaved molecules might represent the fraction of slow diffusing molecules. A bias is thus introduced by the finite measurement

time, the finite photostability of the dye system and the finite temporal resolution.
The aforementioned bias is inevitable, given that no perfect dye system impervious to photodamage exists and that infinite measurement times are generally not feasible. However, it can be reduced to insignificance by extensive experimentation. In essence, a variety of measurements has to be performed in which the cycle time is varied systematically. Nevertheless, the selection process is subject to more personal biases which might be avoided to some degree by automatizing the selection process, i.e., by the use of artificial intelligence (AI). The inclusion of category I donor-acceptor pairs, as well as the exclusion of donor-acceptor pairs of categories II, III and IV, is based on the reasonable selection criteria described in step 7. The selection process, however, is dependent on both the correct recognition and the feasible recognizability of these criteria. Several category II, III and IV donor-acceptor pairs might represent valid donor-acceptor pairs which have been incorrectly excluded from the analysis because they do not match the predefined criteria (see in particular Figure 7.47 **b** and Figure 7.49 **b**). The other way around, several category I donor-acceptor pairs might represent invalid donor-acceptor pairs which have been incorrectly included in the analysis because they happen to match the expectations. It is estimated that the overall statistic of the example measurement is not significantly changed by the exclusion of (some) valid and the inclusion of (some) invalid donor-acceptor pairs.
Lastly, there exists a significant bias in the final step of the analysis (Section 4.6.1 step 9). The example measurement emphasized that the accuracy and precision of the determined diffusion coefficient is heavily dependent on the (arbitrarily) set restriction of the data to certain times. It is estimated that the accuracy of the fit is increased if the data is restricted to measurement times until photobleaching of either donor or acceptor becomes too dominant. The uncorrelated decrease of intensity in either donor or FRET channel is currently not well described by the model. Irrespective of the reasonability of the data restriction, any constraint is ultimately based on the arbitrary recognition of these plausible deviations from the model. Thus, the result is directly influenced by the person performing the analysis. The determined diffusion coefficients D_D and D_F vary significantly for different analyzed time intervals. This is particularly noteworthy for the diffusion coefficient D_D which varies by about 400% depending on the analyzed time interval. The precision of the diffusion coefficient D_F is generally less influenced by the analyzed time, as the photobleaching of the acceptor is conceptually equivalent to the interruption of FRET by sufficient relative movement. The determined values still vary by about 25% depending on the analyzed time interval. It is important to be aware of all these biases to evaluate both accuracy and precision of the determined diffusion coefficients.

To summarize: the method might be the only currently established microscopy technique that is essentially independent from the mechanical stability of the setup, i.e., sample drift. The drift can be corrected by comparatively little computational effort, and still, it is possible to observe diffusion on a sub-pixel level. Unfortunately, the mathematical fit model does not allow for an accurate determination of the diffusion coefficients of individual FRET pairs, as all single molecule intensity-time traces are subject to various statistical fluctuations on comparatively short time scales not accurately described by the long time scale model. These fluctuations, however, are largely compensated if a sufficiently large ensemble is analyzed. The accuracy of these ensemble averaged relative diffusion coefficients might still be improved by including effects like photobleaching and blinking in the model, and by correcting the measured intensities for the local excitation intensity. The method is prone to various biases, in

particular significant biases in the detection and selection process. It is possible that only a specific range of diffusion rates is accessible under certain measurement conditions. Likewise, it is probable that the selection of valid donor-acceptor pairs is biased by the personal recognition and the general recognizability of the time-dependent FRET efficiencies. Last but not least, a bias is introduced by the (reasonable) restriction of the data to specific measurement times. The detection bias can be reduced with extensive control experiments. A selection process guided by AI might reduce the various biases in the analysis.

It is refrained from adjusting the analysis in any way. However, the accuracy of the determined diffusion coefficients can be improved by improving the statistic, i.e., by increasing the amount of donor-acceptor pairs contributing to the summed-up intensity-time traces. In step 9 of the example measurement in Section 4.6.1, it is indicated that the precision of the method is largely independent of the number of donor-acceptor pairs in the statistic, as long as a sufficient amount of FRET pairs is detected overall. Hence, quantitative conclusions can be already drawn from few valid donor-acceptor pairs. Nonetheless, more accurate and therefore trustworthy results are obtained the more valid donor-acceptor pairs are included in the analysis. To this end, measurements in any polymer are repeated several times under the same conditions, i.e., with the same cycle time (see Section 4.6.1), and the summed-up intensity-time traces of each measurement are combined (step 8, see 4.6.1). This way, a reasonable statistic can be achieved irrespective of the number of valid donor-acceptor pairs per measurement.

4.6.2 Poly(vinyl acetate)

In the following, diffusion measurements are presented in poly(vinyl acetate) (PVAc) using the FEDUP method. The diffusion is investigated at various temperatures ranging from room temperature ($T_{\mathrm{r.t.}} \approx 21$ °C) to $T = 45$ °C. The full analysis procedure is not repeated (see Section 4.6.1 for an exemplary complete analysis). Instead, only the important final results, i.e., the final graphs of step 8 and step 9 of the analysis (see 4.6.1), are presented. For a better statistic and more accurate results, the summed-up intensity-time traces of several measurements performed under identical conditions are combined (see also 4.6.1). A brief introduction is given of PVAc in general and the specific polymer sample investigated.

The polymer - PVAc

PVAc is an atactic, non-crystalline polymer produced by free radical polymerization of vinyl acetate.[205] The structure of PVAc is shown in Figure 4.23. PVAc is used in a wide range of applications. Its high flexibility and low toxicity enables its use in the food industry, e.g., as a base for chewing gum and for protective coatings of fruits and vegetables.[205] This extends to uses in the pharmaceutical field, in particular as a binder or as a coating material.[205] Furthermore, PVAc is used as a binding medium for paints, especially in art of the last century.[206] It also represents the precursor for poly vinyl alcohol (PVA), which is produced by the hydrolysis of the acetate groups.[207] No single molecule diffusion studies have been conducted in PVAc films at the time of writing of this work. Diffusion studies in PVAc so far have been restricted to the diffusivity of gases or vapors,[208–211] the tracer diffusion in highly concentrated PVAc solutions,[212] or (ensemble) self-diffusion studies.[213] All given examples are concerned with diffusion rates several orders of magnitude higher than the (expected) diffusion rate of single non-gaseous molecules in thin films.

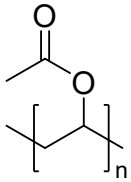

Figure 4.23: Structure of PVAc.

The PVAc investigated in this work was acquired from Sigma-Aldrich and used without further purification. The average molecular weight is specified as $M_W = 184000\,\mathrm{g\,mol^{-1}}$, corresponding to about $n = 2100$ monomer units in Figure 4.23. The glass transition temperature, $T_g = 42.6\,^{\circ}\mathrm{C}$, was determined with differential scanning calorimetry (DSC) (see Figure 7.62 in the appendix for the DSC curve, Section 6.13 for more scientific background of DSC in general and Section 6.13 for the experimental setup). The determined T_g is about 10 °C higher than common literature values.[199,200,206] However, the molecular weight of the investigated PVAc is also significantly higher than the molecular weights in the given literature examples. Given the known dependency of the glass transition temperature on the molecular weight,[206] the determined T_g seems reasonable. A different study using PVAc with more similar molecular weights also reports of a more similar T_g.[214] The glass transition temperature can be reached with comparatively little experimental effort. This makes PVAc an ideal test system for the investigation of the glass transition with the FEDUP method.
To create homogeneous, thin PVAc films, PVAc was dissolved in MeOH at a concentration of about 8 wt%. The concentration is comparatively high and creates slightly thicker polymer films upon deposition than ideal. However, smaller concentrations were noticed to create too inhomogeneous films. Picomolar amounts of dyad **8** in MeOH were added to the polymer solution. A drop of the stained polymer solution was spincoated onto a clean coverslip and dried under vacuum at 80 °C (see Section 6.4.5 for more details of the sample preparation). The surface homogeneity of the film was confirmed with AFM for one exemplary sample. An average film thickness of about 500 nm was also determined with AFM for one exemplary sample. To this end, the polymer film was mechanically cut with a sharp scalpel and the AFM head was scanned across the cut (see Figure 7.56 for the AFM measurement and analysis, Section 2.4 for the scientific background of AFM and Section 6.8 for the experimental setup). Defocused microscopy measurements confirm that the dyad **8** is not notably restricted in its rotational movement in the polymer film (see Figure 7.44 **a** for an exemplary defocused image, Section 6.1.6 for a brief scientific background of defocused microscopy and Section 6.7.3 for the experimental setup). This matches existing experimental evidence that the polymer chains of PVAc continue to move very slowly until temperatures considerably below T_g.[200] Given the rotational freedom of the dyes, Köhler illumination is appropriate for all measurements in PVAc (see Section 2.3.1).

Diffusion at room temperature

In the following, it is attempted to improve on the accuracy of the determined diffusion coefficient D in PVAc with the FEDUP method. The result presented in Section 4.6.1 was derived from a single measurement with 24 valid FRET pairs. These already yielded a reasonable statistic. Frequently, however, arbitrarily fewer FRET pairs are detected per measurement (including none at all). The

exact amount of FRET pairs depends strongly on the exact conditions, i.e., (local) laser power density, irradiation times, labeling density of the polymer film with dyad **8**, the (local) partial oxygen and argon pressure and the measurement delay time. Moreover, inaccuracies particularly in step 1 – 5 of the analysis can further reduce the overall number of interpretable donor-acceptor pairs. Consequently, it is generally not feasible to generate accurate diffusion coefficients with a single measurement.

However, it is conceptually irrelevant if the FRET pairs contributing to the statistic are measured in the same field of view or even on the same substrate. The only conditions for their comparability are reasonably similar measurement conditions, in particular equivalent sample preparation (see also Section 6.4.5) and equal cycle times. A comparable ambient temperature and relative humidity are also important. Higher temperatures are expected to increase the mobility in any polymer film, whereas the water in humid air can plasticize PVAc.[214] Thus, different degrees of humidity during the measurement can also introduce a variance to the mobility. Both temperature and humidity were controlled with a combined air conditioning and humidifier/dehumidifier system in the measurement room. The system was supposed to keep the temperature and humidity constant at $T = 21$ °C and 40%, respectively. Due to technical problems, no entirely rigorous control of the humidity was possible and the relative humidity can fluctuate between 20% – 60% for any given measurement. On average, however, the relative humidity during the measurements was about 40%. The temperature can be regarded as constant for all measurements. Only minor temperature fluctuations of about ± 0.5 °C were observed.

Given a reasonable comparability, the summed-up intensity-time traces of an arbitrary amount of equivalent measurements can be combined to improve the statistical validity of the model and consequently the accuracy of the obtained ensemble-averaged relative diffusion coefficients D_D and D_F. The combined summed-up intensity-time traces of six equivalent FEDUP measurements in PVAc at room temperature, that among the example measurement of Section 4.6.1, are shown in Figure 4.24 **a**. The corresponding separate fits of FRET and donor intensity are shown in subfigure **b**. All six measurements were performed with cycle times of $t_{\text{cycle}} = 30.6$ s. Comparative examples of combined FEDUP measurements with different cycle times ($t_{\text{cycle}} = 10.6$ s and $t_{\text{cycle}} = 32.64$ s) are shown in Figure 7.51 in the appendix. An overview of all determined diffusion coefficients in PVAc is given in Table 4.7, including values at different temperatures and values determined with different analyzed time limits. More details of the experimental setup are presented in Section 6.7.2.

When comparing Figure 4.24 with Figure 4.21, it seems that the accuracy of the fit is indeed increased by the combination of several measurements. When limiting the data to measurement times when photobleaching of the acceptor becomes dominant ($t \approx 2200$ s), the model appears to describe both the increase of donor fluorescence and the decrease of acceptor fluorescence with high accuracy. Otherwise, the summed-up intensity-time trace exhibits the same general problems as before, i.e., the summed-up intensity-time traces of donor and FRET channel are superimposed by further effects not included in the model. The most prominent effect remains (apparent) photobleaching of both donor and acceptor, which leads to significant deviations from the model at times $t > 2200$ s.

Although the accuracy and consequently reliability of the results seem to have been improved, the precision of the method is influenced only little. The diffusion coefficients $D_D = 1.5 \times 10^{-20}$ m^2 s^{-1} and $D_F = 5.0 \times 10^{-21}$ m^2 s^{-1} still differ by a factor of about 3. In this context, the diffusion coefficient D_D still seems to be overestimated (see Section 4.6.1 step 9). Likewise, the strong dependency of especially

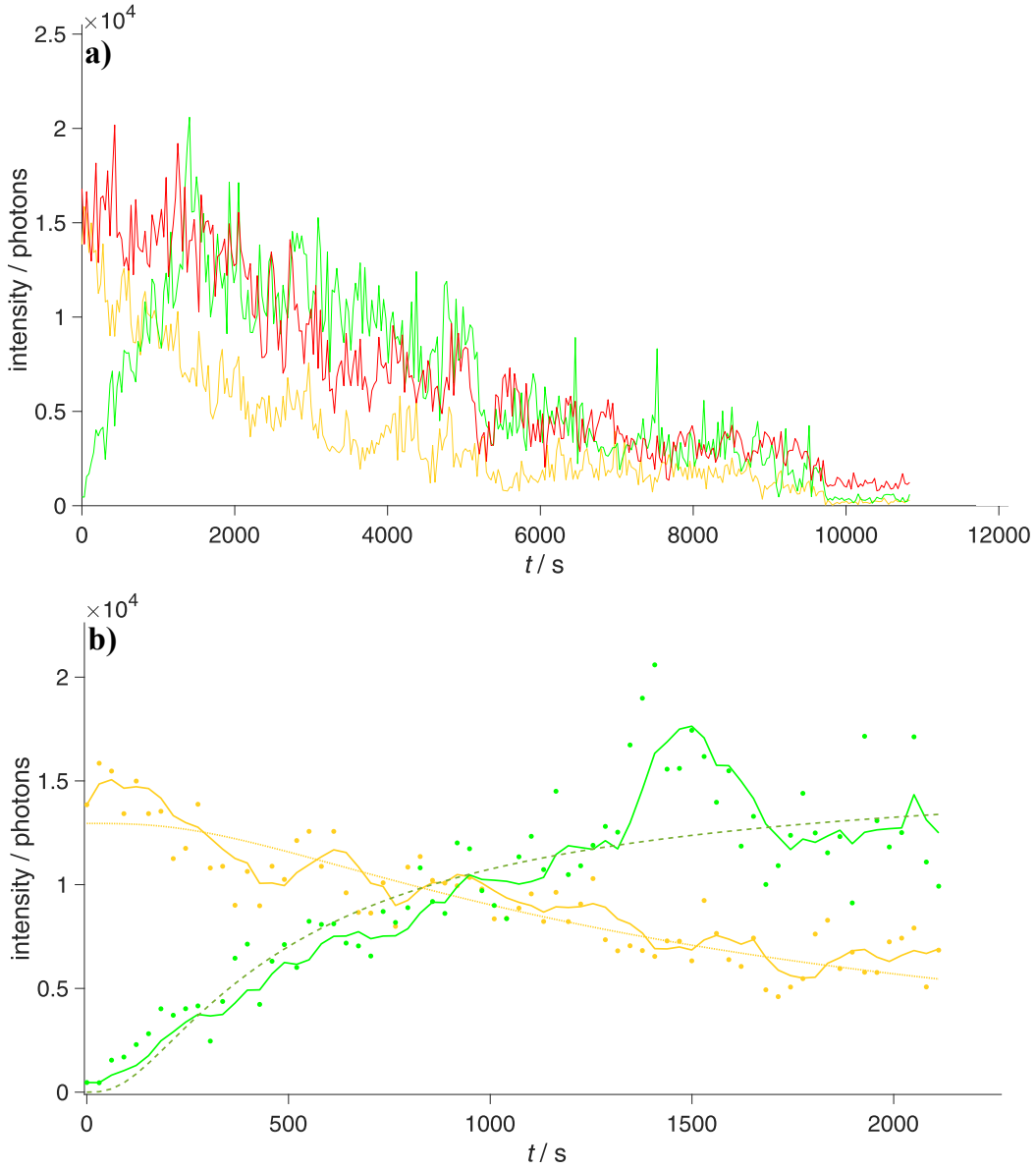

Figure 4.24: (**a**) Summed-up intensity-time traces of 105 FRET pairs from overall six different measurements in tempered PVAc (184 kDa) at room temperature. The intensity-time traces of the FRET-, donor- and acceptor-channel are shown in orange, green and red, respectively. The thin lines in (**a**) and the dots in (**b**) represent the summed-up intensity values at each measured point in time. The solid lines in (**b**) indicate the moving average of these values (binning size = 5). A cycle time of $t_{\mathrm{cycle}} = 30.6$ s was employed for all measurements. (**b**) Separate fits of the FRET and the donor intensity-time trace shown in subfigure (**a**) according to equation (2.30). The dotted orange line corresponds to the fit of the FRET intensity-time trace with a diffusion coefficient of $D_F = 5.0 \times 10^{-21}$ m^2 s^{-1}. The dashed green line corresponds to the fit of the donor intensity-time trace with a diffusion coefficient of $D_D = 1.5 \times 10^{-20}$ m^2 s^{-1}. The fits were restricted to approximately 2200 s diffusion time to counter the effect of photobleaching on the analysis.

D_D on the analyzed time is unchanged. In all measurements, the determined diffusion coefficients are generally larger the longer the analyzed time. The influence on D_F is negligible, as the values only change within the accuracy of the method (see below). The values of D_D can vary by about an order of magnitude

depending on the analyzed time. The determined diffusion coefficients are essentially identical to the values obtained in the example measurement. A reduction of the cycle time to $t_{cycle} = 10.6$ s still yields very similar diffusion coefficients ($D_D = 3.0 \times 10^{-20}$ m^2 s^{-1} and $D_F = 3.5 \times 10^{-21}$ m^2 s^{-1}). Slightly lower values are determined for both $D_D = 1.5 \times 10^{-21}$ m^2 s^{-1} and $D_F = 9.0 \times 10^{-22}$ m^2 s^{-1} in the combined measurements with longer cycle times of $t_{cycle} = 32.64$ s. It is possible that the slower diffusion rate coincides with a lower relative humidity in the measurement room. At least one measurement employing a cycle time of $t_{cycle} = 32.64$ s was unintentionally performed at a relative humidity of 20%, whereas most other measurements are generally performed at 40% relative humidity (see above). Different degrees of plasticization of PVAc with water might have introduced an additional variance of the determined diffusion coefficients. Overall, however, the diffusion coefficients can be considered equal within the general accuracy of the method for all employed cycle times. This indicates that no significant detection bias is present (see Section 4.6.1).

Table 4.7: The relative diffusion coefficients D_D and D_F in PVAc, obtained from fitting the combined summed-up intensity-time traces of several FEDUP measurements at various temperatures T and with different cycle times t_{cycle}. The fits are restricted to analyzed times t according to dominant photobleaching of either donor or acceptor. Donor and FRET intensity-time traces are fitted independently in each case to yield D_D and D_F, respectively.

T / °C	t_{cycle} / s	FRET pairs	fraction of cat. I / %	number of measurements	t / s	D_D / 10^{-21} m^2 s^{-1}	D_F / 10^{-21} m^2 s^{-1}
21	10.60	41	20	3	2000	30	3.5
					3000	40	3.5
					6300[a]	200	5.5
21	30.60	105	28	6	1600	10	5.0
					2200	15	5.0
					11000[a]	150	4.5
21	32.64	17	17	4	8000	1.5	0.9
					9700	1.5	0.7
					84000[a]	X[b]	1.0
30	10.64	8	1	2	4500	3.5	(0.01)[c]
					7700[a]	2.5	0.5
40	10.64	10	6	2	2700	15	8.0
					5400[a]	40	9.5
40	5.64	16	3	2	4500	5.5	10
					5000[a]	5.5	10
45	10.64	3	4	2	2000	6.5	(0.03)[c]

a) Corresponds to the overall measurement time of at least one measurement contributing to the combined result.
b) Since the donor intensity decreases to zero due to photobleaching at approximately 40000 s, no reasonable diffusion coefficient could be determined. A theoretical value of $D_D = 1.0 \times 10^{-16}$ m^2 s^{-1} is obtained.
c) The data cannot be fitted correctly, since no noteworthy decrease of intensity in the FRET channel is observed within the analyzed time. The value is unreasonably low and the statistic unreliable.

Despite the improved accuracy, it is not reasonable to specify the single molecule diffusion coefficient D with the precision given in Table 4.7. In light of the already discussed inaccuracies and uncertainties of the method (see Section 4.6.1), quantified statements should not exceed the determined order of magnitude. Therefore, the average single molecule diffusion coefficient in PVAc at room temperature can

be reasonably estimated to be in the range of $D \approx 1 - 10 \times 10^{-21}$ m^2 s^{-1}. At most, it can be estimated that the real value is closer to the lower end of the specified range, depending on the degree of plasticization due to humid air.

Diffusion at elevated temperatures

Scientifically even more interesting is the diffusion in PVAc at elevated temperatures, in particular close to the glass transition temperature, $T_g = 42.6$ °C. Unfortunately, the measurements at higher temperatures are all accompanied by a (new) set of problems. First and foremost, the quality of the measurements was considerably worse than at room temperature. This included a worse SNR and overall fewer detected fluorescence signals despite the same dye concentration. It is estimated that these effects are to one part introduced by the employed special substrates with implemented heating system (see Section 6.7.2), and to another part related to the heating of the immersion oil on the objective lens. Second, the photobleaching rate of both donor and acceptor increases significantly at higher temperatures. Third, a suitable cycle time has to be found again. The mobility of any donor-acceptor pair should increase with the temperature, thus shorter cycle times have to be employed. However, it is not clear how much the mobility increases and which temporal resolution is required consequently. An extensive scan of suitable cycle times has to be performed for each temperature. Moreover, the demand for a higher temporal resolution is directly opposed to the higher photobleaching rate. All these effects lead to considerably fewer category I donor-acceptor pairs per measurement while increasing the ratio of category II, III and IV pairs (see Table 4.7). The effects become generally more pronounced the higher the measurement temperature. Above $T = 40$ °C, measurements become effectively impossible. Even at $T = 30$ °C, however, the measurements yield unreliable results and the fits are generally not meaningful. A quantitative discussion of the determined diffusion coefficients is not feasible, and at most, qualitative conclusions can be made. Nevertheless, the results of combined FEDUP measurements in PVAc at different temperatures are shown in Figure 4.25. Additional data is presented in Figure 7.52 in the appendix. The determined diffusion coefficients D_D and D_F are summarized in Table 4.7.

It was expected that the mobility of the donor-acceptor pairs increased significantly when approaching T_g, since the glass transition is accompanied by a decrease of viscosity and an increase of the free volume. Hence, measurements were performed with considerably shorter cycle times than at room temperature. These, however, did not yield any interpretable FRET pairs, since the higher photobleaching rate interfered. Only when increasing the cycle time to values more comparable to the ones employed at room temperature, any FRET pairs could be detected in some measurements. The overall statistic of the combined measurements still remains unreliable at all investigated elevated temperatures and generally highly inaccurate and imprecise results are obtained.

At 30 °C, the intensity in the FRET channel remains essentially constant until 5000 s of measurement time. The observed decrease of the intensity afterwards is well correlated with the decrease of the intensity in the acceptor channel. This is assumed to be a sign of photobleaching of the acceptor and the data should not be included in the analysis. Consequently, the diffusion coefficient $D_F = 1.0 \times 10^{-23}$ m^2 s^{-1} is unreasonably small, as the data in the FRET channel implies that no diffusion occurs on the considered time scale. The intensity in the donor channel, in contrast, increases in a more regular fashion comparable to the situation at room temperature. The diffusion coefficient

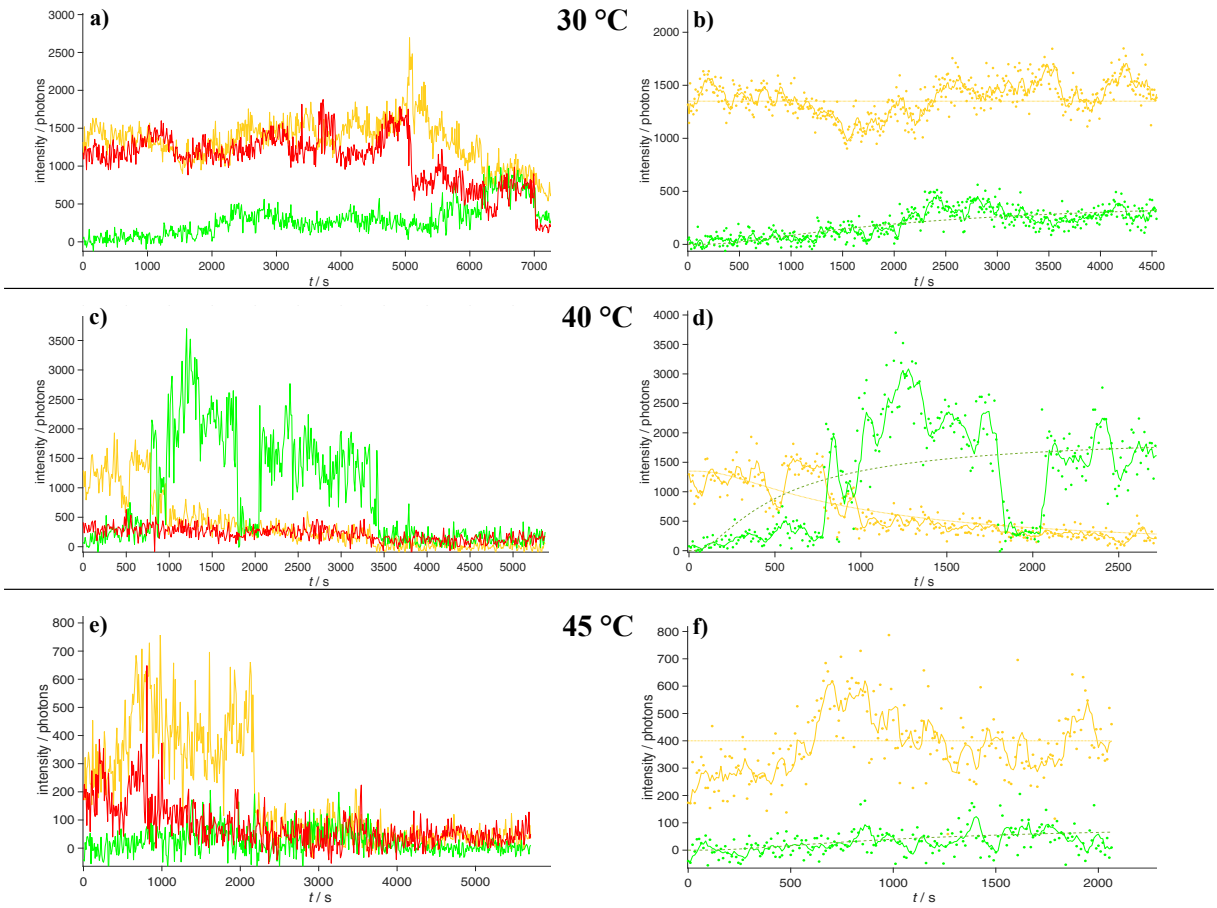

Figure 4.25: (**a,c,e**) Summed-up intensity-time traces of 8, 10 and 3 FRET pairs from each two different measurements in tempered PVAc (184 kDa) at 30 °C, 40 °C and 45 °C, respectively. The intensity-time traces of the FRET-, donor- and acceptor-channel are shown in orange, green and red, respectively. The solid lines in (**a,c,e**) and the dots in (**b,d,f**) represent the summed-up intensity values at each measured point in time. The solid lines in (**b,d,f**) represent the moving average of these values (binning size = 5). A cycle time of $t_{\mathrm{cycle}} = 10.64$ s was employed during all measurements. (**b,d,f**) Separate fits of the FRET and the donor intensity-time traces with equation (2.30). The dotted orange line corresponds to the fit of the FRET intensity-time trace with a diffusion coefficient of (**b**) $D_F = 1.0 \times 10^{-23}$ m^2 s^{-1}, (**d**) $D_F = 8.0 \times 10^{-21}$ m^2 s^{-1} and (**f**) $D_F = 1.0 \times 10^{-23}$ m^2 s^{-1}, respectively. The dashed green line corresponds to the fit of the donor intensity-time trace with a diffusion coefficient of (**b**) $D_D = 3.5 \times 10^{-21}$ m^2 s^{-1}, (**d**) $D_D = 1.5 \times 10^{-20}$ m^2 s^{-1} and (**f**) $D_D = 6.5 \times 10^{-21}$ m^2 s^{-1}.

$D_D = 3.5 \times 10^{-21}$ m^2 s^{-1} is also highly comparable to the diffusion coefficients determined at room temperature. At 40 °C, the measured summed-up intensity-time traces can be described more accurately by the established analysis model. Within the accuracy of the method, both a cycle time of $t_{\mathrm{cycle}} = 10.64$ s and of $t_{\mathrm{cycle}} = 5.64$ s yield the same diffusion coefficients: $D_F = 6.5 - 10 \times 10^{-21}$ m^2 s^{-1} and $D_D = 5.5 - 40 \times 10^{-21}$ m^2 s^{-1}. The values are still in the same order of magnitude as the diffusion coefficients determined at room temperature. The measurement at 45 °C does not yield a reasonably interpretable statistic, as only one or two FRET pairs are obtained per measurement. The effects described above interfere with the measurement to a critical degree. The measurement is only included in Figure 4.25 to emphasize the technical limitations of the method.

Given the inaccuracies of the measurements at elevated temperatures, it is difficult to give any conclusive

statements in general. An investigation of the glass transition in this particular PVAc sample with the fluorophore system used is not feasible at all. Nevertheless, some tentative qualitative conclusions can be drawn, assuming sufficient reliability of the data. The reliability of the data is further discussed below, too. If the measurements are taken as reliable, albeit inaccurate and imprecise, the results suggest that the mobility of the donor-acceptor pairs increases much less when approaching T_g than initially expected. Comparable investigations of the mobility in polymer films with SMT already showed that translational diffusion is only observed at temperatures significantly higher than T_g.[172] This was explained with the finite localization accuracy, as the tracer remains effectively immobilized.[172] Since the FEDUP method is independent of localization accuracy, it was expected that the change of mobility in vicinity of T_g could be seen more accurately with the method. However, no significant increase of mobility is observed with the fluorophore system used. The diffusion coefficient D remains in the same order of magnitude which has been established as the achievable accuracy of the method for the diffusion in PVAc. With some reservations, it can be stated (qualitatively) that the mobility does increase by a factor of about two, as in the 40 °C measurements the generally more accurate diffusion coefficient D_F is about twice as large as in the measurements at room temperature. Still, the increase is too small to be accurately quantified. Moreover, it is possible that the various biases of the method, in particular the detection and selection biases (see Section 4.6.1), prevent the detection of any faster or slower diffusing donor-acceptor pairs. Measurements with shorter cycle times, however, do not seem to suggest a fraction of molecules with higher mobility. In contrast, measurements with longer cycle times might have resulted in less premature photobleaching (category II donor-acceptor pairs) and therefore better overall statistics. It is also possible that the plasticization of PVAc due to humid air differs at different temperatures, so that the measurements are effectively incomparable.

The aforementioned interpretation of the observations, however, is only valid under the assumption that the fluorophore system used does not show significant interactions with the polymer system. It is possible that the donor-acceptor pairs bind physically or even chemically to the polymer strands. The mobility of the polymer strands themselves is not expected to increase as much as the mobility of single molecules within the polymer film in the vicinity of the glass transition temperature. Therefore, the essentially equal diffusion coefficients determined at room temperature and at higher temperatures can alternatively be seen as an indicator of a (strong) interaction between fluorophore and polymer system. In this case, the dyad is fundamentally unsuitable for the method, at least for the investigation of the glass transition in PVAc.

Nonetheless, some experimental evidence points against detrimental interactions of fluorophore and polymer system. First, binding of the dyad to the polymer is likely to restrict not only translational, but also rotational movement. This is observed, for example, at the subtrate-air interface (see Section 4.6.5). In PVAc, however, the dyad does not seem to exhibit any notable rotational restriction (compare the defocused microscopy images in Figure 7.44). Second, it has been shown in Section 4.4.3 and 4.6.1 that the individual intensity-time traces of all valid donor-acceptor pairs suggest random relative movement. Apparent randomness is unlikely to occur if the fluorophore system interacts directly with the polymer system. Third, the diffusion measurements in PVAc are consistent with the results in PBMA (Section 4.6.3). Both polymers have a comparable glass transition temperature, but different polarity. If an interfering interaction dominated, consistency of the results in these diverse polymer system

would indicate approximately equal binding strength of the fluorophore system to both hydrophilic and hydrophobic polymers. This seems improbable, but not necessarily impossible. Hence, the presence of such an interfering interaction cannot be unequivocally confirmed or denied on the basis of the experimental data alone.
The other way around, it also not possible to state with absolute certainty the nature of the relative movement observed for the fluorophore system used. The intensity-time traces do suggest random movement, but this is not necessarily the random translational movement of single molecules in bulk polymer. A more directed, apparently random motion along polymer strands is also fathomable, especially if polymer and fluorophore system interact with each other, after all. Sophisticated molecular simulations are required to ultimately answer these questions.
There are no known other examples of the investigation of the mobility of single molecules at the glass transition of PVAc, hence no definitive comparison with other data is possible, either. The diffusion of single molecules at the glass transition of polymers is not well understood in general. Selected example studies on the topic report of a more clearly observable increase of the diffusion coefficient when approaching T_g of other polymer systems.[215–217] The relative increase of mobility in some of these examples is even approximately similar to the results presented throughout this work. However, the determined diffusion coefficients are orders of magnitude higher and the absolute change is therefore much more drastic. Given the unreliability of the results presented in this work, in particular at higher temperatures, any statements on the nature of the mobility of the employed fluorophore system in the vicinity of the glass transition temperature of any investigated polymer system should be treated with utmost care.

4.6.3 Poly(butyl methacrylate)

In the following, the FEDUP method is applied to polymers other than PVAc. The first alternative polymer investigated is poly(butyl methacrylate) (PBMA). The structure of this section is similar to that of Section 4.6.2. First, a brief introduction on the polymer system is given, then the diffusion is investigated at room temperature ($T_{\text{r.t.}} \approx 21$ °C) and $T = 40$ °C. The results are then compared to diffusion measurements in PBMA in the literature and the diffusion measurements in PVAc.

The polymer - PBMA

PBMA is an apolar polymer, typically produced by radical polymerization of butyl methacrylate. The structure of PBMA is shown in Figure 4.26. The polymer is commonly used in latex coatings[218] and as a binder in the leather industry.[219] In the scientific community, PBMA is often used as a convenient test system. Its properties, in particular optical properties, transparency and chemical inertness, are comparable to the more widespread PMMA.[220] However, the glass transition temperature is significantly lower and in the range of physiological temperatures. This makes PBMA often more convenient to work with. The single molecule diffusion in PBMA has been sparsely investigated. Among the only examples are the first applications of the FEDUP method.[55,204] Although PBMA is apolar and insoluble in polar solvents such as MeOH, diffusion measurements with dyad **8** are attempted. The results are compared with the literature. This is supposed to verify the suitability of dyad **8** for the FEDUP method, as well as the accuracy of the analysis.

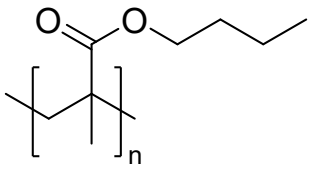

Figure 4.26: Structure of PBMA.

The PBMA investigated in this work was acquired from Polymer Source™ Inc. and used without further purification. The average molecular weight is specified as $M_W = 14500\ \mathrm{g\,mol^{-1}}$ corresponding to approximately $n = 100$ monomer units in Figure 4.26. The glass transition temperature, $T_g = 36.2\ ^\circ\mathrm{C}$, was determined with DSC (see Figure 7.63). To create homogeneous, thin PBMA films, the polymer was dissolved in toluene at a concentration of about 3 wt%. Both the molecular weight and the concentration of the polymer solution are identical to the values specified in older studies.[204] Picomolar amounts of dyad **8** in MeOH were added. It is assumed that the small amount of MeOH does not influence the properties of the toluene polymer solution ($V(\mathrm{MeOH}) \approx 10\ \mu\mathrm{L}$ vs. $V(\mathrm{toluene}) = 3.0\ \mathrm{mL}$). A drop of the stained polymer solution was spincoated onto a clean coverslip and dried under vacuum at 80 °C (see also Section 6.4.5). The surface homogeneity was confirmed with AFM for one exemplary sample. An average film thickness of about 110 nm was also determined with AFM (see Figure 7.57 for the AFM image and analysis). Defocused microscopy measurements indicate rotational restrictions of dyad **8** in PBMA films at room temperature. The rotational restrictions seem to vanish at $T = 40\ ^\circ\mathrm{C}$ (see Figure 7.44 **c** and **d**). Hence, all FEDUP measurements in PBMA at room temperature are performed employing TIRF (see also Section 2.3.2).

Diffusion measurements

It is estimated that the diffusion in PBMA is highly comparable to the diffusion in PVAc, since the glass transition temperatures of both samples are very similar ($T_g(\mathrm{PBMA}) = 36.2\ ^\circ\mathrm{C}$ vs. $T_g(\mathrm{PVAc}) = 42.6\ ^\circ\mathrm{C}$, respectively). However, there exists preliminary evidence that the diffusion rate in PBMA might be even lower. Defocused microscopy measurements imply that the dyad **8** is restricted in its rotational movement in PBMA at room temperature (see Figure 7.44). This, in turn, indicates a lower mobility. It is assumed that the rotational restrictions do not significantly influence the applicability of the model, in particular due to possible alterations of the orientation factor κ^2 and consequently the Förster distance R_0 (see Section 2.2). Given enough FRET pairs, all possible orientations are equally likely on temporal and ensemble average. The rotational restrictions therefore only introduce significant additional uncertainties in the analysis of the intensity-time traces of individual FRET pairs, which is subject to high uncertainties either way (see Section 4.6.1 step 9).

The results of the diffusion measurements in PBMA with the FEDUP method at room temperature ($T \approx 21\ ^\circ\mathrm{C}$) and at $T = 40\ ^\circ\mathrm{C}$ are compared in Figure 4.27. Cycle times of $t_{\mathrm{cycle}} = 30.64$ s and $t_{\mathrm{cycle}} = 5.82$ s were employed during the measurements, respectively. Comparative results at $T = 40\ ^\circ\mathrm{C}$ with a different cycle time ($t_{\mathrm{cycle}} = 10.82$ s) are shown in Figure 7.53 in the appendix. The diffusion coefficients D_D and D_F, determined at different temperatures and with varying analyzed times, are summarized in Table 4.8. More details of the experimental setup are presented in Section 6.7.2.

The established model describes the summed-up intensity-time traces of both donor and FRET channel

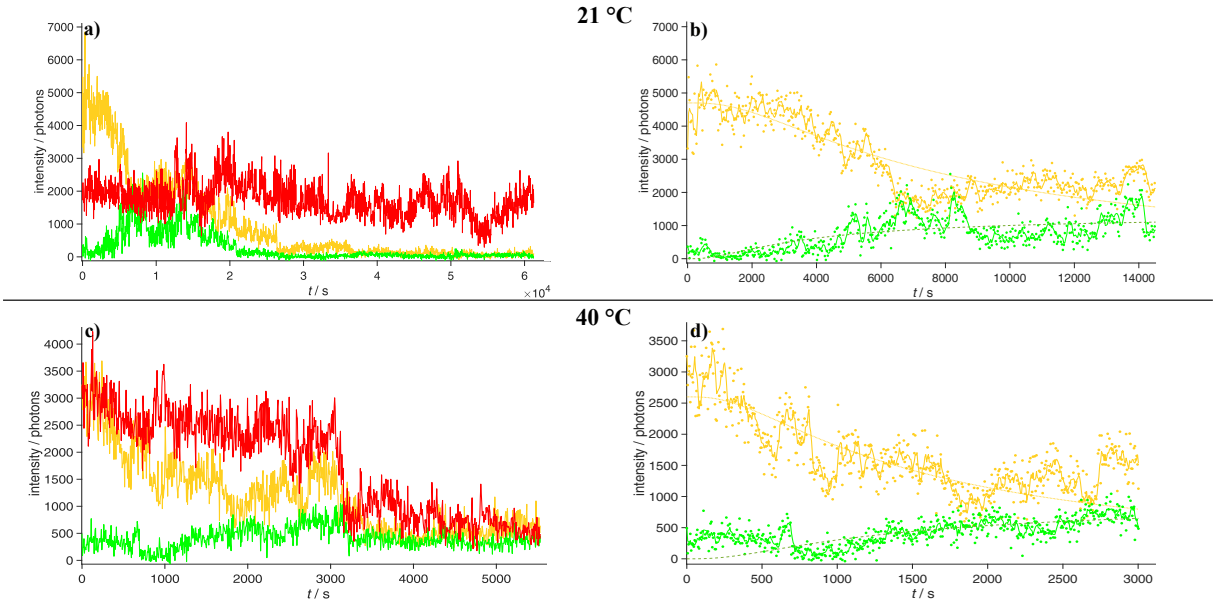

Figure 4.27: (**a, c**) Summed-up intensity-time traces of 20 and 29 FRET pairs from overall six and four different measurements in tempered PBMA (14.5 kDa) at room temperature and at 40 °C, respectively. The intensity-time traces of the FRET-, donor- and acceptor-channel are shown in orange, green and red, respectively. The thin lines in (**a, c**) and the dots in (**b, d**) represent the summed-up intensity values at each measured point in time. The solid lines in (**b, d**) indicate the moving average of these values (binning size = 5). A cycle time of (**a, b**) $t_{\text{cycle}} = 30.64$ s and (**c, d**) $t_{\text{cycle}} = 5.82$ s was employed during the measurements, respectively. (**b, d**) Separate fits of the FRET and the donor intensity-time trace shown in subfigure (**a**) and (**c**), respectively, with equation (2.30). The dotted orange line corresponds to the fit of the FRET intensity-time trace with a diffusion coefficient of (**b**) $D_F = 9.5 \times 10^{-22}$ m^2 s^{-1} and (**d**) $D_F = 5.0 \times 10^{-21}$ m^2 s^{-1}. The dashed green line corresponds to the fit of the donor intensity-time trace with a diffusion coefficient of (**b**) $D_D = 2.0 \times 10^{-21}$ m^2 s^{-1} and (**d**) $D_D = 5.5 \times 10^{-21}$ m^2 s^{-1}. The fits were restricted until photobleaching of the donor or acceptor becomes dominant.

reasonably well, both at room temperature and at $T = 40$ °C. Again, the diffusion coefficient D_D is generally larger than D_F. The value is overestimated due to uncorrelated decreases of the donor intensity caused primarily by photobleaching. However, the mismatch between D_D and D_F is less significant than in PVAc, at least when the data is restricted to analyzed times until photobleaching of the donor becomes dominant. For long analyzed times, D_D still adopts unreasonably big values, as the deviations of the intensity-time trace from the model become too significant, since the effect of photobleaching is not yet implemented in the fits.

The results of the diffusion measurements in PBMA with the FEDUP measurement confirm the initial estimation. The ensemble-averaged single molecule diffusion coefficient in PBMA, $D(\text{PBMA}) \approx 1 \times 10^{-21}$ m^2 s^{-1}, is in the same order of magnitude as the diffusion coefficient in PVAc ($D(\text{PVAc}) \approx 1 - 10 \times 10^{-21}$ m^2 s^{-1}). It was established in Section 4.6.2 that a reasonable precision of the method does not exceed a specification of the order of magnitude, at least for diffusion coefficients below $D < 1 \times 10^{-19}$ m^2 s^{-1}. However, the data presented in Table 4.8 (qualitatively) suggests that the diffusion rate in PBMA at room temperature is indeed slightly lower than the diffusion rate in PVAc. At $T = 40$ °C, thus slightly above the T_g of PBMA and slightly below the T_g of PVAc, the differences appear to vanish almost completely. Very similar diffusion coefficients are measured in PVAc and PBMA

at $T = 40$ °C. However, the diffusion rate in PBMA appears to remain slightly lower, although the T_g is already reached. Assuming no noteworthy interaction of fluorophore and polymer system, as well as a representative observation of translational movement (see Section 4.6.2), it appears as if the mobility in PBMA increases only by a factor of about 3 – 5 at the glass transition temperature. Again, it cannot be confirmed or denied unequivocally if a binding interaction between the dyad and the polymer exists, or if indeed free random translational movement is observed in the first place. The defocused microscopy measurements, however, do not suggest significant interactions. At 40 °C, the rotational restrictions of the dyad present in PBMA at room temperature disappear, thereby indicating an increase of rotational mobility at higher temperatures. If the fluorophore system was bound physically or chemically to the polymer strands, it would be unlikely that the donor-acceptor pairs remain translationally immobilized, while the rotational mobility evidently increases.

Table 4.8: The relative diffusion coefficients D_D and D_F in PBMA, obtained from fitting the combined summed-up intensity-time traces of several FEDUP measurements at various temperatures T and with different cycle times t_{cycle}. The fits are restricted to analyzed times t according to dominant photobleaching of either donor or acceptor. Donor and FRET intensity-time traces are fitted independently in each case to yield D_D and D_F, respectively.

T / °C	t_{cycle} / s	FRET pairs	fraction of cat. I / %	number of measurements	t / s	D_D / 10^{-21} m^2 s^{-1}	D_F / 10^{-21} m^2 s^{-1}
21	30.64	20	2	6	8300	0.65	1.0
					14000	2.0	0.95
					27000	8.0	0.95
					60000[a]	X[b]	1.0
40	5.82	29	16	2	1800	X[b]	6.5
					3000	5.5	5.0
					5500[a]	250	5.0
40	10.82	15	3	4	350	15	(0.01)[c]
					2500	150	2.5
					6500[a]	850	4.0

a) Corresponds to the overall measurement time of at least one measurement contributing to the combined result.
b) No reasonable diffusion coefficient could be determined. A theoretical value of $D_D = 9.5 \times 10^{-15}$ m^2 s^{-1} is obtained.
c) The data cannot be fitted correctly, since no noteworthy decrease of intensity in the FRET channel is observed within the analyzed time. The value is unreasonably low and the statistic unreliable.

Nevertheless, the presence of a detrimental binding interaction cannot be excluded. In particular, comparison to literature values suggests shortcomings of the fluorophore system used. The diffusion coefficient $D(\text{PBMA}, T \approx 21\ ^\circ\text{C}) \approx 1 \times 10^{-21}$ m^2 s^{-1} at room temperature matches the literature value perfectly.[204] The diffusion coefficient $D(\text{PBMA}, T = 40\ ^\circ\text{C}) \approx 5 \times 10^{-21}$ m^2 s^{-1} at $T = 40$ °C, in contrast, differs by about two orders of magnitude.[55,204] Concomitantly, the determined T_g of the sample investigated here is also about $7 - 20$ °C higher, despite comparable[55] or even identical[204] molecular weight of the sample. This could partially explain the smaller diffusion coefficient at $T = 40$ °C. However, it seems improbable that a 7 °C lower T_g increases the diffusion rate at 40 °C this significantly. The strong divergence of the results could potentially indicate the unsuitability of the fluorophore system used in this work.

Still, the results of the diffusion measurement in PBMA are consistent with the results in PVAc, despite

the different polarity of the polymer systems. Given a reasonable reliability and comparability of the data, the correlation between mobility and the glass transition is undeniable, but mobility appears to be dependent on other factors as well. For example, the bigger functional groups of PBMA compared to PVAc might restrict translational and rotational motion more severely, leading to smaller diffusion coefficients despite a lower glass transition temperature.

4.6.4 Polyethylene glycol

In the following, the FEDUP method is applied to poly(ethylene glycol) (PEG). The structure of this section is equivalent to that of Section 4.6.3.

The polymer - PEG

PEG is a highly hydrophilic, semi-crystalline polymer synthesized by ring opening polymerization of ethylene oxide.[221,222] The degree of crystallinity is dependent on the molecular weight and generally increases with increasing chain length.[222] Low molecular weight PEGs ($M_W < 400\ \mathrm{g\,mol^{-1}}$) are typically liquids even.[221] The structure of PEG is shown in Figure 4.28. The polymer has a wide range of applications. It is commonly used in cosmetic and other household products.[221] The low toxicity allows its use as emulsifier in the food industry.[221] Typical biochemical applications include PEG-protein or -enzyme conjugates for pharmaceutical and industrial uses, surface modifications and PEG tethers.[223] A short PEG linker is even present in the acceptor dye ATTO647N azide (see Figure 4.2). Due to the low melting point of low molecular weight PEG, it is increasingly used as a "green" solvent alternative.[224] The single molecule diffusion in PEG has not yet been studied extensively, although selected examples exist.[225,226] Most diffusion studies, however, investigate the polymer surface diffusion of entire PEG chains,[227,228] or the self-diffusion behavior.[224]

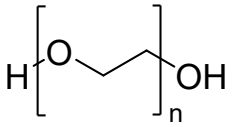

Figure 4.28: Structure of PEG.

The PEG in this work was acquired from Sigma Aldrich and used without further purification. The average molecular weight is specified as $M_W = 35000\ \mathrm{g\,mol^{-1}}$, corresponding to about $n = 760$ monomer units in Figure 4.28. The molecular weight is comparatively high for typical PEGs.[221] No glass transition temperature could be determined in a temperature range of $T = -50\ ^\circ\mathrm{C}$ to $T = 90\ ^\circ\mathrm{C}$ with DSC. However, the DSC measurements determine a melting temperature of $T_m = 70\ ^\circ\mathrm{C}$. The melting process seems to start at approximately $T = 40\ ^\circ\mathrm{C}$ (see Figure 7.64). Both an insufficient sensitivity of DSC to determine a T_g and a defined melting peak are typical indicators of high crystallinity.[222] Literature values for the glass transition temperature of PEG vary between approximately $T_g = -50\ ^\circ\mathrm{C}$ to $T_g = -20\ ^\circ\mathrm{C}$.[225]

To create homogeneous, thin PEG films, the polymer was dissolved in MeOH at a concentration of about 5 wt%. Lower concentrations were noticed to create inhomogeneities. Picomolar amounts of dyad **8** in MeOH were added. A drop of the stained polymer solution was spincoated onto a clean coverslip and

dried under vacuum at 45 °C (see Section 6.4.5). The surface homogeneity was confirmed with AFM for one exemplary sample. An average film thickness of about 350 nm was also determined with AFM (see Figure 7.58 for the AFM image and analysis). Defocused microscopy measurements show no rotational restrictions of dyad **8** in PEG at room temperature (see Figure 7.44).

Diffusion measurements

Despite the comparatively low glass transition and melting temperature, the dyad molecules are largely immobilized in the PEG films. Only spare individual fluorophores show visible translational motion. This observation qualitatively matches literature reports.[225] Depending on the molecular weight and the relative humidity of the environment, between about 10% – 90% of all molecules are classified as immobile.[225] It has been shown that fluorophores in crystalline domains are immobilized whereas mobile fluorophores are observed almost exclusively in amorphous domains.[226] Moreover, a dependency of the general mobility on the humidity of the environment is reported, since water can plasticize PEG.[225] The humidity has not been controlled rigorously during the measurements and generally fluctuates between 20% – 60% relative humidity for any given measurement, although on average the target value of 40% humidity was approximately met. It is estimated that the amorphous domains, and hence the mobile fraction of fluorophores, are more affected by the plasticization. The mobile fraction of fluorophores cannot be reasonably detected with the FEDUP method, since the FRET efficiency decrease typically occurs on a time scale comparable to the UV pulse. It is also likely that more mobile fluorophores are more prone to photobleaching, in particular by the UV pulse. Thus, the mobile fraction might not be recognized as donor-acceptor pairs in the first place, even if relative diffusion of donor and acceptor occurs on a reasonably measurable time scale. Nevertheless, the mobile fraction is significantly smaller than the immobilized fraction, probably due to the high crystallinity of the sample. Thus, the diffusion measured with the FEDUP method is assumed to yield representative average results, if no significant detrimental interactions prevail between fluorophore and polymer system (see Sections 4.6.2 and 4.6.3). However, it is likely that the diffusion measurements presented here report only one part of the more complex diffusion behavior in PEG. In this context, it is also questionable how accurately diffusion coefficients can be determined in crystalline structures with the established Maxwell distribution model in the first place, as diffusion is not necessarily a random (three-dimensional) process anymore. Even cases of one-dimensional diffusion have been reported in PEG.[225] Furthermore, it was shown in Section 4.4.3 already that the photobleaching rate in PEG is significantly higher than in the polymers investigated so far. This included a higher photobleaching rate by the photocleavage UV-laser. All mentioned effects negatively influence the accuracy and reliability of all results presented below.

The results of combined FEDUP measurements in PEG at room temperature and at $T = 40$ °C are compared in Figure 4.29. The measurements were performed with cycle times of $t_{\text{cycle}} = 1.64$ s and $t_{\text{cycle}} = 1.14$ s, respectively. Comparative measurements both at room temperature and at $T = 40$ °C with different cycle times are shown in Figures 7.54 and 7.55 in the appendix, respectively. The diffusion coefficients D_D and D_F determined at different temperatures and with varying analyzed times are summarized in Table 4.9.

Both at room temperature and at $T = 40$ °C, the model describes the summed-up intensity-time traces of the FRET channel in PEG reasonably well. The summed-up intensity-time trace of the donor channel

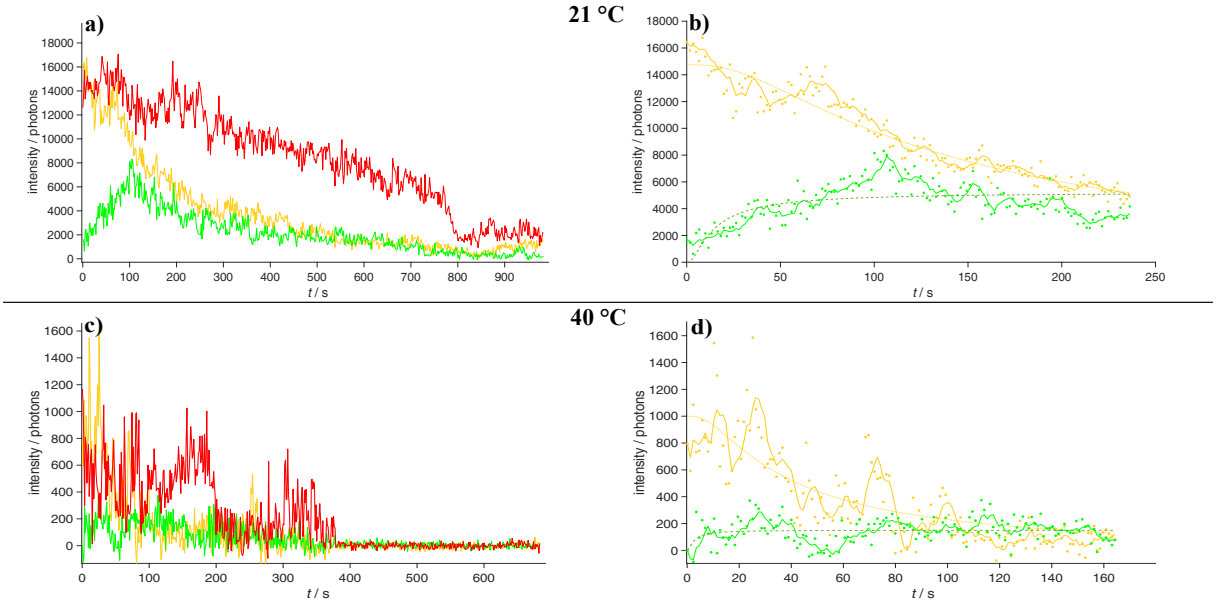

Figure 4.29: (**a, c**) Summed-up intensity-time traces of 95 and 10 FRET pairs from overall nine and four different measurements in tempered PEG (35 kDa) at room temperature and $T = 40$ °C, respectively. The intensity-time traces of the FRET-, donor- and acceptor-channel are shown in orange, green and red, respectively. Thin lines in (**a, c**) and dots in (**b, d**) represent the summed-up intensity values at each measured point in time. Solid lines in (**c, d**) indicate the moving average of these values (binning size = 5). A cycle time of (**a, b**) $t_{\text{cycle}} = 1.64$ s and of (**c, d**) $t_{\text{cycle}} = 1.14$ s was employed, respectively. (**b, c**) Separate fits of the FRET and the donor intensity-time traces with equation (2.30). The dotted orange line corresponds to the fit of the FRET intensity-time trace with a diffusion coefficient of (**b**) $D_F = 5.5 \times 10^{-20}$ m^2 s^{-1} and (**d**) $D_F = 2.0 \times 10^{-19}$ m^2 s^{-1}, respectively. The dashed green line corresponds to the fit of the donor intensity-time trace with a diffusion coefficient of (**b**) $D_D = 5.5 \times 10^{-19}$ m^2 s^{-1} and (**d**) $D_D = 3.0 \times 10^{-18}$ m^2 s^{-1}, respectively. The fits were restricted until photobleaching of the acceptor becomes dominant.

deviates even more strongly from the model than in PVAc and PBMA. The donor has been shown to be generally less photostable than the acceptor under the measurement conditions (see Section 4.4.3). This effect is even more significant in PEG and the diffusion coefficient D_D in PEG is even less accurate and precise than in the measurements shown so far. This is particularly noteworthy for all measurements performed at $T = 40$ °C, where the photobleaching rate increases even further.

Even more problematic is the unambiguous dependency of both diffusion coefficients, D_D and D_F, on the cycle time. Both at room temperature and at $T = 40$ °C, smaller diffusion coefficients are determined the longer the cycle time (see Table 4.9). This has not been observed to this extent in either PVAc or PBMA. The effect does not coincide with a lower relative humidity during the respective measurements. Two possible explanations come to mind. First, the diffusion in PEG could be vastly less homogeneous than in the other polymers. In light of the crystallinity and low phase transition temperatures of PEG, it is possible that the polymer exhibits random domains of drastically different mobility. Especially at $T = 40$ °C, thus close to the melting temperature, some domains of comparatively low crystallinity might begin the transition process before domains of higher order are influenced similarly. Consequently, the mobility might differ in domains with varying degrees of crystallinity. Measurements with shorter cycle times then primarily record the diffusion in domains of high mobility, whereas measurements

Table 4.9: The relative diffusion coefficients D_D and D_F in PEG, obtained from fitting the combined summed-up intensity-time traces of several FEDUP measurements at various temperatures T and with different cycle times t_{cycle}. The fits are restricted to analyzed times t according to dominant photobleaching of either donor or acceptor. Donor and FRET intensity-time traces are fitted independently in each case to yield D_D and D_F, respectively.

T / °C	t_{cycle} / s	FRET pairs	fraction of cat. I / %	number of measurements	t / s	D_D / 10^{-20} m^2 s^{-1}	D_F / 10^{-20} m^2 s^{-1}
21	1.14	79	10	8	50	50	8.5
					110	65	9.5
					2100[a]	X[b]	10
21	1.64	95	16	8	100	35	4.0
					250	55	5.5
					1000[a]	X[b]	5.5
21	30.64	132	20	10	450	5.0	1.5
					2000	9.0	1.0
					6500[a]	X[b]	1.0
40	1.14	10	5	4	160	300	20
					370[a]	700	20
40	1.64	19	15	4	220	X[b]	6.5
					900[a]	X[b]	9.5
40	2.64	20	10	4	250	250	3.5
					1450[a]	X[b]	6.5
40	10.64	12	22	6	150	2.5	2.5
					1500[a]	80	2.0

a) Corresponds to the overall measurement time of at least one measurement contributing to the combined result.
b) No reasonable diffusion coefficient could be determined. A theoretical value of $D_D = 0.9 - 40 \times 10^{-16}$ m^2 s^{-1} is obtained.

with longer cycle times report with higher likelihood on the diffusion in domains with lower mobility. Due to the high photobleaching rate, the slower diffusion could be effectively invisible with shorter cycle times. The second explanation is conceptually similar. It is possible that the dependency of the diffusion coefficients on the cycle time is a sign of the detection bias (see Section 4.6.1). In this context, the diffusion coefficients might be overestimated when employing shorter cycle times, as extensive premature photobleaching prevents the detection of the slower diffusion. Just as well the opposite might be the case, and the temporal resolution of the measurements with long cycle times might be insufficient to accurately report the faster diffusion process.

Despite the obvious correlation between employed cycle times and determined diffusion coefficients, the variance of the results is not too drastic. As has been established in Section 4.6.2, a reasonable precision even of combined FEDUP measurements should not exceed the order of magnitude when talking about diffusion coefficients $D < 10^{-19}$ m^2 s^{-1}. At room temperature, the diffusion coefficients D_F vary between $D_F = 1.0 - 10 \times 10^{-20}$ m^2 s^{-1} depending on the cycle time. At $T = 40$ °C, the diffusion coefficients D_F vary similarly between $D_F = 2.0 - 20 \times 10^{-20}$ m^2 s^{-1}. Thus, the variance introduced by either the heterogeneity of the diffusion process in PEG, or the more significant detection bias in PEG compared to other polymers, does not exceed the inherent imprecision of the method. The accuracy, in contrast, is still high enough to allow drawing qualitative conclusions, assuming reliability of the data (see Section 4.6.2). Only the accuracy of the diffusion coefficients D_D is considered inadequate

due to the extensive photobleaching of the donor and the more significant influence on the analysis compared to photobleaching of the acceptor (see also Section 4.6.1 step 9). Overall, it can be stated with high confidence that the diffusion rate in PEG is about one order of magnitude higher than in PVAc and PBMA. The mobility in PEG does not seem to increase significantly when increasing the temperature from ambient temperature to $T = 40$ °C. It is estimated that this is related to the crystallinity of the polymer, as the crystalline domains remain rigid at $T = 40$ °C. It is assumed that only amorphous domains or domains of comparatively low order show a noticeable increase of mobility at this temperature, whereas highly crystalline domains only start melting at temperatures closer to $T_m = 70$ °C. In this context, it has to be noted that the FEDUP method might be unsuited to report on the broader distribution of diffusion rates in PEG. Likewise, binding interactions between fluorophore and polymer system cannot be excluded, either, but seem unlikely given the rotational freedom of the dyad (see also Sections 4.6.2 and 4.6.3).

4.6.5 Diffusion measurements in further (polymer) systems

In the following, the FEDUP method is applied to a variety of (polymer) systems, namely dextran, poly(acrylic acid) (PAA), poly(ethyl acrylate) (PEA) and the surface of a regular glass substrate. All measurements are performed at room temperature. An investigation of the influence of elevated

Table 4.10: The relative diffusion coefficients D_D and D_F in dextran, PAA, PEA and on the surface of a glass substrate, obtained from fitting the combined summed-up intensity-time traces of several FEDUP measurements at room temperature. Different cycle times t_{cycle} were employed. The fits are restricted to analyzed times t according to dominant photobleaching of either donor or acceptor. Donor and FRET intensity-time traces are fitted independently in each case to yield D_D and D_F, respectively.

(polymer) system	t_{cycle} / s	FRET pairs	fraction of cat. I / %	number of measurements	t / s	D_D / 10^{-21} m^2 s^{-1}	D_F / 10^{-21} m^2 s^{-1}
dextran	32.82	16	4	3	800	15	35
					1600	30	25
					8600[a]	70	3.5
PAA	30.60	37	13	11	900	20	3.0
					1600	75	3.0
					14000[a]	550	6.0
PEA	10.64	28	6	1	4200	0.6	2.5
					9000[a]	0.75	2.0
glass	10.64	40	20	6	150	X[b]	45
					1500	X[b]	20
					4500[a]	X[b]	15

a) Corresponds to the overall measurement time of at least one measurement contributing to the combined result.
b) No reasonable diffusion coefficient could be determined. A theoretical value between $D_D = 1.5 - 250 \times 10^{-18}$ m^2 s^{-1} is obtained.

temperatures was omitted. Each measurement series serves to prove a different point, i.e., advantages or disadvantages of the method. Dextran is a biological polymer which is insoluble in MeOH but well soluble in water. Thereby, the applicability of the method to both biological and aqueous systems is hoped to be confirmed. The glass transition temperature of PAA and PEA is vastly higher and lower than ambient temperature, respectively. The measurements are supposed to emphasize the influence of the

detection and selection bias on the analysis. Measurements on the surface of the glass substrate serve as a final control experiment to prove that all FEDUP measurements presented throughout this work indeed report on the diffusion in polymer films instead of diffusion at the polymer-substrate interface.
The results of the four measurement series are summarized in Table 4.10. Subsequently, each measurement series is presented individually. It is refrained from presenting extended introductions for each system as in Sections 4.6.2 – 4.6.4. Instead, only the most important properties are mentioned.

Dextran

Dextrans are a class of branched polysaccharides. The structure is shown in Figure 4.30. The dextran in this work was acquired from Sigma Aldrich and used without further purification. The average molecular weight is specified as $M_W = 70000\ \mathrm{g\,mol^{-1}}$, corresponding to about $m = n = 190$ repeating units in Figure 4.30, if both subunits occur with equal likelihood.

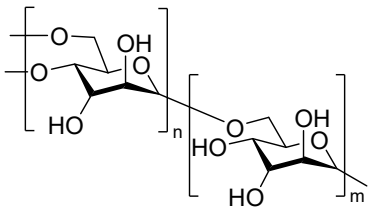

Figure 4.30: Structure of dextran.

The glass transition temperature, $T_g = 98.5\ ^\circ\mathrm{C}$, was determined with DSC (see Figure 7.65). Moreover, the DSC measurement indicates that dextran undergoes a thermal degradation when it is heated to sufficient temperatures. In literature, the thermal degradation temperature of dextran is reported to be around 300 °C,[229] thus far above the temperatures reached in the DSC measurement. However, in a second heating cycle of the DSC measurement, the thermogram of the dextran sample at hand shows drastically different thermal behavior and no phase transition can be observed in the investigated temperature range any more. No single molecule diffusion studies in dextran films are established in literature. Diffusion studies are typically restricted to the movement of dextran in solution.[230]
To create homogeneous, thin dextran films, the polymer was dissolved in water at a concentration of about 2 wt%. Picomolar amounts of a fresh aqueous dyad **8** solution were added. A drop of the stained polymer solution was spincoated onto a clean coverslip and dried under vacuum at 80 °C (see Section 6.4.5). The surface homogeneity was confirmed with AFM for one exemplary sample. An average film thickness of about 120 nm was also determined with AFM (see Figure 7.59 for the AFM image and analysis).
The results of several combined FEDUP measurements are shown in Figure 4.31. Given the high T_g of dextran, a long cycle time of $t_{\mathrm{cycle}} = 32.84$ s was employed. The determined diffusion coefficients D_D and D_F are summarized in Table 4.10.
The established model seems to describe the summed-up intensity both in the donor and FRET channels reasonably well. When restricting the fit to times when photobleaching of the donor appears to become dominant ($t \approx 1600$ s), the diffusion coefficients $D_D = 3.0 \times 10^{-20}\ \mathrm{m^2\,s^{-1}}$ and $D_F = 2.5 \times 10^{-20}\ \mathrm{m^2\,s^{-1}}$ are equal within the accuracy of the method. Despite the detrimental properties of the dye system in water (see Section 4.3.2), FEDUP measurements appear to be possible even in aqueous systems, at least



Figure 4.31: (**a**) Summed-up intensity-time traces of 16 cleaved donor-acceptor pairs of dyad **8** from overall three different measurements in tempered dextran (70 kDa) at room temperature. The intensity-time traces of the FRET-, donor- and acceptor-channel are shown in orange, green and red, respectively. Solid lines in (**a**) and dots in (**b**) represent the summed-up intensity values at each measured point in time. The solid lines in (**b**) indicate the moving average of these values (binning size = 5). A cycle time of $t_{\text{cycle}} = 32.84$ s was employed in all measurements. (**b**) Separate fits of the FRET and the donor intensity-time trace shown in subfigure (**a**) with equation (2.30). The dotted orange line corresponds to the fit of the FRET intensity-time trace with a diffusion coefficient of $D_F = 2.5 \times 10^{-20}$ m^2 s^{-1}. The dashed green line corresponds to the fit of the donor intensity-time trace with a diffusion coefficient of $D_D = 3.0 \times 10^{-20}$ m^2 s^{-1}. The fits were restricted to approximately 1600 s diffusion time to counter the effect of photobleaching on the analysis.

after an appropriate drying step. Nevertheless, the reliability of the results is highly questionable. Given the high T_g of dextran, a considerably slower diffusion rate was expected. The determined diffusion coefficients, however, are in the same order of magnitude as the diffusion coefficients in PEG, whose melting temperature T_m is lower than the T_g of dextran. It seems likely that the drying step induced a certain degree of thermal degradation of the polymer, as is indicated by the DSC measurement. Hence, the determined diffusion coefficients might be accurate, but they do not represent the mobility in real dextran. Instead, they show the mobility in the (unspecified) product of the thermal degradation

of dextran. Regardless of the faulty sample preparation, the experiments confirm that the FEDUP method with dyad **8** is applicable to biological and aqueous polymer systems, given that no noteworthy interactions of polymer and fluorophore system prevail (see Section 4.6.2).

Poly(acrylic acid)

The structure of PAA is shown in Figure 4.32. The PAA in this work was acquired from Sigma Aldrich and used without further purification. The average molecular weight is specified as $M_W = 450000\ \mathrm{g\,mol^{-1}}$, corresponding to about $n = 6200$ monomer units in Figure 4.32. The glass transition temperature, $T_g = 131.1\ ^\circ\mathrm{C}$, was determined with DSC (see Figure 7.66). No single molecule diffusion studies in PAA are established in the literature.

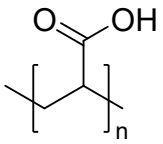

Figure 4.32: Structure of PAA.

To create homogeneous, thin PAA films, the polymer was dissolved in MeOH at a concentration of about 2 wt%. Picomolar amounts of dyad **8** in MeOH were added. A drop of the stained polymer solution was spincoated onto a clean coverslip and dried under vacuum at 90 °C (see Section 6.4.5). The surface homogeneity was confirmed with AFM for one exemplary sample. An average film thickness of about 170 nm was also determined with AFM (see Figure 7.60 for the AFM image and analysis). The results of several combined FEDUP measurements are shown in Figure 4.33. A cycle time of $t_{\mathrm{cycle}} = 30.6$ s was employed in all measurements. The determined diffusion coefficients D_D and D_F are summarized in Table 4.10.

The established model reasonably accurately describes the summed-up intensity in both relevant channels. As usual, the intensity-time trace of the donor channel is subject to more significant deviations from the model due to the bigger influence of photobleaching of the donor. Furthermore, the decay of the summed-up fluorescence intensity in FRET and acceptor channel is essentially identical, indicating an overestimation of the diffusion coefficient D_F due to increased photobleaching of the acceptor, too. It should be noted, however, that the individual intensity-time traces that contribute to the summed-up statistic have all been selected on the basis of the selection criteria presented in Section 4.6.1, thus no premature photobleaching has been observed for individual FRET pairs. Therefore, the comparable decay of the intensity in the FRET and acceptor channel is ultimately less meaningful than it seems at first. Nevertheless, it indicates a potential detection and selection bias due to extensive photobleaching within the time scale of the diffusion process.

The determined diffusion coefficient $D_F \approx 3 \times 10^{-21}\ \mathrm{m^2\,s^{-1}}$ in PAA seems to be much too large in comparison to the diffusion rates in PVAc, PBMA and PEG. The glass transition temperature of PAA is almost 100 °C higher than of either PVAc or PBMA and even about 60 °C higher than the melting temperature of PEG. Hence, it is not reasonable that the diffusion coefficient is in the same order of magnitude as PVAc and PBMA. It is estimated that the drastic overestimation is a sign of the detection bias. On average, only three FRET pairs are detected per measurement in PAA. The majority of all

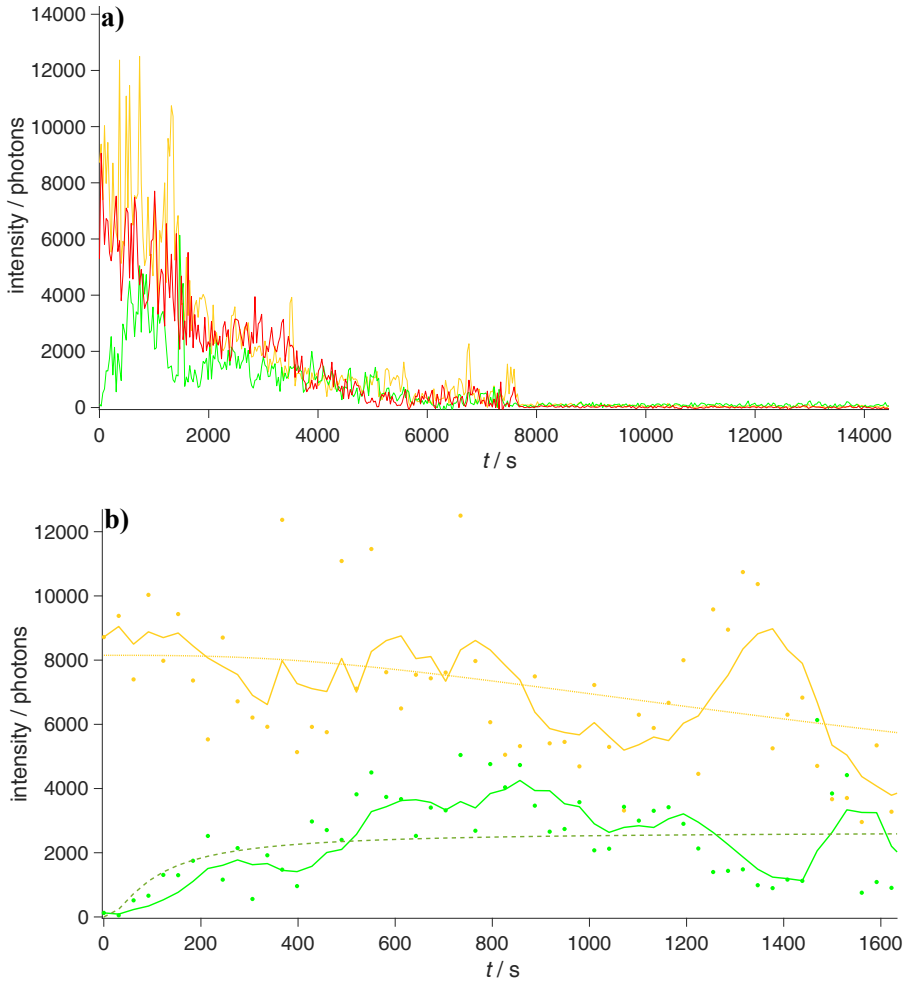

Figure 4.33: (**a**) Summed-up intensity-time traces of 37 cleaved donor-acceptor pairs of dyad **8** from eleven different measurements in tempered PAA (450 kDa) at room temperature. The intensity-time traces of the FRET-, donor- and acceptor-channel are shown in orange, green and red, respectively. Solid lines in (**a**) and dots in (**b**) represent the summed-up intensity values at each measured point in time. Solid lines in (**b**) indicate the moving average of these values (binning size = 5). A cycle time of $t_{\text{cycle}} = 30.6$ s was employed in all measurements. (**b**) Separate fits of the FRET and the donor intensity-time trace shown in subfigure (**a**) with equation (2.30). The dotted orange line corresponds to the fit of the FRET intensity-time trace with a diffusion coefficient of $D_F = 3.0 \times 10^{-21}$ m^2 s^{-1}. The dashed green line corresponds to the fit of the donor intensity-time trace with a diffusion coefficient of $D_D = 7.5 \times 10^{-20}$ m^2 s^{-1}. The fits were restricted to approximately 1600 s diffusion time to counter the effect of photobleaching on the analysis.

donor-acceptor pairs belongs to category II, thus they exhibit premature photobleaching. As almost a dozen measurements are combined, it appears as if a reasonable statistic is achieved. However, it is likely that the statistic is falsified, as only the fraction of faster diffusing FRET pairs contributes to the overall distribution. The majority of donor-acceptor pairs, that would contribute to the summed-up intensity-time traces in all channels at later measurement times, are excluded based on the selection rules, i.e., due to premature photobleaching (see Section 4.6.1). Consequently, it is assumed that the diffusion coefficient in PAA is harshly overestimated, as it is effectively impossible to detect any FRET

pairs that report on the expected slow diffusion. The measurements in PAA thus emphasize the detection bias already mentioned in Section 4.6.1. Moreover, the measurements illustrate one logical limitation of the method; diffusion can no longer be accurately measured when the FRET efficiency decrease due to photobleaching vastly exceeds the FRET efficiency decrease due to relative diffusion of donor and acceptor. As before, this interpretation is only valid given that the fluorophore system used reports representatively on translational movement. If the fluorophore system interacts with the polymer system (see Section 4.6.2), the comparable diffusion rate in PAA, PVAc and PBMA might signify comparable (attractive) interactions. However, any potential interactions between the dyad and the numerous acidic groups of PAA should significantly surpass any interactions of the fluorophore system with the polymers investigated so far, and thus should result in much lower (apparent) diffusion coefficients.

Poly(ethyl acrylate)

The structure of PEA is shown in Figure 4.34. The PEA in this work was acquired from Polymer Source™ Inc. It was attempted to purify the polymer by reprecipitation from MeOH with water. Despite purification, the amount of impurity signals in the donor channel vastly exceeds the amount of impurities in other polymers investigated so far. The average molecular weight is specified as $M_W = 335000\ \mathrm{g\,mol^{-1}}$, corresponding to approximately $n = 3300$ monomer units in Figure 4.34. The glass transition temperature, $T_g = -0.7\ ^\circ\mathrm{C}$, was determined with DSC (see Figure 7.67).

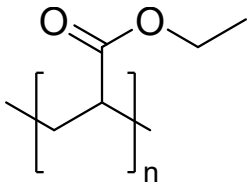

Figure 4.34: Structure of PEA.

To create thin PEA films, the polymer was dissolved in MeOH at a concentration of about 3 wt%. Picomolar amounts of dyad **8** in MeOH were added. A drop of the stained polymer solution was spincoated onto a clean coverslip and dried under vacuum at 50 °C (see Section 6.4.5). An AFM measurement of an exemplary sample revealed that the polymer film is highly inhomogeneous and a landscape of hills and valleys has been formed. An average film thickness of about 120 – 200 nm was also determined with AFM (see Figure 7.61 for the AFM image and analysis). Defocused microscopy measurements indicate that at least part of the dyad molecules embedded in the PEA film experience rotational restrictions at room temperature (see Figure 7.44). The results of a typical FEDUP measurement in PEA are shown in Figure 4.35. The determined diffusion coefficients D_D and D_F are summarized in Table 4.10.

Despite the low T_g, the dyad molecules are perfectly immobilized in the PEA film. The defocused microscopy measurements even indicate that the immobilization is similar to the situation in PBMA at room temperature. At first, this could be seen as an indicator of interactions of polymer and fluorophore system (see also Section 4.6.2). The mobility of single molecules in PEA at room temperature should be high enough that translational motion is comparatively fast and even visible in the measurement videos. Older studies employing TDI in SMT-like measurements confirm this assessment.[55]



Figure 4.35: (**a**) Summed-up intensity-time traces of 28 FRET pairs from a single measurement in tempered PEA (335 kDa) at room temperature. The intensity-time traces of the FRET-, donor- and acceptor-channel are shown in orange, green and red, respectively. Solid lines in (**a**) and dots in (**b**) represent the summed-up intensity values at each measured point in time. Solid lines in (**b**) indicate the moving average of these values (binning size = 5). A cycle time of $t_{\mathrm{cycle}} = 10.64$ s was employed during the measurement. (**b**) Separate fits of the FRET and the donor intensity-time trace shown in subfigure (**a**) with equation (2.30). The dotted orange line corresponds to the fit of the FRET intensity-time trace with a diffusion coefficient of $D_F = 2.0 \times 10^{-21}$ m^2 s^{-1}. The dashed green line corresponds to the fit of the donor intensity-time trace with a diffusion coefficient of $D_D = 7.5 \times 10^{-22}$ m^2 s^{-1}.

However, control experiments were performed in which the polymer solution was infused with other dyes than dyad **8** (ATTO647N in MeOH (slightly polar) and TDI in toluene (highly apolar)). It was also attempted to dissolve PEA in toluene, so that no solvent effects potentially influence the control experiment with TDI. All control experiments confirm that no translational motion is visible at room temperature, even when the drying step is omitted. Given the vastly different structures and polarity, comparable interaction of both the dyad and TDI with PEA is unlikely. It is estimated that, due to the (probably) high mobility in PEA, the fluorescent probes are pushed to the polymer-substrate interface during spincoating where they are terminally immobilized regardless of the polarity of the probe. It is also possible that a disproportionately high fraction of the fluorophores is gathered in the randomly

distributed valleys in the inhomogeneous film. Defocused microscopy measurements of dyad **8** on the surface of a glass substrate confirm that the rotational restriction on a glass substrate is similar to the rotational restriction observed in the PEA films (see below). Consequently, it is likely that the FEDUP measurement shown in Figure 4.35 does not report on the diffusion in (bulk) PEA. A cycle time of $t_{\text{cycle}} = 10.64$ s was employed to account for both the observed immobility and the expected mobility due to the low T_g.

Aside from the conceptual problems, the measurement in PEA appears to work better than in most polymers investigated so far. The summed-up intensity-time trace of the acceptor channel indicates very little photobleaching of the acceptor. Both the summed-up intensity-time traces of the FRET and the donor channel can be accurately described with the established model. Similar diffusion coefficients $D_F = 2.0 \times 10^{-21}$ $\text{m}^2\,\text{s}^{-1}$ and $D_D = 7.5 \times 10^{-22}$ $\text{m}^2\,\text{s}^{-1}$ are obtained for both separate fits. The determined diffusion rates are highly comparable to the results in PBMA but differ greatly from the results on the surface of a glass substrate (see below). In light of the hypothesis of immobilization at the polymer-substrate interface, it seems that the diffusion behavior of single molecules is significantly influenced by interface effects.

Overall, the experiment illustrates a different point than initially aimed for. The measurement was supposed to demonstrate the limitation of the method in the case of comparatively high diffusion rates. Instead, it demonstrates a more common problem of microscopy, and in particular the FEDUP method when employing dyad **8**, in general; only that which can be seen can also be analyzed, but that which can be seen is not necessarily the targeted structure. From the FEDUP measurements alone, the mobility in PEA is likely to be evaluated wrongly. Only in the combination with AFM, defocused microscopy, DSC and control experiments it becomes clear that the FEDUP measurements are faulty, or at least do not report on the diffusion in bulk PEA.

Reference measurements at the glass-air interface

Given the hypothesis that the FEDUP measurements in PEA show the diffusion at the polymer-substrate interface, it is obligatory to make comparative measurements on the substrate-air interface. To this end, a solution of dyad **8** in MeOH ($c \approx 10^{-11}$ $\text{mol}\,\text{L}^{-1}$) was spincoated onto a clean coverslip. The glass substrate was dried under vacuum at 80 °C (see Section 6.4.5). Defocused microscopy measurements indicate that the rotational motion of dyad **8** is restricted at room temperature (see Figure 7.44). The results of FEDUP measurements on the surface of a glass substrate are shown in Figure 4.36. The same cycle time ($t_{\text{cycle}} = 10.64$ s) as in the PEA measurement is employed to grant the best comparability and to avoid potential biases introduced by the cycle time (see also Section 4.6.1). The determined diffusion coefficients D_D and D_F are summarized in Table 4.10.

Perhaps most surprising is the fact that the measurements indicate that single molecules indeed move on a glass surface without any support. The intensity-time trace of the FRET channel can even be described reasonably accurately by the established model. Similar to the measurements in PAA, the decay of the intensity in the acceptor channel correlates exceptionally well with the decay in the FRET channel. Since the individual intensity-time traces do not show premature photobleaching, this is considered to be uncritical for the analysis. Nevertheless, the correlated decay indicates potential detection and selection biases due to the high photobleaching rate. The intensity-time trace of the donor channel deviates in any



Figure 4.36: (**a**) Summed-up intensity-time traces of 40 cleaved donor-acceptor pairs of dyad **8** from six different measurements on a glass substrate at room temperature. The intensity-time traces of the FRET-, donor- and acceptor-channel are shown in orange, green and red, respectively. Solid lines in (**a**) and dots in (**b**) represent the summed-up intensity values at each measured point in time. Solid lines in (**b**) indicate the moving average of these values (binning size = 5). A cycle time of $t_{\text{cycle}} = 10.64$ s was employed in all measurements. (**b**) Separate fits of the FRET and the donor intensity-time trace shown in subfigure (**a**) with equation (2.30). The dotted orange line corresponds to the fit of the FRET intensity-time trace with a diffusion coefficient of $D_F = 2.0 \times 10^{-20}$ m^2 s^{-1}. The dashed green line corresponds to the fit of the donor intensity-time trace with a diffusion coefficient of $D_D = 6.5 \times 10^{-17}$ m^2 s^{-1}. The fits were restricted to approximately 1500 s diffusion time to counter the effect of photobleaching on the analysis.

case from the model, even when the data is restricted to the global maximum at approximately 150 s. It is probable that the photodegradation reactions are faster on an uncovered glass surface compared to a rigid polymer film, since the local partial oxygen pressure is expected to be higher. The partial oxygen pressure has been shown to be one crucial factor in the photobleaching rate of the employed dyes (see Section 4.4.3). In this context, some of the investigated polymer films might act as a protective membrane, limiting the access of fresh oxygen required for the photodegradation reactions. Hence, it is assumed that the high inaccuracy of the diffusion coefficient D_D is to the largest part caused by the excessive photobleaching of the donor. It is possible that other photophysical or -chemical effects play a

role, too. For example, the FRET behavior could be critically influenced by any potential anisotropy of the excitation and emission due to the rotational restrictions. However, measurements in polymer systems with comparable rotational restrictions do not indicate a similar deviation to the expected behavior (in particular PBMA, see Section 4.6.3).
The only thing more surprising than the fact that single molecules move without support on a glass surface might be the apparent speed of that movement. The diffusion coefficient $D_F = 2 \times 10^{-20}$ m^2 s^{-1} indicates a mobility similar to that in PEG despite the differing degrees of rotational freedom. Furthermore, the diffusion rate is an order of magnitude higher than the diffusion rate observed in PEA. In this context it has to be noted that it cannot be stated which kind of movement is observed in the FEDUP measurement. In light of the rotational restrictions of the dyad immobilized on the glass surface, it is possible that the changes in the FRET efficiency are related to rotational instead of translational movement. Irrespective of the reliability of the obtained value, the experiment shows the difference of diffusion at the glass-air interface to all diffusion measurements performed so far. Thus, it is confirmed that the diffusion observed in PEA is not the diffusion of dyad molecules stuck in the valleys of the inhomogeneous film (see above).

4.7 Summary and conclusion (Part 2)

In Chapter 4, the visualization of very slow diffusion processes was set out. In particular, it was attempted to study the glass transition of polymers via the changes of single molecule mobility. In this context, slowness is defined as any diffusion that cannot be reasonably observed with classical tracking methods like SMT ($D < 10^{-17}$ m^2 s^{-1}). It was attempted to improve the FEDUP method introduced in 2013 by *Dill et al.*[55] Improvements included four different aspects. First, the range of systems which can be investigated was increased by switching from an apolar photocleavable dyad to a more polar dyad. Second, the photocleavage wavelength was tuned to optically more convenient longer wavelength UV-A. Third, the measurement procedure was optimized to grant a better simultaneous spectral and spatiotemporal resolution. Last, the analysis, in particular the fit model, was reworked. A novel dyad was synthesized (Section 4.2), fully characterized (Section 4.3) and its suitability for FEDUP measurements was demonstrated (Section 4.4). A summary and conclusion of the aforementioned parts was already given in Section 4.5. In the following, only the application of the new dyad in diffusion measurements is evaluated (Section 4.6).
From a qualitative point of view, one major aim was reached and the otherwise unobservable (translational) motion of single molecules could be visualized in a wide range of rigid (hydrophilic) polymers. In contrast, the second major aim, the investigation of the glass transition via the mobility of single molecules, was reached only partially. It could be shown that diffusion coefficients over about three orders of magnitude ($D \approx 10^{-22} - 10^{-19}$ m^2 s^{-1}) are accessible with the method. Investigated examples included rigid amorphous hydrophilic and hydrophobic polymers (PVAc and PBMA, Sections 4.6.2 and 4.6.3), semi-crystalline polymers (PEG, Section 4.6.4), substrate-air and potentially even substrate-polymer interfaces (glass and PEA, Section 4.6.5).
One of the biggest challenges proved to be the quantification of the tardy movement, especially at elevated temperatures. Photobleaching of donor and acceptor dye interfered with the analysis according

to the established model based on the Maxwell distribution. Further photophysical and -chemical effects, like the blinking behavior of the dyes and the random nature of the relative diffusion of donor and acceptor, made the determination of single molecule diffusion coefficients from individual FRET pairs rather inaccurate and imprecise. Detection and selection biases introduced further uncertainties even when analyzing the entire ensemble. Most importantly, the photobleaching rate in some polymers was too high to obtain a reliable statistic reporting faithfully on the diffusion behavior. This was illustrated most clearly by measurements in PAA, where the determined diffusion coefficient is likely to be overestimated because most of the slow diffusing donor-acceptor pairs were bleached prematurely and only a small fraction of faster diffusing FRET pairs was observed at all. The influence of the sample preparation and the measurement conditions should also not be underestimated. Depending on the investigated system (e.g., PVAc and PEG), even at first glance irrelevant environmental factors like the humidity can significantly affect the measurements. In some cases (e.g., dextran and PEA), the sample preparation was unsuited to study the targeted diffusion inside polymer films because the polymer underwent thermal degradation during the annealing step, or inhomogeneous films were created. Nevertheless, reasonable ensemble-averaged relative diffusion coefficients could be determined in a variety of polymer systems at room temperature.
Measurements at elevated temperatures were plagued by low SNR, bad measurement quality and even higher photobleaching rates. Additionally, the results cast a shadow of doubt over the reliability of all determined diffusion coefficients. In particular, the results indicate that the fluorophore system might interact with the polymer systems. In the measurements at higher temperature, it appears as if the mobility of the fluorophore system in PVAc and PBMA in the vicinity of the glass transition temperature increases only little and the diffusion rates, although increasing, remain in the same order of magnitude. Similar observations were made for the melting process of PEG. Here, the mobility in the crystalline domains appears to be largely unaffected by temperatures at which the amorphous domains begin the phase transition already. These observations do not match the current understanding of polymer physics and can potentially be explained by binding interactions of polymer and fluorophore system. Experimental evidence for or against such interactions is still inconclusive. Therefore, it is impossible to give a definitive statement on the exact nature of the observed movement.

All in all, it can be stated that FEDUP is a valid method to visualize slow translational movement, but the fluorophore system used might be fundamentally unsuitable. Even if the data is reliable, quantification remains problematic. In contrast, it was demonstrated that the method also offers intrinsic advantages like the possibility of drift correction without significantly lowering the accuracy of the determined diffusion coefficients. However, it is estimated that even more accurate diffusion coefficients can be derived from the single molecule data. The comparatively simple model based on the Maxwell distribution seems to be appropriate for the analysis of the ensemble, but it still lacks a description of further important photophysical and -chemical effects, most importantly photobleaching. Similarly, the method clearly offers the possibility to investigate the glass transition of rigid polymers if some of the technical problems can be overcome. To this end, it could prove useful to vary the dye system by employing different, more photostable donor and acceptor dyes. The photocleavable linker based on the NPPOC PPG performed well in regard to photocleavage efficiency. Still, it also appears to introduce an undesirable large variety of further photophysical and -chemical effects, in particular in solution. Some

of the observed problems on the single molecule level might also be related to the altered photo-reactivity imposed by the linker. A different chemical motif might improve the overall performance. Furthermore, the accuracy might be improved by measuring lifetimes instead of intensities.
Last but not least, it should be noted that the method is often rather complementary to existing methods than a simple expansion of the feasible diffusion range. The results, for example, in PEG and PEA indicate a broader distribution of diffusion coefficients that the method fails to detect in its entirety. Complementary diffusion measurements, with e.g., SMT, are still obligatory to obtain the whole picture. Likewise, AFM, DSC and defocused microscopy measurements are required to correctly evaluate the diffusion as observed with the FEDUP method. For example, it cannot be stated if diffusion in bulk or at interfaces is observed from the FEDUP data alone. Detrimental interactions between the fluorophore system used and the polymer systems cannot be fully excluded, either. That said, the method still represents an important step in the visualization of otherwise invisible movement and consequently the understanding of complex processes like the glass transition.

5 Summary and outlook

Understanding comes hand in hand with observation. Therefore, sophisticated tools to reveal the hidden world around us are of essential importance, their existence matched only by the knowledge how to use them. This general principle guided the entire work presented here. This work was laid out to develop new ways of using single molecule fluorescence microscopy to visualize structural aspects of polymer systems that are otherwise difficult to access. In particular, in Chapter 3 it was aimed to visualize bond scission with mechanoresponsive fluorophores, or mechanofluorophores, whereas in Chapter 4 the visualization of single molecule diffusion on a sub-pixel level with a photoresponsive fluorophore system was attempted. Both represent newly established techniques to use the tool of fluorescence microscopy to investigate badly understood phenomena like material failure and the glass transition of polymers, respectively.

Chapter 3 was a continuation of the work of *Baumann et al.*[50] The developed multicolor mechanofluorophore system (BTD) was used as a crosslinker in PVCL/VIM microgels and PHMA networks. It was aimed to visualize bond scission in these polymer systems with improved resolution and information content. To this end, the polymer systems were imaged with FLIM and, if applicable, a controlled activation with AFM was attempted.

The aim, however, was not met. Preliminary tests indicated a generally good spectral separation of unactivated and activated BTD as well as a reasonable contrast of lifetimes at 488 nm excitation in organic solvents. However, they also uncovered unfavorable photochemical and -physical properties of the fluorophore system, in particular a low photostability, fluorescence quantum yield and/or excitation efficiency. These rendered an improvement of the resolution essentially impossible from a technical point of view. Neither it was possible to significantly increase the information content by switching from regular CLSM to FLIM. The determination of lifetimes in all FLIM images was subject to high uncertainties. Within the accuracy of the method, microgels activated *ex-situ* with ultrasonication yielded the same FLIM images as untreated microgels, i.e. comparable lifetime components in a similar ratio and distribution were found. DLS measurements hinted at unspecific thermal or collapse-induced activation of the BTD. Spectral measurements indicated very weak emission of the activated mechanofluorophore in the aqueous environment of microgels, large amounts of remaining unactivated crosslinker in activated microgels and worse spectral separation of the emission of the unactivated and activated BTD in microgels at 488 nm excitation than in the organic solvents used in the preliminary tests. Given the indistinguishability of microgels before and after bulk activation, no controlled activation with AFM was attempted.

The FLIM images of the PHMA networks were plagued by similar problems. Again, determination of lifetimes was subject to high uncertainties. Within the accuracy of the method, the same lifetime components in a similar ratio were observed as in the microgels before. The polymer films exhibited countless fluorescent spots throughout the entire bulk material irrespective of any mechanical activation.

Cutting of the films resulted in an increase of fluorescence intensity at the edges of the cut. However, the fluorescence lifetimes did not differ significantly between the unactivated bulk and the activated cut. Moreover, AFM revealed an unequivocal correlation between film thickness and measured fluorescence intensity. During cutting of a film, polymer material was pushed to the edges and piled up there. It seems likely that the increase in intensity in these areas of locally thicker films coincides with the apparent increase in two dimensional labeling density. No definitive activation with AFM was observed. It is not clear if the results signify widespread unspecific activation due to improper handling, prolonged aging, or other damage of the samples, or insufficient spectral contrast between the unactivated and activated BTD, including fluorescence lifetimes, despite the promising results of the preliminary tests in this regard.

Chapter 4 represented a continuation of the work started by *Dill et al.*[55] and extended by *Schöngen et al.*[59] The further development of the FEDUP method for diffusion measurements below the lower limit of classical tracking methods such as SMT was pursued. To this end, a new photocleavable FRET dyad as well as photoresponsive reference compounds were synthesized, which exhibited an improved solubility in polar media compared to the dyad in the original work.[55] Moreover, the new dyad exhibited a vastly improved photocleavage efficiency at comparatively long wavelength UV-A irradiation. The photoresponsive fluorophore system was characterized extensively, in particular with regard to its photocleavage and photobleaching behavior, and its suitability for the FEDUP method was confirmed. Furthermore, the measurement procedure and the analysis of the FEDUP method were optimized. It was aimed to visualize the tardy diffusion in (hydrophilic) polymers, in particular in vicinity of the glass transition temperature. It was hoped that this approach would provide more insight on the topic of glass transitions.

The aim was met partially. Visualization of slow (translational) motion was possible in a variety of (polymer) systems, that among rigid amorphous hydrophilic polymers (PVAc), polymers in which even rotational diffusion was restricted (PBMA), crystalline polymers (PEG), substrate-polymer interfaces (PEA) or on a glass surface. In all cases, movement was virtually invisible to localization based tracking methods, since the fluorophores appeared to remain immobilized throughout the duration of the measurement. Only observation of the FRET efficiency upon photocleavage revealed a relative movement of donor-acceptor pairs of about 10 nm, thus a sub-pixel level, on a time scale of minutes or even hours.

The investigation of the glass transition, however, was impeded by technical problems. The quality of the measurements at higher temperatures decreased drastically. In particular, they exhibited a worse SNR, a higher laser power was required to recognize any signals and the photobleaching rate was increased. In these measurements, it appears as if fluorophores remain essentially immobilized in the vicinity of the glass transition temperature, and diffusion coefficients, although increasing, remain in the same approximate order of magnitude. This interpretation, however, is only valid if no significant binding interactions occur between the fluorophore and polymer systems. Based on the experimental evidence, the presence of detrimental interactions could be neither fully confirmed nor disproved. Hence, although single molecule movement could be visualized in a wide variety of (polymer) systems, it is not clear if this represents a valid visualization of translational motion, and consequently a representative picture of the glass transition.

All in all, this work presented viable new methods to use fluorescence microscopy for the visualization

of difficult to access structure related properties of polymer systems. At the very least, current shortcomings of these newly established techniques were revealed.

The combined FLIM and AFM measurements of Chapter 3 hint at a hitherto unrecognized relation between the topological changes introduced by mechanical activation and the spectral response of the employed mechanofluorophore system. Moreover, the results emphasize that an extended characterization of mechanofluorophore systems via theoretical calculations and simulations is required for a better or even valid interpretation of the fluorescence microscopy images. Theoretical calculations could help to judge the faithfulness with which any mechanofluorophore reports on material failure. Simulations, in contrast, could assist to evaluate the forces acting on a polymer strand under different conditions. Both are essential to determine the probability and significance of unspecific activation. Since this crucial information is missing for the investigated mechanofluorophore system, it cannot be reliably stated if the FLIM images should be interpreted as random statistical activation, the symptoms of propagating material failure, meaningless over-reporting, or general insufficiencies of the spectral properties of the system.

Speaking of inadequate spectral properties, the measurements show clearly that the originally targeted improvement of resolution demands fluorophores with a higher photostability, fluorescence quantum yield and excitation efficiency. Even super-resolution is conceptually possible, for example, with a photoswitch which is deactivated by mechanolabile bonds. After activation, a PALM-like SRFM approach could lead to super-resolved visualization of bond scission. Controlled activation of individual mechanofluorophores with AFM is also fathomable, even if no activation was observed in this work. It is estimated that this is related to the shortcomings of the system itself. The results indicate that modified AFM tips might be better suited for this purpose.

Similarly, the FEDUP measurements of Chapter 4, although yielding reasonable results at room temperature, indicate several possible improvements. The NPPOC linker shows an excellent photocleavage efficiency at convenient UV wavelengths and no significant undesired photocleavage at visible wavelengths. However, it also seems to introduce a new undesired photochemical reactivity. In particular, the photostability of the used dyes appears to be reduced. The two drastically different possible cleavage pathways are also disadvantageous, even if the more convenient styrene pathway seems to be generally favored. Most importantly, the results at higher temperature hint at possible detrimental interactions of polymer and fluorophore system. A different photolabile linker motif and/or a variation of the linked fluorophores could potentially improve the performance. Nevertheless, the potential of the FEDUP method for the investigation of the glass transition in polymers is undeniable. It is estimated that the technical problems of high temperature measurements in this work can eventually be overcome by skillful experimentation, sophisticated instrumentation and the above mentioned variation of the fluorophore system.

Furthermore, the measurements emphasize the importance of extensive characterization of both the fluorophore and the polymer systems. Without complementary AFM, DSC and defocused microscopy measurements, the diffusion in several polymers can be easily misinterpreted. The spectral characterization of the fluorophore system reveals unexpected properties like the strong dependency of the fluorescence emission on the environment. These are not necessarily disadvantages, but might offer entirely new applications of the photoresponsive dye system, for example as water sensing probes.

Nonetheless, an even more complete characterization should also include theoretical calculations and simulations. The former might help to understand the complex energy transfer. For instance, some experimental evidence points to the existence of reverse FRET, i.e. energy transfer from the expected acceptor to the expected donor. The reasonability of this hypothesized phenomenon can be ultimately answered only with supporting quantum chemical calculations. Simulations might confirm or disprove the reliability of the measurements by revealing possible detrimental interactions of the fluorophore system with the polymer or with itself. They might also deliver a better description of the energy transfer in the dyad, especially in rigid polymer systems with rotational and conformational restrictions, which might drastically alter the FRET behavior and thus influence the analysis of the data.
The analysis can potentially be improved in general. The current statistical model seems to deliver a reasonably accurate description of the relative movement of FRET pairs, especially when a large ensemble is analyzed. However, it was shown that the statistic is influenced by further photophysical and -chemical effects. Most importantly, the intensity decrease due to the independent photobleaching of donor and acceptor has to be implemented in the model to increase the achievable accuracy. Moreover, the analysis is subject to various biases, like the detection and selection bias. It may be possible to reduce the selection bias by making the selection process more objective with the help of AI.
Despite the problems described above, the fluorescence microscopy methods in Chapter 3 and Chapter 4 bear tremendous potential for the investigation of material failure and single molecule mobility in rigid environments, respectively. It is estimated that both methods can be further improved based on the insights presented in this work.

6 Methods and materials

The following chapter is separated into different parts. In Section 6.1, additional scientific background is offered on methods used throughout this work which have not yet been described in Chapter 2. All syntheses related to the synthesis scheme in Figure 4.1 are listed in Section 6.2. Section 6.3 contains protocols on all spectroscopic measurements. Sample preparations are described in Section 6.4. All measurement protocols of confocal time-resolved fluorescence microscopy, i.e., TCSPC, FCS and FLIM, are given in Section 6.5. Section 6.6 contains the setup for all bulk irradiation experiments. All widefield microscopy measurements, including FEDUP measurements, are given in Section 6.7. Protocols for AFM and DLS measurements are listed in Sections 6.8 and 6.9, respectively. NMR, MS, HPLC and DSC measurements are described in Sections 6.10 – 6.13.

6.1 Additional scientific background

6.1.1 Dynamic light scattering

A standard technique for the determination of particle sizes is dynamic light scattering (DLS). To this end, the sample, typically a transparent dispersion, is irradiated with a coherent visible laser. The light is scattered by any scattering particles and detected at an angle θ relative to the incident light beam. The scattering angle θ is dependent on the refractive index n of the medium and the wavelength λ of the scattered light. The relationship of these quantities is typically expressed in form of the scattering vector q according to equation (6.1).[231]

$$q = 4\pi \cdot n \cdot \frac{\sin\left(\frac{\theta}{2}\right)}{\lambda} \tag{6.1}$$

As the particles in solution undergo random Brownian motion, the detected intensity of the scattered light fluctuates. The temporal intensity fluctuations are used to calculate the intensity time correlation function $G^{(2)}(q,t)$. Here, t describes the time between two arbitrary intensity values. The correlation function $G^{(2)}(q,t)$ can be transformed to the normalized electric field time correlation function $|g^{(1)}(q,t)|$ via the Siegert relation.[231] The normalized correlation function allows the calculation of the translational diffusion coefficient D with equation (6.2).

$$|g^{(1)}(q,t)| = \int_0^\infty G(D)\exp\left(-q^2 Dt\right)\mathrm{d}D \tag{6.2}$$

Where $G(D)$ is the distribution of diffusion coefficients. For spherical particles, the diffusion coefficient D can be translated to the hydrodynamic radius R_H according to the Stokes–Einstein equation (2.32).
In this work, DLS is used for the size determination of approximately spherical microgels in Chapter 3.

6.1.2 Nuclear magnetic resonance

The collective spin of protons and neutrons leads to a nuclear magnetic moment in most atomic nuclei. This nuclear magnetic moment μ is defined by the gyromagnetic ratio γ according to equation (6.3).[232] The gyromagnetic ratio is a characteristic constant for different nuclei.

$$\mu = \gamma \times p = \gamma\sqrt{I(I+q)}\hbar \tag{6.3}$$

Here, p is the intrinsic angular momentum, $\hbar$ is the reduced Planck-constant and I is the spin quantum number which determines the overall spin of a nucleus. The spin quantum number can have integral or half-integral values. Within a homogeneous static magnetic field B_0, the angular momentum vector of the magnetic moment of a nucleus adopts quantized orientations to the B_0-vector.[232] The quantized spin component along the applied magnetic field is described by the magnetic quantum number m, which can take values from $-I$ to I in integer steps. Hence, there exist $2I+1$ angular momentum states. Without an external magnetic field, these states are degenerate. Within a magnetic field, however, these so-called nuclear-Zeeman-levels lose their degeneracy.[232] The energy of a nuclear-Zeeman-level depends on the orientation of the spin to the magnetic field vector B_0. The most prominent NMR-nucleus, the proton, has got a spin of $I = 1/2$ and therefore two nuclear-Zeeman-levels, corresponding to $m = \pm 1/2$. In the energetically more favorable state, the spin is aligned with the external magnetic field, in the less favorable state the spin is aligned against B_0. The energy difference ΔE between the two states is dependent on the strength of the applied magnetic field. The resonance condition $\Delta E = h\nu$ can be calculated with equation (6.4).[232]

$$\Delta E = \gamma\hbar B_0 = h\nu \tag{6.4}$$

The energy difference ΔE is so small that radio-frequency pulses are sufficient to obtain a spin-inversion and a population of the upper nuclear-Zeeman-level. During the relaxation of the nuclei to the lower nuclear-Zeeman-level the vectorial magnetization of the nuclei in direction of the magnetic field necessarily changes. Likewise, the equatorial magnetization is affected. The equatorial magnetization is influenced by the interaction of the nuclear magnetic moments and its relaxation time can be measured. A subsequent Fourier-transformation yields the NMR-spectrum.[232]

For the interpretation of ^{1}H-NMR-spectra, the phenomena of chemical shift and spin-spin-coupling are crucial. Chemical shift denominates the subtle changes of the resonance frequencies ν due to the environment of a given nucleus. In essence, the small nuclear magnetic moments of the surrounding nuclei interact with the external magnetic field B_0. This interaction weakens the magnetic field experienced by the considered nucleus.[232] Hence, the amount of shielding reveals information about the surrounding structure of a nucleus. Since the resonance frequency is also dependent on the external magnetic field itself (equation (6.4)), ^{1}H-NMR-spectra are represented as the dimensionless chemical shift δ of the nuclei compared to the reference substance tetramethylsilane (TMS). The chemical shift of the twelve chemically equal protons of TMS is defined as $\delta = 0$. The chemical shift of any other proton is defined by the ratio of the difference between the resonance frequencies of the investigated nucleus and TMS, and the measuring frequency.

Spin-spin-coupling also plays an important role in the interpretation of ^{1}H-NMR-spectra. The coupling

of different neighboring nuclei results in a fine structure in the signal of an arbitrary observed nucleus. The coupling is quantified by the coupling constant J. Contrary to the resonance frequencies, coupling constants are independent of the external magnetic field.[232] Coupling is only observed between nuclei which are chemically not equivalent.[232] To prevent the coupling of protons to, for example, ^{13}C-nuclei, special measurement protocols can effect decoupling. Therefore, in ^{1}H-NMR-spectroscopy only the coupling between different chemically nonequivalent protons is observed. Coupling of one specific proton to n chemically equivalent protons results in a $n+1$ multiplicity of the observed proton's signal. Further coupling of the first proton to m other interchangeable protons results in an additional splitting of the signal with an overall multiplicity of $(m+1)\times(n+1)$. Integrating the measured peaks of an ^{1}H-NMR-spectrum gives information about the relative frequency of the associated proton. Hence, the amount of protons leading to any given signal can be determined by comparing the areas of all peaks.
In this research, ^{1}H-NMR-spectroscopy (and ^{13}C-NMR) is used for the characterization of almost all synthesized compounds in Chapter 4.

6.1.3 Mass spectrometry

When accelerating charged gas particles inside a homogeneous magnetic field, they are redirected by the field. According to Newton's second law of motion, the redirecting force is proportional to the mass of the charged particles.[232] This proportionality can be used to separate charged particles according to their masses. Moreover, their mass, or rather mass-to-charge ratio, can be determined from the magnitude of their deflection. The lighter the particles and the higher their charge, the more they are deflected.[232] These quantifiable effects are utilized in mass spectrometry (MS). One of the main conditions of MS is the ability to ionize and evaporate the sample. Both ionization and evaporation are achieved by various methods even for non-volatile substances (see below). The ionized gaseous molecules are injected into a high vacuum chamber with an applied magnetic field. The ions are deflected towards a detector. Their mass-to-charge ratio is determined from the degree of deflection.
Different species of charged particles are produced in MS. Molecules can be ionized directly to molecule-ions whenever an electron is abstracted or added.[232] More common are adduct-ions which are created by the attachment of cations such as H^+ or Na^+.[232] Molecule-ions or adduct-ions usually represent the highest mass peaks in a mass spectrum. Furthermore, molecule-ions and adduct-ions can fragment. As ionization requires high energies, weaker molecular bonds can be cleaved heterolytically and smaller ionic fragments are formed. These fragments are often characteristic, since cleavage occurs at specific bonds within the investigated compounds. Thus, whereas molecule- or adduct-ions reveal the mass of the measured substance, the fragmentary patterns reveal more details about the structure.[232]
In this research, MS is used for the identification of several compounds. The fragmentation patterns are not of relevance. Adduct-ion peaks are used to ensure the presence of the desired compound. In all cases, electrospray ionization (ESI)-MS is employed. ESI is a mild ionization technique suitable for the possibly fragile structures investigated in this work. In ESI-MS, the sample solution is sprayed through a fused silica capillary into a chamber with a cathode. Within the chamber an electric potential between 1 — 5 kV is applied.[232] The tip of the fused silica capillary narrows to a filament. As the liquid solution flows into the filament, the Rayleigh-limit is reached.[232] Above this limit, the electrostatic repulsion of surficial charges is greater than the surface tension. Consequently, highly-charged droplets are expelled

from the filament. Evaporation of the solvent leads to an increasing charge density on the shrinking droplets' surfaces until the droplets split explosively due to the electrostatic repulsion. This process is called Coulomb-explosion.[232] Evaporation and Coulomb-explosion are repeated until single ions desorb from the droplets' surfaces. The formed ions are released from the chamber through a hole in the cathode. Afterwards, they are focused through another capillary and brought into the high vacuum chamber with the applied magnetic field.
In this work, ESI-MS is used for the characterization of all synthesized compounds in Chapter 4 which cannot be reasonably characterized by NMR.

6.1.4 High perfomance liquid chromatography

The separation and identification of chemical components in mixtures is termed chromatography. Fundamentally, chromatography requires a stationary phase, which exhibits interactions of varying strength to the various components to be separated, and a mobile phase which moves the components through the stationary phase.[233] Both gaseous and liquid mobile phases are possible. The stationary phase often consists of uniform particles like silica particles packed tightly in a so-called column. Separation of components with high performance liquid chromatography (HPLC) is based on the same principle. A small volume of the liquid sample is injected into a liquid stream moving into the HPLC column where the components of the sample mixture are separated based on their retention times. Detection is achieved by a flow-through device, usually a UV-vis detector. The biggest advantage compared to manual chromatography are the high pressures that can be applied to the mobile phase. The high pressure increases the speed, efficiency and sensitivity of the method.[233]
In this work, HPLC is used to confirm the purity of the dyad **8** in Section 4.2.

6.1.5 Differential scanning calorimetry

Differential scanning calorimetry (DSC) is a universal method to characterize physical properties of e.g. polymers. Phase transitions, such as melting, crystallization or glass transition, can be observed according to changes in heat capacity.[234] According to thermodynamics, the heat capacity at constant pressure C_p and at constant volume C_V defines the most important material properties, i.e., enthalpy H, inner energy U, entropy S and Gibbs energy G. The relations between these material properties, the heat capacity and the temperature T are shown in the following equations (6.5 – 6.8).[234]

$$H = \int_0^T C_p \mathrm{d}T \tag{6.5}$$

$$U = \int_0^T C_V \mathrm{d}T \tag{6.6}$$

$$S = \int_0^T \frac{C_p}{T} \mathrm{d}T \tag{6.7}$$

$$G = H - TS \tag{6.8}$$

The heat capacity C is in turn determined by the fundamental relationship of DSC summarized in equation (6.9).[234]

$$\frac{\partial Q}{dt} = \Phi = C\frac{dT}{dt} = c \cdot m \cdot \beta \tag{6.9}$$

The exchanged heat ∂Q or the heat flow rate Φ, the temperature changes dT and the sample mass m are measured, the heating and cooling rate β can be defined freely. Thus, the heat capacity C or the specific heat capacity $c = C/m$ can be determined with equation (6.9). Phase transitions, in particular the glass transition and melting, can be recognized according to the characteristic change of the heat capacity, or equivalently, the change of the heat flow.[234]
In this work, DSC is used for the determination of the glass transition temperatures of all polymers investigated in Chapter 4.

6.1.6 Defocused microscopy

The fundamental requirement of all spectroscopy is a transition dipole moment $\hat{\mu} \neq 0$ (see also Section 2.1). The transition dipole moment is oriented along any arbitrary axis of a molecule. Hence, rotation of a molecule generally results in rotation of the transition dipole moment. The excitation probability of a molecule dependents on both the magnitude of the transition dipole moment, as well as the orientation of the dipole moment relative to the incident light. The highest probability is achieved for an orientation of the transition dipole moment parallel to the polarization of the excitation light. The maximum emission, in contrast, occurs perpendicular to the transition dipole moment which tends to have the same orientation for absorption and emission. As emission occurs with different probability in various orientations, emission of a single molecule is defined by an according pattern. However, the transition dipole moments of freely rotating (fluorescent) molecules can adopt all possible orientations in a frequency so fast that the pattern is obscured for all currently achievable finite temporal resolutions. The inevitable temporal averaging of the patterns of individual emission events then yields a simple ring pattern.[235] Only when the rapid reorientation of the fluorophores and consequently their transition dipole moments is restricted, different characteristic patterns are recognized depending on the angle between the emitter and the detector.[235] The recognition of these patterns is only feasible when the emitter is not perfectly in focus, as the orientation pattern is otherwise obscured by the diffraction pattern. Hence, the technique is termed defocused microscopy. The time-dependent change of the patterns can be used to determine rotational diffusion.
In this work, defocused microscopy is used throughout Section 4.6 to confirm or disprove the existence of rotational restrictions of fluorophores in polymer films.

6.2 Syntheses

All chemicals except the dyes and reverse phase columns were purchased from Merck™ and used without further purification. Solvents were dried over sodium and stored over molecular sieve (3 Å). The dyes ATTO565 (NHS-ester modification) and ATTO647N (azide modification) were purchased from ATTO-Tec™. Prepacked octadecyl-modified silica gel columns (Chromabond©, C_{18} SPE PP columns,

1000 mg adsorbent weight) were purchased from Macherey-Nagel™.

6.2.1 Synthesis of methyl(2-nitrophenyl)acetate (1)

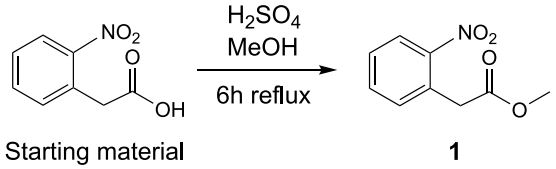

Figure 6.1: Esterification of nitrophenyl acetic acid with methanol to methyl(2-nitrophenyl)acetate (**1**).

The synthesis procedure was taken from literature.[191] 15.033 g (83 mmol) nitrophenyl acetic acid (starting material) were dissolved in methanol (MeOH, 150 mL). Concentrated sulphuric acid (H_2SO_4, 10 mL) was added dropwise. The reaction mixture was refluxed at 64 °C for 6 h. The solvent was evaporated and the residue was dissolved dichloromethane (DCM, 100 mL). The solution was neutralised with saturated K_2CO_3 solution. Afterwards, the aqueous phase was extracted with DCM. The united organic phase was dried over $MgSO_4$. The solvent was evaporated again. At lowered temperature, the ester **1** crystallised as a colourless solid (14.361 g, 74 mmol, 89%). The product was characterized with ^{1}H-NMR.

Molecular formula: $C_9H_9NO_4$, **Molecular mass:** 195.17 g mol^{-1}

^{1}H-NMR(600 MHz, $CDCl_3$, see Figure 7.74) δ/ppm 8.05 (d, $J = 12.2$ Hz, 1 H), 7.53 (t, $J = 11.2$ Hz, 1 H), 7.41 (t, $J = 11.2$ Hz, 1 H), 7.29 (d, $J = 12.2$ Hz, 1 H), 3.96 (s, 2 H), 3.65 (s, 3 H)

6.2.2 Synthesis of methyl 2-(2-nitrophenyl)pent-4-ynoate (2)

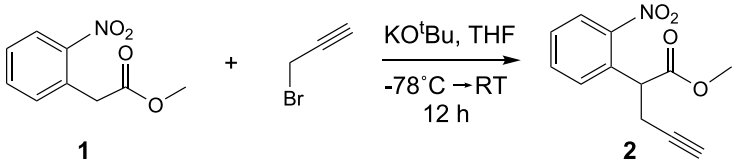

Figure 6.2: Benzylic functionalization of **1** to methyl 2-(2-nitrophenyl)pent-4-ynoate (**2**).

Compound **2** was synthesized according to literature.[192] The reaction was performed under N_2 atmosphere. The ester **1** (4.938 g, 25 mmol, 1 eq.) was dissolved in dry tetrahydrofuran (THF) (15 mL) and cooled down to −80 °C. Tertiary potassium butanolate (KO^{t}Bu, 2.985 g, 27 mmol, 1.1 eq.) was added. Dropwise, a cooled solution of propargyl bromide (3.00 mL, 4.14 g, 35 mmol, 1.4 eq.) in THF (5 mL) was added. Subsequently, the reaction mixture was slowly heated to room temperature and stirred for 20 h. At −70 °C, the reaction was quenched with saturated NH_4Cl solution. The mixture was extracted with DCM (4×50 mL). The united organic phase was washed with water and dried over $MgSO_4$. The solvent was evaporated. The raw product was purified chromatographically (silica gel, hexane/ethyl acetate (EtOAc) 4:1) to yield compound **2** as a yellow-orange oil (3.70 g, 0.016 mmol, 63%). The product was characterized with ^{1}H-NMR.

Molecular formula: $C_{12}H_{11}NO_4$, **Molecular mass:** 233.22 g mol^{-1}

^{1}H-NMR(600 MHz, $CDCl_3$, see Figure 7.75) δ/ppm 7.98 (dd, $J_1 = 8.1$ Hz, $J_2 = 1.3$ Hz, 1H), 7.62 (td, $J_1 = 7.6$ Hz, $J_2 = 1.3$ Hz, 1H), 7.53 (dd, $J_1 = 7.8$ Hz, $J_2 = 1.3$ Hz, 1H), 7.47 (td, $J_1 = 7.8$ Hz, $J_2 = 1.3$ Hz, 1H), 4.46 (dd, $J_1 = 8.3$ Hz, $J_2 = 6.2$ Hz, 1H), 3.70 (s, 3H), 3.05 (ddd, $J_1 = 17.1$ Hz, $J_2 = 6.2$ Hz, $J_3 = 2.7$ Hz, 1H), 2.85 (ddd, $J_1 = 17.1$ Hz, $J_2 = 8.3$ Hz, $J_3 = 2.7$ Hz, 1H), 1.96 (t, 2.7 Hz, 1H)

6.2.3 Synthesis of 2-(2-nitrophenyl)pent-4-yn-1-ol (3)

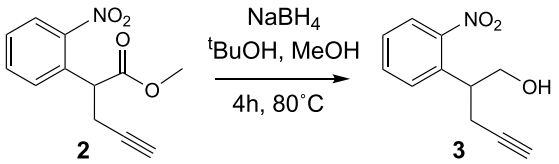

Figure 6.3: Reduction of the ester **2** to the alcohol **3**.

The reduction of compound **2** to the corresponding terminal alcohol **3** was performed according to literature.[192] The reactant **2** (1.36 g, 6 mmol, 1 eq.) was dissolved in tertiary butanol (^{t}BuOH, 40 mL). An excess of sodium borohydride ($NaBH_4$, 0.552 g, 15 mmol, 2.5 eq.) was added. The suspension was heated to 80 °C and stirred for 4 h. Small amounts of MeOH were added in regular intervals. The reaction mixture was quenched with saturated NH_4Cl solution and the pH was neutralized. Afterwards, the reaction mixture was extracted with diethyl ether (Et_2O, 3×20 mL). The residue was purified with flash chromatography (silica gel, hexane:EtOAc 3:1 $\rightarrow$ 1:1) to yield the alcohol **3** as an orange oil (581 mg, 3 mmol, 50%). The product was characterized with ^{1}H-NMR.
Molecular formula: $C_{11}H_{11}NO_3$, **Molecular mass:** 205.22 g mol^{-1}
^{1}H-NMR(600 MHz, $CDCl_3$, see Figure 7.76) 7.81 (dd, $J_1 = 8.1$ Hz, $J_2 = 1.2$ Hz, 1H), 7.61–7.56 (m, 2H), 7.40 (td, $J_1 = 7.5$ Hz, $J_2 = 1.9$ Hz), 4.02–3.97 (m, 2H), 3.64 (quint. $J = 6.5$ Hz, 1H), 2.74 (ddd, $J_1 = 17.0$ Hz, $J_2 = 6.8$ Hz, $J_3 = 2.7$ Hz, 1H), 2.67 (ddd, $J_1 = 17.0$ Hz, $J_2 = 6.9$ Hz, $J_3 = 2.7$ Hz, 1H), 1.98 (t, $J = 2.7$ Hz, 1H)

6.2.4 Synthesis of tert-butyl (2-(2-nitrophenyl)pent-4-yn-1-yl) ethane-1,2-diyldicarbamate (4, protected photocleavable linker)

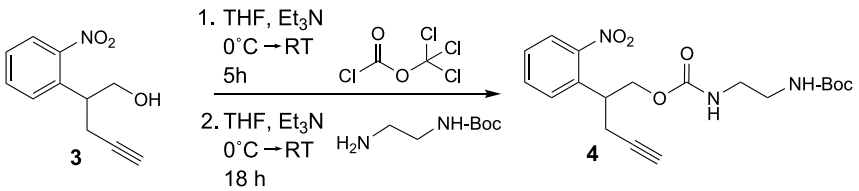

Figure 6.4: Synthesis of compound **4**.

The synthesis was adapted from literature.[193] The entire reaction was performed under a nitrogen atmosphere. Trichloromethyl chloroformate (diphosgene, 0.5 mL, 0.825 g, 4 mmol, 1.3 eq.) was dissolved in dry THF (10 mL) at 0 °C. A solution of compound **3** (580 mg, 3 mmol, 1 eq.) and triethylamine (NEt_3, 0.40 mL, 3 mmol, 1 eq.) in dry THF (15 mL) was added dropwise and stirred

for 1 h at 0 °C. The reaction mixture was stirred for another 2 h at room temperature. Next, the reaction mixture was transferred into a dropping funnel. A new solution of N-Boc-ethylene diamine (0.80 mL, 0.81 g, 5 mmol, 1.7 eq.) and NEt_3 (0.10 mL, 0.7 mmol, 0.25 eq.) in dry THF (5 mL) was prepared and cooled to 0 °C. The first reaction mixture was slowly added to the new solution and stirred for 1 h at 0 °C. Afterwards, the united reaction mixture was stirred for another 16 h at room temperature. All reactive components were quenched with water (15 mL). The mixture was extracted with EtOAc (4×30 mL), dried over $MgSO_4$ and concentrated under reduced pressure. The raw product was purified chromatographically (silica gel, hexane:EtOAc 2:1) to yield compound **4** as a yellow oil (240 mg, 0.6 mmol, 22%). The product was characterized with ^{1}H-NMR and ESI-MS.

Molecular formula: $C_{19}H_{25}N_3O_6$, **Molecular mass:** 391.42 g mol^{-1}

ESI-MS (m/z): calculated for $C_{19}H_{25}N_3O_6$ $[M+Na]^+$: 414.16, found 414.1632 (100% relative abundance, see Figure 7.80)

^{1}H-NMR(600 MHz, $CDCl_3$, see Figure 7.77) 7.83 (d, $J = 7.8$ Hz, 1H), 7.61 (t, $J = 7.4$ Hz, 1H), 7.55 (d, $J = 7.8$ Hz, 1H), 7.43 (t, $J = 7.4$ Hz, 1H), 5.08 (brs, 1H), 4.85 (brs, 1H), 4.48 (dd, $J_1 = 10.7$ Hz, $J_2 = 6.3$ Hz, 1H), 4.33 (dd, $J_1 = 10.7$ Hz, $J_2 = 7.2$ Hz, 1H), 3.84 (quint., $J = 6.5$ Hz, 1H), 3.25 (br, 4H), 2.72 (ddd, $J_1 = 17.0$ Hz, $J_2 = 10.6$ Hz, $J_3 = 2.5$ Hz, 1H), 2.68 (ddd, $J_3 = 17.0$ Hz, $J_2 = 6.8$ Hz, $J_3 = 2.5$ Hz, 1H), 2.01 (t, $J = 2.3$ Hz, 1H), 1.45 (s, 9H)

6.2.5 Synthesis of the photocleavable linker 2-(2-nitrophenyl)pent-4-yn-1-yl (2-aminoethyl)carbamate (5)

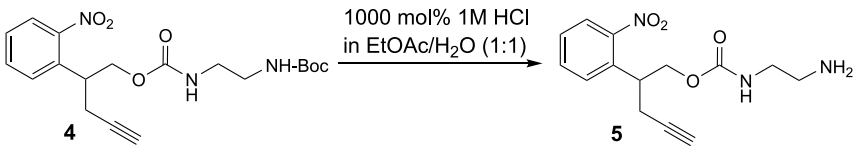

Figure 6.5: Deprotection of compound **4** to compound **5**.

The deprotection of compound **4** was performed according to the literature procedure for selective deprotection of Boc-groups in the presence of other acid-sensitive groups.[194] To compound **4** (240 mg, 0.6 mmol) was added a solution of 1000 mol% 1 M HCl in a H_2O/EtOAc emulsion (1:1, 6 mL). The reaction mixture was stirred vigorously for 4 h at room temperature. The solvent was evaporated. The raw product was purified via flash chromatography (silica gel, EtOAc:DCM:MeOH 1:0:0 $\rightarrow$ 0:9:1) to yield the product **5** as a brown powder (40 mg, 0.1 mmol, 22%). The product was characterized with ESI-MS and ^{13}C-NMR.

Molecular formula: $C_{14}H_{17}N_3O_4$, **Molecular mass:** 291.31 g mol^{-1}

^{13}C-NMR(150 MHz, decoupling at 600 MHz, $CDCl_3$, see Figure 7.79): 210.92, 156.81, 150.53, 134.54, 130.81, 129.31, 125.29, 81.24, 73.02, 69.57, 54.57, 38.14, 29.64, 23.18

ESI-MS (m/z): calculated for $C_{14}H_{17}N_3O_4$ $[M+H]^+$: 292.13, found 292.1292 (100% relative abundance, see Figure 7.81)

6.2.6 Synthesis of the reference donor (6)

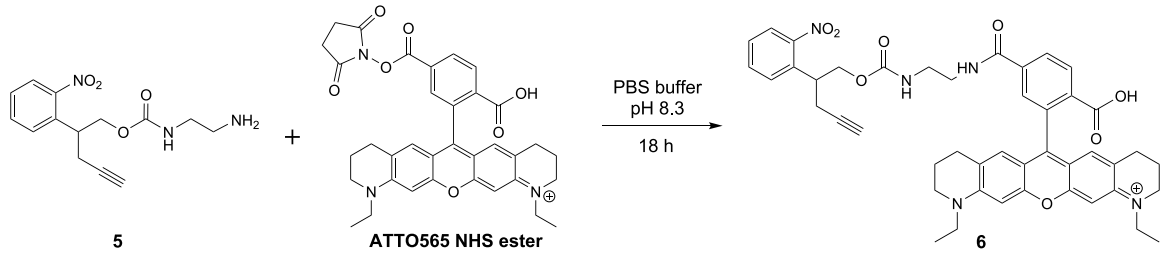

Figure 6.6: Labelling reaction with ATTO565 NHS ester to the reference donor compound (**6**).

The labeling reaction of the photocleavable linker **5** with ATTO565 NHS-ester to the donor **6** was performed according to the labeling protocol specified by the manufacturer (see also Figure 7.89). To prevent fast hydrolysis of the ATTO565 NHS-ester, the reaction was done under inert gas atmosphere. Compound **5** (1.75 mg, 6.0 µmol) was dissolved in phosphate-buffered saline (PBS, 1 mL). ATTO565 NHS-ester (1 mg, 1.4 µmol) was added and the reaction mixture was stirred for 18 h at room temperature. The solvent was evaporated. The pink residue was purified chromatographically (octadecyl-modified silica gel (reverse phase), MeOH:H_2O 1:1 $\rightarrow$ 1:0). The yield (67%) was determined with UV-Vis spectroscopy according to the Lambert-Beer law. The product was characterized with ESI-MS, UV-Vis- and fluorescence spectroscopy.

Molecular formula: $C_{45}H_{46}N_5O_8^+$ (as cation), **Molecular mass:** 784.89 g mol^{-1}

ESI-MS (m/z): calculated for $C_{45}H_{46}N_5O_8^+$ $[M]^+$: 784.33, found 784.3364 (100% relative abundance), calculated for $C_{45}H_{45}N_5O_8$ $[M+Na]^+$: 806.32, found 806.3184 (30% relative abundance, see Figure 7.82)

6.2.7 Synthesis of the reference acceptor (7)

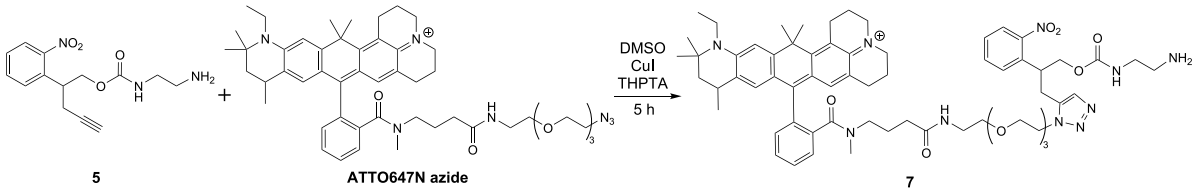

Figure 6.7: Labelling reaction of compound **5** with ATTO647N azide to the acceptor **7**.

The labeling reaction of the photocleavable linker **5** with **ATTO647N azide** to the acceptor **7** was performed according to the labeling protocol specified by the manufacturer (see also Figure 7.89). Compound **5** (0.15 mg, 0.5 µmol), tris(3-hydroxypropyltriazolylmethyl)amine (THPTA) (0.44 mg, 1.0 µmol), copper(I) iodide (CuI, 0.10 mg, 0.5 µmol) and **ATTO647N azide** (0.03 mg, 26 nmol) were dissolved in dimethyl sulfoxide (DMSO, 70 µL). The reaction mixture was shaken for 3 h at room temperature. The solvent was partly evaporated. The residue was purified with reverse phase chromatography (octadecyl-modified silica gel, MeOH:acetic acid:NEt_3 99:1:0 $\rightarrow$ 199:0:1. Reactants can be flushed out with the MeOH:acetic acid mixture. For an efficient retrieval of the product, the MeOH:acetic acid and MeOH:NEt_3 eluent mixtures have to be used alternating.) The yield (45%) was

determined with UV-Vis spectroscopy according to the Lambert-Beer law. The product was characterized with ESI-MS, UV-Vis- and fluorescence spectroscopy.
Molecular formula: $C_{64}H_{85}N_{10}O_9^+$ (as cation), **Molecular mass:** 1138.44 g mol^{-1}
ESI-MS (m/z): calculated for $C_{64}H_{85}N_{10}O_9^+$ $[M]^+$: 1137.65, found 1137.6525 (100% relative abundance, see Figure 7.83)

6.2.8 Synthesis of the dyad (8)

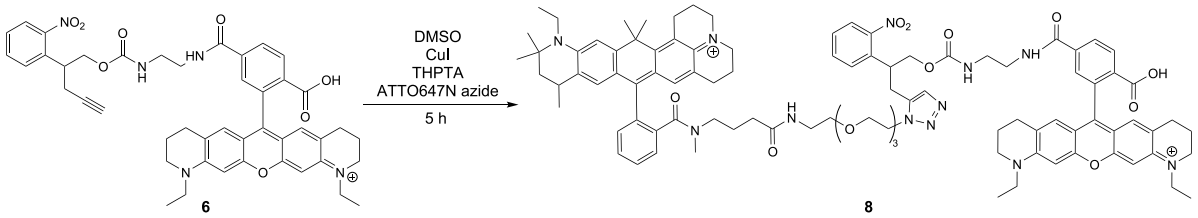

Figure 6.8: Labelling reaction of compound **6** with ATTO647N azide to the Dyad **8**.

The labeling reaction of compound **6** with ATTO647N azide to the dyad **8** was done analogously to the procedure outlined in synthesis 6.2.7 (see also Figure 7.89). To a solution of compound **6** in MeOH (80 µL, 4.7 mmol L^{-1}, 0.38 µmol) was added a solution of THPTA (0.65 mg, 1.5 µmol), CuI (0.14 mg, 0.8 µmol) and ATTO647N azide (0.18 mg, 0.18 µmol) in DMSO (365 µL). The reaction mixture was shaken for 3 h at room temperature. The solvent was partly evaporated. The residue was purified with reverse phase chromatography (octadecyl-modified silica gel, MeOH:acetic acid:NEt_3 1:0:0 $\rightarrow$ 99:1:0 $\rightarrow$ 199:0:1. Reactants can be flushed out with pure MeOH and the MeOH:acetic acid mixture. For an efficient retrieval of the product, the MeOH:acetic acid and MeOH:NEt_3 eluent mixtures have to be used alternating.) The yield (20%) was determined with UV-Vis spectroscopy according to the Lambert-Beer law. The product was characterized with ESI-MS, UV-Vis- and fluorescence spectroscopy.
Molecular formula: $C_{95}H_{114}N_{12}O_{13}{}^{2+}$ (as cation, protonated), **Molecular mass:** 1632.03 g mol^{-1}
ESI-MS (m/z): calculated for $C_{95}H_{113}N_{12}O_{13}^+$ $[M]^+$: 1630.86, found 1630.8575 (1% relative abundance, see Figure 7.84)

6.3 Spectroscopy

6.3.1 UV-Vis Spectroscopy

All absorption spectra were recorded with an Agilent Cary 60 UV-Vis spectrophotometer at room temperature. The scan range was set from 800 nm to 200 nm at a scanning speed of 300 nm min^{-1}. A baseline correction was performed with pure solvent.

6.3.2 Fluorescence Spectroscopy

All emission spectra in Chapter 3 were recorded at room temperature with a Jasco FP-6500 Spectrofluorometer. An excitation wavelength of 380 nm or 488 nm was used. The scan range was adjusted to 400 – 700 nm or 500 – 750 nm, respectively.

All emission spectra in Chapter 4 were recorded at room temperature with an Edinburgh FS5 spectrofluorometer using the standard SC-05 sample holder. An excitation wavelength of 530 nm or 600 nm was used, and the scan range was adjusted to 540 – 800 nm or 610 – 800 nm, respectively. Both excitation and emission bandwidths were set to 1 nm. The step size was set to 0.5 nm and the dwell time was set to 0.5 s. These settings, apart from the excitation and emission wavelengths, were used for all measurements in the main text. Stern–Volmer experiments were performed with 530 nm and 620 nm excitation wavelength for ATTO565 and ATTO647N, respectively. Excitation bandwidth was increased to 2.5 nm, emission bandwidth was 2.0 nm. The step size was set to 1.0 nm and the dwell time was set to 1.0 s.

6.3.3 Quantum Yields

All quantum yields in Chapter 4 were determined at room temperature with an Edinburgh FS5 spectrofluorometer using the SC-30 integrating sphere holder. An excitation wavelength of 510 nm or 600 nm was used and the scan range was adjusted to 480 – 800 nm or 570 – 800 nm, respectively. The excitation bandwidth was set to 5 nm, and the emission bandwidth to 0.3 nm. The step size was set to 0.25 nm and the dwell time to 0.5 s. These settings were used for all measurements.

6.4 Sample preparation

6.4.1 Cleaning of glass substrates

All regular glass substrates (Marienfeld GmbH, DIN ISO 8255, approx. 130 µm thickness) used for the combined FLIM and AFM measurements in Chapter 3 were first cleaned with isopropanol. All other glass substrates were cleaned with 2 v% Hellmanex©solution. Afterwards, the glass substrates were rinsed with water. Only purified water (Milli-Q©) was used for both the cleaning solution and the rinsing step. The substrates were dried at 60 °C in a heating cabinet. Finally, the substrates were plasma-cleaned for fifteen minutes with oxygen plasma (Femto Plasma-Surface-Technology, Diener Electronic).
VaHeat© substrates (SMS-SR-P-XX-XX Smart Substrate VaHeat for VA-SR: VaHeat Standard Range, Interherence/Bruker) for measurements at higher temperatures were cleaned with analytical grade solvent, in particular iso-propanol, acetone and ethanol to avoid contact of the electronics with water. The substrates were finally rinsed with spectroscopic grade MeOH and dried at 60 °C in a heating cabinet. Finally, the substrates were plasma-cleaned for five minutes with oxygen plasma (Femto Plasma-Surface-Technology, Diener Electronic). Again, the reduced time compared to regular substrates is supposed to reduce any technical defects of the sensitive electronics.
For all FEDUP measurements, plasma cleaning of any substrates, both regular and smart substrates, was typically performed one week in advance. The procedure introduces negative surface charges, which could influence the diffusion behavior of the slightly cationic probes. It is estimated that no negative surface charges remain after several days of storage in a closed nontransparent plastic box.

6.4.2 TCSPC

Approximately 16 µL of dye solutions (approx. 3×10^{-9} mol L^{-1}) in either toluene, methanol or water were sealed airtight between two coverslips (Marienfeld GmbH, DIN ISO 8255, approx. 130 µm thickness). The sealing was accomplished with an imaging spacer (SecureSeal™, 1 well, diameter 8 – 20 mm, thickness 9 – 13 mm). For lifetime measurements in PS films, a 2 wt% PS solution in toluene was stained with the respective dye solution. A drop of the solution was spincoated onto a clean coverslip.

6.4.3 PAINT

The microgel sample was spincoated onto a clean coverslip. About 100 µL of an approximately 5×10^{-11} mol L^{-1} aqueous Nile Red solution was added.

6.4.4 FLIM

Microgel samples

The microgel suspensions (approx. 0.1 mg mL^{-1}) were either spincoated or drop-casted onto a clean coverslip (see Section 6.4.1). The substrate was placed onto the microscope without further preparation.

PHMA networks

The PHMA networks were prepared as described in literature.[50] Hexyl methacrylate was mixed with dibenzoylperoxide as initiator, 0.98 wt% tetraethylene glycol dimethacrylate and 0.02 wt% BTD crosslinker. The mixture was put in a Teflon mold directly on a coverslip and stored for 6 h at 60 °C under nitrogen atmosphere. Films of varying thickness were produced.

6.4.5 FEDUP

To a polymer solution (2 – 8 wt%, solvent and concentration depending on the polymer) was added dyad **8** (or donor **6** / acceptor **7**) in picomolar concentrations (final concentration $c \approx 1 - 50 \times 10^{-12}$ mol L^{-1}). The dyad was typically pre-dissolved to low concentrations in MeOH or H_2O, depending on the solvent of the polymer solution. Approximately 20 µL of the measurement solution were spincoated onto clean coverslides (see Section 6.4.1). It was taken care that only plasma-cleaned glass pipettes were used during the entire sample preparation. The spincoated samples were stored overnight under reduced pressure at up to 40 °C above the T_g to remove remaining solvent and release mechanical stress. The heating device was incapable of reaching temperatures above $T > 100$ °C, therefore polymer samples with particularly high T_g were annealed at approximately 90 °C instead.
VaHeat© substrates (SMS-SR-P-XX-XX Smart Substrate VaHeat for VA-SR: VaHeat Standard Range, Interherence/Bruker) for measurement at higher temperatures were treated equally. However, during the spincoating the electric contacts had to be protected with sticky foil in order to prevent polymer film from blocking the contacts.

6.5 Confocal microscopy

6.5.1 Lifetime measurements and FCS

All lifetimes were determined at room temperature with time correlated single photon counting (TCSPC) using a customized Picoquant Microtime 200 setup. FCS curves were recorded on the same setup under the same conditions. Samples prepared according to Section 6.4.2 were placed on an Olympus IX83 inverted fluorescence microscope. A 60x water objective (Olympus UPLSAPO60XW, NA = 1.20) was used. For the measurements in Chapter 3, a white laser (NKT Photonics, SuperK EVO) set to 488 nm was employed. The laser was reflected by a dichroic mirror (Chroma, zt 488 RDC). As emission filters a 500 nm long pass filter (Semrock, 500 LP Edge) and 715 nm short pass filter (Semrock, BrightLine HC Shortpass Filter 715/SP) were used. For the measurements in Chapter 4, the white-light NKT laser was set to 527 nm or 635 nm and reflected into the microscope by a dichroic mirror (Di03-R532-t3-25×36 for 527 nm and Di03-R405/488/532/635-t3-25×36 for 635 nm, both Semrock). The fluorescence light was guided back through the same dichroic mirrors. For measurements with 527 nm excitation, an additional 532 long pass filter (532 LP Edge Basic, Semrock) and a 582/75 band pass filter (582/75 BrightLine HC, Semrock) or a 685/70 band pass filter (685/70 ET, Chroma) were placed in the optical path. For measurements with 635 nm excitation, a 655 long pass filter (655 LP ET, Chroma) in combination with a 685/70 band pass filter (685/70 ET, Chroma) were used. The light was further guided through a 100 µm pinhole and recorded on a SPAD (SPCM-AQRH, Excelitas). For FCS, the confocal volume was determined using the standard ATTO655 in water. The accuracy of the TCSPC was tested with the standard Rhodamine 6G in water.

6.5.2 FLIM

FLIM measurements were performed with an Olympus IX83 inverted microscope. A MicroTime 200 (PicoQuant) in combination with a galvano scanner (PicoQuant, FLIMbee) and picosecond histogram accumulating real-time processor (PicoQuant, PicoHarp 300) is used to achieve the necessary temporal resolution. A white laser (NKT Photonics, SuperK EVO) set to 488 nm was employed. The laser was reflected by a dichroic mirror (Chroma, zt 488 RDC) into either an 60x water objective (Olympus UPLSAP60XW, NA = 1.20) for microgel samples or a 100x oil objective (Olympus, U Apo N Oil 100x, NA = 1.49) for polymer films. As emission filters a 500 nm long pass filter (Semrock, 500 LP Edge) and 715 nm short pass filter (Semrock, BrightLine HC Shortpass Filter 715/SP) were used. The light was further guided through a 100 µm pinhole and recorded on a SPAD. The pixel dwell time was set to 1.3 – 3 µs. The measurement and the analysis of the data was performed with the SymPhoTime 64 software (PicoQuant). The intensity decay curves were fitted with n-exponential tail fits and FLIM fit was performed.

6.6 Irradiation experiments

All irradiation experiments were performed in a custom-made Quantum Yield Determination Setup (QYDS).[236] An LED was placed in a lightproof box. Depending on the experiment, a 365 nm LED operated at $U = 3.25$ V and $I = 0.08$ A (measured power density = 400 – 450 $\mathrm{W\,m^{-1}}$), a 400 nm LED

operated at $U = 3.0$ V and $I = 0.16$ A (measured power density = 210 $W\,m^{-1}$), a 455 nm LED operated at $U = 2.7$ V and $I = 0.07$ A (measured power density = 350 $W\,m^{-1}$), a 567 nm LED operated at $U = 2.7$ V and $I = 0.09$ A (measured power density = 112 $W\,m^{-1}$), or a 645 nm LED operated at $U = 2.48$ V and $I = 0.99$ A (measured power density = 1.675 $kW\,m^{-1}$) was used. The light was guided through a lens to illuminate the sample in a constantly stirred cuvette homogeneously in a 1 cm^2 area. Behind the sample holder a 555 short pass filter (ET 555 SP, AHF) was placed to eliminate all fluorescence light for measurements with LEDs of lower wavelength in Chapter 4. For measurements with the 645 nm LED, an OD1 filter was implemented. The irradiation power was measured with a calibrated solar cell. For this purpose, a cuvette filled only with the used solvent was placed in the sample holder and the power behind the cuvette was measured. At preset time intervals, the irradiation was stopped with a manually controlled shutter. The exact irradiation time and power at the time of the shutter closing was recorded with a custom LabView script.

6.7 Widefield microscopy

6.7.1 PAINT measurements

All measurements were performed with an inverted fluorescence microscope (IX-83, Olympus) employing a 100x 1.3 NA oil immersion objective (UPLFLN 100XO2, Olympus). Illumination was achieved with a 488 nm diode laser (Cobolt MLD, 200 mW). The beam was guided through a beam expander (BE06R/M, Thorlabs) and a widefield lens (LA1380-A, $f = 500$ mm, Thorlabs) and finally reflected into the microscope by a dichroic mirror (ZT488/640rpc-UF2, Chroma). A combination of a 510 nm long pass filter (ET510 LP, Semrock) and a 770 nm short pass filter (Multiphoton-Emitter HC 770/SP, Semrock) served as emission filters. The emission light was channeled through two further magnification lenses (AC245-200-A, $f_1 = 200$ mm and AC254-400-A, $f_2 = 400$ mm, Thorlabs) and imaged on an EMCCD chip (Andor iXon 897, 512×512 pixels, pixel size 16 µm). 3D measurements were performed with astigmatism. To this end, a cylindrical lens of focal length 500 mm was implemented after the last magnification lenses. The overall imaging pixel size was 80 nm. Individual frames were recorded with an exposure time of 20 ms with a readout rate of 17 MHz at 16-bit, a pre-amplifier gain of 3 and an EM gain of 150. Localization and drift correction was performed with the ThunderSTORM[201] ImageJ plug-in. Images were generated with ViSP[237] or with custom Mathematica scripts.

6.7.2 FEDUP measurements

FEDUP measurements at room temperature

The samples prepared according to Section 6.4.5 were placed on an Olympus IX-83 inverted fluorescence microscope. A 100x oil objective (Olympus UPLAPO100XOHR) was used. A 561 nm laser (Cobolt, Jive 150, 0.006 – 0.04 $kW\,cm^{-2}$ depending on the measurement) was used for the excitation of the donor dye, a 640 nm laser (Cobolt, Rogue 1000, 0.003 – 0.03 $kW\,cm^{-2}$ depending on the measurement) was employed to control for acceptor dye fluorescence. Photocleavage was performed with a 378 nm laser (Toptica, iBeam-Smart-375-S, 0.05 – 0.1 $kW\,cm^{-2}$ depending on the measurement). All three

lasers were guided along the same path through a beam expander (Thorlabs, BE06R/M), a widefield lens (Thorlabs, ACT508-400-A-ML) and finally reflected into the microscope by the same dichroic mirror (Chroma, ZT405/488/561/640rpc-UF2). Alternating laser excitation as well as a defined time interval for UV-irradiation were ensured via a custom LabView routine. A 561 nm notch filter (Chroma, ZET561NF) was used as primary emission filter. The fluorescence light was spectrally split into two spatially identical wavelength channels on the same camera using an Optosplit (Cairn Research, Optosplit II) with an implemented dichroic mirror (Chroma, ZT 640 RDC flat). In the short wavelength channel, a 570 nm long pass filter (Chroma, 570 LP ET) and a 633 nm short pass filter (Chroma, 633 SP Edge Basic) were employed. In the long wavelength channel, a 655 nm long pass filter (Chroma, 655 LP ET) was used. The measurements were recorded with a camera (pco.edge 4.2 CLHS (s)CMOS, 6.5 µm pixel size). The camera exposure time varied between 200 – 300 ms. Measurements were performed either in Köhler or TIRF illumination (see below).

FEDUP measurements at elevated temperatures

The same setup as described above was used. The VaHeat substrates were set to the desired temperature via software control. The temperature was set to its target value about 1 h before the first measurement to reach the thermal equilibrium. Due to a generally worse SNR than at room temperature, laser power densities are generally higher for measurements at elevated temperatures (upper limit of the laser powers defined above).

Argon flow

The Argon for all FEDUP measurements with additional Argon flow was channeled through a hose attached to an open syringe. The syringe was aimed directly at the focused field of view of any sample. The sample holder was additionally covered to minimize losses of Argon. The Argon pressure at the final valve was set to approximately 0.5 bar overpressure compared to ambient pressure.

TIRF

TIRF was either employed to increase the SNR, or if the defocused microcopy measurements indicate rotational restrictions of the dyes. Objective-based TIRF was used in all cases (see also Section 2.3.2). To this end, the incident angle of all lasers was changed by a collective movement of the widefield lens and last directing mirror until the SNR visibly reached its maximum.

6.7.3 Defocused microscopy

Defocused microscopy measurements were performed on the same setup as the one described in Section 6.7.2, using the 640 nm laser (Cobolt, Rogue 1000). Signals in the acceptor channel (640 nm excitation, emission $\lambda > 655$ nm) were first brought into focus. Then, the focus was manually changed to a focal plane above the focal plane of the fluorophores until the full diffraction patterns of the signals reached maximum visibility. About ten frames were recorded with a camera exposure time of 200 ms.

6.8 AFM

All AFM measurements were performed with a *JPK Instruments NanoWizard 3* microscope in tapping mode. The employed cantilever (Bruker, *OTESPA-R3*) has a nominal frequency of 300 kHz, a nominal spring constant of 26 $\mathrm{N\,m^{-1}}$ and a rectangular geometry with a nominal tip radius of 7 nm. The backside of the cantilever is coated with reflective aluminum. The cantilever and the associated infrared (IR) laser were aligned manually via a 20x air objective (Olympus Plan N Air 20x, NA = 0.4) mounted on an Olympus IX53 inverted microscope. The laser was positioned on the backside of the cantilever and the detector position was optimized to achieve the highest voltage. The resonance frequency and the spring constant were measured via the thermal noise method. The spring constant varied between 32 $\mathrm{N\,m^{-1}}$ and 35 $\mathrm{N\,m^{-1}}$, the resonance frequency varied between 252.3 kHz and 256.3 kHz for all all measurements. The drive frequency was manually set to approximately 80% of the amplitude maximum. Image size, resolution, scan speed, setpoint and gain were varied depending on the measurement. Analysis of the data was achieved with the open source software *Gwyddion*. Typical post-processing steps include leveling of the data, application of basic filters, correction of horizontal scars and setting the lowest height value to zero, corresponding to the surface of the glass substrates. The AFM belongs to the Institute of Physical Chemistry at RWTH Aachen University.

6.9 DLS

All DLS measurements were performed with an ALV setup from ALV GmbH (ALV-5000/EPP Multiple Tau Digital Correlator, ALV goniometer, equipped with a laser (λ = 633 nm) and two avalanche photodiodes). A toluene bath was employed to index-match the surrounding medium. An external programmable thermostat (JULABO GmbH) was used to regulate the temperature. Highly dilute suspensions were used to avoid multiple scattering. All suspensions were filtered through a 1.2 µm pore to get rid of dust particles. Heating and cooling cycles were performed in 5 °C temperature steps from 20 °C to 50 °C. At each temperature, angles between 30° and 90° were measured with either 5° or 10° steps. The data was analyzed with a custom Excel script. The DLS apparatus belongs to the Institute of Physical Chemistry at RWTH Aachen University.

6.10 NMR

All ^{1}H-NMR spectra were recorded with the *Varian VNMRS 600* at 600 MHz belonging to the Institute of Organic Chemistry at RWTH Aachen University. Samples were dissolved in deuterated chloroform ($CDCl_3$), deuterated water (D_2O) or deuterated methanol (CD_3OD) and scanned in a range of about 0 to +12 ppm. ^{13}C-NMR spectra were recorded with the same spectrometer with an observation frequency of 150 MHz and a decoupling frequency of 600 MHz. Analysis of the spectra was performed with the software MestReNova.

6.11 MS

All MS measurements employed ESI as ionization method. Measurements were performed with the *ThermoFinnigan LCQ Deca XP plus* mass spectrometer at the Institute of Organic Chemistry at RWTH Aachen University.

6.12 HPLC

Additional purification of dyad **8** with HPLC was performed at the Institute of Organic Chemistry at RWTH Aachen University. A reverse phase column was used. Eluent was methanol with 0.02% acetic acid and 0.01% trifluoroacetic acid. Detection was achieved by a UV-absorption scanner.

6.13 DSC

All DSC measurements were performed with *Netzsch DSC 204 F1 Phoenix* belonging to the Institute of Building Materials Research at RWTH Aachen University. Heating/cooling rates of 20 $\mathrm{K\,min^{-1}}$ were employed. Samples were placed in aluminum crucibles with perforated caps. The glass transition temperature was determined during the second heating cycle, if possible.

7 Supplementary information

7.1 Spectra

7.1.1 Absorption coefficients of BTD reference compounds

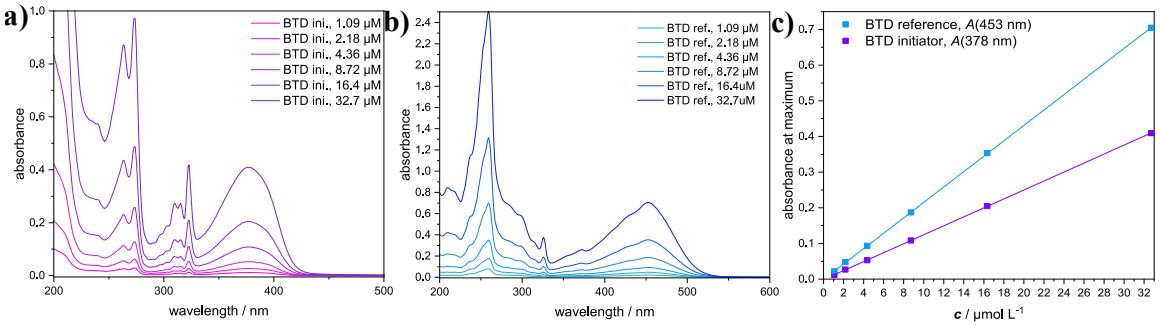

Figure 7.1: Absorption spectra at different defined concentrations of (**a**) the BTD initiator (shades of violet) and (**b**) the BTD reference (shades of blue) in MeCN. (**c**) Determination of the absorption coefficient ε at the most red-shifted local maxima of the BTD initiator (violet, $\varepsilon_{\text{BTD ini.}} = 12600\ \text{L}\,\text{mol}^{-1}\,\text{cm}^{-1}$) and the BTD reference (blue, $\varepsilon_{\text{BTD ref.}} = 21600\ \text{L}\,\text{mol}^{-1}\,\text{cm}^{-1}$) with the Lambert-Beer law (equation (2.9))

7.1.2 Irradiation experiments

Irradiation of BTD reference compounds at 400 nm

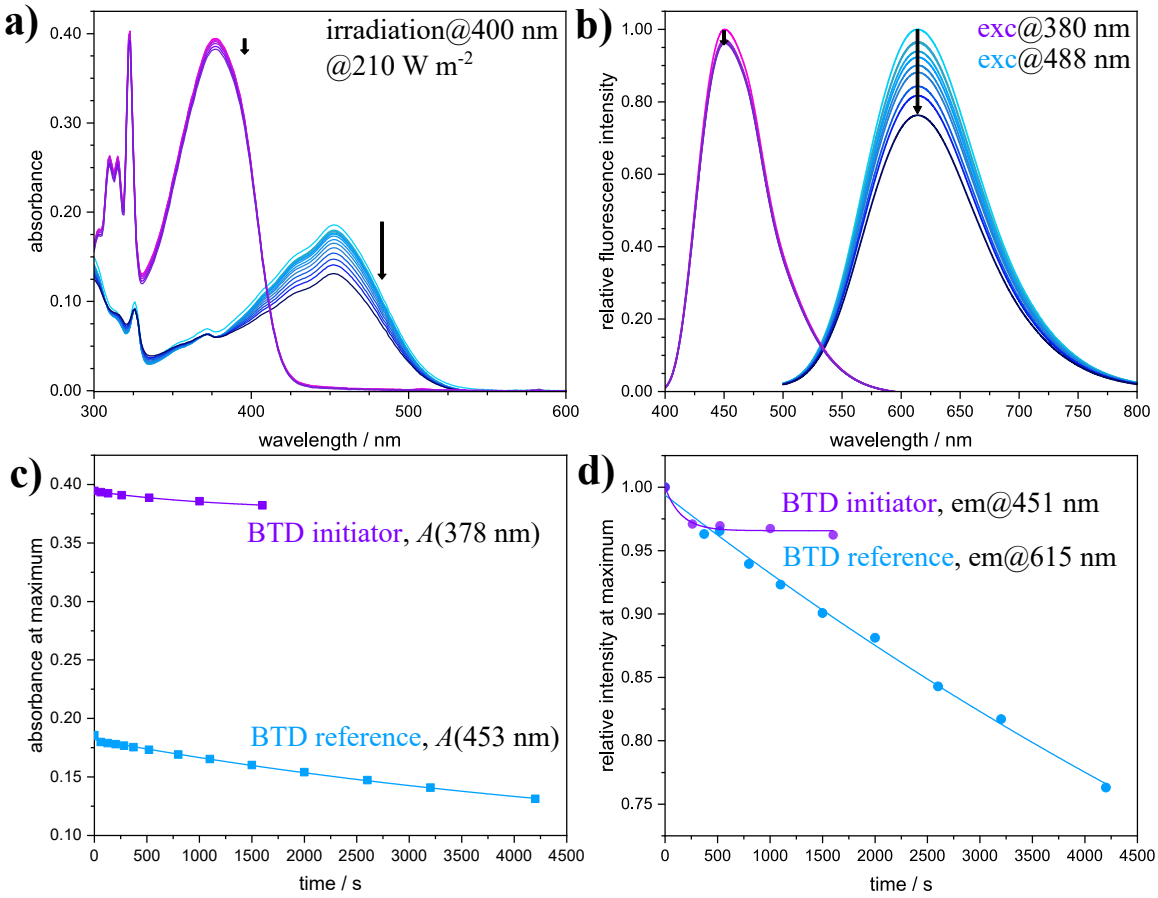

Figure 7.2: Spectral changes of BTD initiator and BTD reference in MeCN during selected irradiation times with a 400 nm LED @ 210 $W m^{-2}$. Changes of (**a**) absorption spectra and (**b**) relative emission spectra at 380 nm and 488 nm excitation for the BTD initiator (light to dark violet) and the BTD reference (light to dark blue) respectively. The black arrows indicate the changes with increasing irradiation time. Emission intensity is given relative to the maximum intensity of the respective compound at 0 s irradiation. (**c**) Temporal evolution of the absorbance at the different wavelengths of the (local) maxima shown in (**a**). (**d**) Temporal evolution of the relative fluorescence intensities at the different wavelength of the (local) maxima depicted in (**b**). All solid lines in (**c**) and (**d**) represent fits with single exponential decay functions. The colors correspond to the primary colors of the color gradients used for the spectra of the different compounds in (**a**) and (**b**).

Irradiation of dyad 8 with green light

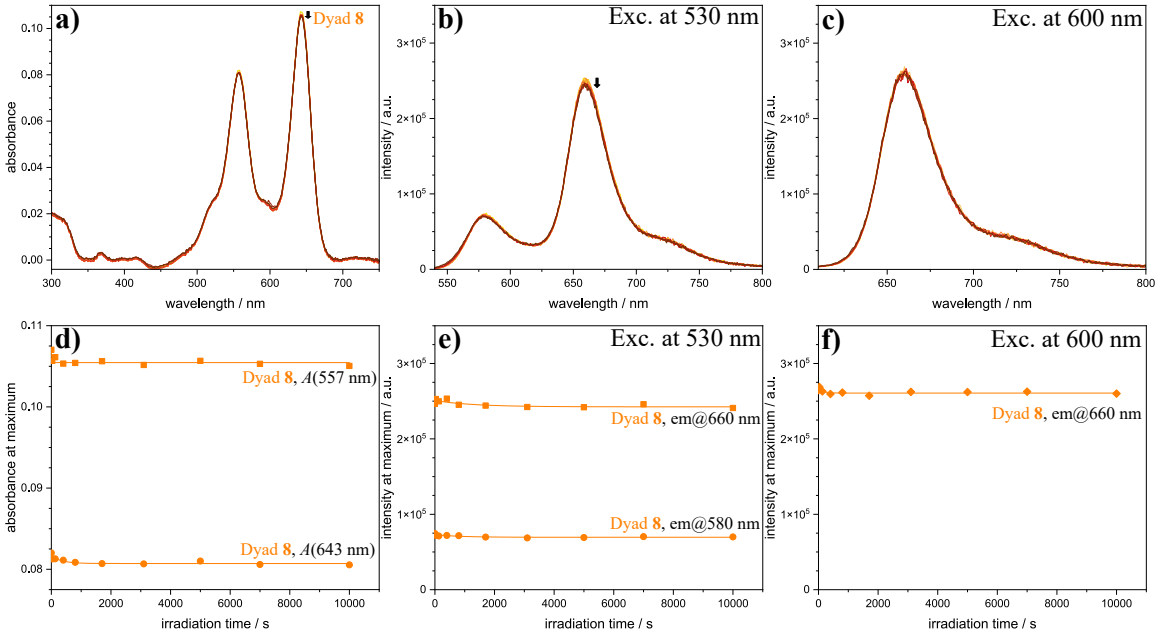

Figure 7.3: Spectral changes of the dyad **8** in methanol during selected irradiation times with a 567 nm LED @ 112 $W\,m^{-2}$. The first column from the left shows the changes of absorption spectra, the second column depicts changes of emission spectra at 530 nm excitation and the third column represents changes of the emission spectra at 600 nm excitation. Changes of (a) absorption and (b) / (c) emission spectra the dyad **8** (light to dark orange), respectively. The black arrows in subfigures (a) – (c) indicate the changes with increasing irradiation time. (d) Temporal evolution of the absorbance at the different wavelengths of the (local) maxima shown in (a). (e) Temporal evolution of the fluorescence intensities (excitation at 530 nm) at the different wavelengths of the (local) maxima depicted in (b). (f) Temporal evolution of the fluorescence intensities (excitation 600 nm) at the different wavelengths of the (local) maxima presented in (c) In subfigures (d) – (f), circles refer to absorbance and emission maxima values related to the ATTO565 chromophore, while squares denote absorbance and emission maxima values related to the ATTO647N chromophore. All solid lines represent fits with single exponential decay functions. The colour corresponds to the primary colour of the colour gradient used for the spectra in subfigures (a) – (c).

7.1.3 Emission map of ATTO647N

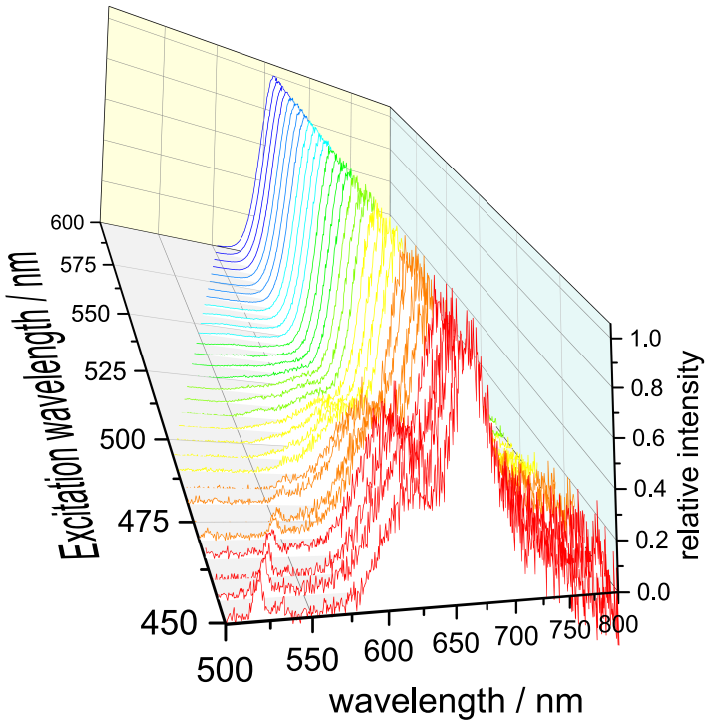

Figure 7.4: Emission map of ATTO647N azide. The excitation wavelength was varied in 5 nm steps from 450 – 600 nm. The fluorescence intensity was normalized relative to the maximum value of each spectrum, respectively.

7.1.4 Comparison of dyad 8 in water and methanol

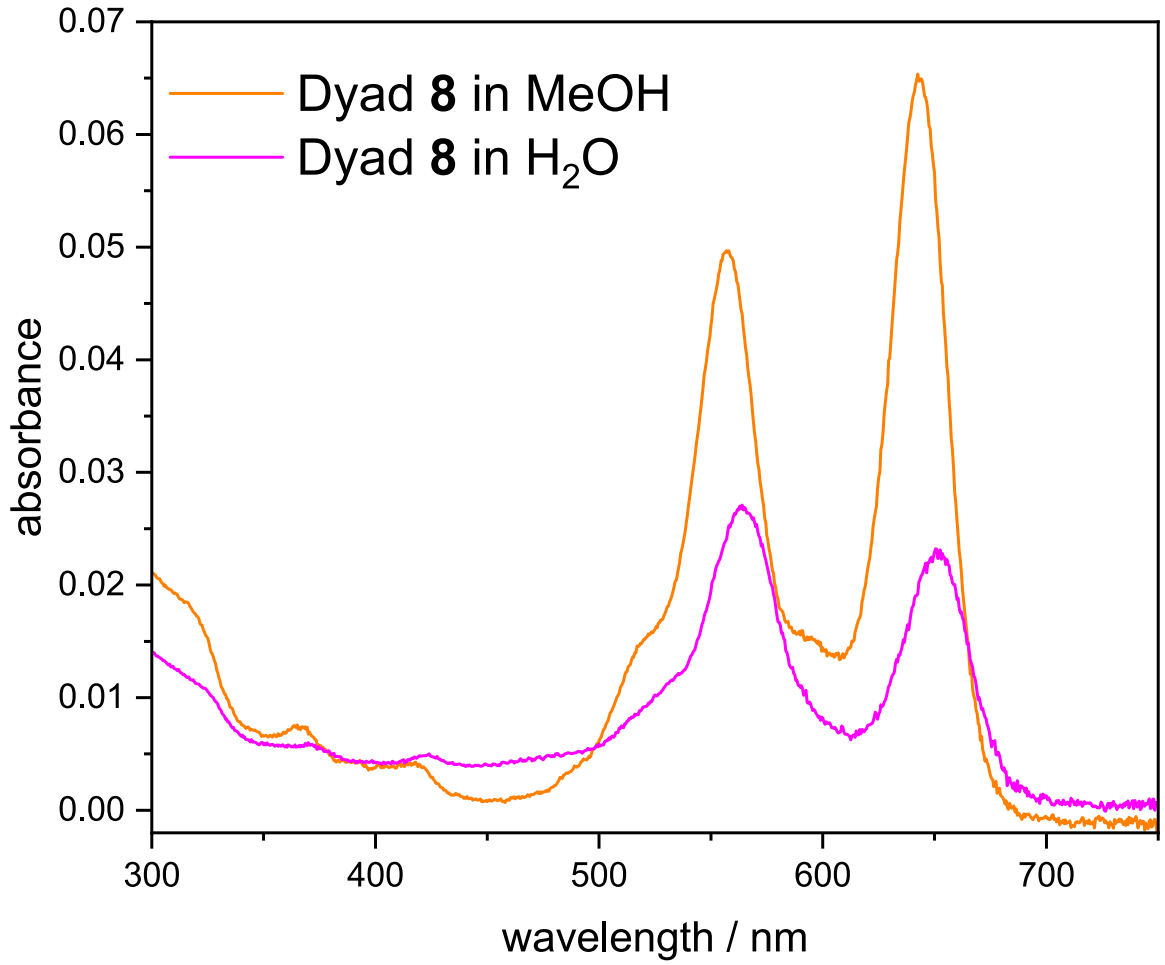

Figure 7.5: Absorption spectra of the exact same amount of dyad **8** dissolved in methanol (orange) and water (pink).

7.1.5 Stern-Volmer Analysis

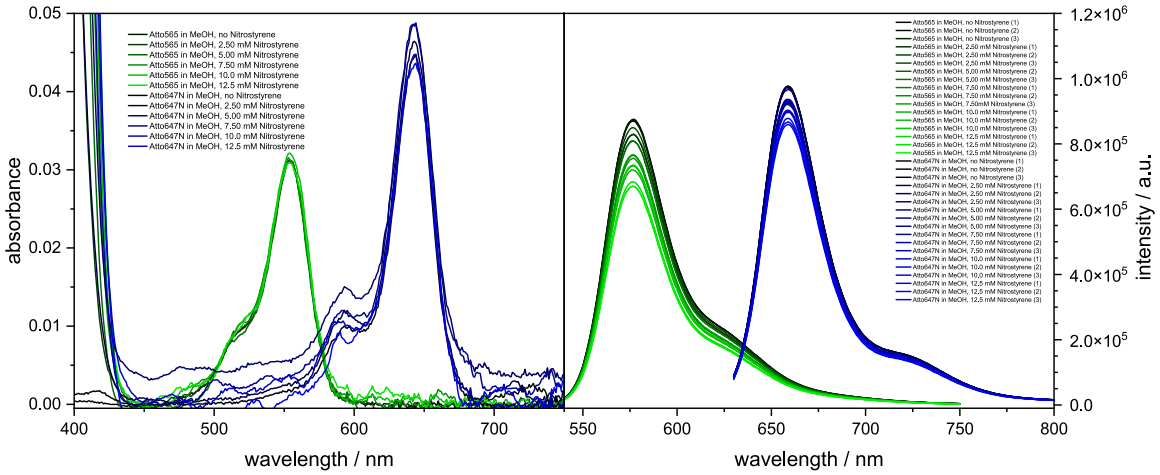

Figure 7.6: Absorption and fluorescence spectra of ATTO565 and ATTO647N in methanol with 4-nitrostyrene as quencher. The dyes were kept at constant concentration of approximately 0.25 µmol L^{-1}, the quencher was varied between 2.50 mM – 12.50 mM in 2.50 mM steps (dark green to light green for ATTO565 and black to blue for ATTO647N, respectively). Each solution was prepared and measured three times. Excitation wavelength were 530 nm and 620 nm, respectively.[59]

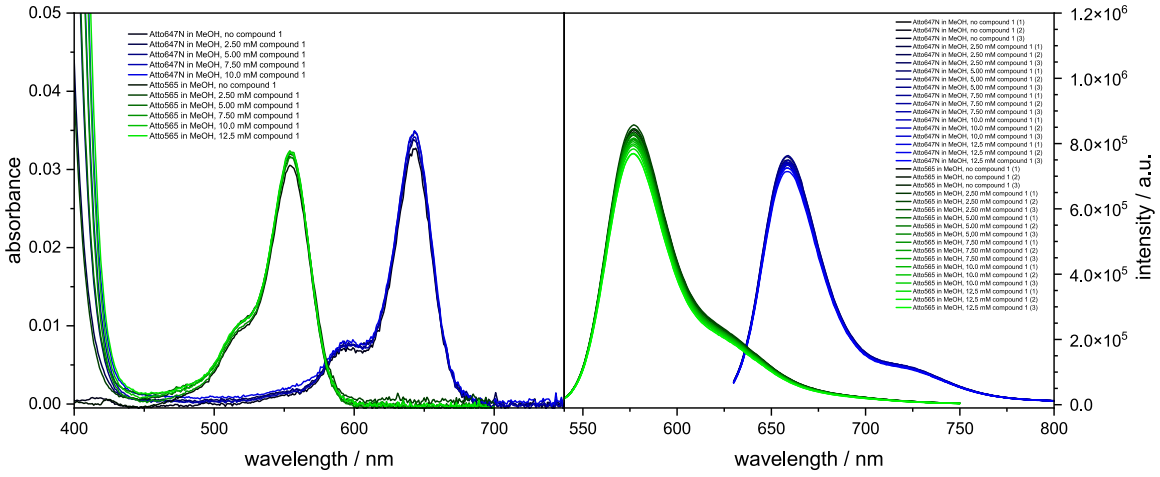

Figure 7.7: Absorption and fluorescence spectra of ATTO565 and ATTO647N in methanol with compound **1** as quencher. The dyes were kept at constant concentration of approximately 0.25 µmol L^{-1}, the quencher was varied between 2.50 mM – 12.50 mM in 2.50 mM steps (dark green to light green for ATTO565 and black to blue for ATTO647N, respectively). Each solution was prepared and measured three times. Excitation wavelength were 530 nm and 620 nm, respectively.[59]

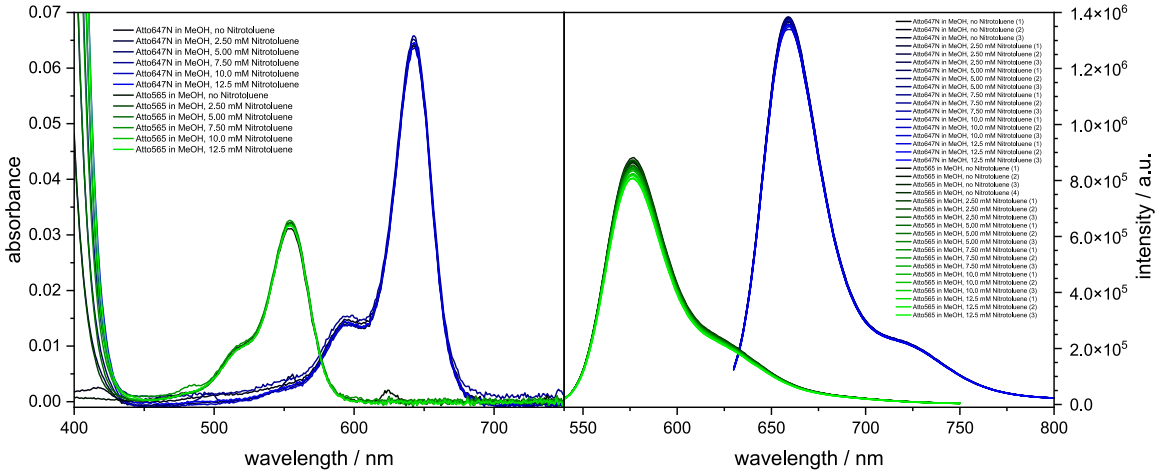

Figure 7.8: Absorption and fluorescence spectra of ATTO565 and ATTO647N in methanol with nitrotoluene as quencher. The dyes were kept at constant concentration of approximately 0.25 µmol L^{-1}, the quencher was varied between 2.50 mM – 12.50 mM in 2.50 mM steps (dark green to light green for ATTO565 and black to blue for ATTO647N, respectively). Each solution was prepared and measured three times. Excitation wavelength were 530 nm and 620 nm, respectively.[59]

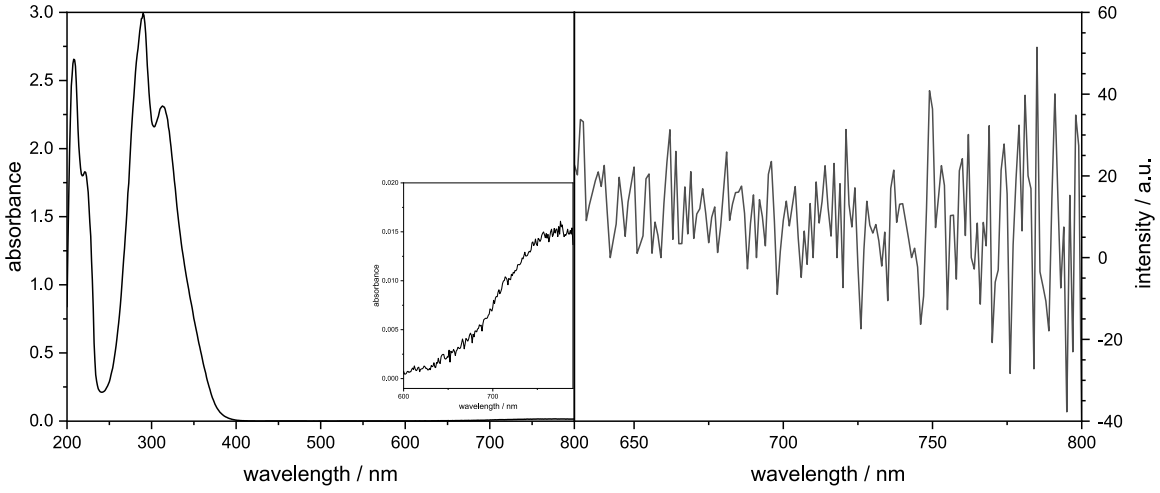

Figure 7.9: Absorption and emission spectra of 2-nitrosotoluene in methanol at 0.25 mM. Excitation wavelength was 620 nm. No emission was detectable. The inset in the absorption spectrum shows the absorption above 600 nm in closer detail.[59]

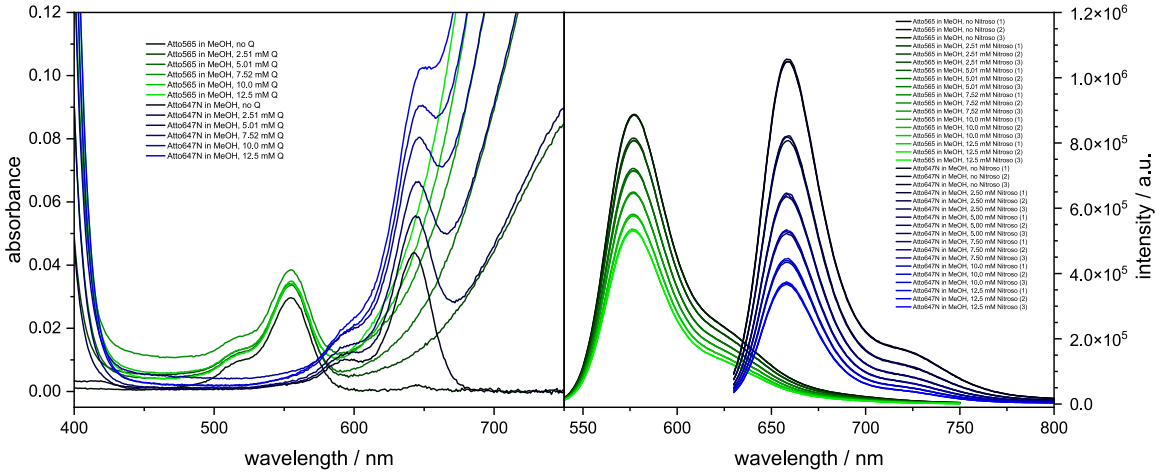

Figure 7.10: Absorption and fluorescence spectra of ATTO565 and ATTO647N in methanol with 2-nitrosotoluene as quencher. The dyes were kept at constant concentration of approximately 0.25 µmol L^{-1}, the quencher was varied between 2.50 mM – 12.50 mM in 2.50 mM steps (dark green to light green for ATTO565 and black to blue for ATTO647N, respectively). Each solution was prepared and measured three times. Excitation wavelength were 530 nm and 620 nm, respectively.[59]

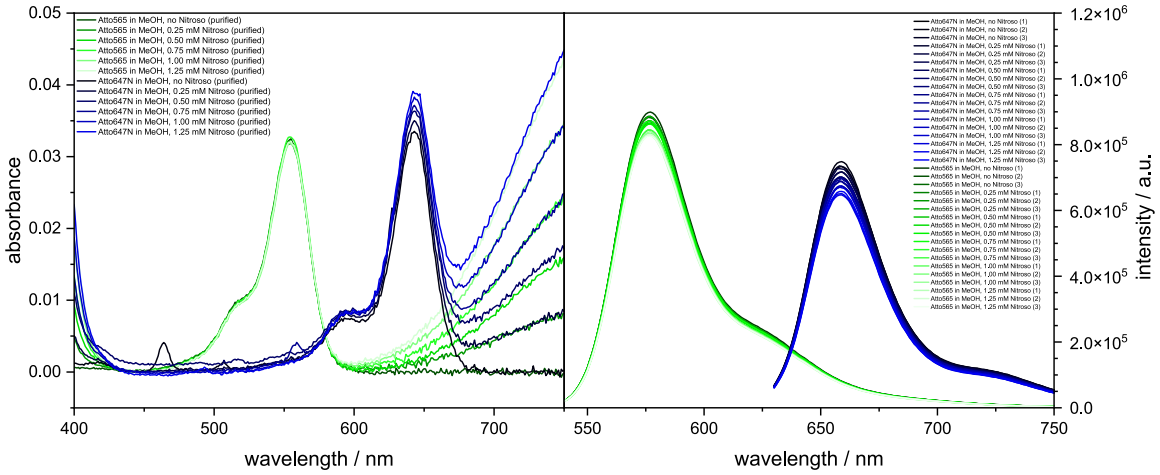

Figure 7.11: Absorption and fluorescence spectra of ATTO565 and ATTO647N in methanol with purified 2-nitrosotoluene as quencher. The dyes were kept at constant concentration of approximately 0.25 µmol L^{-1}, the quencher was varied between 0.25 mM – 1.25 mM in 0.25 mM steps (dark green to light green for ATTO565 and black to blue for ATTO647N, respectively). Each solution was prepared and measured three times. Excitation wavelength were 530 nm and 620 nm, respectively.[59]

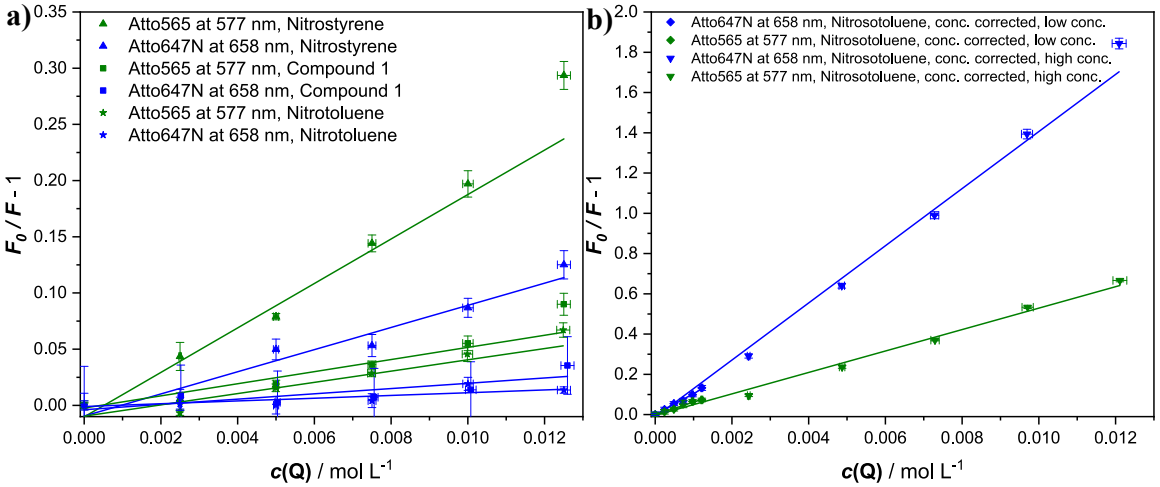

Figure 7.12: Stern-Volmer plots of ATTO565 NHS-ester and ATTO647N azide with different quenchers in methanol using the data presented in figures 7.6 – 7.11. All data related to the ATTO565 chromophore is coloured olive, all data related to the ATTO647N chromophore is coloured blue. In graph **a)**, all quenchers contain a nitro moiety, in graph **b)** all quenchers contain a nitroso moiety. Upright triangles correspond to 4-nitrostyrene, squares correspond to compound **1**, stars correspond to 2-nitrotoluene and downright triangles correspond to nitrosotoluene as quencher, respectively.[59]

Table 7.1: Quenching constants of ATTO565 NHS-ester and ATTO647N azide for different quenchers in methanol solutions. For the calculation of the bimolecular quenching constants k_q the lifetimes of the dyes were used as determined in the main text. Stern-Volmer quenching behaviour was assumed for each quencher. The Stern-Volmer constant K_{SV} corresponds to the slopes of the linear fits presented in figure 7.12 **a)** and **b)**

quencher	dye	K_{SV} / L mol^{-1}	intercept	R^2	k_q / 10^9 L mol^{-1} s^{-1}
2-nitrosotoluene (low conc.)[a,b]	ATTO565	62.9 ± 4.1	-0.0008 ± 0.003	0.979	15.2 ± 0.97
2-nitrosotoluene (low conc.)[a,b]	ATTO647N	104.5 ± 5.5	-0.0002 ± 0.004	0.987	24.3 ± 1.29
2-nitrosotoluene[a]	ATTO565	53.3 ± 1.8	-0.004 ± 0.007	0.994	12.5 ± 0.40
2-nitrosotoluene[a]	ATTO647N	141.9 ± 5.4	-0.01 ± 0.02	0.993	33.0 ± 1.26
4-nitrostyrene	ATTO565	19.8 ± 2.2	-0.01 ± 0.01	0.941	4.79 ± 0.53
4-nitrostyrene	ATTO647N	9.9 ± 1.2	-0.01 ± 0.008	0.934	2.29 ± 0.27
compound **1**	ATTO565	5.4 ± 0.7	-0.002 ± 0.004	0.920	1.30 ± 0.17
compound **1**	ATTO647N	2.4 ± 0.8	-0.004 ± 0.007	0.583	0.55 ± 0.19
2-nitrotoluene	ATTO565	5.0 ± 1.3	-0.01 ± 0.006	0.748	1.21 ± 0.30
2-nitrotoluene	ATTO647N	1.2 ± 0.3	-0.001 ± 0.003	0.749	0.29 ± 0.07

a) The concentration of 2-nitrosotoluene was corrected for the mole fraction of dimer in solution according to the equilibrium as approximated in figure 7.73. We assume negligible quenching contribution from the dimer.
b) 2-nitrosotoluene purchased from Merck™ was purified via flash chromatography (silica, DCM:MeOH 20:1) and the concentration was reduced compared to the second measurement to avoid possible secondary effects due to the absorption band of nitrosotoluene in the visible region, compare figure 7.9.

7.2 TCSPC curves

7.2.1 Lifetimes of the mechanofluorophore reference compounds

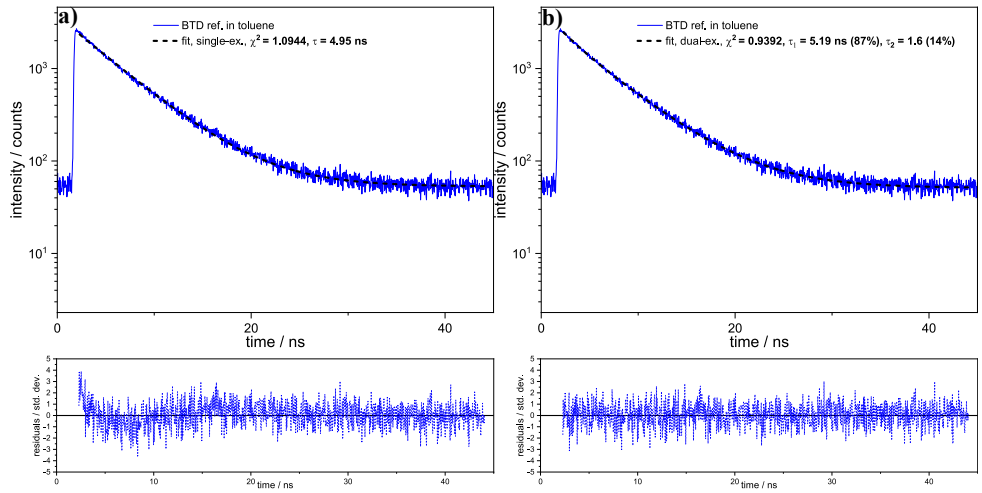

Figure 7.13: TCSPC curves of the activated BTD reference compound in toluene. Excitation wavelength was 488 nm, the observed spectral window was from 532 – 715 nm. In graph **a)**, the curve was fitted with a single exponential tail fit. In graph **b)**, the same data was fitted with a dual exponential tail fit. Below the curves, the residuals of the fits are given as well.

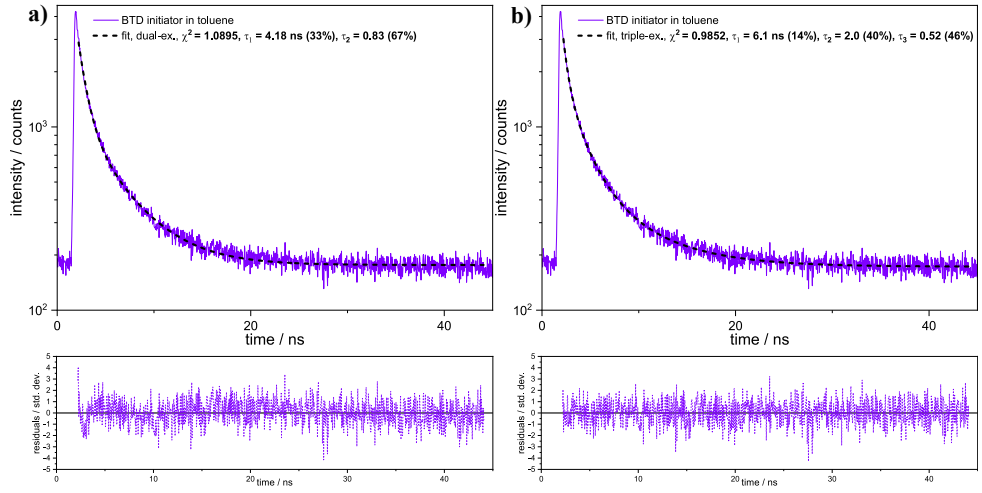

Figure 7.14: TCSPC curves of the unactivated BTD initiator compound in toluene. Excitation wavelength was 488 nm, the observed spectral window was from 532 – 715 nm. In graph **a)**, the curve was fitted with a dual exponential tail fit. In graph **b)**, the same data was fitted with a triple exponential tail fit. Below the curves, the residuals of the fits are given as well.

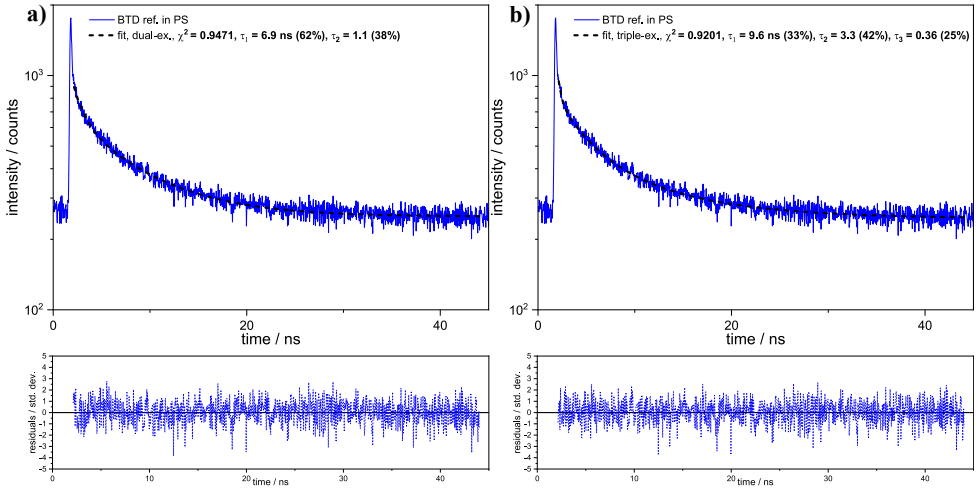

Figure 7.15: TCSPC curves of the activated BTD reference compound in a poly styrene matrix. Excitation wavelength was 488 nm, the observed spectral window was from 532 – 715 nm. In graph **a)**, the curve was fitted with a dual exponential tail fit. In graph **b)**, the same data was fitted with a triple exponential tail fit. Below the curves, the residuals of the fits are given as well.

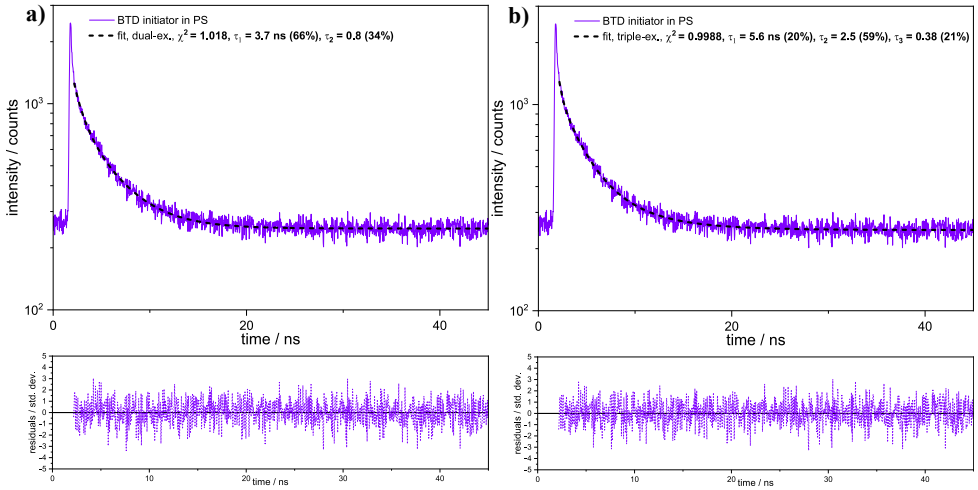

Figure 7.16: TCSPC curves of the unactivated BTD initiator compound in a poly styrene matrix. Excitation wavelength was 488 nm, the observed spectral window was from 532 – 715 nm. In graph **a)**, the curve was fitted with a dual exponential tail fit. In graph **b)**, the same data was fitted with a triple exponential tail fit. Below the curves, the residuals of the fits are given as well.

7.2.2 Lifetimes of the FLIM images

FLIM of microgels

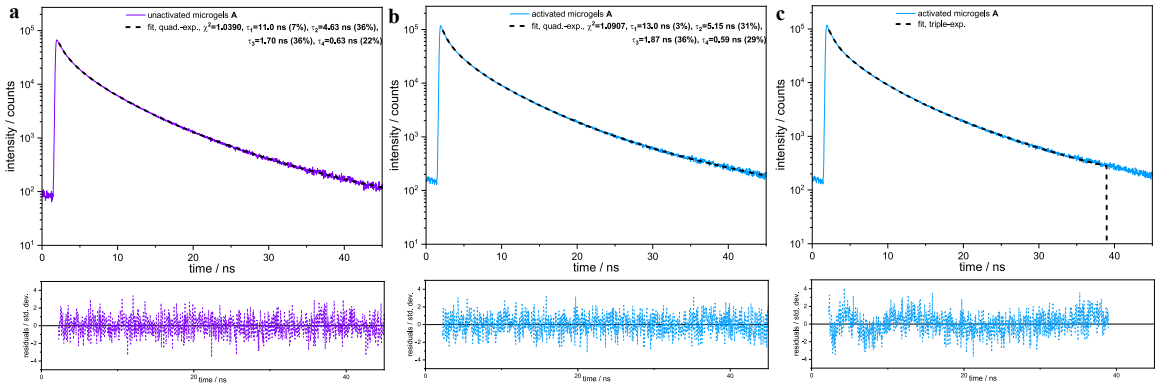

Figure 7.17: TCSPC curves of the FLIM images of unactivated (**a**, violet) and activated (**b,c**, blue) microgels **A** (figure 3.7). Excitation wavelength was 488 nm, the observed spectral window was from 500 – 715 nm. The data in (**a,b**) was fitted with quadruple exponential tail fits. For comparison, the same data as in (**b**) was fitted again in (**c**) with a triple exponential tail fit. The result, in particular the residual curve, is representative for all FLIM measurements with four determined lifetime components. Below the curves, the residuals of the fits are given as well.

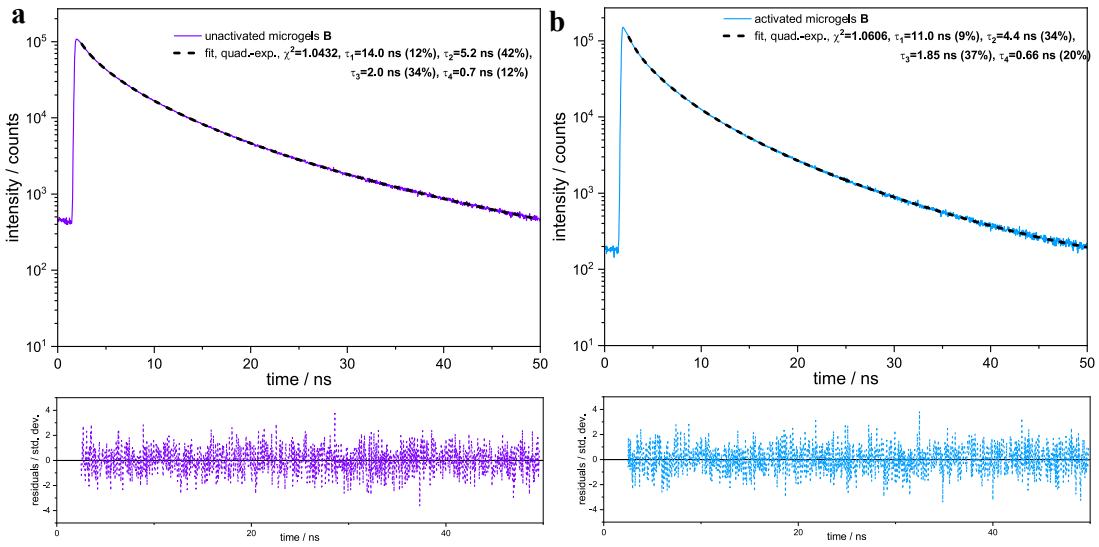

Figure 7.18: TCSPC curves of the FLIM images of unactivated (**a**, violet) and activated (**b**, blue) microgels **B** (figure 3.8). Excitation wavelength was 488 nm, the observed spectral window was from 500 – 715 nm. All data was fitted with quadruple exponential tail fits. Below the curves, the residuals of the fits are given as well.

FLIM of PHMA networks

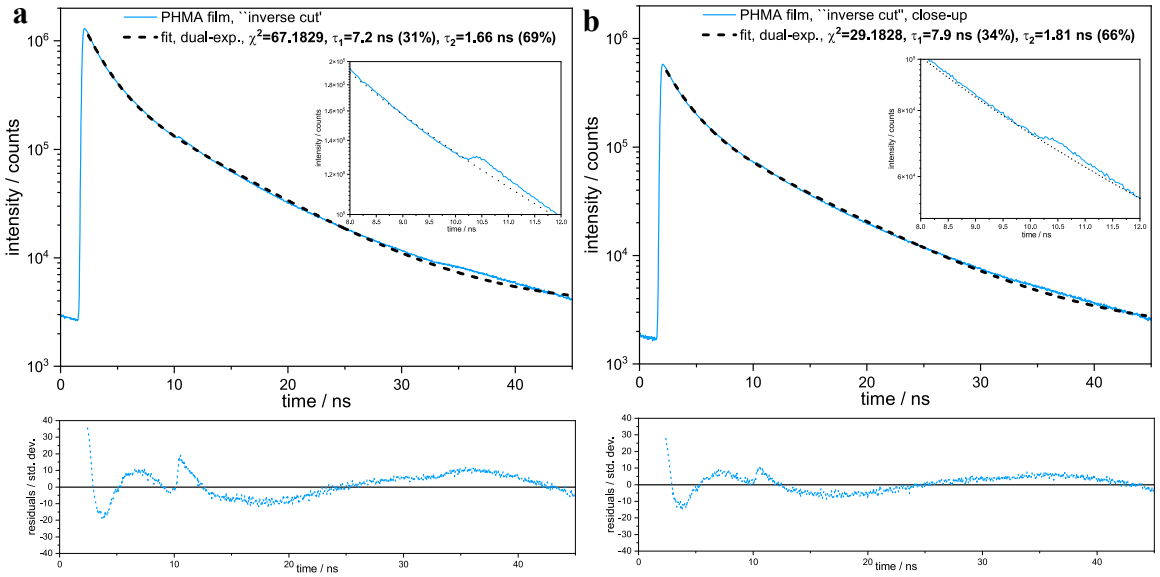

Figure 7.19: TCSPC curves of the FLIM images of BTD-PHMA networks (figure 3.9). The insets show the TCSPC around 10 ns when a second maximum / a shoulder is visible in the decay curves. Excitation wavelength was 488 nm, the observed spectral window was from 500 – 715 nm. All data was fitted with dual exponential tail fits. Below the curves, the residuals of the fits are given as well.

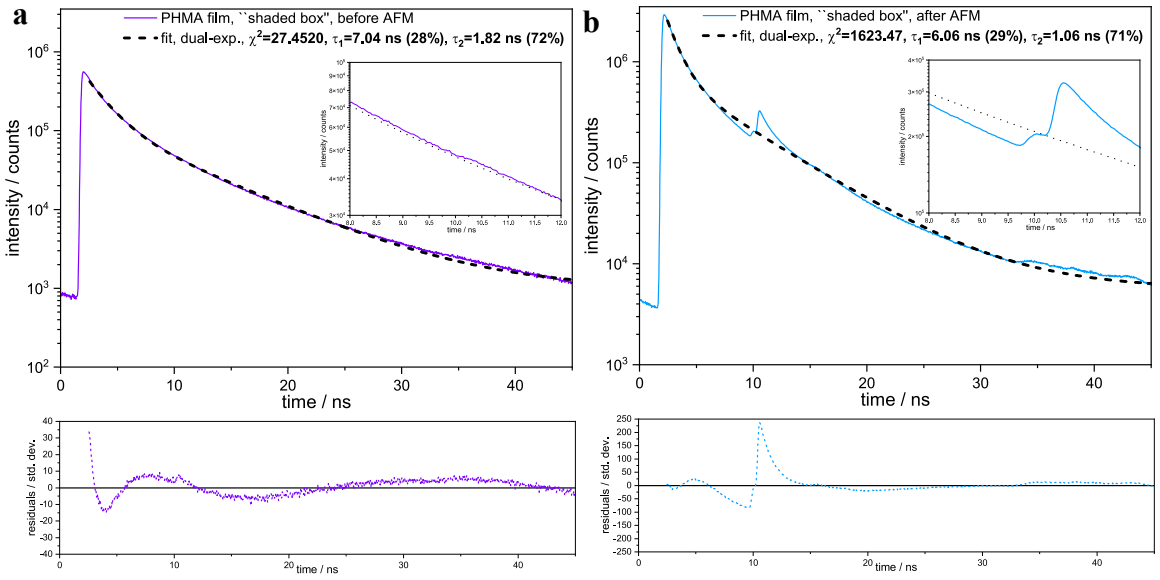

Figure 7.20: TCSPC curves of the FLIM images of BTD-PHMA networks before (**a**, violet) and after (**b**, blue) an AFM measurement (figure 3.10). The insets show the TCSPC around 10 ns when a second maximum / a shoulder is visible in the decay curves. Excitation wavelength was 488 nm, the observed spectral window was from 500 – 715 nm. All data was fitted with dual exponential tail fits. Below the curves, the residuals of the fits are given as well.

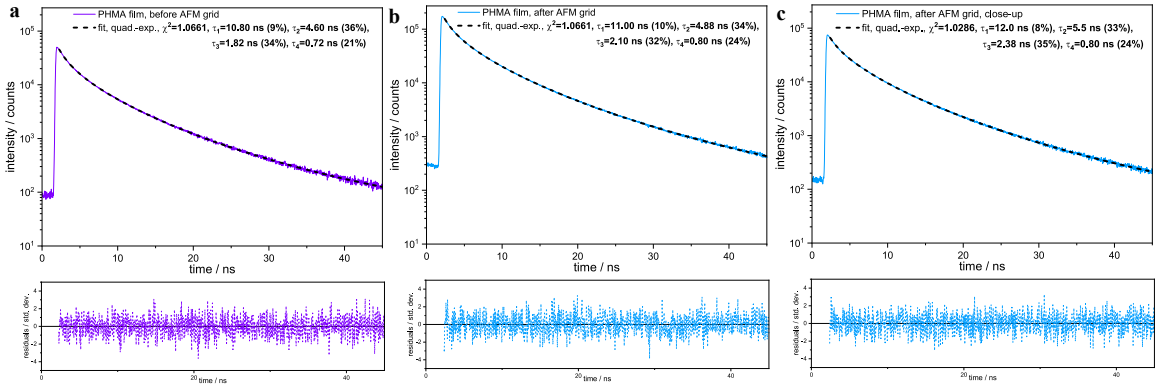

Figure 7.21: TCSPC curves of the FLIM images of BTD-PHMA networks before (**a**, violet) and after (**b,c**, blue) the AFM grid measurement (figure 3.11). Excitation wavelength was 488 nm, the observed spectral window was from 500 – 715 nm. All data was fitted with quadruple exponential tail fits. Below the curves, the residuals of the fits are given as well.

7.2.3 Lifetimes of the FEDUP system before and after UV irradiation

Methanol solutions – Emission window 545 – 620 nm

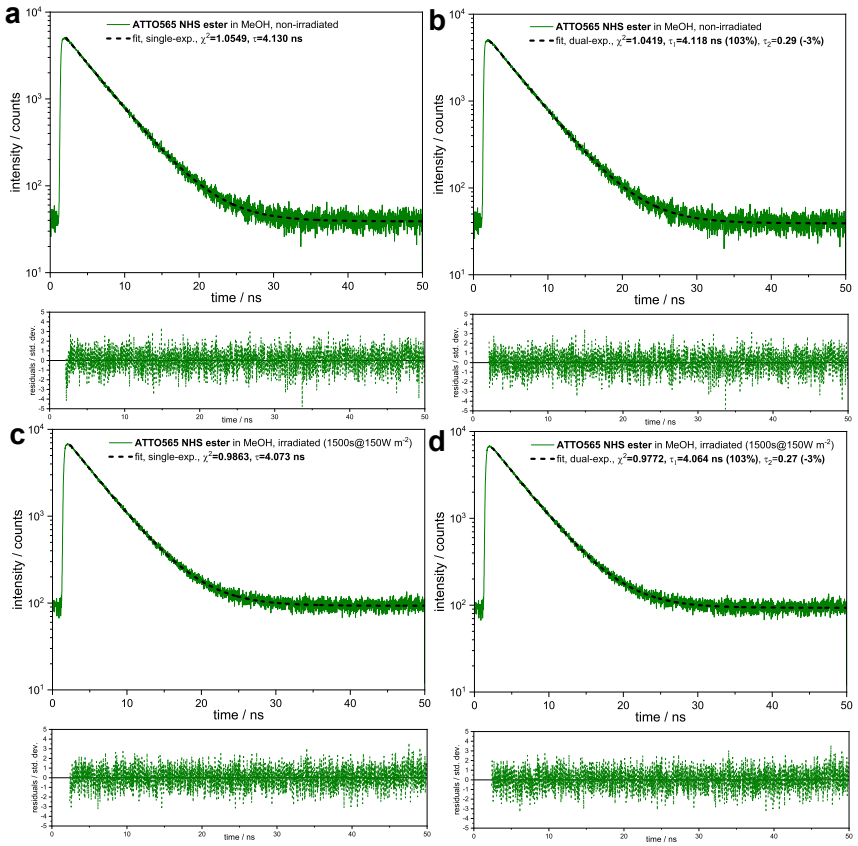

Figure 7.22: TCSPC curves of ATTO565 in methanol before (**a**) and **b**)) and after UV irradiation (**c**) and **d**)). Excitation wavelength was 527 nm, the observed spectral window was from 545 – 620 nm. In graphs **a**) and **c**) the curves were fitted with single exponential tail fits. For comparison, in graphs **b**) and **d**) the same data was fitted with dual exponential tail fits. Below the curves, the residuals of the fits are given as well.

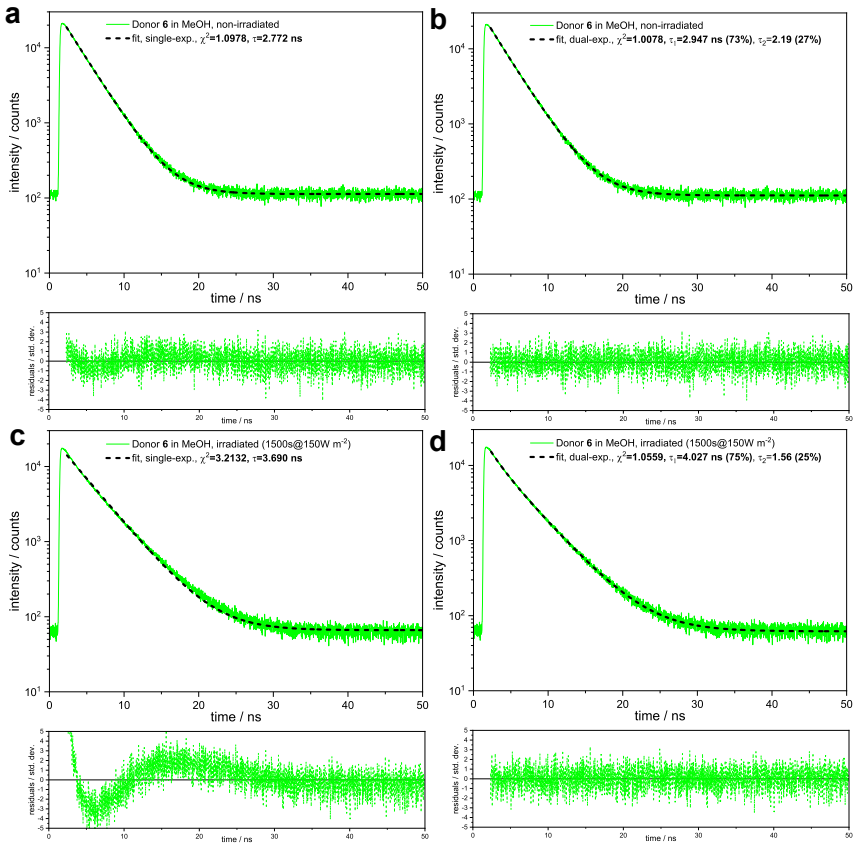

Figure 7.23: TCSPC curves of Donor **6** in methanol before (**a)** and **b)**) and after UV irradiation (**c)** and **d)**). Excitation wavelength was 527 nm, the observed spectral window was from 545 – 620 nm. In graphs **a)** and **c)** the curves were fitted with single exponential tail fits. For comparison, in graphs **b)** and **d)** the same data was fitted with dual exponential tail fits. Below the curves, the residuals of the fits are given as well.

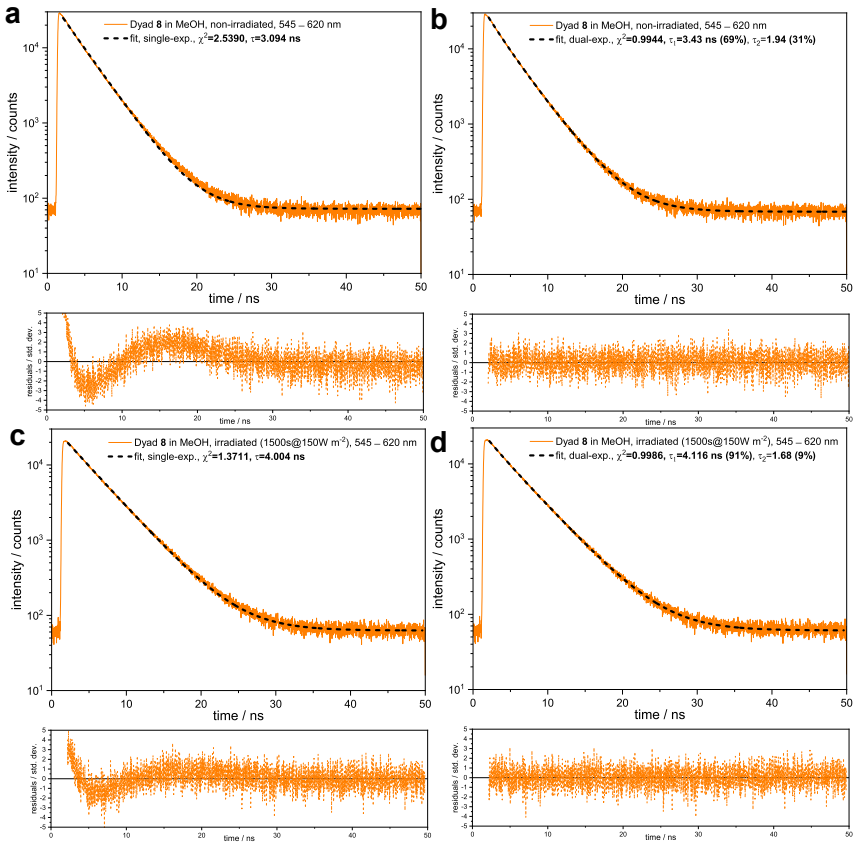

Figure 7.24: TCSPC curves of Dyad **8** in methanol before (**a)** and **b)**) and after UV irradiation (**c)** and **d)**). Excitation wavelength was 527 nm, the observed spectral window was from 545 – 620 nm. In graphs **a)** and **c)** the curves were fitted with single exponential tail fits. For comparison, in graphs **b)** and **d)** the same data was fitted with dual exponential tail fits. Below the curves, the residuals of the fits are given as well.

Methanol solutions – Emission window 655 – 715 nm

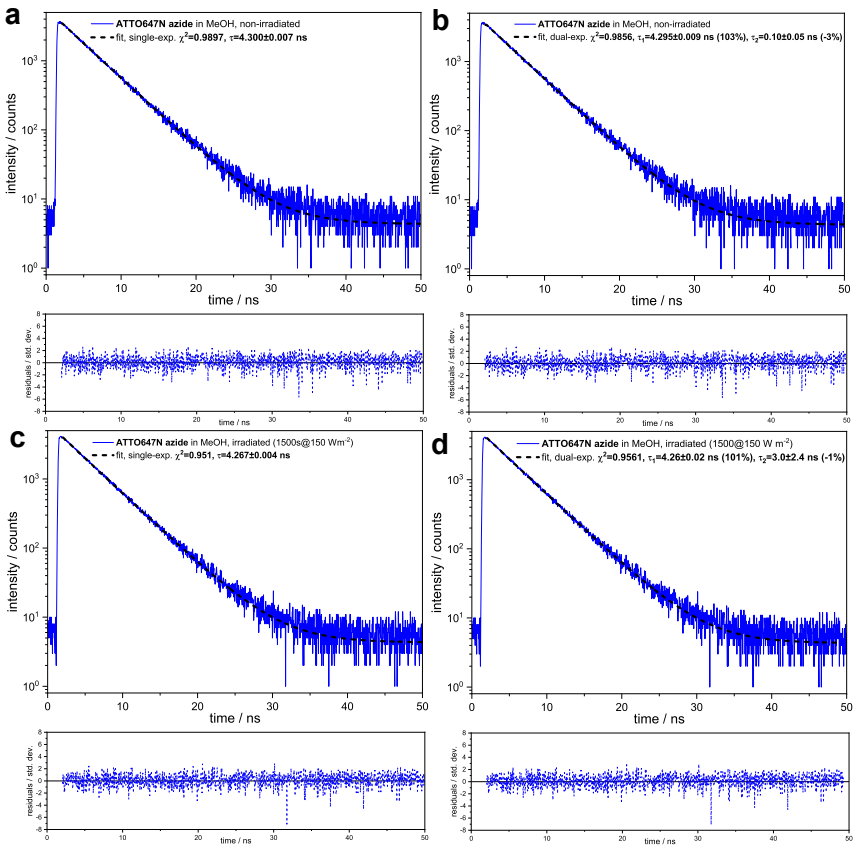

Figure 7.25: TCSPC curves of ATTO647N in methanol before (**a)** and **b)**) and after UV irradiation (**c)** and **d)**). Excitation wavelength was 635 nm, the observed spectral window was from 655 – 715 nm. In graphs **a)** and **c)** the curves were fitted with single exponential tail fits. For comparison, in graphs **b)** and **d)** the same data was fitted with dual exponential tail fits. Below the curves, the residuals of the fits are given as well.

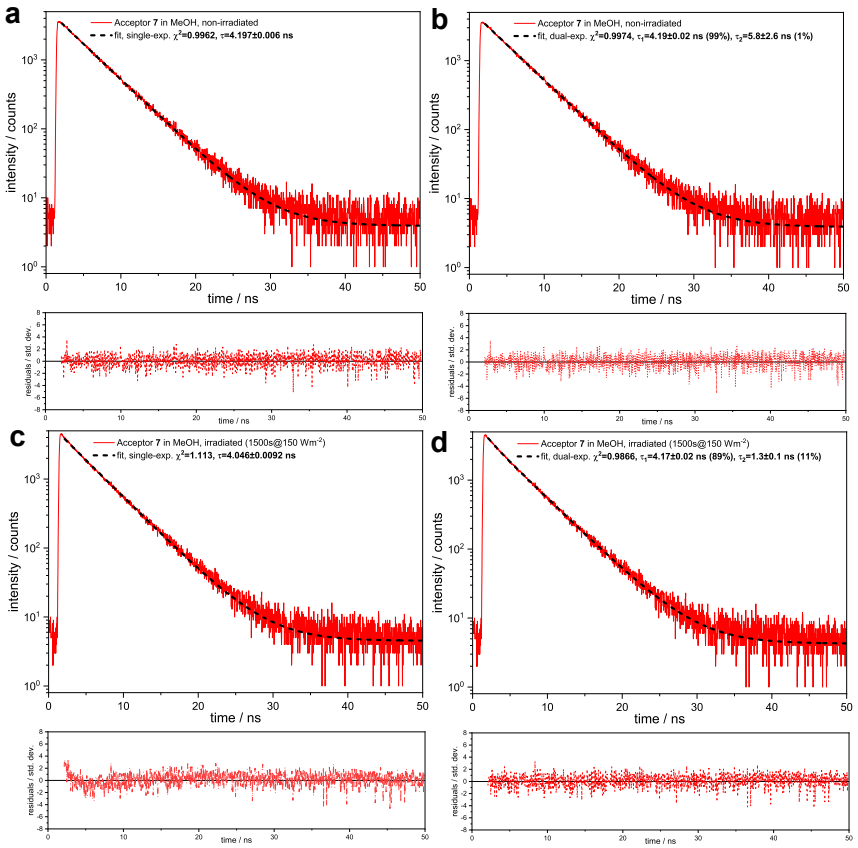

Figure 7.26: TCSPC curves of the acceptor **7** in methanol before (**a)** and **b)**) and after UV irradiation (**c)** and **d)**). Excitation wavelength was 635 nm, the observed spectral window was from 655 – 715 nm. In graphs **a)** and **c)** the curves were fitted with single exponential tail fits. For comparison, in graphs **b)** and **d)** the same data was fitted with dual exponential tail fits. Below the curves, the residuals of the fits are given as well.

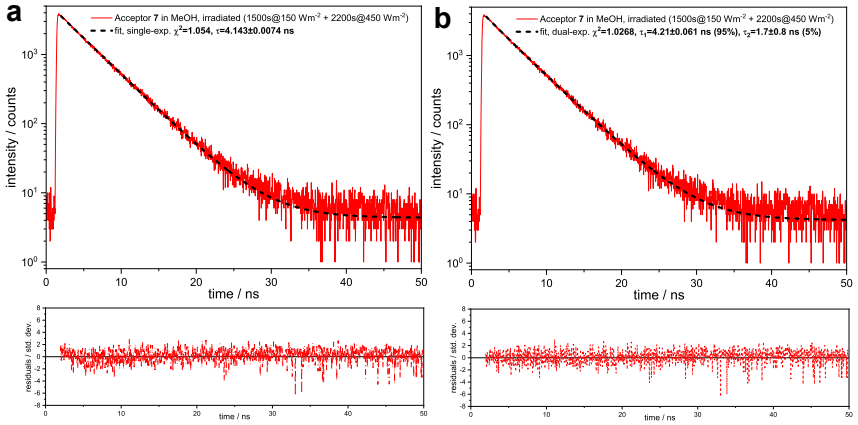

Figure 7.27: TCSPC curves of the acceptor **7** in methanol after additional UV irradiation. Excitation wavelength was 635 nm, the observed spectral window was from 655 – 715 nm. In graph **a)** the curve was fitted with a single exponential tail fit. For comparison, in graph **b)** the same data was fitted with a dual exponential tail fit. Below the curves, the residuals of the fits are given as well.

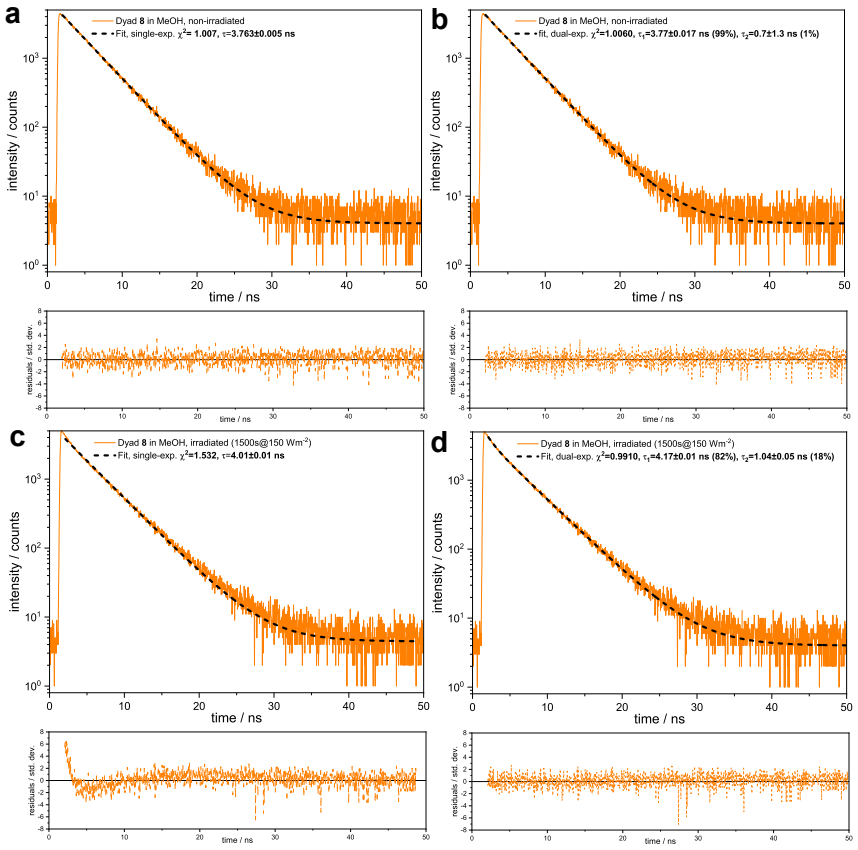

Figure 7.28: TCSPC curves of the dyad **8** in methanol before (**a)** and **b)**) and after UV irradiation (**c)** und **d)**). Excitation wavelength was 635 nm, the observed spectral window was from 655 – 715 nm. In graphs **a)** and **c)** the curves were fitted with single exponential tail fits. For comparison, in graphs **b)** and **d)** the same data was fitted with dual exponential tail fits. Below the curves, the residuals of the fits are given as well.

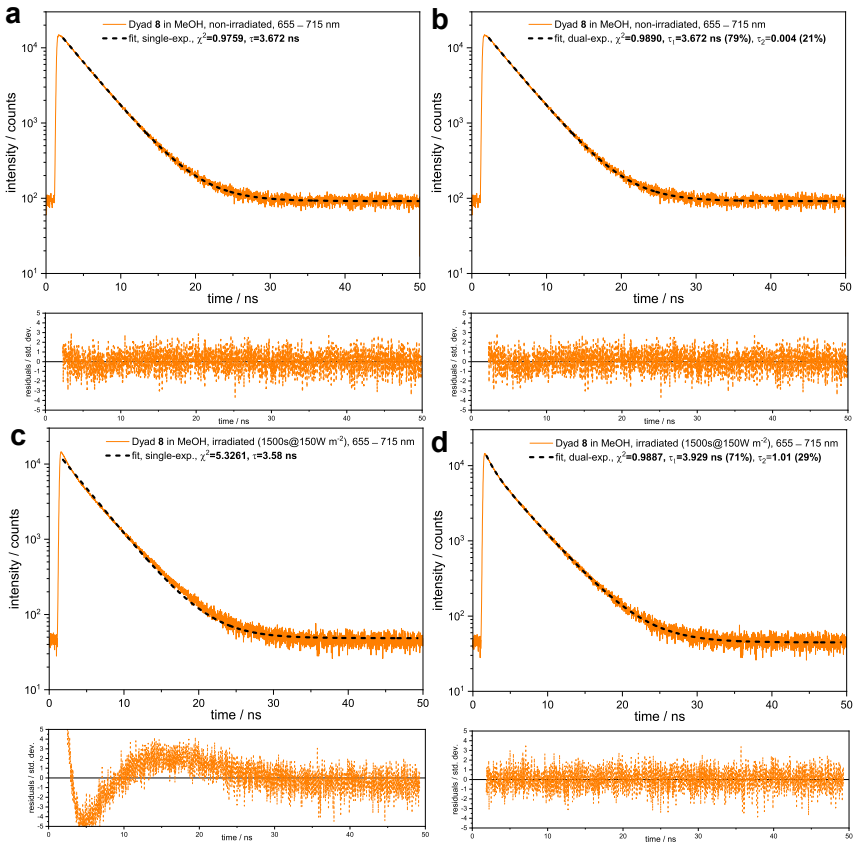

Figure 7.29: TCSPC curves of Dyad **8** in methanol before (**a)** and **b)**) and after UV irradiation (**c)** and **d)**). Excitation wavelength was 527 nm, the observed spectral window was from 655 – 715 nm. In graphs **a)** and **c)** the curves were fitted with single exponential tail fits. For comparison, in graphs **b)** and **d)** the same data was fitted with dual exponential tail fits. Below the curves, the residuals of the fits are given as well.

Aqueous solutions – Emission window 545 – 620 nm

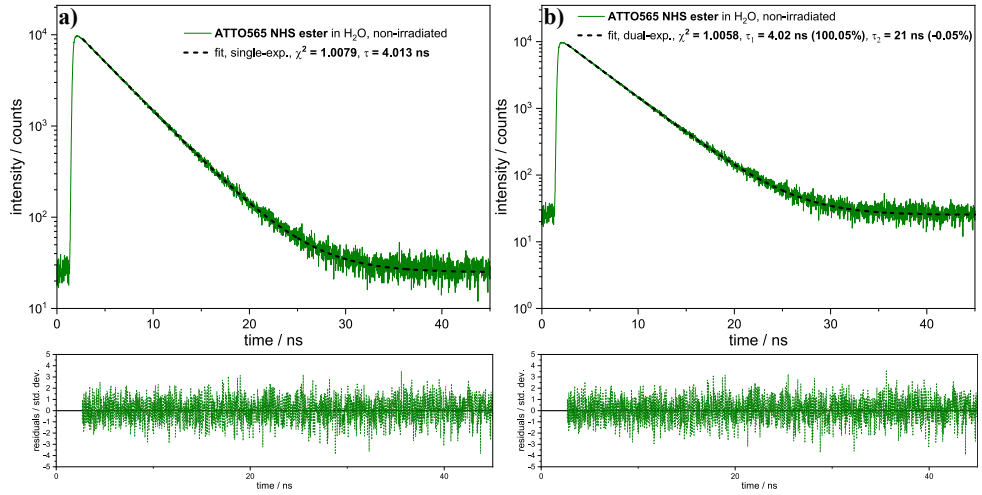

Figure 7.30: TCSPC curves of ATTO565 in water before (**a)** and **b)**) and after UV irradiation (**c)** and **d)**). Excitation wavelength was 527 nm, the observed spectral window was from 545 – 620 nm. In graphs **a)** and **c)** the curves were fitted with single exponential tail fits. For comparison, in graphs **b)** and **d)** the same data was fitted with dual exponential tail fits. Below the curves, the residuals of the fits are given as well.

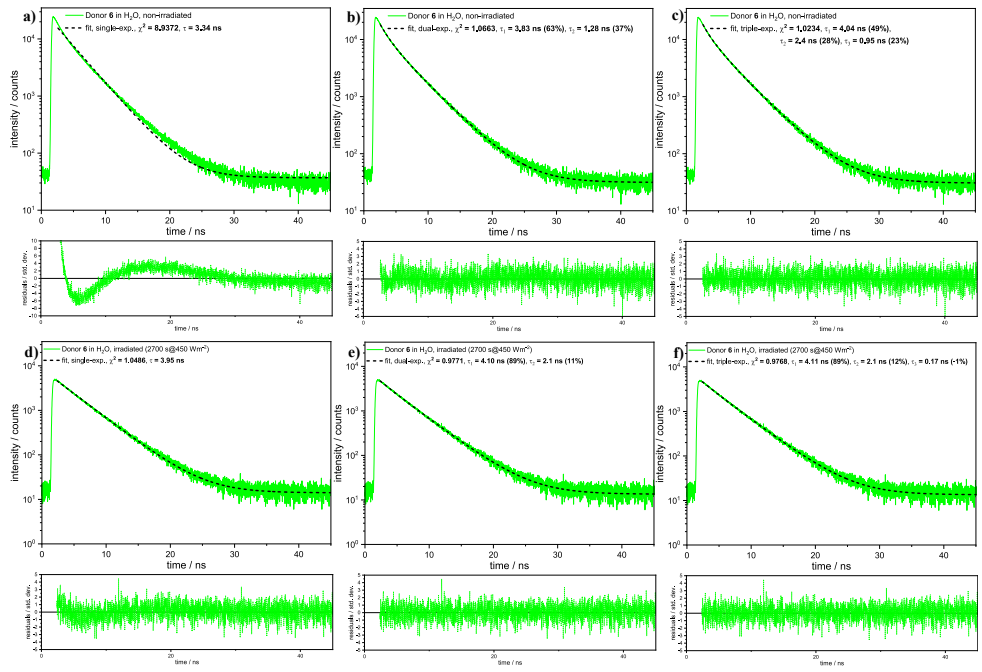

Figure 7.31: TCSPC curves of Donor **6** in water before (**a)**, **b)** and **c)**) and after UV irradiation (**d)**, **e)** and **f)**). Excitation wavelength was 527 nm, the observed spectral window was from 545 – 620 nm. In graphs **a)** and **d)** the curves were fitted with single exponential tail fits. For comparison, in graphs **b)** and **e)** the same data was fitted with dual exponential tail fits, and in graphs **c)** and **f)** with triple exponential tail fits. Below the curves, the residuals of the fits are given as well.

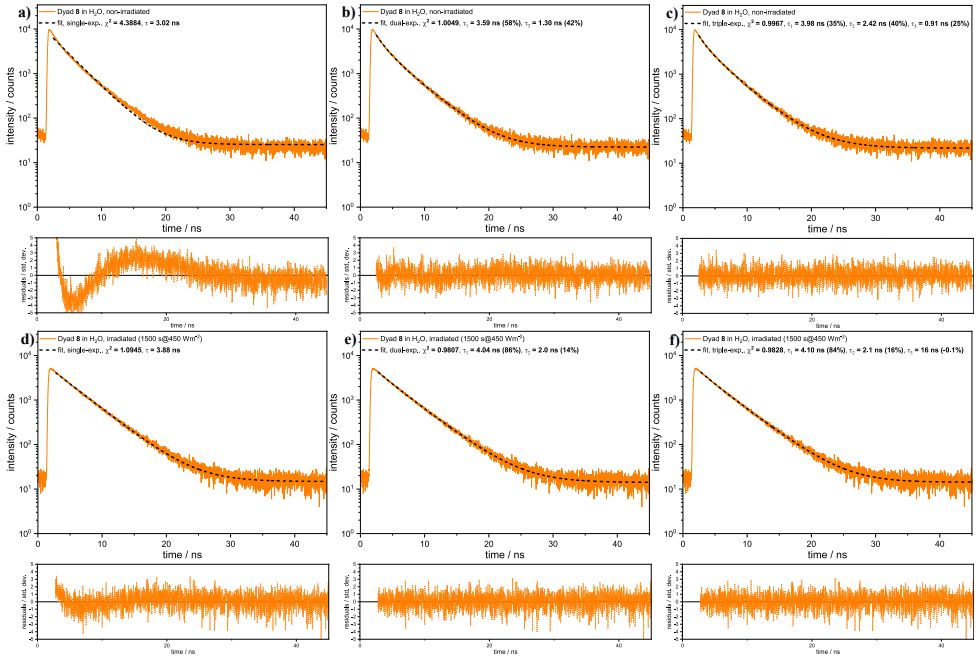

Figure 7.32: TCSPC curves of Dyad **8** in water before (**a)**, **b)** and **c)**) and after UV irradiation (**d)**, **e)** and **f)**). Excitation wavelength was 527 nm, the observed spectral window was from 545 – 620 nm. In graphs **a)** and **d)** the curves were fitted with single exponential tail fits. For comparison, in graphs **b)** and **e)** the same data was fitted with dual exponential tail fits, and in graphs **c)** and **f)** with triple exponential tail fits. Below the curves, the residuals of the fits are given as well.

Aqueous solutions – Emission window 655 – 715 nm

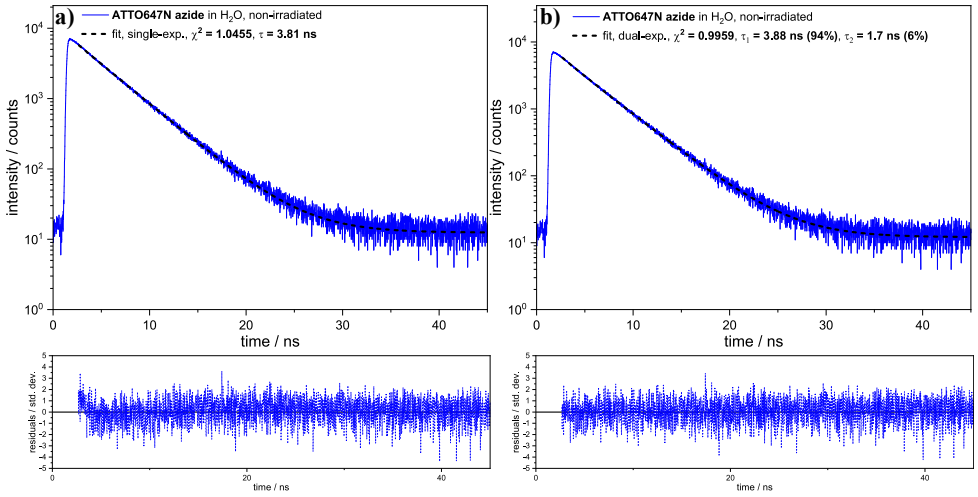

Figure 7.33: TCSPC curves of ATTO647N in water before (**a)** and **b)**) and after UV irradiation (**c)** and **d)**). Excitation wavelength was 635 nm, the observed spectral window was from 655 – 715 nm. In graphs **a)** and **c)** the curves were fitted with single exponential tail fits. For comparison, in graphs **b)** and **d)** the same data was fitted with dual exponential tail fits. Below the curves, the residuals of the fits are given as well.

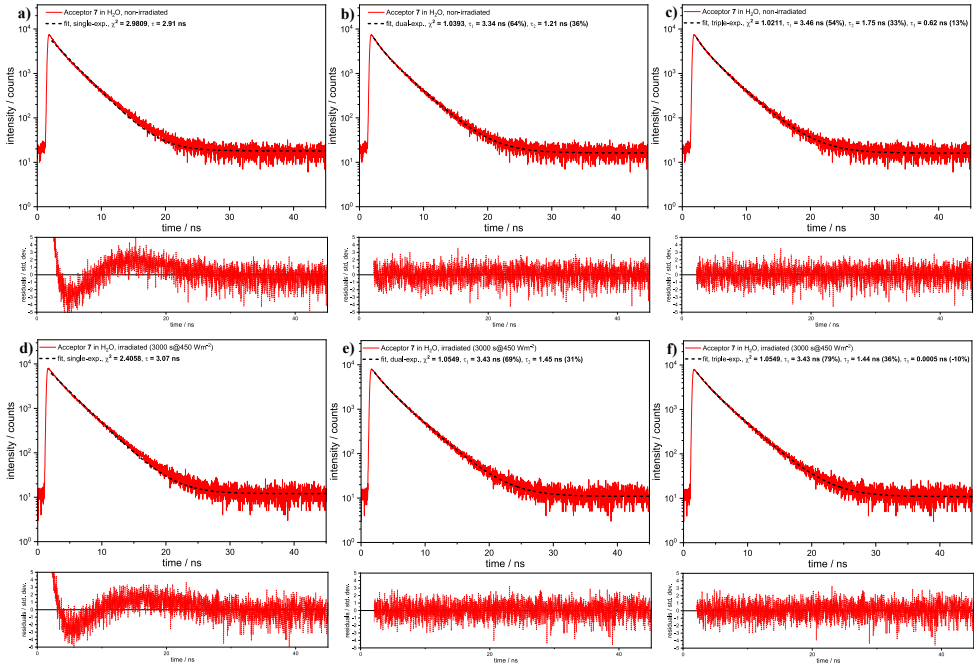

Figure 7.34: TCSPC curves of the acceptor **7** in water before (**a)**, **b)** and **c)**) and after UV irradiation (**d)**, **e)** and **f)**). Excitation wavelength was 635 nm, the observed spectral window was from 655 – 715 nm. In graphs **a)** and **d)** the curves were fitted with single exponential tail fits. For comparison, in graphs **b)** and **e)** the same data was fitted with dual exponential tail fits, and in graphs **c)** and **f)** with triple exponential tail fits. Below the curves, the residuals of the fits are given as well.

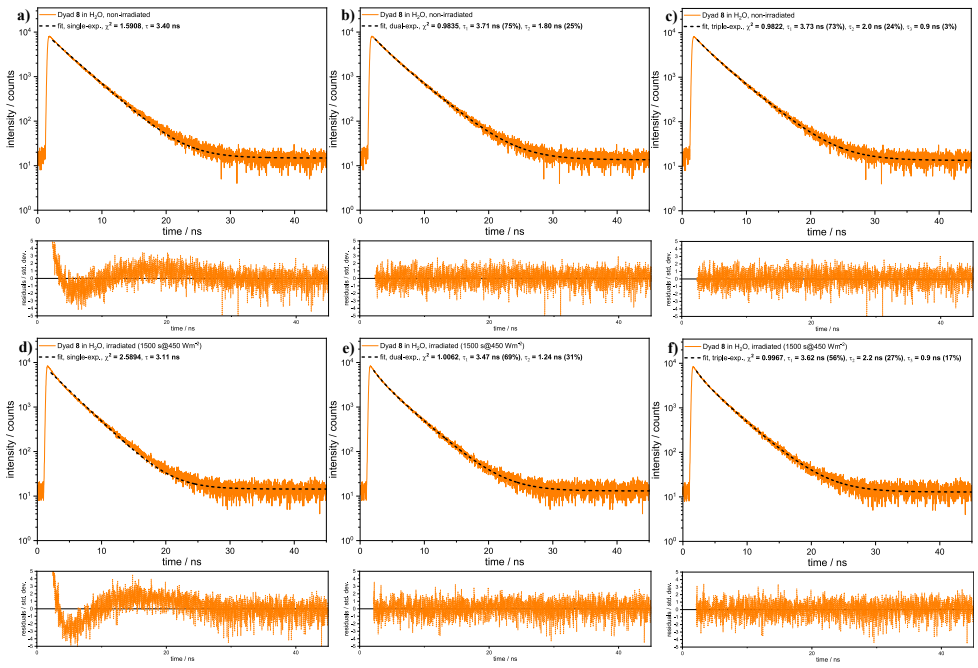

Figure 7.35: TCSPC curves of the dyad **8** in water before (**a)**, **b)** and **c)**) and after UV irradiation (**d)**, **e)** and **f)**). Excitation wavelength was 635 nm, the observed spectral window was from 655 – 715 nm. In graphs **a)** and **d)** the curves were fitted with single exponential tail fits. For comparison, in graphs **b)** and **e)** the same data was fitted with dual exponential tail fits, and in graphs **c)** and **f)** with triple exponential tail fits. Below the curves, the residuals of the fits are given as well.

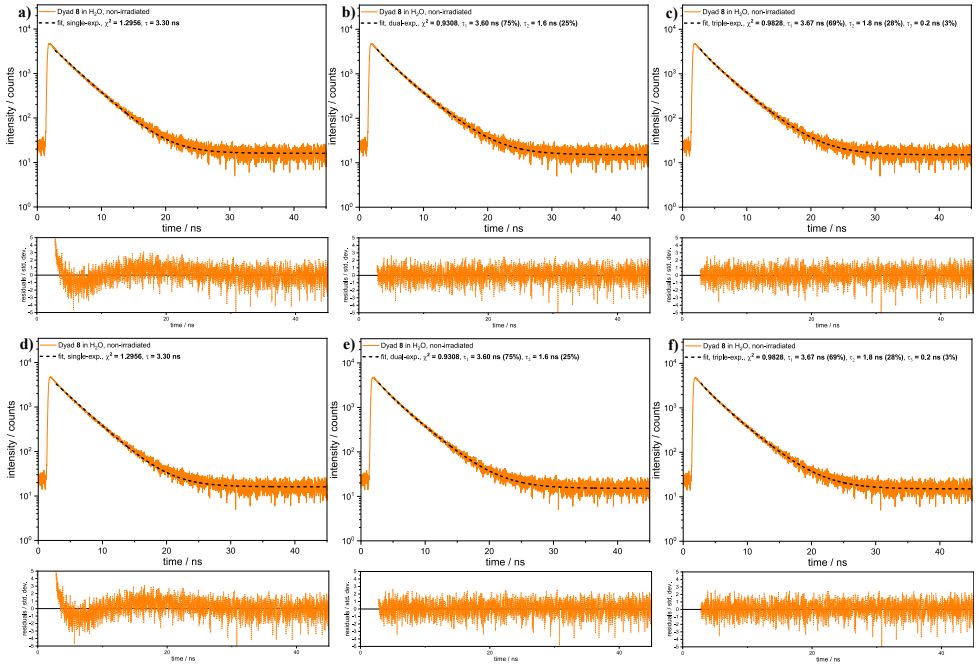

Figure 7.36: TCSPC curves of Dyad **8** in water before (**a**), **b**) and **c**)) and after UV irradiation (**d**), **e**) and **f**)). Excitation wavelength was 635 nm, the observed spectral window was from 655 – 715 nm. In graphs **a**) and **d**) the curves were fitted with single exponential tail fits. For comparison, in graphs **b**) and **e**) the same data was fitted with dual exponential tail fits, and in graphs **c**) and **f**) with triple exponential tail fits. Below the curves, the residuals of the fits are given as well.

7.2.4 Lifetimes of the FEDUP system after irradiation with red light

Emission window 545 – 620 nm

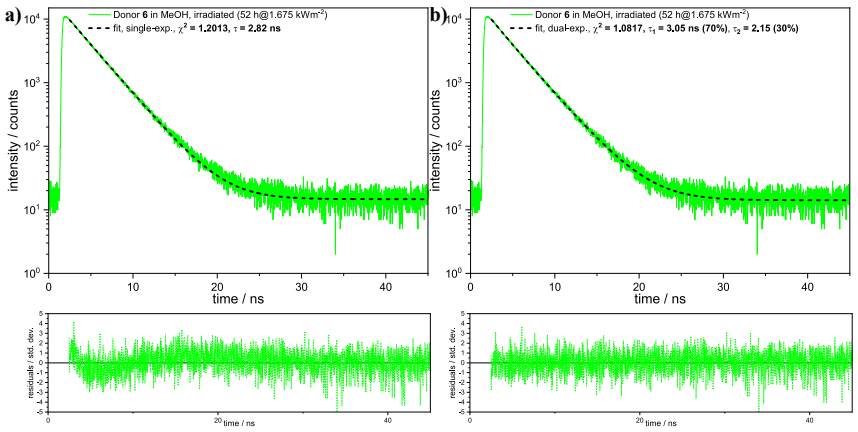

Figure 7.37: TCSPC curves of Donor **6** in methanol after irradiation with red light. Excitation wavelength was 527 nm, the observed spectral window was from 545 – 620 nm. In graphs **a**) the curve was fitted with a single exponential tail fit. For comparison, in graph **b**) the same data was fitted with a dual exponential tail fit. Below the curves, the residuals of the fits are given as well.

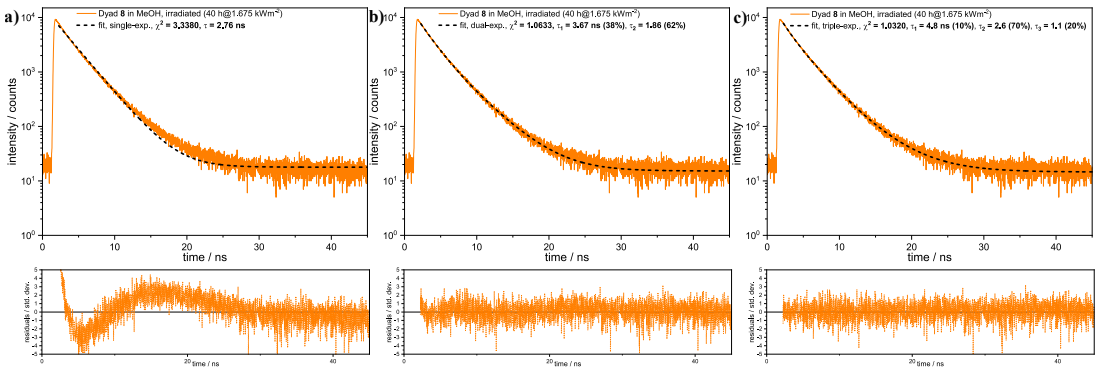

Figure 7.38: TCSPC curves of dyad **8** in methanol after irradiation with red light. Excitation wavelength was 527 nm, the observed spectral window was from 545 – 620 nm. In graphs **a)** the curve was fitted with a single exponential tail fit. For comparison, in graph **b)** the same data was fitted with a dual exponential tail fit and in graph **c)** with a triple exponential tail fit. Below the curves, the residuals of the fits are given as well.

Emission window 655 – 715 nm

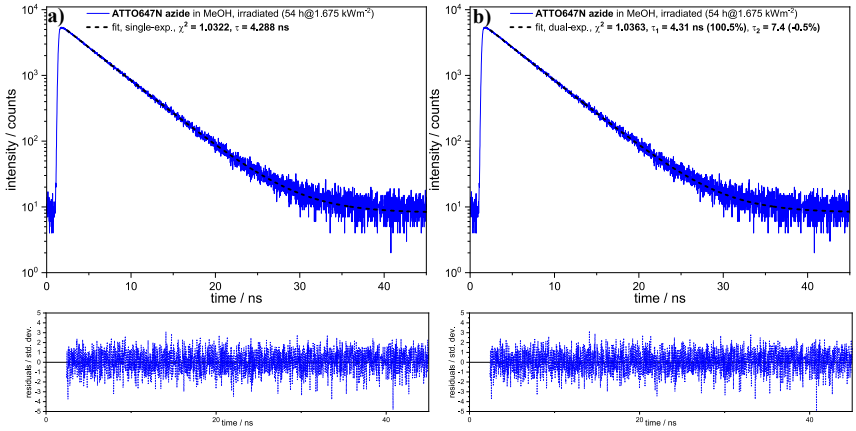

Figure 7.39: TCSPC curves of **ATTO647N azide** in methanol after irradiation with red light. Excitation wavelength was 635 nm, the observed spectral window was from 655 – 715 nm. In graphs **a)** the curve was fitted with a single exponential tail fit. For comparison, in graph **b)** the same data was fitted with a dual exponential tail fit. Below the curves, the residuals of the fits are given as well.

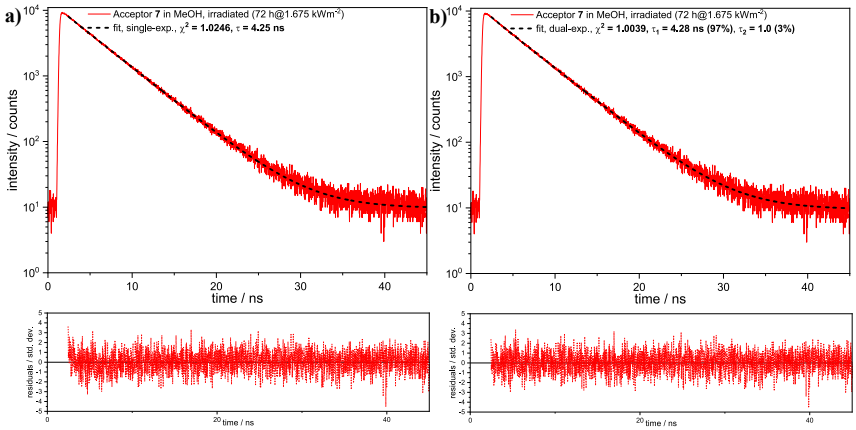

Figure 7.40: TCSPC curves of acceptor **7** in methanol after irradiation with red light. Excitation wavelength was 635 nm, the observed spectral window was from 655 – 715 nm. In graphs **a)** the curve was fitted with a single exponential tail fit. For comparison, in graph **b)** the same data was fitted with a dual exponential tail fit. Below the curves, the residuals of the fits are given as well.

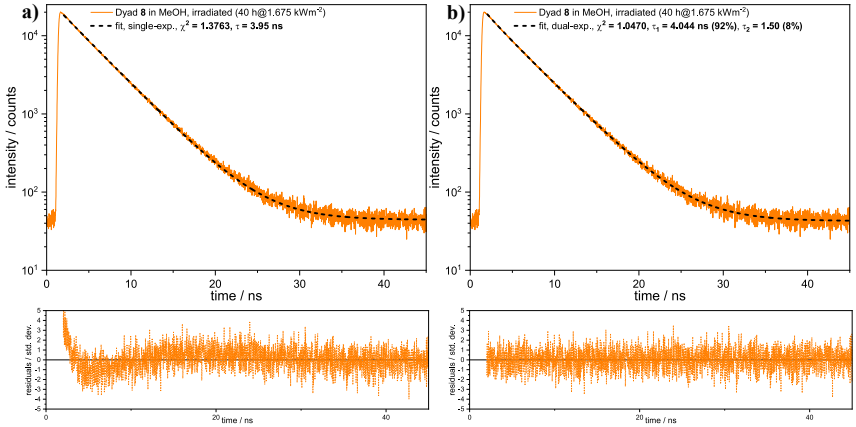

Figure 7.41: TCSPC curves of dyad **8** in methanol after irradiation with red light. Excitation wavelength was 635 nm, the observed spectral window was from 655 – 715 nm. In graphs **a)** the curve was fitted with a single exponential tail fit. For comparison, in graph **b)** the same data was fitted with a dual exponential tail fit. Below the curves, the residuals of the fits are given as well.

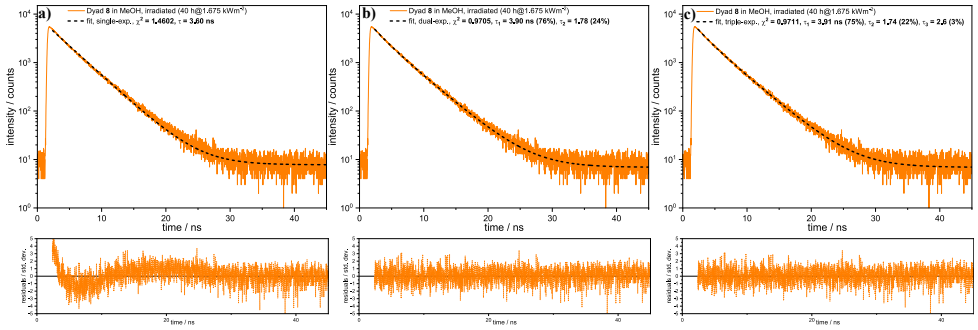

Figure 7.42: TCSPC curves of dyad **8** in methanol after irradiation with red light. Excitation wavelength was 527 nm, the observed spectral window was from 655 – 715 nm. In graphs **a)** the curve was fitted with a single exponential tail fit. For comparison, in graph **b)** the same data was fitted with a dual exponential tail fit and in graph **c)** with a triple exponential tail fit. Below the curves, the residuals of the fits are given as well.

7.3 FCS curves

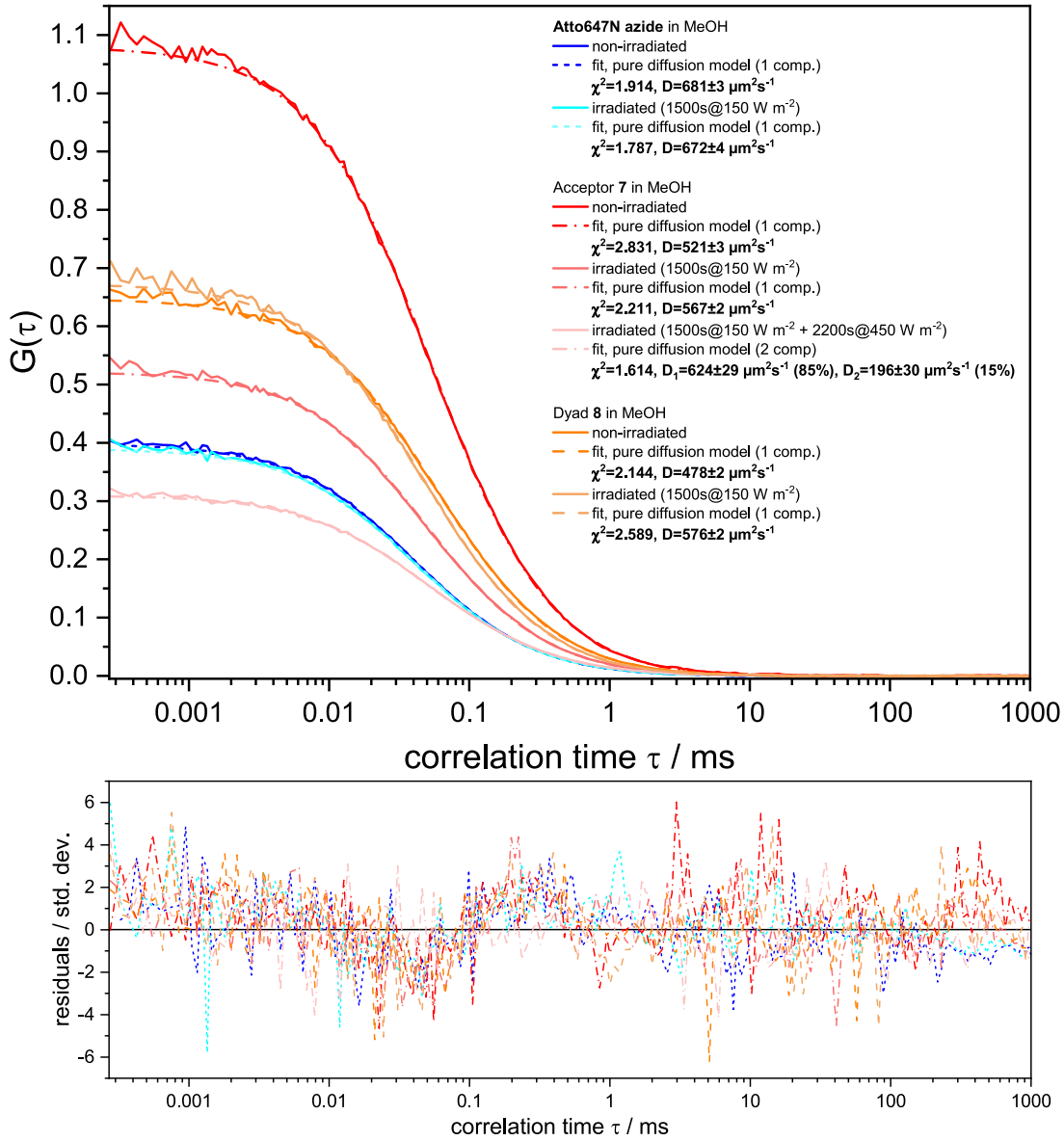

Figure 7.43: FCS curves of ATTO647N (blue and cyan), the acceptor (dark to light red) and the dyad (dark and light orange) in methanol before and after irradiation, respectively. Excitation wavelength was 635 nm. All curves have been fitted with the pure diffusion model and the least amount of components that still led to reasonable fits. Below the curves, the residuals of the fits are given as well.[59]

7.4 Microscopy measurements

7.4.1 Defocused images

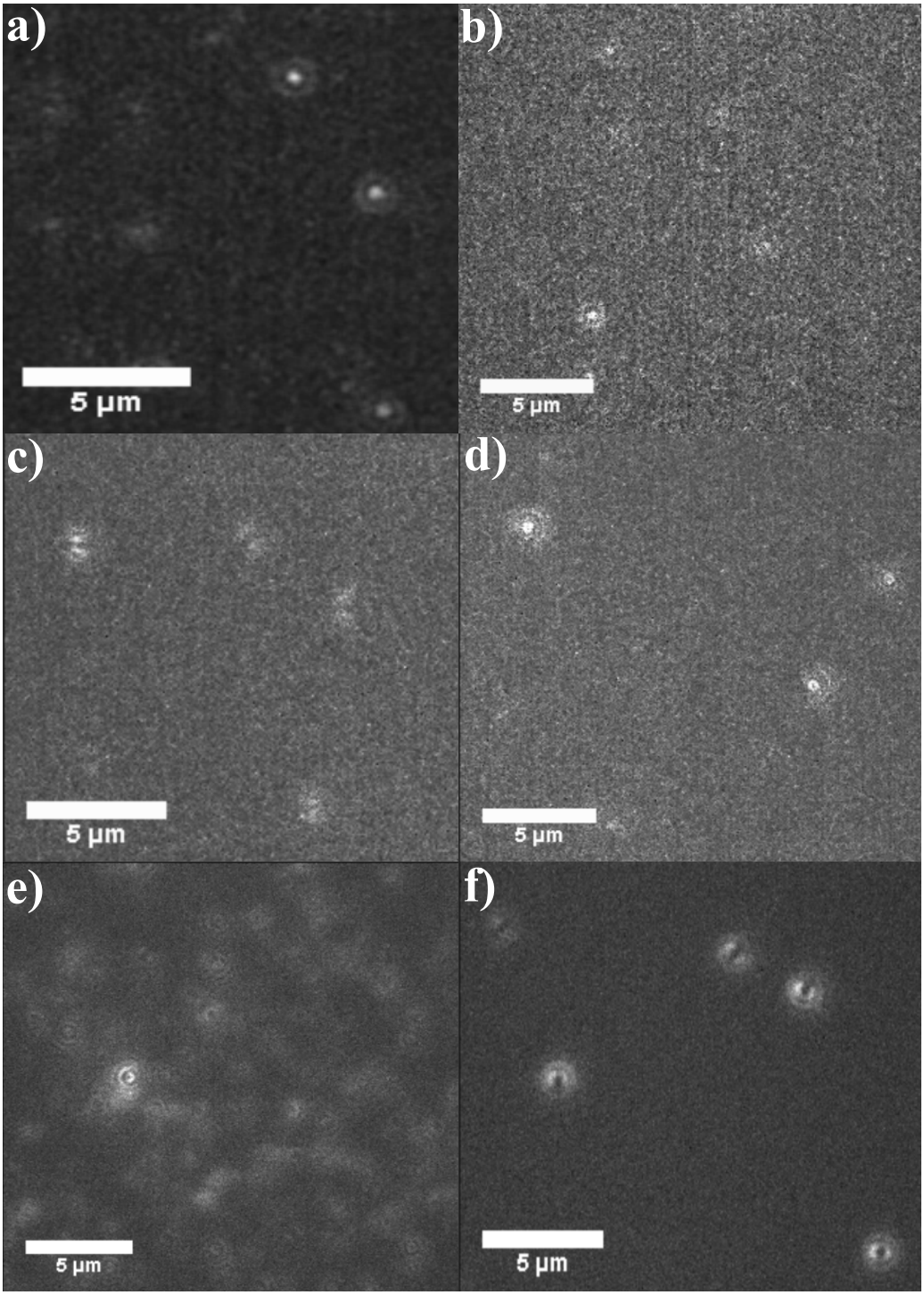

Figure 7.44: Defocused image of dyad **8** in **a**) PVAc at room temperature, **b**) PEG at room temperature, **c, d**) PBMA at room temperature and 40 °C, respectively, **e**) PEA at room temperature and **f**) on a glass substrate at room temperature. All images were recorded with 640 nm excitation. The imaging pixel size was 65 nm.

7.4.2 FEDUP images

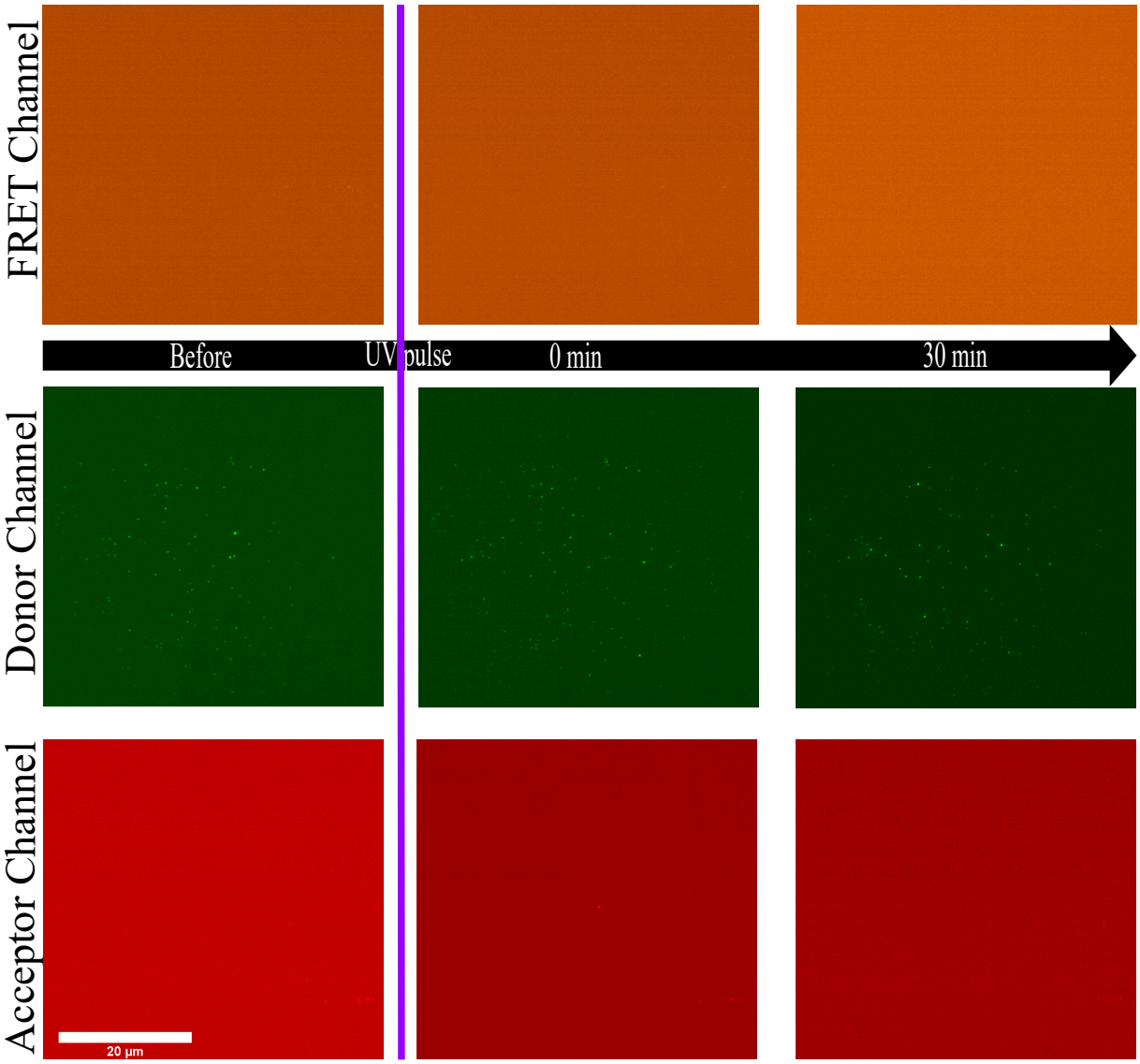

Figure 7.45: Series of false-color images taken from a widefield microscopy movie of a tempered PVAc film before and after 0.5 s of UV irradiation (378 nm at 50 $W cm^{-2}$). No dye was added to the film. A selection of images recorded with 200 ms integration time is shown which were taken at the times indicated in the central time arrow. In the top row, the long wavelength channel ($>$ 655 nm) at 561 nm excitation is shown (orange, FRET channel). In the middle row, the short wavelength channel (570 – 633 nm) at 561 nm excitation is displayed (green, donor channel). In the bottom row, the long wavelength channel at 640 nm excitation is shown (red, acceptor channel). All images were colored according to the established color scheme. The vertical purple line symbolizes the UV irradiation. The imaging pixel size was 65 nm.

7.4.3 FEDUP data

Data from the example measurement

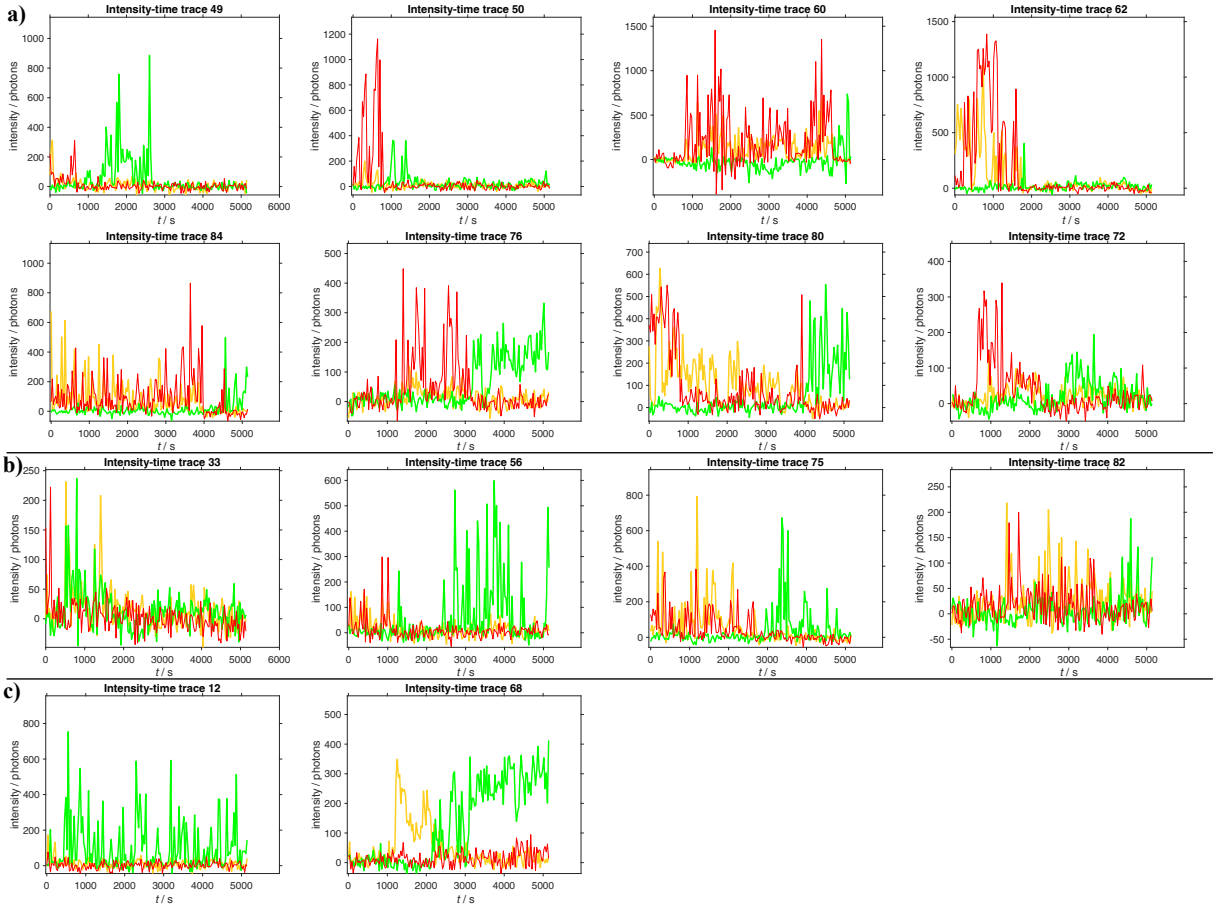

Figure 7.46: All intensity-time traces of the example measurement that have been identified as exhibiting premature photobleaching (donor-acceptor pair category II), with (**a**) perfect correlation of donor and acceptor channel, (**b**) short delay between the rise of donor intensity and the drop of acceptor intensity, or (**c**) without reasonably interpretable intensity in the acceptor at all. The numbers above each trace correspond to the numbers given to the initially identified donor-acceptor pairs in figure 4.18.

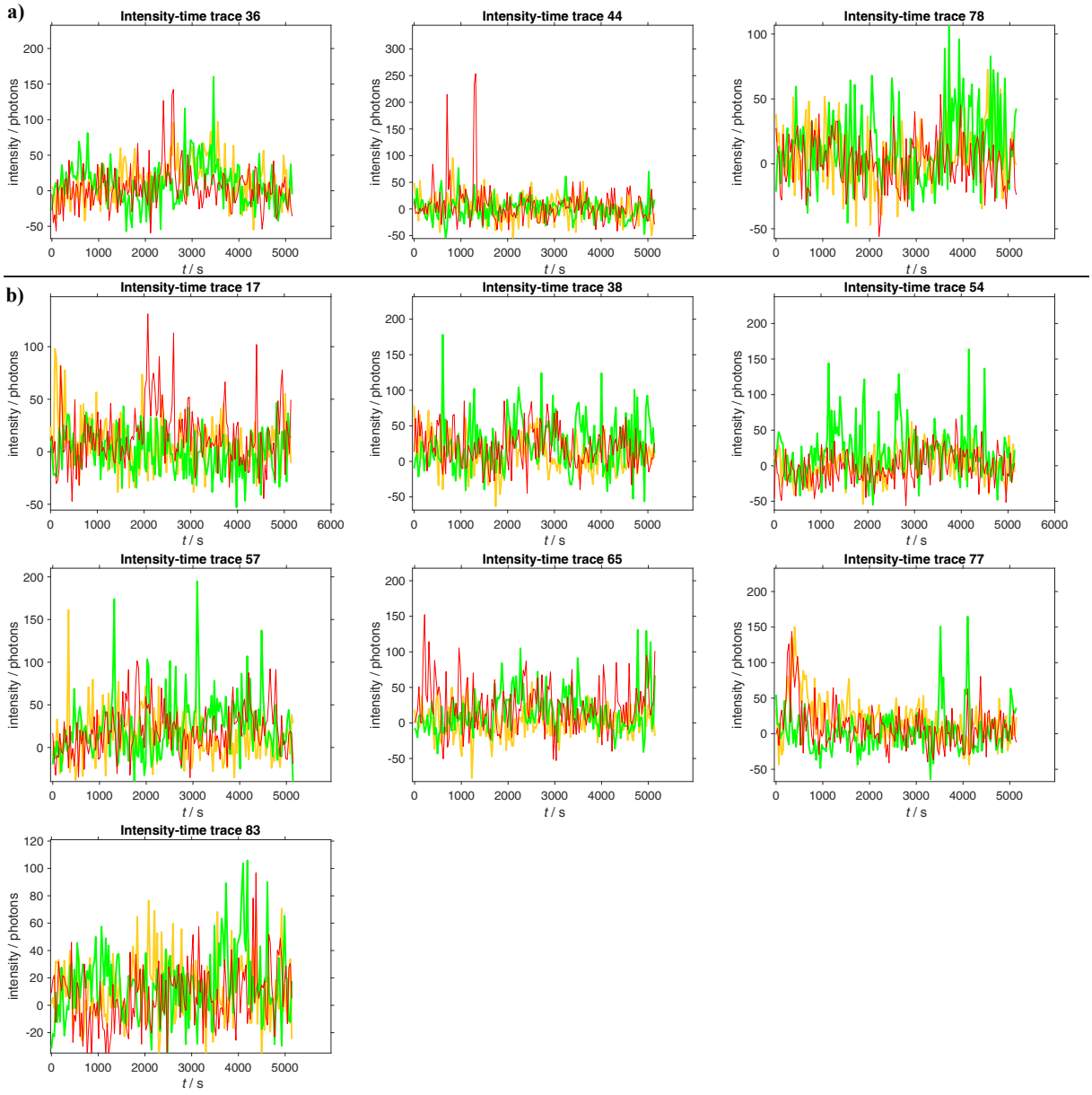

Figure 7.47: All intensity-time traces of the example measurement that are assumed to be either noise (**a**) or whose features are hidden by noise (**b**) (donor-acceptor pairs of category III). The numbers above each trace correspond to the numbers given to the initially identified donor-acceptor pairs in figure 4.18.

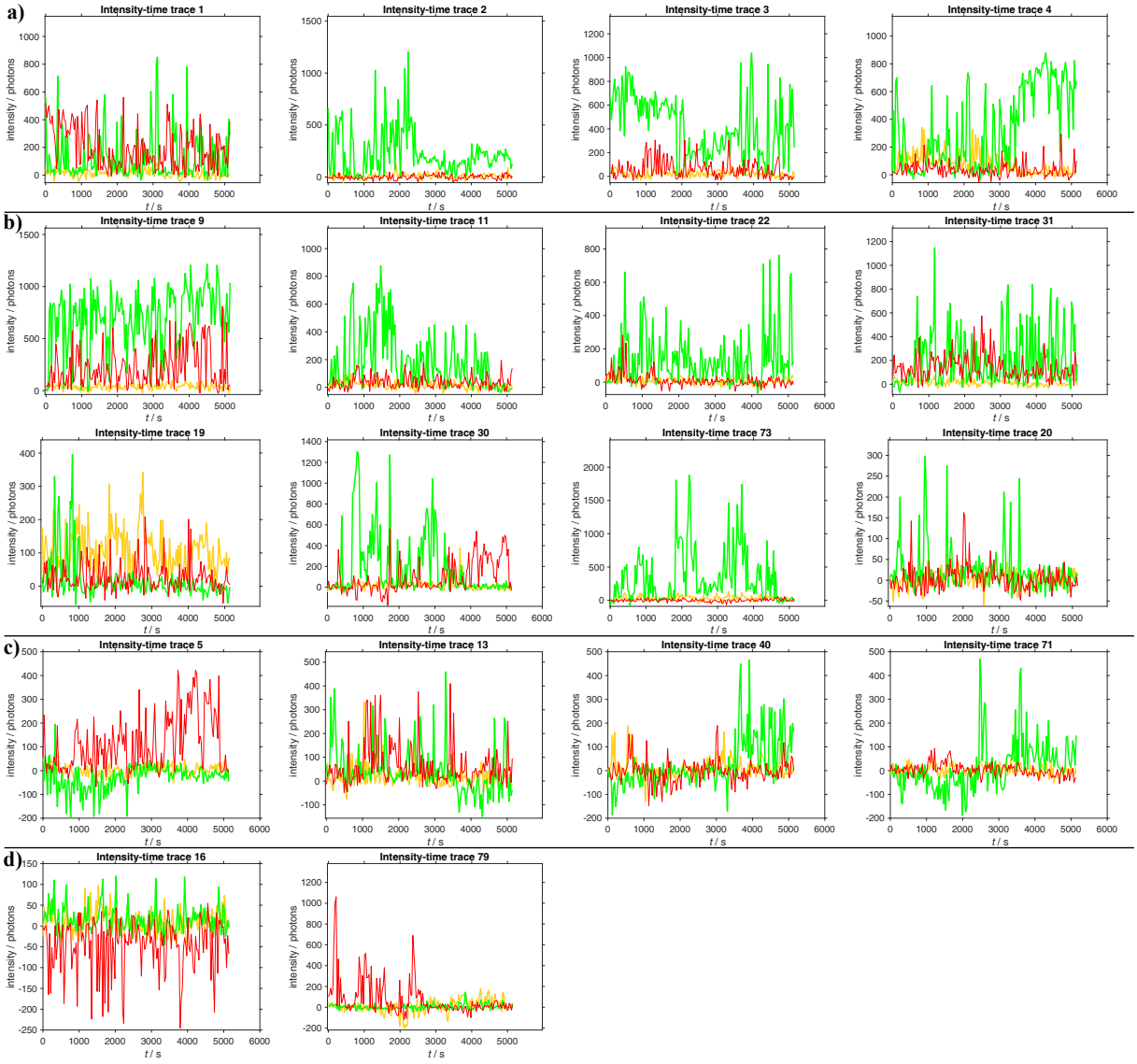

Figure 7.48: First part of all intensity-time traces of the example measurement that have been identified as irregular (category IV). In particular, (**a**) signals are detected in the donor channel starting from $t = 0$ s, (**b**) signals are detected in the donor channel shortly after the beginning while while no reasonable correlation is observed between the signals in the donor channel and the FRET and/or acceptor channel, (**c**) the background correction results in significantly negative intensity in the donor channel, or (**d**) the background correction results in significantly negative intensity in the FRET and/or acceptor channel. The negative intensity values are probably caused by fluorescence events within the background circle in any of the three channels (see slso section 4.6.1 step 5) The numbers above each trace correspond to the numbers given to the initially identified donor-acceptor pairs in figure 4.18.



Figure 7.49: Second part of all intensity-time traces of the example measurement that have been identified as irregular (category IV). In particular, (**a**) the intensity in the FRET channel remains approximately constant, (**b**) no reasonable correlated signal is detected in the donor channel, or (**c**) noteworthy intensity is only detected in the acceptor channel. The numbers above each trace correspond to the numbers given to the initially identified donor-acceptor pairs in figure 4.18.

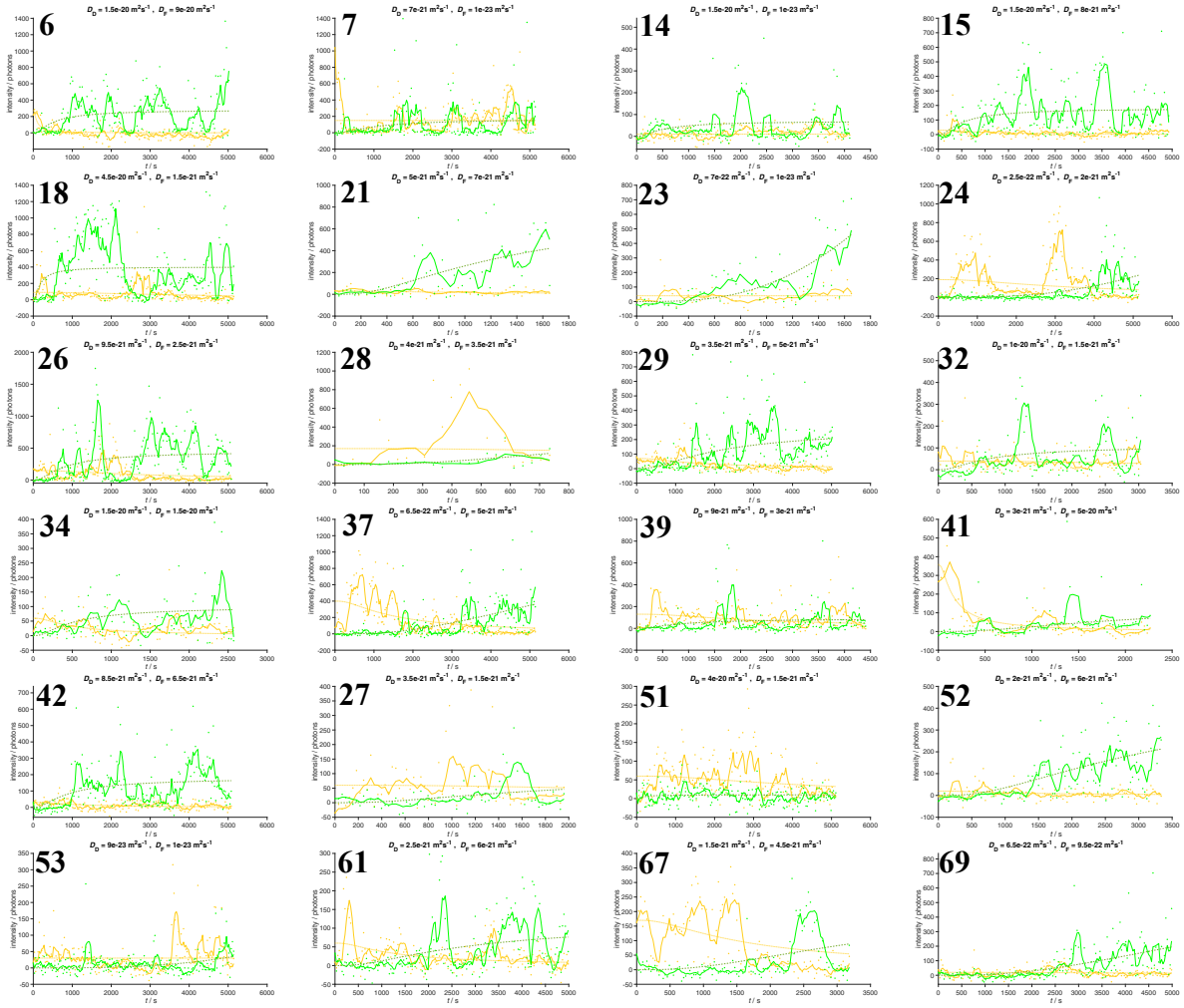

Figure 7.50: Separate fits of the individual FRET (orange) and donor (green) intensity-time traces shown in figure 4.19. The order of the individual fits is the same as order of intensity-time traces in figure 4.19. For a better overview, the identification number of the corresponding donor-acceptor pair is given in the upper left corner of each graph. The dots represent the summed-up intensity values, the solid lines indicate the moving average of these values. The dots are always 30.6 s apart corresponding to the temporal resolution of the measurement. The dotted orange lines corresponds to the fit of the FRET intensity-time traces. The dashed green lines corresponds to the fit of the donor intensity-time traces. The determined diffusion coefficients are listed above each graph. The data in each fit was restricted according to photobleaching of the donor. All fits are performed with equation (2.30).

Comparative FEDUP data in PVAc

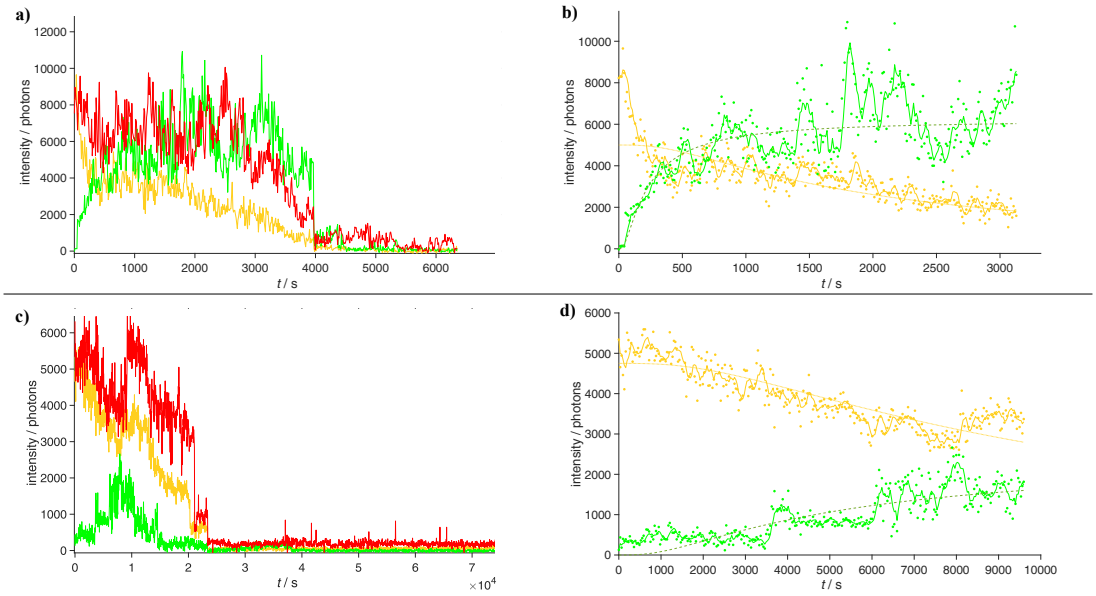

Figure 7.51: (**a, c**) Summed-up intensity-time traces of (**a**) 41 and (**c**) 17 FRET pairs of dyad **8** from overall (**a**) three and (**c**) four different measurements in tempered PVAc (184 kDa) at room temperature, respectively. The intensity-time traces of the FRET-, donor- and acceptor-channel are shown in orange, green and red, respectively. Thin lines in **a, c** and dots in **b, d** represent the summed-up intensity values at each measured point in time. Solid lines in (**b, d**) indicate the moving average of these values. A cycle time of (**a, b**) $t_{\mathrm{cycle}} = 10.6$ s and of (**c, d**) $t_{\mathrm{cycle}} = 32.64$ s was employed, respectively. (**b, d**) Separate fits of the FRET and the donor intensity-time traces with equation (2.30). The dotted orange line corresponds to the fit of the FRET intensity-time trace with a diffusion coefficient of (**b**) $D_F = 4.0 \times 10^{-21}$ m^2 s^{-1} and (**d**) $D_F = 7.0 \times 10^{-22}$ m^2 s^{-1}, respectively. The dashed green line corresponds to the fit of the donor intensity-time trace with a diffusion coefficient of (**b**) $D_D = 3.5 \times 10^{-20}$ m^2 s^{-1} and (**d**) $D_D = 1.5 \times 10^{-21}$ m^2 s^{-1}. The fits were restricted to approximately 10000 s diffusion time to counter the effect of photobleaching on the analysis.

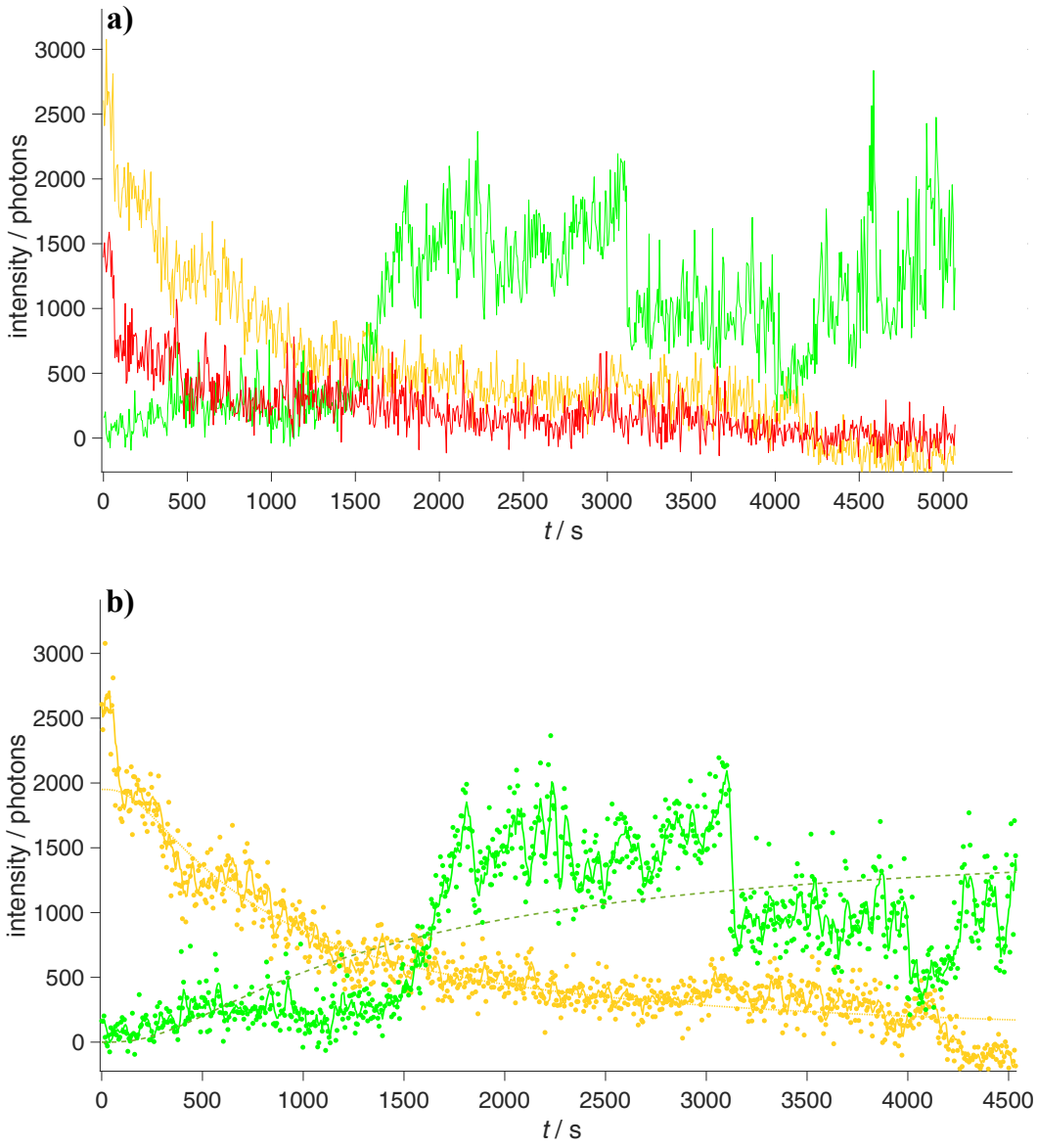

Figure 7.52: (a) Summed-up intensity-time traces of 16 cleaved donor-acceptor pairs of dyad **8** from overall two different measurements in tempered PVAc (184 kDa) at 40 °C. The intensity-time traces of the FRET-, donor- and acceptor-channel are shown in orange, green and red, respectively. Dots represent the summed-up intensity values at each measured point in time, solid lines indicate the moving average of these values. Between consecutive frames, a delay time of 5 s was employed during the measurements. (b) Separate fits of the FRET and the donor intensity-time trace shown in subfigure (a) according to equation (2.30). The dotted orange line corresponds to the fit of the FRET intensity-time trace with a diffusion coefficient of $D_F = 1.0 \times 10^{-20}$ m^2 s^{-1}. The dashed green line corresponds to the fit of the donor intensity-time trace with a diffusion coefficient of $D_D = 5.5 \times 10^{-21}$ m^2 s^{-1}.

Comparative FEDUP data in PBMA

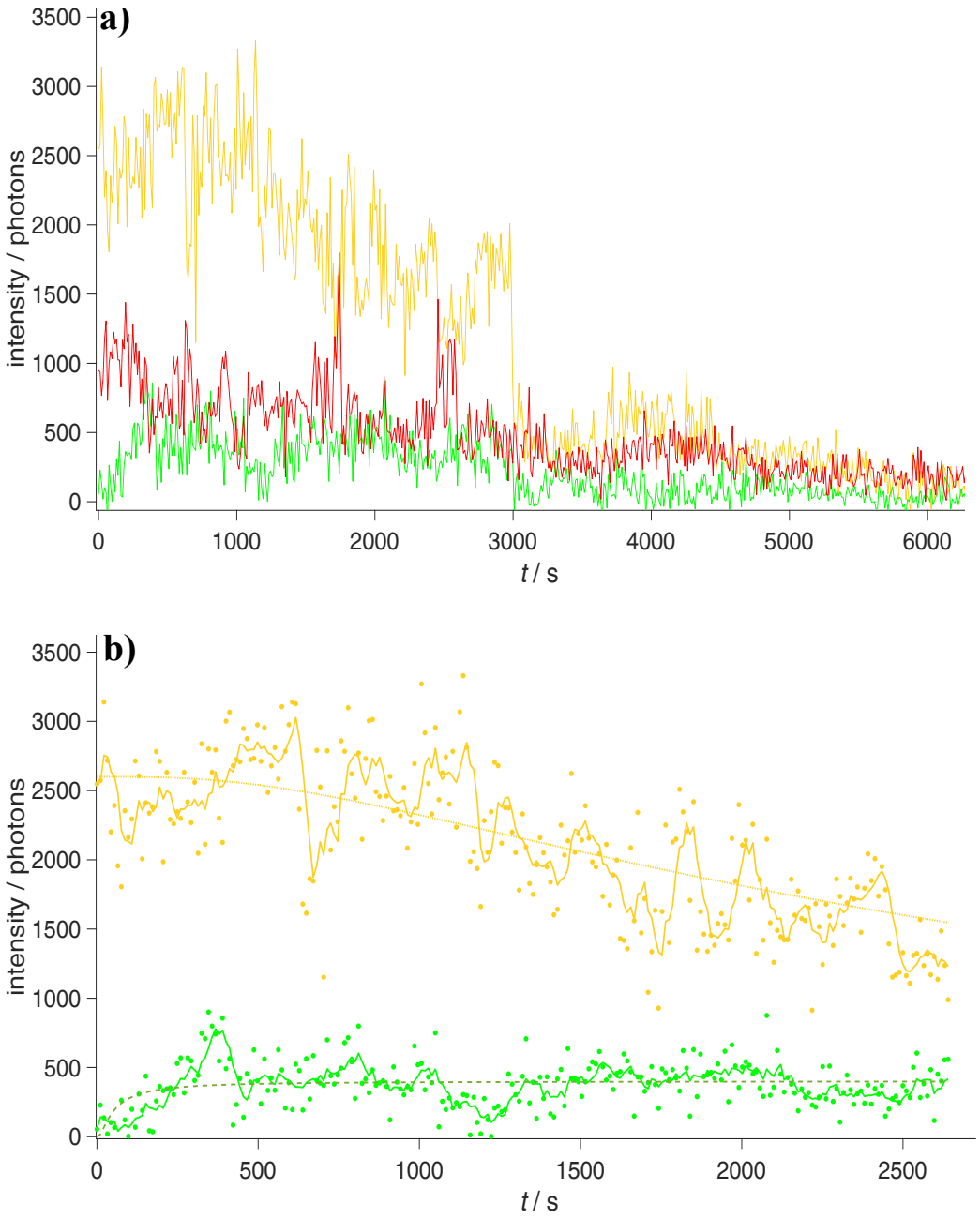

Figure 7.53: (**a**) Summed-up intensity-time traces of 15 FRET pairs from overall four different measurements in tempered PBMA (14.5 kDa) at 40 °C. The intensity-time traces of the FRET-, donor- and acceptor-channel are shown in orange, green and red, respectively. Thin lines and dots represent the summed-up intensity values at each measured point in time, solid lines indicate the moving average of these values. The cycle time was $t_{\mathrm{cycle}} = 10.82$ s. (**b**) Separate fits of the FRET and the donor intensity-time trace shown in subfigure (a) according to equation (2.30). The dotted orange line corresponds to the fit of the FRET intensity-time trace with a diffusion coefficient of $D_F = 2.5 \times 10^{-21}$ m^2 s^{-1}. The dashed green line corresponds to the fit of the donor intensity-time trace with a diffusion coefficient of $D_D = 1.5 \times 10^{-19}$ m^2 s^{-1}.

Comparative FEDUP data in PEG

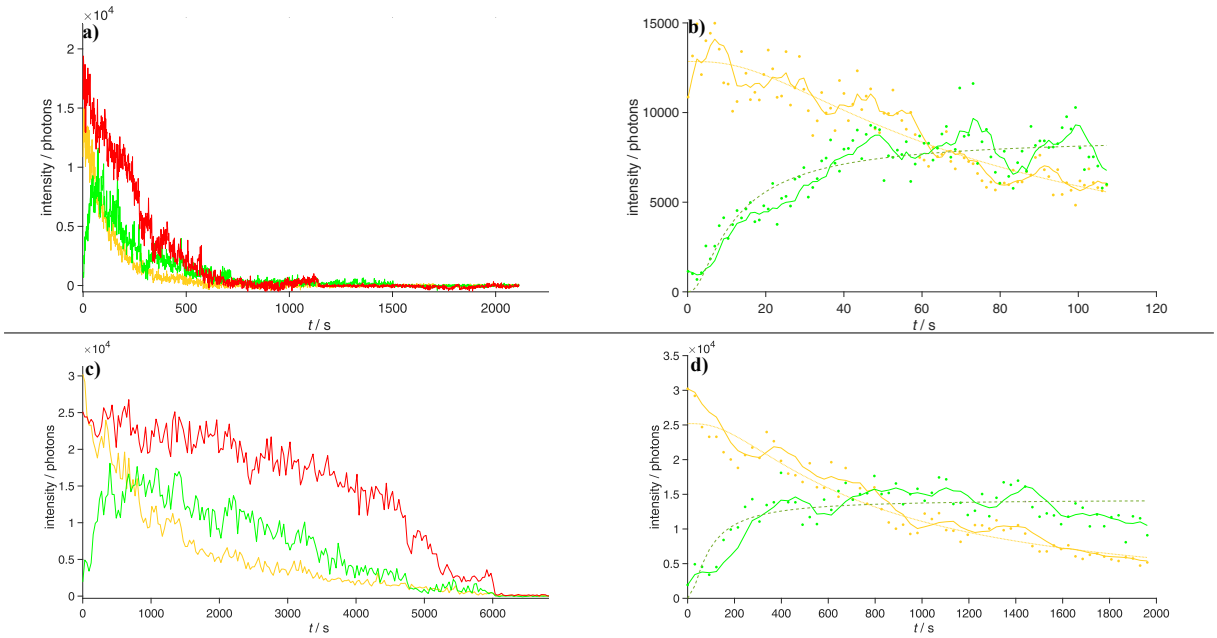

Figure 7.54: (**a, c**) Summed-up intensity-time traces of 79 and 132 FRET pairs from overall eight and ten different measurements in tempered PEG (35 kDa) at room temperature, respectively. The intensity-time traces of the FRET-, donor- and acceptor-channel are shown in orange, green and red, respectively. Solid lines in (**a, c**) and dots in (**b, d**) represent the summed-up intensity values at each measured point in time, solid lines in (**b, d**) indicate the moving average of these values. Cycle times of (**a, b**) $t_{\mathrm{cycle}} = 1.14$ s and (**c, d**) $t_{\mathrm{cycle}} = 30.64$ s were employed, respectively. (**b, d**) Separate fits of the FRET and the donor intensity-time trace shown in subfigure (**a**) and (**c**) with equation (2.30). The dotted orange line corresponds to the fit of the FRET intensity-time trace with a diffusion coefficient of (**b**) $D_F = 9.5 \times 10^{-20}$ m^2 s^{-1} and (**d**) $D_F = 1.0 \times 10^{-20}$ m^2 s^{-1}. The dashed green line corresponds to the fit of the donor intensity-time trace with a diffusion coefficient of (**b**) $D_D = 6.5 \times 10^{-19}$ m^2 s^{-1} and (**d**) $D_D = 9.0 \times 10^{-20}$ m^2 s^{-1}. The fits were restricted until photobleaching of either donor or acceptor becomes dominant.

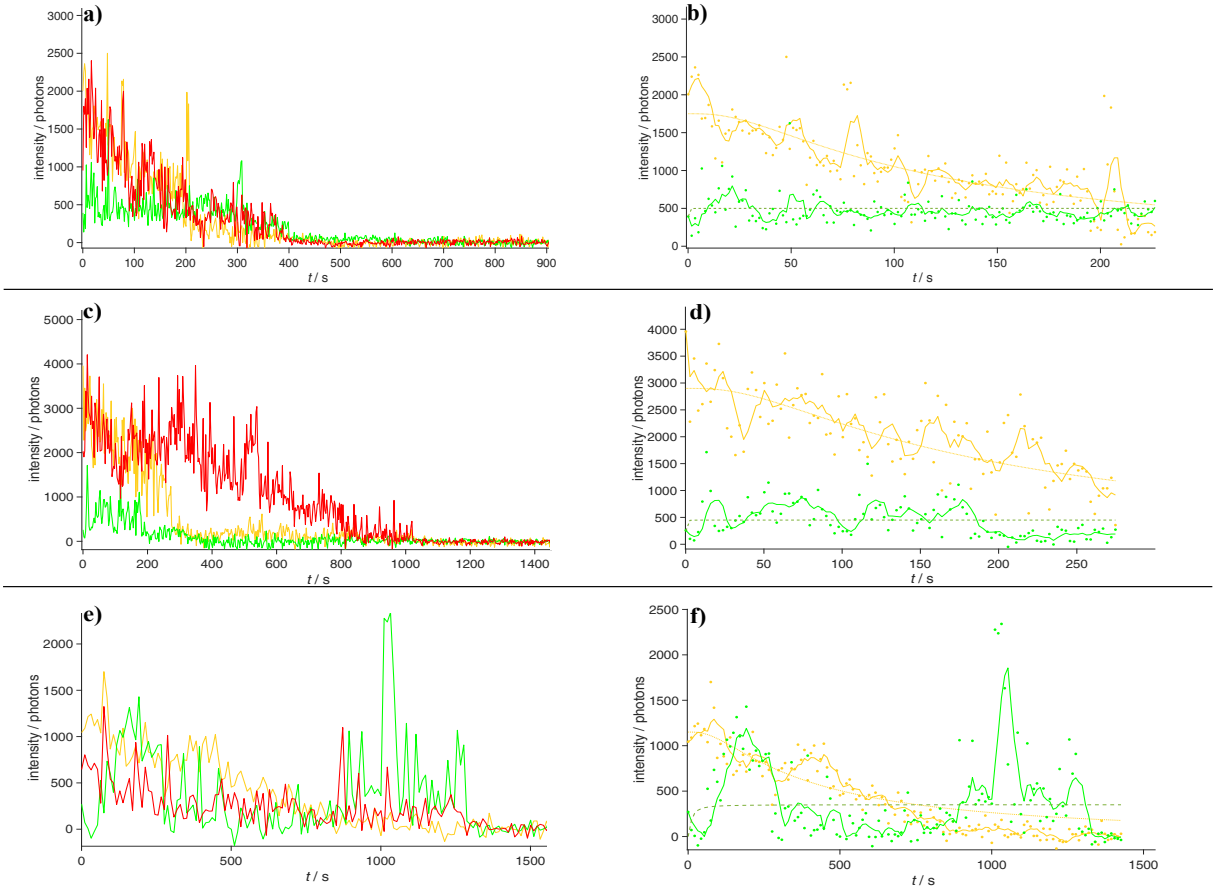

Figure 7.55: (**a, c, e**) Summed-up intensity-time traces of (**a**) 19, (**c**) 20 and (**e**) 12 FRET pairs from (**a, c**) four and (**e**) six different measurements in tempered PEG (35 kDa) at 40 °C, respectively. The intensity-time traces of the FRET-, donor- and acceptor-channel are shown in orange, green and red, respectively. Thin lines in (**a, c, e**) and dots in (**c, d, f**) represent the summed-up intensity values at each measured point in time. The solid lines in (**c, d, f**) indicate the moving average of these values. A cycle time of (**a, b**) $t_{\text{cycle}} = 1.64$ s, (**c, d**) $t_{\text{cycle}} = 2.64$ s and (**e, f**) $t_{\text{cycle}} = 10.64$ s was employed, respectively. (**b, d, f**) Separate fits of the FRET and the donor intensity-time traces with equation (2.30). The dotted orange line corresponds to the fit of the FRET intensity-time trace with a diffusion coefficient of (**b**) $D_F = 6.5 \times 10^{-20}$ m^2 s^{-1}, (**d**) $D_F = 3.5 \times 10^{-20}$ m^2 s^{-1} and (**f**) $D_F = 2.5 \times 10^{-20}$ m^2 s^{-1}, respectively. The dashed green line corresponds to the fit of the donor intensity-time trace with a diffusion coefficient of (**b**) $D_D = 2.0 \times 10^{-16}$ m^2 s^{-1} and (**d**) $D_D = 2.5 \times 10^{-18}$ m^2 s^{-1} and (**f**) $D_D = 8.0 \times 10^{-19}$ m^2 s^{-1}, respectively. The fits were restricted to measurement times when photobleaching of the donor becomes dominant.

7.5 AFM images of thin polymer films

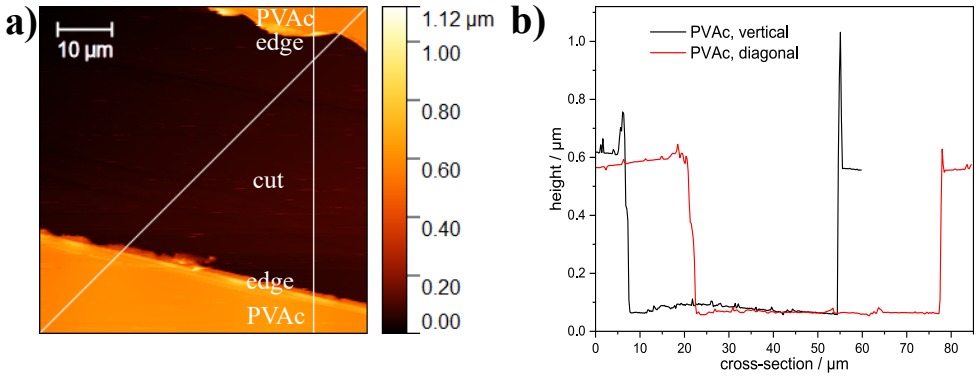

Figure 7.56: a) AFM image of manual cut in a PVAc film (100 kDa, 8w% MeOH solution, spincoated and tempered). The image was recorded in tapping mode with a setpoint of 30 nm, a scan size of 60×60 µm with 256×256 pixels and a line rate of 0.5 lines per second. The white lines represent the measured height profiles in image (b). b) Height profile from bottom to top along the vertical (black) and the diagonal (red) line shown in image (a). An average film thickness of about 500 nm is derived. Material from the region of the cut is pushed to the edges resulting in a local height increase which has to be ignored for the estimation of the average thickness.

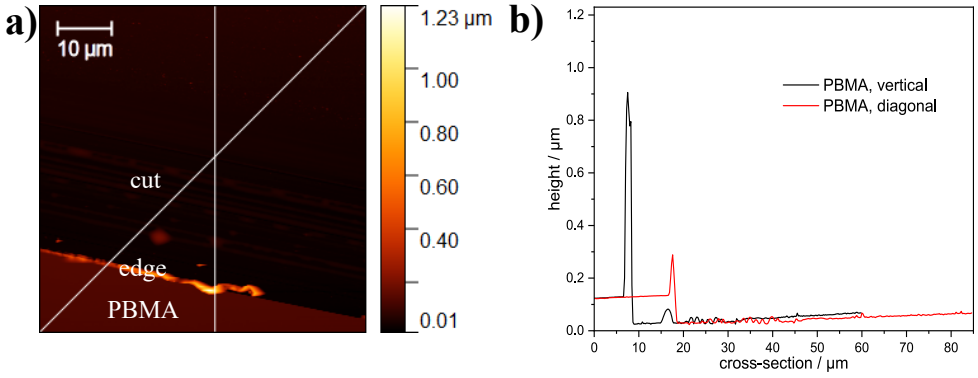

Figure 7.57: a) AFM image of manual cut in a PBMA film (14 kDa, 3w% toluene solution, spincoated and tempered). The image was recorded in tapping mode with a setpoint of 30 nm, a scan size of 60×60 µm with 256×256 pixels and a line rate of 0.5 lines per second. The white lines represent the measured height profiles in image (b). b) Height profile from bottom to top along the vertical (black) and the diagonal (red) line shown in image (a). An average film thickness of about 110 nm is derived. Material from the region of the cut is pushed to the edges resulting in a local height increase which has to be ignored for the estimation of the average thickness.

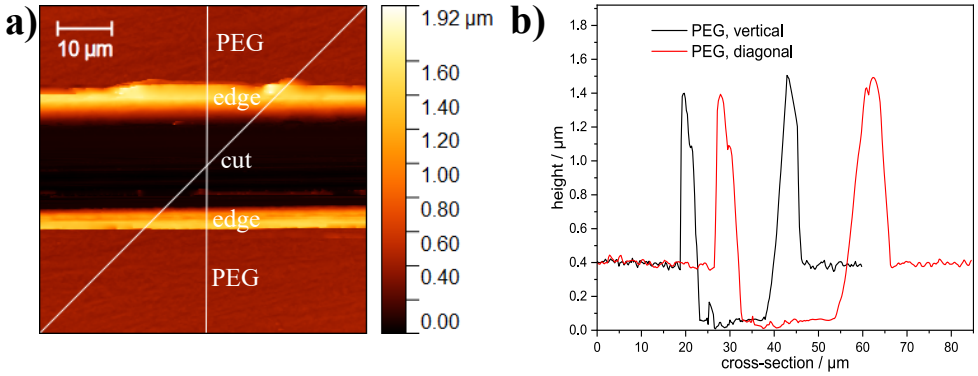

Figure 7.58: a) AFM image of manual cut in a PEG film (35 kDa, 5w% MeOH solution, spincoated and tempered). The image was recorded in tapping mode with a setpoint of 30 nm, a scan size of 60×60 µm with 256×256 pixels and a line rate of 0.5 lines per second. The white lines represent the measured height profiles in image (b). b) Height profile from bottom to top along the vertical (black) and the diagonal (red) line shown in image (a). An average film thickness of about 350 nm is derived. Material from the region of the cut is pushed to the edges resulting in a local height increase which has to be ignored for the estimation of the average thickness.

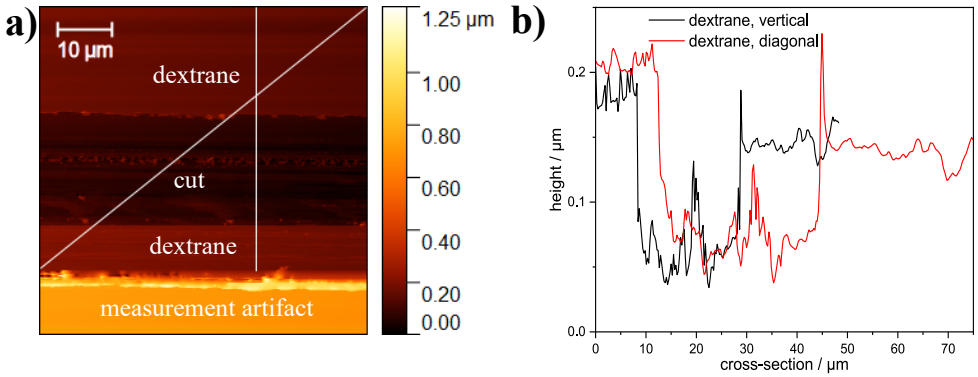

Figure 7.59: a) AFM image of manual cut in a dextrane film (70 kDa, 3w% aqueous solution, spincoated and tempered). The image was recorded in tapping mode with a setpoint of 30 nm, a scan size of 60×60 µm with 256×256 pixels and a line rate of 0.5 lines per second. The white lines represent the measured height profiles in image (b). The inhomogeneous area at the bottom of the image is estimated to be a measurement artifact. b) Height profile from bottom to top along the vertical (black) and the diagonal (red) line shown in image (a). An average film thickness of about 100 – 150 nm is derived. Material from the region of the cut is pushed to the edges resulting in a local height increase which has to be ignored for the estimation of the average thickness.

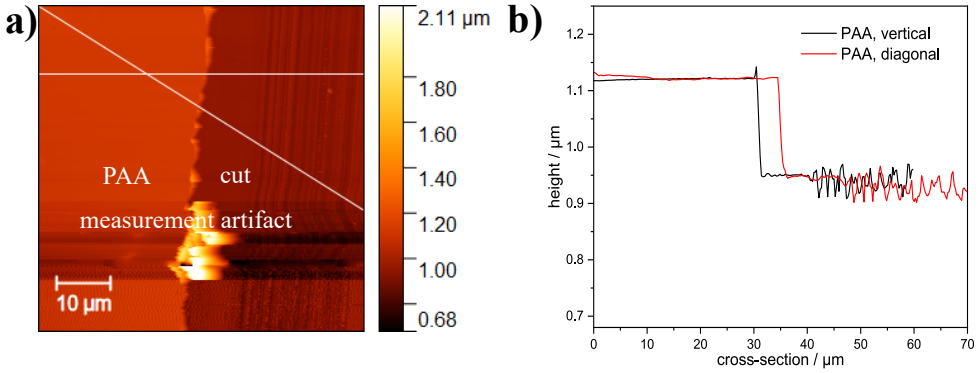

Figure 7.60: a) AFM image of manual cut in a PAA film (450 kDa, 2w% MeOH solution, spincoated and tempered). The image was recorded in tapping mode with a setpoint of 30 nm, a scan size of 60×60 µm with 256×256 pixels and a line rate of 0.5 lines per second. The white lines represent the measured height profiles in image (b). The inhomogeneous area at the bottom of the image is estimated to be a measurement artifact due to some particularly high features in the polymer film stemming from the cut. b) Height profile from left to right along the horizontal (black) and the diagonal (red) line shown in image (a). An average film thickness of about 170 nm is derived. Material from the region of the cut is pushed to the edges resulting in a local height increase which has to be ignored for the estimation of the average thickness.

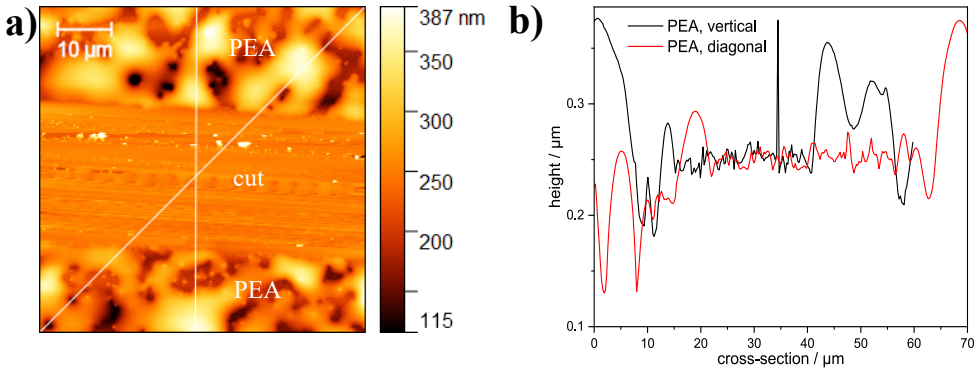

Figure 7.61: a) AFM image of manual cut in a PEA film (335 kDa, 3w% MeOH solution, spincoated and tempered). The image was recorded in tapping mode with a setpoint of 30 nm, a scan size of 60×60 µm with 256×256 pixels and a line rate of 0.5 lines per second. The white lines represent the measured height profiles in image (b). b) Height profile from bottom to top along the vertical (black) and the diagonal (red) line shown in image (a). An average film thickness of about 120 – 200 nm is derived. The polymer film shows major inhomogeneities all throughout the image.

7.6 DSC curves

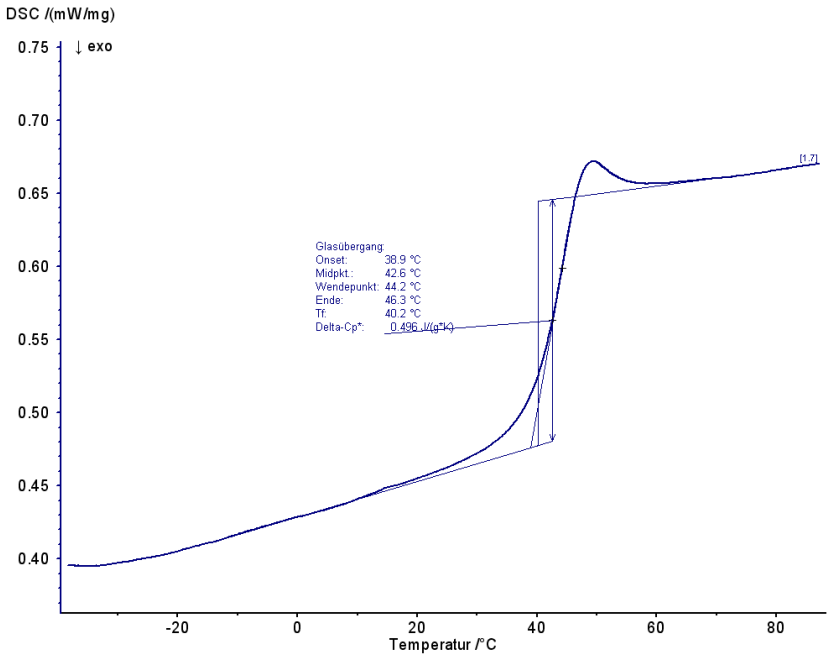

Figure 7.62: DSC curve of PVAc (184 kDa). Heating and cooling rate was 20 $\mathrm{K\,min^{-1}}$. The glass transition temperature $T_g = 42.6$ °C was determined during the second heating process as the midpoint of the curve.

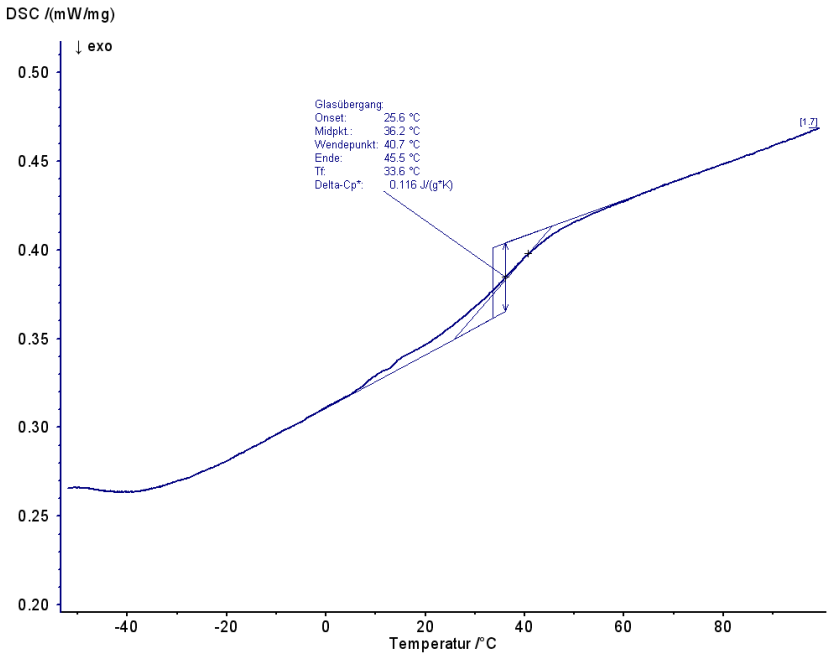

Figure 7.63: DSC curve of PBMA (14 kDa). Heating and cooling rate was 20 $\mathrm{K\,min^{-1}}$. The glass transition temperature $T_g = 36.2$ °C was determined during the second heating process as the midpoint of the curve.

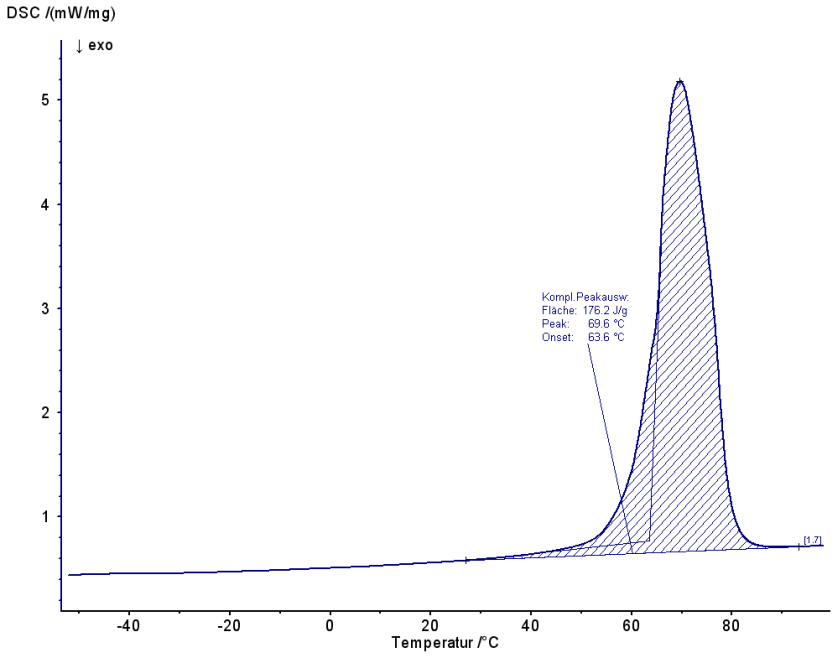

Figure 7.64: DSC curve of PEG (35 kDa). Heating and cooling rate was 20 K min^{-1}. No glass transition could be determined. The band between 40 – 90 °C indicates melting of the polymer.

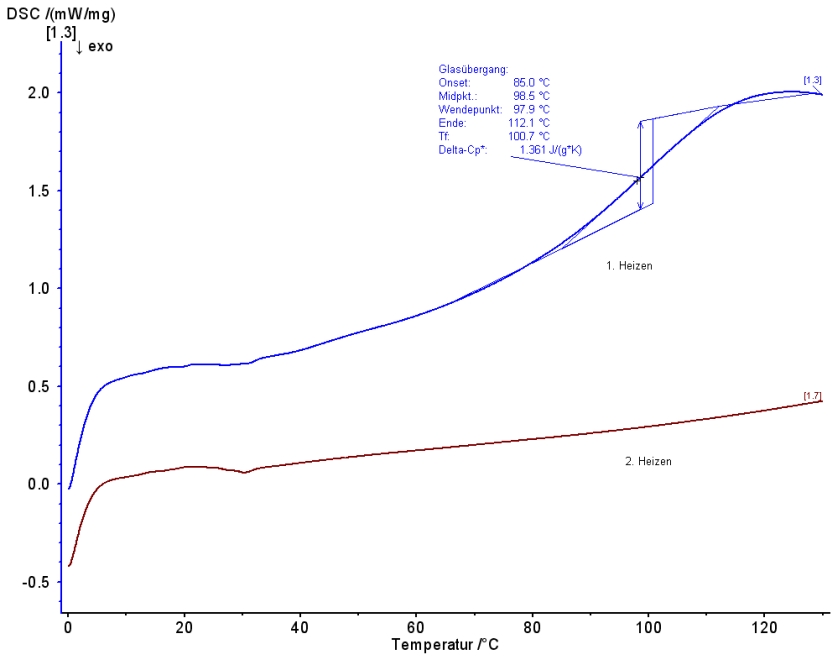

Figure 7.65: DSC curve of dextrane (70 kDa). Heating and cooling rate was 20 K min^{-1}. The glass transition temperature $T_g = 98.5$ °C was determined during the first heating process (blue curve) as the midpoint of the curve. The structure of the curve fades entirely during the second heating process indicating a thermal decomposition at elevated temperatures.

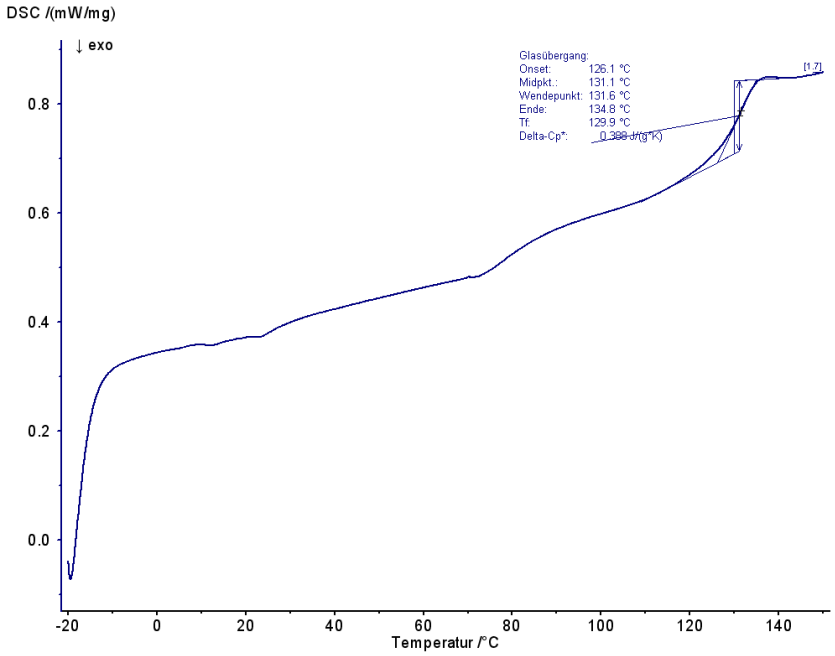

Figure 7.66: DSC curve of PAA (450 kDa). Heating and cooling rate was 20 K min^{-1}. The glass transition temperature $T_g = 131.1$ °C was determined during the second heating process as the midpoint of the curve.

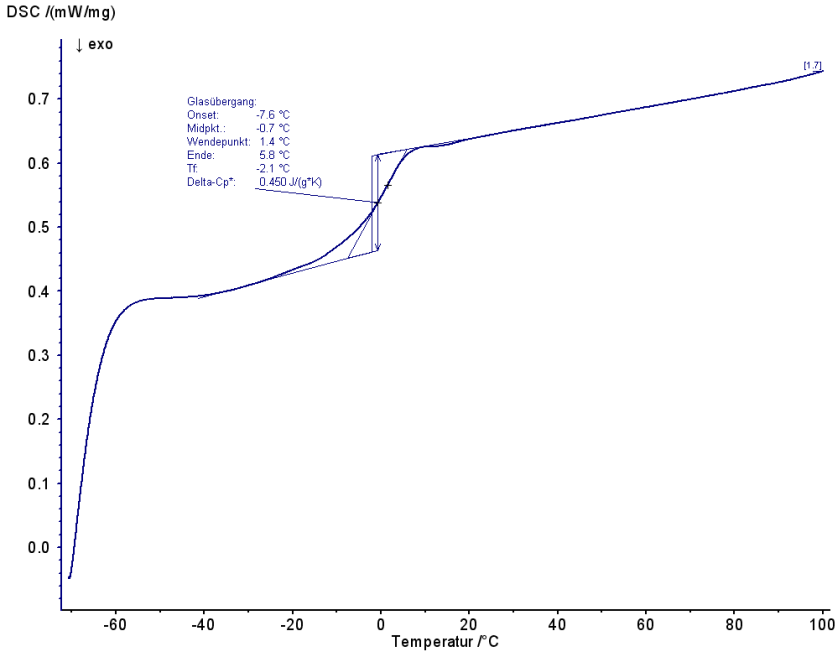

Figure 7.67: DSC curve of PEA (335 kDa). Heating and cooling rate was 20 K min^{-1}. The glass transition temperature $T_g = -0.7$ °C was determined during the second heating process as the midpoint of the curve.

7.7 NMR spectra

7.7.1 2-Nitrosotoluene

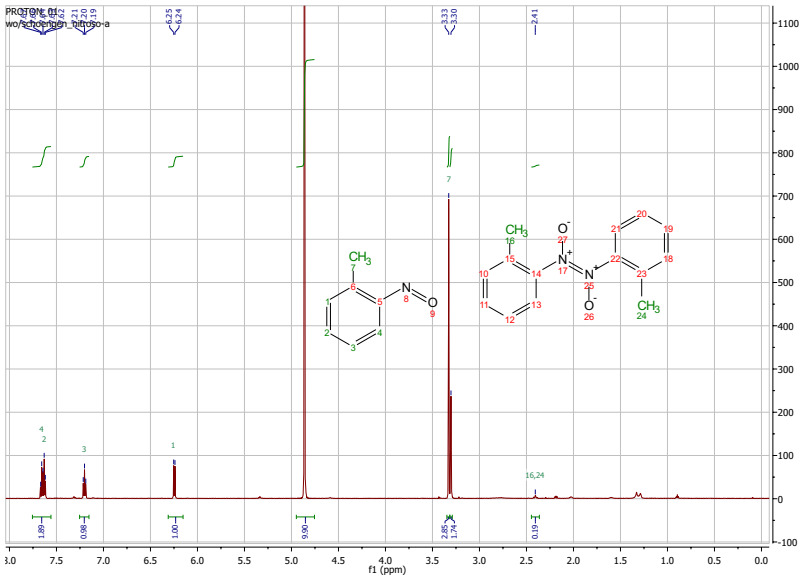

Figure 7.68: ^{1}H-NMR spectrum of 2-nitrosotoluene at a concentration of 12.7 mM in MeOH$-$d$_4$ at 600 MHz. The singlet peaks at 2.40 ppm and 2.42 ppm correspond to the methyl peaks of the dimer in trans- and cis-conformation, respectively.[59]

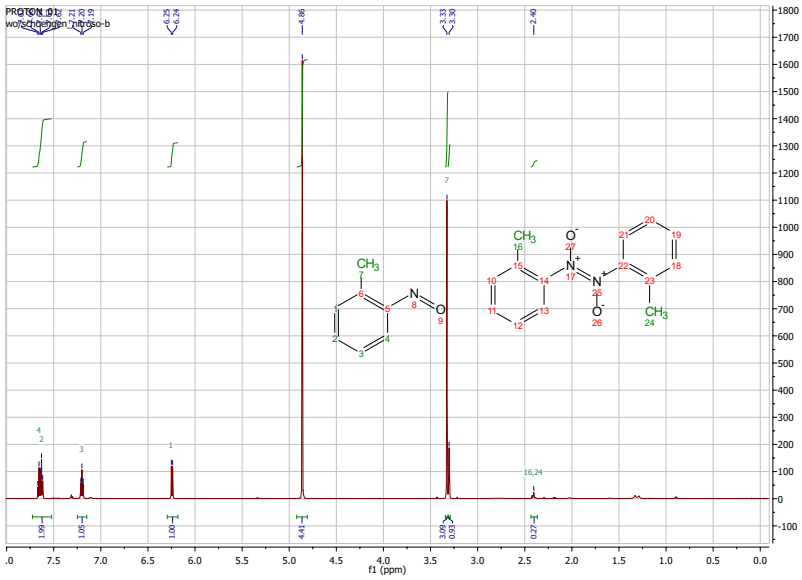

Figure 7.69: ^{1}H-NMR spectrum of 2-nitrosotoluene at a concentration of 25.5 mM in MeOH$-$d$_4$ at 600 MHz. The singlet peaks at 2.40 ppm and 2.42 ppm correspond to the methyl peaks of the dimer in trans- and cis-conformation, respectively.[59]

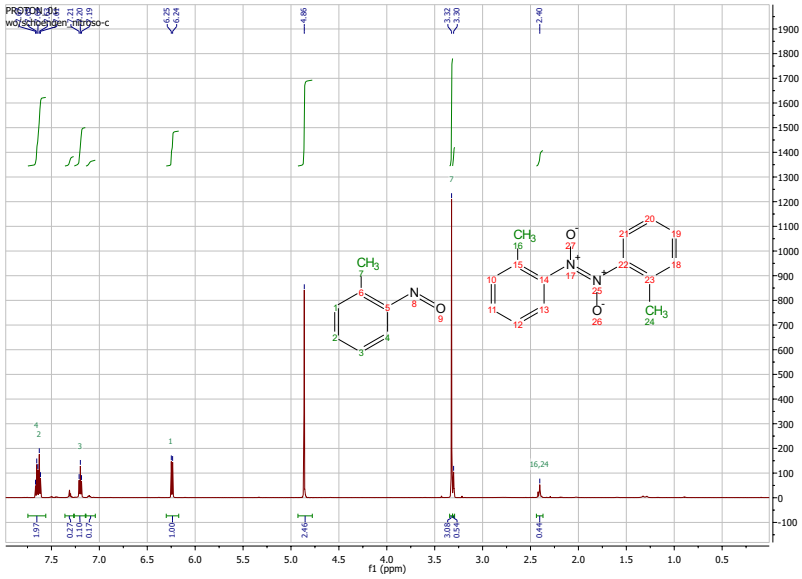

Figure 7.70: ^{1}H-NMR spectrum of 2-nitrosotoluene at a concentration of 49.7 mM in MeOH$-$d$_4$ at 600 MHz. The singlet peaks at 2.40 ppm and 2.42 ppm correspond to the methyl peaks of the dimer in trans- and cis-conformation, respectively.[59]

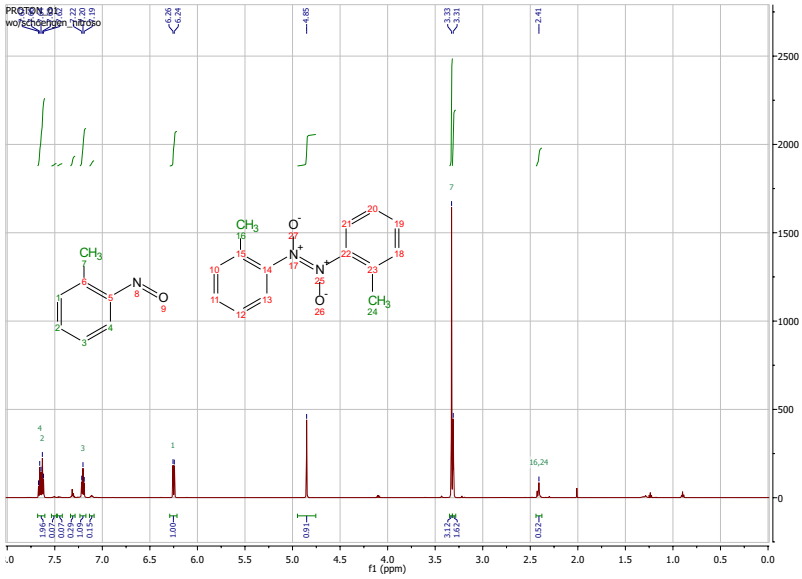

Figure 7.71: ^{1}H-NMR spectrum of 2-nitrosotoluene at a concentration of 82.4 mM in MeOH$-$d$_4$ at 600 MHz. The singlet peaks at 2.40 ppm and 2.42 ppm correspond to the methyl peaks of the dimer in trans- and cis-conformation, respectively.[59]

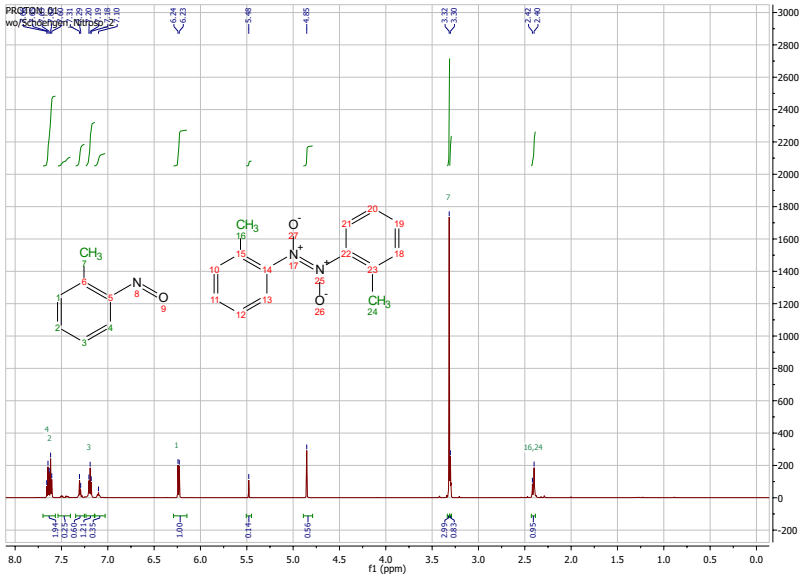

Figure 7.72: ^{1}H-NMR spectrum of 2-nitrosotoluene at a concentration of 154 mM in MeOH$-$d$_4$ at 600 MHz. The singlet peaks at 2.40 ppm and 2.42 ppm correspond to the methyl peaks of the dimer in trans- and cis-conformation, respectively.[59]

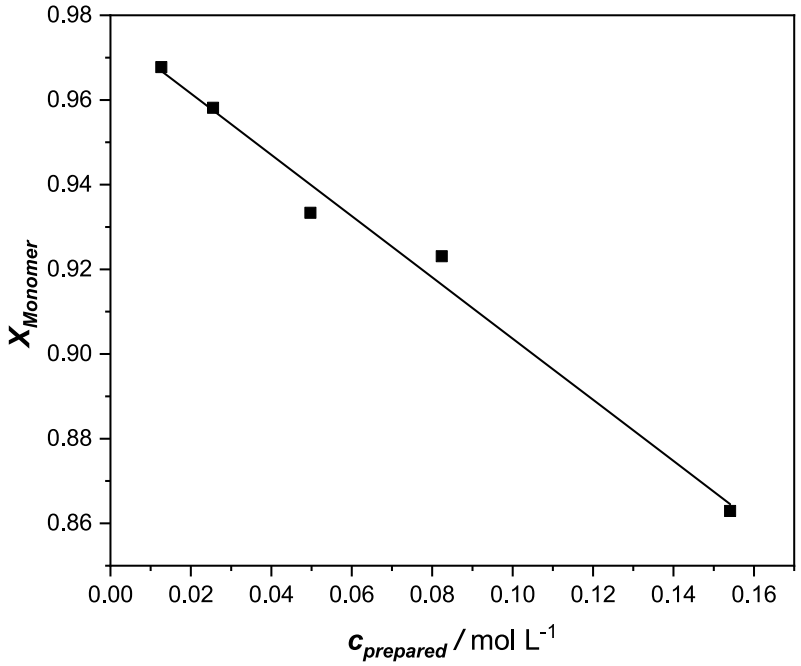

Figure 7.73: Plot of the prepared concentration of 2-nitrosotoluene as determined from the weighted mass assuming complete dissociation vs. the mole fraction of the monomeric form as determined by ^{1}H-NMR. The data was fitted with a linear function with a slope of $m = -0.7232\,\mathrm{L\,mol^{-1}}$ and intercept of $y = 0.9760$. We assume that the concentrations used in our Stern-Volmer experiments are within the linear regime of the monomer-dimer equilibrium of 2-nitrosotoluene.[59]

7.7.2 Synthesis

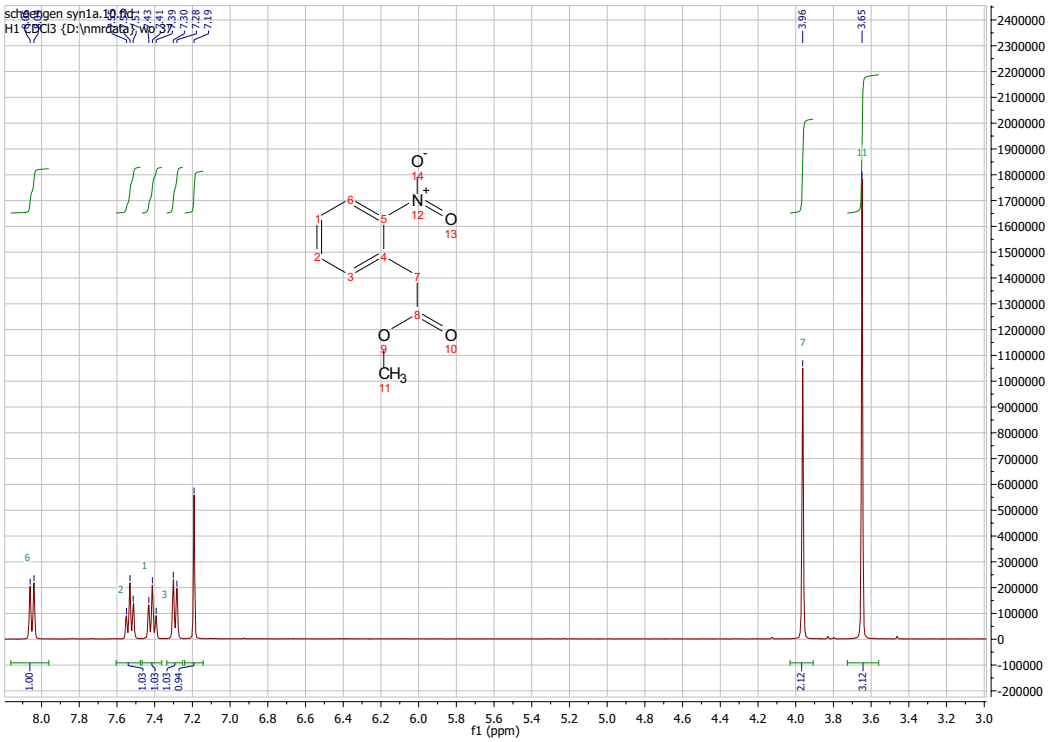

Figure 7.74: ^{1}H-NMR spectrum of methyl (2-nitrophenyl)acetate (**1**) in $CDCl_3$ at 600 MHz.[59]

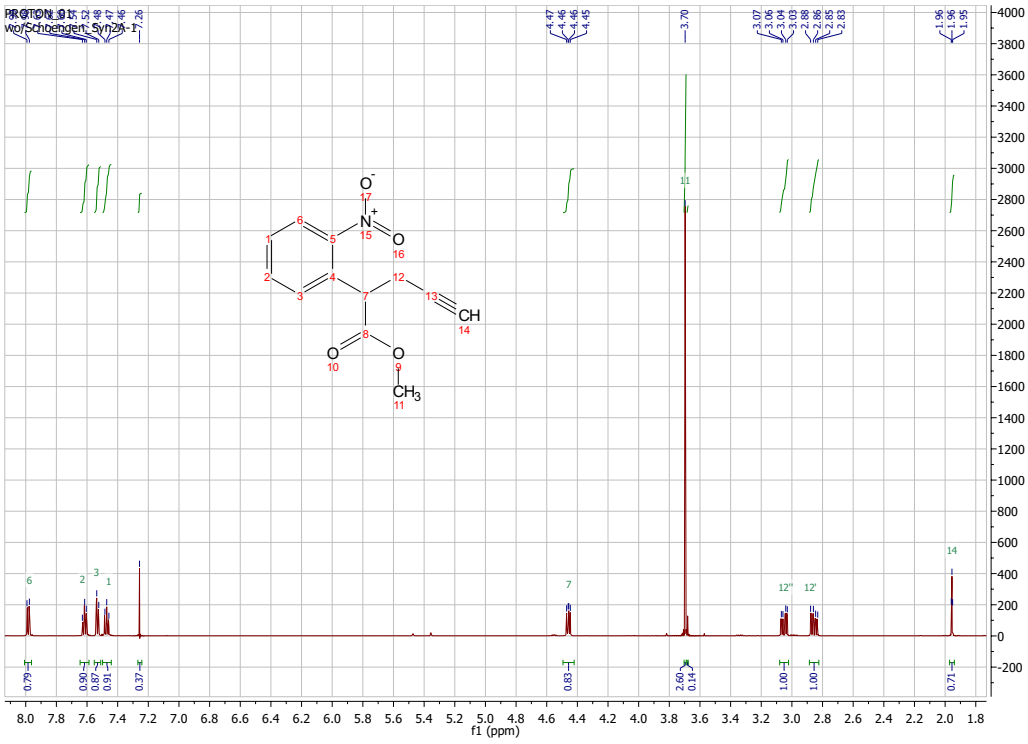

Figure 7.75: ^{1}H-NMR spectrum of methyl 2-(2-nitrophenyl)pent-4-ynoate (**2**) in $CDCl_3$ at 600 MHz.[59]

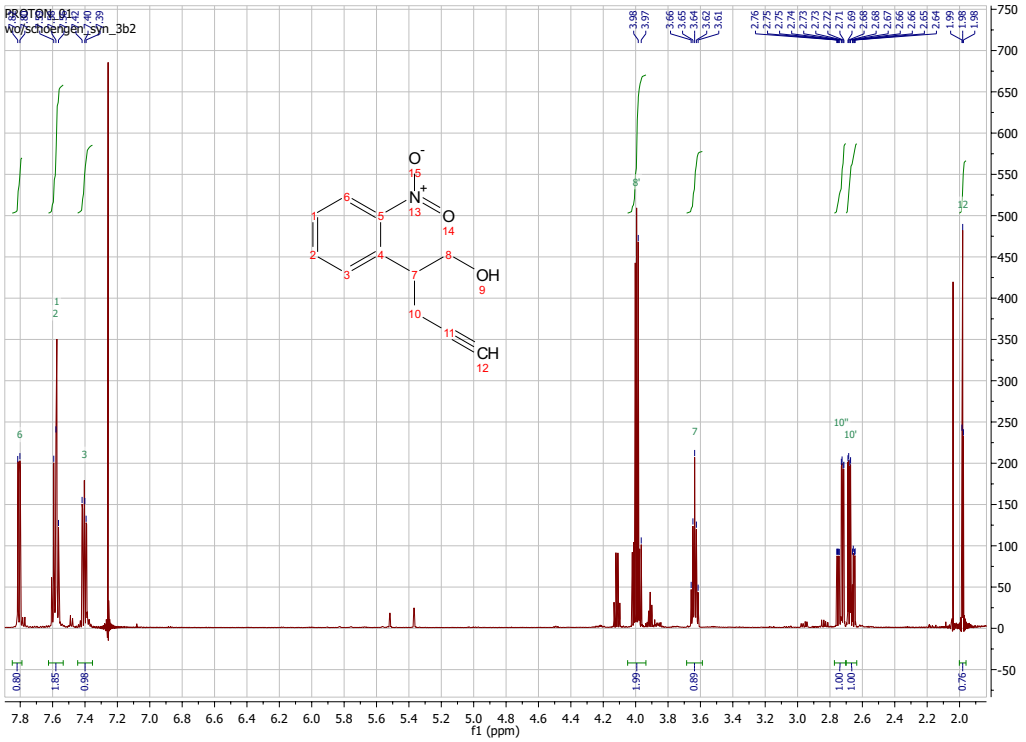

Figure 7.76: ^{1}H-NMR spectrum of methyl 2-(2-nitrophenyl)pent-4-yn-1-ol (**3**) in $CDCl_3$ at 600 MHz.[59]

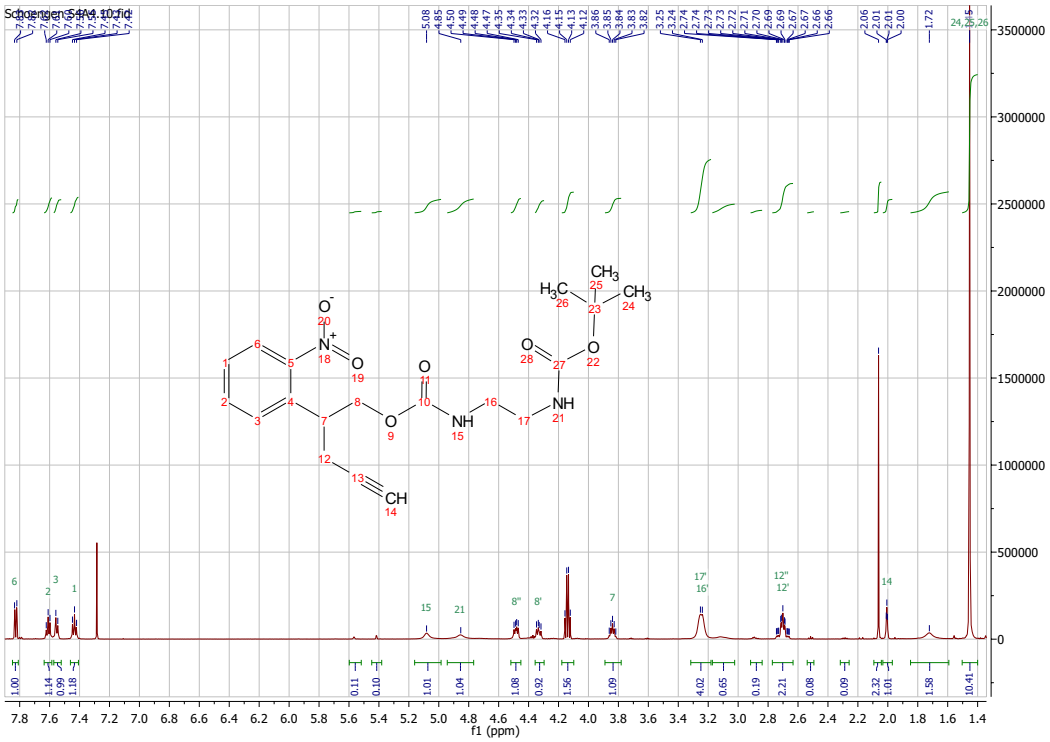

Figure 7.77: ^{1}H-NMR spectrum of tert-butyl (2-(2-nitrophenyl)pent-4-yn-1-yl) ethane-1,2-diyldicarbamate (**4**) in $CDCl_3$ at 600 MHz.[59]

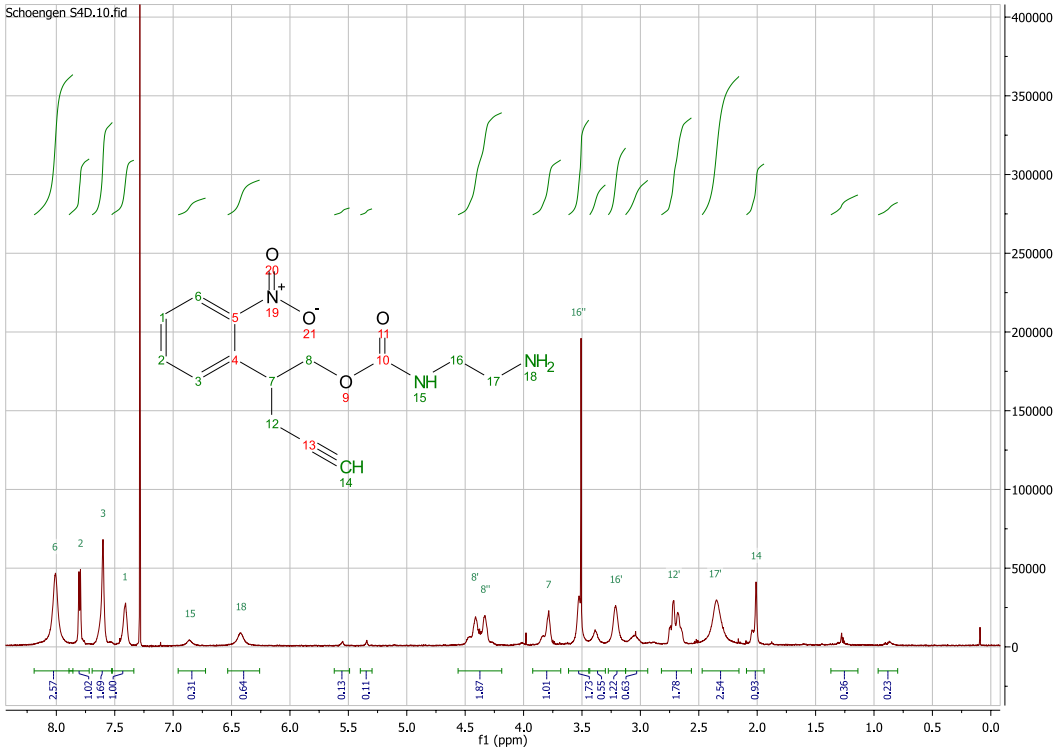

Figure 7.78: ^{1}H-NMR spectrum of 2-(2-nitrophenyl)pent-4-yn-1-yl (2-aminoethyl)carbamate (**5**) in $CDCl_3$ at 600 MHz.

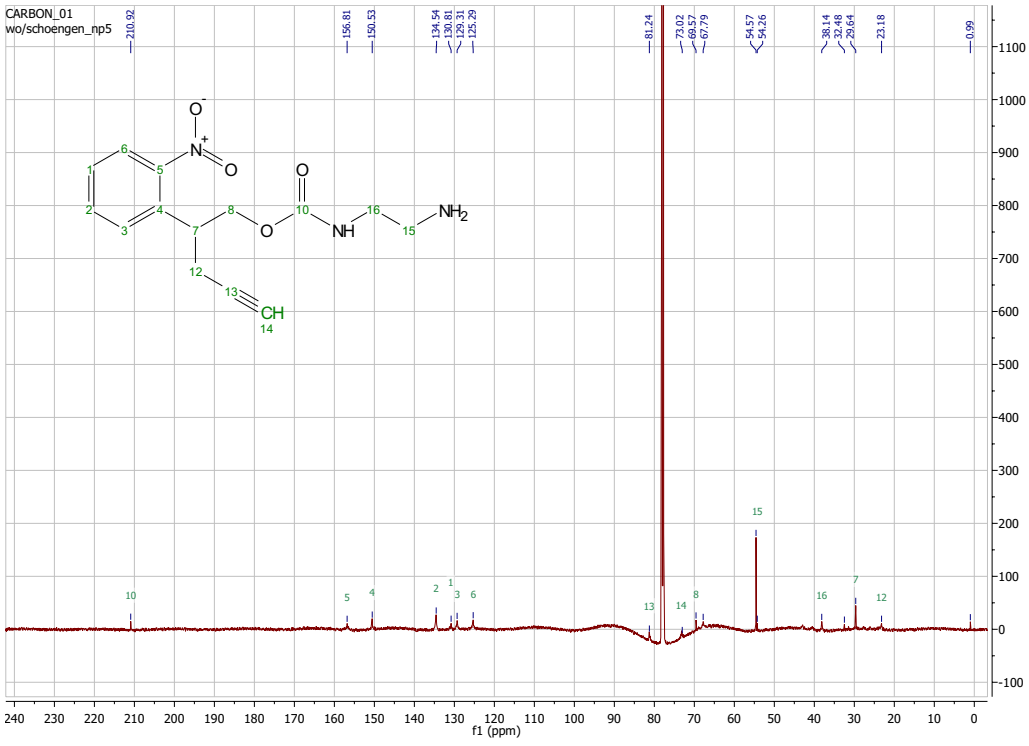

Figure 7.79: ^{13}C-NMR spectrum of 2-(2-nitrophenyl)pent-4-yn-1-yl (2-aminoethyl)carbamate (**5**) in $CDCl_3$ at 150 MHz, decoupling at 600 MHz.[59]

7.8 ESI-MS spectra

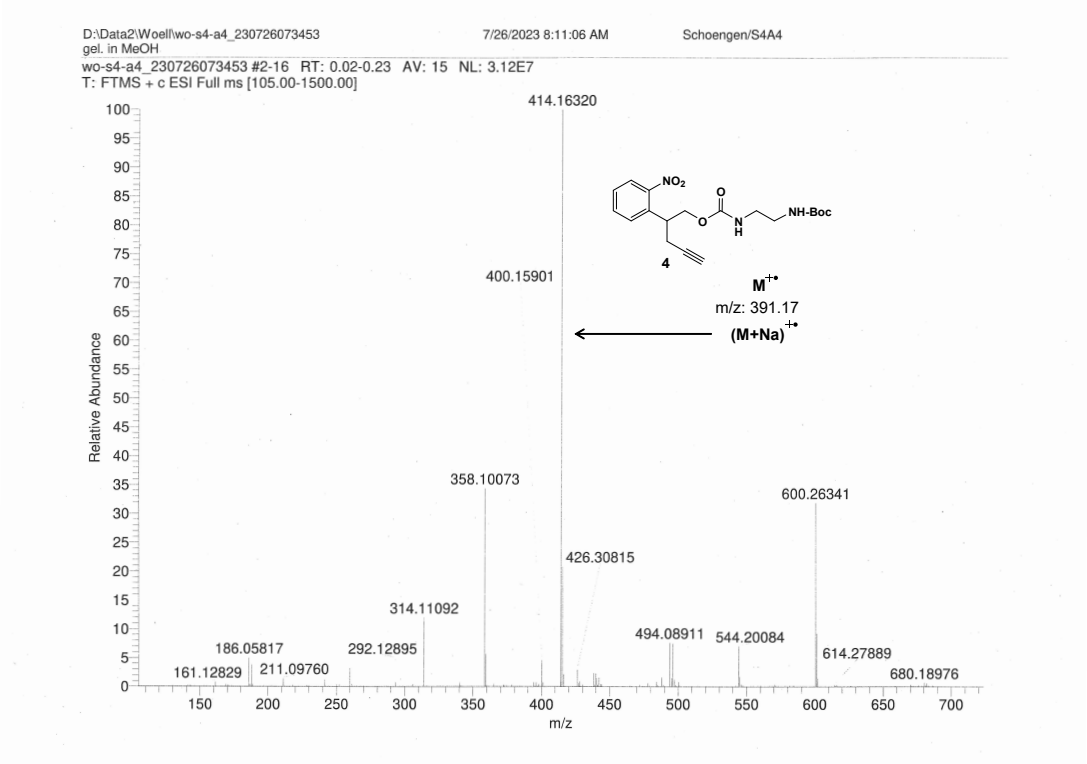

Figure 7.80: ESI-MS spectrum of tert-butyl (2-(2-nitrophenyl)pent-4-yn-1-yl) ethane-1,2-diyldicarbamate (**4**).[59]

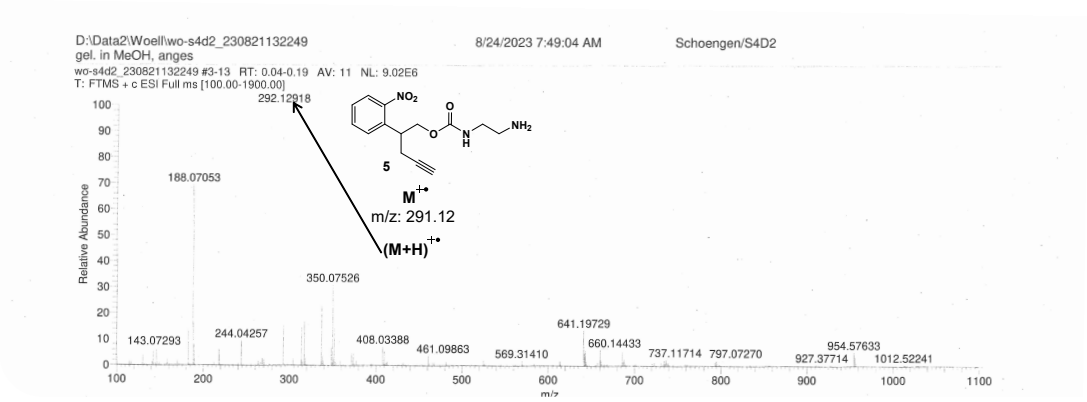

Figure 7.81: ESI-MS spectrum of (2-(2-nitrophenyl)pent-4-yn-1-yl) (2-aminoethyl)carbamate (**5**).[59]

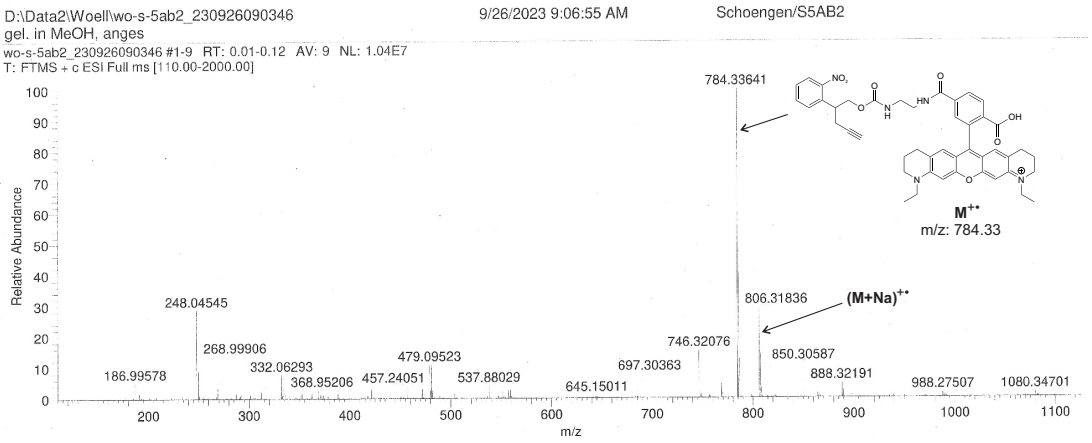

Figure 7.82: ESI-MS spectrum of donor **6**.[59]

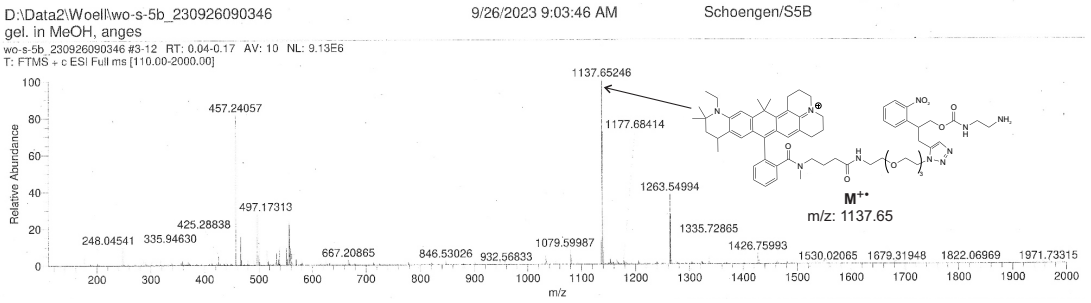

Figure 7.83: ESI-MS spectrum of acceptor **7**.[59]

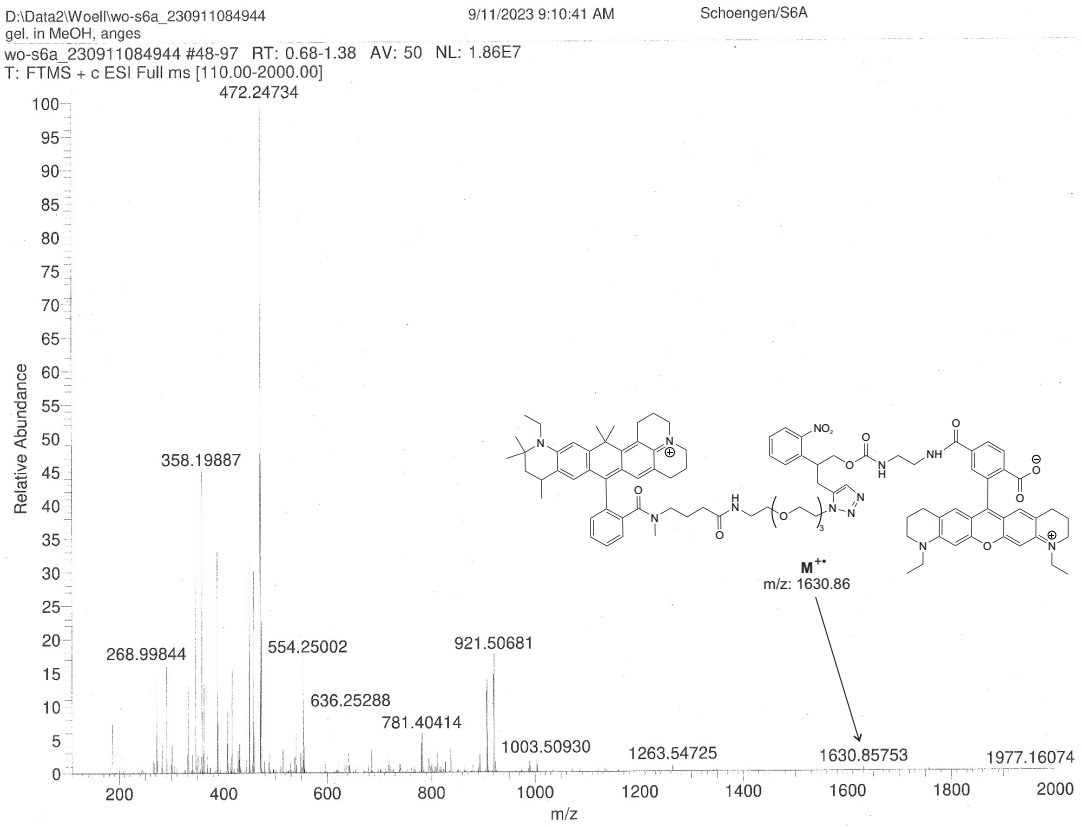

Figure 7.84: ESI-MS spectrum of dyad **8**.[59]

7.9 HPLC

Chromatogram : AK-Woell-DS-Dyad-8_channel1

System : PREP
Method : varian-1
User : Varian
Run Time: 91.52

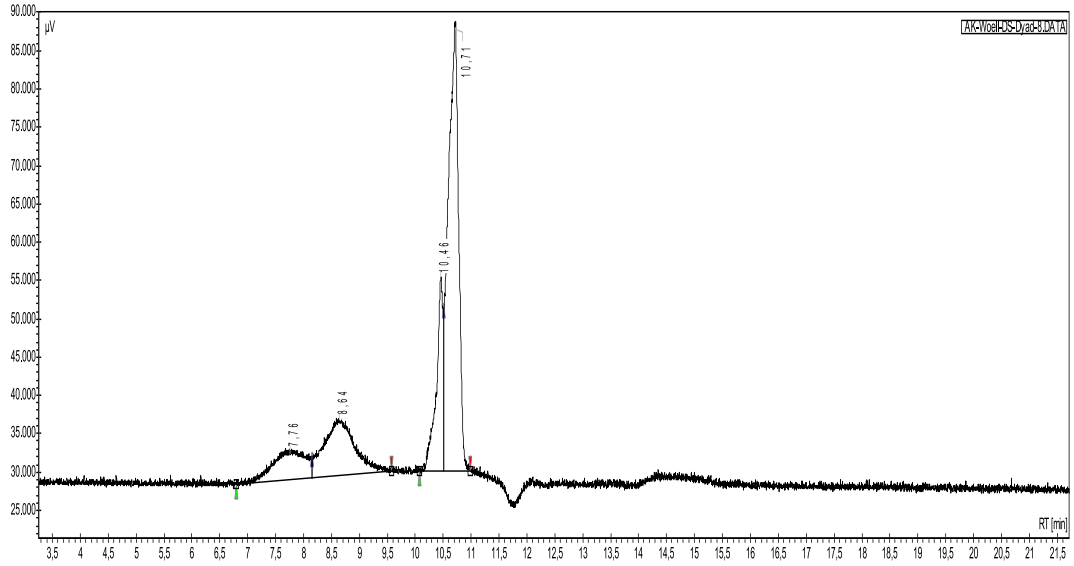

Peak results :

AK-Woell-DS-Dyad-8.DATA [UV Kanal]

Index	Name	Time [Min]	Quantity [% Area]	Height [µV]	Area [µV.Min]	Area % [%]
1	UNKNOWN	7,76	11,36	3404,9	2675,6	11,364
3	UNKNOWN	8,64	19,73	7230,0	4644,4	19,725
2	UNKNOWN	10,46	15,17	24954,2	3573,0	15,175
4	UNKNOWN	10,71	53,74	58154,6	12652,6	53,737
Total			100,00	93743,6	23545,5	100,000

Figure 7.85: HPLC chromatogram of the dyad **8** pre-purified according to synthesis of dyad **8**. Eluent was methanol with 0.02% acetic acid and 0.01% trifluoroacetic acid. Everything between retention times from 6 – 9.5 min was united to fraction 1, everything between retention times from 10 – 11 min was united to fraction 2. Both fractions were characterized with UV-Vis and fluorescence spectroscopy, see figure 7.86. The detection in the HPLC was performed at 275 nm. The characterization with UV-Vis spectroscopy revealed that impurities absorbing or scattering in the UV region accumulated in the sample after the HPLC. Hence, the chromatogram is not quantitative.[59]

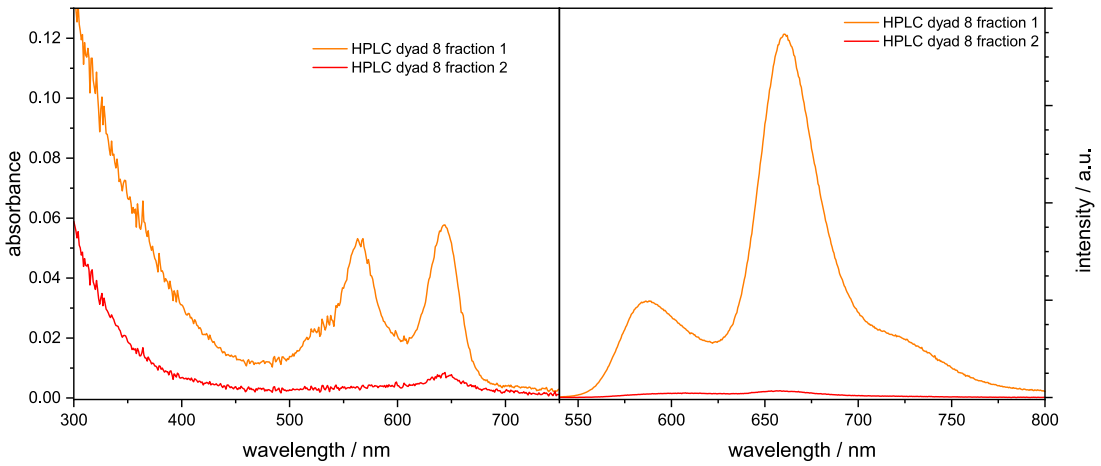

Figure 7.86: Absorption and emission spectra of the two HPLC fraction seen in figure 7.85. The excitation wavelength was 530 nm. Fraction 1 was identified as dyad **8**, fraction 2 is assumed to be unreacted free ATTO647N-azide. No significant changes to the spectra in the main text are observed apart from a different behavior in the UV region. We assume these to stem from impurities, in particular column material, from the HPLC column.[59]

7.10 ATTO-TEC product information

ATTO-TEC GmbH
Martinshardt 7
D-57074 Siegen
Germany
Phone: +49 271 23853 – 0
FAX: +49 271 23853 – 11
E-mail: info@atto-tec.com
http: www.atto-tec.com



ATTO-TEC

Revised: 2024-02-19

Product Information: ATTO 565



ATTO 565 is a novel fluorescent label belonging to the class of Rhodamine dyes. The dye is intended for application in the area of life science, e.g. labeling of DNA, RNA or proteins. Characteristic features of the label are strong absorption, high fluorescence quantum yield, high thermal and photo-stability, and very little triplet formation. The dye is highly suitable for single-molecule detection applications and high-resolution microscopy.

As supplied **ATTO 565** consists of a mixture of two isomers with practically identical absorption and fluorescence. On request the dye can also be supplied as single isomer. For details of coupling see our recommended labeling procedure at www.atto-tec.com - Support - User Guides & Protocols.

Optical data of the carboxy derivative (in PBS, pH 7.4):

λ_{abs}	=	564 nm
ε_{max}	=	1.2 x 10^5 M^{-1} cm^{-1}
λ_{fl}	=	590 nm
η_{fl}	=	90 %
τ_{fl}	=	4.0 ns
CF_{260}	=	0.27
CF_{280}	=	0.12

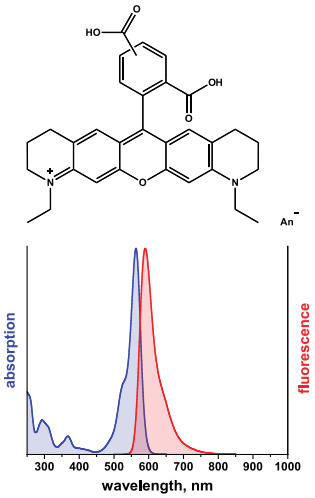

Spectra available in digitized form (excel file) on http://www.atto-tec.com

Modification	MW, g/mol	M^+, g/mol	Order Code Unit (1 mg)	Order Code Unit (5 mg)
carboxy	611	511	AD 565-21	AD 565-25
NHS-ester	708	608	AD 565-31	AD 565-35
maleimide	733	633	AD 565-41	AD 565-45
biotin	922	821	AD 565-71	AD 565-75
phalloidin	1394	1280	AD 565-81*	AD 565-82**
amine	781	553	AD 565-91	AD 565-95
Peg(3)-azide	811	711	AD 565-101	AD 565-105
iodoacetamide	835	721	AD 565-111	AD 565-115
hydrazide	752	525	AD 565-121	AD 565-125
alkyne	648	548	AD 565-141	AD 565-145
cadaverine	796	596	AD 565-231	AD 565-235
tetrazine (MeTet)	794	694	AD 565-2502#	AD 565-2505##
Peg(4)-DBCO *new*	1016	1016	AD 565-291	AD 565-295

* 10 nmol **20 nmol #0.2 mg ##0.5 mg

Figure 7.87: Product information sheet of ATTO565 as provided by the manufacturer. (https://www.leica-microsystems.com/de/produkte/atto-tec-consumables/p/atto-565/downloads/)

ATTO-TEC GmbH
Martinshardt 7
D-57074 Siegen
Germany
Phone: +49 271 23853 – 0
FAX: +49 271 23853 – 11
E-mail: info@atto-tec.com
http: www.atto-tec.com



ATTO-TEC

Revised: 2024-02-09

Product Information: ATTO 647N



ATTO 647N belongs to a new generation of fluorescent labels for the red spectral region. Characteristic features of the label are strong absorption, excellent fluorescence quantum yield, high photostability, excellent ozone resistance, good solubility, and very little triplet formation. The dye is highly suitable for single-molecule detection applications and high-resolution microscopy.
ATTO 647N is a cationic dye. After coupling to a substrate the dye carries a net electrical charge of +1. In common with most **ATTO**-labels, absorption and fluorescence are independent of pH in the range of 2 to 11, used in typical applications.
As supplied **ATTO 647N** consists of a mixture of two isomers with practically identical absorption and fluorescence properties. For details of coupling see our recommended labeling procedure at www.atto-tec.com - Support - User Guides & Protocols.

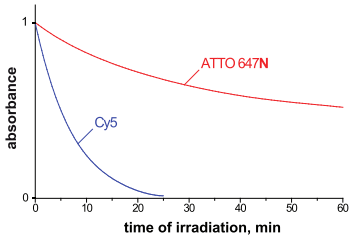

Optical data of the carboxy derivative *(in PBS, pH 7.4):*

λ_{abs}	=	646 nm
ε_{max}	=	1.5 x 10^5 M^{-1} cm^{-1}
λ_{fl}	=	664 nm
η_{fl}	=	65 %
τ_{fl}	=	3.5 ns
CF_{260}	=	0.04
CF_{280}	=	0.03

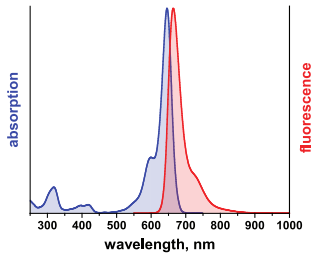

Spectra available in digitized form (excel file) on http://www.atto-tec.com

Modification	MW, g/mol	M^+, g/mol	Order Code Unit (1 mg)	Order Code Unit (5 mg)
carboxy	746	646	AD 647**N**-21	AD 647**N**-25
NHS-ester	843	743	AD 647**N**-31	AD 647**N**-35
maleimide	868	768	AD 647**N**-41	AD 647**N**-45
biotin	1057	956	AD 647**N**-71	AD 647**N**-75
phalloidin	1530	1415	AD 647**N**-81*	AD 647**N**-82**
amine	889	688	AD 647**N**-91	AD 647**N**-95
Peg(3)-azide	960	846	AD 647**N**-101	AD 647**N**-105
iodoacetamide	956	856	AD 647**N**-111	AD 647**N**-115
hydrazide	861	660	AD 647**N**-121	AD 647**N**-125
alkyne	783	683	AD 647**N**-141	AD 647**N**-145
cadaverine	958	731	AD 647**N**-231	AD 647**N**-235
tetrazine (MeTet)	930	830	AD 647**N**-2502#	AD 647**N**-2505##
Peg(4)-DBCO *new*	1252	1153	AD 647**N**-291	AD 647**N**-295
phosphoramidite *new*	1035	890	AD 647**N**-3050§	AD 647**N**-30100§§

*10 nmol **20 nmol #0.2 mg ##0.5 mg §50 mg §§100 mg

Figure 7.88: Product information sheet of ATTO647N as provided by the manufacturer. (https://www.leica-microsystems.com/de/produkte/atto-tec-consumables/p/atto-647n/downloads/)

ATTO-TEC

Revised: March 23, 2021

Product Information: ATTO NHS-Esters

Compound	Storage information	Shelf Life
Amine-reactive NHS-ester, Crystalline solid	Freeze upon receipt < -20 °C Protect from light and moisture	When stored as indicated, ATTO NHS-esters are stable for at least 3 years.
For optical properties see table on page 4.		

Introduction

ATTO-TEC offers a large variety of high-quality amine-reactive dyes for labeling proteins and other amine-containing substrates. The dyes cover the spectral region from 350 nm in the UV to 750 nm in the NIR.
The most commonly used amine-reactive reagents are N-hydroxysuccinimidyl(NHS)-esters. NHS-esters readily react with compounds containing amino groups, forming a chemically stable amide bond between the dye and e.g. a protein. However, the amino group ought to be unprotonated to be reactive. Hence the pH of the solution must be adjusted sufficiently high to obtain a high concentration of unprotonated amino groups. On the other hand, the NHS-ester also reacts with the hydroxyl ions in the solution to yield "free" dye, which is no longer reactive. As the rate of this unavoidable hydrolysis increases with the concentration of hydroxyl ions, the pH should be kept as low as possible. Buffering the solution at pH 8.3 has been found to be a good compromise between the contradicting requirements.

Labeling Proteins with ATTO NHS-Esters

ATTO NHS-esters readily react with amino groups of proteins. The optimum pH-range for NHS-ester coupling is pH 8.0 – 9.0. At this pH amino groups of proteins, i.e. the ε-amino groups of lysines are unprotonated to a degree sufficiently high for fast coupling.

Required Materials

- **Solution A**: PBS buffer (Phosphate-Buffered Saline, pH 7.4): Dissolve 8 g NaCl, 0.2 g KCl, 1.44 g $Na_2HPO_4 \cdot 2\,H_2O$, and 0.24 g KH_2PO_4, in 1 liter distilled water.
- **Solution B**: 0.2 M sodium bicarbonate solution, adjusted to pH 9.0 with 2 M sodium hydroxide.
- **Solution C**: To 20 parts of **Solution A** add 1 part of **Solution B** to obtain a labeling buffer of pH 8.3. Kept in an air-tight bottle, this solution will be stable for a long period of time.
- **Solution D**: Dissolve 1.0 mg of dye NHS-ester in 50 – 200 µl of an-hydrous, amine-free DMSO or acetonitrile. For detailed information on preparation and handling of dye stock-solutions see page 2.
- Gel filtration column filled with Sephadex G-25 or equivalent.

Preparation and Handling of Dye Stock-Solutions

For the preparation of dye stock-solutions a solvent recommendation for each dye is given in the table on page 4. To determine the concentration of a dye stock-solution we recommend to take an aliquot and dilute with acidified ethanol (0.1 vol.-% trifluoroacetic acid) to avoid dye aggregation and in some cases (ATTO 565 and ATTO 590) formation of a colorless spiro-lacton.
Depending on solvent quality such stock-solutions are not stable at room temperature and for storage purposes must be kept, protected from light, at -20 °C. Additionally, it may be difficult to avoid humidity entering a solution in continuous use. The reactive moiety may hydrolyze and become non-reactive. We advise to freshly prepare, whenever possible, the dye stock-solutions immediately before starting the labeling reaction. One should keep in mind that solvents like DMSO or DMF are never free of nucleophilic and/or basic impurities. Such compounds will react with the NHS-ester functionality and consequently reduce coupling efficiency. In some cases (ATTO 610, ATTO 647, ATTO 725, ATTO 740) they also undergo reactions with the dye chromophore resulting in dye-degradation.

Conjugate Preparation

- Dissolve 1 – 5 mg of protein in 1 ml of **Solution C**. Protein solutions must be free of any amine-containing substances such as tris-(hydroxymethyl)-aminomethane (TRIS), free amino acids or ammonium ions. Antibodies that are dissolved in amine containing buffers should be dialyzed against **Solution A**, and the desired coupling pH of 8.3 will be obtained by the procedure given above for **Solution C**. The presence of sodium azide in low concentration (< 3 mM) will not interfere with the labeling reaction.
- To obtain an average degree of labeling (DOL, dye-to-protein ratio) of 2 – 3, add while gently shaking a threefold molar excess of reactive dye (**Solution D**) to the protein solution. Variations due to different reactivities of both the protein and the labeling reagent may occur. This may necessitate optimization of the dye-to-protein ratio used in the reaction in order to obtain the desired DOL. To increase the degree of labeling a higher ratio of NHS-ester to protein has to be used and vice versa.
- Incubate the reaction mixture protected from light for up to 1 hour at room temperature. For ATTO 565-NHS and ATTO 590-NHS we recommend an incubation time of 18 hours at ambient temperature for the reaction to be completed.

Conjugate Purification – Removal of Unbound Dye

- Due to an unavoidable side reaction part of the applied dye NHS-ester will hydrolyze during the labeling reaction and must be removed from the protein conjugate. We recommend using a Sephadex G-25 (or equivalent) gel filtration column of 1 – 2 cm diameter and 10 – 20 cm length. For very hydrophilic dyes, e. g. ATTO 488, ATTO 532, ATTO 542, ATTO 594, ATTO 643 the column has to be at least 30 cm in length to achieve a satisfactory result.
- Preequilibrate the column with **Solution A**.
- Elute the dye-protein conjugate using **Solution A**.
- The first colored and fluorescent zone to elute will be the desired dye-protein conjugate. A second colored and fluorescent, but slower moving zone contains the unbound free dye (hydrolyzed NHS-ester).
- To prevent denaturation of the conjugate after elution, bovine serum albumin (BSA) or another stabilizer may be added.
- For re-use of the Sephadex column one can elute with either 0.01 % sodiumhydroxide solution and/or water/ethanol 80:20 to remove any residues of dye or dye-conjugate. The treatment is followed by exhaustive washing with water.

Storage of the Protein Conjugate

In general, conjugates should be stored under the same conditions used for the unlabeled protein. For storage in solution at 4 °C, sodium azide (2 mM final concentration) can be added as a preservative. Removal of preservatives prior to use may be necessary to avoid inhibitory effects in applications in which conjugates are added to live cell specimens. The conjugate should be stable at 4 °C for several months. For long-term storage, divide the solution into small aliquots and freeze at -20 °C. Avoid repeated freezing and thawing. Protect dye conjugates from light as much as possible.

ATTO-TEC

Revised: November 12, 2021

Product Information: ATTO-Reagents for Click Chemistry (Alkyne- or azide-modified ATTO-label)

Compound	Storage information	Shelf Life
Alkyne- or azide-modified reactive label Lyophilized or crystalline solid	Freeze upon receipt < -20°C Protect from light and moisture	When stored as indicated, ATTO reagents for Click Chemistry are stable for at least 3 years.
For optical properties see table on page 3.		

Introduction:

The term **"Click Chemistry"** describes chemical reactions that are able to quickly and reliably generate substances by joining together small units. One of the most popular reactions within the Click Chemistry concept is the copper (I) catalyzed Huisgen azide alkyne cycloaddition forming a covalent linking unit (triazole) between the label and the target molecule (Figure 1).

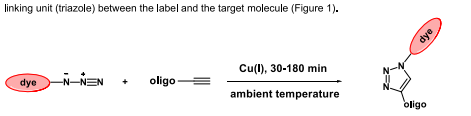

Figure 1: Cu(I) catalysed alkyne-azide "Click Reaction". The azide and the alkyne residues are interchangeable e.g. the fluorophore can be labeled with an azide moiety and the target molecule could carry the alkyne functionality.

The alkyne and azide groups are biologically unique and therefore the click reaction is very selective and specific. The fluorescent labeled click conjugates can be easily detected with high sensitivity and low background, unlike conventional labeling reactions using succinimidyl ester or maleimides which react with amines and sulfhydryls, which are common functionalities in biological environment.
ATTO-TEC offers a large variety of alkyne- or azide-modified fluorophores for Clikck Chemistry.

Protocol for Oligonucleotide Labeling via Click Chemistry

General Remarks

The following protocol describes the labeling procedure for 5 nmol of a single alkyne modified oligonucleotide.

The reaction is most efficient if the azide and alkyne are dissolved in a minimal amount of solvent and the solutions are of high concentration.
The reaction can be accelerated by raising the temperature and is generally finished in 30 min at around 40 – 45 °C.

Required Materials

- **Solution A**: Dissolve the azide- or alkyne-modified oligonucleotide in the appropriate amount of water to obtain a 2 mM solution and centrifuge shortly.
- **Solution B**: Dissolve 1.0 mg of the click reagent (azide- or alkyne-modified ATTO-dye) in the appropriate amount of DMSO/t-BuOH-solution 1:1 to obtain a 50 mM stock-solution. In case of azide or alkyne of ATTO 725, ATTO 740, ATTO 647, and ATTO 610 we recommend using ACN/t-BuOH.
- **Solution C**: Click Solution: Dissolve 54 mg TBTA (tris[(1-benzyl-1*H*-1,2,3-triazole-4-yl)methyl]amine) in 1 ml DMSO/t-BuOH 3:1 for a 0.1 M solution. The solution can be stored at -20 °C.
- **Solution D**: Dissolve 1 mg CuBr in 70 µl DMSO/t-BuOH 3:1 to obtain a 0.1 M solution. NOTE: This solution must be freshly prepared and cannot be stored!
- **Solution E**: The final click solution is prepared by quickly adding 1 volume of **Solution D** to 2 volumes of **Solution C**.

Conjugate Preparation

In general, the labeling reaction works more efficiently with concentrated solutions of alkynes (e.g. oligo) and azides (dye label). In the case the reaction does not work in water, rising the pH by performing the reaction in Tris-HCl (50 mM) at pH 8.3 might be helpful.

- Pipette 5 µl of **Solution A** (10 nmol of oligonucleotide) in a 0.5 reaction vial.
- Add 1 – 2 µl of **Solution B** (50 – 100 nmol; 5 – 10 eq.) to the reaction vial.
- Pipette the correct amount of **Solution B** corresponding to a 2 – 10 times molar excess of the alkyne-or azide modified ATTO-dye into the reaction vial.
- 3 µl of freshly prepared **Solution E** is added and the reaction vial is thoroughly mixed by shaking at 25 °C for 3 h. As previously mentioned, by rising the temperature to 40 – 45 °C the reaction is generally finished in 30 minutes.

Conjugate Purification – Removal of Excess Reagents

- Add 100 µl of a 0.3 M NaOAc solution and precipitate the oligonucleotide by adding 1 ml cold ethanol (containing 5 % diethylether; -20 °C). Centrifuge for at least 20 min at 6000 rpm or higher. Remove the supernatant and wash the residue with 100 µl cold ethanol (containing 5 % diethyl ether; -20 °C). Centrifuge again for at least 10 min and remove the supernatant. Dry the residue on air.

Storage of the Conjugate

In general, conjugates should be stored under the same conditions used for the unlabeled oligonucleotide. For long-term storage we recommend freezing at -20 °C. Protect dye conjugates from light as much as possible.

Figure 7.89: Labeling procedure of ATTO dyes with (top) NHS ester modification and (bottom) alkyne or azide modification as specified by the manufacturer.

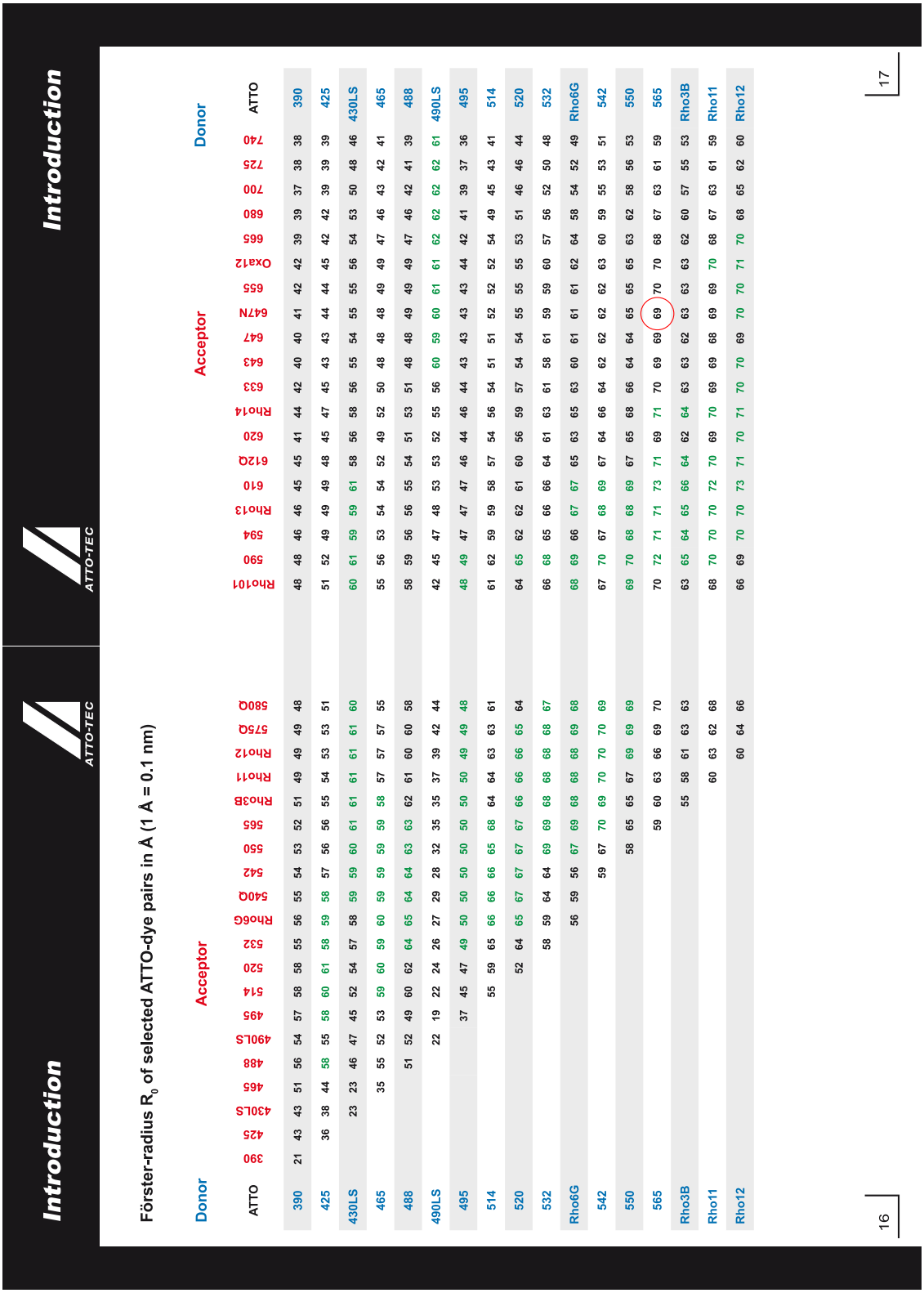

Figure 7.90: Förster distance for a variety of ATTO-dye pairs as provided by the manufacturer. The relevant Förster distance of ATTO565 and ATTO647N is marked by a red circle.

8 Lists

8.1 List of Tables

3.1 Fluorescence lifetimes τ of the BTD initiator and the BTD reference in toluene and in thin PS films. Lifetimes were determined at 488 nm excitation in a spectral window from 532 – 715 nm. The relative amplitudes of the fluorescence lifetime components τ_1, τ_2 and τ_3 are mentioned in square brackets after the lifetimes. The errors of the lifetime components are always in the order of magnitude of the last decimal place specified. . . 44

3.2 Absorption coefficients ε, fluorescence quantum yields Φ and photobleaching quantum yields Φ_b at different irradiation wavelengths $\lambda_{irrad.}$ of the BTD initiator and the BTD reference in MeCN. Absorption coefficients were determined according to the Lambert–Beer law at 378 nm and 453 nm for the BTD initiator and the BTD reference, respectively. Fluorescence quantum yields were determined at 366 nm and 488 nm excitation in MeCN relative to the standard Rhodamine 6G in ethanol ($\Phi_s = 94\%$)[67] according to equation (2.4). 48

3.3 Fluorescence lifetimes τ determined in the FLIM images of microgels **A** and **B**. The excitation wavelength was 488 nm, the analyzed emission wavelengths 500 – 715 nm. The relative amplitudes of the fluorescence lifetime components τ_1, τ_2, τ_3 and τ_4 are mentioned in the square brackets. The errors of the lifetime components are in the order of magnitude of the last decimal place specified. 55

3.4 Fluorescence lifetimes τ determined in the various FLIM images shown in Figure 3.11. The excitation wavelength was 488 nm. The relative amplitudes of the fluorescence lifetime components τ_1, τ_2, τ_3 and τ_4 are mentioned in the square brackets. The errors of the lifetime components are in the order of magnitude of the last decimal place specified. 63

4.1 Fluorescence lifetimes τ and fluorescence quantum yields Φ of compounds **ATTO565 NHS ester**, **ATTO647N azide**, energy donor reference compound **6**, energy acceptor reference compound **7**, and dyad **8** in methanol. Quantum yields were determined with either 510 nm or 600 nm excitation. Lifetimes were determined either with 527 nm or 635 nm excitation. For the lifetimes of **ATTO565 NHS ester** and donor **6** the emission between 545 – 620 nm was analyzed. For the lifetimes of **ATTO647N azide** and acceptor **7** the emission between 655 – 715 nm was analyzed. For dyad **8**, both spectral windows were analyzed separately. The amplitudes of the fluorescence lifetime components τ_1 and τ_2 are mentioned in square brackets after the lifetimes. The errors of the lifetime components are always in the order of magnitude of the last decimal place specified. . . 76

4.2 Fluorescence lifetimes τ and fluorescence quantum yields Φ of compounds **ATTO565 NHS ester**, **ATTO647N azide**, energy donor reference compound **6**, energy acceptor reference compound **7**, and dyad **8** in water. Quantum yields were determined with either 510 nm or 600 nm excitation. Lifetimes were determined either with 527 nm or 635 nm excitation. For the lifetimes of **ATTO565 NHS ester** and donor **6** the emission between 545 – 620 nm was analyzed. For the lifetimes of **ATTO647N azide** and acceptor **7** the emission between 655 – 715 nm was analyzed. For dyad **8**, both spectral windows were analyzed separately. The amplitudes of the fluorescence lifetime components τ_1, τ_2 and τ_3 are mentioned in square brackets after the lifetimes. The errors of the lifetime components are always in the order of magnitude of the last decimal place specified. . . 81

4.3 Fluorescence lifetimes τ and fluorescence quantum yield Φ of compounds **ATTO565 NHS ester**, **ATTO647N azide**, energy donor reference compound **6**, energy acceptor reference compound **7**, and dyad **8** in methanol before and after 1500 s of irradiation with a 365 nm LED @ 450 $\mathrm{W\,m^{-2}}$. Quantum yields were determined with either 510 nm or 600 nm excitation. Lifetimes were determined either with 527 nm or 635 nm excitation. For **ATTO565 NHS ester** and donor **6** the emission between 545 – 620 nm was analyzed. For **ATTO647N azide** and acceptor **7** the emission between 655 – 715 nm was analyzed. For dyad **8**, both spectral windows were analyzed separately. The amplitudes of the fluorescence lifetime components τ_1 and τ_2 are mentioned in square brackets underneath the lifetimes. The errors of the lifetime components are always in the order of magnitude of the last decimal place specified. 89

4.4 Fluorescence lifetimes τ and fluorescence quantum yield Φ of the energy donor reference compound **6**, the energy acceptor reference compound **7**, and the dyad **8** in water before and after up to 3000 s of irradiation with a 365 nm LED @ 450 $\mathrm{W\,m^{-2}}$. Quantum yields were determined with either 510 nm or 600 nm excitation. Lifetimes were determined either with 527 nm or 635 nm excitation. For donor **6** the emission between 545 – 620 nm was analyzed. For acceptor **7** the emission between 655 – 715 nm was analyzed. For dyad **8**, both spectral windows were analyzed separately. The amplitudes of the fluorescence lifetime components τ_1, τ_2 and τ_3 are mentioned in square brackets underneath the lifetimes. The errors of the lifetime components are always in the order of magnitude of the last decimal place specified. 93

4.5 Fluorescence lifetimes τ and fluorescence quantum yield Φ of compounds **ATTO647N azide**, energy donor reference compound **6**, energy acceptor reference compound **7**, and dyad **8** in methanol before and after up to 73 h of irradiation with a 645 nm LED @ 1.675 $kW\,m^{-2}$. Quantum yields were determined with either 510 nm or 600 nm excitation. Lifetimes were determined either with 527 nm or 635 nm excitation. For donor **6** the emission between 545 – 620 nm was analyzed. For **ATTO647N azide** and acceptor **7** the emission between 655 – 715 nm was analyzed. For dyad **8**, both spectral windows were analyzed separately. The amplitudes of the fluorescence lifetime components τ_1 and τ_2 are mentioned in square brackets underneath the lifetimes. The errors of the lifetime components are always in the order of magnitude of the last decimal place specified. 99

4.6 The relative diffusion coefficients D_D and D_F obtained from fitting the summed-up intensity-time trace of the example measurement until different analyzed times, corresponding to, in that order, photobleaching of the donor, acceptor or the overall measurement time, respectively. Donor and FRET intensity-time traces are fitted independently in each case to yield D_D and D_F, respectively. 136

4.7 The relative diffusion coefficients D_D and D_F in PVAc, obtained from fitting the combined summed-up intensity-time traces of several FEDUP measurements at various temperatures T and with different cycle times t_{cycle}. The fits are restricted to analyzed times t according to dominant photobleaching of either donor or acceptor. Donor and FRET intensity-time traces are fitted independently in each case to yield D_D and D_F, respectively. 145

4.8 The relative diffusion coefficients D_D and D_F in PBMA, obtained from fitting the combined summed-up intensity-time traces of several FEDUP measurements at various temperatures T and with different cycle times t_{cycle}. The fits are restricted to analyzed times t according to dominant photobleaching of either donor or acceptor. Donor and FRET intensity-time traces are fitted independently in each case to yield D_D and D_F, respectively. 152

4.9 The relative diffusion coefficients D_D and D_F in PEG, obtained from fitting the combined summed-up intensity-time traces of several FEDUP measurements at various temperatures T and with different cycle times t_{cycle}. The fits are restricted to analyzed times t according to dominant photobleaching of either donor or acceptor. Donor and FRET intensity-time traces are fitted independently in each case to yield D_D and D_F, respectively. 156

4.10 The relative diffusion coefficients D_D and D_F in dextran, PAA, PEA and on the surface of a glass substrate, obtained from fitting the combined summed-up intensity-time traces of several FEDUP measurements at room temperature. Different cycle times t_{cycle} were employed. The fits are restricted to analyzed times t according to dominant photobleaching of either donor or acceptor. Donor and FRET intensity-time traces are fitted independently in each case to yield D_D and D_F, respectively. 157

7.1 Quenching constants of ATTO565 NHS-ester and ATTO647N azide for different quenchers in methanol solutions. For the calculation of the bimolecular quenching constants k_q the lifetimes of the dyes were used as determined in the main text. Stern-Volmer quenching behaviour was assumed for each quencher. The Stern-Volmer constant K_{SV} corresponds to the slopes of the linear fits presented in figure 7.12 **a)** and **b)** 198

8.2 List of Figures

1.1 Schematic depiction of the activation of the BTD mechanofluorophore investigated in Chapter 3. Before activation, the chromophore can only be excited with UV light (violet lightning) and emits fluorescence from roughly 400–600 nm (violet star).[50] It is assumed that when (opposing) pulling forces act upon the linked polymer strands x and y (depicted in the brackets, here polyacrylate), one of the two Diels–Alder anthracene-maleimide adducts undergoes a retro Diels–Alder reaction restoring the aromaticity of the central anthracene moiety (see also Section 2.6.5). This results in a spectral shift, such that excitation with blue light (blue lightning) becomes possible and the fluorescence emission shifts to the range of 450–800 nm (blue star).[50] The color scheme shown here is used consistently throughout this work, i.e., the unactivated mechanofluorophore is coded in violet, whereas the activated mechanofluorophore is coded in blue. 3

1.2 Schematic depiction of the photocleavage of the dyad **8** investigated in Chapter 4. Before irradiation with UV light (purple lightning), the dyad exhibits efficient energy transfer from the ATTO565 moiety to the ATTO647N moiety. Upon irradiation with UV light, the central NPPOC moiety undergoes photocleavage (for mechanism, see Section 2.5.1). After photocleavage, the two chromophores can move independently from each other. Thereby, they will statistically move further apart than the distance required for energy transfer (about 10 nm, see Section 2.2). The color scheme shown here is used consistently throughout this work, i.e., donor fluorescence is coded in bright green, acceptor fluorescence in red, FRET in orange and the chromophores ATTO565 and ATTO647N are coded in olive and blue, respectively. 5

2.1 Schematic Jablonski diagram depicting excitation and various radiative and non-radiative relaxation pathways of an arbitrary fluorophore. The bold horizontal lines constitute the vibrational ground state of any particular electronic state. The thin horizontal correspond to the various excited vibrational states of any particular electronic state. Vibrational states are also indicated with the vibrational quantum number v. Electronic singlet states are denoted S_N with $N = 0,1,2,...$ for the electronic ground state and higher excited states, respectively. Electronic triplet states are likewise denoted T_N. The vertical blue arrows represent the absorption process resulting in excitation into higher electronic states. The vertical green arrows illustrate fluorescence and the vertical red arrows illustrate phosphorescence, respectively. The dashed vertical black arrows mark VR within any particular electronic state. The dashed horizontal black arrows represent IC from any particular electronic state to another electronic state of the same multiplicity. The solid horizontal black arrows depict ISC from any particular electronic state to another electronic state of different multiplicity. 7

2.2 Schematic Jablonski diagram depicting the FRET mechanism. The bold horizontal lines constitute the vibrational ground state of any particular electronic state. The thin horizontal lines correspond to the various excited vibrational states of any particular electronic state. Vibrational states are also indicated with the vibrational quantum number v. Electronic singlet states are denoted S_N with $\mathrm{N} = 0,1,2,...$ for the electronic ground state and higher excited states, respectively. The solid vertical blue arrow represents the absorption process resulting in excitation into higher electronic states. The dashed vertical green arrow illustrates the non-radiative relaxation of the FRET-donor that replaces relaxation via fluorescence emission. The dashed vertical blue arrow represents the excitation of the FRET-acceptor via energy transfer. The curved black arrows indicate the energy transfer from donor to acceptor. The vertical red arrow marks the fluorescence of the acceptor following the energy transfer. The dashed vertical grey arrows depict VR within any particular electronic state. 12

2.3 Schematic setup of an inverted fluorescence microscope. The excitation beam is colored in light blue, the emission light is colored in green. 15

2.4 Schematic representation of the imaging path in a confocal microscope. The solid green lines represent the in-focus fluorescence, whereas the dotted blue lines represent fluorescence from a position outside of the focal plane and the dotted red lines depict fluorescence from a position in the focal plane but outside of the focus. 19

2.5 General principle of single molecule localization microscopy (SMLM). The structure of interest is symbolized by the spiral pattern. Single molecule fluorescence is depicted as broad orange two-dimensional signals appearing along the structure. The centroids are determined by fitting two-dimensional Gaussians to the measured signals. The sum of all these localizations results in a super-resolved image. Reprinted from Developmental Cell, *23*, P. Sengupta, S. Van Engelenburg, J. Lippincott-Schwartz, Visualizing Cell Structure and Function with Point-Localization Superresolution Imaging, 1092–1102, **2012**, with permission from Elsevier.[31] 23

2.6 Schematic procedure of a single molecule tracking (SMT) measurement. (**a**) Schematic representation of the fluorescence signals of three single molecules at eight different points in time. (**b**) Detection and linking of single molecule positions. The distance threshold (here "link range") is symbolized by the dashed blue circles. (**c**) The resulting single-molecule trajectories of the three single molecules captured in the eight frames shown in (**a**). Reprinted from K.-H. Tran-Ba, K. Foreman, "Single-Molecule Tracking of Dye Diffusion in Synthetic Polymers: A Tutorial Review", *J. Appl. Phys.* **2023**, *133*, 101101, with the permission of AIP Publishing.[104] 26

2.7 Schematic microscopy setup for all FEDUP measurements in Chapter 4. All laser beams (640 nm, red, acceptor excitation, 561 nm, green, donor excitation, 378 nm, violet, photocleavage) are guided along the same optical path. Fluorescence emission is split into two spectral channels. The green channel records all emission between 570 – 633 nm, the red channel records all emission above 655 nm. 30

2.8 Schematic AFM setup. A laser beam is reflected from the backside of the cantilever and detected on the quad photodiode. Upon interaction of the tip with the sample, the cantilever deforms, thereby changing the reflection of the laser beam on the quad photodiode. A feedback loop between the photodiode and the chip or the sample holder constantly adjusts the height between cantilever and the surface of the sample to keep the interaction between tip and sample constant. 32

2.9 Proposed photocleavage mechanism adapted from literature.[111] Dependent on the reaction conditions, either the styrene or the nitroso pathway is the main reaction pathway. The formation of the nitroso product 2 is mainly dependent on the solvent.[111] 34

3.1 (**a**) Absorption (dotted-dashed lines) and normalized emission spectra (solid lines) of the BTD initiator (violet, 380 nm excitation) and the BTD reference (blue, 488 nm excitation) in toluene. Both emission spectra are normalized to their maximum intensity at 447 nm and 555 nm, respectively. The absorption spectra are scaled to the absorption coefficients determined at the local absorption maxima at 382 nm and 465 nm, respectively. (**b**) Structure of the unactivated (purple, BTD initiator / crosslinker) and activated (blue, BTD reference) reference compounds. (**c**) Comparative emission spectra of both reference compounds at 488 nm excitation. The emission intensity of both spectra is given relative to the maximum of the BTD reference at 555 nm. (**d**) Close-up of (**c**). . 43

3.2 Spectral changes of BTD initiator and BTD reference in MeCN during selected irradiation times with a 365 nm LED @ 400 $\mathrm{W\,m^{-2}}$ and a 455 nm LED @ 300 $\mathrm{W\,m^{-2}}$, respectively. Changes of (**a**) absorption spectra and (**b**) relative emission spectra at 380 nm and 488 nm excitation for the BTD initiator (light to dark violet) and the BTD reference (light to dark blue) respectively. The black arrows indicate the changes with increasing irradiation time. Emission intensity is given relative to the maximum intensity of the respective compound at 0 s irradiation. (**c**) Temporal evolution of the absorbance at the different wavelengths of the (local) maxima shown in (**a**). (**d**) Temporal evolution of the relative fluorescence intensities at the different wavelengths of the (local) maxima depicted in (**b**). All solid lines in (**c**) and (**d**) represent fits with single exponential decay functions. The colors correspond to the primary colors of the color gradients used for the spectra of the different compounds in (**a**) and (**b**). 45

3.3 Hydrodynamic radii R_H determined via DLS at various temperatures for unactivated BTD microgels (violet) and activated BTD microgels (blue). Upright triangles denote heating cycles (increasing temperature), downright triangles signify cooling cycles (decreasing temperature). The microgels in (**a**) are synthesized with the following ratios by mass: 100% PVCL (monomer), 1.0% of the total monomer mass BTD crosslinker (microgels **A**). The microgels in (**b**) are synthesized with the following ratios by mass: 80% PVCL (monomer), 20% VIM (co-monomer), 1.0% of the total monomer mass BTD crosslinker (microgels **B**). Activation was in both cases achieved with 30 s of ultrasonication. 50

3.4 Absorption (**a**) and emission spectra (**b**) of an aqueous solution of microgels **B** before (violet) and after activation (blue). Emission spectra were once recorded at 400 nm excitation (solid lines) and once at 488 nm excitation (dotted lines). The intensity at 400 nm and at 488 nm excitation is given relative to the maximum intensity of the emission spectrum of the unactivated and the activated microgels, respectively. 52

3.5 Widefield microscopy measurements of BTD microgels before (**a** – **c**) and after 30 s of sonication (**d** – **g**). A different sample with comparable composition to the ones investigated in the DLS and FLIM measurements is shown. (**a**, **e**) Fluorescence image of the field of view. The red circle marks the single microgels shown in (**b,c**) and (**f,g**), respectively. (**b,f**) 3D Nile Red PAINT images of the microgels marked in (**a,e**), respectively. 3D data was measured with astigmatism. (**c,g**) XY-projection of the microgels shown in (**b,f**), respectively. The color scale denotes the amount of localizations in a 50 nm radius around any given localization. (**d**) Brightfield image of the field of view shown in (**e**). 53

3.6 Structure of (**a**) PVCL (co-polymerized with VIM) and (**b**) PHMA. Microgels **A** have a ratio of $n : m = 1 : 0$, microgels **B** have a ratio of $n : m = 4 : 1$. Both microgels and PHMA networks in this work are crosslinked with BTD crosslinker. 54

3.7 FLIM images of unactivated (top) and activated (bottom) microgels **A**. A 40×40 µm region of interest was imaged with 512×512 pixels and a pixel dwell time of 1.3 µs. 100 and 250 frames were recorded, respectively. Each FLIM fit was performed with four lifetime components. Unactivated: $\tau_1 = 11.0$ ns [7%], $\tau_2 = 4.63$ ns [36%], $\tau_3 = 1.70$ ns [36%] and $\tau_4 = 0.63$ ns [22%]. Activated: $\tau_1 = 13.0$ ns [3%], $\tau_2 = 5.15$ ns [31%], $\tau_3 = 1.87$ ns [36%] and $\tau_4 = 0.59$ ns [29%]. (**a,d**) The color scale represents the average lifetime, the grey scale depicts the measured intensity. (**b,e**) The intensity of the fluorescence ascribed to the two dominant lifetime components (τ_2, τ_3) is depicted in scales of red and blue for the long and the short lifetime component, respectively. (**c,f**) Close-up of the region of interest marked by the red square in (**a,b**) and (**d,e**), respectively. 56

3.8 FLIM images of unactivated (top) and activated (bottom) microgels **B**. A cut-out is shown of the 40×40 µm region of interest which was imaged with 512×512 pixels and a pixel dwell time of 1.3 µs. 250 frames were recorded. Four lifetime components were determined in both cases. Unactivated: $\tau_1 = 14.0$ ns [12%], $\tau_2 = 5.2$ ns [42%], $\tau_3 = 2.0$ ns [34%] and $\tau_4 = 0.68$ ns [12%]. Activated: $\tau_1 = 11.0$ ns [9%], $\tau_2 = 4.4$ ns [34%], $\tau_3 = 1.85$ ns [37%] and $\tau_4 = 0.66$ ns [20%]. (**a,d**) The color scale represents the average lifetime, the grey scale depicts the measured intensity. (**b,e**) The intensity of the fluorescence ascribed to the two dominant lifetime components (τ_2, τ_3) is depicted in scales of red and blue for the long and the short lifetime component, respectively. (**c,f**) Close-up of the region of interest marked by the red square in (**a,b**) and (**d,e**), respectively. 57

3.9 FLIM (**a,b,d,e**) and AFM height images (**c,f**) of a manually activated PHMA network crosslinked with BTD crosslinker. Images (**d,e,f,**) are separate measurements with higher resolution of the regions of interest marked by the red square in images (**a,b,c**). Images (**c,d,e**) all show approximately the same region of interest. (**a,b**) A 264 µm × 264 µm, (**c,d,e**) a 40 µm × 40 µm and (**f**) a 10 µm × 10 µm region of interest was imaged. All FLIM images were recorded with 512×512 pixels, 1.3 µs dwell time and 250 frames. Due to technical measurement problems, only two lifetime components yielded any reasonable fit of the global TCSPC curves. Lifetime components of (**a,b**) $\tau_1 = 7.2$ ns [31%] and $\tau_2 = 1.66$ ns [69%], as well as (**d,e**) $\tau_1 = 7.9$ ns [34%] and $\tau_2 = 1.81$ ns [66%], were determined. (**a,d**) The color scale represents the average lifetime, the grey scale depicts the measured intensity. (**b,e**) The intensity of the fluorescence ascribed to the two lifetime components τ_1 and τ_2 is depicted in scales of red and blue, respectively. (**c,f**) The color scale depicts the relative height. 60

3.10 FLIM images before (**a,b,f,g**) and after (**d,e,h,i**) an AFM measurement, as well as the corresponding AFM height image (**c**) of a cut PHMA network crosslinked with BTD crosslinker. The red square in (**a,b**) marks the approximate area of the AFM scan shown in (**c**). In the FLIM images (**d,e**), an apparent change of intensity occurred in a precise rectangular area corresponding approximately to the area of the AFM scan. The violet / magenta and dark / light blue squares in (**a**) and (**d**) mark the regions of interest shown in greater magnification in (**f,g**) and (**h,i**), respectively. (**a,b,d,e**) A 264 µm × 264 µm and (**c**) a 40 µm × 40 µm region of interest was imaged with FLIM and AFM respectively. All FLIM images were recorded with 512 × 512 pixels, 1.3 µs dwell time and 250 frames. Due to technical measurement problems, only two lifetime components yielded any reasonable fit of the global TCSPC curves. Lifetime components of (**a,b,f,g**) $\tau_1 = 7.4$ ns [28%] and $\tau_2 = 1.82$ ns [72%], as well as (**d,e,h,i**) $\tau_1 = 6.06$ ns [29%] and $\tau_2 = 1.06$ ns [71%] were determined. (**a,d,f,g,h,i**) The color scale represents the average lifetime, the grey scale depicts the measured intensity. (**b,e**) The intensity of the fluorescence ascribed to the two lifetime components τ_1 and τ_2 is depicted in scales of red and blue, respectively. (**c**) The color scale depicts the relative height. 61

3.11 FLIM images before (**a,b**) and after (**d,e,f,g**) sixteen AFM measurements with varying settings, as well as the corresponding AFM height images (**e**) of a cut PHMA network crosslinked with BTD crosslinker. The red square in (**a,b,c,d**) marks the approximate area of the AFM scan shown in (**e**) and the separate FLIM measurement shown in (**f,g**). (**a,b,c,d,f,g**) All FLIM images were recorded with 512 × 512 pixels, 3 µs dwell time and 250 frames. Four lifetime components were determined in each case (see Table 3.4). (**a,c,f**) The color scale represents the average lifetime, the grey scale depicts the measured intensity. (**b,d,g**) The intensity of the fluorescence ascribed to the two dominant lifetime components τ_2 and τ_3 is depicted in scales of red and blue, respectively. (**e**) The color scale depicts the relative height. 64

4.1 Overview of the synthesis route of the dyad **8**. Reactants and solvents are written in bold next to the reaction arrows. Reaction yields are given below the compound numbers. For the most essential reactants, the structure is given next to the reaction arrows, too. The structures of the commercially available dyes ATTO565 NHS ester (olive) and ATTO647N azide (blue) can be found in Figure 4.2. 72

4.2 (**a**) Absorption and (**b**) emission (excitation at 530 nm) spectra of **ATTO565 NHS ester** (olive), **ATTO647N azide** (blue), reference donor **6** (bright green), reference acceptor **7** (red), and dyad **8** (orange) in MeOH. The structures of all compounds are shown in (**c**). The corresponding emission spectra with 600 nm excitation are presented in (**d**). No significant excitation was observed for the compounds without ATTO647N moiety. The concentration of all compounds was adjusted to approximately 0.6 µmol L^{-1}.[59] 75

4.3 (**a**) Absorption and (**b**) emission (excitation at 530 nm) spectra of **ATTO565 NHS ester** (olive), **ATTO647N azide** (blue), reference donor **6** (green), reference acceptor **7** (red), and dyad **8** (orange) in water. The corresponding emission spectra with 600 nm excitation are presented in (**c**). No significant excitation was observed for the compounds without ATTO647N moiety. (**d**) Emission spectra (**b**) in about ten-fold enhancement for a better visualization of the weakly fluorescent species. The intensity I of all emission spectra is normed to the concentration c of the respective compound. 80

4.4 Overview of the possible photocleavage products of dyad **8**. 85

4.5 Spectral changes of **ATTO565 NHS ester**, **ATTO647N azide**, the reference donor **6**, the reference acceptor **7** and the dyad **8** in methanol during selected irradiation times with a 365 nm LED @ 450 $\mathrm{W\,m^{-2}}$. The first column from the left shows the changes of absorption spectra, the second column depicts changes of emission spectra at 530 nm excitation and the third column represents changes of the emission spectra at 600 nm excitation. Changes of (**a**) absorption and (**b**) / (**c**) emission spectra of **ATTO565 NHS ester** (light to dark olive), the reference donor **6** (dark to light green) and the dyad **8** (light to dark orange), respectively. Changes of (**d**) absorption and (**e**) / (**f**) emission spectra of **ATTO647N azide** (dark to light blue), the reference acceptor **7** (dark to light red) and the dyad **8** (light to dark orange), respectively. The black arrows in subfigures (**a**) – (**f**) indicate the changes with increasing irradiation time. (**g**) Temporal evolution of the absorbance at the different wavelengths of the (local) maxima shown in (**a**) and (**d**). (**h**) Temporal evolution of the fluorescence intensities (excitation at 530 nm) at the different wavelengths of the (local) maxima depicted in (**b**) and (**e**). (**i**) Temporal evolution of the fluorescence intensities (excitation at 600 nm) at the different wavelengths of the (local) maxima presented in (**c**) and (**f**). In subfigures (**g**) – (**i**), circles refer to absorbance and emission maxima values related to the ATTO565 chromophore, while squares denote absorbance and emission maxima values related to the ATTO647N chromophore. All solid lines represent fits with single exponential decay functions. The colors correspond to the primary colors of the color gradients used for the spectra of the different compounds in subfigures (**a**) – (**f**).[59] 87

4.6 Spectral changes of the reference donor **6**, the reference acceptor **7** and the dyad **8** in water during selected irradiation times with a 365 nm LED @ 450 $W\,m^{-2}$. The first column from the left shows the changes of absorption spectra, the second column depicts changes of emission spectra at 530 nm excitation and the third column represents changes of the emission spectra at 600 nm excitation. Changes of (**a**) absorption and (**b**) / (**c**) emission spectra of the reference donor **6** (dark to light green), the reference acceptor **7** (dark to light red) and the dyad **8** (light to dark orange), respectively. The black arrows in subfigures (**a**) – (**c**) indicate the changes with increasing irradiation time. (**d**) Temporal evolution of the absorbance at the different wavelengths of the (local) maxima shown in (**a**). (**e**) Temporal evolution of the fluorescence intensities (excitation at 530 nm) at the different wavelengths of the (local) maxima depicted in (**b**). (**f**) Temporal evolution of the fluorescence intensities (excitation 600 nm) at the different wavelengths of the (local) maxima presented in (**c**). In subfigures (**d**) – (**f**), circles refer to absorbance and emission maxima values related to the ATTO565 chromophore, while squares denote absorbance and emission maxima values related to the ATTO647N chromophore. All solid lines represent fits with single exponential decay functions. The colors correspond to the primary colors of the color gradients used for the spectra of the different compounds in subfigures (**a**) – (**c**). The intensity I of all emission data is normed to the concentration c of the respective compound. 92

4.7 Spectral changes of ATTO647N azide, the reference donor **6**, the reference acceptor **7** and the dyad **8** in methanol during selected irradiation times with a 645 nm LED @ 1.675 $kW\,m^{-2}$. The first column from the left shows the changes of absorption spectra, the second column depicts changes of emission spectra at 530 nm excitation and the third column represents changes of the emission spectra at 600 nm excitation. Changes of (**a**) absorption and (**b**) / (**c**) emission spectra of ATTO647N azide (dark to light blue) and the dyad **8** (light to dark orange), respectively. Changes of (**d**) absorption and (**e**) / (**f**) emission spectra of the reference donor **6** (dark to light green) and the reference acceptor **7**, respectively. The black arrows in subfigures (**a**) – (**f**) indicate the changes with increasing irradiation time. (**g**) Temporal evolution of the absorbance at the different wavelengths of the (local) maxima shown in (**a**) and (**d**). (**h**) Temporal evolution of the fluorescence intensities (excitation at 530 nm) at the different wavelengths of the (local) maxima depicted in (**b**) and (**e**). (**i**) Temporal evolution of the fluorescence intensities (excitation 600 nm) at the different wavelengths of the (local) maxima presented in (**c**) and (**f**). In subfigures (**g**) – (**i**), circles refer to absorbance and emission maxima values related to the ATTO565 chromophore, while squares denote absorbance and emission maxima values related to the ATTO647N chromophore. Triangles denote the absorbance and emission values at the wavelengths of the shifted maxima of the dyad **8**. All solid lines represent fits with single exponential decay functions. The colors correspond to the primary colors of the color gradients used for the spectra of the different compounds in subfigures (**a**) – (**f**). 97

4.8 Series of false-color images taken from a widefield microscopy movie of (**a**) donor **6** and (**b**) acceptor **7** in a tempered PVAc film before and after 0.5 s of UV irradiation (378 nm at 100 $W\,cm^{-2}$). A selection of images recorded with 200 ms integration time is shown which were taken at the times indicated in the central time arrow. In the top row, the long wavelength channel ($>$ 655 nm) at 561 nm excitation is shown (orange, FRET channel). In the middle row, the short wavelength channel (570 – 633 nm) at 561 nm excitation is displayed (green, donor channel). In the bottom row, the long wavelength channel at 640 nm excitation is shown (red, acceptor channel). All images were colored according to the established color scheme. The vertical purple line symbolizes the UV irradiation. The imaging pixel size was 65 nm. A few selected signals are marked with black squares to help guide the eye. The squares were positioned over the clearly visible signals in the donor and the acceptor channel, respectively, and then translated to the corresponding coordinates in the other channels. Three arbitrarily chosen signals of each sample are additionally labeled with numbers. The corresponding intensity-time traces are shown in Figure 4.9. 103

4.9 Typical intensity-time traces of donor **6** (left) and acceptor **7** (right) in PVAc. The numbers above each graph coincide with the labels given in Figure 4.8 **a** and **b**. The intensities detected in the different spectral channels are shown as orange, green and red lines for the FRET, donor and acceptor channel, respectively. The time is given relative to the UV pulse. The insets depict the measured intensity in the first five frames before and the first few dozen frames after the UV pulse which is symbolized by the vertical purple line. All signals are corrected for background (see Section 4.6.1 for a more detailed description of the analysis algorithm). 105

4.10 Series of false-color images taken from a widefield microscopy movie of dyad **8** in a tempered PVAc film before and at different times after 4 s of UV irradiation (378 nm at 50 $W\,cm^{-2}$). A selection of images recorded with 200 ms integration time is shown which were taken at the times indicated in the central time arrow. In the top row, the long wavelength channel ($>$ 655 nm) at 561 nm excitation is shown (orange, FRET channel). In the middle row, the short wavelength channel (570 – 633 nm) at 561 nm excitation is displayed (green, donor channel). In the bottom row, the long wavelength channel at 640 nm excitation is shown (red, acceptor channel). All images were colored according to the established color scheme. The vertical purple line symbolizes the UV irradiation. The imaging pixel size was 65 nm. All signals are marked with black squares and labeled with white numbers to help with the recognition of the signal pattern. The corresponding intensity-time traces are shown in Figure 4.11.[59] 108

4.11 The intensity-time traces of the six signals identified in Figure 4.10. The time is counted relative to the UV pulse. The numbers above each graph coincide with the labels given in Figure 4.10. The intensities detected in the different spectral channels are shown as orange, green and red lines for the FRET, donor and acceptor channel, respectively. The insets in the upper right corner of each graph show the intensity in the first five frames before and the first few frames after the UV pulse which is symbolized by the vertical purple line.[59] 109

4.12 (**a** – **c**) Three exemplary intensity-time traces from the same measurement as the one shown in Figure 4.10. It is assumed that in all three cases photobleaching occurs, since the intensities in acceptor and donor channel are well correlated. (**d** – **f**) Three exemplary intensity-time traces from a control experiment without a UV pulse. Otherwise, the measurement was performed under identical conditions. The intensity-time traces of the donor-acceptor pairs depicted in **d** and **e** show conceptually similar behavior to their counterparts in **a** and **b**. The intensity-time traces of the FRET, donor and acceptor channel are shown in orange, green and red, respectively. 112

4.13 Categorization of the intensity-time traces of all initially identified donor-acceptor pairs in the experiments (**a**) without and (**b**) with application of a UV pulse. Category I, II and III donor-acceptor pairs are symbolized by green, red and blue. Category IV pairs are divided into the sub-categories “unspecified irregular” (dark red) and “no cleavage” (purple). 113

4.14 Comparison of photobleaching in PVAc and PEG. All fluorescence signals were localized with the ImageJ plugin ThunderSTORM[201]. Subsequently, the number of localizations were normalized to ensure comparability. Data shown in one particular graph was recorded on the same day under identical measurement conditions and analyzed with the same localization threshold value. All measurements were performed according to the regular FEDUP measurement protocol. Each frame corresponds to 220 ms of irradiation with a 561 nm laser (0.028 $\mathrm{kW\,cm^{-2}}$) and additional 220 ms of irradiation with a 640 nm laser (0.022 $\mathrm{kW\,cm^{-2}}$). Additionally, a 500 ms pulse with 378 nm laser (0.1 $\mathrm{kW\,cm^{-2}}$) was applied between frame 5 and 6. All dye components were added in sub-nanomolar concentration to ensure single molecule behavior. (**a**) Localizations in the donor channel when embedding donor **6** in PVAc (light green) and PEG (olive), respectively. (**b**) Localizations in the acceptor channel when embedding acceptor **7** in PVAc (red) and PEG (magenta), respectively. (**c**) Localizations in the FRET channel (orange and dark yellow), the donor channel (light green and olive) and the acceptor channel (red and magenta) when embedding dyad **8** in PVAc and PEG, respectively. 114

4.15 Comparison of photobleaching of dyad **8** on glass with and without a constant flow of Argon across the coverslip. All fluorescence signals were localized with the ImageJ plugin ThunderSTORM[201]. The number of localizations were normalized to ensure comparability. All data was recorded on the same day under identical measurement conditions and analyzed with the same localization threshold value. The same sample was used for both measurement series. All measurements were performed according to the regular FEDUP measurement protocol. Each frame corresponds to 220 ms of irradiation with a 561 nm laser (0.006 $kW\,cm^{-2}$) and additional 220 ms of irradiation with a 640 nm laser (0.003 $kW\,cm^{-2}$). Additionally, a 300 ms pulse with a 378 nm laser (0.1 $kW\,cm^{-2}$) was applied between frames 5 and 6. TIRF illumination was employed for all lasers. The dyad was added in sub-nanomolar concentration to ensure single molecule behavior. Normalized amounts of localizations are separately compared in the (**a**) donor channel, (**b**) acceptor channel and (**c**) FRET channel with (olive, magenta and dark yellow) and without (light green, red and orange) a constant Ar flow, respectively. . 117

4.16 (**a**) Overlay of the FRET channel (red) and donor channel (green) of a single exemplary frame of the spatial correlation with TetraSpeck™ beads. The white square shows the approximate area that is referenced in subfigures **b** and **c**. (**b**) Calculated shift vectors connecting the pixels in the donor channel with the corresponding pixels in the FRET channel. A cut-out corresponding to the white square in subfigure **a** is shown. The magnitude of the vectors corresponds to the distance between correlated pixels in amount of pixels, the orientation of the vectors signifies the direction of the shift. (**c**) Application of the shift vectors to the donor signals (green, measured donor positions) from 250 summed up frames of the donor channel. Again, the approximate area of the white square in **a** is shown. The signals detected in the FRET channel are depicted in red (measured acceptor positions), the expected positions calculated by applying the shift vectors to the signals in the donor channel are marked by blue circles (calculated acceptor positions). The area signed by the white square in subfigure **a** approximately corresponds to the region of interest shown both in Figure 4.10 and 4.18. 123

4.17 (**a**) Summed-up localizations of all frames of the acceptor channel. (**b**) The identified average collective movement of all localizations in the acceptor channel over the whole measurement time. The x- and y-axis show the relative drift in x- and y-direction, respectively. The distance from the first localization is expressed in numbers of pixels. The drift is equivalent in all three channels. 125

4.18 (**a**) All detected pairs of signals in the donor and the FRET channel that match the initial condition to be identified as donor-acceptor pairs. 84 donor-acceptor pairs were identified by the algorithm overall. (**b**) Close up of the region of interest marked by the black square. The calibrated local vector field of this specific region is shown in Figure 4.16 **c**. The donor-acceptor pairs marked with the numbers 49, 26, 48, 39, 43 and 37 by the identification algorithm correspond to the re-branded donor-acceptor pairs 1, 2, 3, 4, 5 and 6 in Figure 4.10. The green and red dots correspond to all localizations detected in the donor and FRET channel, respectively, after application of the drift correction. The green and red squares around the dots represent the accepted search radius when moving along the local shift vector to the correlated signal in the other channel. An overlap of green and red squares is not critical, as the areas are not spatially correlated. Only an overlap of two green or two red squares can lead to errors. 126
4.19 All intensity-time traces of the example measurement belonging to valid donor-acceptor pairs (category I). The numbers above each trace correspond to the numbers given to the initially identified donor-acceptor pairs in Figure 4.18. 130
4.20 (**a**) Sum of the intensity-time traces of all valid donor-acceptor pairs depicted in Figure 4.19. (**b**) Sum of the intensity-time traces of all valid donor-acceptor pairs, if the second identification criterion in step 2 is implemented. The summed-up intensity values are shown as thin lines. The thick lines represent the moving average of the intensity values (binning size = 5). The intensity in the donor, FRET and acceptor channel is colored in green, orange and red, respectively. The vertical green line represents the point at which (partial) photobleaching of the donor appears to become significant, the vertical red line represents the point at which (partial) photobleaching of the acceptor appears to become significant. 133
4.21 Separate fits of the summed-up FRET (orange) and donor (green) intensity-time traces shown in Figure 4.20 **a** until (**a**) photobleaching of the (free) donor becomes dominant, (**b**) photobleaching of the (free) acceptor becomes dominant, or (**c**) when including all data. (**d**) Separate fits of the summed-up FRET (orange) and donor (green) intensity-time traces shown in Figure 4.20 **b** when including all data. The dots represent the summed-up intensity values, the solid lines indicate the moving average of these values (binning size = 5). The cycle time is $t_{\text{cycle}} = 30.6$ s. The dotted orange line corresponds to the fit of the FRET intensity-time trace with a diffusion coefficient of (**a**) $D_F = 3.5 \times 10^{-21}\ \text{m}^2\,\text{s}^{-1}$, (**b**) $D_F = 3.0 \times 10^{-21}\ \text{m}^2\,\text{s}^{-1}$, (**c**) $D_F = 4.0 \times 10^{-21}\ \text{m}^2\,\text{s}^{-1}$, and (**d**) $D_F = 4.5 \times 10^{-21}\ \text{m}^2\,\text{s}^{-1}$, respectively. The dashed green line corresponds to the fit of the donor intensity-time trace with a diffusion coefficient of (**a**) $D_D = 3.5 \times 10^{-21}\ \text{m}^2\,\text{s}^{-1}$ and (**b**, **c**, **d**) $D_D = 1.5 \times 10^{-20}\ \text{m}^2\,\text{s}^{-1}$, respectively. All fits are performed with equation (2.30). 135
4.22 Histogram of the relative single molecule diffusion coefficients D_D (green) and D_F (orange). D_D and D_F were determined with separate fits of the individual FRET and donor intensity-time traces shown in Figure 4.19 (see Figure 7.50 for the fits). All fits are performed with equation (2.30). 137
4.23 Structure of PVAc. 142

4.24 (**a**) Summed-up intensity-time traces of 105 FRET pairs from overall six different measurements in tempered PVAc (184 kDa) at room temperature. The intensity-time traces of the FRET-, donor- and acceptor-channel are shown in orange, green and red, respectively. The thin lines in (**a**) and the dots in (**b**) represent the summed-up intensity values at each measured point in time. The solid lines in (**b**) indicate the moving average of these values (binning size = 5). A cycle time of $t_{\text{cycle}} = 30.6$ s was employed for all measurements. (**b**) Separate fits of the FRET and the donor intensity-time trace shown in subfigure (**a**) according to equation (2.30). The dotted orange line corresponds to the fit of the FRET intensity-time trace with a diffusion coefficient of $D_F = 5.0 \times 10^{-21}$ m^2 s^{-1}. The dashed green line corresponds to the fit of the donor intensity-time trace with a diffusion coefficient of $D_D = 1.5 \times 10^{-20}$ m^2 s^{-1}. The fits were restricted to approximately 2200 s diffusion time to counter the effect of photobleaching on the analysis. 144

4.25 (**a,c,e**) Summed-up intensity-time traces of 8, 10 and 3 FRET pairs from each two different measurements in tempered PVAc (184 kDa) at 30 °C, 40 °C and 45 °C, respectively. The intensity-time traces of the FRET-, donor- and acceptor-channel are shown in orange, green and red, respectively. The solid lines in (**a,c,e**) and the dots in (**b,d,f**) represent the summed-up intensity values at each measured point in time. The solid lines in (**b,d,f**) represent the moving average of these values (binning size = 5). A cycle time of $t_{\text{cycle}} = 10.64$ s was employed during all measurements. (**b,d,f**) Separate fits of the FRET and the donor intensity-time traces with equation (2.30). The dotted orange line corresponds to the fit of the FRET intensity-time trace with a diffusion coefficient of (**b**) $D_F = 1.0 \times 10^{-23}$ m^2 s^{-1}, (**d**) $D_F = 8.0 \times 10^{-21}$ m^2 s^{-1} and (**f**) $D_F = 1.0 \times 10^{-23}$ m^2 s^{-1}, respectively. The dashed green line corresponds to the fit of the donor intensity-time trace with a diffusion coefficient of (**b**) $D_D = 3.5 \times 10^{-21}$ m^2 s^{-1}, (**d**) $D_D = 1.5 \times 10^{-20}$ m^2 s^{-1} and (**f**) $D_D = 6.5 \times 10^{-21}$ m^2 s^{-1}. 147

4.26 Structure of PBMA. 150

4.27 (**a, c**) Summed-up intensity-time traces of 20 and 29 FRET pairs from overall six and four different measurements in tempered PBMA (14.5 kDa) at room temperature and at 40 °C, respectively. The intensity-time traces of the FRET-, donor- and acceptor-channel are shown in orange, green and red, respectively. The thin lines in (**a, c**) and the dots in (**b, d**) represent the summed-up intensity values at each measured point in time. The solid lines in (**b, d**) indicate the moving average of these values (binning size = 5). A cycle time of (**a, b**) $t_{\text{cycle}} = 30.64$ s and (**c, d**) $t_{\text{cycle}} = 5.82$ s was employed during the measurements, respectively. (**b, d**) Separate fits of the FRET and the donor intensity-time trace shown in subfigure (**a**) and (**c**), respectively, with equation (2.30). The dotted orange line corresponds to the fit of the FRET intensity-time trace with a diffusion coefficient of (**b**) $D_F = 9.5 \times 10^{-22}$ m^2 s^{-1} and (**d**) $D_F = 5.0 \times 10^{-21}$ m^2 s^{-1}. The dashed green line corresponds to the fit of the donor intensity-time trace with a diffusion coefficient of (**b**) $D_D = 2.0 \times 10^{-21}$ m^2 s^{-1} and (**d**) $D_D = 5.5 \times 10^{-21}$ m^2 s^{-1}. The fits were restricted until photobleaching of the donor or acceptor becomes dominant. 151

4.28 Structure of PEG. 153
4.29 (**a, c**) Summed-up intensity-time traces of 95 and 10 FRET pairs from overall nine and four different measurements in tempered PEG (35 kDa) at room temperature and $T = 40\,^{\circ}\mathrm{C}$, respectively. The intensity-time traces of the FRET-, donor- and acceptor-channel are shown in orange, green and red, respectively. Thin lines in (**a, c**) and dots in (**b, d**) represent the summed-up intensity values at each measured point in time. Solid lines in (**c, d**) indicate the moving average of these values (binning size = 5). A cycle time of (**a, b**) $t_{\mathrm{cycle}} = 1.64$ s and of (**c, d**) $t_{\mathrm{cycle}} = 1.14$ s was employed, respectively. (**b, c**) Separate fits of the FRET and the donor intensity-time traces with equation (2.30). The dotted orange line corresponds to the fit of the FRET intensity-time trace with a diffusion coefficient of (**b**) $D_F = 5.5 \times 10^{-20}\ \mathrm{m^2\,s^{-1}}$ and (**d**) $D_F = 2.0 \times 10^{-19}\ \mathrm{m^2\,s^{-1}}$, respectively. The dashed green line corresponds to the fit of the donor intensity-time trace with a diffusion coefficient of (**b**) $D_D = 5.5 \times 10^{-19}\ \mathrm{m^2\,s^{-1}}$ and (**d**) $D_D = 3.0 \times 10^{-18}\ \mathrm{m^2\,s^{-1}}$, respectively. The fits were restricted until photobleaching of the acceptor becomes dominant. 155
4.30 Structure of dextran. 158
4.31 (**a**) Summed-up intensity-time traces of 16 cleaved donor-acceptor pairs of dyad **8** from overall three different measurements in tempered dextran (70 kDa) at room temperature. The intensity-time traces of the FRET-, donor- and acceptor-channel are shown in orange, green and red, respectively. Solid lines in (**a**) and dots in (**b**) represent the summed-up intensity values at each measured point in time. The solid lines in (**b**) indicate the moving average of these values (binning size = 5). A cycle time of $t_{\mathrm{cycle}} = 32.84$ s was employed in all measurements. (**b**) Separate fits of the FRET and the donor intensity-time trace shown in subfigure (**a**) with equation (2.30). The dotted orange line corresponds to the fit of the FRET intensity-time trace with a diffusion coefficient of $D_F = 2.5 \times 10^{-20}\ \mathrm{m^2\,s^{-1}}$. The dashed green line corresponds to the fit of the donor intensity-time trace with a diffusion coefficient of $D_D = 3.0 \times 10^{-20}\ \mathrm{m^2\,s^{-1}}$. The fits were restricted to approximately 1600 s diffusion time to counter the effect of photobleaching on the analysis. 159
4.32 Structure of PAA. 160

4.33 (**a**) Summed-up intensity-time traces of 37 cleaved donor-acceptor pairs of dyad **8** from eleven different measurements in tempered PAA (450 kDa) at room temperature. The intensity-time traces of the FRET-, donor- and acceptor-channel are shown in orange, green and red, respectively. Solid lines in (**a**) and dots in (**b**) represent the summed-up intensity values at each measured point in time. Solid lines in (**b**) indicate the moving average of these values (binning size = 5). A cycle time of $t_{\text{cycle}} = 30.6$ s was employed in all measurements. (**b**) Separate fits of the FRET and the donor intensity-time trace shown in subfigure (**a**) with equation (2.30). The dotted orange line corresponds to the fit of the FRET intensity-time trace with a diffusion coefficient of $D_F = 3.0 \times 10^{-21}$ m^2 s^{-1}. The dashed green line corresponds to the fit of the donor intensity-time trace with a diffusion coefficient of $D_D = 7.5 \times 10^{-20}$ m^2 s^{-1}. The fits were restricted to approximately 1600 s diffusion time to counter the effect of photobleaching on the analysis. 161
4.34 Structure of PEA. 162
4.35 (**a**) Summed-up intensity-time traces of 28 FRET pairs from a single measurement in tempered PEA (335 kDa) at room temperature. The intensity-time traces of the FRET-, donor- and acceptor-channel are shown in orange, green and red, respectively. Solid lines in (**a**) and dots in (**b**) represent the summed-up intensity values at each measured point in time. Solid lines in (**b**) indicate the moving average of these values (binning size = 5). A cycle time of $t_{\text{cycle}} = 10.64$ s was employed during the measurement. (**b**) Separate fits of the FRET and the donor intensity-time trace shown in subfigure (**a**) with equation (2.30). The dotted orange line corresponds to the fit of the FRET intensity-time trace with a diffusion coefficient of $D_F = 2.0 \times 10^{-21}$ m^2 s^{-1}. The dashed green line corresponds to the fit of the donor intensity-time trace with a diffusion coefficient of $D_D = 7.5 \times 10^{-22}$ m^2 s^{-1}. 163
4.36 (**a**) Summed-up intensity-time traces of 40 cleaved donor-acceptor pairs of dyad **8** from six different measurements on a glass substrate at room temperature. The intensity-time traces of the FRET-, donor- and acceptor-channel are shown in orange, green and red, respectively. Solid lines in (**a**) and dots in (**b**) represent the summed-up intensity values at each measured point in time. Solid lines in (**b**) indicate the moving average of these values (binning size = 5). A cycle time of $t_{\text{cycle}} = 10.64$ s was employed in all measurements. (**b**) Separate fits of the FRET and the donor intensity-time trace shown in subfigure (**a**) with equation (2.30). The dotted orange line corresponds to the fit of the FRET intensity-time trace with a diffusion coefficient of $D_F = 2.0 \times 10^{-20}$ m^2 s^{-1}. The dashed green line corresponds to the fit of the donor intensity-time trace with a diffusion coefficient of $D_D = 6.5 \times 10^{-17}$ m^2 s^{-1}. The fits were restricted to approximately 1500 s diffusion time to counter the effect of photobleaching on the analysis. 165

6.1 Esterification of nitrophenyl acetic acid with methanol to methyl(2-nitrophenyl)acetate (**1**). 178
6.2 Benzylic functionalization of **1** to methyl 2-(2-nitrophenyl)pent-4-ynoate (**2**). 178
6.3 Reduction of the ester **2** to the alcohol **3**. 179
6.4 Synthesis of compound **4**. 179
6.5 Deprotection of compound **4** to compound **5**. 180

6.6 Labelling reaction with ATTO565 NHS ester to the reference donor compound (**6**). . . . 181
6.7 Labelling reaction of compound **5** with ATTO647N azide to the acceptor **7**. 181
6.8 Labelling reaction of compound **6** with ATTO647N azide to the Dyad **8**. 182

7.1 Absorption spectra at different defined concentrations of (**a**) the BTD initiator (shades of violet) and (**b**) the BTD reference (shades of blue) in MeCN. (**c**) Determination of the absorption coefficient ε at the most red-shifted local maxima of the BTD initiator (violet, $\varepsilon_{\text{BTD ini.}} = 12600\,\text{L}\,\text{mol}^{-1}\,\text{cm}^{-1}$) and the BTD reference (blue, $\varepsilon_{\text{BTD ref.}} = 21600\,\text{L}\,\text{mol}^{-1}\,\text{cm}^{-1}$) with the Lambert-Beer law (equation (2.9)) 190
7.2 Spectral changes of BTD initiator and BTD reference in MeCN during selected irradiation times with a 400 nm LED @ 210 $\text{W}\,\text{m}^{-2}$. Changes of (**a**) absorption spectra and (**b**) relative emission spectra at 380 nm and 488 nm excitation for the BTD initiator (light to dark violet) and the BTD reference (light to dark blue) respectively. The black arrows indicate the changes with increasing irradiation time. Emission intensity is given relative to the maximum intensity of the respective compound at 0 s irradiation. (**c**) Temporal evolution of the absorbance at the different wavelengths of the (local) maxima shown in (**a**). (**d**) Temporal evolution of the relative fluorescence intensities at the different wavelength of the (local) maxima depicted in (**b**). All solid lines in (**c**) and (**d**) represent fits with single exponential decay functions. The colors correspond to the primary colors of the color gradients used for the spectra of the different compounds in (**a**) and (**b**). 191
7.3 Spectral changes of the dyad **8** in methanol during selected irradiation times with a 567 nm LED @ 112 $\text{W}\,\text{m}^{-2}$. The first column from the left shows the changes of absorption spectra, the second column depicts changes of emission spectra at 530 nm excitation and the third column represents changes of the emission spectra at 600 nm excitation. Changes of (a) absorption and (b) / (c) emission spectra the dyad **8** (light to dark orange), respectively. The black arrows in subfigures (a) – (c) indicate the changes with increasing irradiation time. (d) Temporal evolution of the absorbance at the different wavelengths of the (local) maxima shown in (a). (e) Temporal evolution of the fluorescence intensities (excitation at 530 nm) at the different wavelengths of the (local) maxima depicted in (b). (f) Temporal evolution of the fluorescence intensities (excitation 600 nm) at the different wavelengths of the (local) maxima presented in (c) In subfigures (d) – (f), circles refer to absorbance and emission maxima values related to the ATTO565 chromophore, while squares denote absorbance and emission maxima values related to the ATTO647N chromophore. All solid lines represent fits with single exponential decay functions. The colour corresponds to the primary colour of the colour gradient used for the spectra in subfigures (a) – (c). 192
7.4 Emission map of ATTO647N azide. The excitation wavelength was varied in 5 nm steps from 450 – 600 nm. The fluorescence intensity was normalized relative to the maximum value of each spectrum, respectively. 193
7.5 Absorption spectra of the exact same amount of dyad **8** dissolved in methanol (orange) and water (pink). 194

7.6 Absorption and fluorescence spectra of ATTO565 and ATTO647N in methanol with 4-nitrostyrene as quencher. The dyes were kept at constant concentration of approximately 0.25 $\mu mol L^{-1}$, the quencher was varied between 2.50 mM – 12.50 mM in 2.50 mM steps (dark green to light green for ATTO565 and black to blue for ATTO647N, respectively). Each solution was prepared and measured three times. Excitation wavelength were 530 nm and 620 nm, respectively.[59] 195
7.7 Absorption and fluorescence spectra of ATTO565 and ATTO647N in methanol with compound **1** as quencher. The dyes were kept at constant concentration of approximately 0.25 $\mu mol L^{-1}$, the quencher was varied between 2.50 mM – 12.50 mM in 2.50 mM steps (dark green to light green for ATTO565 and black to blue for ATTO647N, respectively). Each solution was prepared and measured three times. Excitation wavelength were 530 nm and 620 nm, respectively.[59] 195
7.8 Absorption and fluorescence spectra of ATTO565 and ATTO647N in methanol with nitrotoluene as quencher. The dyes were kept at constant concentration of approximately 0.25 $\mu mol L^{-1}$, the quencher was varied between 2.50 mM – 12.50 mM in 2.50 mM steps (dark green to light green for ATTO565 and black to blue for ATTO647N, respectively). Each solution was prepared and measured three times. Excitation wavelength were 530 nm and 620 nm, respectively.[59] 196
7.9 Absorption and emission spectra of 2-nitrosotoluene in methanol at 0.25 mM. Excitation wavelength was 620 nm. No emission was detectable. The inset in the absorption spectrum shows the absorption above 600 nm in closer detail.[59] 196
7.10 Absorption and fluorescence spectra of ATTO565 and ATTO647N in methanol with 2-nitrosotoluene as quencher. The dyes were kept at constant concentration of approximately 0.25 $\mu mol L^{-1}$, the quencher was varied between 2.50 mM – 12.50 mM in 2.50 mM steps (dark green to light green for ATTO565 and black to blue for ATTO647N, respectively). Each solution was prepared and measured three times. Excitation wavelength were 530 nm and 620 nm, respectively.[59] 197
7.11 Absorption and fluorescence spectra of ATTO565 and ATTO647N in methanol with purified 2-nitrosotoluene as quencher. The dyes were kept at constant concentration of approximately 0.25 $\mu mol L^{-1}$, the quencher was varied between 0.25 mM – 1.25 mM in 0.25 mM steps (dark green to light green for ATTO565 and black to blue for ATTO647N, respectively). Each solution was prepared and measured three times. Excitation wavelength were 530 nm and 620 nm, respectively.[59] 197
7.12 Stern-Volmer plots of ATTO565 NHS-ester and ATTO647N azide with different quenchers in methanol using the data presented in figures 7.6 – 7.11. All data related to the ATTO565 chromophore is coloured olive, all data related to the ATTO647N chromophore is coloured blue. In graph **a)**, all quenchers contain a nitro moiety, in graph **b)** all quenchers contain a nitroso moiety. Upright triangles correspond to 4-nitrostyrene, squares correspond to compound **1**, stars correspond to 2-nitrotoluene and downright triangles correspond to nitrosotoluene as quencher, respectively.[59] 198

7.13 TCSPC curves of the activated BTD reference compound in toluene. Excitation wavelength was 488 nm, the observed spectral window was from 532 – 715 nm. In graph **a)**, the curve was fitted with a single exponential tail fit. In graph **b)**, the same data was fitted with a dual exponential tail fit. Below the curves, the residuals of the fits are given as well. 199
7.14 TCSPC curves of the unactivated BTD initiator compound in toluene. Excitation wavelength was 488 nm, the observed spectral window was from 532 – 715 nm. In graph **a)**, the curve was fitted with a dual exponential tail fit. In graph **b)**, the same data was fitted with a triple exponential tail fit. Below the curves, the residuals of the fits are given as well. 199
7.15 TCSPC curves of the activated BTD reference compound in a poly styrene matrix. Excitation wavelength was 488 nm, the observed spectral window was from 532 – 715 nm. In graph **a)**, the curve was fitted with a dual exponential tail fit. In graph **b)**, the same data was fitted with a triple exponential tail fit. Below the curves, the residuals of the fits are given as well. 200
7.16 TCSPC curves of the unactivated BTD initiator compound in a poly styrene matrix. Excitation wavelength was 488 nm, the observed spectral window was from 532 – 715 nm. In graph **a)**, the curve was fitted with a dual exponential tail fit. In graph **b)**, the same data was fitted with a triple exponential tail fit. Below the curves, the residuals of the fits are given as well. 200
7.17 TCSPC curves of the FLIM images of unactivated (**a**, violet) and activated (**b,c**, blue) microgels **A** (figure 3.7). Excitation wavelength was 488 nm, the observed spectral window was from 500 – 715 nm. The data in (**a,b**) was fitted with quadruple exponential tail fits. For comparison, the same data as in (**b**) was fitted again in (**c**) with a triple exponential tail fit. The result, in particular the residual curve, is representative for all FLIM measurements with four determined lifetime components. Below the curves, the residuals of the fits are given as well. 201
7.18 TCSPC curves of the FLIM images of unactivated (**a**, violet) and activated (**b**, blue) microgels **B** (figure 3.8). Excitation wavelength was 488 nm, the observed spectral window was from 500 – 715 nm. All data was fitted with quadruple exponential tail fits. Below the curves, the residuals of the fits are given as well. 201
7.19 TCSPC curves of the FLIM images of BTD-PHMA networks (figure 3.9). The insets show the TCSPC around 10 ns when a second maximum / a shoulder is visible in the decay curves. Excitation wavelength was 488 nm, the observed spectral window was from 500 – 715 nm. All data was fitted with dual exponential tail fits. Below the curves, the residuals of the fits are given as well. 202

7.20 TCSPC curves of the FLIM images of BTD-PHMA networks before (**a**, violet) and after (**b**, blue) an AFM measurement (figure 3.10). The insets show the TCSPC around 10 ns when a second maximum / a shoulder is visible in the decay curves. Excitation wavelength was 488 nm, the observed spectral window was from 500 – 715 nm. All data was fitted with dual exponential tail fits. Below the curves, the residuals of the fits are given as well. 202
7.21 TCSPC curves of the FLIM images of BTD-PHMA networks before (**a**, violet) and after (**b,c**, blue) the AFM grid measurement (figure 3.11). Excitation wavelength was 488 nm, the observed spectral window was from 500 – 715 nm. All data was fitted with quadruple exponential tail fits. Below the curves, the residuals of the fits are given as well. 203
7.22 TCSPC curves of ATTO565 in methanol before (**a)** and **b)**) and after UV irradiation (**c)** and **d)**). Excitation wavelength was 527 nm, the observed spectral window was from 545 – 620 nm. In graphs **a)** and **c)** the curves were fitted with single exponential tail fits. For comparison, in graphs **b)** and **d)** the same data was fitted with dual exponential tail fits. Below the curves, the residuals of the fits are given as well. 203
7.23 TCSPC curves of Donor **6** in methanol before (**a)** and **b)**) and after UV irradiation (**c)** and **d)**). Excitation wavelength was 527 nm, the observed spectral window was from 545 – 620 nm. In graphs **a)** and **c)** the curves were fitted with single exponential tail fits. For comparison, in graphs **b)** and **d)** the same data was fitted with dual exponential tail fits. Below the curves, the residuals of the fits are given as well. 204
7.24 TCSPC curves of Dyad **8** in methanol before (**a)** and **b)**) and after UV irradiation (**c)** and **d)**). Excitation wavelength was 527 nm, the observed spectral window was from 545 – 620 nm. In graphs **a)** and **c)** the curves were fitted with single exponential tail fits. For comparison, in graphs **b)** and **d)** the same data was fitted with dual exponential tail fits. Below the curves, the residuals of the fits are given as well. 205
7.25 TCSPC curves of ATTO647N in methanol before (**a)** and **b)**) and after UV irradiation (**c)** and **d)**). Excitation wavelength was 635 nm, the observed spectral window was from 655 – 715 nm. In graphs **a)** and **c)** the curves were fitted with single exponential tail fits. For comparison, in graphs **b)** and **d)** the same data was fitted with dual exponential tail fits. Below the curves, the residuals of the fits are given as well. 206
7.26 TCSPC curves of the acceptor **7** in methanol before (**a)** and **b)**) and after UV irradiation (**c)** and **d)**). Excitation wavelength was 635 nm, the observed spectral window was from 655 – 715 nm. In graphs **a)** and **c)** the curves were fitted with single exponential tail fits. For comparison, in graphs **b)** and **d)** the same data was fitted with dual exponential tail fits. Below the curves, the residuals of the fits are given as well. 207
7.27 TCSPC curves of the acceptor **7** in methanol after additional UV irradiation. Excitation wavelength was 635 nm, the observed spectral window was from 655 – 715 nm. In graph **a)** the curve was fitted with a single exponential tail fit. For comparison, in graph **b)** the same data was fitted with a dual exponential tail fit. Below the curves, the residuals of the fits are given as well. 207

7.28 TCSPC curves of the dyad **8** in methanol before (**a)** and **b)**) and after UV irradiation (**c)** und **d)**). Excitation wavelength was 635 nm, the observed spectral window was from 655 – 715 nm. In graphs **a)** and **c)** the curves were fitted with single exponential tail fits. For comparison, in graphs **b)** and **d)** the same data was fitted with dual exponential tail fits. Below the curves, the residuals of the fits are given as well. 208
7.29 TCSPC curves of Dyad **8** in methanol before (**a)** and **b)**) and after UV irradiation (**c)** and **d)**). Excitation wavelength was 527 nm, the observed spectral window was from 655 – 715 nm. In graphs **a)** and **c)** the curves were fitted with single exponential tail fits. For comparison, in graphs **b)** and **d)** the same data was fitted with dual exponential tail fits. Below the curves, the residuals of the fits are given as well. 209
7.30 TCSPC curves of ATTO565 in water before (**a)** and **b)**) and after UV irradiation (**c)** and **d)**). Excitation wavelength was 527 nm, the observed spectral window was from 545 – 620 nm. In graphs **a)** and **c)** the curves were fitted with single exponential tail fits. For comparison, in graphs **b)** and **d)** the same data was fitted with dual exponential tail fits. Below the curves, the residuals of the fits are given as well. 210
7.31 TCSPC curves of Donor **6** in water before (**a)**, **b)** and **c)**) and after UV irradiation (**d)**, **e)** and **f)**). Excitation wavelength was 527 nm, the observed spectral window was from 545 – 620 nm. In graphs **a)** and **d)** the curves were fitted with single exponential tail fits. For comparison, in graphs **b)** and **e)** the same data was fitted with dual exponential tail fits, and in graphs **c)** and **f)** with triple exponential tail fits. Below the curves, the residuals of the fits are given as well. 210
7.32 TCSPC curves of Dyad **8** in water before (**a)**, **b)** and **c)**) and after UV irradiation (**d)**, **e)** and **f)**). Excitation wavelength was 527 nm, the observed spectral window was from 545 – 620 nm. In graphs **a)** and **d)** the curves were fitted with single exponential tail fits. For comparison, in graphs **b)** and **e)** the same data was fitted with dual exponential tail fits, and in graphs **c)** and **f)** with triple exponential tail fits. Below the curves, the residuals of the fits are given as well. 211
7.33 TCSPC curves of ATTO647N in water before (**a)** and **b)**) and after UV irradiation (**c)** and **d)**). Excitation wavelength was 635 nm, the observed spectral window was from 655 – 715 nm. In graphs **a)** and **c)** the curves were fitted with single exponential tail fits. For comparison, in graphs **b)** and **d)** the same data was fitted with dual exponential tail fits. Below the curves, the residuals of the fits are given as well. 211
7.34 TCSPC curves of the acceptor **7** in water before (**a)**, **b)** and **c)**) and after UV irradiation (**d)**, **e)** and **f)**). Excitation wavelength was 635 nm, the observed spectral window was from 655 – 715 nm. In graphs **a)** and **d)** the curves were fitted with single exponential tail fits. For comparison, in graphs **b)** and **e)** the same data was fitted with dual exponential tail fits, and in graphs **c)** and **f)** with triple exponential tail fits. Below the curves, the residuals of the fits are given as well. 212

7.35 TCSPC curves of the dyad **8** in water before (**a**), **b)** and **c)**) and after UV irradiation (**d**), **e)** and **f)**). Excitation wavelength was 635 nm, the observed spectral window was from 655 – 715 nm. In graphs **a)** and **d)** the curves were fitted with single exponential tail fits. For comparison, in graphs **b)** and **e)** the same data was fitted with dual exponential tail fits, and in graphs **c)** and **f)** with triple exponential tail fits. Below the curves, the residuals of the fits are given as well. 212
7.36 TCSPC curves of Dyad **8** in water before (**a**), **b)** and **c**)) and after UV irradiation (**d**), **e)** and **f)**). Excitation wavelength was 635 nm, the observed spectral window was from 655 – 715 nm. In graphs **a)** and **d)** the curves were fitted with single exponential tail fits. For comparison, in graphs **b)** and **e)** the same data was fitted with dual exponential tail fits, and in graphs **c)** and **f)** with triple exponential tail fits. Below the curves, the residuals of the fits are given as well. 213
7.37 TCSPC curves of Donor **6** in methanol after irradiation with red light. Excitation wavelength was 527 nm, the observed spectral window was from 545 – 620 nm. In graphs **a)** the curve was fitted with a single exponential tail fit. For comparison, in graph **b)** the same data was fitted with a dual exponential tail fit. Below the curves, the residuals of the fits are given as well. 213
7.38 TCSPC curves of dyad **8** in methanol after irradiation with red light. Excitation wavelength was 527 nm, the observed spectral window was from 545 – 620 nm. In graphs **a)** the curve was fitted with a single exponential tail fit. For comparison, in graph **b)** the same data was fitted with a dual exponential tail fit and in graph **c)** with a triple exponential tail fit. Below the curves, the residuals of the fits are given as well. 214
7.39 TCSPC curves of **ATTO647N azide** in methanol after irradiation with red light. Excitation wavelength was 635 nm, the observed spectral window was from 655 – 715 nm. In graphs **a)** the curve was fitted with a single exponential tail fit. For comparison, in graph **b)** the same data was fitted with a dual exponential tail fit. Below the curves, the residuals of the fits are given as well. 214
7.40 TCSPC curves of acceptor **7** in methanol after irradiation with red light. Excitation wavelength was 635 nm, the observed spectral window was from 655 – 715 nm. In graphs **a)** the curve was fitted with a single exponential tail fit. For comparison, in graph **b)** the same data was fitted with a dual exponential tail fit. Below the curves, the residuals of the fits are given as well. 215
7.41 TCSPC curves of dyad **8** in methanol after irradiation with red light. Excitation wavelength was 635 nm, the observed spectral window was from 655 – 715 nm. In graphs **a)** the curve was fitted with a single exponential tail fit. For comparison, in graph **b)** the same data was fitted with a dual exponential tail fit. Below the curves, the residuals of the fits are given as well. 215

7.42 TCSPC curves of dyad **8** in methanol after irradiation with red light. Excitation wavelength was 527 nm, the observed spectral window was from 655 – 715 nm. In graphs **a)** the curve was fitted with a single exponential tail fit. For comparison, in graph **b)** the same data was fitted with a dual exponential tail fit and in graph **c)** with a triple exponential tail fit. Below the curves, the residuals of the fits are given as well. 215
7.43 FCS curves of ATTO647N (blue and cyan), the acceptor (dark to light red) and the dyad (dark and light orange) in methanol before and after irradiation, respectively. Excitation wavelength was 635 nm. All curves have been fitted with the pure diffusion model and the least amount of components that still led to reasonable fits. Below the curves, the residuals of the fits are given as well.[59] 216
7.44 Defocused image of dyad **8** in **a**) PVAc at room temperature, **b**) PEG at room temperature, **c, d**) PBMA at room temperature and 40 °C, respectively, **e**) PEA at room temperature and **f**) on a glass substrate at room temperature. All images were recorded with 640 nm excitation. The imaging pixel size was 65 nm. 217
7.45 Series of false-color images taken from a widefield microscopy movie of a tempered PVAc film before and after 0.5 s of UV irradiation (378 nm at 50 $W\,cm^{-2}$). No dye was added to the film. A selection of images recorded with 200 ms integration time is shown which were taken at the times indicated in the central time arrow. In the top row, the long wavelength channel ($>$ 655 nm) at 561 nm excitation is shown (orange, FRET channel). In the middle row, the short wavelength channel (570 – 633 nm) at 561 nm excitation is displayed (green, donor channel). In the bottom row, the long wavelength channel at 640 nm excitation is shown (red, acceptor channel). All images were colored according to the established color scheme. The vertical purple line symbolizes the UV irradiation. The imaging pixel size was 65 nm. 218
7.46 All intensity-time traces of the example measurement that have been identified as exhibiting premature photobleaching (donor-acceptor pair category II), with (**a**) perfect correlation of donor and acceptor channel, (**b**) short delay between the rise of donor intensity and the drop of acceptor intensity, or (**c**) without reasonably interpretable intensity in the acceptor at all. The numbers above each trace correspond to the numbers given to the initially identified donor-acceptor pairs in figure 4.18. 219
7.47 All intensity-time traces of the example measurement that are assumed to be either noise (**a**) or whose features are hidden by noise (**b**) (donor-acceptor pairs of category III). The numbers above each trace correspond to the numbers given to the initially identified donor-acceptor pairs in figure 4.18. 220

7.48 First part of all intensity-time traces of the example measurement that have been identified as irregular (category IV). In particular, (**a**) signals are detected in the donor channel starting from $t = 0$ s, (**b**) signals are detected in the donor channel shortly after the beginning while while no reasonable correlation is observed between the signals in the donor channel and the FRET and/or acceptor channel, (**c**) the background correction results in significantly negative intensity in the donor channel, or (**d**) the background correction results in significantly negative intensity in the FRET and/or acceptor channel. The negative intensity values are probably caused by fluorescence events within the background circle in any of the three channels (see slso section 4.6.1 step 5) The numbers above each trace correspond to the numbers given to the initially identified donor-acceptor pairs in figure 4.18. 221

7.49 Second part of all intensity-time traces of the example measurement that have been identified as irregular (category IV). In particular, (**a**) the intensity in the FRET channel remains approximately constant, (**b**) no reasonable correlated signal is detected in the donor channel, or (**c**) noteworthy intensity is only detected in the acceptor channel. The numbers above each trace correspond to the numbers given to the initially identified donor-acceptor pairs in figure 4.18. 222

7.50 Separate fits of the individual FRET (orange) and donor (green) intensity-time traces shown in figure 4.19. The order of the individual fits is the same as order of intensity-time traces in figure 4.19. For a better overview, the identification number of the corresponding donor-acceptor pair is given in the upper left corner of each graph. The dots represent the summed-up intensity values, the solid lines indicate the moving average of these values. The dots are always 30.6 s apart corresponding to the temporal resolution of the measurement. The dotted orange lines corresponds to the fit of the FRET intensity-time traces. The dashed green lines corresponds to the fit of the donor intensity-time traces. The determined diffusion coefficients are listed above each graph. The data in each fit was restricted according to photobleaching of the donor. All fits are performed with equation (2.30). 223

7.51 (**a, c**) Summed-up intensity-time traces of (**a**) 41 and (**c**) 17 FRET pairs of dyad **8** from overall (**a**) three and (**c**) four different measurements in tempered PVAc (184 kDa) at room temperature, respectively. The intensity-time traces of the FRET-, donor- and acceptor-channel are shown in orange, green and red, respectively. Thin lines in **a, c** and dots in **b, d** represent the summed-up intensity values at each measured point in time. Solid lines in (**b, d**) indicate the moving average of these values. A cycle time of (**a, b**) $t_{\text{cycle}} = 10.6$ s and of (**c, d**) $t_{\text{cycle}} = 32.64$ s was employed, respectively. (**b, d**) Separate fits of the FRET and the donor intensity-time traces with equation (2.30). The dotted orange line corresponds to the fit of the FRET intensity-time trace with a diffusion coefficient of (**b**) $D_F = 4.0 \times 10^{-21}$ m^2 s^{-1} and (**d**) $D_F = 7.0 \times 10^{-22}$ m^2 s^{-1}, respectively. The dashed green line corresponds to the fit of the donor intensity-time trace with a diffusion coefficient of (**b**) $D_D = 3.5 \times 10^{-20}$ m^2 s^{-1} and (**d**) $D_D = 1.5 \times 10^{-21}$ m^2 s^{-1}. The fits were restricted to approximately 10000 s diffusion time to counter the effect of photobleaching on the analysis. 224

7.52 (a) Summed-up intensity-time traces of 16 cleaved donor-acceptor pairs of dyad **8** from overall two different measurements in tempered PVAc (184 kDa) at 40 °C. The intensity-time traces of the FRET-, donor- and acceptor-channel are shown in orange, green and red, respectively. Dots represent the summed-up intensity values at each measured point in time, solid lines indicate the moving average of these values. Between consecutive frames, a delay time of 5 s was employed during the measurements. (b) Separate fits of the FRET and the donor intensity-time trace shown in subfigure (a) according to equation (2.30). The dotted orange line corresponds to the fit of the FRET intensity-time trace with a diffusion coefficient of $D_F = 1.0 \times 10^{-20}$ m^2 s^{-1}. The dashed green line corresponds to the fit of the donor intensity-time trace with a diffusion coefficient of $D_D = 5.5 \times 10^{-21}$ m^2 s^{-1}. 225

7.53 (**a**) Summed-up intensity-time traces of 15 FRET pairs from overall four different measurements in tempered PBMA (14.5 kDa) at 40 °C. The intensity-time traces of the FRET-, donor- and acceptor-channel are shown in orange, green and red, respectively. Thin lines and dots represent the summed-up intensity values at each measured point in time, solid lines indicate the moving average of these values. The cycle time was $t_{\text{cycle}} = 10.82$ s. (**b**) Separate fits of the FRET and the donor intensity-time trace shown in subfigure (a) according to equation (2.30). The dotted orange line corresponds to the fit of the FRET intensity-time trace with a diffusion coefficient of $D_F = 2.5 \times 10^{-21}$ m^2 s^{-1}. The dashed green line corresponds to the fit of the donor intensity-time trace with a diffusion coefficient of $D_D = 1.5 \times 10^{-19}$ m^2 s^{-1}. 226

7.54 (**a, c**) Summed-up intensity-time traces of 79 and 132 FRET pairs from overall eight and ten different measurements in tempered PEG (35 kDa) at room temperature, respectively. The intensity-time traces of the FRET-, donor- and acceptor-channel are shown in orange, green and red, respectively. Solid lines in (**a, c**) and dots in (**b, d**) represent the summed-up intensity values at each measured point in time, solid lines in (**b, d**) indicate the moving average of these values. Cycle times of (**a, b**) $t_{\text{cycle}} = 1.14$ s and (**c, d**) $t_{\text{cycle}} = 30.64$ s were employed, respectively. (**b, d**) Separate fits of the FRET and the donor intensity-time trace shown in subfigure (**a**) and (**c**) with equation (2.30). The dotted orange line corresponds to the fit of the FRET intensity-time trace with a diffusion coefficient of (**b**) $D_F = 9.5 \times 10^{-20}$ m^2 s^{-1} and (**d**) $D_F = 1.0 \times 10^{-20}$ m^2 s^{-1}. The dashed green line corresponds to the fit of the donor intensity-time trace with a diffusion coefficient of (**b**) $D_D = 6.5 \times 10^{-19}$ m^2 s^{-1} and (**d**) $D_D = 9.0 \times 10^{-20}$ m^2 s^{-1}. The fits were restricted until photobleaching of either donor or acceptor becomes dominant. . . . 227

7.55 (**a, c, e**) Summed-up intensity-time traces of (**a**) 19, (**c**) 20 and (**e**) 12 FRET pairs from (**a, c**) four and (**e**) six different measurements in tempered PEG (35 kDa) at 40 °C, respectively. The intensity-time traces of the FRET-, donor- and acceptor-channel are shown in orange, green and red, respectively. Thin lines in (**a, c, e**) and dots in (**c, d, f**) represent the summed-up intensity values at each measured point in time. The solid lines in (**c, d, f**) indicate the moving average of these values. A cycle time of (**a, b**) $t_{\text{cycle}} = 1.64$ s, (**c, d**) $t_{\text{cycle}} = 2.64$ s and (**e, f**) $t_{\text{cycle}} = 10.64$ s was employed, respectively. (**b, d, f**) Separate fits of the FRET and the donor intensity-time traces with equation (2.30). The dotted orange line corresponds to the fit of the FRET intensity-time trace with a diffusion coefficient of (**b**) $D_F = 6.5 \times 10^{-20}$ m^2 s^{-1}, (**d**) $D_F = 3.5 \times 10^{-20}$ m^2 s^{-1} and (**f**) $D_F = 2.5 \times 10^{-20}$ m^2 s^{-1}, respectively. The dashed green line corresponds to the fit of the donor intensity-time trace with a diffusion coefficient of (**b**) $D_D = 2.0 \times 10^{-16}$ m^2 s^{-1} and (**d**) $D_D = 2.5 \times 10^{-18}$ m^2 s^{-1} and (**f**) $D_D = 8.0 \times 10^{-19}$ m^2 s^{-1}, respectively. The fits were restricted to measurement times when photobleaching of the donor becomes dominant. . . . 228

7.56 a) AFM image of manual cut in a PVAc film (100 kDa, 8w% MeOH solution, spincoated and tempered). The image was recorded in tapping mode with a setpoint of 30 nm, a scan size of 60×60 µm with 256×256 pixels and a line rate of 0.5 lines per second. The white lines represent the measured height profiles in image (b). b) Height profile from bottom to top along the vertical (black) and the diagonal (red) line shown in image (a). An average film thickness of about 500 nm is derived. Material from the region of the cut is pushed to the edges resulting in a local height increase which has to be ignored for the estimation of the average thickness. . . . 229

7.57 a) AFM image of manual cut in a PBMA film (14 kDa, 3w% toluene solution, spincoated and tempered). The image was recorded in tapping mode with a setpoint of 30 nm, a scan size of 60×60 µm with 256×256 pixels and a line rate of 0.5 lines per second. The white lines represent the measured height profiles in image (b). b) Height profile from bottom to top along the vertical (black) and the diagonal (red) line shown in image (a). An average film thickness of about 110 nm is derived. Material from the region of the cut is pushed to the edges resulting in a local height increase which has to be ignored for the estimation of the average thickness. 229
7.58 a) AFM image of manual cut in a PEG film (35 kDa, 5w% MeOH solution, spincoated and tempered). The image was recorded in tapping mode with a setpoint of 30 nm, a scan size of 60×60 µm with 256×256 pixels and a line rate of 0.5 lines per second. The white lines represent the measured height profiles in image (b). b) Height profile from bottom to top along the vertical (black) and the diagonal (red) line shown in image (a). An average film thickness of about 350 nm is derived. Material from the region of the cut is pushed to the edges resulting in a local height increase which has to be ignored for the estimation of the average thickness. 230
7.59 a) AFM image of manual cut in a dextrane film (70 kDa, 3w% aqueous solution, spincoated and tempered). The image was recorded in tapping mode with a setpoint of 30 nm, a scan size of 60×60 µm with 256×256 pixels and a line rate of 0.5 lines per second. The white lines represent the measured height profiles in image (b). The inhomogeneous area at the bottom of the image is estimated to be a measurement artifact. b) Height profile from bottom to top along the vertical (black) and the diagonal (red) line shown in image (a). An average film thickness of about 100 – 150 nm is derived. Material from the region of the cut is pushed to the edges resulting in a local height increase which has to be ignored for the estimation of the average thickness. 230
7.60 a) AFM image of manual cut in a PAA film (450 kDa, 2w% MeOH solution, spincoated and tempered). The image was recorded in tapping mode with a setpoint of 30 nm, a scan size of 60×60 µm with 256×256 pixels and a line rate of 0.5 lines per second. The white lines represent the measured height profiles in image (b). The inhomogeneous area at the bottom of the image is estimated to be a measurement artifact due to some particularly high features in the polymer film stemming from the cut. b) Height profile from left to right along the horizontal (black) and the diagonal (red) line shown in image (a). An average film thickness of about 170 nm is derived. Material from the region of the cut is pushed to the edges resulting in a local height increase which has to be ignored for the estimation of the average thickness. 231

7.61 a) AFM image of manual cut in a PEA film (335 kDa, 3w% MeOH solution, spincoated and tempered). The image was recorded in tapping mode with a setpoint of 30 nm, a scan size of 60×60 µm with 256×256 pixels and a line rate of 0.5 lines per second. The white lines represent the measured height profiles in image (b). b) Height profile from bottom to top along the vertical (black) and the diagonal (red) line shown in image (a). An average film thickness of about 120 – 200 nm is derived. The polymer film shows major inhomogeneities all throughout the image. 231
7.62 DSC curve of PVAc (184 kDa). Heating and cooling rate was 20 $\mathrm{K\,min^{-1}}$. The glass transition temperature $T_g = 42.6$ °C was determined during the second heating process as the midpoint of the curve. 232
7.63 DSC curve of PBMA (14 kDa). Heating and cooling rate was 20 $\mathrm{K\,min^{-1}}$. The glass transition temperature $T_g = 36.2$ °C was determined during the second heating process as the midpoint of the curve. 232
7.64 DSC curve of PEG (35 kDa). Heating and cooling rate was 20 $\mathrm{K\,min^{-1}}$. No glass transition could be determined. The band between 40 – 90 °C indicates melting of the polymer. 233
7.65 DSC curve of dextrane (70 kDa). Heating and cooling rate was 20 $\mathrm{K\,min^{-1}}$. The glass transition temperature $T_g = 98.5$ °C was determined during the first heating process (blue curve) as the midpoint of the curve. The structure of the curve fades entirely during the second heating process indicating a thermal decomposition at elevated temperatures. . . 233
7.66 DSC curve of PAA (450 kDa). Heating and cooling rate was 20 $\mathrm{K\,min^{-1}}$. The glass transition temperature $T_g = 131.1$ °C was determined during the second heating process as the midpoint of the curve. 234
7.67 DSC curve of PEA (335 kDa). Heating and cooling rate was 20 $\mathrm{K\,min^{-1}}$. The glass transition temperature $T_g = -0.7$ °C was determined during the second heating process as the midpoint of the curve. 234
7.68 ^{1}H-NMR spectrum of 2-nitrosotoluene at a concentration of 12.7 mM in MeOH$-\mathrm{d_4}$ at 600 MHz. The singlet peaks at 2.40 ppm and 2.42 ppm correspond to the methyl peaks of the dimer in trans- and cis-conformation, respectively.[59] 235
7.69 ^{1}H-NMR spectrum of 2-nitrosotoluene at a concentration of 25.5 mM in MeOH$-\mathrm{d_4}$ at 600 MHz. The singlet peaks at 2.40 ppm and 2.42 ppm correspond to the methyl peaks of the dimer in trans- and cis-conformation, respectively.[59] 235
7.70 ^{1}H-NMR spectrum of 2-nitrosotoluene at a concentration of 49.7 mM in MeOH$-\mathrm{d_4}$ at 600 MHz. The singlet peaks at 2.40 ppm and 2.42 ppm correspond to the methyl peaks of the dimer in trans- and cis-conformation, respectively.[59] 236
7.71 ^{1}H-NMR spectrum of 2-nitrosotoluene at a concentration of 82.4 mM in MeOH$-\mathrm{d_4}$ at 600 MHz. The singlet peaks at 2.40 ppm and 2.42 ppm correspond to the methyl peaks of the dimer in trans- and cis-conformation, respectively.[59] 236
7.72 ^{1}H-NMR spectrum of 2-nitrosotoluene at a concentration of 154 mM in MeOH$-\mathrm{d_4}$ at 600 MHz. The singlet peaks at 2.40 ppm and 2.42 ppm correspond to the methyl peaks of the dimer in trans- and cis-conformation, respectively.[59] 237

7.73 Plot of the prepared concentration of 2-nitrosotoluene as determined from the weighted mass assuming complete dissociation vs. the mole fraction of the monomeric form as determined by ^{1}H-NMR. The data was fitted with a linear function with a slope of $m = -0.7232\ \mathrm{L\,mol^{-1}}$ and intercept of $y = 0.9760$. We assume that the concentrations used in our Stern-Volmer experiments are within the linear regime of the monomer-dimer equilibrium of 2-nitrosotoluene.[59] 237
7.74 ^{1}H-NMR spectrum of methyl (2-nitrophenyl)acetate (**1**) in $CDCl_3$ at 600 MHz.[59] 238
7.75 ^{1}H-NMR spectrum of methyl 2-(2-nitrophenyl)pent-4-ynoate (**2**) in $CDCl_3$ at 600 MHz.[59] 238
7.76 ^{1}H-NMR spectrum of methyl 2-(2-nitrophenyl)pent-4-yn-1-ol (**3**) in $CDCl_3$ at 600 MHz.[59] 239
7.77 ^{1}H-NMR spectrum of tert-butyl (2-(2-nitrophenyl)pent-4-yn-1-yl) ethane-1,2-diyldicarbamate (**4**) in $CDCl_3$ at 600 MHz.[59] 239
7.78 ^{1}H-NMR spectrum of 2-(2-nitrophenyl)pent-4-yn-1-yl (2-aminoethyl)carbamate (**5**) in $CDCl_3$ at 600 MHz. 240
7.79 ^{13}C-NMR spectrum of 2-(2-nitrophenyl)pent-4-yn-1-yl (2-aminoethyl)carbamate (**5**) in $CDCl_3$ at 150 MHz, decoupling at 600 MHz.[59] 240
7.80 ESI-MS spectrum of tert-butyl (2-(2-nitrophenyl)pent-4-yn-1-yl) ethane-1,2-diyldicarbamate (**4**).[59] 241
7.81 ESI-MS spectrum of (2-(2-nitrophenyl)pent-4-yn-1-yl) (2-aminoethyl)carbamate (**5**).[59] 241
7.82 ESI-MS spectrum of donor **6**.[59] 242
7.83 ESI-MS spectrum of acceptor **7**.[59] 242
7.84 ESI-MS spectrum of dyad **8**.[59] 243
7.85 HPLC chromatogram of the dyad **8** pre-purified according to synthesis of dyad **8**. Eluent was methanol with 0.02% acetic acid and 0.01% trifluoroacetic acid. Everything between retention times from 6 – 9.5 min was united to fraction 1, everything between retention times from 10 – 11 min was united to fraction 2. Both fractions were characterized with UV-Vis and fluorescence spectroscopy, see figure 7.86. The detection in the HPLC was performed at 275 nm. The characterization with UV-Vis spectroscopy revealed that impurities absorbing or scattering in the UV region accumulated in the sample after the HPLC. Hence, the chromatogram is not quantitative.[59] 244
7.86 Absorption and emission spectra of the two HPLC fraction seen in figure 7.85. The excitation wavelength was 530 nm. Fraction 1 was identified as dyad **8**, fraction 2 is assumed to be unreacted free ATTO647N-azide. No significant changes to the spectra in the main text are observed apart from a different behavior in the UV region. We assume these to stem from impurities, in particular column material, from the HPLC column.[59] 245
7.87 Product information sheet of ATTO565 as provided by the manufacturer. (https://www.leica-microsystems.com/de/produkte/atto-tec-consumables/p/atto-565/downloads/) 246
7.88 Product information sheet of ATTO647N as provided by the manufacturer. (https://www.leica-microsystems.com/de/produkte/atto-tec-consumables/p/atto-647n/downloads/) 247
7.89 Labeling procedure of ATTO dyes with (top) NHS ester modification and (bottom) alkyne or azide modification as specified by the manufacturer. 248

7.90 Förster distance for a variety of ATTO-dye pairs as provided by the manufacturer. The relevant Förster distance of ATTO565 and ATTO647N is marked by a red circle. 249

8.3 List of Abbreviations

AFM atomic force microscopy

AI artificial intelligence

ALEX alternating laser excitation

ATRP atom transfer radical polymerization

BTD benzo thiadiazole

CCD charge-coupled device

CLSM confocal laser scanning microscopy

(s)CMOS (scientific) complementary metal-oxide-semiconductor

DLS dynamic light scattering

DSC differential scanning calorimetry

DNA deoxyribonucleic acid

ESI electrospray ionization

FCS fluorescence correlation spectroscopy

FEDUP FRET efficiency diffusion measurement upon photocleavage

FLIM fluorescence lifetime imaging

FM fluorescence microscopy

FRAP fluorescence recovery after photobleaching

FRET Förster resonance energy transfer

HPLC high performance liquid chromatography

IC internal conversion

IR infrared

ISC intersystem crossing

IUPAC International Union of Pure and Applied Chemistry

laser light amplification by stimulated emission radiation

LCST lower critical solution temperature

LED light-emitting diode

MeCN acetonitrile

MeOH methanol

MINFLUX minimal fluorescence photon fluxes microscopy

MP-LSM multiphoton-laser scanning microscopy

MS mass spectrometry

MSD mean square displacement

NA numerical aperture

NMR nuclear magnetic resonance

NPPOC 2-(2-nitrophenyl)propyloxycarbonyl

OFP optical force probe

PAA poly(acrylic acid)

PAINT point accumulation for imaging in nanoscale topography

PALM photoactivation localization microscopy

PBMA poly(butyl methacrylate)

PBS phosphate-buffered saline

PDI perylene diimide

PEA poly(ethyl acrylate)

PEG poly(ethylene glycol)

PFG pulsed field gradient

PHMA poly(hexyl methacrylate)

PMMA poly(methyl methacrylate)

PNIPAM poly(*N*-isopropylacrylamide)

PPG photolabile protecting group

PSF point spread function

PVA poly vinyl alcohol

PVAc poly(vinyl acetate)

PVCL poly(vinyl caprolactam)

PS poly styrene

RESOLFT reversible saturable optical fluorescence transitions

SDCM spinning disk confocal microscopy

SEM scanning electron microscopy

SIM structured illumination microscopy

SMLM single molecule localization microscopy

SMT single molecule tracking

SNR signal-to-noise ratio

SPAD single photon avalanche diode

SPT single particle tracking

SRFM super-resolution fluorescence microscopy

(d)STORM (direct) stochastic optical reconstruction microscopy

STED stimulated emission depletion

TCSPC time correlated single photon counting

TDI terrylene diimide

TEM transmission electron microscopy

THF tetrahydrofuran

THPTA tris(3-hydroxypropyltriazolylmethyl)amine

TIRF total internal reflection fluorescence

TMS tetramethylsilane

UV ultraviolet

vis visible

VIM N-vinyl-imidazole

VPTT volume phase transition temperature

VR vibrational relaxation

VFT Vogel-Fulcher-Tammann

8.4 List of Symbols

A	absorbance
A_i	amplitude of component i
a	pixel size or (irradiation) area
α	diffusion parameter
B	material constant
b	background signal
c	speed of light
$c(x)$ or c_x	concentration of substance x
D	diffusion coefficient
D_D	collective diffusion coefficient of the relative movement of donor and acceptor determined via donor fluorescence (see also glossary 8.5)
D_F	collective diffusion coefficient of the relative movement of donor and acceptor determined via FRET fluorescence (see also glossary 8.5)
d	sample thickness, diffraction limit or penetration depth
ΔE	energy gap between two arbitrary states
E	energy
E_{abs}	total absorbed energy
ε	absorption coefficient
h	Planck constant
η	viscosity
η_{FRET}	FRET efficiency
$\eta(r,t)$	FRET efficiency in dependency of distance and time
$\eta(t,D)$	FRET efficiency in dependency of time and diffusion
F	(fluorescence) emission intensity
F_D	(fluorescence) emission intensity of the donor in absence of the acceptor
F_{DA}	(fluorescence) emission intensity of the donor in presence of the acceptor
I	transmission intensity
K_{SV}	Stern-Volmer constant
k	arbitrary rate constant
k_{fl}	fluorescence rate constant
k_{nr}	collective rate constant of all non radiative relaxation pathways
k_B	Boltzmann constant
k_q	bimolecular quenching constant
κ	orientation factor
λ	wavelength
$\lambda_{\text{irrad.}}$	wavelength of irradiation
$\hat{\mu}$	transition dipole moment
ν	frequency
n	refractive index, or dimensionality
N	number (of light-absorbing molecules per volume, detected photons, etc.)
N_A	Avogadro constant
P_A	(absorbed) power density
$P_{A,0}$	power density measured after the reference cuvette filled with solvent
$P_{A,s}(t)$	power density measured behind the sample at time t
$P_{3\text{D}}(r,t,D)$	Maxwell distribution (of distances r at times t due to diffusion with D)

q	scattering angle
r	distance (between FRET-donor and -acceptor)
$\langle r^2 \rangle$	mean square displacement (MSD)
R_H	hydrodynamic radius
R_0	Förster distance
ρ_{label}	labeling density
σ	absorption cross section or standard deviation
$\sigma(\Phi_{\text{pb}})$	standard deviation of the photobleaching quantum yield
σ_{loc}	localization accuracy
σ_{Nyquist}	Nyquist resolution
σ_{final}	overall image resolution
S_0, S_1, S_{N}	singlet states
θ_{in}	angle of incidence
θ_{out}	angle of refraction
θ_c	critical angle
t	time
t_{cycle}	cycle time (see also glossary 8.5)
t_{delay}	delay time (see also glossary 8.5)
T_0, T_1, T_{N}	triplet states
T	temperature or transmission
T_g	glass transition temperature
T_∞	Vogel-temperature
τ	time constant of a single exponential decay function
τ_A	time constant of a single exponential decay function describing the decrease of maximum absorbance A
τ_F	time constant of a single exponential decay function describing the decrease of maximum fluorescence emission F
τ_{fl}	fluorescence lifetime
τ_x	fluorescence lifetime component x
τ_D	fluorescence lifetime of the donor in absence of the acceptor
τ_{DA}	fluorescence lifetime of the donor in presence of the acceptor
Φ	fluorescence quantum yield
Φ_D	fluorescence quantum yield of the donor
Φ_{b}	photobleaching quantum yield
v	vibrational quantum number
z	vertical distance

8.5 Glossary

8.5.1 Glossary of Chapter 3

- **activation**: refers to the mechanical activation of mechanophores (e.g. via ultrasonication)
- **activated BTD**: can refer to the activated reference compound (see BTD reference), or the activated mechanofluorophore inside a polymer system
- **activated (BTD) microgel**: microgels with BTD crosslinker that have already been activated (e.g. by ultrasonication)
- **BTD initiator / BTD crosslinker / unactivated BTD**: reference compound for the investigated

BTD mechanofluorophore system before mechanical activation. The compound can be used as initiator in ATRP and acts as crosslinker, hence the various names.

- **BTD reference / activated BTD**: reference compound for the investigated BTD mechanofluorophore system after mechanical activation.
- **BTD-PHMA network**: A PHMA polymer film crosslinked with BTD crosslinker
- **mechanophore**: any chemical motif that undergoes any kind of reaction upon application of mechanical force
- **mechanofluorophore**: a mechanophore that exhibits a change of optical properties, in particular fluorescence emission, upon application of mechanical force
- microgels **A**: 100% PVCL, 1 w% of total monomer mass BTD crosslinker
- microgels **B**: 80% PVCL, 20 % VIM, 1 w% of total monomer mass BTD crosslinker
- **optical force probe (OFP)**: a mechanofluorophore that reports quantitatively on the mechanical force applied to the system
- **shadow / shaded rectangle**: a highly regular rectangular shape of lower intensity observed in the approximate area of the AFM scan in the FLIM images presented in figure 3.10
- **unactivated BTD**: can refer to the unactivated reference compound (see BTD initiator) or the unactivated mechanofluorophore inside a polymer system
- **unactivated (BTD) microgel**: microgels with BTD crosslinker that have not yet been purposefully activated

8.5.2 Glossary of Chapter 4

- **acceptor**: the chromophore the energy is transferred to via FRET. Not to be confused with reference acceptor **7** (see reference compound). Usually used to denote the ATTO647N chromophore attached to the nitrostyrene or nitroso product of the linker after photocleavage of dyad **8**
- **analyzed time**: time restriction for the fit of the data of a FEDUP measurement. All data at subsequent times is neglected in the fit.
- **bias**: (personal) influence on the analysis lowering the reliability of the results
  - **detection bias**: error in the analysis due to faulty measurement conditions that prevent the correct detection of all valid donor-acceptor pairs
  - **selection bias**: error in the analysis due to misinterpretation of the intensity-time traces of all initially identified donor-acceptor pairs
- **channel**: spectrally separated field of view
  - **donor channel**: excitation at 561 nm, emission between 570 – 633 nm

  - **FRET channel**: excitation at 561 nm, emission above 655 nm
  - **acceptor channel**: excitation at 640 nm, emission above 655 nm

- **crosstalk**: leakage of donor fluorescence in the FRET channel or acceptor channel, acceptor fluorescence in the FRET channel due to direct excitation or generally acceptor fluorescence in the donor channel

- **cycle time**: time between two successive frames recorded with 561 nm excitation. The cycle time is composed of the irradiation times of the green and the red laser (200 – 300 ms), the internal delay between the two irradiation times (200 ms) and the delay time

- **delay time**: time between two excitation cycles when the sample is not irradiated in any way

- **donor**: the (excited) chromophore the energy is transferred from via FRET. Not to be confused with reference donor **6** (see reference compound). Usually used to denote the (free) ATTO565 chromophore after photocleavage of dyad **8**

- **donor-acceptor pair**: any pair of localizations in corresponding areas of donor and FRET channel
  - **initially identified donor-acceptor pair**: any pair of localizations in corresponding areas of donor and FRET channel as identified in step 4 of the analysis (section 4.6.1)
  - **valid donor-acceptor pair / FRET pair / category I pair**: a pair of signals in corresponding areas of donor and FRET channel that has been identified as a cleaved dyad molecule according to the selection criteria in step 7 of the analysis (section 4.6.1)
  - **invalid donor-acceptor pair**: any pair of signals in corresponding areas of donor and FRET channel that has been excluded from the analysis according to the selection criteria in step 7 of the analysis (section 4.6.1)
    * **category II pair**: invalid donor-acceptor pair due to premature photobleaching
    * **category III pair**: invalid donor-acceptor pair due to obscurity of the signals by noise
    * **category IV pair**: invalid donor-acceptor pair due to (often uninterpretable) irregular behavior of the intensity-time traces, that among missing intensity in any of the three channels or intensity in the donor channel at unreasonably early times

- **drift**: concerted uniform movement of all signals in the field of view due to mechanical instability of the measurement setup

- **FRET pair**: a different expression for a valid donor-acceptor pair

- **intensity-time trace**: graphic depiction of the intensities measured in time intervals corresponding to the cycle time in donor, FRET or acceptor channel in a FEDUP measurement
  - **summed-up intensity-time trace / summed-up statistic**: sum of all intensity-time traces of valid donor-acceptor pairs

- **nitroso pathway**: photocleavage of NPPOC that results in a nitroso product (see the mechanism in figure 2.9)

- **nitroso product**: product of the photocleavage of dyad **8** when the reaction proceeds according to the nitroso pathway (see the mechanism in figure 2.9)
- **nitrostyrene product**: product of the photocleavage of dyad **8** when the reaction proceeds according to the styrene pathway (see the mechanism in figure 2.9)
- **pixel**: the smallest square detection unit on a camera
  - **sub-pixel**: a pixel is subdivided with an arbitrary grid into theoretical smaller squares (computational necessity for a better calculation of intensities and background)
- **precursor dyes**: a different name for **ATTO565 NHS ester** and **ATTO647N azide**. Not to be confused with reference compounds.
- **premature photobleaching**: photobleaching of the acceptor occurs before the donor-acceptor pair exhibits measurable intensity in the donor channel
- **reference compound**: a different name for donor **6** and acceptor **7**.
- **relative diffusion**: the average change of relative distances between the donor and acceptor of an individual FRET pair or of an ensemble of FRET pairs
- **reverse FRET**: energy transfer from the expected acceptor to the expected donor
- **spatial correlation**: fluorescence signals are measured in corresponding areas in at least two of the three measurement channels (donor, FRET and acceptor channel)
- **styrene pathway**: photocleavage of NPPOC that results in a nitrostyrene product (see the mechanism in figure 2.9)

9 Bibliography

[1] S. S. Pendhari, T. Kant, Y. M. Desai, "Application of Polymer Composites in Civil Construction: A General Review", *Composite Structures* **2008**, *84*, 114–124, DOI 10.1016/j.compstruct.2007.06.007.

[2] P. Jagadeesh, M. Puttegowda, O. P. Oladijo, C. W. Lai, S. Gorbatyuk, D. Matykiewicz, S. M. Rangappa, S. Siengchin, "A Comprehensive Review on Polymer Composites in Railway Applications", *Polymer Composites* **2022**, *43*, 1238–1251, DOI 10.1002/pc.26478.

[3] V. Siracusa, P. Rocculi, S. Romani, M. D. Rosa, "Biodegradable Polymers for Food Packaging: A Review", *Trends in Food Science & Technology* **2008**, *19*, 634–643, DOI 10.1016/j.tifs.2008.07.003.

[4] I. A. Ignatyev, W. Thielemans, B. Vander Beke, "Recycling of Polymers: A Review", *ChemSusChem* **2014**, *7*, 1579–1593, DOI 10.1002/cssc.201300898.

[5] S. Ramakrishna, J. Mayer, E. Wintermantel, K. W. Leong, "Biomedical Applications of Polymer-Composite Materials: A Review", *Composites Science and Technology* **2001**, *61*, 1189–1224, DOI 10.1016/S0266-3538(00)00241-4.

[6] A. M. E. Arefin, N. R. Khatri, N. Kulkarni, P. F. Egan, "Polymer 3D Printing Review: Materials, Process, and Design Strategies for Medical Applications", *Polymers* **2021**, *13*, 1499, DOI 10.3390/polym13091499.

[7] R. A. Auras, S. P. Singh, J. J. Singh, "Evaluation of Oriented Poly(Lactide) Polymers vs. Existing PET and Oriented PS for Fresh Food Service Containers", *Packaging Technology and Science* **2005**, *18*, 207–216, DOI 10.1002/pts.692.

[8] H. Nishida, "Development of Materials and Technologies for Control of Polymer Recycling", *Polym J* **2011**, *43*, 435–447, DOI 10.1038/pj.2011.16.

[9] M. Hong, E. Y.-X. Chen, "Chemically Recyclable Polymers: A Circular Economy Approach to Sustainability", *Green Chemistry* **2017**, *19*, 3692–3706, DOI 10.1039/C7GC01496A.

[10] B. Salam, G. A. El-Hiti, M. Bufaroosha, D. S. Ahmed, A. Ahmed, M. H. Alotaibi, E. Yousif, "Tin Complexes Containing an Atenolol Moiety as Photostabilizers for Poly(Vinyl Chloride)", *Polymers* **2020**, *12*, 2923, DOI 10.3390/polym12122923.

[11] O. G. Mousa, G. A. El-Hiti, M. A. Baashen, M. Bufaroosha, A. Ahmed, A. A. Ahmed, D. S. Ahmed, E. Yousif, "Synthesis of Carvedilol–Organotin Complexes and Their Effects on Reducing Photodegradation of Poly(Vinyl Chloride)", *Polymers* **2021**, *13*, 500, DOI 10.3390/polym13040500.

[12] J. Kern, Y.-L. Su, W. Gutekunst, R. Ramprasad, "An Informatics Framework for the Design of Sustainable, Chemically Recyclable, Synthetically Accessible, and Durable Polymers", *npj Comput Mater* **2025**, *11*, 182, DOI 10.1038/s41524-025-01683-6.

[13] M. Rubinstein, S. Panyukov, "Elasticity of Polymer Networks", *Macromolecules* **2002**, *35*, 6670–6686, DOI 10.1021/ma0203849.

[14] J. Samuel, S. Sinha, "Elasticity of Semiflexible Polymers", *Phys. Rev. E* **2002**, *66*, 050801, DOI 10.1103/PhysRevE.66.050801.

[15] J. H. Snoeijer, A. Pandey, M. A. Herrada, J. Eggers, "The Relationship between Viscoelasticity and Elasticity", *Proceedings of the Royal Society A: Mathematical Physical and Engineering Sciences* **2020**, *476*, 20200419, DOI 10.1098/rspa.2020.0419.

[16] N. Sakumichi, Y. Yoshikawa, T. Sakai, "Linear Elasticity of Polymer Gels in Terms of Negative Energy Elasticity", *Polym J* **2021**, *53*, 1293–1303, DOI 10.1038/s41428-021-00529-4.

[17] A. Rudawska, "The Impact of the Acidic Environment on the Mechanical Properties of Epoxy Compounds in Different Conditions", *Polymers* **2020**, *12*, 2957, DOI 10.3390/polym12122957.

[18] A. Maléchaux, J. Colombani, S. Amat, S. R. A. Marque, N. Dupuy, "Influence of Gamma Irradiation on Electric Cables Models: Study of Additive Effects by Mid-Infrared Spectroscopy", *Polymers* **2021**, *13*, 1451, DOI 10.3390/polym13091451.

[19] E. Blázquez-Blázquez, J. Lahoz, E. Pérez, M. L. Cerrada, "An Effective Package of Antioxidants for Avoiding Premature Failure in Polypropylene Random Copolymer Plastic Pipes under Hydrostatic Pressure and High Temperature", *Polymers* **2021**, *13*, 2825, DOI 10 . 3390 / polym13162825.

[20] M. Frigione, A. Rodríguez-Prieto, "Can Accelerated Aging Procedures Predict the Long Term Behavior of Polymers Exposed to Different Environments?", *Polymers* **2021**, *13*, 2688, DOI 10.3390/polym13162688.

[21] M. Frigione, "Assessment of the Ageing and Durability of Polymers", *Polymers* **2022**, *14*, 1934, DOI 10.3390/polym14101934.

[22] L. A. Wall, J. H. Flynn, "Degradation of Polymers", *Rubber Chemistry and Technology* **1962**, *35*, 1157–1221, DOI 10.5254/1.3539991.

[23] A. Göpferich in The Biomaterials: Silver Jubilee Compendium, (Ed.: D. F. Williams), Elsevier Science, Oxford, **1996**, pp. 117–128, DOI 10.1016/B978-008045154-1.50016-2.

[24] A. Kulkarni, H. Dasari, "Current Status of Methods Used In Degradation of Polymers: A Review", *MATEC Web Conf.* **2018**, *144*, 02023, DOI 10.1051/matecconf/201814402023.

[25] T. Ishida, R. Kitagaki, "Mathematical Modeling of Outdoor Natural Weathering of Polycarbonate: Regional Characteristics of Degradation Behaviors", *Polymers* **2021**, *13*, 820, DOI 10.3390/polym13050820.

[26] G. Gałko, M. Sajdak, "Trends for the Thermal Degradation of Polymeric Materials: Analysis of Available Techniques, Issues, and Opportunities", *Applied Sciences* **2022**, *12*, 9138, DOI 10.3390/app12189138.

[27] C. Stoffelen, J. Voskuhl, P. Jonkheijm, J. Huskens, "Dual Stimuli-Responsive Self-Assembled Supramolecular Nanoparticles", *Angewandte Chemie International Edition* **2014**, *53*, 3400–3404, DOI 10.1002/anie.201310829.

[28] K. Geisel, L. Isa, W. Richtering, "The Compressibility of pH-Sensitive Microgels at the Oil–Water Interface: Higher Charge Leads to Less Repulsion", *Angewandte Chemie* **2014**, *126*, 5005–5009, DOI 10.1002/ange.201402254.

[29] H. Cui, Z. Chen, S. Zhong, K. L. Wooley, D. J. Pochan, "Block Copolymer Assembly via Kinetic Control", *Science* **2007**, *317*, 647–650, DOI 10.1126/science.1141768.

[30] R. Fenyves, M. Schmutz, I. J. Horner, F. V. Bright, J. Rzayev, "Aqueous Self-Assembly of Giant Bottlebrush Block Copolymer Surfactants as Shape-Tunable Building Blocks", *J. Am. Chem. Soc.* **2014**, *136*, 7762–7770, DOI 10.1021/ja503283r.

[31] P. Sengupta, S. Van Engelenburg, J. Lippincott-Schwartz, "Visualizing Cell Structure and Function with Point-Localization Superresolution Imaging", *Developmental Cell* **2012**, *23*, 1092–1102, DOI 10.1016/j.devcel.2012.09.022.

[32] M. D. Lew, S. F. Lee, J. L. Ptacin, M. K. Lee, R. J. Twieg, L. Shapiro, W. E. Moerner, "Three-Dimensional Superresolution Colocalization of Intracellular Protein Superstructures and the Cell Surface in Live Caulobacter Crescentus", *PNAS* **2011**, *108*, E1102–E1110, DOI 10.1073/pnas.1114444108.

[33] E. Abbe, "Beiträge zur Theorie des Mikroskops und der mikroskopischen Wahrnehmung", *Archiv f. mikrosk. Anatomie* **1873**, *9*, 413–468, DOI 10.1007/BF02956173.

[34] S. W. Hell, J. Wichmann, "Breaking the Diffraction Resolution Limit by Stimulated Emission: Stimulated-Emission-Depletion Fluorescence Microscopy", *Opt. Lett. OL* **1994**, *19*, 780–782, DOI 10.1364/OL.19.000780.

[35] E. Betzig, G. H. Patterson, R. Sougrat, O. W. Lindwasser, S. Olenych, J. S. Bonifacino, M. W. Davidson, J. Lippincott-Schwartz, H. F. Hess, "Imaging Intracellular Fluorescent Proteins at Nanometer Resolution", *Science* **2006**, *313*, 1642–1645, DOI 10.1126/science.1127344.

[36] S. T. Hess, T. P. K. Girirajan, M. D. Mason, "Ultra-High Resolution Imaging by Fluorescence Photoactivation Localization Microscopy", *Biophysical Journal* **2006**, *91*, 4258–4272, DOI 10.1529/biophysj.106.091116.

[37] M. J. Rust, M. Bates, X. Zhuang, "Sub-Diffraction-Limit Imaging by Stochastic Optical Reconstruction Microscopy (STORM)", *Nat Methods* **2006**, *3*, 793–796, DOI 10.1038/nmeth929.

[38] M. Heilemann, S. van de Linde, M. Schüttpelz, R. Kasper, B. Seefeldt, A. Mukherjee, P. Tinnefeld, M. Sauer, "Subdiffraction-Resolution Fluorescence Imaging with Conventional Fluorescent Probes", *Angewandte Chemie International Edition* **2008**, *47*, 6172–6176, DOI 10.1002/anie.200802376.

[39] M. Heilemann, S. van de Linde, A. Mukherjee, M. Sauer, "Super-Resolution Imaging with Small Organic Fluorophores", *Angewandte Chemie International Edition* **2009**, *48*, 6903–6908, DOI 10.1002/anie.200902073.

[40] A. Sharonov, R. M. Hochstrasser, "Wide-Field Subdiffraction Imaging by Accumulated Binding of Diffusing Probes", *PNAS* **2006**, *103*, 18911–18916, DOI 10.1073/pnas.0609643104.

[41] H. Deschout, T. Lukes, A. Sharipov, D. Szlag, L. Feletti, W. Vandenberg, P. Dedecker, J. Hofkens, M. Leutenegger, T. Lasser, A. Radenovic, "Complementarity of PALM and SOFI for Super-Resolution Live-Cell Imaging of Focal Adhesions", *Nat Commun* **2016**, *7*, 13693, DOI 10.1038/ncomms13693.

[42] L. Schubert, C. Nenninger, M. Nöth, T. Belthle, R. D. de Lange, A. Pich, U. Schwaneberg, D. Wöll, "Nanoscopic Visualization of Microgel-Immobilized Cytochrome P450 Enzymes and Their Local Activity", *Nanoscale* **2024**, *16*, 20194–20201, DOI 10.1039/D4NR03435J.

[43] P. Lenßen, R. Hengsbach, A. Frommelius, S. Cammeraat, K. Linssen, U. Simon, D. Wöll, "Nanosized Core–Shell Bio-Hybrid Microgels and Their Internal Structure", *Nanoscale* **2025**, *17*, 4570–4577, DOI 10.1039/D4NR04677C.

[44] J. Maillard, K. Klehs, C. Rumble, E. Vauthey, M. Heilemann, A. Fürstenberg, "Universal Quenching of Common Fluorescent Probes by Water and Alcohols", *Chem. Sci.* **2021**, *12*, 1352–1362, DOI 10.1039/D0SC05431C.

[45] S. Jana, O. Nevskyi, H. Höche, L. Trottenberg, E. Siemes, J. Enderlein, A. Fürstenberg, D. Wöll, "Local Water Content in Polymer Gels Measured with Super-Resolved Fluorescence Lifetime Imaging", *Angewandte Chemie International Edition* **2024**, *63*, e202318421, DOI 10.1002/anie.202318421.

[46] S. Jana, D. Wöll, "Moisture Changes inside Hydrogel Particles during Their Drying Process Investigated with Fluorescence Lifetime Imaging", *Physical Chemistry Chemical Physics* **2024**, *26*, 23250–23255, DOI 10.1039/D4CP02684E.

[47] A. Purohit, S. P. Centeno, S. K. Wypysek, W. Richtering, D. Wöll, "Microgel PAINT – Nanoscopic Polarity Imaging of Adaptive Microgels without Covalent Labelling †Dedicated to Prof. Dr Ulrich E. Steiner (Retired Professor, University of Konstanz) for His 75th Birthday. ‡Electronic Supplementary Information (ESI) Available. See DOI: 10.1039/C9sc03373d", *Chem Sci* **2019**, *10*, 10336–10342, DOI 10.1039/c9sc03373d.

[48] M. Paez-Perez, M. K. Kuimova, "Molecular Rotors: Fluorescent Sensors for Microviscosity and Conformation of Biomolecules", *Angewandte Chemie* **2024**, *136*, e202311233, DOI 10.1002/ange.202311233.

[49] M. Stratigaki, R. Göstl, "Methods for Exerting and Sensing Force in Polymer Materials Using Mechanophores", *ChemPlusChem* **2020**, *85*, 1095–1103, DOI 10.1002/cplu.201900737.

[50] C. Baumann, M. Stratigaki, S. P. Centeno, R. Göstl, "Multicolor Mechanofluorophores for the Quantitative Detection of Covalent Bond Scission in Polymers", *Angewandte Chemie International Edition* **2021**, *60*, 13287–13293, DOI 10.1002/anie.202101716.

[51] K. S. Ngai, S. Ramesh, K. Ramesh, J. C. Juan, "A Review of Polymer Electrolytes: Fundamental, Approaches and Applications", *Ionics* **2016**, *22*, 1259–1279, DOI 10.1007/s11581-016-1756-4.

[52] B. Stempfle, M. Dill, M. J. Winterhalder, K. Müllen, D. Wöll, "Single Molecule Diffusion and Its Heterogeneity during the Bulk Radical Polymerization of Styrene and Methyl Methacrylate", *Polym. Chem.* **2012**, *3*, 2456–2463, DOI 10.1039/C2PY20268A.

[53] H. Geerts, M. D. Brabander, R. Nuydens, S. Geuens, M. Moeremans, J. D. Mey, P. Hollenbeck, "Nanovid Tracking: A New Automatic Method for the Study of Mobility in Living Cells Based on Colloidal Gold and Video Microscopy", *Biophysical Journal* **1987**, *52*, 775–782, DOI 10.1016/S0006-3495(87)83271-X.

[54] T. Schmidt, G. J. Schütz, W. Baumgartner, H. J. Gruber, H. Schindler, "Imaging of Single Molecule Diffusion.", *Proceedings of the National Academy of Sciences* **1996**, *93*, 2926–2929, DOI 10.1073/pnas.93.7.2926.

[55] M. Dill, M. C. Baier, S. Mecking, D. Wöll, "Enhanced Accuracy of Single-Molecule Diffusion Measurements with a Photocleavable Energy-Transfer Dyad", *Angew. Chem. Int. Ed.* **2013**, *52*, 12435–12438, DOI 10.1002/anie.201303658.

[56] K. I. Mortensen, L. S. Churchman, J. A. Spudich, H. Flyvbjerg, "Optimized Localization Analysis for Single-Molecule Tracking and Super-Resolution Microscopy", *Nat Methods* **2010**, *7*, 377–381, DOI 10.1038/nmeth.1447.

[57] X. Michalet, A. J. Berglund, "Optimal Diffusion Coefficient Estimation in Single-Particle Tracking", *Phys. Rev. E* **2012**, *85*, 061916, DOI 10.1103/PhysRevE.85.061916.

[58] J. Enderlein, E. Toprak, P. R. Selvin, "Polarization Effect on Position Accuracy of Fluorophore Localization", *Opt. Express OE* **2006**, *14*, 8111–8120, DOI 10.1364/OE.14.008111.

[59] D. Schöngen, D. Wöll, "Synthesis and Characterization of a Novel Photocleavable Fluorescent Dye Dyad for Diffusion Imaging", *Chemical & Biomedical Imaging* **2025**, *3*, 199–207, DOI 10.1021/cbmi.4c00084.

[60] F. Balzarotti, Y. Eilers, K. C. Gwosch, A. H. Gynnå, V. Westphal, F. D. Stefani, J. Elf, S. W. Hell, "Nanometer Resolution Imaging and Tracking of Fluorescent Molecules with Minimal Photon Fluxes", *Science* **2017**, *355*, 606–612, DOI 10.1126/science.aak9913.

[61] R. Göstl, R. P. Sijbesma, "π-Extended Anthracenes as Sensitive Probes for Mechanical Stress", *Chem. Sci.* **2015**, *7*, 370–375, DOI 10.1039/C5SC03297K.

[62] E. Izak-Nau, D. E. Demco, S. Braun, C. Baumann, A. Pich, R. Göstl, "Shear-Induced Structural and Functional Transformations of Poly(N-vinylcaprolactam) Microgels", *ACS Appl. Polym. Mater.* **2020**, *2*, 1682–1691, DOI 10.1021/acsapm.0c00111.

[63] A. Hasan, K.-P. Stengele, H. Giegrich, P. Cornwell, K. R. Isham, R. A. Sachleben, W. Pfleiderer, R. S. Foote, "Photolabile Protecting Groups for Nucleosides: Synthesis and Photodeprotection Rates", *Tetrahedron* **1997**, *53*, 4247–4264, DOI 10.1016/S0040-4020(97)00154-3.

[64] H. Giegrich, S. Eisele-Bühler, C. Hermann, E. Kvasyuk, R. Charubala, W. Pfleiderer, "New Photolabile Protecting Groups in Nucleoside and Nucleotide Chemistry—Synthesis, Cleavage Mechanisms and Applications", *Nucleos Nucleot* **1998**, *17*, 1987–1996, DOI 10.1080/07328319808004738.

[65] H. Yi, S. Maisonneuve, J. Xie, "Synthesis, Glycosylation and Photolysis of Photolabile 2-(2-Nitrophenyl)Propyloxycarbonyl (NPPOC) Protected Glycopyranosides", *Org. Biomol. Chem.* **2009**, *7*, 3847–3854, DOI 10.1039/B908404E.

[66] J. R. Lakowicz, Principles of Fluorescence Spectroscopy, 3rd ed., Springer Science & Business Media, New York, **2006**.

[67] A. M. Brouwer, "Standards for photoluminescence quantum yield measurements in solution (IUPAC Technical Report)", *Pure and Applied Chemistry* **2011**, *83*, 2213–2228, DOI 10.1351/PAC-REP-10-09-31.

[68] B. Fückel, A. Köhn, M. E. Harding, G. Diezemann, G. Hinze, T. Basché, J. Gauss, "Theoretical Investigation of Electronic Excitation Energy Transfer in Bichromophoric Assemblies", *J. Chem. Phys.* **2008**, *128*, DOI 10.1063/1.2829531.

[69] T. Förster, "Zwischenmolekulare Energiewanderung und Fluoreszenz", *Ann Phys* **1948**, *437*, 55–75, DOI 10.1002/andp.19484370105.

[70] R. M. Clegg, "Fluorescence Resonance Energy Transfer", *Current Opinion in Biotechnology* **1995**, *6*, 103–110, DOI 10.1016/0958-1669(95)80016-6.

[71] L. Stryer, "Fluorescence Energy Transfer as a Spectroscopic Ruler", *Annual Review of Biochemistry* **1978**, *47*, 819–846, DOI 10.1146/annurev.bi.47.070178.004131.

[72] B. Schuler, W. A. Eaton, "Protein Folding Studied by Single-Molecule FRET", *Current Opinion in Structural Biology*, Folding and Binding / Protein-nucleic Acid Interactions **2008**, *18*, 16–26, DOI 10.1016/j.sbi.2007.12.003.

[73] X. Michalet, S. Weiss, M. Jäger, "Single-Molecule Fluorescence Studies of Protein Folding and Conformational Dynamics", *Chem. Rev.* **2006**, *106*, 1785–1813, DOI 10.1021/cr0404343.

[74] A. K. Woźniak, G. F. Schröder, H. Grubmüller, C. A. M. Seidel, F. Oesterhelt, "Single-Molecule FRET Measures Bends and Kinks in DNA", *Proceedings of the National Academy of Sciences* **2008**, *105*, 18337–18342, DOI 10.1073/pnas.0800977105.

[75] X. A. Feng, M. F. Poyton, T. Ha, "Multicolor Single-Molecule FRET for DNA and RNA Processes", *Current Opinion in Structural Biology*, Biophysical Methods **2021**, *70*, 26–33, DOI 10.1016/j.sbi.2021.03.005.

[76] U. Kubitscheck, Fluorescence Microscopy, 2nd ed., Wiley-VCH, Weinheim, **2017**.

[77] M. Sticker, R. Elsässer, M. Neumann, H. Wolff, "How to Get Better Fluorescence Images with Your Widefield Microscope: A Methodology Review", *Micros Today* **2020**, *28*, 36–43, DOI 10.1017/S155192952000156X.

[78] H. Schneckenburger, V. Richter, "Laser Scanning versus Wide-Field—Choosing the Appropriate Microscope in Life Sciences", *Applied Sciences* **2021**, *11*, 733, DOI 10.3390/app11020733.

[79] N. S. Poulter, W. T. E. Pitkeathly, P. J. Smith, J. Z. Rappoport in Advanced Fluorescence Microscopy: Methods and Protocols, (Ed.: P. J. Verveer), Springer, New York, NY, **2015**, pp. 1–23, DOI 10.1007/978-1-4939-2080-8_1.

[80] S. W. Paddock, "Confocal Laser Scanning Microscopy", *BioTechniques* **1999**, *27*, 992–1004, DOI 10.2144/99275ov01.

[81] R. Datta, T. M. Heaster, J. T. Sharick, A. A. Gillette, M. C. Skala, "Fluorescence Lifetime Imaging Microscopy: Fundamentals and Advances in Instrumentation, Analysis, and Applications", *JBO* **2020**, *25*, 071203, DOI 10.1117/1.JBO.25.7.071203.

[82] J. Maillard, C. A. Rumble, A. Fürstenberg, "Red-Emitting Fluorophores as Local Water-Sensing Probes", *J. Phys. Chem. B* **2021**, *125*, 9727–9737, DOI 10.1021/acs.jpcb.1c05773.

[83] S. Strauss, P. C. Nickels, M. T. Strauss, V. Jimenez Sabinina, J. Ellenberg, J. D. Carter, S. Gupta, N. Janjic, R. Jungmann, "Modified Aptamers Enable Quantitative Sub-10-Nm Cellular DNA-PAINT Imaging", *Nat Methods* **2018**, *15*, 685–688, DOI 10.1038/s41592-018-0105-0.

[84] L. Möckl, D. C. Lamb, C. Bräuchle, "Super-Resolved Fluorescence Microscopy: Nobel Prize in Chemistry 2014 for Eric Betzig, Stefan Hell, and William E. Moerner", *Angewandte Chemie International Edition* **2014**, *53*, 13972–13977, DOI 10.1002/anie.201410265.

[85] M. G. L. Gustafsson, "Surpassing the Lateral Resolution Limit by a Factor of Two Using Structured Illumination Microscopy", *Journal of Microscopy* **2000**, *198*, 82–87, DOI 10.1046/j.1365-2818.2000.00710.x.

[86] S. W. Hell, "Far-Field Optical Nanoscopy", *Science* **2007**, *316*, 1153–1158, DOI 10.1126/science.1137395.

[87] S. Hell, S. Jakobs, L. Kastrup, "Imaging and Writing at the Nanoscale with Focused Visible Light through Saturable Optical Transitions", *Appl Phys A* **2003**, *77*, 859–860, DOI 10.1007/s00339-003-2292-4.

[88] R. M. Dickson, A. B. Cubitt, R. Y. Tsien, W. E. Moerner, "On/off Blinking and Switching Behaviour of Single Molecules of Green Fluorescent Protein", *Nature* **1997**, *388*, 355–358, DOI 10.1038/41048.

[89] M. Lakadamyali, H. Babcock, M. Bates, X. Zhuang, J. Lichtman, "3D Multicolor Super-Resolution Imaging Offers Improved Accuracy in Neuron Tracing", *PLOS ONE* **2012**, *7*, e30826, DOI 10.1371/journal.pone.0030826.

[90] C. Shannon, "Communication in the Presence of Noise", *Proceedings of the IRE* **1949**, *37*, 10–21, DOI 10.1109/JRPROC.1949.232969.

[91] G.-e. Go, U. Jeong, H. Park, S. Go, D. Kim, "Photoswitching Reagent for Super-Resolution Fluorescence Microscopy", *Angewandte Chemie International Edition* **2024**, *63*, e202405246, DOI 10.1002/anie.202405246.

[92] Y. Gidi, L. Payne, V. Glembockyte, M. S. Michie, M. J. Schnermann, G. Cosa, "Unifying Mechanism for Thiol-Induced Photoswitching and Photostability of Cyanine Dyes", *J. Am. Chem. Soc.* **2020**, *142*, 12681–12689, DOI 10.1021/jacs.0c03786.

[93] M. N. Bongiovanni, J. Godet, M. H. Horrocks, L. Tosatto, A. R. Carr, D. C. Wirthensohn, R. T. Ranasinghe, J.-E. Lee, A. Ponjavic, J. V. Fritz, C. M. Dobson, D. Klenerman, S. F. Lee, "Multi-Dimensional Super-Resolution Imaging Enables Surface Hydrophobicity Mapping", *Nature Communications* **2016**, *7*, 13544, DOI 10.1038/ncomms13544.

[94] R. Jungmann, C. Steinhauer, M. Scheible, A. Kuzyk, P. Tinnefeld, F. C. Simmel, "Single-Molecule Kinetics and Super-Resolution Microscopy by Fluorescence Imaging of Transient Binding on DNA Origami", *Nano Lett.* **2010**, *10*, 4756–4761, DOI 10 . 1021 / nl103427w.

[95] E. L. Elson, "Fluorescence Correlation Spectroscopy Measures Molecular Transport in Cells", *Traffic* **2001**, *2*, 789–796, DOI 10.1034/j.1600-0854.2001.21107.x.

[96] A. S. Verkman, "Solute and Macromolecule Diffusion in Cellular Aqueous Compartments", *Trends in Biochemical Sciences* **2002**, *27*, 27–33, DOI 10.1016/S0968-0004(01)02003-5.

[97] B. L. Sprague, J. G. McNally, "FRAP Analysis of Binding: Proper and Fitting", *Trends Cell Biol.* **2005**, *15*, 84–91, DOI 10.1016/j.tcb.2004.12.001.

[98] M. J. Saxton, K. Jacobson, "SINGLE-PARTICLE TRACKING:Applications to Membrane Dynamics", *Annu Rev Bioph Biom* **1997**, *26*, 373–399, DOI 10.1146/annurev.biophys.26.1.373.

[99] D. Chetverikov, J. Verestói, "Feature Point Tracking for Incomplete Trajectories", *Computing* **1999**, *62*, 321–338, DOI 10.1007/s006070050027.

[100] D. Sage, F. Neumann, F. Hediger, S. Gasser, M. Unser, "Automatic Tracking of Individual Fluorescence Particles: Application to the Study of Chromosome Dynamics", *IEEE Transactions on Image Processing* **2005**, *14*, 1372–1383, DOI 10.1109/TIP.2005.852787.

[101] K. Jaqaman, D. Loerke, M. Mettlen, H. Kuwata, S. Grinstein, S. L. Schmid, G. Danuser, "Robust Single-Particle Tracking in Live-Cell Time-Lapse Sequences", *Nat Methods* **2008**, *5*, 695–702, DOI 10.1038/nmeth.1237.

[102] D. Ernst, J. Köhler, "Measuring a Diffusion Coefficient by Single-Particle Tracking: Statistical Analysis of Experimental Mean Squared Displacement Curves", *Physical Chemistry Chemical Physics* **2013**, *15*, 845–849, DOI 10.1039/C2CP43433D.

[103] D. Wöll, C. Kölbl, B. Stempfle, A. Karrenbauer, "A Novel Method for Automatic Single Molecule Tracking of Blinking Molecules at Low Intensities", *Physical Chemistry Chemical Physics* **2013**, *15*, 6196–6205, DOI 10.1039/C3CP44693J.

[104] K.-H. Tran-Ba, K. Foreman, "Single-Molecule Tracking of Dye Diffusion in Synthetic Polymers: A Tutorial Review", *J. Appl. Phys.* **2023**, *133*, 101101, DOI 10.1063/5.0139719.

[105] A. N. Kapanidis, T. A. Laurence, N. K. Lee, E. Margeat, X. Kong, S. Weiss, "Alternating-Laser Excitation of Single Molecules", *Acc. Chem. Res.* **2005**, *38*, 523–533, DOI 10.1021/ar0401348.

[106] E. Meyer, "Atomic Force Microscopy", *Progress in Surface Science* **1992**, *41*, 3–49, DOI 10.1016/0079-6816(92)90009-7.

[107] G. Binnig, C. F. Quate, C. Gerber, "Atomic Force Microscope", *Phys. Rev. Lett.* **1986**, *56*, 930–933, DOI 10.1103/PhysRevLett.56.930.

[108] G. Haugstad, Atomic Force Microscopy: Understanding Basic Modes and Advanced Applications, 1st ed., John Wiley & Sons, Inc., Hoboken, New Jersey, **2012**.

[109] M. Schelhaas, H. Waldmann, "Protecting Group Strategies in Organic Synthesis", *Angewandte Chemie International Edition in English* **1996**, *35*, 2056–2083, DOI 10.1002/anie.199620561.

[110] C. G. Bochet, "Chromatic Orthogonality in Organic Synthesis", *Synlett* **2004**, 2268–2274.

[111] D. Wöll, J. Smirnova, M. Galetskaya, T. Prykota, J. Bühler, K.-P. Stengele, W. Pfleiderer, U. E. Steiner, "Intramolecular Sensitization of Photocleavage of the Photolabile 2-(2-Nitrophenyl)Propoxycarbonyl (NPPOC) Protecting Group: Photoproducts and Photokinetics of the Release of Nucleosides", *Chem. Eur. J.* **2008**, *14*, 6490–6497, DOI 10.1002/chem.200800613.

[112] P. O. Brown, D. Botstein, "Exploring the New World of the Genome with DNA Microarrays", *Nat Genet* **1999**, *21*, 33–37, DOI 10.1038/4462.

[113] M. C. Pirrung, L. Wang, M. P. Montague-Smith, "3'-Nitrophenylpropyloxycarbonyl (NPPOC) Protecting Groups for High-Fidelity Automated 5' → 3' Photochemical DNA Synthesis", *Org. Lett.* **2001**, *3*, 1105–1108, DOI 10.1021/ol0069150.

[114] P. Berroy, M. L. Viriot, M. C. Carré, "Photolabile Group for 5*I*-OH Protection of Nucleosides: Synthesis and Photodeprotection Rate", *Sensors and Actuators B: Chemical*, Proceedings of the 5th European Conference on Optical Chemical Sensors and Biosensors **2001**, *74*, 186–189, DOI 10.1016/S0925-4005(00)00731-0.

[115] W. Xi, M. Krieger, C. J. Kloxin, C. N. Bowman, "A New Photoclick Reaction Strategy: Photo-Induced Catalysis of the Thiol-Michael Addition via a Caged Primary Amine", *Chemical Communications* **2013**, *49*, 4504–4506, DOI 10.1039/C3CC41123K.

[116] S. Walbert, W. Pfleiderer, U. E. Steiner, "Photolabile Protecting Groups for Nucleosides: Mechanistic Studies of the 2-(2-Nitrophenyl)Ethyl Group", *Helvetica Chimica Acta* **2001**, *84*, 1601–1611, DOI 10.1002/1522-2675(20010613)84:6<1601::AID-HLCA1601>3.0.CO;2-S.

[117] D. Wöll, S. Laimgruber, M. Galetskaya, J. Smirnova, W. Pfleiderer, B. Heinz, P. Gilch, U. E. Steiner, "On the Mechanism of Intramolecular Sensitization of Photocleavage of the 2-(2-Nitrophenyl)Propoxycarbonyl (NPPOC) Protecting Group", *J. Am. Chem. Soc.* **2007**, *129*, 12148–12158, DOI 10.1021/ja072355p.

[118] D. Wöll, J. Smirnova, W. Pfleiderer, U. E. Steiner, "Highly Efficient Photolabile Protecting Groups with Intramolecular Energy Transfer", *Angew. Chem. Int. Ed.* **2006**, *45*, 2975–2978, DOI 10.1002/anie.200504091.

[119] D. F. Wöll, PhD thesis, Universität Konstanz, **2006**.

[120] D. Feldman, "Polymer History", *Designed Monomers and Polymers* **2008**, *11*, 1–15, DOI 10.1163/156855508X292383.

[121] A. Galeski, "Strength and Toughness of Crystalline Polymer Systems", *Progress in Polymer Science* **2003**, *28*, 1643–1699, DOI 10.1016/j.progpolymsci.2003.09.003.

[122] Y. Yuan, K. Raheja, N. B. Milbrandt, S. Beilharz, S. Tene, S. Oshabaheebwa, U. A. Gurkan, A. C. S. Samia, M. Karayilan, "Thermoresponsive Polymers with LCST Transition: Synthesis, Characterization, and Their Impact on Biomedical Frontiers", *RSC Applied Polymers* **2023**, *1*, 158–189, DOI 10.1039/D3LP00114H.

[123] M. D. Ediger, C. A. Angell, S. R. Nagel, "Supercooled Liquids and Glasses", *J. Phys. Chem.* **1996**, *100*, 13200–13212, DOI 10.1021/jp953538d.

[124] R. Zorn, "Microscopic Dynamics of Glass-Forming Polymers", *J. Phys.: Condens. Matter* **2003**, *15*, R1025, DOI 10.1088/0953-8984/15/23/201.

[125] A. Alegria, E. Guerrica-Echevarria, L. Goitiandia, I. Telleria, J. Colmenero, "α-Relaxation in the Glass Transition Range of Amorphous Polymers. 1. Temperature Behavior across the Glass Transition", *Macromolecules* **1995**, *28*, 1516–1527, DOI 10.1021/ma00109a025.

[126] V. A. Bershtein, V. M. Egorov, Y. A. Emelyanov, V. A. Stepanov, "The Nature of β-Relaxation in Polymers", *Polymer Bulletin* **1983**, *9*, 98–105, DOI 10.1007/BF00275575.

[127] P. Gheysoori, A. Paydayesh, M. Jafari, H. Peidayesh, "Thermoresponsive Nanocomposite Hydrogels Based on Gelatin/Poly (N–Isopropylacrylamide) (PNIPAM) for Controlled Drug Delivery", *European Polymer Journal* **2023**, *186*, 111846, DOI 10.1016/j.eurpolymj.2023.111846.

[128] D. Iohara, M. Okubo, M. Anraku, S. Uramatsu, T. Shimamoto, K. Uekama, F. Hirayama, "Hydrophobically Modified Polymer/α-Cyclodextrin Thermoresponsive Hydrogels for Use in Ocular Drug Delivery", *Mol. Pharmaceutics* **2017**, *14*, 2740–2748, DOI 10.1021/acs.molpharmaceut.7b00291.

[129] K. J. Hogan, A. G. Mikos, "Biodegradable Thermoresponsive Polymers: Applications in Drug Delivery and Tissue Engineering", *Polymer* **2020**, *211*, 123063, DOI 10.1016/j.polymer.2020.123063.

[130] M. Sponchioni, U. Capasso Palmiero, D. Moscatelli, "Thermo-Responsive Polymers: Applications of Smart Materials in Drug Delivery and Tissue Engineering", *Materials Science and Engineering: C* **2019**, *102*, 589–605, DOI 10.1016/j.msec.2019.04.069.

[131] International Union of Pure and Applied Chemistry, "Microgel", *IUPAC Compendium of Chemical Terminology* **2025**, *5*, DOI doi:10.1351/goldbook.M03901.

[132] E. Ponomareva, B. Tadgell, M. Hildebrandt, M. Krüsmann, S. Prévost, P. Mulvaney, M. Karg, "The Fuzzy Sphere Morphology Is Responsible for the Increase in Light Scattering during the Shrinkage of Thermoresponsive Microgels", *Soft Matter* **2022**, *18*, 807–825, DOI 10.1039/D1SM01473K.

[133] B. R. Saunders, N. Laajam, E. Daly, S. Teow, X. Hu, R. Stepto, "Microgels: From Responsive Polymer Colloids to Biomaterials", *Advances in Colloid and Interface Science*, Colloids, Polymers and Surfactants. Special Issue in Honour of Brian Vincent **2009**, *147–148*, 251–262, DOI 10.1016/j.cis.2008.08.008.

[134] K. Kumar, U. Reddicherla, G. M. Rani, V. Pannuru, "How Do Biological Stimuli Modulate Conformational Changes of Biomedical Thermoresponsive Polymer?", *Colloids and Surfaces B: Biointerfaces* **2019**, *178*, 479–487, DOI 10.1016/j.colsurfb.2019.03.014.

[135] P. Rawat, S. Mor, R. Yadav, P. Narang, M. Bisht, P. Venkatesu, "The Hydrophobic Collapse of Thermoresponsive Polymer Poly(N -Vinyl Caprolactam): A New Class of Biocompatible Solvents", *New Journal of Chemistry* **2024**, *48*, 1771–1780, DOI 10.1039/D3NJ04754G.

[136] F. A. Plamper, W. Richtering, "Functional Microgels and Microgel Systems", *Acc. Chem. Res.* **2017**, *50*, 131–140, DOI 10.1021/acs.accounts.6b00544.

[137] S. V. Vinogradov, "Colloidal Microgels in Drug Delivery Applications", *Current Pharmaceutical Design* **2006**, *12*, 4703–4712, DOI 10.2174/138161206779026254.

[138] S. Wiese, A. C. Spiess, W. Richtering, "Microgel-Stabilized Smart Emulsions for Biocatalysis", *Angewandte Chemie* **2013**, *125*, 604–607, DOI 10.1002/ange.201206931.

[139] M. Nöth, E. Gau, F. Jung, M. D. Davari, I. El-Awaad, A. Pich, U. Schwaneberg, "Biocatalytic Microgels (μ-Gelzymes): Synthesis, Concepts, and Emerging Applications", *Green Chem.* **2020**.

[140] Q. Hu, P. S. Katti, Z. Gu, "Enzyme-Responsive Nanomaterials for Controlled Drug Delivery", *Nanoscale* **2014**, *6*, 12273–12286, DOI 10.1039/C4NR04249B.

[141] Y. Jiang, J. Chen, C. Deng, E. J. Suuronen, Z. Zhong, "Click Hydrogels, Microgels and Nanogels: Emerging Platforms for Drug Delivery and Tissue Engineering", *Biomaterials* **2014**, *35*, 4969–4985, DOI 10.1016/j.biomaterials.2014.03.001.

[142] A. Cutivet, C. Schembri, J. Kovensky, K. Haupt, "Molecularly Imprinted Microgels as Enzyme Inhibitors", *J. Am. Chem. Soc.* **2009**, *131*, 14699–14702, DOI 10.1021/ja901600e.

[143] C. Calvino, C. Weder, "Microcapsule-Containing Self-Reporting Polymers", *Small* **2018**, *14*, 1802489, DOI 10.1002/smll.201802489.

[144] J. W. Woodcock, R. J. Sheridan, R. Beams, S. J. Stranick, W. F. Mitchell, L. C. Brinson, V. Gudapati, D. Hartman, A. Vaidya, J. W. Gilman, G. A. Holmes, "Damage Sensing Using a Mechanophore Crosslinked Epoxy Resin in Single-Fiber Composites", *Composites Science and Technology* **2020**, *192*, 108074, DOI 10.1016/j.compscitech.2020.108074.

[145] Y. Sagara, H. Traeger, J. Li, Y. Okado, S. Schrettl, N. Tamaoki, C. Weder, "Mechanically Responsive Luminescent Polymers Based on Supramolecular Cyclophane Mechanophores", *J. Am. Chem. Soc.* **2021**, *143*, 5519–5525, DOI 10.1021/jacs.1c01328.

[146] F. F. C. Dubach, W. G. Ellenbroek, C. Storm, "How Accurately Do Mechanophores Report on Bond Scission in Soft Polymer Materials?", *Journal of Polymer Science* **2021**, *59*, 1188–1199, DOI 10.1002/pol.20210025.

[147] F. Verstraeten, R. Göstl, R. P. Sijbesma, "Stress-Induced Colouration and Crosslinking of Polymeric Materials by Mechanochemical Formation of Triphenylimidazolyl Radicals", *Chem. Commun.* **2016**, *52*, 8608–8611, DOI 10.1039/C6CC04312G.

[148] Z. Shi, Q. Song, R. Göstl, A. Herrmann, "The Mechanochemical Release of Naphthalimide Fluorophores from β-Carbonate and β-Carbamate Disulfide-Centered Polymers", *CCS Chemistry* **2021**, DOI 10.31635/ccschem.021.202101147.

[149] S. He, M. Stratigaki, S. P. Centeno, A. Dreuw, R. Göstl, "Tailoring the Properties of Optical Force Probes for Polymer Mechanochemistry", *Chemistry – A European Journal* **2021**, *27*, 15889–15897, DOI 10.1002/chem.202102938.

[150] D. A. Davis, A. Hamilton, J. Yang, L. D. Cremar, D. Van Gough, S. L. Potisek, M. T. Ong, P. V. Braun, T. J. Martínez, S. R. White, J. S. Moore, N. R. Sottos, "Force-Induced Activation of Covalent Bonds in Mechanoresponsive Polymeric Materials", *Nature* **2009**, *459*, 68–72, DOI 10.1038/nature07970.

[151] J. R. Hemmer, P. D. Smith, M. van Horn, S. Alnemrat, B. P. Mason, J. R. de Alaniz, S. Osswald, J. P. Hooper, "High Strain-Rate Response of Spiropyran Mechanophores in PMMA", *Journal of Polymer Science Part B: Polymer Physics* **2014**, *52*, 1347–1356, DOI 10.1002/polb.23569.

[152] M. Stratigaki, C. Baumann, L. C. A. van Breemen, J. P. A. Heuts, R. P. Sijbesma, R. Göstl, "Fractography of Poly(N -Isopropylacrylamide) Hydrogel Networks Crosslinked with Mechanofluorophores Using Confocal Laser Scanning Microscopy", *Polymer Chemistry* **2020**, *11*, 358–366, DOI 10.1039/C9PY00819E.

[153] J. F. Patrick, M. J. Robb, N. R. Sottos, J. S. Moore, S. R. White, "Polymers with Autonomous Life-Cycle Control", *Nature* **2016**, *540*, 363–370, DOI 10.1038/nature21002.

[154] S. Huo, P. Zhao, Z. Shi, M. Zou, X. Yang, E. Warszawik, M. Loznik, R. Göstl, A. Herrmann, "Mechanochemical Bond Scission for the Activation of Drugs", *Nat. Chem.* **2021**, *13*, 131–139, DOI 10.1038/s41557-020-00624-8.

[155] Y. Chen, A. J. H. Spiering, S. Karthikeyan, G. W. M. Peters, E. W. Meijer, R. P. Sijbesma, "Mechanically Induced Chemiluminescence from Polymers Incorporating a 1,2-Dioxetane Unit in the Main Chain", *Nature Chem* **2012**, *4*, 559–562, DOI 10.1038/nchem.1358.

[156] J. M. Lenhardt, A. L. Black, B. A. Beiermann, B. D. Steinberg, F. Rahman, T. Samborski, J. Elsakr, J. S. Moore, N. R. Sottos, S. L. Craig, "Characterizing the Mechanochemically Active Domains in Gem-Dihalocyclopropanated Polybutadiene under Compression and Tension", *J. Mater. Chem.* **2011**, *21*, 8454–8459, DOI 10.1039/C0JM04117C.

[157] C. M. Kingsbury, P. A. May, D. A. Davis, S. R. White, J. S. Moore, N. R. Sottos, "Shear Activation of Mechanophore-Crosslinked Polymers", *J. Mater. Chem.* **2011**, *21*, 8381–8388, DOI 10.1039/C0JM04015K.

[158] J. Sung, M. J. Robb, S. R. White, J. S. Moore, N. R. Sottos, "Interfacial Mechanophore Activation Using Laser-Induced Stress Waves", *J. Am. Chem. Soc.* **2018**, *140*, 5000–5003, DOI 10.1021/jacs.8b01427.

[159] J. M. Clough, J. van der Gucht, R. P. Sijbesma, "Mechanoluminescent Imaging of Osmotic Stress-Induced Damage in a Glassy Polymer Network", *Macromolecules* **2017**, *50*, 2043–2053, DOI 10.1021/acs.macromol.6b02540.

[160] G. Cravotto, E. C. Gaudino, P. Cintas, "On the Mechanochemical Activation by Ultrasound", *Chem. Soc. Rev.* **2013**, *42*, 7521–7534, DOI 10.1039/C2CS35456J.

[161] A. R. Sulkanen, J. Sung, M. J. Robb, J. S. Moore, N. R. Sottos, G.-y. Liu, "Spatially Selective and Density-Controlled Activation of Interfacial Mechanophores", *J. Am. Chem. Soc.* **2019**, *141*, 4080–4085, DOI 10.1021/jacs.8b10257.

[162] E. Blatt, F. E. Treloar, K. P. Ghiggino, R. G. Gilbert, "Viscosity and Temperature Dependence of Fluorescence Lifetimes of Anthracene and 9-Methylanthracene", *J. Phys. Chem.* **1981**, *85*, 2810–2816, DOI 10.1021/j150619a022.

[163] M. Mitsui, Y. Kawano, R. Takahashi, H. Fukui, "Photophysics and Photostability of 9,10-Bis(Phenylethynyl)Anthracene Revealed by Single-Molecule Spectroscopy", *RSC Advances* **2012**, *2*, 9921–9931, DOI 10.1039/C2RA21100A.

[164] P. S. Mohanty, S. Nöjd, K. van Gruijthuijsen, J. J. Crassous, M. Obiols-Rabasa, R. Schweins, A. Stradner, P. Schurtenberger, "Interpenetration of Polymeric Microgels at Ultrahigh Densities", *Sci Rep* **2017**, *7*, 1487, DOI 10.1038/s41598-017-01471-3.

[165] T. Belthle, D. E. Demco, A. Pich, "Nanostructuring the Interior of Stimuli-Responsive Microgels by N-Vinylimidazoles Quaternized with Hydrophobic Alkyl Chains", *Macromolecules* **2022**, *55*, 844–861, DOI 10.1021/acs.macromol.1c02276.

[166] S. Bhattacharya, F. Eckert, V. Boyko, A. Pich, "Temperature-, pH-, and Magnetic-Field-Sensitive Hybrid Microgels", *Small* **2007**, *3*, 650–657, DOI 10.1002/smll.200600590.

[167] E. Gau, D. M. Mate, Z. Zou, A. Oppermann, A. Töpel, F. Jakob, D. Wöll, U. Schwaneberg, A. Pich, "Sortase-Mediated Surface Functionalization of Stimuli-Responsive Microgels", *Biomacromolecules* **2017**, *18*, 2789–2798, DOI 10.1021/acs.biomac.7b00720.

[168] M. Nöth, L. Hussmann, T. Belthle, I. El-Awaad, M. D. Davari, F. Jakob, A. Pich, U. Schwaneberg, "MicroGelzymes: pH-Independent Immobilization of Cytochrome P450 BM3 in Microgels", *Biomacromolecules* **2020**, DOI 10.1021/acs.biomac.0c01262.

[169] V. V. Klimov, A. K. Shilin, D. A. Kusakovskiy, O. V. Kolyaganova, V. O. Kharlamov, A. V. Rudnev, M. D. Le, E. V. Bryuzgin, A. V. Navrotskii, "Formation of Superhydrophobic Coatings Based on Dispersion Compositions of Hexyl Methacrylate Copolymers with Glycidyl Methacrylate and Silica Nanoparticles", *Polymers* **2024**, *16*, 3094, DOI 10.3390/polym16213094.

[170] M. Worzakowska, "Experimental Studies on the Preparation and Properties of Starch-Graft-Poly(Hexyl Acrylate) Copolymers", *Journal of Applied Polymer Science* **2023**, *140*, e54029, DOI 10.1002/app.54029.

[171] G. Zhu, Q. Zhang, T. Yu, J. Chen, R. Hu, G. Yang, Y. Zeng, Y. Li, "Multiple Force-Triggered Downconverted and Upconverted Emission in Polymers Containing Diels-Alder Adducts", *Chemistry – An Asian Journal* **2024**, *19*, e202301147, DOI 10.1002/asia.202301147.

[172] B. M. I. Flier, M. C. Baier, J. Huber, K. Müllen, S. Mecking, A. Zumbusch, D. Wöll, "Heterogeneous Diffusion in Thin Polymer Films As Observed by High-Temperature Single-Molecule Fluorescence Microscopy", *J. Am. Chem. Soc.* **2012**, *134*, 480–488, DOI 10.1021/ja208581r.

[173] J. J. E. Maris, D. Fu, F. Meirer, B. M. Weckhuysen, "Single-Molecule Observation of Diffusion and Catalysis in Nanoporous Solids", *Adsorption* **2021**, *27*, 423–452, DOI 10.1007/s10450-020-00292-7.

[174] G. Pagès, V. Gilard, R. Martino, M. Malet-Martino, "Pulsed-Field Gradient Nuclear Magnetic Resonance Measurements (PFG NMR) for Diffusion Ordered Spectroscopy (DOSY) Mapping", *Analyst* **2017**, *142*, 3771–3796, DOI 10.1039/C7AN01031A.

[175] J. Kärger, D. Freude, J. Haase, "Diffusion in Nanoporous Materials: Novel Insights by Combining MAS and PFG NMR", *Processes* **2018**, *6*, 147, DOI 10.3390/pr6090147.

[176] M. Wachsmuth, "Molecular Diffusion and Binding Analyzed with FRAP", *Protoplasma* **2014**, *251*, 373–382, DOI 10.1007/s00709-013-0604-x.

[177] H. C. Ishikawa-Ankerhold, R. Ankerhold, G. P. C. Drummen, "Advanced Fluorescence Microscopy Techniques—FRAP, FLIP, FLAP, FRET and FLIM", *Molecules* **2012**, *17*, 4047–4132, DOI 10.3390/molecules17044047.

[178] A. Gupta, J. Sankaran, T. Wohland, "Fluorescence Correlation Spectroscopy: The Technique and Its Applications in Soft Matter", *Physical Sciences Reviews* **2019**, *4*, DOI 10.1515/psr-2017-0104.

[179] M. Kinjo, R. Rigler, "Ultrasensitive Hybridization Analysis Using Fluorescence Correlation Spectroscopy", *Nucleic Acids Res* **1995**, *23*, 1795–1799, DOI 10.1093/nar/23.10.1795.

[180] H. Shen, L. J. Tauzin, R. Baiyasi, W. Wang, N. Moringo, B. Shuang, C. F. Landes, "Single Particle Tracking: From Theory to Biophysical Applications", *Chem. Rev.* **2017**, *117*, 7331–7376, DOI 10.1021/acs.chemrev.6b00815.

[181] D. Wöll, E. Braeken, A. Deres, F. C. D. Schryver, H. Uji-i, J. Hofkens, "Polymers and Single Molecule Fluorescence Spectroscopy, What Can We Learn?", *Chem. Soc. Rev.* **2009**, *38*, 313–328, DOI 10.1039/B704319H.

[182] H. Zou, S. Li, X. Kou, Z. Gu, J. Wang, "The advantage of MINFLUX nanoscopy in single molecular tracking within living cells.", *Journal of Innovative Optical Health Sciences* **2025**, *18*, 1, DOI 10.1142/S1793545825300083.

[183] L. Yao, D. Si, L. Chen, S. Li, J. Guan, Q. Zhang, J. Wang, J. Ma, L. Wang, M. Gu, "Gradual Labeling with Fluorogenic Probes: A General Method for MINFLUX Imaging and Tracking", *Science Advances* **2025**, *11*, eadv5971, DOI 10.1126/sciadv.adv5971.

[184] R. Schmidt, T. Weihs, C. A. Wurm, I. Jansen, J. Rehman, S. J. Sahl, S. W. Hell, "MINFLUX Nanometer-Scale 3D Imaging and Microsecond-Range Tracking on a Common Fluorescence Microscope", *Nat Commun* **2021**, *12*, 1478, DOI 10.1038/s41467-021-21652-z.

[185] B. T. L. Vogler, G. De Angelis, Z. Zhao, C. Eggeling, F. Reina, "Parameter Optimization for MINFLUX Microscopy Enabled Single Particle Tracking", *Commun Biol* **2025**, *8*, 1573, DOI 10.1038/s42003-025-09060-1.

[186] L. W. Fitzpatrick, L. Woythe, Z. Huang, S. Schnorrenberg, T. Zimmermann, L. Albertazzi, "MINFLUX: μs and Nm Precision 3D Tracking of Dynamic Lipid Mobility on Nanoparticles", *Nanoscale* **2025**, *17*, 16609–16615, DOI 10.1039/D5NR00948K.

[187] J. D. Rickert, M. O. Held, J. Engelhardt, S. W. Hell, "4Pi MINFLUX Arrangement Maximizes Spatio-Temporal Localization Precision of Fluorescence Emitter", *Proceedings of the National Academy of Sciences* **2024**, *121*, e2318870121, DOI 10.1073/pnas.2318870121.

[188] J. O. Wirth, L. Scheiderer, T. Engelhardt, J. Engelhardt, J. Matthias, S. W. Hell, "MINFLUX Dissects the Unimpeded Walking of Kinesin-1", *Science* **2023**, *379*, 1004–1010, DOI 10.1126/science.ade2650.

[189] Y. Eilers, H. Ta, K. C. Gwosch, F. Balzarotti, S. W. Hell, "MINFLUX Monitors Rapid Molecular Jumps with Superior Spatiotemporal Resolution", *Proceedings of the National Academy of Sciences* **2018**, *115*, 6117–6122, DOI 10.1073/pnas.1801672115.

[190] J. Rocha, J. Corbitt, T. Yan, C. Richardson, A. Gahlmann, "Resolving Cytosolic Diffusive States in Bacteria by Single-Molecule Tracking", *Biophysical Journal* **2019**, *116*, 1970–1983, DOI 10.1016/j.bpj.2019.03.039.

[191] T. Yoshida, N. Matsuura, K. Yamamoto, M. Doi, K. Shimada, T. Morie, S. Kato, "Practical Synthesis of 1H-indazole-3-carboxylic Acid and Its Derivatives", *Heterocycles* **1996**, *12*, 2701–2712.

[192] J. Smirnova, D. Wöll, W. Pfleiderer, U. E. Steiner, "Synthesis of Caged Nucleosides with Photoremovable Protecting Groups Linked to Intramolecular Antennae", *Helv. Chim. Acta* **2005**, *88*, 891–904, DOI 10.1002/hlca.200590067.

[193] K. R. Bhushan, C. DeLisi, R. A. Laursen, "Synthesis of Photolabile 2-(2-Nitrophenyl)Propyloxycarbonyl Protected Amino Acids", *Tetrahedron Lett* **2003**, *44*, 8585–8588, DOI 10.1016/j.tetlet.2003.09.155.

[194] F. S. Gibson, S. C. Bergmeier, H. Rapoport, "Selective Removal of an N-BOC Protecting Group in the Presence of a Tert-Butyl Ester and Other Acid-Sensitive Groups", *J. Org. Chem.* **1994**, *59*, 3216–3218, DOI 10.1021/jo00090a045.

[195] K. Mutai, "Intramolecular Fluorescence Quenching Effect by P-Nitrophenyl and p-Nitrophenoxy Groups", *bull. Chem. Soc. Jpn.* **1971**, *44*, 2537–2541, DOI 10.1246/bcsj.44.2537.

[196] A. Pandith, A. Kumar, H. S. Kim, "Imidazole-Appended 9,10-Anthracenedicarboxamide Probe for Sensing Nitrophenols and Selective Determination of 2,4,6-Trinitrophenol in an EtOH–Water Medium", *RSC Adv.* **2016**, *6*, 68627–68637, DOI 10.1039/C6RA17407H.

[197] D. Beaudoin, J. D. Wuest, "Dimerization of Aromatic C-Nitroso Compounds", *Chem. Rev.* **2016**, *116*, 258–286, DOI 10.1021/cr500520s.

[198] E. Hadjoudis, A. Tsoka, "A Flash Photolytic Study of O-Nitrosotoluene", *J. Photochem.* **1978**, *8*, 233–238, DOI 10.1016/0047-2670(78)80024-0.

[199] A. N. Adhikari, N. A. Capurso, D. Bingemann, "Heterogeneous Dynamics and Dynamic Heterogeneities at the Glass Transition Probed with Single Molecule Spectroscopy", *The Journal of Chemical Physics* **2007**, *127*, 114508, DOI 10.1063/1.2768955.

[200] S. Saito, T. Nakajima, "Glass Transition in Polymers", *Journal of Applied Polymer Science* **1959**, *2*, 93–99, DOI 10.1002/app.1959.070020414.

[201] M. Ovesný, P. Křížek, J. Borkovec, Z. Švindrych, G. M. Hagen, "ThunderSTORM: A Comprehensive ImageJ Plug-in for PALM and STORM Data Analysis and Super-Resolution Imaging", *Bioinformatics* **2014**, *30*, 2389–2390, DOI 10.1093/bioinformatics/btu202.

[202] H. Lin, B. D. Freeman, "Gas Solubility, Diffusivity and Permeability in Poly(Ethylene Oxide)", *Journal of Membrane Science*, Special Issue in Honor of Dr. Ora Kedem **2004**, *239*, 105–117, DOI 10.1016/j.memsci.2003.08.031.

[203] M. A. Semsarzadeh, B. Ghalei, "Characterization and Gas Permeability of Polyurethane and Polyvinyl Acetate Blend Membranes with Polyethylene Oxide–Polypropylene Oxide Block Copolymer", *Journal of Membrane Science* **2012**, *401–402*, 97–108, DOI 10.1016/j.memsci.2012.01.035.

[204] M. Dill, "Synthese, Charakterisierung und Anwendungen photospaltbarer Fluoreszenzfarbstoff-Dyaden mit intramolekularer Energieübertragung", *Dissertation*, Universität Konstanz **2014**.

[205] K. Kolter, A. Dashevsky, M. Irfan, R. Bodmeier, "Polyvinyl Acetate-Based Film Coatings", *International Journal of Pharmaceutics*, Progress in Film Coating **2013**, *457*, 470–479, DOI 10.1016/j.ijpharm.2013.08.077.

[206] M. Novak, B. Ormsby, "Poly(Vinyl Acetate) Paints: A Literature Review of Material Properties, Ageing Characteristics, and Conservation Challenges", *Polymers* **2023**, *15*, 4348, DOI 10.3390/polym15224348.

[207] E. S. Marín Cardona, J. J. Rojas Camargo, Y. A. Ciro Monsalve, "A Review of Polyvinyl Alcohol Derivatives : Promising Materials for Pharmaceutical & Biomedical Applications", **2014**.

[208] P. Meares, "The Diffusion of Gases Through Polyvinyl Acetate1", *J. Am. Chem. Soc.* **1954**, *76*, 3415–3422, DOI 10.1021/ja01642a015.

[209] R. J. Kokes, F. A. Long, "Diffusion of Organic Vapors into Polyvinyl Acetate", *J. Am. Chem. Soc.* **1953**, *75*, 6142–6146, DOI 10.1021/ja01120a011.

[210] P. Meares, "The Diffusion of Gases in Polyvinyl Acetate in Relation to the Second-Order Transition", *Trans. Faraday Soc.* **1957**, *53*, 101–106, DOI 10.1039/TF9575300101.

[211] P. Meares, "Diffusion of Allyl Chloride in Polyvinyl Acetate. Part I. The Steady State of Permeation", *Journal of Polymer Science* **1958**, *27*, 391–404, DOI 10 . 1002 / pol . 1958 . 1202711530.

[212] T. P. Lodge, J. A. Lee, T. S. Frick, "Probe Diffusion in Poly (Vinyl Acetate) / Toluene Solutions", *Journal of Polymer Science Part B: Polymer Physics* **1990**, *28*, 2607–2627, DOI 10.1002/polb.1990.090281310.

[213] S. A. Willis, G. R. Dennis, G. Zheng, W. S. Price, "Hydrodynamic Size and Scaling Relations for Linear and 4 Arm Star PVAc Studied Using PGSE NMR", *Journal of Molecular Liquids*, Transport Processes in Molecular Liquids-Special Issue in Honour of Prof. Victor Lobo on the Occasion of His 70th Birthday **2010**, *156*, 45–51, DOI 10.1016/j.molliq.2010.04.026.

[214] J. S. Royal, J. M. Torkelson, J. M. Torkelson, "Molecular-Scale Asymmetry and Memory Behavior in Poly(Vinyl Acetate) Monitored with Mobility-Sensitive Fluorescent Molecules", *Macromolecules* **1992**, *25*, 1705–1710, DOI 10.1021/ma00032a013.

[215] D. D. Deppe, A. Dhinojwala, J. M. Torkelson, "Small Molecule Probe Diffusion in Thin Polymer Films Near the Glass Transition: A Novel Approach Using Fluorescence Nonradiative Energy Transfer", *Macromolecules* **1996**, *29*, 3898–3908, DOI 10.1021/ma960024j.

[216] D. Champion, M. Le Meste, D. Simatos, "Towards an Improved Understanding of Glass Transition and Relaxations in Foods: Molecular Mobility in the Glass Transition Range", *Trends in Food Science & Technology* **2000**, *11*, 41–55, DOI 10.1016/S0924-2244(00)00047-9.

[217] D. Ehlich, H. Sillescu, "Tracer Diffusion at the Glass Transition", *Macromolecules* **1990**, *23*, 1600–1610, DOI 10.1021/ma00208a008.

[218] Y. Liu, J. C. Haley, K. Deng, W. Lau, M. A. Winnik, "Synthesis of Branched Poly(Butyl Methacrylate) via Semicontinuous Emulsion Polymerization", *Macromolecules* **2008**, *41*, 4220–4225, DOI 10.1021/ma800215m.

[219] O. A. Mohamed, A. B. Moustafa, M. A. Mehawed, N. H. El-Sayed, "Styrene and Butyl Methacrylate Copolymers and Their Application in Leather Finishing", *Journal of Applied Polymer Science* **2009**, *111*, 1488–1495, DOI 10.1002/app.29022.

[220] K. Suhailath, M. T. Ramesan, B. Naufal, P. Periyat, V. C. Jasna, P. Jayakrishnan, "Synthesis, Characterisation and Flame, Thermal and Electrical Properties of Poly (n-Butyl Methacrylate)/Titanium Dioxide Nanocomposites", *Polym. Bull.* **2017**, *74*, 671–688, DOI 10.1007/s00289-016-1737-9.

[221] s. A. Gaballa, Y. Naguib, F. M. Mady, K. A. Khaled, "Polyethylene Glycol: Properties, Applications, and Challenges", *Journal of Advanced Biomedical and Pharmaceutical Sciences* **2024**, DOI 10.21608/jabps.2023.241685.1205.

[222] S. Bistac, M. Brogly, D. Bindel, "Crystallinity of Amphiphilic PE-b-PEG Copolymers", *Polymers* **2022**, *14*, 3639, DOI 10.3390/polym14173639.

[223] S. Zalipsky, J. M. Harris in Poly(Ethylene Glycol), ACS Symposium Series, American Chemical Society, **1997**, Chapter 1, pp. 1–13, DOI 10.1021/bk-1997-0680.ch001.

[224] M. M. Hoffmann, J. D. Kealy, T. Gutmann, G. Buntkowsky, "Densities, Viscosities, and Self-Diffusion Coefficients of Several Polyethylene Glycols", *J. Chem. Eng. Data* **2022**, *67*, 88–103, DOI 10.1021/acs.jced.1c00759.

[225] K.-H. Tran-Ba, R. E. Willis, K. Foreman, K. Ajmani, P. Gujarati, "Single-Molecule Tracking in Poly(Ethylene Oxide) Films: Revealing the Effects of Molecular Weight, Network Plasticization, and Thermal Annealing on Anionic Dye Diffusion", *J. Phys. Chem. B* **2021**, *125*, 382–392, DOI 10.1021/acs.jpcb.0c08122.

[226] T. D. Roberts, R. Yuan, L. Xiang, M. Delor, R. Pokhrel, K. Yang, E. Aqad, T. Marangoni, P. Trefonas, K. Xu, N. S. Ginsberg, "Direct Correlation of Single-Particle Motion to Amorphous Microstructural Components of Semicrystalline Poly(Ethylene Oxide) Electrolytic Films", *J. Phys. Chem. Lett.* **2020**, *11*, 4849–4858, DOI 10.1021/acs.jpclett.0c01318.

[227] M. J. Skaug, J. N. Mabry, D. K. Schwartz, "Single-Molecule Tracking of Polymer Surface Diffusion", *J. Am. Chem. Soc.* **2014**, *136*, 1327–1332, DOI 10.1021/ja407396v.

[228] S. A. Sukhishvili, Y. Chen, J. D. Müller, E. Gratton, K. S. Schweizer, S. Granick, "Surface Diffusion of Poly(Ethylene Glycol)", *Macromolecules* **2002**, *35*, 1776–1784, DOI 10.1021/ma0113529.

[229] L. Katsikas, K. Jeremic, S. Jovanovic, J. Velickovic, I. Popovic, "The Thermal Degradation Kinetics of Dextran and Pullulan", *Journal of Thermal Analysis and Calorimetry* **2007**, *40*, 511–517, DOI 10.1007/bf02546620.

[230] J. G. Ritter, R. Veith, A. Veenendaal, J. P. Siebrasse, U. Kubitscheck, "Light Sheet Microscopy for Single Molecule Tracking in Living Tissue", *PLoS One* **2010**, *5*, e11639, DOI 10.1371/journal.pone.0011639.

[231] R. Borsali, R. Pecora, Soft-Matter Characterization, Springer Science & Business Media, **2008**.

[232] S. Bienz, L. Bigler, T. Fox, H. Meier, Spektroskopische Methoden in Der Organischen Chemie, 9., Thieme, Stuttgard, **2016**.

[233] A. H. Ali, "High-Performance Liquid Chromatography (HPLC): A Review", *Ann. Adv. Chem* **2022**, *6*, 10–20, DOI 10.29328/journal.aac.1001026.

[234] C. Schick, "Differential Scanning Calorimetry (DSC) of Semicrystalline Polymers", *Anal Bioanal Chem* **2009**, *395*, 1589–1611, DOI 10.1007/s00216-009-3169-y.

[235] D. Wöll, E. Braeken, A. Deres, F. C. D. Schryver, H. Uji-i, J. Hofkens, "Polymers and Single Molecule Fluorescence Spectroscopy , What Can We Learn?", *Chemical Society Reviews* **2009**, *38*, 313–328, DOI 10.1039/B704319H.

[236] U. Megerle, R. Lechner, B. König, E. Riedle, "Laboratory Apparatus for the Accurate, Facile and Rapid Determination of Visible Light Photoreaction Quantum Yields", *Photochem Photobiol Sci* **2010**, *9*, 1400–1406, DOI 10.1039/c0pp00195c.

[237] M. E. Beheiry, M. Dahan, "ViSP: Representing Single-Particle Localizations in Three Dimensions", *Nature Methods* **2013**, *10*, 689–690, DOI 10.1038/nmeth.2566.